Connection of Thermodynamics, Kinetics, Mechanics and Structure in a model Pt-Pd-metallic glass-forming System

Dissertation

zur Erlangung des Grades

des Doktors der Ingenieurswissenschaften

der Naturwissenschaftlich-Technischen Fakultät

der Universität des Saarlandes

von

Nico Neuber

Saarbrücken

2024

Tag des Kolloquiums: 22.08.2025

Dekan: Prof. Dr.-Ing. Dirk Bähre

Berichterstatter: Prof. Dr. Ralf Busch

Prof. Dr.-Ing. Frank Mücklich

Prof. Dr. Jörg F. Löffler

Akad. Mitglied: Dr.-Ing. Oliver Maurer

Vorsitz: Prof. Dr. mont. Christian Motz

Abstract

Bulk metallic glasses have long been considered a pipe dream in solid state physics, as metallic liquids, when cooled below their liquidus temperature, show an extremely high tendency towards crystallization. To engineer bulk metallic glasses, in-depth metallurgic knowledge was needed to find the correct interplay of sluggish crystallization kinetics, accompanied with slow atomic mobility in the melt and a low thermodynamic driving force to form a crystal. One system that fulfils these criteria is the noble metal based Pd-Cu-Ni-P, as well as its compositionally similar Pt-Cu-Ni-P system. In this work the main thermophysical properties that enable the glass-formation in these systems are evaluated regarding kinetic, dynamic and thermodynamic properties. On the base of this data, high-energy X-rays are utilized to study the microscopic structure and its thermal evolution. The work revealed direct connections between these thermophysical properties and the thermally induced changes of the structure. Further, the connection of different structural units to mechanical and thermodynamic properties is suggested and experimentally underlined contributing to the understanding of the embrittlement mechanism of metallic glasses. Further progress in fundamental research was made in the field of atomic dynamics. We report first experimental evidence of a dynamic slow-down in a metallic liquid at wave-vectors corresponding to a spacing larger than the average interatomic distance.

Zusammenfassung

Metallische Massivgläser wurden in der Festkörperphysik lange Zeit für einen unerfüllbaren Traum gehalten, da Metallschmelzen, wenn sie unter ihre Liquidustemperatur gekühlt werden eine hohe Kristallisationsneigung haben. Um metallische Massivgläser herzustellen ist tiefgehendes metallurgisches Wissen vonnöten, um ein Legierungssystem mit dem richtigen Zusammenspiel aus langsamer Kristallisationskinetik und einer geringen thermodynamischen Triebkraft zur Kristallisation zu finden. Ein System, das dies erfüllt ist das Pt/Pd-Cu-Ni-P-System. Im Rahmen dieser Arbeit werden die wichtigsten thermophysikalischen Charakteristika, die die Glasbildung in diesen Systemen ermöglichen, hinsichtlich kinetischer, dynamischer und thermodynamischer Eigenschaften bewertet. Zwischen diesen thermophysikalischen Eigenschaften wurden direkte Abhängigkeiten zu den thermisch bedingten Veränderungen der vorliegenden Struktur gezeigt. Darüber hinaus wurde ein Zusammenhang von unterschiedlichen Struktureinheiten mit den mechanischen und thermodynamischen Eigenschaften erarbeitet und experimentell untermauert, was grundlegend zum Verständnis des Versprödungsmechanismus von metallischen Gläsern beiträgt. Weitere Fortschritte in der Grundlagenforschung wurden im Bereich der atomaren Dynamik erzielt. Erstmals wurde eine verlangsamte Dynamik bei Wellenvektoren, welche einem größeren Abstand als dem mittleren interatomaren Abstand entsprechen, in metallischer Flüssigkeit experimentell nachgewiesen.

Acknowledgement

First of all, I would like to express my sincere gratitude to my supervisor, Prof. Dr. Ralf Busch, for sharing his expertise on metallic glasses and liquids and giving me the opportunity to write my dissertation at his chair of metallic materials in Saarbrücken. Many facets of this work reflect the results of many fruitful discussions with him on thermodynamics, structure and fragility in metallic systems. Likewise, I want to deeply thank Dr. Oliver Gross for his excellent support, as well as his expertise and pre-work on the topic of noble metal based metallic glasses, which laid the foundation of all the following work. His ongoing input during the last years has been invaluable for the creation of the numerous mutual publications.

Accordingly, I want to thank the whole chair of metallic materials with its senior researchers, Dr. Isabella Gallino and Dr. Frank Aubertin, as well as my fellow PhD students Maximilian Frey, Bastian Adam, Lucas Ruschel, Benedikt Bochtler, Alexander Kuball, Simon Hechler, Haoran Jiang and Sascha Riegler that provided fruitful discussions concerning experimental settings as well as interpretation of data. Especially the countless hours and measurements at the synchrotron and neutron facilities would have not been the same without you. At this point I also want to praise the technical support by Jörg Eiden and Hermann Altmeyer, who always helped reliably and fast solving technical problems with the machines and equipment and supporting the construction of numerous casting molds. I also want to thank our metallographer Martina Stemmler for taking care of XRD and SEM measurements. Likewise the administrative support through our secretaries Sigrid Neusius and later Alexandra Hirth need to be mentioned thankfully, too.

Along with this a special section is needed to account for all the external project partners that helped tremendously at synchrotron and neutron source research facilities.

Regarding the external partners I would like to thank Dr. Beatrice Ruta for her outstanding support, particularly in the field of X-ray photon correlation spectroscopy, but in general in terms of introducing me into the world of science. Without her expertise and motivation, the detailed works on the microscopic dynamics would not have been possible.

Furthermore, I want to thank Dr. Fan Yang, a project partner from the DLR cologne within a DFG project and several beam-times. His expertise on metallic liquids and their thermophysical behavior regarding X-ray and neutron radiation experiments frequently provided new insights and a deeper understanding of the topic during our numerous discussions. Without his expertise on levitation techniques the realization of several synchrotron experiments would not have been possible. In this context also Dr. Eloi Pineda has to be mentioned, who spent many beamtimes with me and has contributed to my works through his expertise on dynamics and disordered systems through long and motivating discussions.

Additionally, the partners from the FEM Schwäbisch Gmünd have to be mentioned for the fruitful collaborations in the framework of several AiF projects. Namely, I want to thank Dr. Ulrich Klotz, Dr. Miriam Eisenbart and Lisa-Yvonn Schmitt for their time and expertise in the wide field of noble metals and their applications.

Moreover, I want to deeply thank those people who enabled me to study at the university by teaching me so well in various natural sciences at my prior school, Max-Planck-Gymnasium. Numerous teachers provided knowledge and were always motivational to move towards a scientific career. In particular I would like to thank and mention Thomas Klein, Benjamin Brück, Michael Grittmann, Inge Plitzko-Schels and Willi Göbel, whose words came back to me more than once during my pursuit of my doctorate, as they did provide me the basic tools that are so important in science.

Also I want to thank all of my personal friends and whole family, who supported me throughout my academic life, particularly over the last years here in Saarbrücken at the Saarland University.

Last but not least I want to express my deepest gratitude to my beloved partner Victoria, who has always had my back and supported me no matter what. Thank you for always strengthening me in doing the right thing and making me a better person.

Contributions and Publications

In the framework of his dissertation and his time working at the Chair of Metallic Materials Nico Neuber contributed to the following articles:

[1]   N. Neuber*, O. Gross, M. Frey, B. Bochtler, A. Kuball, S. Hechler, F. Yang, E. Pineda, F. Westermeier, M. Sprung, F. Schäfer, I. Gallino, R. Busch, B. Ruta, Disentangling structural and kinetic components of the α-relaxation in supercooled metallic liquids, Commun. Phys. 5 (2022) 316. https://doi.org/10.1038/s42005-022-01099-4.

[2]   N. Neuber*, M. Sadeghilaridjani, N. Ghodki, O. Gross, B. Adam, L. Ruschel, M. Frey, S. Muskeri, M. Blankenburg, I. Gallino, R. Busch, S. Mukherjee, Effect of composition and thermal history on deformation behavior and cluster connections in model bulk metallic glasses, Sci. Rep. 12 (2022) 17133. https://doi.org/10.1038/s41598-022-20938-6.

[3]   N. Neuber*, O. Gross, M. Frey, B. Bochtler, A. Kuball, S. Hechler, I. Gallino, R. Busch, On the thermodynamics and its connection to structure in the Pt-Pd-Cu-Ni-P bulk metallic glass forming system, Acta Mater. 220 (2021) 117300. https://doi.org/10.1016/j.actamat.2021.117300.

[4]   N. Neuber*, O. Gross, M. Eisenbart, A. Heiss, U.E. Klotz, J.P. Best, M.N. Polyakov, J. Michler, R. Busch, I. Gallino, The role of Ga addition on the thermodynamics, kinetics, and tarnishing properties of the Au-Ag-Pd-Cu-Si bulk metallic glass forming system, Acta Mater. 165 (2019) 315–326. https://doi.org/10.1016/j.actamat.2018.11.052.

[5]   N. Neuber*, M. Frey, O. Gross, J. Baller, I. Gallino, R. Busch, Ultrafast scanning calorimetry of newly developed Au-Ga bulk metallic glasses, J. Phys. Condens. Matter. 32 (2020) 324001. https://doi.org/10.1088/1361-648X/ab8252.

[6]   O. Gross*, N. Neuber, A. Kuball, B. Bochtler, S. Hechler, M. Frey, R. Busch, Signatures of structural differences in Pt–P- and Pd–P-based bulk glass-forming liquids, Commun. Phys. 2 (2019). https://doi.org/10.1038/s42005-019-0180-2.

[7]   H. Voigt*, N. Neuber, O. Vaerst, M. Demming, R. Busch, M. Peterlechner, H. Rösner, G. Wilde, Differences in structure and dynamics of ternary Pd–Ni-based bulk metallic glasses

containing sulfur or phosphorous, Acta Mater. 264 (2024) 119574. https://doi.org/10.1016/j.actamat.2023.119574.

[8]   M. Frey*, N. Neuber, M. Müller, O. Gross, S.S.S. Riegler, I. Gallino, R. Busch, Determining and modelling a complete time-temperature-transformation diagram for a Pt-based metallic glass former through combination of conventional and fast scanning calorimetry, Scr. Mater. 215 (2022) 114710. https://doi.org/10.1016/j.scriptamat.2022.114710.

[9]   M. Frey*, N. Neuber, O. Gross, B. Zimmer, W. Possart, R. Busch, Determining the fragility of bulk metallic glass forming liquids via modulated DSC, J. Phys. Condens. Matter. 32 (2020) 324004. https://doi.org/10.1088/1361-648X/ab8526.

[10]   L.Y. Schmitt*, N. Neuber, M. Eisenbart, L. Cifci, O. Gross, U.E. Klotz, R. Busch, Study on technical parameters and suitability of Pt-based metallic glasses for jewellery applications, Johnson Matthey Technol. Rev. 44 (2022) 1–33. https://doi.org/10.1595/205651323x16577027080875.

[11]   B. Ruta*, S. Hechler, N. Neuber, D. Orsi, L. Cristofolini, O. Gross, B. Bochtler, M. Frey, A. Kuball, S.S. Riegler, M. Stolpe, Z. Evenson, C. Gutt, F. Westermeier, R. Busch, I. Gallino, Wave-Vector Dependence of the Dynamics in Supercooled Metallic Liquids, Phys. Rev. Lett. 125 (2020) 055701. https://doi.org/10.1103/PhysRevLett.125.055701.

[12]   V. Di Lisio, I. Gallino*, S.S. Riegler, M. Frey, N. Neuber, G. Kumar, J. Schroers, R. Busch, D. Cangialosi*, Size-dependent vitrification in metallic glasses, Nat. Commun. 14 (2023) 4698. https://doi.org/10.1038/s41467-023-40417-4.

[13]   C. Mahajan, V. Hasannaeimi, N. Neuber, X. Wang, R. Busch, I. Gallino, S. Mukherjee*, Model Metallic Glasses for Superior Electrocatalytic Performance in a Hydrogen Oxidation Reaction, ACS Appl. Mater. Interfaces. 15 (2023) 6697–6707. https://doi.org/10.1021/acsami.2c18266.

[14]   A. Cornet*, G. Garbarino, F. Zontone, Y. Chushkin, J. Jacobs, E. Pineda, T. Deschamps, S. Li, A. Ronca, J. Shen, G. Morard, N. Neuber, M. Frey, R. Busch, I. Gallino, M. Mezouar, G. Vaughan, B. Ruta*, Denser glasses relax faster: Enhanced atomic mobility and anomalous particle displacement under in-situ high pressure compression of metallic glasses, Acta Mater. 255 (2023) 119065. https://doi.org/10.1016/j.actamat.2023.119065.

[15]   H.-R. Jiang, J.-Y. Hu, N. Neuber, M. Frey, L. Xu, K. Sun, Y.-D. Jia, G. Wang, R. Busch, J. Shen*, Influence of sulfur addition on the glass formation, phase transformation and mechanical properties of $Cu_{50}Zr_{50}$ alloy, Acta Mater. 255 (2023) 119064. https://doi.org/https://doi.org/10.1016/j.actamat.2023.119064.

[16]   H.R. Jiang, J. Tseng, N. Neuber, J. Barrirero, B. Adam, M. Frey, A.C. Dippel, S. Banerjee, I. Gallino, A.H. Feng*, G. Wang, F. Mücklich, R. Busch, J. Shen*, On the devitrification of Cu–Zr–Al alloys: Solving the apparent contradiction between polymorphic liquid-liquid transition and phase separation, Acta Mater. 226 (2022) 117668. https://doi.org/10.1016/j.actamat.2022.117668.

[17]   H.R. Jiang, J.Y. Hu, N. Neuber, B. Bochtler, B. Adam, S.S. Riegler, M. Frey, L. Ruschel, W.F. Lu, A.H. Feng*, R. Busch, J. Shen*, Effect of sulfur on the glass-forming ability, phase transformation, and thermal stability of Cu-Zr-Al bulk metallic glass, Acta Mater. 212 (2021) 116923. https://doi.org/10.1016/j.actamat.2021.116923.

[18]   H.R. Jiang, B. Bochtler, S.S. Riegler, X.S. Wei*, N. Neuber, M. Frey, I. Gallino, R. Busch, J. Shen*, Thermodynamic and kinetic studies of the Cu–Zr–Al(–Sn) bulk metallic glass-forming system, J. Alloys Compd. 844 (2020) 156126. https://doi.org/10.1016/j.jallcom.2020.156126.

[19]   L.M. Ruschel*, O. Gross, B. Bochtler, B. Li, B. Adam, N. Neuber, M. Frey, S. Jakovlev, F. Yang, H. Jiang, B. Gludovatz, J.J. Kruzic, R. Busch, Ni-Nb-P-based bulk glass-forming alloys: Superior material properties combined in one alloy family, Acta Mater. 253 (2023) 118968. https://doi.org/10.1016/j.actamat.2023.118968.

[20]   L.M. Ruschel*, B. Adam, O. Gross, N. Neuber, M. Frey, H.J. Wachter, R. Busch, Development and optimization of novel sulfur-containing Ti-based bulk metallic glasses and the correlation between primarily crystallizing phases, thermal stability and mechanical properties, J. Alloys Compd. 960 (2023) 170614. https://doi.org/10.1016/j.jallcom.2023.170614.

[21]   M. Frey*, J. Wegner, N. Neuber, B. Reiplinger, B. Bochtler, B. Adam, L. Ruschel, S.S. Riegler, H.R. Jiang, S. Kleszczynski, G. Witt, R. Busch, Thermoplastic forming of additively manufactured Zr-based bulk metallic glass: A processing route for surface finishing of complex structures, Mater. Des. 198 (2021) 109368. https://doi.org/10.1016/j.matdes.2020.109368.

[22]   E. Soares Barreto*, M. Frey, J. Wegner, A. Jose, <u>N. Neuber</u>, R. Busch, S. Kleszczynski, L. Mädler, V. Uhlenwinkel, Properties of gas-atomized Cu-Ti-based metallic glass powders for additive manufacturing, Mater. Des. 215 (2022) 110519. https://doi.org/10.1016/j.matdes.2022.110519.

[23]   L. Thorsson, M. Unosson, M. Teresa Pérez-Prado, X. Jin, P. Tiberto, G. Barrera, B. Adam, <u>N. Neuber</u>, A. Ghavimi, M. Frey, R. Busch, I. Gallino*, Selective laser melting of a Fe-Si-Cr-B-C-based complex-shaped amorphous soft-magnetic electric motor rotor with record dimensions, Mater. Des. 215 (2022) 110483. https://doi.org/10.1016/j.matdes.2022.110483.

[24]   J. Wegner*, M. Frey, M. Piechotta, <u>N. Neuber</u>, B. Adam, S. Platt, L. Ruschel, N. Schnell, S.S. Riegler, H.R. Jiang, G. Witt, R. Busch, S. Kleszczynski, Influence of powder characteristics on the structural and the mechanical properties of additively manufactured Zr-based bulk metallic glass, Mater. Des. 209 (2021) 109976. https://doi.org/10.1016/j.matdes.2021.109976.

[25]   O. Gross*, M. Eisenbart, L.Y. Schmitt, <u>N. Neuber</u>, L. Ciftci, U.E. Klotz, R. Busch, I. Gallino, Development of novel 18-karat, premium-white gold bulk metallic glasses with improved tarnishing resistance, Mater. Des. 140 (2018) 495–504. https://doi.org/10.1016/j.matdes.2017.12.007.

[26]   M. Frey*, J. Wegner, E.S. Barreto, L. Ruschel, <u>N. Neuber</u>, B. Adam, S.S. Riegler, H.-R. Jiang, G. Witt, N. Ellendt, V. Uhlenwinkel, S. Kleszczynski, R. Busch, Laser powder bed fusion of Cu-Ti-Zr-Ni bulk metallic glasses in the Vit101 alloy system, Addit. Manuf. 66 (2023) 103467. https://doi.org/10.1016/j.addma.2023.103467.

[27]   B. Adam*, A. Kuball, L.M. Ruschel, <u>N. Neuber</u>, M. Frey, R. Busch, Sulphuric precipitates in novel titanium-based, sulphur-bearing bulk metallic glass–a BMG composite?, Philos. Mag. Lett. 104 (2024) 1–11. https://doi.org/10.1080/09500839.2024.2376614.

[28]   N. Grund, D. Holland-Moritz, S. Khademorezaian, L.P. Kreuzer, <u>N. Neuber</u>, L.M. Ruschel, H. Voigt, J. Wilden, F. Yang*, S. Banerjee, M. Blankenburg, A.C. Dippel, J.P. Embs, S. Divinski, R. Busch, A. Meyer, G. Wilde, Impact of sulfur addition on the structure and dynamics of Ni-Nb alloy melts, APL Mater. 12 (2024). https://doi.org/10.1063/5.0205058.

[29]   L.M. Ruschel*, S. Jakovlev, O. Gross, <u>N. Neuber</u>, B. Adam, M. Frey, B. Schmidt, B. Bochtler, R. Busch, Unraveling the role of relaxation and rejuvenation on the structure and

deformation behavior of the Zr-based bulk metallic glass Vit105, Mater. Today Adv. 23 (2024) 100522. https://doi.org/10.1016/j.mtadv.2024.100522

[30]   H.R. Jiang, M. Frey, N. Neuber, Y.F. Gao, B. Zhang, J. Ren, G. Wang*, R. Busch, J. Shen, In-situ scattering and calorimetric studies of crystallization pathway and kinetics in a Cu-Zr-Al bulk metallic glass, J. Alloys Compd. 1006 (2024) 176243. https://doi.org/10.1016/j.jallcom.2024.176243.

[31]   B. Li, L.M. Ruschel, K. Nomoto, O. Gross, B. Adam, N. Neuber, M. Frey, S.P. Ringer, B. Gludovatz, R. Busch, J.J. Kruzic*, Fracture behavior of NiNb and NiNbP bulk metallic glasses, J. Alloys Compd. 1010 (2025) 177369. https://doi.org/10.1016/j.jallcom.2024.177369.

*- Corresponding Author

Ordered by Journals:

Nature Communication :	1
Communication Physics:	2
Acta Materialia:	8
Scientific Reports:	1
Physical Review Letters:	1
Materials Today Advances:	1
Materials and Design:	5
ACS Applied Materials Interfaces:	1
Scripta Materialia:	1
Journal of Alloys and Compounds:	4
Journal of Physics: Condensed Matter:	2
APL Materials:	1
Additive Manufacturing:	1
Philosophical Magazine Letters:	1
Johnson Mathey Technology Review:	1

Proposals and Education

Research Grants accepted

IGF 21469N "Entwicklung der Prozesstechnologie für massive metallische Gläser auf Platinbasis mit dem Ziel einer Industrialisierung am Beispiel des Uhren- und Schmucksektors", <u>N. Neuber</u> and L.Y. Schmitt (Funding 420,328 €)

DFG BU 2276/15-1 „Untersuchung der kompositionellen Abhängigkeit struktureller Änderungen von Pt/Pd-Cu-Ni-P massivglasbildenden Flüssigkeiten und deren Verbindung zur Thermodynamik, Kinetik, Dynamik und mechanischen Eigenschaften" <u>N. Neuber</u> and O. Gross (Funding: 211,300 €)

Landesforschungsförderungsprogramm Saarland "Nanoindentation an metallischen Massivgläsern - ", F. Schäfer and <u>N. Neuber</u> (Funding 36,028.30 €)

Anschubsfinanzierung Universität des Saarlandes "Verarbeitung Platin-basierter metallischer Massivgläser im Schmuckbereich", O. Gross and <u>N. Neuber</u> (Funding 9,896 €)

Flight time for Parabola Flights (TEMPUS)

I-2022-01720 TEMPUS PF Campaign "Viscosity and surface tension in the liquid state of an ultra-fragile bulk glass forming composition $Pd_{58}Ni_{12}Se_{30}$", proposed by **<u>N. Neuber</u>**, B. Adam, L. Ruschel, F. Yang, Ralf Busch, number of parabolas allocated: 10

Beamtime at Synchrotron Facilities accepted:

Deutsches Elektronen Synchrotron (DESY)

In the following all proposals that successfully led to the scheduling of beamtimes at the Deutsches Elektronen Synchrotron (DESY) Hamburg are listed. The principal investigator and

main proposer of each experiment is written in bold letters and the length of the allocated beamtime is added.

I-20170938 "Investigation of the compositional dependence of structural changes of Pt/Pd-Cu-Ni-P bulk glass forming liquids and their connection to kinetic fragility", proposed by **O. Gross**, A. Kuball, B. Bochtler, <u>N. Neuber</u> , R. Busch, beamtime allocated: 48 h at P02.1

I-20180284 "Investigation of the cooling rate dependent structural changes of the relaxation mechanisms in bulk metallic glass forming alloys", proposed by **A. Kuball**, O. Gross, B. Bochtler, <u>N. Neuber</u>, B. Busch, beamtime allocated: 48 h at P02.1

I-20180946 "Dynamics on the medium range order length scale in a metallic glass-former", proposed by **O. Gross**, I. Gallino, B. Ruta , A. Kuball, B. Bochtler, <u>N. Neuber</u>, R. Busch, beamtime allocated: 96 h at P10

I-20191456 "Dispersion relation of metallic glasses across the glass transition" proposed by **B. Ruta**, I. Gallino, <u>N. Neuber</u> and G. Baldi, beamtime allocated: 96 h at P10

I-20200218 "Investigation of the structural change in the supercooled liquid region of CuZr-based bulk metallic glasses and its influence on crystallization", proposed by **H. Jiang**, B. Bochtler, <u>N. Neuber</u> and J. Chen, beamtime allocated: 72 h at P21.1

I-20200684 "In-situ structural investigation of sulfuric precipitates and intermetallic nano-crystallization in novel sulfur bearing Bulk Metallic Glass formers", proposed by **B. Adam**, A. Kuball, O. Gross, <u>N. Neuber,</u> M. Frey and R. Busch, beamtime allocated: 96 h at P21.2

I-20200650 EC "In-situ structural analysis of a liquid-liquid transition in a metallic glass former during dynamic mechanical analysis", proposed by **M. Frey**, <u>N. Neuber,</u> O. Gross, R. Busch and E. Pineda, beamtime allocated: 96 h at P21.1

I-20200052 EC "Wave-vector and temperature dependence of the dynamics in PtPdCuNiP metallic glass forming liquid", proposed by <u>**N. Neuber**</u>, O. Gross, M. Frey, I. Gallino and B. Ruta, beamtime allocated: 144 h at P10

I-20210859 "Large-scale density fluctuations during structural transition in metallic glass forming liquid beyond medium range order", proposed by F. Yang, <u>N. Neuber</u>, R. Busch and A. Meyer, beamtime allocated: 72 h at P21.2

I-20210883 "Study of the influence of metalloid addition on the structure and crystallization behavior of Ni-Nb based metallic liquids by combination of In-situ X-ray diffraction with electrostatic levitation", proposed by <u>**N. Neuber**</u>, B. Adam, L. Ruschel, F. Yang, N. Grund, D. Holland-Moritz, Ralf Busch, and A. Meyer, beamtime allocated: 96 h at P21.1

I-20210803 "The influence of shear on the liquid-liquid transition and crystallization of undercooled $Zr41.2Ti13.8Cu12.5Ni10.0Be22.5$ bulk metallic glass forming alloy studied by WAXS and SAXS in the electrostatic levitator", proposed by <u>**N. Neuber**</u>, I. Gallino, F. Yang, A. Meyer and R. Busch, beamtime allocated: 72 h at P21.2

I-20210971 "Investigation of interface diffusion and early phase transformation of various Ni/Al nanoscaled multilayered thin films by SAXS/WAXS" **S. S Riegler**, I. Gallino1, S. Matthes, <u>N. Neuber</u>, R. Busch and Peter Schaaf, beamtime allocated: 72 h at P21.2

I-20210781 "Structural investigation of an anomalous exothermic event in the supercooled liquid region of refractory Ni-Nb-P-based amorphous alloys", proposed by **L. Ruschel**, B. Adam, <u>N. Neuber</u> and R. Busch, beamtime allocated: 96 h at P21.1

I-20210687 "The effect of micro-alloying on the phase separation and crystallization behavior of Cu-Zr-Al-based bulk metallic glasses", proposed by **H. Jiang**, <u>N. Neuber</u>, J. Tseng, R. Busch and J. Chen, beamtime allocated 72 h at P21.2

I-20221413 "Correlation length scale during vitrification of Pd/Pt-based BMG alloys", proposed by <u>**N. Neuber,**</u> F. Yang, I. Gallino and R. Busch, beamtime allocated: 72 h at P21.2

I-20221106 EC "Atomic scale dynamics of metallic glass under high pressure", proposed by **A. Cornet**, <u>N. Neuber,</u> F. Yang and B. Ruta, beamtime allocated: 96 h at P10

I-20221413 "Study on the crystallization behavior and the melt structure in glass forming Pd-Ni-S", proposed by **M. R. Chegeni**, <u>N. Neuber</u>, J. Wilden, P. Eckstein, F. Yang, R. Busch and I. Gallino, beamtime allocated: 70 h at P21.1

European Synchrotron Radiation Facility (ESRF)

In the following all proposals that successfully led to the scheduling of beamtimes at the European Synchrotron Radiation Facility (ESRF) Grenoble are listed.

HC-4260 "Probing the wave-vector dependence of the atomic motion of glass-formers across the glass transition", proposed by **N. Neuber**, B. Ruta ,M. Frey, I. Gallino and R. Busch, beamtime allocated 96 h

HC-4479 "Study of the microscopic dynamics during a liquid-liquid transition in supercooled metallic melt", proposed by E. Pineda, M. Frey, N. Neuber, R. Busch and B. Ruta, beamtime allocated 120 h

HC-4429 "Dynamical processes in out-of-equilibrium materials at extreme conditions", Longtime Proposal proposed by B. Ruta, collaboration on-site for several beamtimes (2x 120 h)

HC-4902 "Wave-vector dependence of dynamics in deeply undercooled metallic liquids", proposed by **N. Neuber**, A. Cornet, S. Li, I. Gallino, L. Ruschel, E. Pineda, R. Busch and B. Ruta, beamtime allocated 144 h

Supervised or partially supervised thesis

Master-Thesis: Lamia Ciftci, "Crystallization and Physical Aging Behavior Studies on Bulk Metallic Glass Forming Liquids", Saarland University 2019

Master-Thesis: Marvin Müller, "Crystallization and Physical Aging Behavior Studies on Bulk Metallic Glass Forming Liquids via Fast Differential Scanning Calorimetry", Saarland University 2022

Master-Thesis: Viktor Carl Harry Svenonius, "Alloy development and thermophysical properties of new bulk metallic PdNiSe glasses", Saarland University 2022

Bachelor-Thesis: Marvin Müller, "Entwicklung einer biokompatiblen metallischen Massivglaslegierung auf Platinbasis", Saarland University 2020

AMASE Master-Project (6-month mandatory Laboratory-internship): Gonzalo Molina "Glass-forming ability improvement in the PtCuP system", Saarland University 2020

Teaching

<u>"Praktikum Master Material science"</u>: Lab Course "Legierungsentwicklung" (Synthesis of metallic Glasses) Winter terms 2017-2022 (4 h/week)

<u>"Praktikum Master Material science"</u>: Lab Course "Legierungscharakterisierung" (Introduction to Differential Calorimetry) Winter terms 2017-2022 (4 h/week)

<u>„Praktikum II Bachelor Material science"</u>: Lab Course "Gießen von Metallen" (Casting of Metals) Winter terms 2017-2021 (4 h/week)

<u>„Projektpraktikum II Master Material Chemistry"</u>: Lab Course "Amorphous Metals" (Casting of Metals) Winter terms 2019, 2021, 2022 (16 h/course)

<u>"Kinetics of Amorphous Systems"</u> Stand-in Lecturer Summer term 2019 (2 h)

<u>"Amorphous Metals"</u> Stand-in Lecturer Summer term 2018+2019 (4 h)

Ringvorlesung MINT "Amorphous Metals" Lecturer Summer term 2022 (2 h)

Oral Contributions to Conferences and Colloquia

2022.

The 19th International Conference on Liquid and Amorphous Metals (LAM18), Hiroshima, JAPAN

Oral presentation (Online): "On the thermodynamics and its connection to structure in the Pt-Pd-Cu-Ni-P bulk metallic glass forming system "

User-Meeting of the Deutsches Elektronensynchrotron (DESY) – Swedish Materials Science beamline

Invited Oral presentation (online):" Usage of combined in situ SAXS/WAXS setup to understand decomposition and crystallization sequences in metallic glasses"

Oral presentation at the Open Day of Saarland University: "Amorphe Metalle – Härter als Stahl, elastisch wie Kunststoff"

2021.

Condensed Matter Physics and Chemistry (CMPC) research group meeting of the Deutsches Elektronensynchrotron (DESY)

Invited Oral presentation (online): "Experimental investigations of metallic glasses utilizing synchrotron radiation"

2019.

The 18th International Conference on Liquid and Amorphous Metals (LAM17), Lyon, FRANCE

Oral presentation: "The role of the Ga addition to the thermodynamics, kinetics, and tarnishing properties of the Au-Pd-Cu-Ag-Si bulk metallic glass forming system"

2018.

DPG (Deutsche Physikalische Gesellschaft) Frühjahrstagung Berlin, GERMANY.

Oral presentation: "The role of the Ga addition to the thermodynamics, kinetics, and tarnishing properties of the Au-Pd-Cu-Ag-Si bulk metallic glass forming system"

2017.

The 16th International Conference on Rapidly Quenched and Metastable Materials (RQ16) Leoben, AUSTRIA.

Oral presentation: "Alloy Development of 18-karat premium-white gold bulk metallic glasses with improved tarnishing resistance"

List of papers regarding the thesis

This cumulative thesis is based on the following papers:

I. N. Neuber*, O. Gross, M. Frey, B. Bochtler, A. Kuball, S. Hechler, I. Gallino, R. Busch, On the thermodynamics and its connection to structure in the Pt-Pd-Cu-Ni-P bulk metallic glass forming system, Acta Mater. 220 (2021) 117300. https://doi.org/10.1016/j.actamat.2021.117300.

II. N. Neuber*, O. Gross, M. Frey, B. Bochtler, A. Kuball, S. Hechler, F. Yang, E. Pineda, F. Westermeier, M. Sprung, F. Schäfer, I. Gallino, R. Busch, B. Ruta Disentangling structural and kinetic components of the α-relaxation in supercooled metallic liquids. Commun Phys 5, 316 (2022). https://doi.org/10.1038/s42005-022-01099-4

III. N. Neuber*, M. Sadeghilaridjani, N. Ghodki, O. Gross, B. Adam, L. Ruschel, M. Frey, S. Muskeri, M. Blankenburg R. Busch, I. Gallino, S. Mukherjee Effect of composition and thermal history on deformation behavior and cluster connections in model bulk metallic glasses, Scient. Rep. 165 (2022). https://doi.org/10.1038/s41598-022-20938-6

IV. O. Gross* N. Neuber, A. Kuball, B. Bochtler, S. Hechler, M. Frey, R. Busch, Signatures of structural differences in Pt–P- and Pd–P-based bulk glass-forming liquids, Commun. Phys. 2 (2019) 83. https://doi.org/10.1038/s42005-019-0180-2.

V. B. Ruta,* S. Hechler, N. Neuber, D. Orsi, L. Cristofolini, O. Gross, B. Bochtler, M. Frey, A. Kuball, S.S. Riegler, M. Stolpe, Z. Evenson, C. Gutt, F. Westermeier, R. Busch, I. Gallino, Wave-Vector Dependence of the Dynamics in Supercooled Metallic Liquids, Phys. Rev. Lett. 125 (2020) 055701. https://doi.org/10.1103/PhysRevLett.125.055701.

Reprints are made with the permission of the respective publishers. The explicit permissions can be found in the Appendix.

Author's contribution to the papers

In the following a more detailed overview on the contributions to the papers of this thesis is provided. It should be stressed that also the contributions of the other authors is provided in Papers II to IV. For all papers an additional author contribution sheet was signed by all coauthors.

I.   The author conceptualized and planned the study together with the second and last author. He also synthesized the samples and measured and analyzed the data of the calorimetric study. He performed the synchrotron X-ray diffraction together with the coauthors and analyzed the data with input from the second author. The manuscript was outlined and written by the author with input of the second and last author. Plots are made by the author with input from the coauthors.

II. The author conceptualized and planned the study together with the second and last author. The author synthesized the samples. The X-ray photon correlation spectroscopy measurements were performed during several beamtimes with groups consisting out of different pairings of the coauthors. The data was analyzed and interpreted by the author with input of the second and last author. The manuscript was mutually written by the first and last author with input of the other authors. Plots are made by the author with input from the coauthors.

III. The author conceptualized and planned the study together with the equally contributing second author and last author. The micro-mechanical characterization and analysis was performed by the second author, Nandita Ghodki and Saideep Muskeri. The author performed the synchrotron X-ray diffraction with help of the coauthors from the Chair of Metallic Materials. The analysis of the structural data was performed by himself. The manuscript was mutually written by the first and equally contributing second author with focus on the structural data. Additional input was provided by the other authors. Plots are made by the author with input from the coauthors.

IV.   The author synthesized the samples and planned and performed the synchrotron X-ray diffraction experiments with the coauthors. The author contributed to the discussion and gave input to the manuscript.

V.   The author synthesized the Pd-based samples. The X-ray photon correlation spectroscopy measurements of the Pd-based sample were performed by the author with the coauthors from the Chair of Metallic Materials and the first author of the publication. The data on the Pd-based system was analyzed and interpreted by the author with input of the first author of the Publication. Plots containing data on the Pd-based system are made by the author with input from the first author of the publication.

Content

Content

List of Figures

List of Tables

Abbreviations

ABBREVIATION	FULL NAME
3PBB	three-point beam bending
bcc	body-centered cubic
BMG	bulk metallic glass
CCR	critical cooling rate
CSM	cooperative shear model
CSRO	chemical short-range order
DESY	Deutsches Elektronensynchtrotron
DSC	differential scanning calorimeter
DCT	decoupling temperature (mode coupling)
DTA	differential thermal analysis
ECP	efficient cluster packing
ESRF	European Synchrotron Radiation Facility
fcc	face-centered cubic
FSDP	first sharp diffraction peak
FWHM	full width at half maximum
GFA	glass-forming ability
hcp	hexagonal closest packed
HEXRD	high energy XRD
INS	inelastic neutron scattering
JMAK	Johnson-Mehl-Avrami-Kolmogorov
KWW	Kohlrausch-Williams-Watts
LLPT	Liquid-liquid phase transition
MCT	mode coupling theory
MRO	medium-range order
MDSC	modulated differential scanning calorimetry
PDF	(radial) pair distribution function
SCL	supercooled liquid
SRO	short-range order
SRS	strain rate sensitivity
STZ	shear-transformation zone

TMA	thermo-mechanical analyzer
TTP	tri-capped trigonal prism
TTCF	Two-times correlation function
TTT	Time-temperature transformation
VFT	Vogel-Fulcher-Tamann
XPCS	X-ray photon correlation spectroscopy
XRD	X-ray diffraction

Symbols

SYMBOL	FULL NAME
A_T	amplitude of temperature modulation
A_x	area of the crystalline nucleus
α_{th}	volumetric thermal expansion coefficient
$\alpha_{th,Dil}$	volumetric thermal expansion coefficient measured in dilatometry
$\alpha_{th,XRD}$	volumetric thermal expansion coefficient derived from XRD
a	fitting parameter of isobaric heat capacity in the liquid state
b	fitting parameter of isobaric heat capacity in the liquid state
β	stretching exponent in KWW equations
β'	proportionality factor between volume and enthalpy
c	fitting parameter of isobaric heat capacity in the crystalline state
c(Q,T)	contrast parameter in XPCS
c_i	concentration of the atomic species i
c_p	isobaric heat capacity
c_p^x	isobaric heat capacities of the crystal
c_p^l	isobaric heat capacities of the liquid
Δc_p^{l-x}	difference in isobaric heat capacity between the liquid and crystalline state
Δc_p^{l-g}	difference in isobaric heat capacity between the liquid and glassy state
$\gamma_{cluster}$	shear strain imposed on an atomic cluster
γ_c	experimental contrast
$\gamma_{imposed}$	macroscopic shear strain
γ_{l-x}	interfacial energy between the crystalline and liquid phase
D^*	fragility parameter
d	fitting parameter of isobaric heat capacity in the crystalline state
d_c	critical casting thickness
E_A	activation energy
$E_{elastic}$	elastic energy
E_{young}	Young's modulus
ε_{4-3}	volume dilatation between the 3rd and 4th coordination cell

f_r	atomic roughness factor
f_i	atomic form factor
$f_q(Q,T)$	non-ergodicity factor
$G(r)$	reduced pair distribution function
G	Gibb's free energy
$\Delta G^{l\text{-}x}$	molar difference in Gibbs free energy between the liquid and crystalline state
$\Delta g^{l\text{-}x}$	difference in Gibbs free energy between the liquid and crystalline state per volume
ΔG^{*}	nucleation barrier for crystallization
G_{∞}	high frequency shear modulus
$G_{\tau\text{-}\eta}$	proportionality factor between viscosity and time domain
$g(r)$	pair distribution function
$g_2(Q,t,T)$	Intensity autocorrelation function
H	enthalpy
H_f	enthalpy of fusion
$\Delta H^{l\text{-}x}$	difference in enthalpy between the liquid and crystalline state
H_{mech}	micromechanical hardness
HF_{tot}	total heat flow in MDSC
$HF_{non\text{-}rev}$	non reversible heat flow in MDSC
HF_{rev}	reversible heat flow in MDSC
h	Planck's constant ($h = 6.626 \times 10^{-34}$ m^{2}kgs^{-1})
η	dynamic viscosity
η_0	upper limit of viscosity at infinite temperature
η_{eq}	(supercooled) liquid equilibrium viscosity
$\Delta\eta_{eq\text{-}g}$	difference of glassy non-equilibrium viscosity to equilibrium
η_g	glassy non-equilibrium viscosity
I_T	transmitted scattering intensity
I_C	coherently scattered intensity
I_{IC}	incoherently scattered intensity
I_{BG}	the intensity of photons scattered by the experimental background
I_{MC}	multiple-scattering intensity
I_v	critical nucleation rate for steady state
k_B	Boltzmann constant ($k_B = 1.380649 \times 10^{-23}$ m^2 kg s^{-2} K^{-1})

λ	wavelength
m	m-fragility index
$m_{kinetic}$	kinetic m-fragility index
$m_{str}^{V4\text{-}3}$	structural fragility index
m_{SSR}	strain rate sensitivity
m_S	sample mass in DSC
m_R	reference mass in DSC
n_0	number of atoms in a system
n^*	number of these supercritical clusters per volume
N_A	Avogadro's number ($N_A = 6.022 \times 10^{23}$)
P	period time in MDSC
Φ	observational quantity (representative for e.g. H, η, V)
Φ_{eq}	equilibrium state of Φ
$\Phi_{n\text{-}eq}$	non-equilibrium state of Φ
φ	packing fraction
$\Psi(Q)$	sample scattering amplitude
Q	wave-vector
Q_i	wave-vector position of the i-th diffraction peak
Q_{FSDP}	wave-vector position of the first sharp diffraction peak
$\dot{Q} = dQ/dt$	heat flow
R	universal Gas constant ($R = 8.314$ J mol^{-1}K^{-1})
R_c	critical cooling rate for crystallization
r	radius
r_i	peak position of the i-th peak in the PDF
r^*	critical radius for nucleation
ρ	mass density
ρ_0	average number density
S	entropy
S_{ij}	partial structure function of the atomic pair of species i and j
S_c	configurational entropy
S_f	entropy of fusion
S_{vib}	vibrational entropy
$\Delta S^{l\text{-}x}$	difference in enthalpy between the liquid and crystalline state
$S(Q)$	total structure factor

$S(Q_i)$	height of the i-th diffraction peak
$d\sigma_C/d\Omega$	coherent scattering cross-section
T_{ann}	annealing temperature
T_f	temperature of fusion
T_{fic}	fictive temperature
$T_{fic,c}$	critical fictive temperature
$T_{g,on}$	onset temperature of (kinetic) glass transition
$T_{g,end}$	end temperature of (kinetic) glass transition
T_g^*	glass transition temperature defined through $\eta = 10^{12}$ Pas
$T_{g,dyn}$	dynamic glass transition temperature
T_l	liquidus temperature
T_m	melting temperature
T_s	solidus temperature
T_x	temperature of crystallization
T_0	temperature of divergence of the VFT temperature
$\dot{T} = dT/dt$	heating/cooling rate
ΔT	undercooling of the liquid with respect to T_f
ΔT_{SR}	temperature difference between sample and reference in DSC
t_x	crystallization time
τ_x^*	critical crystallization time
τ_c	critical shear stress for flow
τ_d	average relaxation time, connected to dynamic glass transition
τ_{trans}	transition time from glassy to liquid state
τ_0	relaxation time of the liquid in the high temperature limit ($T\rightarrow\infty$)
θ	scattering angle
u	crystal growth rate
V_{atomic}	atomic average volume
V_m	molar volume
V_x	volume of the crystalline nucleus
ΔV_f	volumetric change during the melting
V_{free}	free volume
ΔV^*	shear activation volume
ΔV_{4-3}	change in volume between the 3rd and 4th shell of the PDF
w_{ij}	atomic weighting factor of the atoms of species i and j

x(T,t)	crystalline fraction
X	dynamic quantity
ξ	coherence length
dΩ	solid angle between detector and scatterer
ω	angular frequency

1. Introduction

Conventionally solid metallic materials feature a periodic structure with a translational symmetry. This state of atoms being arranged in a long-range ordered lattice structure, with well-defined positions of the atoms, is called crystalline. In contrast, metallic liquids do not feature such a long-range order, but are seemingly disordered, which is called amorphous. Nevertheless, it must be pointed out that even in a liquid, there are certain degrees of ordering relations as the metallic atoms tend to form clusters. These different kinds of arrangements are called short-range (SRO) or medium-range order (MRO). Whereas SRO is just involving ordering relations between directly neighboring atoms, covering length scales around 2-3 Å, the MRO already involves the surroundings up to the third or fourth neighboring atomic shell, leading to length scales of around 10 Å or even more. In simplified terms the SRO merely describes the type(s) of cluster(s) the atoms prefer to be arranged in, whereas the MRO can basically originate in specific arrangements of these clusters between each other. The term amorphous, whose origin is found in Greek and literally translates to "without a shape", is often connected to the word "disordered". However knowing about the existence of SRO and MRO in it should not be taken too literally, as it would rather describe an ideal gas that is actually disordered, instead of a liquid or a glassy structure.

Amorphous metals or metallic glasses combine characteristics of both liquid and solid state: while being solid they do lack the long-range order and translational symmetry of a crystalline metal but resemble the structure of a liquid. This lack of long-range order leads to a unique combination of thermophysical and mechanical properties and even allows so-called thermo-plastic forming [1–3]. The latter is a property originally known for thermoplastic polymers or silicate glasses (or in general glasses[1]), but not for metals. The absence of a crystalline lattice leads to completely different deformation behavior leading to close to theoretical strength, a high hardness, combined with an elastic limit of up to 2% [1].

---

[1] Different to ordinary language the term glass describes an amorphous solid, no-matter of being a metal, a polymer, or a silicate, for which the term is conventionally used.

In order to obtain the desired glassy state, the amorphous structure of the liquid somehow needs to be preserved. This means that the crystallization of the respective liquid needs to be successfully suppressed during cooling.

During cooling below the melting point, certain numbers of atoms can accumulate through thermal fluctuations and form a so-called crystalline nucleus. Fortunately, this process creates an interface between the energetically favorable volume of the crystalline nucleus and the surrounding liquid state, that is energetically unfavorable. In the end, the initial size of the nucleus with a radius r^2 decides on the balance between energetic gain due to the crystalline volume ($\propto r^3$) and the effort to create the interface between liquid and crystal ($\propto r^2$), which determines whether the crystalline nucleus prefers to dissolve or to grow. Without this additional energetic contribution of the interface, undercooling of liquids below their melting point would be virtually impossible. Ultimately, the statistical nature of the thermal fluctuations that are needed to create the nuclei, resulting in a time dependence of the nucleation process, can be used to successfully limit the number of overcritical nucleation events by rapid cooling.

In this context, this means that any liquid has the general ability to form a glass. However, its propensity to do so varies significantly among different systems. One of the determining factors is the mobility of particles in the liquid, which strongly depends on the structural units that are formed by the atoms or even molecules in the liquid. It is one of the determining properties of a liquid, on how much effort, i.e. sufficiently high cooling, is needed to successfully bypass the crystallization event. For conventional glasses of everyday use, such as silicate glasses or most polymers, no rapid quenching is needed to form a glass. The governing structural units, SiO_4 tetrahedra or long chain-molecules, are found to be substantially large with strong interactions, making them rather sluggish for ordering processes on a long range. In comparison the simple structure of a metallic melt leads to a very high mobility of atoms rising the tendency to ultimately end up rearranging in the highly ordered and energetically favorable crystalline structure.

---

[2] The nucleus is in a first approximation assumed to be spherical, as a sphere geometrically provides the highest volume to surface ratio.
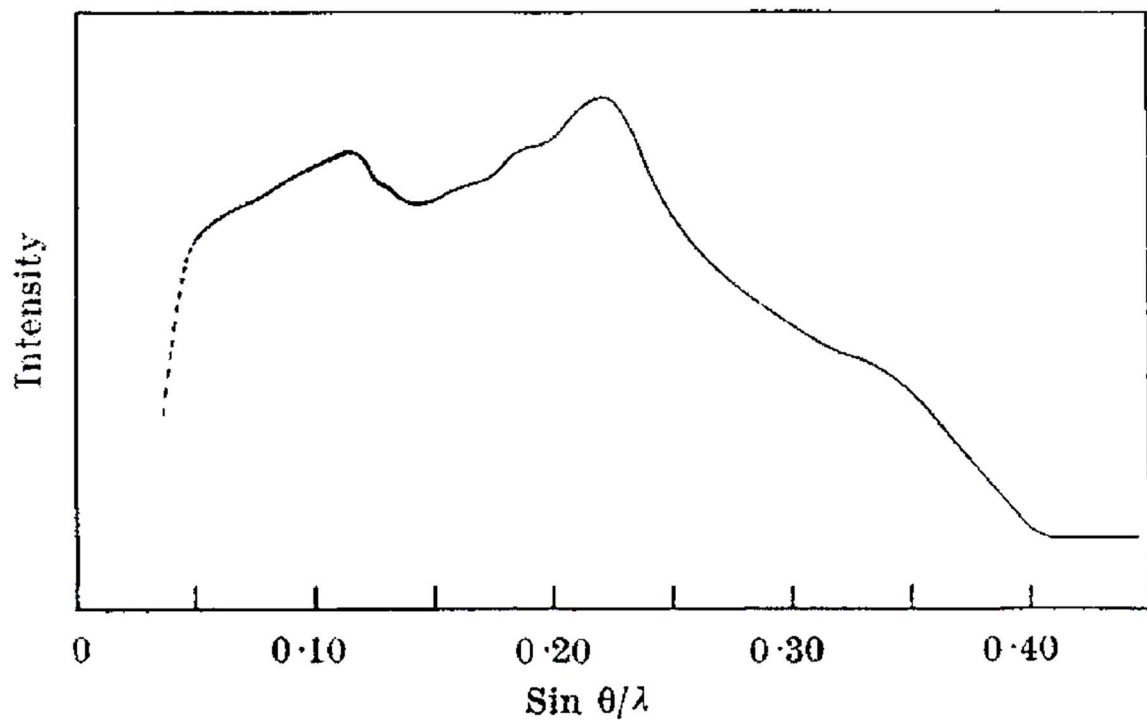
Figure 1-1: X-ray diffraction pattern of the first amorphous metallic alloy ($Au_{75}Si_{25}$) reported by Duwez et al [4]. The absence of sharp diffraction peaks (Bragg-peaks) verifies the amorphous structure of the splat-quenched specimen. Taken from Ref. [4].

Based on all these adverse conditions it was assumed for a long time that the cooling rates needed to achieve the glassy state in metals cannot be technologically realized. Still, the concept was challenged by the scientific community by the likes of David Turnbull [5], until a group around Pol Duwez successfully created the first non-crystalline metallic solid by splat-quenching a mixture of Au and Si to an amorphous flake of 10 μm thickness [4]. This small thickness of the obtainable amorphous specimen mirrors the high critical cooling rate R_c that was still needed to prevent the formation of crystals, as thickness and cooling rate are inverse proportional ($R_c \propto d_c^{-2}$)[6]. The critical casting thickness yields a practical tool to describe and determine the glass-forming ability (GFA) of a liquid experimentally.
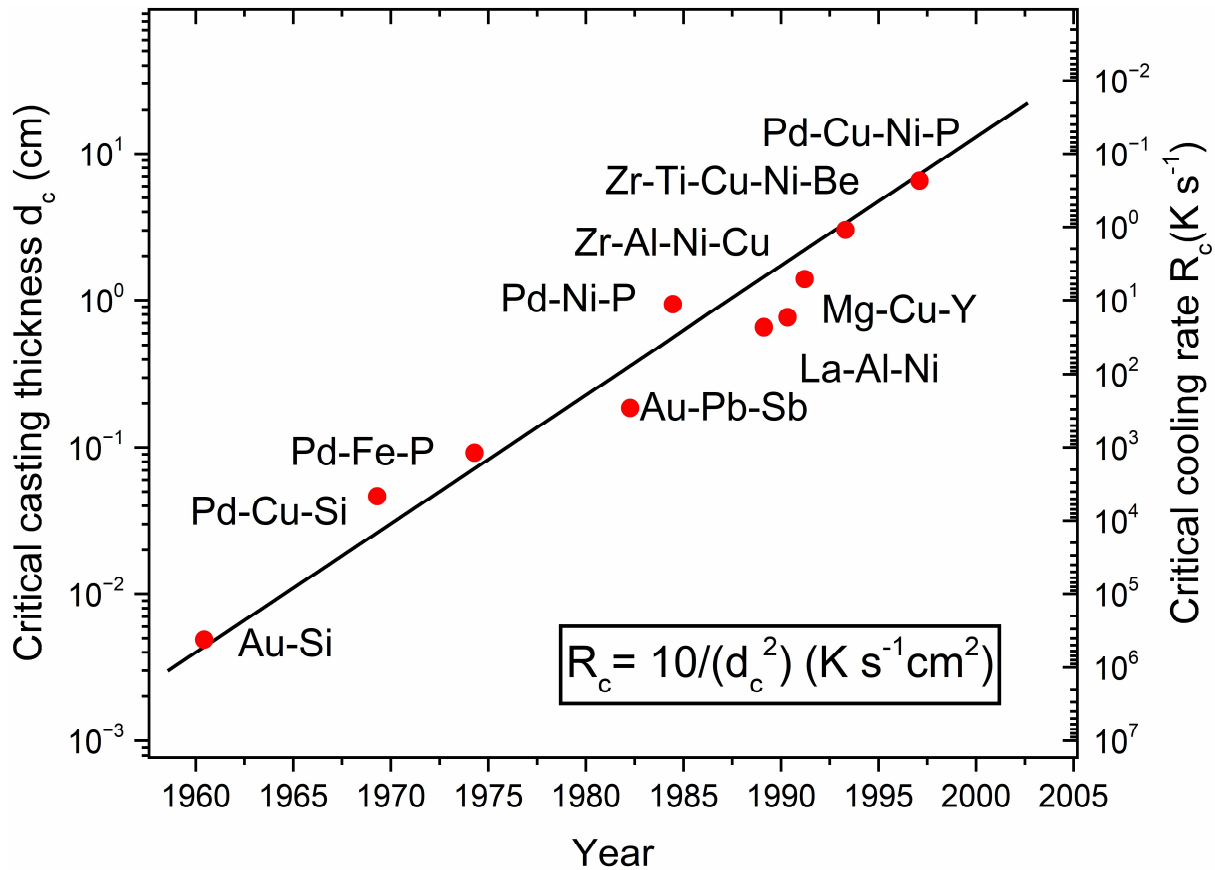
Figure 1-2: History of the development of the critical casting thickness and respective critical cooling rate since the first discovery in the 1960s. The data are reproduced from Löffler et al. [3].

Since the production of first thin films in the 1960s, amorphous metals/metallic glasses have undergone tremendous development over the past 60 years, reaching critical casting diameters of up to 80 mm and critical cooling rates as low as 0.067 K s^{-1} [7]. During the alloy development soon, the trend went towards more complex systems with a larger number of components. Up until now a large number of metallic glass forming systems based on almost any metal in combination with various different metals and metalloids can be found, most famously including Zr- [8–10], Mg- [11,12], Fe-[13,14] or Ni-based [15,16] systems to just name a few. Next to Zr-based systems, especially Pd-based systems emerged on the front of the best glass formers but were often disregarded for industrial applications due to their high cost. However, even amorphous alloys based on noble metals (Pt, Pd, Au, etc), which are the main subject in the current work, have recently attracted serious interest in jewelry applications [17–21], but also highly functional applications ranging from energy conversion [22–25] to biomedical implants [26–28]. One example on the size and quality of a cast metallic glass is provided in Figure 1-3, which depicts an amorphous ring made out of a Pt-based ($Pt_{58}Cu_{21}P_{21}$) alloy, with an inner diameter of 19 mm and a width of 6 mm and a wall thickness of 1 mm.
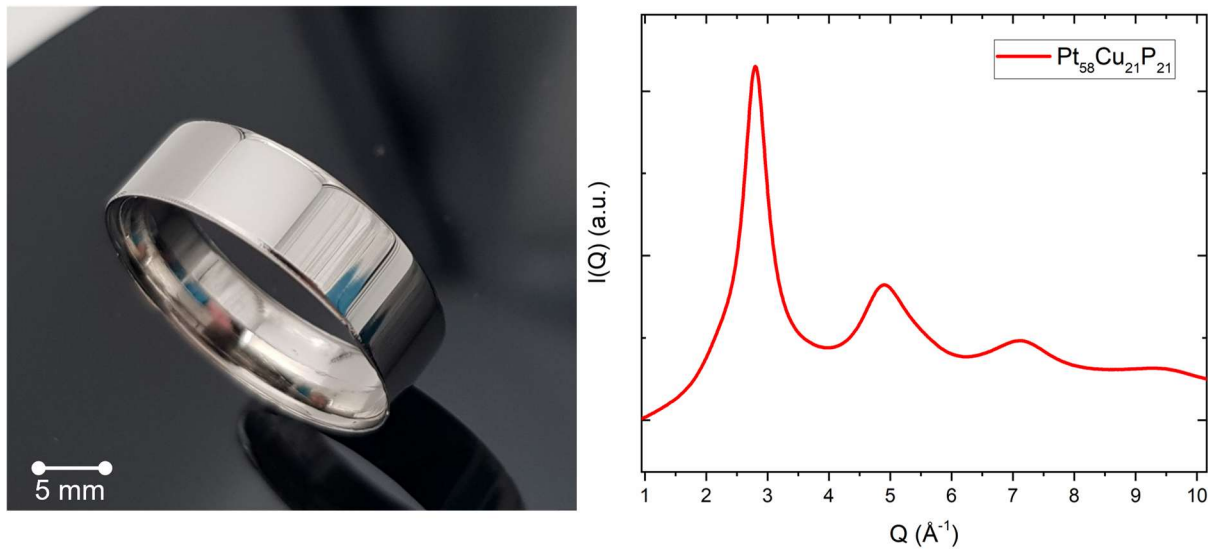
Figure 1-3: Example for the application of noble metal containing metallic glass : left side: an amorphous ring with a 19 mm diameter and 6 mm width out of $Pt_{58}Cu_{21}P_{21}$ (850 Pt hallmark). The outer part of the ring was turned down from 1.7 mm to a wall thickness of 1 mm and polished, whereas the visible inside is still in the as-cast state.

right side: High-energy synchrotron diffraction pattern of the cross-section cut out of a similar ring out of $Pt_{58}Cu_{21}P_{21}$. The amorphous halo, combined with the absence of sharp crystalline Bragg-peaks, verifies the amorphous structure of the ring.

This tremendous improvement of glass-forming ability was possible due to a better understanding of the glass formation process and the underlying concepts to strengthen the liquid against crystallization. Based on their past success in the development of new compositions Akihisa Inoue and coworkers laid down the first set of empirical rules on how to design bulk metallic glass forming liquids [3,29]. In their rules they defined the need to have a system with at least three components, while also demanding a size difference of more than 12% and negative heats of mixing between the main components involved. From a physical point of view the rules can be explained by simple and descriptive models. First of all, the substantial number of different atomic species can facilitate the occurrence of a large number of possible complex crystalline structures, which will hinder each other during their attempt to form. When assuming a hard sphere model the mixture of different sized spheres leads to good topological packing of space, reducing the free volume between the atoms, decreasing the mobility of the individual atoms. The negative heat of mixing is needed to ensure a chemical contribution for the intermixing of the different sized atoms, while also impeding the movement of the individual atoms through the melt by the chemical interaction with the other atoms. The rules contribute to a dense packed liquid that is energetically close to the crystal with assumably

sluggish atomic mobility, often mirrored by a highly viscous melt of a good glass forming liquid. This picturesque description already summarizes well the interrelation of the thermodynamics (energetically close to the crystal), the dynamics (sluggish mobility of the atoms) and the structure of the liquid. Still, a detailed understanding of its intercorrelation is still deficient and a prevailing research topic.

Subsequently, the present work aims to further facilitate the understanding of structure property correlations in multicomponent bulk metallic glass forming systems. Therefore, a detailed investigation of thermodynamics, dynamics, kinetics, mechanics, and structure on a systematic series of compositions shall be carried out.

For this task it is crucial to select a suitable alloy system, which possesses enough stability of the SCL against crystallization to experimentally assess the properties of the supercooled liquid state (SCL) without the interference through crystallization. Further, a systematic change of composition should be possible without a loss of this high stability while maintaining a good GFA. The latter is extremely challenge as often the region of good glass forming ability is limited to a narrow compositional space [30]. Promising systems are provided by the Pt-Cu-Ni-P and Pd-Cu-Ni-P, where the outstanding glass forming compositions (at least 20 mm) are found in the same stoichiometric range of $(Pt/Pd)_{42.5}Cu_{27}Ni_{9.5}P_{21}$ [31]. When considering simple hard sphere structural models of metallic liquids that are based on the efficient packing of representative structural units (clusters), Pt and Pd can be, due to their similar size, deemed topologically equivalent[3] [32]. Based on this, a good interchangeability of the two elements is suggested and also supported by literature for PtPd-based BMGs [33–35], making the $(Pt/Pd)_{42.5}Cu_{27}Ni_{9.5}P_{21}$ composition with different Pt/Pd ratios an ideal "case-study" system.

Special interest is raised by the properties of the two boundary systems for several reasons. The first is the discrepancy in their GFA (80 mm for $Pd_{42.5}Cu_{30}Ni_{7.5}P_{20}$ [7] vs. 20 mm for $Pt_{42.5}Cu_{27}Ni_{9.5}P_{21}$ [19]). While both are exceptionally good glass-formers, this difference by a factor of four in critical thickness (which is roughly about 1.5 orders of magnitude in R_c) can neither be explained by the structural models, assuming similar behavior, nor by the almost identical temperature dependence of viscosity in the supercooled liquid (fragility)[36,37]. Further both boundary systems feature similar liquidus temperatures (863 K for the Pt-based

---

[3] Based on the efficient cluster packing model (EPC) elements with atomic radii that differ by less than 2 % are considered as topologically equivalent [86]

and 869 K for the Pd-based system [21]), while showing a difference in the glass transition temperature T_g of 57 K (517 K and 574 K for Pt and Pd respectively). Thus, this model system not only enables to study the undercooled state through its good stability but also raises questions and shows irregularities that need to be solved. To further study and understand the different structural and thermodynamic behaviors of the two somehow similar, but at the same time remarkably different, alloy-families the compositional space on the Pt-Pd axis is thoroughly examined. Therefore, Pt is subsequently replaced by Pd in the composition $(Pt/Pd)_{42.5}Cu_{27}Ni_{9.5}P_{21}$.

On the base of this strategy, the different contributions of this cumulative thesis work out connections between the intrinsic structure (Paper IV) of the undercooled liquid and its thermally induced changes with the thermodynamic (Paper I) and dynamic (Paper II+V) properties. Throughout these published works, the evolution of structure with temperature is assessed in reciprocal as well as real space, utilizing in-situ X-ray diffraction with high energy synchrotron light sources. Further, the microscopic dynamics of the metallic liquids is investigated by X-ray photon electron spectroscopy, being another synchrotron-based technique. For the thermodynamic and kinetic properties calorimetric techniques are applied in combination with thermomechanical and rheological methods. Further, correlations of the resulting structure of the deeply undercooled liquid that has eventually vitrified, and its mechanical properties is presented (Paper III). For the micromechanical characterization, nano-indentation and micro-pillar compression tests were used to monitor the strength and in particular the strain-rate sensitivity and ductility of the material. The resulting embrittlement through composition (higher Pd content) and thermal history (more relaxed state) seems to be correlated to structural changes in the connecting schemes of the atomic clusters, based on structural data in real space.

All results are summarized in chapter 4 of this current work and then holistically discussed in the context of literature and partially extended through additional unpublished data, covering kinetic, dynamic and structural information on the alloy system, in the discussion section.

2. State of the Art and Theory

2.1   Crystallization

In the following subchapter fundamental principles and concepts to understand how a liquid is crystallizing and which measures have to be undertaken to possibly prevent it. In a first section the basic thermodynamic concept will be discussed, basically describing the tendency and motivation of a liquid to form a crystal, followed by kinetic considerations, that basically describe how much time the liquid needs to actually form the crystal that is predicted by the thermodynamics.

2.1.1 Thermodynamic Considerations

The formation of the crystal, such as any system out of condensed matter, is always motivated by the minimization of the Gibbs free energy. At constant pressure and temperature, the Gibbs free energy is defined as:

$$G = H - TS \tag{2.1}$$

, where H is the enthalpy, T the temperature and S the entropy. The Gibbs free energy incorporates the two main driving forces for a system to undergo a transformation by any means. On the one hand the urgency of the system to minimize its potential energy through ordering, described by the enthalpic term of Eq. (**2.1**). On the other hand, its striving towards the highest possible entropic state caused by the thermal energy that is stored in the system included via the second term of Eq. (**2.1**).[4] When more than one phase is occurring in a system, such as the liquid and crystalline state, each state can be described by an individual Gibbs free energy curve. The system will then always strive towards the state that possesses the lowest Gibbs free energy at given pressure and temperature. Hence, the most stable for a given temperature and pressure is always well defined.

---

[4] The counteraction of enthalpic minimization and entropic maximization leads to the negative sign in Eq. (2.1)

To understand the process of glass formation and how cooling of a liquid below its original thermodynamic boundaries of existence is possible, one has to review how a crystal, the natural enemy of the liquid below its temperature of fusion T_f is formed. The temperature of fusion itself is defined as the point of equilibrium between the Gibbs free energy of the liquid G_l and the crystal G_x, which marks the intersection of both curves in the graphic of Figure 2-1 [5]. Below T_f, the difference between the liquid and crystalline Gibbs free energy ΔG^{l-x} creates a thermodynamic driving force for the transition of the liquid to the crystal. It is defined by

$$\Delta G^{l-x}(T) = \ G_l(T) - G_x(T)$$

$$= (H^l(T) - TS^l(T)) - (H^x(T) - TS^x(T)) \tag{2.2}$$

$$= \ \Delta H^{l-x}(T) - T\Delta S^{l-x}(T)$$

, with ΔH^{l-x} being the difference in enthalpy between the liquid and crystalline state, also called excess enthalpy and ΔS^{l-x} being the difference in enthalpy between the liquid and crystalline state, also called excess entropy. The latter quantities can be derived from the isobaric heat capacities of the liquid c_p^l and crystalline state c_p^x together with knowledge of the enthalpy of fusion and the temperature of fusion by using:

$$\Delta H^{l-x}(T) = \ \Delta H_f + \int_{T_f}^{T} \Delta c_p^{l-x}\,(T')dT' \tag{2.3}$$

$$\Delta S^{l-x}(T) = \ \Delta S_f + \int_{T_f}^{T} \frac{\Delta c_p^{l-x}}{T'}(T')dT' \tag{2.4}$$

, with Δc_p^{l-x} being the excess isobaric heat capacity being defined as:

$$\Delta c_p^{l-x} = \ c_p^l - c_p^x \tag{2.5}$$

---

[5] Whereas, the temperature of fusion is rather a definition from a theoretical point of view, in application the temperature of melting T_m or liquidus temperature T_l are used. However, using them synonymously would be incorrect. In a multi-component system, as it is mainly the case, (outside the eutectic point) no congruent melting point, but a melting region is found that has its upper (the liquidus temperature) and lower limit (the solidus temperature or melting point). The melting temperature and liquidus temperature do only coincide for a one-component system or in the eutectic point of a multicomponent system, marking the only case where they are identical to the temperature of fusion.

Both the isobaric heat capacity of the liquid and of the crystalline state can be described by different polynomials, often called "Kubaschewski equation" [38]:

$$c_p^l(T) = 3R + aT + bT^{-2} \qquad (2.6)$$

$$c_p^l(T) = 3R + cT + dT^2 \qquad (2.7)$$

, with R being the universal gas constant (R = 8.314 J mol^{-1}K^{-1}) and a, b ,c and d being fitting parameters.

A detailed justification on the interpretation of $\Delta G^{l\text{-}x}$ in multi-component systems is being presented in Refs. [37,39]
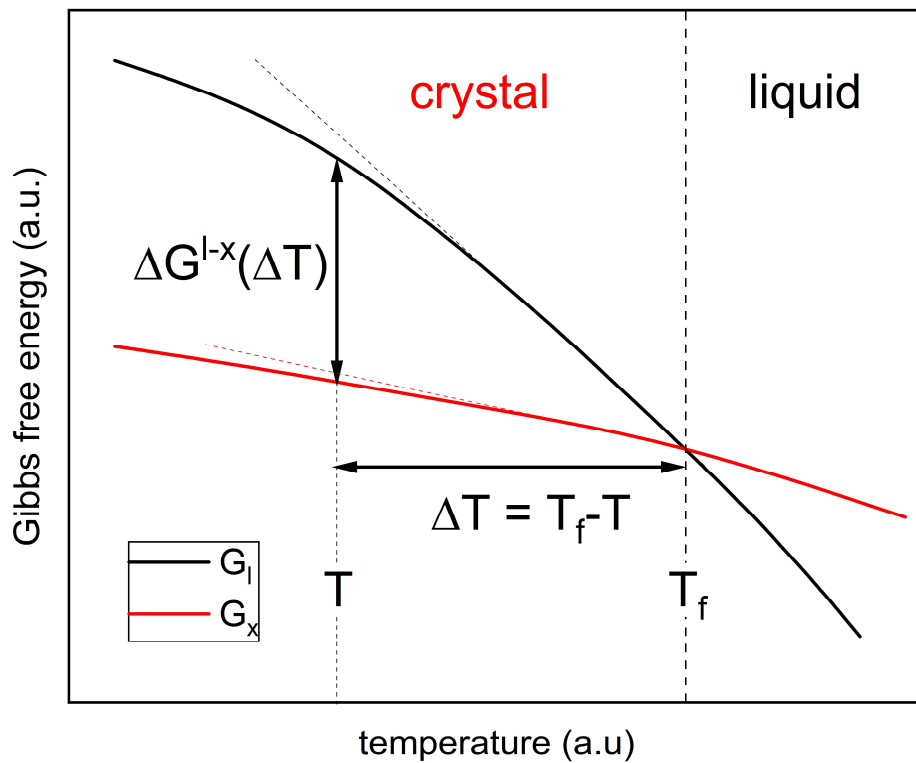
Figure 2-1: Gibbs free energy of the liquid G_l and the crystalline state G_x as a function of temperature . Below the temperature of fusion T_f the difference between G_l and G_x, $\Delta G^{l\text{-}x}$ is acting as the thermodynamic driving force for crystallization of the liquid.

Whenever a volume V_x of the liquid crystallizes the Gibbs free energy of the system changes by a volumetric contribution $\Delta G_V = V_x \, \Delta g^{l\text{-}x}$, with $\Delta g^{l\text{-}x}$ being the difference in Gibbs free

energy between the liquid and the crystalline phase per volume[6]. It shall be noted that below the temperature of fusion Δg^{l-x} becomes negative, which makes the whole ΔG_V term negative, which means that the systems energy is decreased. However, the crystalline surface A_x that is creates an interface to the surrounding liquid phase, which is energetically unfavorable, generating a surface dependent contribution $\Delta G_A = A_x \, \gamma_{l-x}$, with γ_{l-x} being the surface energy between the liquid and the crystalline state. In total the change of the Gibbs free energy due to the formation of a crystalline particle can be described by:

$$\Delta G(r,T) = V_x \Delta g^{l-x}(T) + A_x \, \gamma_{l-x}$$

(2.8)

Under the assumption of a spherical crystalline particle, which itself has the highest volume to surface ratio, Eq. (2.8) becomes:

$$\Delta G(r,T) = \frac{4}{3} \pi r^3 \Delta g^{l-x}(T) + 2\pi r^2 \gamma_{l-x}$$

(2.9)

In Figure 2-2 the volume and surface contribution as well as its balance are illustrated for a spherical particle as a function of its radius. The question whether a given crystalline particle will start to grow or even shrink mainly depends on the change of ΔG with respect to the change of the radius. Mathematically speaking, this means that

$$\frac{d\Delta G(r^*)}{dr} = 0$$

(2.10)

, with r^* being the critical radius, which marks the turning point, graphically described by the maximum of the balance curve in Figure 2-2. On the one hand, if the slope of the curve is positive, additional energy is needed for the growth of the particle and it will be energetically motivated to dissolve. On the other hand, if the slope of the curve is negative, the system will gain energy by further growth of the nuclei. Applying the Eq. (2.10) to Eq. (2.9) the critical radius can be described as

---

[6] The volumetric Δg^{l-x} can be easily derived from the molar ΔG^{l-x} by dividing it by the molar volume V_m.

$$r^*(T) = \frac{2\,\gamma_{l-x}}{\Delta g^{l-x}(T)} \tag{2.11}$$

For the given size of a critical particle r^* the Gibbs free energy already possesses a value, which acts as an activation energy or nucleation barrier for supercritical growth of nuclei ΔG^*. This amount of energy is needed to form supercritical nuclei. It can be calculated by inserting Eq. (2.11) into Eq. (2.9) and leads to

$$\Delta G^*(T) = \frac{16\pi\,\gamma_{l-x}{}^3}{3\Delta g^{l-x}(T)^2} \tag{2.12}$$

Both the nucleation barrier ΔG^* as well as the critical radius r^* have a temperature dependence, based on the growth of the difference in Gibbs free energy between the liquid and crystalline state Δg^{l-x} when the undercooling $\Delta T = T_f - T$ is becoming larger. The temperature dependence of ΔG^* and r^* can be estimated by applying the Turnbull approximation, which assumes a constant c_p for small undercoolings. Therefore, the Δg^{l-x} can be linearly approximated by:

$$\Delta g^{l-x}(T) = V_m{}^{-1}\frac{\Delta H_f}{T_f}\,\Delta T = \Delta S_f \Delta T \tag{2.13}$$

with ΔH_f being the enthalpy of fusion and ΔS_f being the entropy of fusion[7]. From Eq. (2.13) it also becomes obvious that the melting entropy plays decisive role on the driving force for crystallization, as it in a first approximation is describing its temperature dependence with undercooling. Applying this approximation to Eqs. (2.11) and (2.12) leads to:

$$r^*(T) = \frac{2\,\gamma_{l-x}T_f}{\Delta H_f \Delta T} \tag{2.14}$$

$$\Delta G^*(T) = \frac{16\pi\,\gamma_{l-x}{}^3}{3\Delta H_f{}^2 \Delta T^2} \tag{2.15}$$

---

[7] The entropy of fusion is derived from the quotient of enthalpy of fusion and temperature of fusion, which is derived from $\Delta G(T_f) = 0 = \Delta H_f - T_f \Delta S_f$.
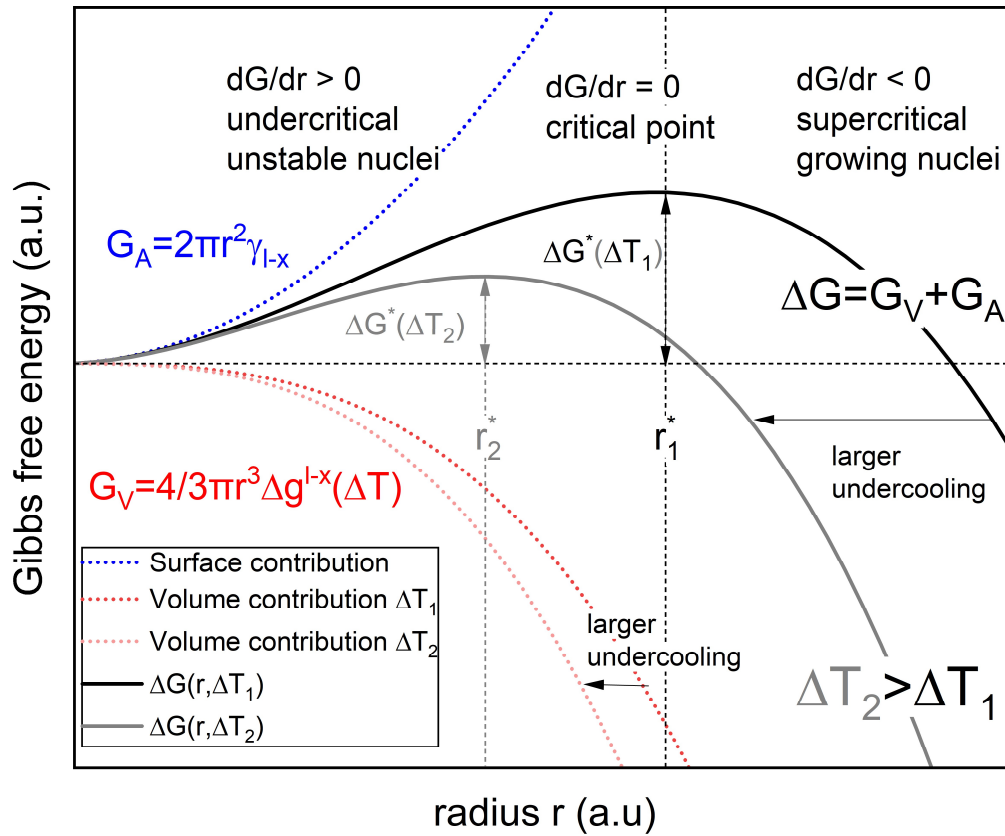
Figure 2-2: Change Gibbs free energy during the formation of a spherical crystalline nuclei with radius r, together with the individual contributions of surface and volume. The maximum in the net-contribution marks the critical radius r^* with its activation energy for crystallization ΔG^{*}[8]. Crystalline particles with larger radii than r^* are named supercritical as their growth is energetically favorable. Vice versa, smaller undercritical particles are energetically motivated to shrink and finally dissolve again. For larger undercoolings (ΔT_2) the volume contribution becomes stronger, as the conversion from liquid to crystalline structure is associated to a larger gain in energy (Δg^{l-x} becomes larger). This shifts the absolute Gibbs free energy curve to lower radii, leading to smaller critical radii ($\Delta r^{*}_2 < \Delta r^{*}_1$) as well as a decrease of the activation energy for crystallization ($\Delta G^{*}(\Delta T_2) < \Delta G^{*}(\Delta T_1)$).

Hence, from a thermodynamic point of view the tendency of the liquid to crystallize is growing as the critical radius is decreasing linearly and the nucleation barrier is decreasing quadratically with further undercooling. A depiction of the interplay of difference in Gibbs free energy and the critical radii and nucleation barrier is exemplarily shown in Figure 2-3, based on actual experimental data. The initial formation of nuclei is driven by thermal fluctuations in the melt that lead to the occurrence of locally ordered clusters of size r. As these thermal fluctuations

---

[8] The quantity ΔG^{*} is also called nucleation barrier for crystallization.

are stochastically distributed in size and location throughout the melt volume, the described lowering of r* will lead to a higher probability or higher number of these ordered clusters to become supercritical. The number of these supercritical clusters per volume n* can be described by [40]:

$$n^*(T) = n_0 exp \left(\frac{\Delta G^*(T)}{k_B T} \right)$$

(2.16)

with k$_B$ being the Boltzmann constant (k$_B$ = 1.380649 × 10^{-23} m^2 kg s^{-2} K^{-1}) and n$_0$ being the number of atoms in the system. While for the supercritical nuclei further and further growth through new atoms attaching on its surface is predicted by the thermodynamics, no predication about the rate can be provided.
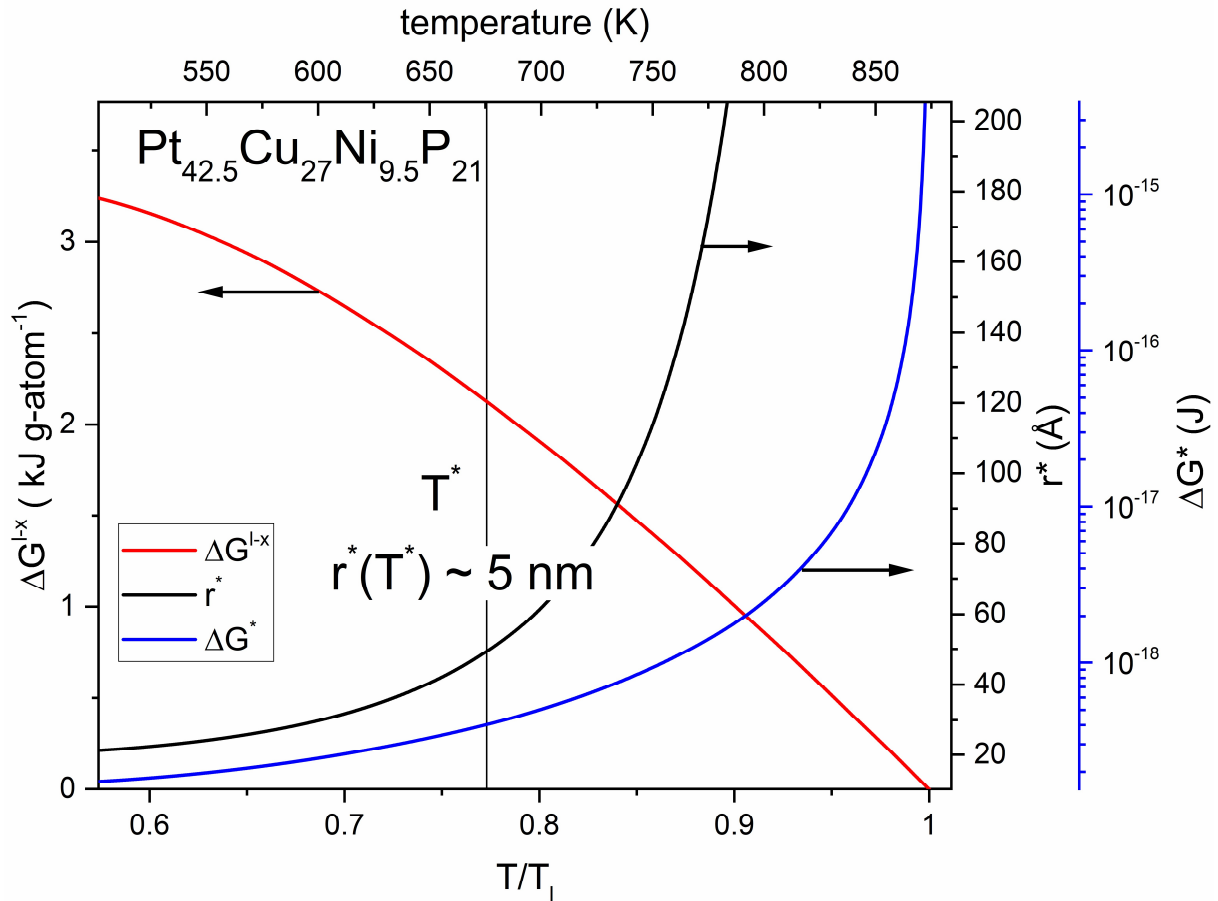
Figure 2-3: Effect of undercooling on the difference in Gibbs free energy between the liquid and crystalline ΔG^{L-x}(T) and the resulting changes in the critical radius r* and the energy barrier for nucleation ΔG^* for the Pt$_{42.5}$Cu$_{27}$Ni$_{9.5}$P$_{21}$ liquid. The curves are derived from experimental data from Gross et al. [41]. The calculations further reveal a critical radius for crystallization at the temperature of minimum isothermal crystallization time T* of 5 nm.

2.1.2 Dynamic Considerations

Based on the thermodynamic considerations, that show the continuous lowering of the activation energy and the critical radius of nucleation, the crystallization of the liquid seems inevitable. Still as thermodynamics is describing equilibrium processes, the factor of time is basically neglected. This means that the mobility of the structural units and atoms, which need to rearrange to the form a crystal, namely the dynamics of the liquid needs to be considered. Especially the rate in which they attach to the growing nucleus.

One way to describe the mobility of atoms is their diffusivity. The diffusivity of atoms in a multicomponent system can be described by an average atomic diffusion coefficient D:

$$D(T) = a_0{}^2 v(T) = a_0{}^2 v_0 \, exp\left(\frac{E_A}{k_B T}\right) \tag{2.17}$$

, where a_0 is the average atomic diameter, v is the atomic jump frequency and v_0 the vibration frequency of the atoms. The average atomic diffusion coefficient D, a microscopic property, can be connected to the shear viscosity η, a macroscopic property of the liquid, via the Stokes-Einstein (SE) relation[9]:

$$D(T) = \frac{k_B T}{6\pi\eta(T)a_0} \tag{2.18}$$

This relation provides a vital tool as the macroscopic measurements of shear viscosity can be used to estimate the mobility of atoms, which itself is often hard to access experimentally. A more detailed description of the SE-relation and general description of viscosity is given in the section 2.2 "Liquid State".

2.1.3 Crystal Nucleation and Growth

As described in the former subchapters the nucleation and growth of a crystal depends on the thermodynamic and kinetic properties of the system. Both attributes are combined in the critical

---

[9] The temperature region in which the Stokes-Einstein relation is valid is an ongoing research topic with numerous experimental evidence of good agreement but also significant deviations at various systems and temperatures.

nucleation rate for steady state[10] I_v, which is a product of the relative available number of overcritical nuclei (Eq. (2.16)) and the atomic jump frequency (Eq. (2.17)).

$$I_v(T) = Av(T)\frac{n^*(T)}{n_0} = Av(T)exp\left(\frac{\Delta G^*}{k_BT}\right) \qquad (2.19)$$

, with A being a constant. Applying the Eqs. (2.15) and (2.18) to Eq. (2.19) leads to [42]:

$$I_v(T) = \frac{A_v}{\eta(T)}exp\left[\frac{-16\pi\gamma_{l-x}^3}{3k_bT[\Delta g^{l-x}(T)]^2}\right] \qquad (2.20)$$

, where A_v is a constant.

The rate at which the surface of an overcritical crystalline nucleus is growing is described by [43]

$$u(T) = \frac{f_rk_bT}{3\pi a_0^2\eta(T)}\left[1 - exp\frac{V_{atomic}\Delta g^{l-x}(T)}{k_bT}\right] \qquad (2.21)$$

where V_{atomic} is the atomic average volume, and a_0 is the average atomic diameter. The factor f_r depends on the roughness of the interface between the crystal and liquid on an atomic scale [44].

Ultimately, the crystallization process is based on the interplay of both, crystal nucleation and growth, originating from thermodynamics of crystal and liquid and dynamic properties of the liquid. In Figure 2-4 the temperature dependence of both, $I_v(T)$ and $u(T)$, are depicted. The interplay of thermodynamics, which will always favor crystallization of the undercooled liquid, and dynamics which will consecutively become more sluggish during cooling leads to $I_v(T)$ and $u(T)$ each possessing a maximum. The crystal growth rate $u(T)$ is showing its maximum at high temperature and low undercooling, whereas the nucleation rate is still very low, as there is not enough driving force for crystallization compared to the interfacial energy. This is based on the high mobility of atoms and low viscosity at this elevated temperature close to T_l. Once an overcritical nucleus is formed in this temperature region, rapid crystallization will occur directly based on the very high growth rate. A small number of fast-growing crystals will then lead to a

---

[10] The steady state describes a state which is time independent. The steady state is an assumption that may not always apply in the application.

coarse microstructure. Hence, the crystallization is nucleation controlled and therefore highly statistical in the temperature regime close to T_l. In contrast, at lower temperatures, mainly observed upon heating from the glassy state, the supply of overcritical nuclei is not the limiting factor but their ability to grow, as atomic mobility and therefore crystal growth has slowed down tremendously due to the exponential increase of viscosity. Consequently, the large number of slowly growing overcritical nuclei leads to a fine-grained even nanocrystalline microstructure that is growth controlled.
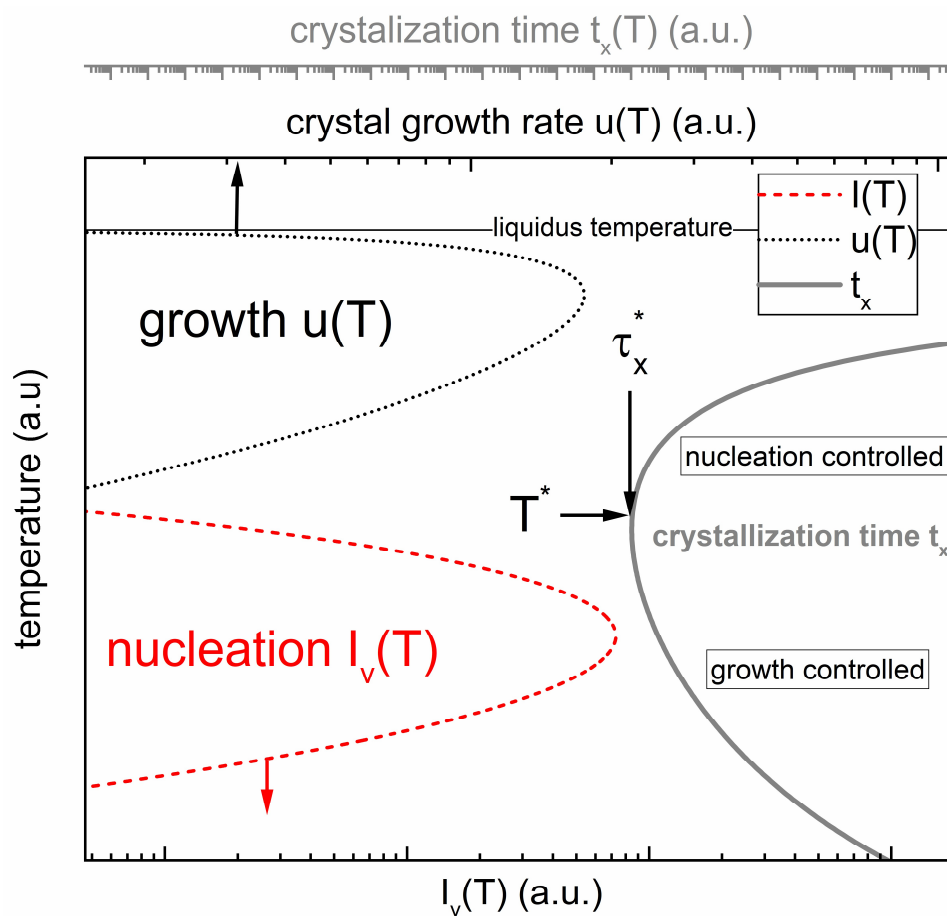
Figure 2-4: Temperature dependence of crystal nucleation and growth rate and its connection to the crystallization time. The maximum of the crystal growth rate u is located at temperature close to the liquidus temperatures and the maximum of the nucleation rate $I_v(T)$ is located at higher undercooling, where the driving forces for crystallization are already sufficiently high. The interaction of both, nucleation and growth, leads to the typical shape of the isothermal crystallization times (grey). The minimal crystallization time t_x^* is located between the two maxima of I_v and u at the temperature T^*, where the interaction of both is the highest. In the upper temperature range a high growth rate will lead to a rapid crystallization once a supercritical nuclei is formed (nucleation-controlled crystallization), whereas in the lower temperature regime the availability of overcritical nuclei is not the issue, but its ability to grow (growth-controlled crystallization).

A good description of crystallization, combining $I_v(T)$ and $u(T)$, that is derived from classical nucleation theory, is given by the Johnson-Mehl-Avrami-Kolmogorov model. It contains several further assumptions such as a spherical growth of the nuclei and a polymorphic crystallization. Under these restraints the crystallized fraction $x(t)$ at a given time t of an undercooled liquid under isothermal conditions can be described [45]:

$$x(T) = 1 - exp\left(\frac{\pi}{3}I_v(T)u(T)^3 t^4\right) \tag{2.22}$$

Vice versa the time for a given fraction of the system to crystallize can be calculated by:

$$t_x(T) = \left[\frac{-3ln(1-x)}{\pi I(T)[u(T)]^3}\right]^{1/4} \tag{2.23}$$

Time-temperature transformation (TTT) diagrams are often used in application, for a graphical description of the crystallization behavior. A TTT diagram in general describes the stability of phases and their transformation with time at a given temperature (isothermal) or during an applied cooling/heating rate (continuous). In following a focus is put on the isothermal crystallization behavior as it can be directly modeled with the JMAK-equation. In Figure 2-5 an example is provided how the JMAK equation is being applied to fit experimental data of isothermal crystallization experiments.

Ultimately, $I_v(T)$ and $u(T)$ determine the C-like or nose-like shape of the TTT diagram, as well as the localization of the minimum crystallization time τ_x^*. The minimum crystallization time τ_x^* is located at the temperature T^*, where the declining growth rate and the growing nucleation rate superimpose in the most constructive way. It is directly connected to the critical cooling rate (CCR) and critical casting thickness d_c via the empirical relation developed by Johnson et al. [46]:

$$\tau_x^* = 0.00419(d_c/mm)^{2.54}s \tag{2.24}$$
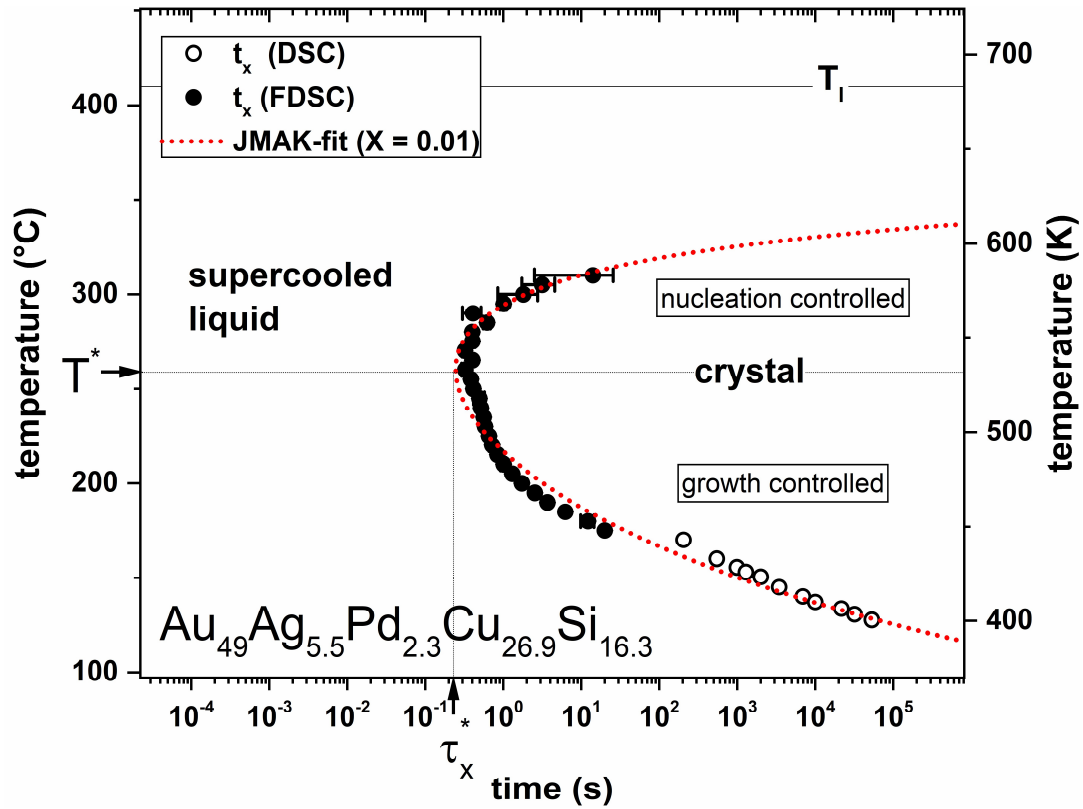
Figure 2-5: Time-temperature transformation diagram of $Au_{49}Ag_{5.5}Pd_{2.3}Cu_{26.9}Si_{16.3}$ based on actual isothermal crystallization data described by the JMAK equation. Adapted from Neuber et al. [47].

2.2 Liquid State

With glasses being often described as frozen-in liquids, it is highly important to understand the basic phenomena of transport and diffusion occurring in the liquid and its connection to thermodynamic and structural properties. Especially, the dynamic slowdown during the supercooling of densely packed metallic liquids plays an essential role during glass formation and the microscopic effects are widely not well understood and are subject to current research.

2.2.1 Dynamics of the Liquid: Viscosity and Fragility concept

The dynamics of the liquid state is a property of the (metastable) equilibrium liquid basically covering different length scales down from atomic motion up to the resulting macroscopic flow behavior. One common way to characterize the dynamics of the liquid is the shear viscosity. The shear viscosity of a liquid describes its fluidity and is a measure of its inner resistance against external forces to flow. The dynamic viscosity η is defined as the proportionality factor between the shear rate $\dot{\gamma}$ and shear stress τ_{xy}:

$$\eta = \frac{\tau_{xy}}{\dot{\gamma}}$$
(2.25)

The dynamic viscosity of a liquid depends on the cooperative motion of the individual structural units that have to overcome energy barriers E_A to be able to flow. This process can be described by a constant activation energy, a simple Arrhenius behavior, following the exponential behavior:

$$\eta(T) \propto exp\left(\frac{E_A}{k_B T}\right)$$
(2.26)

This most straightforward description of thermally activated processes is assuming a temperature invariant energy barrier, which in reality is not the case. In liquids it is observed that the activation energy is actually growing with further undercooling. However, this growth of the activation energy is strongly differing between the different liquids and seems to be strongly connected to their structure [48–50]. This makes the viscosity of a liquid a highly temperature-dependent and sensitive quantity that can change by several orders of magnitude over small temperature intervals. Therefore, it qualifies to be used to characterize and classify different types of liquids. One concept to distinguish between the different sensitivities of viscosity to temperature changes is the so-called fragility concept [51]. Alike its name it describes the sensitivity of viscosity towards changes in temperature. If it undergoes large changes due to changes in temperature, it behaves fragile, or vice versa. Besides this pictorial explanation, from a physical point of view, the fragility concept actually characterizes the deviation of viscosity from the aforementioned Arrhenius behavior. Arrhenius behavior means that the thermally activated process can be described by a temperature invariant activation energy E_A. Consequently, liquids with less temperature dependent activation energies are labeled strong, whereas liquids with larger changes in their activation energies during cooling are termed fragile.

In a typical depiction, the logarithmic viscosity is plotted over inverse temperature, which leads to a linear behavior in the case of a strong liquid, whereas a fragile liquid shows exponential changes on the logarithmic scale (compare Figure 2-6). In this so-called "Angell-plot" the inverse temperature is normalized by the glass transition temperature T_g^*. It is defined as the temperature, at which the liquid possesses a viscosity value of 10^{12} Pas and leads to all liquids sharing the same point at $T_g^*/T = 1$. The use of the 10^{12} Pas value comes from the first studies of glass-forming liquids carried out on silicate glasses, which are strong liquids. Therefore,

from a physical point of view, this value should be regarded as a rough empirical guide, especially as it does not consider the rate dependence of the glass transition. Hence the value of T_g^* does not have to be equal to the calorimetrically determined T_g. This divergence between the two temperatures originates from a lower viscosity at the calorimetric glass transition. For molecular glass formers, which are more fragile liquids, viscosities down to 10^{10} Pas are observed at the calorimetric glass transition [52].

The temperature dependence of viscosity that takes the evolution of the activation energy into account, can be mathematically described by the empirical Vogel-Fulcher-Tamann equation:

$$\eta(T) = \eta_0 exp \left(\frac{D^* T_0}{T - T_0} \right) \qquad (2.27)$$

with D^* being the fragility parameter and T_0 the so called VFT temperature, at which the viscosity would diverge to infinity. The physical value of this VFT temperature is widely discussed, but it is suggested that for good glass formers T_0 lays further away from T_g than for bad glass forming liquids [51,53]. The η_0 parameter describes the lowest possible viscosity in the theoretical limit of infinite temperature. It is physically connected to the Debye frequency and can be estimated by [54]:

$$\eta_0 = \frac{N_A \cdot h}{V_m} \qquad (2.28)$$

With $N_A = 6.022$ x 10^{23} being Avogadro's number, $h = 6.626$ x 10^{-34} m^{2}kgs^{-1} being Planck's constant and V_m being the molar volume.

In the framework of the fragility concept being described by eq. (2.27), strong liquids possess large D^* values, for example SiO_2 with a D* of 100 and fragile liquids possess a small D^* for example ortho-terphenyl with a D^* of around 5. Metallic glass forming systems have a D^* between values of about 10 to around 30.
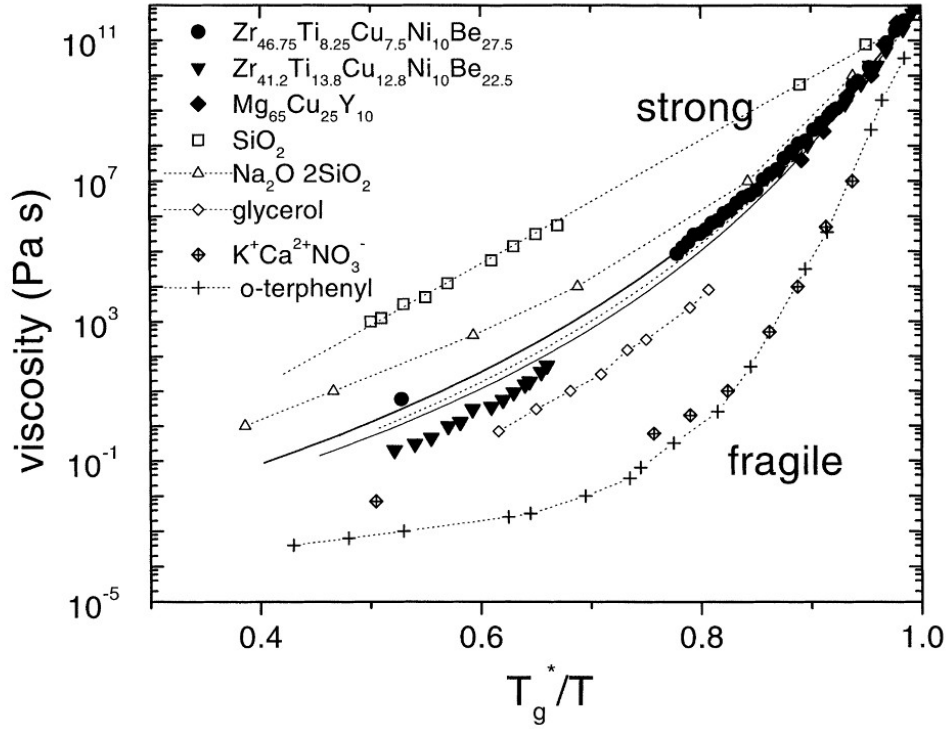
Figure 2-6: Angell plot for various glass formers reaching from strong glass formers like SiO_2, that show a linear Arrhenius behavior, over metallic glass forming liquids with mediocre fragilities to extremely fragile systems like o-terphenyl. Taken from Busch et al. [53].

Another way to describe fragility is via the steepness of the shear viscosity around the glass transition. This parameter is often useful, when only viscosity values around the glass transition are known. In this case the fragility is directly quantified by the linear slope of the viscosity in the Angell plot at T_g^*. Fragile behavior is therefore characterized by a steep slope and stronger behavior vice versa. Mathematically this so called steepness index or m-fragility can be expressed by [55]:

$$m = \left. \frac{\partial log_{10}\left(\eta\right)}{\partial \frac{T_g^*}{T}} \right|_{T=T_g^*} \tag{2.29}$$

To further understand the meaning of the viscosity and its connection to the atomic mobility one has to interpret it as the ability of a liquid to transfer a momentum, which in a first approximation is similar to a diffusive process. This approach is the base of the so-called Stokes-Einstein equation, that combines the viscosity and diffusion coefficient. The basic idea is the internal friction that a particle with given radius r experiences whilst travelling through a

liquid with viscosity η, which leads to the Stokes-Einstein relation (2.18) mentioned in section 2.1.2

Based on the validity of this equation, measurements and classifications of viscosity allow a direct insight into the atomic mobility of the melt. Still, it seems surprising that an initially macroscopic model, such as the Stokes-friction model, is still valid on the atomic scale, where the particle is of the same size as the structural units of the surrounded liquid. Its validity was widely accepted under stable equilibrium, while studies have shown a good agreement of this relation, even in the deeply undercooled state of a $Pd_{43}Cu_{27}Ni_{10}P_{20}$ metallic liquid [56]. However, recent studies described its break-down already in the equilibrium liquid [57], while the breakdown itself has been assigned to the rise of dynamic heterogeneities below a critical point. However, the detailed process is far from well understood and part of ongoing research.

Another way to connect a timescale to the viscosity of the liquid is the viscoelastic model. Under the assumption of the liquid being described by a Maxwell unit, which is a series connection of a damper and a spring, a relaxation time τ can be described by

$$\tau = \frac{\eta}{G_\infty} \tag{2.30}$$

, where G_∞ is the high frequency shear modulus. It characterizes the viscous response of a Maxwell unit at an infinite loading frequency. It can be used to connect the intrinsic relaxation time of the liquid with the macroscopic viscosity. In actual experiments with the aim to determine relaxation times, this relation has to be used with caution, as the probed timescale does not have to be similar to the intrinsic relaxation time of the mechanical model described in eq. (2.30). As a consequence the proportionality between the experimental relaxation time τ_{exp} is not described by the high frequency shear modulus G_∞ but a different proportionality generic factor $G_{\tau\text{-}\eta}$ that is specific for the actual measurement method [36]. While it might seem arbitrary at first, the need of several $G_{\tau\text{-}\eta}$ can be physically justified by the fact that not a single relaxation time in the liquid but a relaxation spectrum is expected, but only a single macroscopic viscosity can be probed. Therefore, depending on the part of the spectrum being probed, it becomes a natural need of different proportionality factors. However, the general proportionality of τ and η allows to also use the VFT equation (2.26) to also describe the temperature dependence of the relaxation time, featuring the same temperature dependence [58].

2.2.2 Thermodynamics of the Liquid: Heat Capacity, Entropy and Thermodynamic Fragility

As mentioned in the prior chapter, as a liquid cools, there is an increase in the cooperativity of the structural units, which is accompanied by changes in the dynamic properties, i.e. an increase in viscosity and a slowing of the intrinsic relaxation time. Hence, the question arises how the thermodynamic properties such as heat capacity, enthalpy and entropy change in the meantime.

The Adam Gibbs model, that originally aimed to better understand the super-exponential growth of the relaxation time in the vicinity of the glass transition, ultimately provided an idea of the changes of configurational entropy in an undercooled liquid [59]. Their theory was built upon the idea that during undercooling a decreasing number of possible configurations will be assessable to the atoms/molecules of the liquid. This decreased access would then be directly characterized by a decrease of the configurational entropy of the liquid. Therefore, they considered that the dynamic quantity X, i.e. viscosity η or relaxation time τ can be described as a function of the configurational entropy S_c by:

$$X(T) = X_0 \, exp \left(\frac{C}{T S_c(T)} \right) \tag{2.31}$$

with C being the energy barrier for cooperative rearrangements and X_0 being the value of the dynamic quantity that is described at infinite temperature. However, the actual experimental quantification of the configurational entropy is far from trivial and not directly possible. Instead, the experimentally easier assessable quantity of the excess entropy between liquid and crystalline state ΔS^{l-x} is used, which can be calculated from heat capacity measurements of crystalline and liquid state, as well as a determination of the entropy of fusion ΔS_f (compare section 2.1.1). The excess entropy however consists out of a vibrational term S_{vib} together with the configurational term S_c described by[11]:

$$\Delta S^{l-x} = S_{vib}^{l-x} + S_c^{l-x} \tag{2.32}$$

---

[11] It is important to note that here the configurational and the vibrational terms describe the difference between the liquid and the crystalline state as well.

An actual decoupling of these quantities is possible by neutron scattering experiments that allow the determination of the vibrational entropy of the liquid and the glassy state, exemplarily shown by Fultz et al. [60]. These measurements showed similar vibrational entropies in the crystalline and liquid state in the case of Zr-based metallic glasses, which would lead to a cancelation of the first part of equation (2.32), making the difference in excess entropy purely configurational. Under this assumption the dynamics can be described well using the excess enthalpy in eq. (2.31). However, besides this explicit experimental data the assumption is still highly controversial in the scientific community [58,61].

A possible reasoning on the success of this assumption is provided by Martinez et al. [62], noting the similar temperature dependence of S_c and ΔS^{l-x}. When reviewing the changes of configurational entropy with respect to temperature

$$\left.\frac{\partial \Delta S^{l-x}}{\partial T}\right|_p = \frac{\Delta c_p^{l-x}}{T} \tag{2.33}$$

It becomes obvious that large changes are connected to large differences in excess heat capacity. With the differences in isobaric heat capacity of crystalline and glassy state being insignificantly small, Δc_p^{l-x} can be seen equal to the excess heat capacity with respect to the glassy state Δc_p^{l-g12}. Based on this, the T_g normalized height of the c_p step at the glass transition temperature, $\Delta c_p^{l-x}(T_g)/T_g$, should already entail information on the thermodynamic fragility. A large value of $\Delta c_p^{l-x}(T_g)/T_g$ would be the signature of a faster rising liquid heat capacity associated with the high rate of loss in configurational entropy of the liquid during cooling, which would be a fragile behavior. Vice versa small $\Delta c_p^{l-x}(T_g)/T_g$ suggest a flatter course of the liquid heat capacity, smaller rate of loss in the configurational entropy, typical for a stronger behavior. However, this direct correlation may only be valid if the absolute entropy of the systems is not significantly changing, as the fragility is mainly based on the relative change. These changes of absolute entropic level may be due to changes in the entropy of fusion, as the high temperature limit of ΔS^{l-x} is actually determined by it. (compare eq. (2.4))

For a better understanding the course of the thermodynamic functions of heat capacity and entropy of the liquid state shall be reviewed for an exemplary fragile and strong liquid in the

---

[12] Similar argumentation applies for the use of the excess entropy with respect to crystal or glass.

following and also compared to the respective course of the viscosity in Figure 2-7. The more fragile liquid, depicted by the black lines, shows a more rapid ascending isobaric heat capacity during cooling. As a consequence a larger c_p - step between the liquid and the crystalline/glassy state is observed at T_g, as the heat capacity of the crystal or the glass is usually of the magnitude of 3 R, following the Dulong-Petite rule [58]. The larger specific isobaric heat capacity of the fragile liquid translates into the larger slope of the excess entropy following the aforementioned argumentation and eq. (2.33). Finally the viscosity of section c) shows a larger change in slope at the glass transition temperature for the fragile system, due to the larger entropic changes described through eq. (2.31).
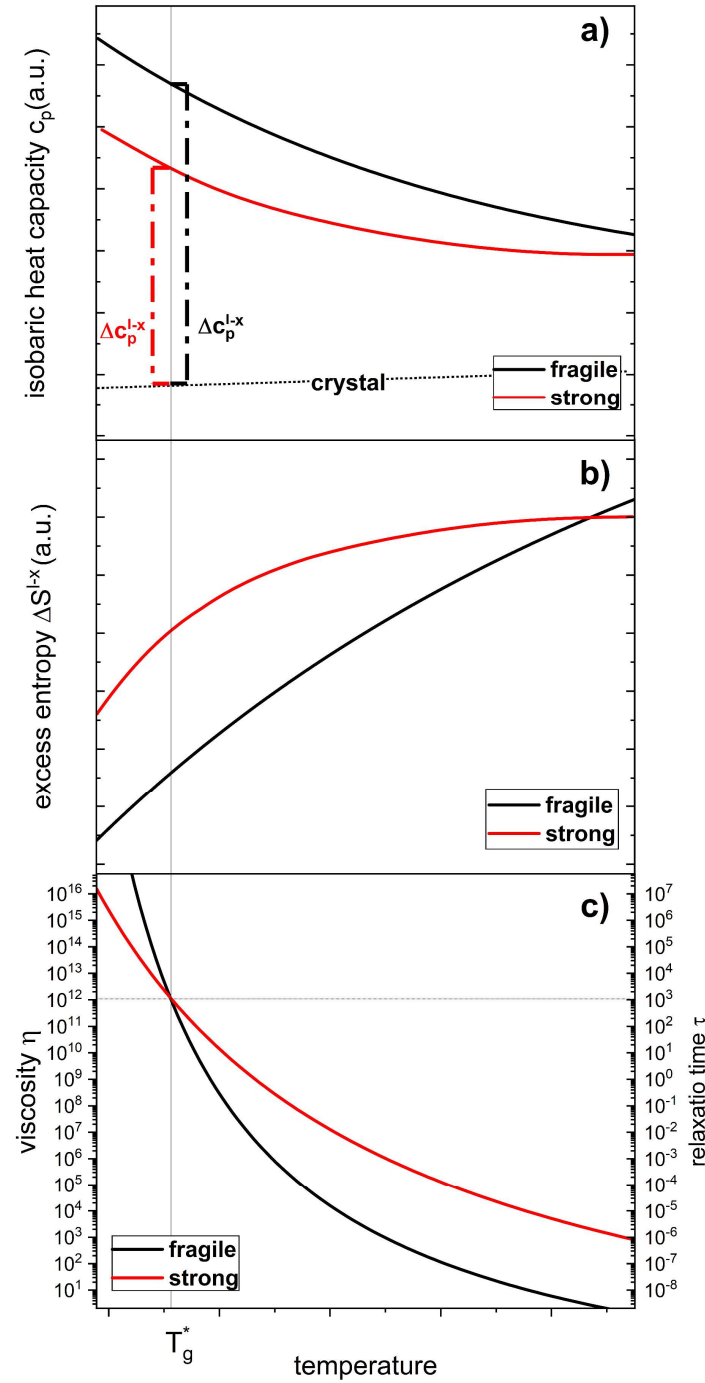
Figure 2-7: Schematic drawing of thermodynamic and dynamic properties of the liquid state as a function of temperature for a strong and a fragile metallic liquid with thermodynamic properties in a) the isobaric heat capacity and b) the excess entropy and the dynamic property in c), the viscosity and relaxation time (translated with a generic $G_{\tau\text{-}\eta} = 10^9$ Pa s). In all cases the fragile system shows more significant changes in the observable compared to the strong system. In section a) also the step in heat capacity between the liquid and crystalline state is depicted, showing a much larger step in $\Delta c_p^{l\text{-}x}$ at the glass transition temperature for the fragile liquid compared to the strong one. Due to the similar values of the heat capacity of the crystalline and glassy state, this difference in $\Delta c_p^{l\text{-}x}$ is also representative for the heat capacity step during the glass transition event $\Delta c_p^{l\text{-}g}(T_g)$

2.3   Glass Transition and Glassy State

In the following section, the basic principles of the glass transition process are presented in a similar manner to the crystallization process.

2.3.1 The Glass Transition process

For a better understanding of the glass transition process in contrast to the crystallization event, it is helpful to study the evolution of the thermodynamic properties i.e. volume V or enthalpy H as a function of temperature. To simplify the problem a one-component system is assumed in the following discussion. The advantage of a one-component system is found in the congruent melting of the system. This means that the melting point T_m and the liquidus temperature T_l becomes one. In contrast, in multicomponent systems, outside of a eutectic, thermodynamic equilibrium is including more than a single phase, leading to a melting interval that is framed by T_m and T_l. Therefore, the temperature of fusion T_f is used in the following, marking the temperature of thermodynamic equilibrium between crystalline and liquid state.

At first the scenario of crystallization shall be reviewed, which resembles the pathway (1) in Figure 2-8. During cooling the volume V and enthalpy H of the liquid decreases, with the slope of the curve being a measure of the volumetric thermal expansion coefficient α_{th} or the specific isobaric heat capacity c_p. Once a liquid is cooled below its temperature of fusion, the crystal becomes the thermodynamically favorable configuration. Below this temperature any volume of the liquid that transforms to a crystal leads to gain of energy. Hence, any nucleus that is large enough to compensate for the energy needed to form the interface between itself and liquid will start to grow. A more detailed description of the process can be reviewed in the section 2.1.3 "Crystal Nucleation and Growth". The ordering during the crystallization process goes in hand with an abrupt jump in volume ΔV_f, due to the denser atomic packing of the crystal, as well as a release of enthalpy ΔH_f[13] because of the enthalpically deeper state of the crystal. It shall be noted that the slope of the crystalline curve is much shallower than that of the liquid

---

[13] In this case the released enthalpy is rather a crystallization enthalpy ΔH_x, which in this ideal case of a crystallization at the melting point would be of the same magnitude as the enthalpy of fusion ΔH_f but with the inverse sign.

curve, which is an expression of the decreased α_{th} and c_p due to the closer packing and reduced number of degrees of freedom in the crystal.
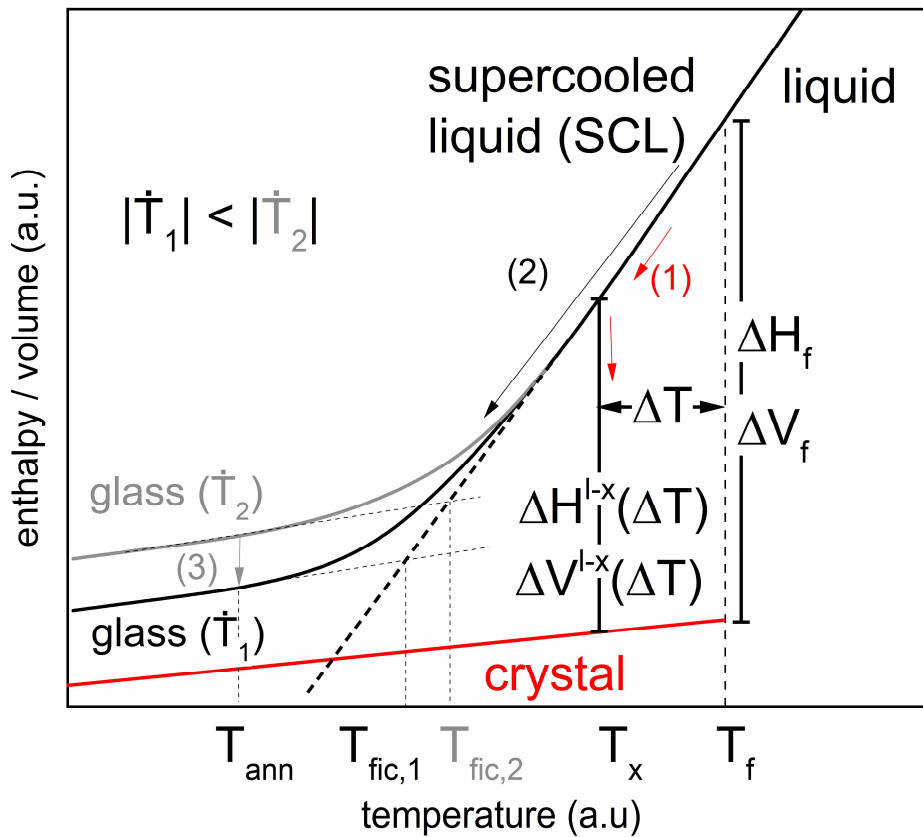
Figure 2-8: Schematic on the evolution of the volume following different pathways during cooling. (1) Slow cooling leading to crystallization and volume shrinkage or release of crystallization enthalpy after certain amount of undercooling

(2) Fast cooling at different rates that lead to a falling out of equilibrium at different fictive temperatures T_{fic} with volumetrically and enthalpically distinct glassy states.

(3) Isothermal annealing at T_{ann} that leads to relaxation of free volume (aging) out of the system, lowering its enthalpic state and consequently the fictive temperature of the glassy state is striving towards T_{ann} over time. The internal equilibrium of the supercooled liquid reached when $T_{fic} = T_{ann}$.

Pathway (2) of Figure 2-8 describes the vitrification process of the liquid. As soon as the liquid is cooled below the temperature of its thermodynamical stability T_f, it is called supercooled liquid (SCL). From a thermodynamic standpoint the SCL is a metastable equilibrium[14], with

---

[14] A system is considered metastable, if it is not the most stable thermodynamic configuration that would be possible under the given conditions.

the crystalline state representing the stable equilibrium. To reach this state, the growth of overcritical nuclei has to be suppressed by a sufficiently high cooling rate q_c as the volume and enthalpy of the system continuously decreases. In the SCL the viscosity of the liquid increases exponentially (compare section 2.5.4.2), which reflects the slowdown of atomic mobility at decreasing temperature. At a certain point the system is cooled faster than it can restore its internal equilibrium based on its mobility. This restoration of the equilibrium due to the external perturbation is called relaxation and defines the temperature dependent relaxation time that is connected to the viscosity. If this relaxation of the system is not possible within the timeframe dictated by the external perturbation, it falls out of equilibrium and the glass transition process progresses. The liquid is then vitrified to a glass. The temperature at which the system undergoes the glass transition in cooling is called fictive temperature T_{fic} and provides a vital tool to define the volumetric, enthalpic and structural state of a glass. In the case of cooling with q_{c1} this leads to the volumetric state of "glass 1". Obviously, the glass transition is not only dependent on the intrinsic properties of the liquid itself but strongly on the external disturbance, in this case the cooling rate. For a higher cooling rate $|\dot{T}_2|>|\dot{T}_1|$ the system is falling out of equilibrium at higher temperatures, leading to a higher T_{fic} combined with a larger volumetric state of "glass 2". Both states merely differ in their packing density, as "glass 2" is even further away from the equilibrium crystal incorporating more so-called free volume V_{free}.

The third pathway (3) in Figure 2-8 shows the influence of isothermal annealing on the glassy state at T_{ann}, which is called relaxation or aging. It is a manifestation of the striving of a system that is brought out of equilibrium, such as any glassy state, towards its (metastable) equilibrium, here the supercooled liquid or crystalline state. Relaxation is a universal phenomenon that is happening to any glass below T_g but can be negligibly slow if $T_{ann} \ll T_{fic}$. During aging the fictive temperature of the system is consecutively striving towards the ambient temperature T_{ann}. A more detailed review on relaxation and aging will be provided in section 2.4.

2.3.2 Thermodynamics of the Glass

Whenever the metastable supercooled liquid is unable to recover and ultimately falls out of equilibrium its momentary structure is frozen in. This frozen-in structure is energetically unfavorable compared to a crystal, which can be characterized by a residual enthalpy or excess free volume, depending on the preferred view. Experimentally, the relative changes in volume and enthalpy of liquids and glasses have been shown to be in good agreement for the relative changes in both quantities, for glasses in general [63] and particularly for metallic glasses [64–

67]. Hence, knowledge of the excess residual enthalpy ΔH_{res} from calorimetric experiments allows to estimate the free volume V_{free} that is stored in the glass [68]. Both quantities can be linked by the empirical equation of Van den Beukel and Sietsma [63] and the experimental validation of Evenson et al. :

$$\Delta H_{res} = \beta' \left(\frac{\Delta V_{free}}{V_m} \right)_{glass} \tag{2.34}$$

,where V_m is the molar volume and β' is the proportionality constant, describing the enthalpy of free volume formation per atomic volume. Knowledge of the free volume is of high consequence for the glassy state as it is connected to manifold properties e.g. diffusion, viscosity and especially plastic flow (more detailed justification is found in section 2.6) [69–71].
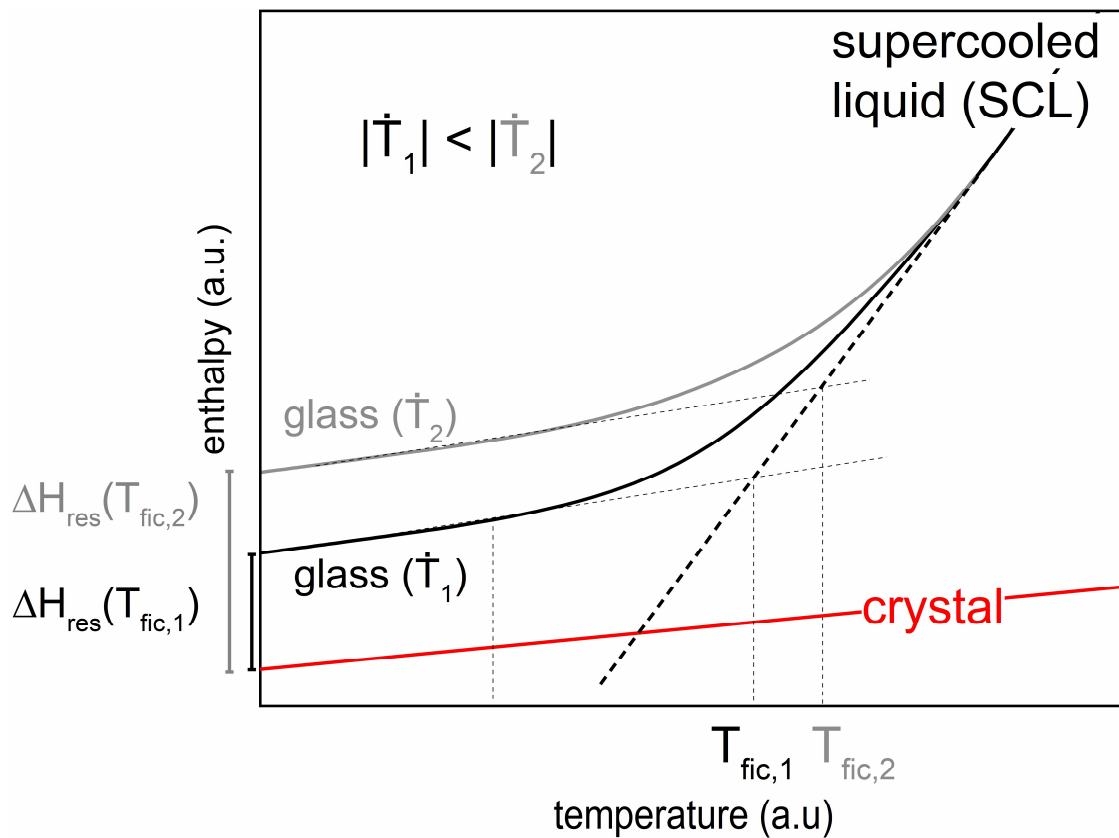
Figure 2-9: Schematic drawing of different residual enthalpies and free volumes of the glassy state created by different cooling protocols . The residual enthalpy of the respective glassy state can be characterized by its fictive temperature.

2.4 Relaxation of the Liquid and Aging of the Glassy State

As the glassy state is thermodynamically characterized as an unstable non-equilibrium state it is always striving towards a more stable configuration closer to equilibrium over time, starting from the very second it is formed. The temporal evolution of the glassy state towards its actual equilibrium is called aging. It is important to distinguish between the two terms relaxation and aging, which are often redundantly used. Unlike aging, which involves a system that is out of equilibrium, relaxation is carried out by a system that is still in equilibrium.

A relaxation phenomenon is always observed, when the system is somehow perturbed. Due to this perturbation a quantity Φ is brought to an out-of-equilibrium state $\Phi_{n\text{-eq}}$. The quantity will immediately strive to recover its equilibrium value Φ_{eq}. The temporal evolution towards its equilibrium, or rather the distance between the temporal state $\Phi(t)$ and the Φ_{eq}, can then be described by a exponential decay function with a relaxation time τ. However, in reality relaxation phenomena of enthalpy, viscosity or volume in glassy systems cannot be well modeled by a simple exponential approach, but rather by a so-called multiexponential or stretched exponential approach, mathematically described by the Kohlrausch-Williams-Watts (KWW) equation [72]:

$$\Phi(t) - \Phi_{eq} = \Delta\Phi(t) = \Delta\Phi(0)\,exp\left(-\left(\frac{t}{\tau}\right)^{\beta}\right) \qquad (2.35)$$

with β being the stretch exponent or shape parameter. In Figure 2-10 the influence of β on the appearance of the relaxation function is depicted. For $\beta = 1$ the KWW describes a single exponential decay, whereas it behaves compressed for $\beta > 1$ and stretched for $\beta < 1$. The stretched relaxation behavior originates from the superposition of multiple relaxation times, i.e. a relaxation spectrum. Hence, the stretch exponent can also be interpreted as a heterogeneity parameter, as a more heterogeneous distribution of relaxation times will lead to a more stretched relaxation event, described by a smaller value of β. To illustrate the influence of multiple relaxation times on the observed relaxation function a combination of seven distinct single exponential decays is depicted in Figure 2-11. In contrast a compressed behavior leads to the relaxation phenomenon being faster than exponential, a so-called Debye relaxation [73]. While this behavior is experimentally observed in the relaxation of the glassy state, a general theoretical explanation is still lacking [73]. Still in some works it is associated to a ballistic or avalanche-like dynamics [74–77]

Within the framework of this thesis the KWW equation is used to describe the viscosity relaxation in thermomechanical analysis (TMA) (compare section 3.5.1) and the decorrelation of density fluctuations in X-ray photon correlation spectroscopy (XPCS) (compare section 3.4.1). More detailed information and peculiarities in the use of the KWW in the individual cases is provided in the specific sections.
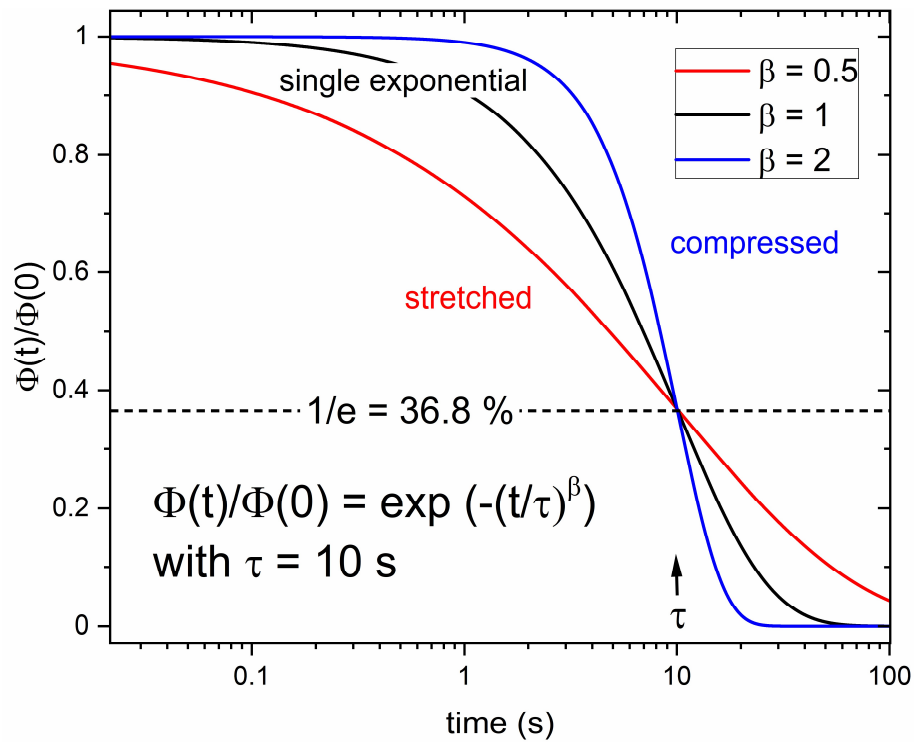
Figure 2-10: Influence of the stretching exponent β on the shape of the multiexponential relaxation function.
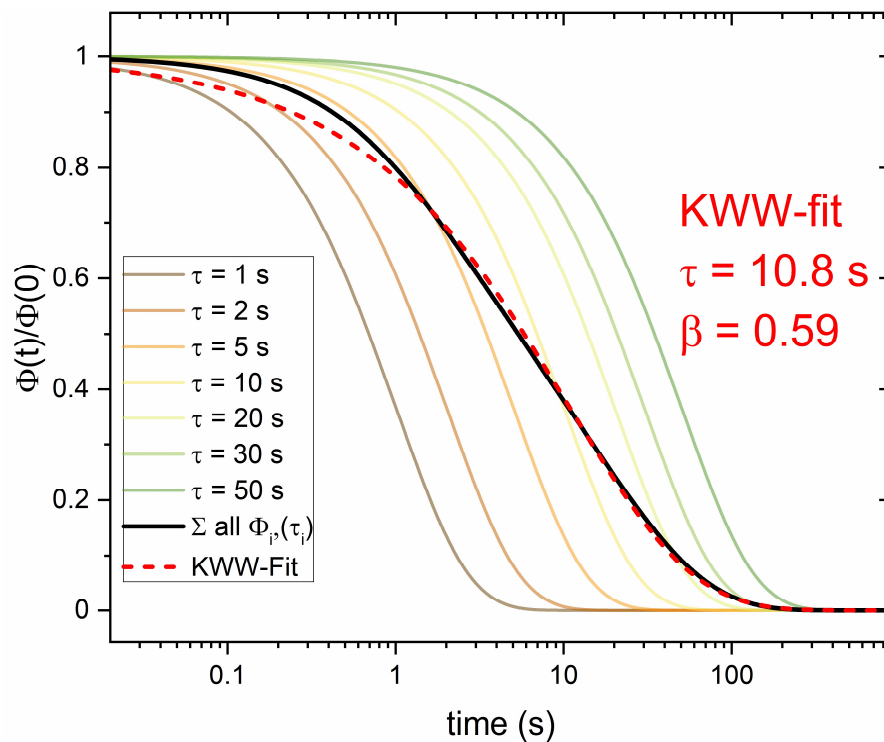
Figure 2-11: Schematic drawing of a relaxation function composed out of multiple single exponential functions ($\beta = 1$) with different relaxation times. The superposition of all relaxation times can be described by the stretched multiexponential relaxation function with a stretching exponent of $\beta = 0.59$. Depiction adapted from Ref. [78].

2.5   Structure of Liquids and Metallic Glasses

In this section a general structure of metallic liquids and glasses shall be provided with basic structural models and present what information can be derived from scattering experiments and how this information is processed.

2.5.1 Order in an Amorphous Structure

Whereas the term amorphous is synonymously used for unordered, this is not completely true. Even the liquid and the glassy state, both amorphous, do possess certain ordering relations and therefore structure. Experimentally this can be easily evaluated by X-ray diffraction, where still a signal can be obtained: broad maxima, also called "amorphous halo". This signal is clearly different to the distinct Bragg peaks that are created from crystalline long-range order, which are more numerous and much sharper. Still, there has to be some certain distribution of order that creates the scattering signal in the liquid and glassy state. Indeed, certain correlations between the nearest atomic neighbors (short-range order, SRO) up to length scales of 1 nm (medium-range order, MRO) can be found. [79] Its origin is motivated by the topology/size of the atoms as well as their chemical nature and resulting preference to be located next to each other (basically characterized by their enthalpy of mixing). In the past 60 years numerous works have been conducted to understand the "order" in the disorder of amorphous solids and liquids and to derive certain laws and rules of how they are composed. A good historical review on the early evolution of structural models in disordered condensed matter can be found from Finney [80], while a more detailed and general overview on the different models of metallic liquids and especially glasses and their connection to the resulting thermophysical properties can be found from Cheng and Ma. [79]

2.5.2 Structural Models

One of the earliest descriptions of the disorder in metallic (monatomic) liquids was provided by Bernal [81,82], even shortly before the first amorphous metallic solid was created. In one of his most famous works Bernal used monoatomic liquids and described their structure through a dense, randomly packing of irregular polyhedra, such a octahedra or tetrahedra, defining the existence of a structural short-range order (SRO). Based on this he proposed five fundamental structural units, called "Bernal's holes" (compare Figure 2-12). While the tetrahedron features

the highest packing efficiency, it needs to be noted, that to successfully cover the space in 3D more than one kind of these polyhedra and/or a significant distortion is needed [79]. In an experiment that used steel bearings he found a distribution of holes, indicating around 70% tetrahedra. 20% half octahedra and the rest being the remaining other holes as well as distorted versions of them [83]
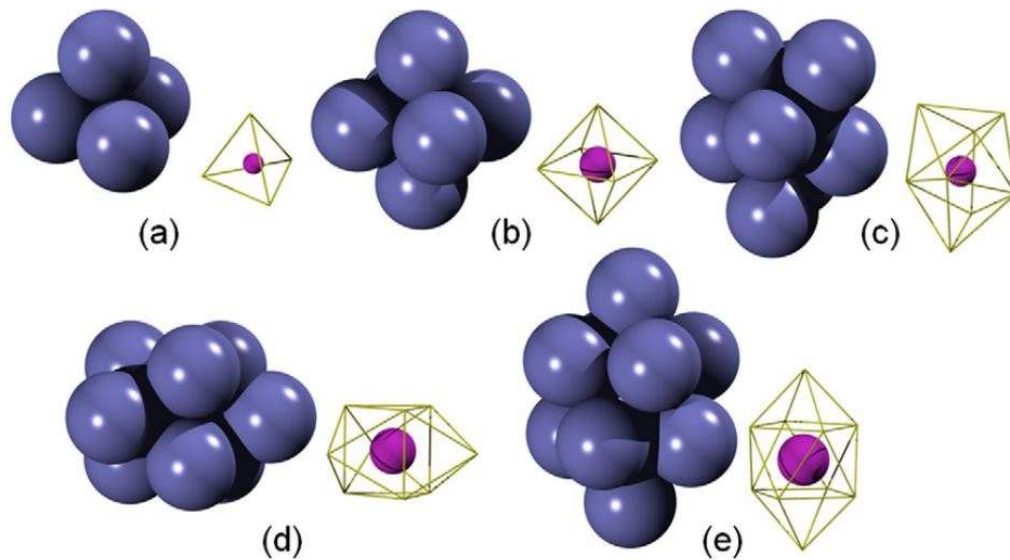
Figure 2-12: Solid sphere-model of Bernal's canonical holes : a) tetrahedron, b) octahedron, c) tetragonal dodecahedron, d) trigonal prism capped with three half octahedra and e) Archimedean antiprism capped with two half octahedra. Taken from Ref. [79].

Further important considerations of structure, particularly in metal-metalloid glasses, which are the main focus of this work was provided by Gaskell et al. [84,85]. He proposed a structural model in which the SRO was well defined in the glass, being highly similar to the corresponding crystalline structure. For the Ni-P system he proposed a tri-capped trigonal prism (TTP) that consists out of a trigonal prism (6 Ni-atoms) with a P-atom inside, that is capped by three additional Ni atoms (see Figure 2-13). The idea of similar motifs in the equivalent crystalline system was supported by the observation of similar structural motifs in the Ni_3P crystalline compound. For the TTPs Gaskell also explained their ability to be connected with each other via edge sharing, leading to chain-like arrangements. This description that covers spatial correlations beyond the nearest-neighbor shell, can be seen as a kind of medium-range order, in which Gaskell saw the main difference between glassy and crystalline systems. Whereas the structural units are packed in an ordered way in crystals, they are packed randomly in the glass.
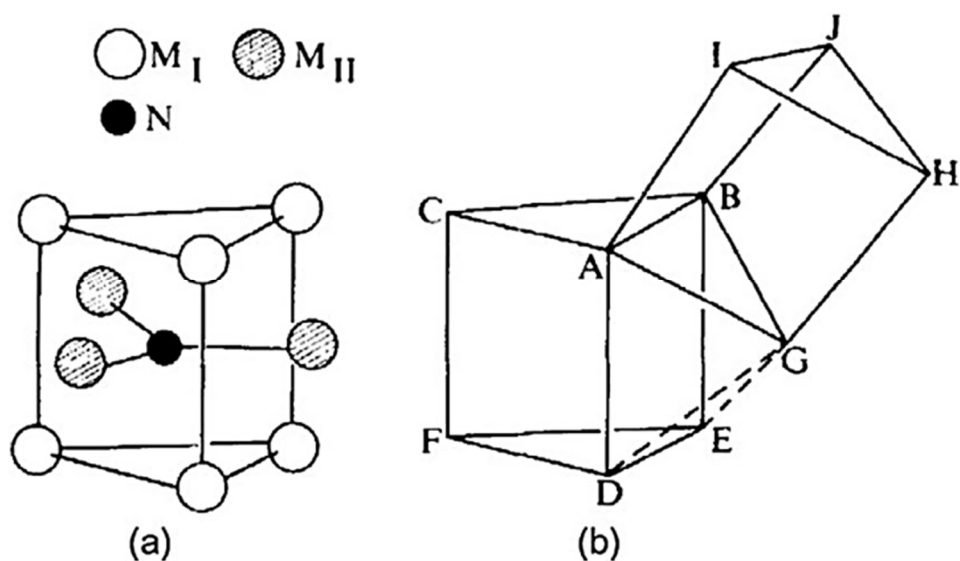
Figure 2-13: Depiction of tricapped trigonal prisms (TTP) from Gaskell's stereochemical model for metal-metalloid glasses . In a) the trigonal prism as a structural unit is shown with metallic atoms M_I and M_{II} together with the metalloid atom N. In part b) the chain-like connection via edge sharing of the TTP is shown, explaining its ability to form larger ordered regions. Original from Gaskell [84], reproduced from Ref. [79].

A model that included both concepts of MRO and SRO is the "efficient cluster packing model", created by Miracle et al, in the early 2000s [32,86], refined over the years taking into account the most recent experimental results [31,87]. Principally, it is assuming the formation of densely packed atomic clusters in the amorphous state. These clusters itself describe the average direct environment of an atom in the system, which is created due to topological constraints, describing the SRO. The model further includes a description of the MRO, as the arrangement of the individual clusters in the style of a densely packed superstructure, resembling hexagonal closest packed (hcp) and face-centered cubic (fcc) lattice structures. However, as the basic name-giving idea of "efficient cluster packing" is based on the geometrical close packing of spherical bodies, it is taking only geometric, topological aspects of the hard-sphere atoms into account, neglecting any chemical interactions. Elements with a difference in their atomic radii smaller than 2 % are considered topological equivalent, irrespective of their chemical properties. In reality of course the chemical interactions and the question whether atom A likes to be in the nearest neighborhood of atom B plays a tremendous role.

Table 2-1: Atomic radii in metallic glasses used in the ECP model. Taken from Ref. [31])

Element	Pt	Pd	Cu	Ni	P
Radius (pm)	139	140	126	126	106

The ECP clusters consist of the solvent atoms Ω, which are the predominant atomic species of the system, together with the solute atoms labeled as α, β, and γ in descending order of size. The different clusters occurring in the system are named by their centered solute atom, e.g. α-cluster, depicted in Figure 2-14. The number of solvent atoms involved in the respective cluster is directly derived from the ratio of the radii between the involved species e.g. r_α and r_Ω in the case of the α-cluster. The irregularly shaped clusters are now randomly arranged in the hcp or fcc structure to efficiently fill the space, without forming a long-range translational symmetry. Similar to actual crystals, that have separate atoms on the lattice positions instead of clusters, there are similar defects (vacancies) and interstices (octahedral or tetrahedral sites), which can remain vacant or can be occupied by other atoms [87]. One of the strengths of this model is its ability to describe the different kinds of MRO, as well as different types of cluster connections.

The concept of connecting schemes distinguishes between different types of cluster connections, based on the number of atoms share between adjacent clusters [88–90]. The different clusters may share 1 to 4 atoms with each other. In the following these connections will be labeled as 1-atom connection or vertex sharing, 2-atom connection or edge sharing, 3-atom connection or face sharing and 4-atom connection or distorted quadrilateral sharing. The occurrence of these different schemes experimentally can be derived if the radial pair distribution function (PDF) is known from structural experiments. The information is located in the splitting of the second peak of the radial PDF [89]. From this the apparent connecting schemes can be derived from geometrical considerations [90]. As the first peak r_1 determines the nearest neighbor distance the respective distance between the second nearest neighbors for each connection can be calculated for adjacent clusters that share one ($2\,r_1$), two ($\sqrt{2}\,r_1$), three ($\sqrt{8/3}\,r_1$) or four atoms ($\sqrt{3}\,r_1$). In Figure 2-15 b) these different connections are shown for some exemplary polyhedra. Yet, it needs to be stressed once again, that in multicomponent systems, such as most metallic glass forming liquids, the radial pair distribution function is composed out of the weighted superposition of all partial pair distribution functions, leading to, in a first approximation, the detected r_1 only being the interatomic distance of the most prominent scattering partial in the system. Consequently, if not all partials are known the analysis of second nearest neighbors will also not yield a full picture of the respective structure.
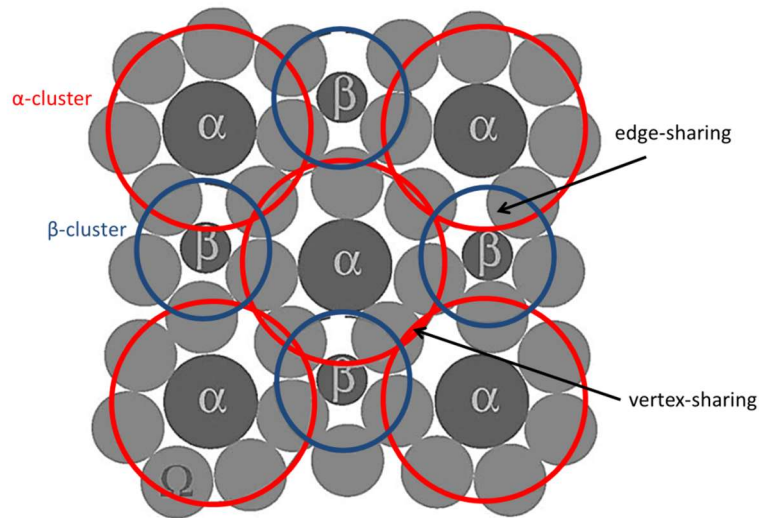
Figure 2-14: Schematic drawing of a 2D-Projection of the different atomic species α, β and Ω in a {100} plane of an fcc-unit cell. The red and blue circles highlight the different α-centered and β-centered clusters surrounded by the solvent atoms Ω. The drawing was originally adapted from Ref. [86], taken out of Ref. [91].
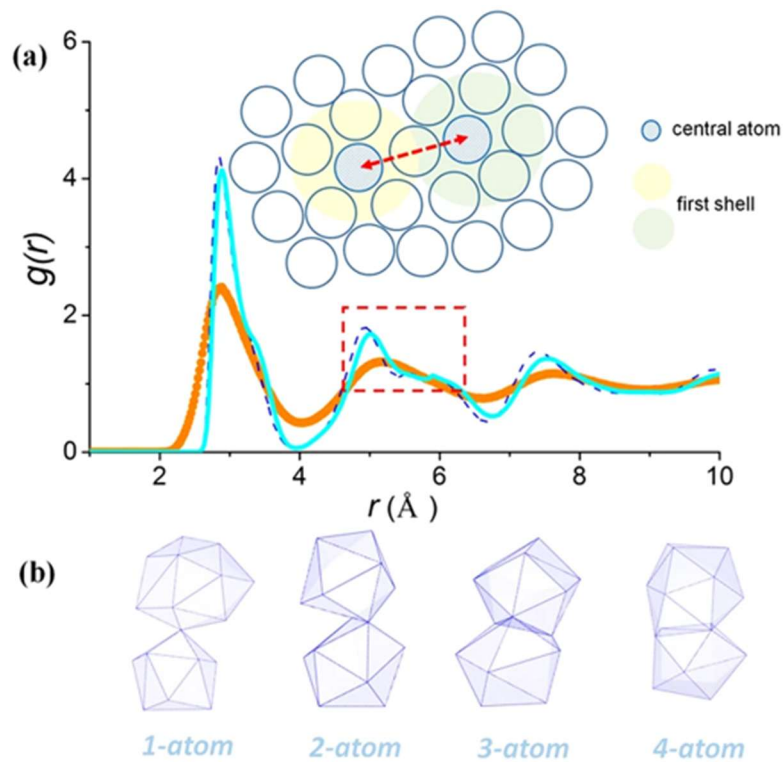
Figure 2-15: Connecting schemes and their connection to the pair distribution function : a) Schematic connection of the second peak of the radial pair distribution function g(r) of liquid Ta at 3300 K (orange) and glassy Ta at 300 K with the atomic order and relation between the second nearest neighbor shell. b) Schematic drawing or coordination polyhedra sharing different amounts of atoms. The connections are labeled regarding the number of shared atoms. Taken from Ding et al. [88]

2.5.3 Structural Information from Scattering Experiments

One way to actually determine structural information on the atomic scale, is the application of scattering techniques such as neutron or X-ray diffraction. When carried out correctly, it is possible to extract the total structure factor as well as the (reduced) pair distribution function from the captured scattered intensity. Methodological information on the acquisition of structural data is provided in section 3.3 In this section we want to give an overview on the interpretation of the structural functions in disordered systems.

The first quantity to describe the structure of the disordered system is the total structure factor S(Q), which is derived from the normalized intensity of the diffraction pattern (compare section 3.3.1 for a more detailed mathematical description). A representative depiction of S(Q) determined by high energy synchrotron X-ray diffraction is shown in Figure 2-16. Compared to a lab-scale X-ray diffraction pattern with a Cu-Kα source, the higher energy allows to cover a larger Q-range[15] (compare eq. (3.20)), combined with a severely improved signal-to-noise ratio.

For the analysis each peak, shown in Figure 2-16 can be analyzed regarding its peak position Q_i, peak height $S(Q_i)$ and peak width or full width at half maximum (FWHM) $FWHM_i$, with i being the order of the respective quantity, each delivering different information on underlying the structure.

The peak position of the first sharp diffraction peak (FSDP) provides information on the average distance between the atoms. As long as no significant structural rearrangements are possible, it was shown that the change of Q_{FSDP} correlates well with the thermal expansion coefficient α_{th} determined in actual dilatometric experiments [92], leading to:

$$\left(\frac{Q_{FSDP}(T_{ref})}{Q_{FSDP}(T)}\right)^3 = 1 + \alpha_{th}(T - T_{ref}) = \frac{V(T)}{V(T_{ref})} \tag{2.36}$$

with T_{ref} being a reference temperature, whose initial volume is used as a reference (mainly room temperature). This correlation is mainly valid in the glassy state.

---

[15] The maximum Q with Cu-Kα would be around 8 Å^{-1}.

Regarding the interpretation of the peak height $S(Q_i)$, one has to understand that a perfect long-range ordered crystal would lead to a divergence in $S(Q)$, whereas a value of $S(Q) = 1$ would correspond to a complete loss of structural order [93]. From this one can understand the peak height, in particular the height of the first peak $S(Q_{FSDP})$ as a measure of order in the system. Consequently, when a liquid is cooled it will strive towards a more ordered state, which is manifested in a growth of $S(Q)$ [93].

The peak width, or FWHM of the FSDP, has been shown to correlate with the correlation length over which a repeated unit period persists in non-crystalline systems [94].Also connections to the free volume and the relaxation state of the glass have been established experimentally, particularly connecting the changes of the FWHM of the FSDP to changes in the MRO of the system[77].
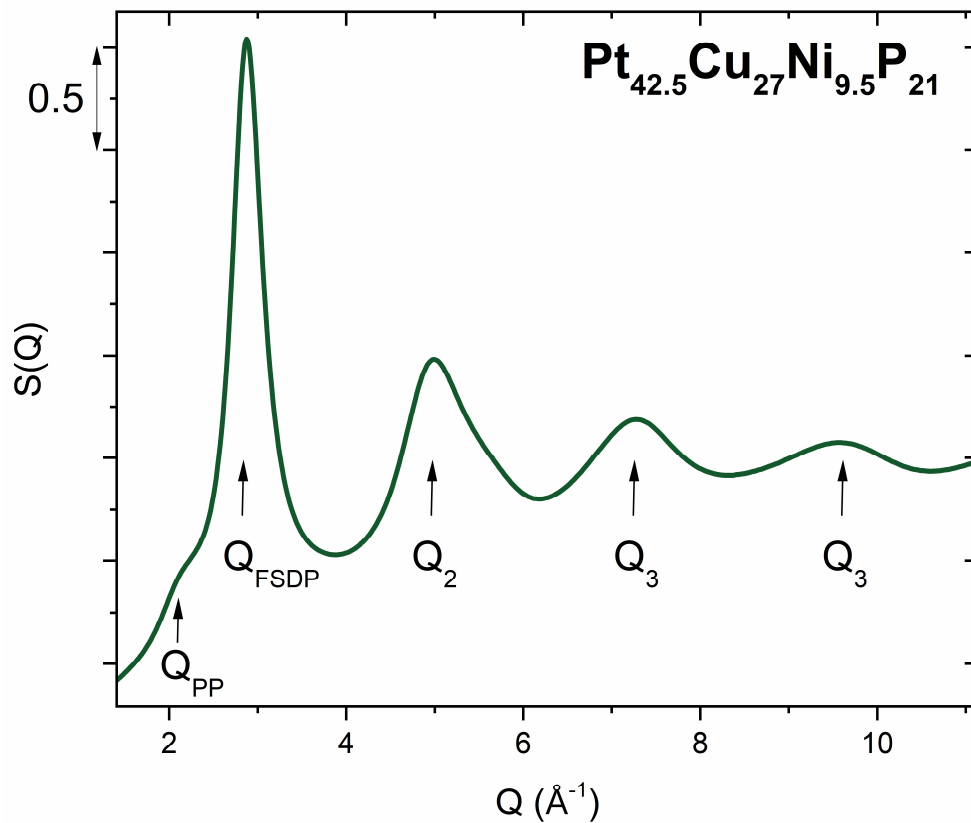
Figure 2-16: Total structure factor $S(Q)$ of $Pt_{42.5}Cu_{27}Ni_{9.5}P_{21}$ at room temperature in the glassy state . The respective maxima Q_i are labeled up to the 4th maxima. The first sharp diffraction peak (FSDP) is differently labeled by Q_{FSDP} (alternatively Q_1) and the distinct pre-peak of the FSDP is also highlighted with Q_{PP}

A more accessible description is provided by the reduced pair distribution function (PDF) $G(r)$, as it describes the structure in real space instead of the reciprocal space, used in $S(Q)$. A representative depiction of $G(r)$ is shown in Figure 2-17. A more detailed description can be found in the later chapter on X-ray diffraction (see section 3.3.1).

In a PDF the individual peak positions r_i describe the average separation between atoms of the n-th coordination shell of atoms. As $G(r)$ contains the information of all atomic pairs in the system, which also contribute differently to the signal (compare section 3.3.1 for general considerations and in particular for the examined systems section 6.3.4.1), a broadening of the peaks with increasing n is naturally observed in systems that lack long-range order. While the average next neighbor distances are rather limited (SRO) each additional atomic shell becomes less well defined, which leads to the a broadening of the individual peaks in disordered systems [95].
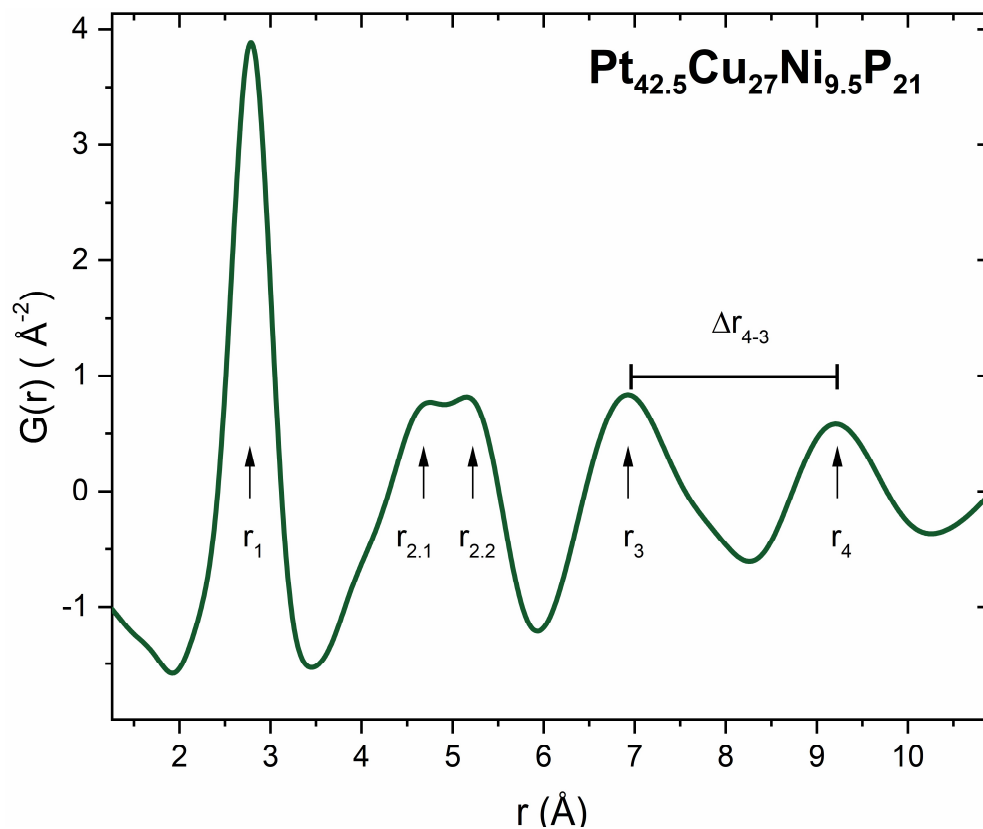
Figure 2-17: Reduced total pair distribution function $G(r)$ of $Pt_{42.5}Cu_{27}Ni_{9.5}P_{21}$ at room temperature in the glassy state . The different peak positions r_i are labeled, marking the different atomic shells. The splitting of the second peak, displaying the second nearest neighboring atoms originates from the occurrence of different cluster connecting schemes [88]. Further the difference between the 3rd and 4th peak is highlighted, marking the linear dilation of the respective shells. This quantity is connected to the structural fragility model of Wei et al. [96].

The decreasing order relations at larger distances further corresponds to the decrease of the intensity of G(r) with growing r that can be observed in Figure 2-17. The exponential decay behavior of the individual peaks in G(r) can be connected to a structural coherence length of the system, which represents a parameter to describe the degree of order that is present in a system [95]. In contrast a perfectly long-range ordered system G(r) would never fully decay, whereas any structural incoherence does lead to the decay of G(r) at growing r. Based on the descriptions of Ornstein and Zernike the exponential decay of the peak values of the reduced PDF $G(r)_{max}$ can be described in a strongly simplified form by [97]:

$$G(r)_{max} = A_0 \exp\left(-\frac{r}{\xi}\right) \tag{2.37}$$

,where A_0 describes a pre-factor and ξ is the coherence length. In Figure 2-18 the fitting procedure used to determine the coherence length is shown. Here the peak values beyond length of 6 Å is used to determine the exponential decay of the medium range order and all parameters are kept free. In particular the amplitude A_0 has to be kept free to account for the changes in G(r) with respect to temperature. Commonly the pair distribution function g(r) (compare eq. (3.30)) would have to be used for the actual calculations instead of the reduced PDF, as it already entails the changes in the number density with temperature. However, as the explicit determination of the (number) density as a function of temperature, particularly in the liquid state is not trivial the use of G(r) is much simpler. The useability of G(r) instead of g(r) was recently shown by Stolpe, leading to similar results in the absolute values and temperature dependence of ξ extracted from either G(r) and g(r) [78]. A detailed discussion on the physical interpretation and experimental determination of the coherence length from X-ray scattering experiments for the case of metallic liquids and glasses is provided in his work [78].
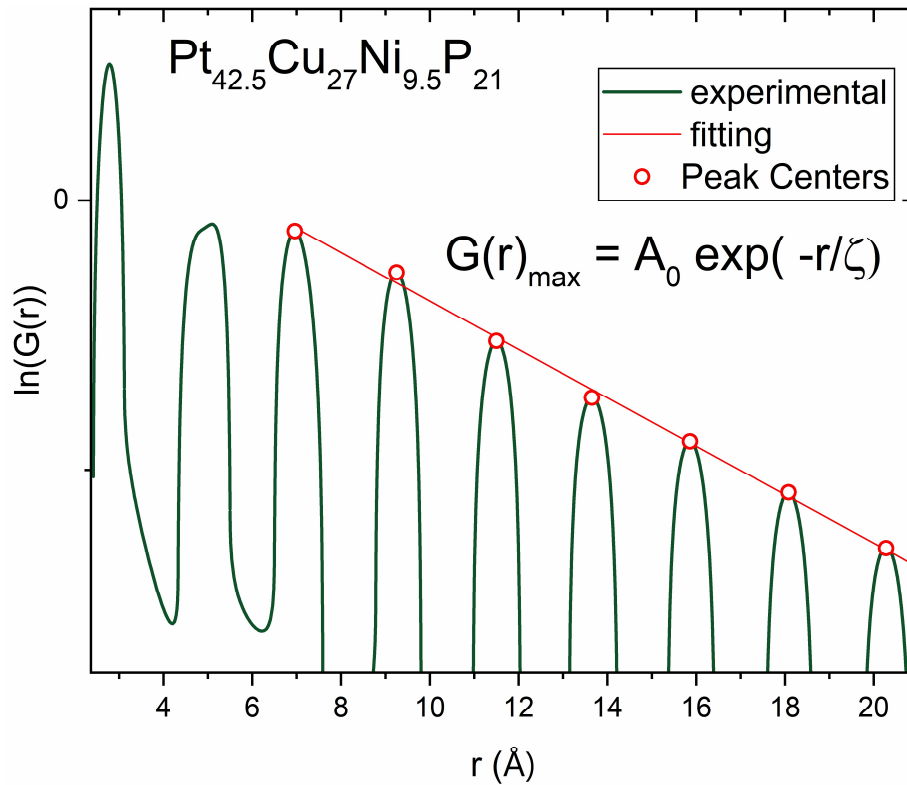
Figure 2-18: Natural logarithm of the reduced pair distribution function . The peak values including the 3rd peak and beyond are used for the determination of the correlation length according to the methodology by Stolpe [78]

Further knowledge on the structure can be extracted from the peak area of the individual peaks of the PDF. It provides information on the coordination number of the individual atomic shell. The coordination number describes the number of neighboring atoms at the given distance. However, for an actual quantitative analysis the knowledge of the partial PDFs would be needed instead of the total PDF. To experimentally determine the $n(n+1)/2$ partial PDFs of an n component system, the same number of $n(n+1)/2$ individual independent measurements with different contrasts would be needed. Different contrasts can be created by using different radiation e.g. neutron scattering techniques that also allow to exchange the different components with different isotopic variants. The different isotopes possess unalike scattering contributions, leading to a change in contrasts. This technique is mainly applied to resolve the partial structures in binary systems such as ZrNi [98]. Another possible technique is anomalous X-ray scattering, which uses the energy dependence of the scattering contribution, in particular in the vicinity of the absorption edges of individual elements that are contained in the system. Here, several works even tried to resolve ternary systems or parts of quaternary systems under isothermal conditions [99–101]. However, the experimental effort, even under isothermal conditions is extremely high and up to now not applied to study the temperature dependence of

the individual partial structures. This might be related to the comparably low flux of neutron sources and the low yield of photons that is possible around the absorption edges, which lead to the need of long exposure times and limit the possibility of dynamic measurements. At this point it needs to be noted that in the context of this work only total diffraction experiments are carried out as the main goal is to study the temperature dependence of the underlying structure. Nevertheless, neutron scattering as well as anomalous X-ray scattering experiments in the glassy state and liquid state would be highly beneficial to facilitate the structural understanding.

2.5.4 Structural Signatures of Fragility

2.5.4.1 Fragility of Metallic Liquids based on changes of SRO

During the cooling of the liquid its order or ordering can be described by the changes of the configurational entropy, which itself can be interpreted as the thermodynamic signature of fragility (compare chapter 2.2.2). The changes of the configurational entropy during cooling are directly related to the growth of the isobaric heat capacity of the liquid c_p[1], indicating their thermodynamic fragility. From a structural point of view the degree and rate of chemical or topological ordering of the liquid should be reflected by the heat capacity and entropic changes. The actual influence of different short-range order on the fragility and the course of c_p is well described in a numerical simulation by Ding et al. [102]. In their study Ding et al. compared a fragile system, $Cu_{64}Zr_{36}$, with a rather strong system, $Pd_{82}Si_{18}$ (compare Figure 2-19). In the case of the fragile $Cu_{64}Zr_{36}$ significant energy minimization was observed through icosahedral short-range ordering. The SRO was motivated by the chemistry of both components, as well as their topology[16]. The rapidly ascending heat capacity was directly traced back as a signature of the growing ratio of full icosahedra (compare Figure 2-20a) and b)). In contrast, such significant ordering was not observed in $Pd_{82}Si_{18}$, where the fraction of structural motifs was only changing linear with undercooling (compare Figure 2-20c) and d)). Hence, the heat capacity of the liquid was also growing less rapid than in the $Cu_{64}Zr_{36}$ liquid. At his point it shall be noted that the location of such ordering processes are randomly distributed through the volume of the sample. Together with an increased intrinsic lifetime these structure are also seemingly related to the

---

[16] It shall be noted, that a real separation of both effects (chemical and topological order) is rather complicated, as in the end any chemical affinity will lead to a change in topology and vice versa chemical ordering is only possible if the intrinsic topology is allowing it. Ultimately it has to be recognized that both effects go hand in hand and their interplay leads to the final structure.

often observed dynamic heterogeneity of metallic undercooled liquids that leads to their complex non-linear stretched exponential relaxation behavior (compare section 2.4 and 3.4) [103].
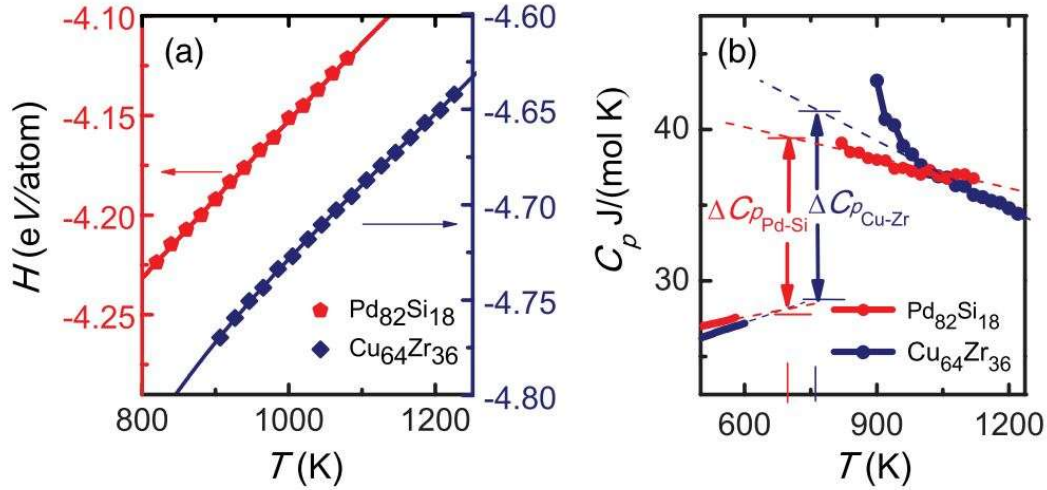
Figure 2-19: Computer simulation of the thermal evolution of enthalpy and specific isobaric heat capacity with undercooling for $Cu_{64}Zr_{36}$ and $Pd_{82}Si_{18}$. The two different glass forming liquids feature different temperature dependence of both parameters, with $Cu_{64}Zr_{36}$ featuring a thermodynamically fragile behavior with large thermally induced changes, compared to $Pd_{81}Si_{18}$, showing thermodynamically strong behavior. The Figure is rearranged out of partial Figures from Ding et al. [102].
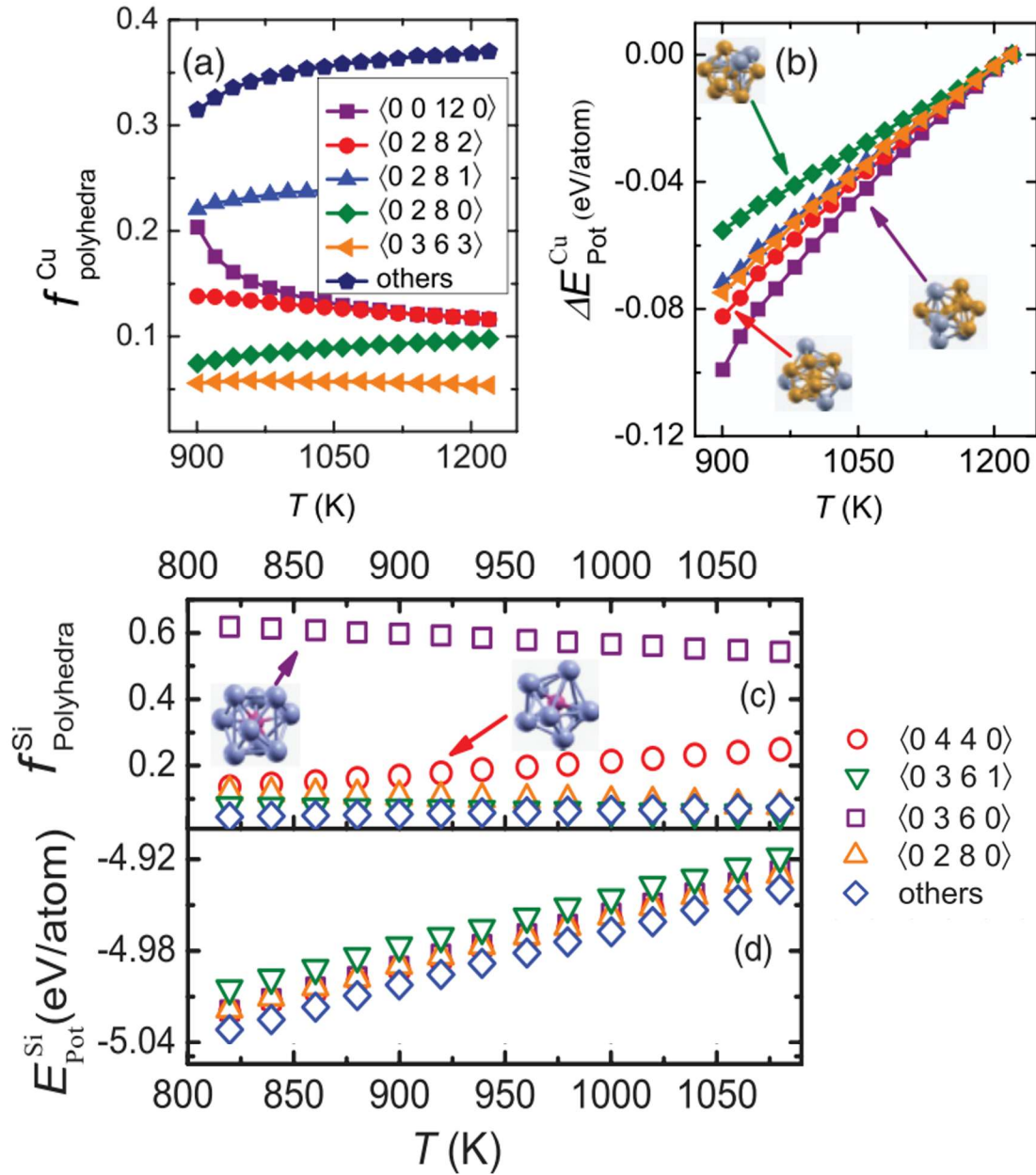
Figure 2-20 Change of different cluster species in the supercooled liquid state for two different metallic liquids : $Cu_{64}Zr_{36}$ (a) fractions and b) the potential energy) and $Pd_{82}Si_{18}$ (c) fractions and d) potential energy). In the case of $Cu_{64}Zr_{36}$ the fraction of <0 0 12 0> undergoes a significant increase, as it is featuring the most stable configuration, underlined by the largest potential energy difference in b). This icosahedral short-range ordering directly manifests in the decrease of enthalpy and entropy and ultimately the rapid ascending heat capacity. In c) and d) the fraction of Si-centered polyhedra and their potential energy are shown as a function of temperature. In contrast here no significant structural ordering effects are observed, reflecting the minor reductions in enthalpy, entropy and ultimately the rather flat ascend of the heat capacity upon cooling (compare Figure 2-19). The Figure is rearranged out of partial Figures from Ding et al. [102].

2.5.4.2 Fragility of Metallic Liquids based on changes of MRO

Another experimental approach to characterize the structural signature of fragility is the so-called structural fragility parameter, m_{str}^{V4-3}, proposed by Wei et al. [96]. Instead of focusing on the SRO, this parameter quantifies the changes on the length-scale of the 3rd and 4th coordination shell (~0.7-1 nm, MRO). Instead of the aforementioned simulations it is based on X-ray diffraction that is used to determine the reduced pair distribution function G(r). Large thermally induced expansions on the MRO length-scale are typically observed for fragile liquids whereas smaller thermal expansions are found for strong liquids. In order to quantify m_{str}^{V4-3} Wei et al. obtained structural data by total X-ray diffraction during a constant heating with 20 K min^{-1} and the reduced pair distribution function G(r) is calculated. From G(r) the volume dilatation ε_{4-3} between the 3rd and 4th coordination cell can then be calculated by

$$\varepsilon_{4-3} = -\Delta V_{4-3}(T)/V_{4-3}(T_g^*), \tag{2.38}$$

with the change in volume between the 3rd and 4th shell ΔV_{4-3} being

$$\Delta V_{4-3}(T) = \frac{4}{3}\pi(r_4^3 - r_3^3), \tag{2.39}$$

with r_4 and r_3 being the peak positions of the 3rd and 4th peak of G(r). From the volume dilatation the structural fragility parameter $m_{str}^{V}{}_{4-3}$ is determined by a linear fitting of the data in the supercooled liquid region on a T_g-normalized inverse temperature scale, mathematically expressed by

$$m_{str}^{V4-3} = d\varepsilon_{4-3}/d(\frac{T_g'}{T})\Big|_{T=T_g'} \tag{2.40}$$

Based on observations on seven different alloys spanning over the spectrum of fragilities covered by metallic glass forming liquids (Figure 2-21) Wei et al. proposed a quantitative empirical correlation between the kinetic m-fragility parameter $m_{kinetic,calc}$ and m_{str}^{V4-3}, with

$$m_{str}^{V4-3} = 2.95 \cdot 10^{-3}\, m_{kinetic,calc} - 0.124 \tag{2.41}$$
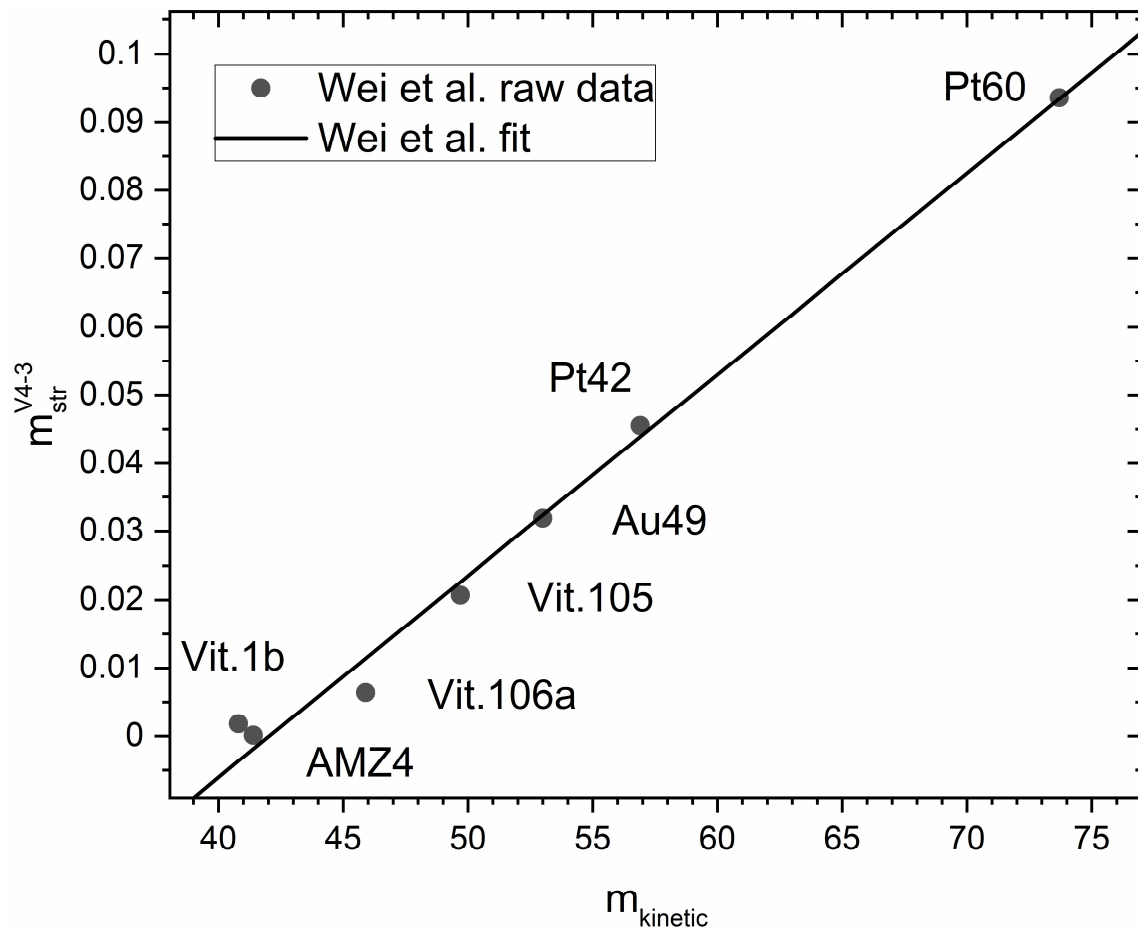
Figure 2-21: Empirical connection of the kinetic m-fragility parameter and the structural fragility parameter . The plot was reproduced and the labelling of the alloys was adapted according to Wei et al. [96].

2.6   Mechanical Properties of Metallic Glasses

2.6.1 Plasticity of Metallic Glasses

Crystalline metallic systems consist out of a periodic lattice, featuring well defined symmetries and are known to be full of defects of different sizes, ranging from unoccupied sites in the lattice, called vacancies, over linear defects such as dislocations or grain boundaries. While these defects lead to the fact that the theoretical strength of a material is never reached, but plastic flow is setting in at significantly smaller stresses applied, it is exactly those defects that facilitate the large plasticity observed in metallic crystalline materials. Classically this deformation takes place through the movement of dislocations, but also through the sliding of grain boundaries to just name some example. In contrast, amorphous metals that lack a long-range ordered crystalline lattice in general, they of course also lack dislocations and grain

boundaries, being the carrier of plastic deformation. This implies, that the amorphous structure can withstand stresses close to theoretical strength, leading to yield strengths σ_y of 0.3 GPa for Ca-based systems up to 6 GPa in Co-Ta-B[104]. However, the absence of these classical mechanisms also means that the stresses applied cannot be distributed by plastic deformation by the same mechanisms as in crystalline metals. Further the limit for elastic strain ε_y of amorphous metals is around 2%, which is much higher than the conventional 0.2% for crystalline material, being rather in the range of polymeric materials. This combination leads to amorphous metals being tagged as "Harder than steel and as elastic as polymers". But this is not the end of exceptional mechanical properties, as two other interesting features can be derived: a) the large elastic deformation and high strength gives the material a large capacitance to store elastic energy $E_{elastic}$ ($E_{elastic} = \frac{1}{2}\sigma_y\,\varepsilon_y$) and b) a relatively small Young's modulus E_{young}, which can be derived from the ratio of yield strength and elastic limit ($E_{young} = \frac{\sigma_y}{\varepsilon_y}$).
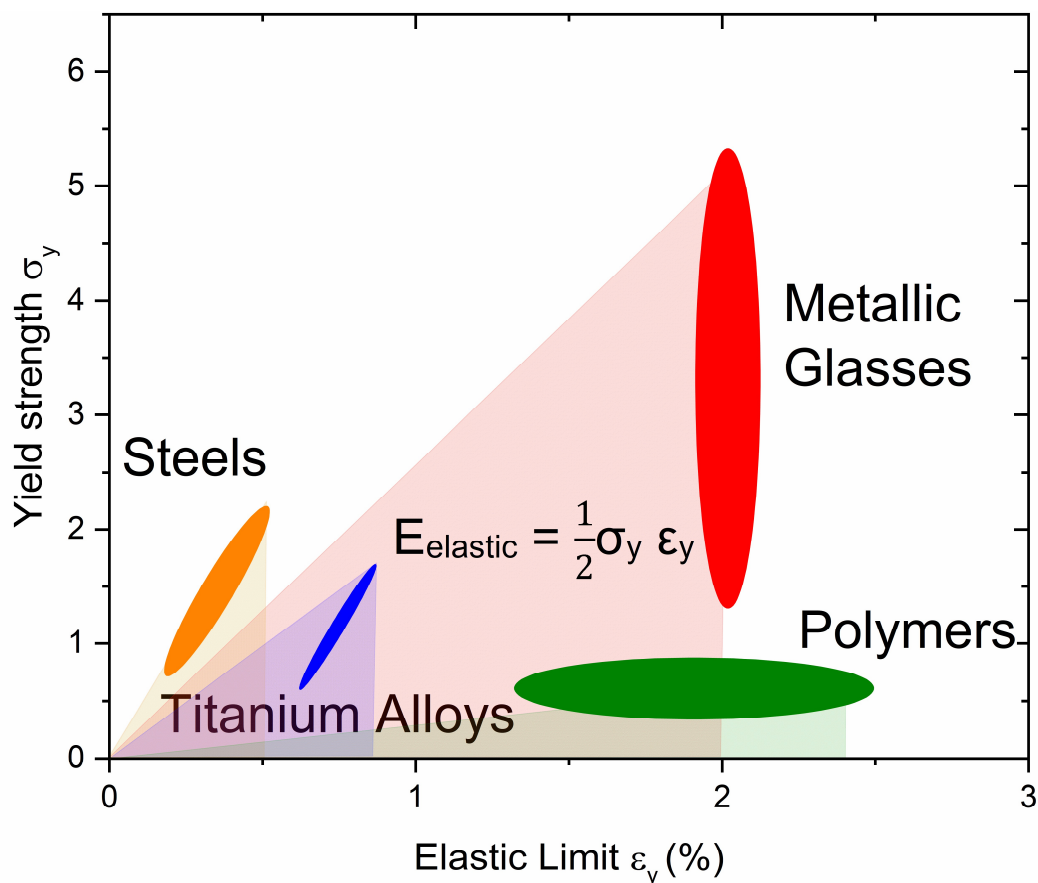
Figure 2-22: Strength of different classes of materials as a function of elastic limit for different groups of materials . The area of the shaded triangle is representative of the elastic energy that can be stored in the respective class of materials. The slope of the hypothenuse is representative of the Young's modulus of the respective class of materials.

To understand the deformation behavior, one has to differ between two regimes. The first one is a so-called homogeneous deformation, which can be observed at elevated temperatures around the glass transition when applying moderate strain rates. This homogeneous deformation mode is possible due to the unfreezing of the atoms in the vicinity of the glass transition temperature, leading to a highly viscous flow of the material. In this regime, (compare right side of both diagrams in Figure 2-23) severe "superplastic" deformations of several 1000% are possible, comparable to a silicate melt or a thermoplastic polymer [71,105]. In a large contrast to that is the inhomogeneous deformation mode, which is present at temperatures well below the glass transition temperature or at high deformation rates. For its activation large stresses are needed. In comparison to the cooperative flow of the homogeneous scenario, here a small volume is activated, called shear transformation zone (STZ) (compare Figure 2-24). In the STZ shear-induced local inelastic rearrangements take place that transfer the system locally from one low energy configuration to another, bypassing an intermediate "activated configuration" of higher energy [71]. While the STZ could be seen in analogy to a dislocation, it is important to note that the STZ is no inherent structural defect, but rather a transient effect during the deformation. However, the location of a STZ is not independent of the underlying structure of the glass. STZs prefer to be initiated in regions of lower stiffness featuring a less densely packed structure, i.e., in regions of higher free volume. The latter is ununiformly distributed promoting the inhomogeneous nature of this deformation process. Another critical point during this deformation process is the fact that within these STZs a local volume dilation is occurring [68,106,107], which goes in hand with a further softening of the local structure. This less dense local structure is unable to heal through local atomic redistributions due to the limited diffusion at the given low temperatures of inhomogeneous flow. This promotes an even higher localization of the STZ in their direct surroundings, ultimately leading to an accumulation of many STZs to so called shear bands. These shear bands can easily migrate through the mechanically stressed material, as there are no hindering mechanisms i.e. grain boundaries, until they reach a free surface where they lead to a macroscopic shear offset and often failure of the material [108]. Under tensile load this leads to an apparent brittle behavior on the macroscopic scale with a single shear band cutting through the sample at an angle of 45 °[109], whereas large plastic flow is occurring localized inside the shear bands [110]. To achieve macroscopic plasticity the movement of the shear bands needs to be hindered by some internal barriers. For example during bending of a metallic glass the neutral fiber in the middle of the beam can act as such a barrier, leading to the observability of plasticity in bending, even at room temperature [109,111]. In this neutral fiber the bending stress becomes zero, which

blocks the propagation of the shear band. This does lead to the formation of new shear bands, so called shear band multiplication, to compensate for the imposed macroscopic strain. The multiple shear bands are detectable as serrations in the stress-strain curves due to the stick-slip behavior in their propagation [112–114]. The ability of multiple shear banding itself facilitates the observation of plasticity and is therefore an intrinsic property of the material. It was shown that intersecting, branching and slipping, resulting from the interaction of the multiple shear bands is playing an important role when large plasticity is observed in metallic glasses [109,115,116]. Numerous studies have shown that the thermal history, composition and the resulting underlying structure play a crucial factor on the ductility of metallic glasses [33,117,118]. But the question, on how to exactly facilitate the multiple shear banding through manipulation of composition and structure, is still not fully answered.
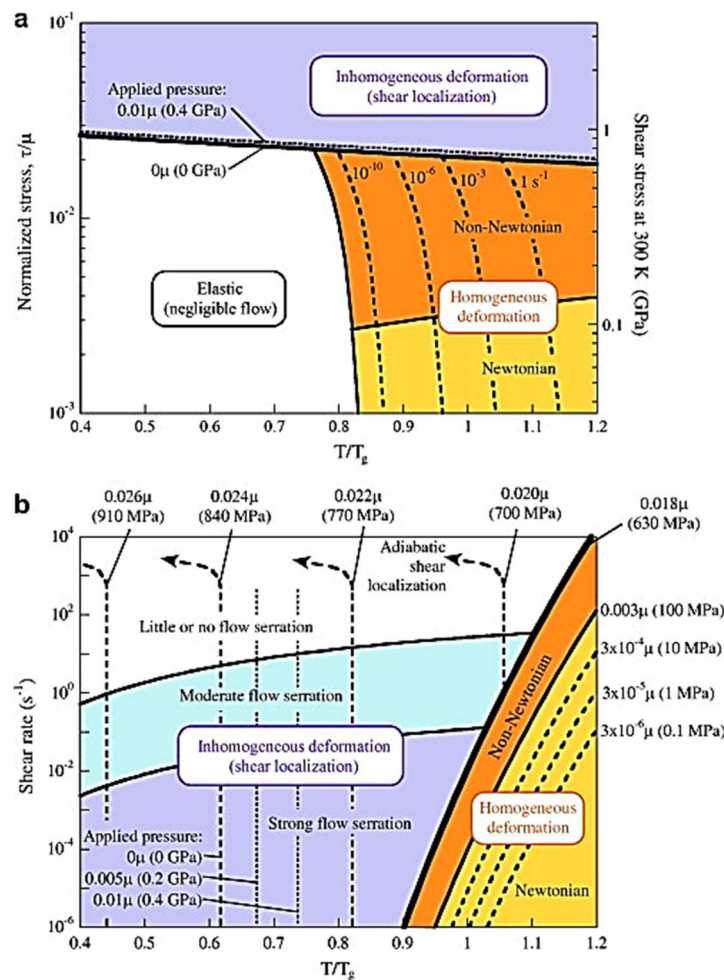
Figure 2-23: Deformation map of metallic glasses for stress and strain-rate as a function of temperature. The main focus for this work lies on the distinction between homogeneous and inhomogeneous deformation taking place at different temperatures and deformation rates. Taken from Schuh et al. [71]
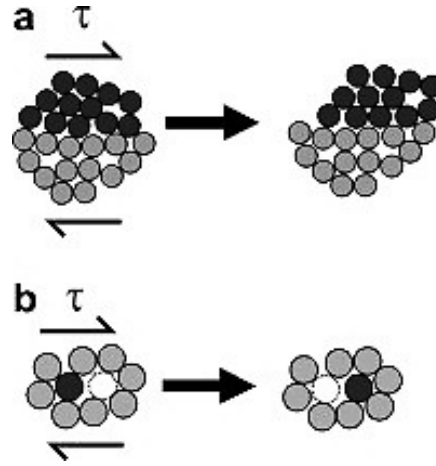
Figure 2-24: Schematic illustration of deformation mechanisms in metallic glasses , depicting the models of a shear transformation zone (a) or a local atomic jump (b). Taken from Schuh et al. [71].

2.6.2 Cooperative Shear Model and Time-dependent deformation behavior

Over the years the concept of shear transition zones (STZs) was further elaborated in many ways. One model, used in the context of this works, was established by Johnson, Samwer and coworkers [119,120]. The so called Cooperative Shear Model (CSM) combines deformation mechanisms together with rheological properties such as the shear modulus to predict the failure of metallic glasses. It is based on the concepts of inherent states and the potential energy landscapes [121,122]. It leads to a universal scaling law of the critical flow stress (yield stress) as a function of temperature:

$$\frac{\tau_C}{G}(T) = \gamma_{C0} - \gamma_{C1}\left(\frac{T}{T_g}\right)^{2/3} \tag{2.42}$$

, with τ_C being the critical shear stress for flow (yield stress), G being the shear modulus and $\gamma_{C0} = 0.036$ and $\gamma_{C1} = 0.016$ being empirical coefficient in the dimension of a shear strain [119]. Ultimately, it is anticipated that the ductility of BMGs intrinsically depends on the actual volumes of the STZs [119,122,123]. Hence, an accurate determination of the sizes of STZs, is of key importance, when aiming to understand the plastic deformation process. In the context of the CSM Pan et al. derived a formula for the activation volume ΔV^*[123]:

$$\Delta V^* = \frac{k_B\,T}{\tau}\left(\frac{d\ln(\dot{\gamma})}{d\ln(\tau)}\right)_{p,T} = \frac{k_B\,T}{\tau\,m_{SRS}} \tag{2.43}$$

with the strain rate sensitivity m_{SRS}. This quantity can experimentally be determined through the strain-rate dependence of the hardness:

$$m_{SRS} = \left(\frac{d\ln(H_{mech})}{d\ln(\dot{\varepsilon})}\right)_{p,T} \tag{2.44}$$

,where H_{mech} is the micromechanical hardness and $\dot{\varepsilon}$ is the strain rate.
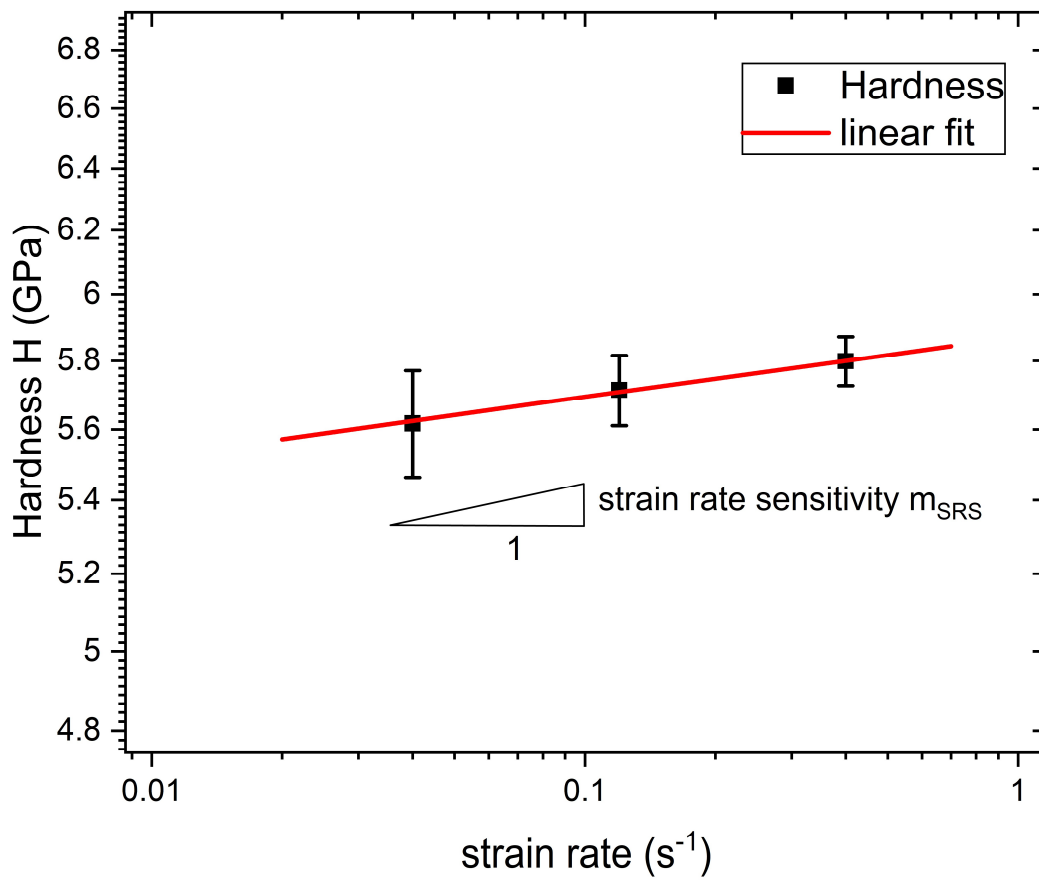
Figure 2-25: Strain rate dependence of Hardness reported on a log-log scale. A linear fit of the hardness values is used to determine the strain-rate sensitivity m_{SRS}. Plot created from experimental data for $Pt_{42.5}Cu_{27}Ni_{9.5}P_{21}$.

2.6.3 Embrittlement of Metallic Glasses

As already coarsely outlined in section 2.6.1, the ductility of metallic glasses can be affected by various intrinsic and extrinsic factors. In the following a short overview on some of these factors shall be provided. First the extrinsic influence of the thermal history, characterized by fictive temperature and resulting free volume, then the more intrinsic influence of the composition and in the end also how the structure is influenced by both, composition and thermal history, ultimately condensing in the macroscopic embrittlement.

2.6.3.1 Influence of Thermal History: Fictive Temperature

One effect that was observed and studied is the general influence of the thermal history of a metallic glass on the mechanical properties. The term thermal history summarizes the effects of the cooling rate at which the glass was obtained, but also incorporates the annealing steps the glass has experienced afterwards (compare section 2.4). Ultimately, the thermal history allows a description of a defined enthalpic, volumetric and structural state of the glass. In literature the influence of thermal history is often described separately regarding annealing or variated cooling rates [117,124–126]. The effects of the different thermal histories on the ductility are often traced back to the amount of so-called free volume in the mechanically probed glass [68]. The free volume model describes the residual excess volume that is frozen in the glass, when the supercooled liquid is leaving its metastable equilibrium. Similar to the residual enthalpy, the free volume is higher, if the glass was obtained by fast cooling, i.e. it possesses a large fictive temperature T_{fic} (compare section 2.3.1). Experimentally validated, a reduction of the free volume and the respective fictive temperature leads to an embrittlement and lowered fracture toughness with a decreased ability of shear band formation, together with an increase in the hardness and Youngs modulus [67,126–130]. Vice versa an increase of the free volume and the fictive temperature, through processes like faster cooling out of the SCL [131–133] or severe plastic deformation e.g. cold-rolling [134–136], leads to a more ductile and tougher metallic glass.
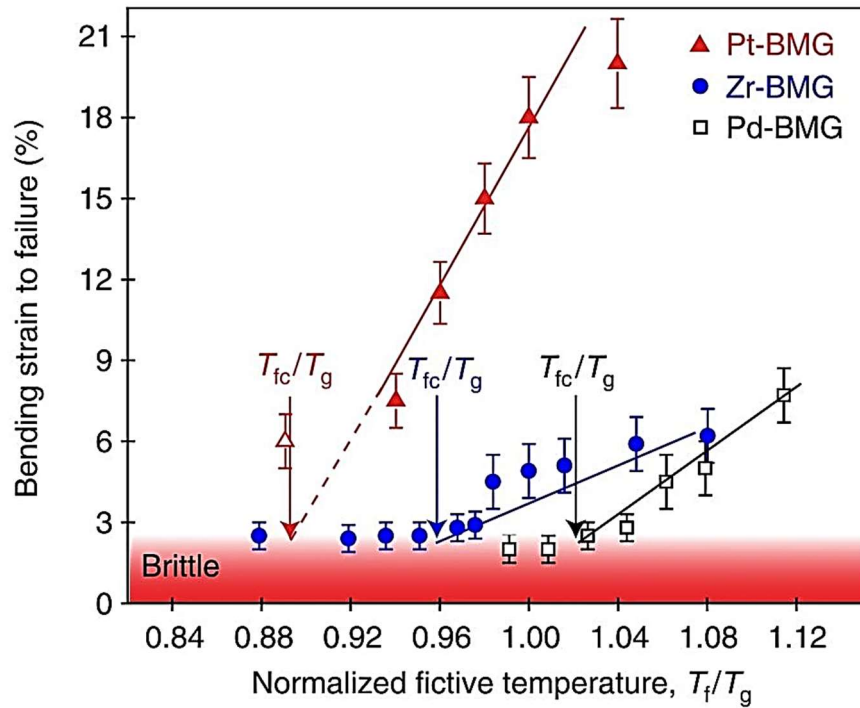
Figure 2-26: Critical bending strain to failure at room-temperature for three different classes of metallic glasses with different fictive temperatures . The fictive temperatures are normalized with respect to the glass transition temperature at 0.33 K s⁻¹. [17]Taken from Kumar et al. [117]

A good phenomenological criterion is provided by the "critical fictive temperature model" established by Kumar et al. [117]. It describes the thermal history of the glass through a single parameter, the fictive temperature, which can be assessed through calorimetric measurements [137]. Within one chemical composition they determine a specific critical fictive temperature $T_{fic,c}$, below which a brittle mechanical behavior of the material can be observed. Especially the location of this critical fictive temperature with respect to the glass transition temperature is of special interest, as it directly provides a tendency if conventionally casted material will behave brittle or ductile. In Figure 2-26 the fictive temperature normalized by the glass transition temperature is depicted for three different metallic glass-forming compositions. Within each system the plastic deformation decreases linearly with a decreasing fictive temperature, mirroring the decrease in free volume. However, significant changes in the slope of this decrease as well as the location $T_{fic,c}$ with respect to T_g can be observed between the

---

[17] It shall be noted that the fictive temperature is here labeled as T_f and its critical value as T_{fc}. In the context of the current work T_{fic} and $T_{fic,c}$ are used to make it well distinguishable to the temperature of fusion T_f.

different studied alloys, underlining the influence of the composition and atomic species incorporated in the glass itself.

2.6.3.2 Influence of Composition

From the depiction in Figure 2-26, the drastic changes of mechanical performance with respect to the composition in different metallic glass-forming systems becomes eminent. Within the material family of metallic glasses there are intrinsically extremely brittle compositions such as Fe-based BMGs that feature a fracture toughness comparable to silicates, whereas other compositions behave as ductile as conventional Al-based crystalline alloys. Finding the specific mechanisms of this compositional embrittlement is still an ongoing research topic. The understanding of these mechanism is of high importance for the usage of metallic glasses in structural applications as it would facilitate the development of ductile, more damage tolerant compositions. For this purpose, systematic variations of composition can enable the understanding in specific systems and are one way to find more general implications.

In the context of this work especially the work by Kumar et al. on the embrittlement of Pd-based metallic glasses is of interest [33]. He investigated the difference of ductility between (stoichiometrically) different metallic glasses containing Pd and Pt. He observed a larger tendency to embrittle in the glasses that contain more Pd. This fits well the tendency of the fictive temperatures in Figure 2-26, where the critical fictive temperature of the Pd-BMG is found above its glass transition temperature at 0.33 K s^{-1} ($T_{\text{fic,c}}(\text{Pd-BMG}) \approx 1.03 \, T_{\text{g}}$), in comparison to the Pt-BMG, where the critical fictive temperature is located well below T_{g} ($T_{\text{fic,c}}(\text{Pt-BMG}) \approx 0.9 \, T_{\text{g}}$).
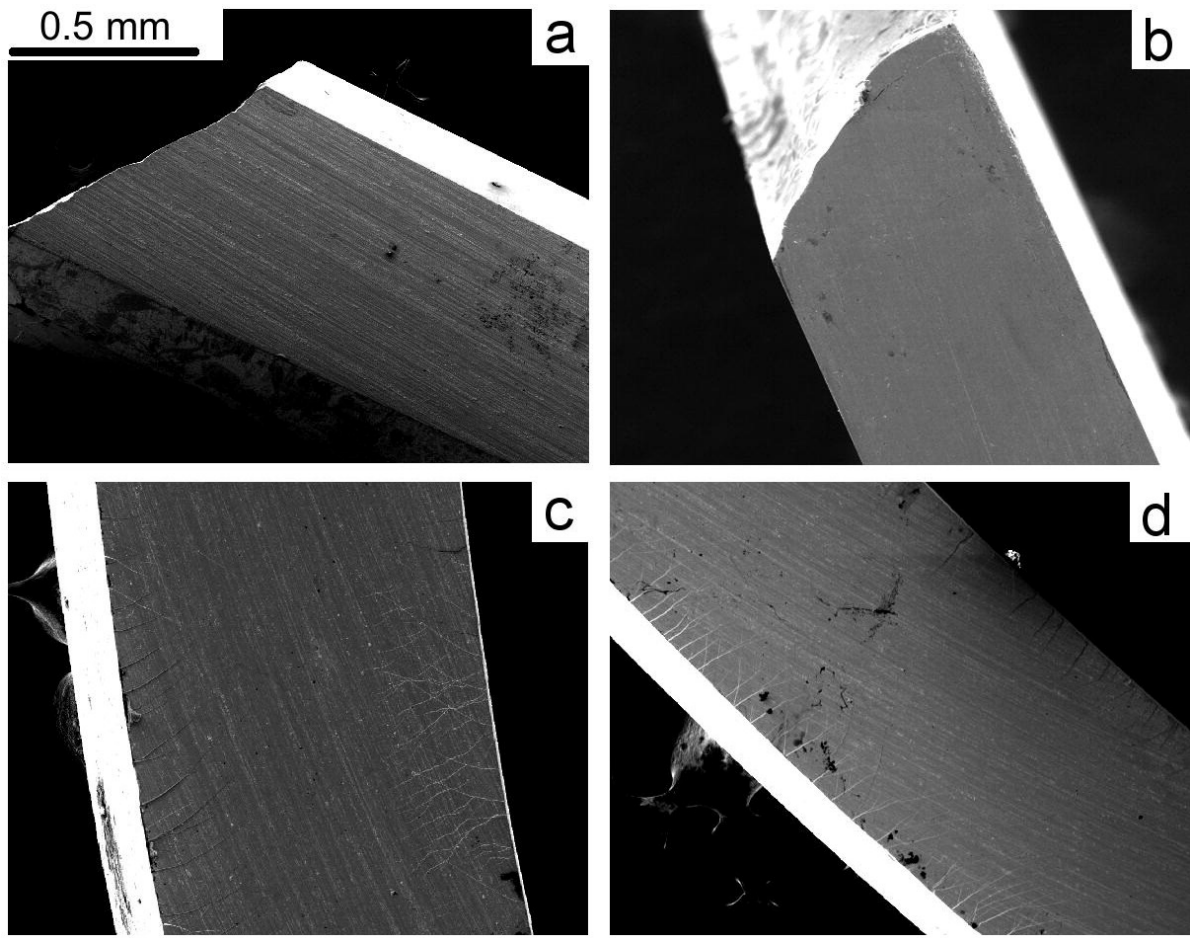
Figure 2-27: Scanning electron microscopy images of the as-cast beams with different Pt/Pd content after a bending experiment. The Pt content is rising from a) to d) with a) being a Pd-BMG ($Pd_{43}Cu_{27}Ni_{10}P_{20}$) , b) being a Pd-Pt ratio of about 3:1 ($Pd_{36}Pt_{9.3}Cu_{25}Ni_{9.3}P_{20.4}$), c) being an almost equal amount of Pd-Pt ($Pd_{27.5}Pt_{21}Cu_{22.4}Ni_{8.1}P_{21}$), and d) being a Pt-BMG ($Pt_{57.5}Cu_{14.7}Ni_{5.3}P_{22.5}$). Whereas for the Pd-rich beams a brittle fracture without visible shear bands is observed, multiple shear band are visible of the surface of the beams containing a higher amount of Pt in c) and d). Taken from Kumar et al. [33].

The scanning electron microscopic images in Figure 2-27 give a good phenomenological impression of the different mechanical performance of the glasses with different Pt-Pd contents, with Pd-rich ones showing a brittle fracture, in a stark contrast to the multiple shear banding observed in glasses containing an equal amount or more Pt than Pd. Unfortunately, the compared systems do differ in their overall noble metal content as well as the ratio of the other components, which makes it hard to make a quantitative statement. However, it is one of the starting points for this current work, to systematically study the influence of the Pt-Pd ratio in $(Pt/Pd)_{42.5}Cu_{27}Ni_{9.5}P_{21}$.

2.6.3.3 Influence of Structure

From the preceding sections it becomes clear that the mechanical performance is defined by the combination of the specific chemical composition, which basically sets the frame of which ductility can be reached, and the then applied thermal protocol, ultimately defining the mechanical properties. The respective explanation of specific free volume being determined by the interplay of both and then leading to the mechanical response of the material might be satisfying but is rather phenomenological. Deeper insights are anticipated by structural considerations. Unfortunately, with the lack of translational long-range order in the material the derivation of direct structure-property relations is extremely challenging from an experimental point of view. However, the established concepts of specific atomic clusters, establishing a short-range order (SRO) and these cluster sometimes possessing ordering relations among themselves, the medium-range order (MRO) are helpful tools to describe the order in the perceived disordered structure [138,139] (compare section 2.5.2).

 Especially the medium range order, reaching beyond the nearest neighbor (NN) relation in the pair distribution function and especially the number of atoms shared between neighboring cluster, i.e. how they are connected, was shown to be important for the respective mechanical properties [88]. In particular it was shown that these different cluster connections do react differently to external loads. In a recent simulation study, Ding et al. imposed a shear strain to eight different metallic glasses and simulated the resulting shear strain of differently connected clusters. The results of the simulations, depicted in Figure 2-28, show significant differences between the actual shear strains on the respective clusters compared to the imposed macroscopic strain. When reflecting that different connecting schemes are basically always present in any amorphous system, this further underlines the inhomogeneous nature of any elastic deformation state present in an amorphous material. Whereas for the 1-atom connection almost no difference between the external and microscopic strain can be observed, the 2-atom and especially the 4-atom connections show a much higher deformation, meaning they behave less rigid compared to the average. In a stark contrast the 3-atom connection is the only atomic arrangement that behaves stiffer than the macroscopic sample. This heterogeneous distribution of shear within the probed sample due to the different connections underlines the importance of also including the structure of the glass, when interpreting the macroscopic properties i.e. the shear modulus to bulk modulus ratio to predict a mechanical response [109,118].
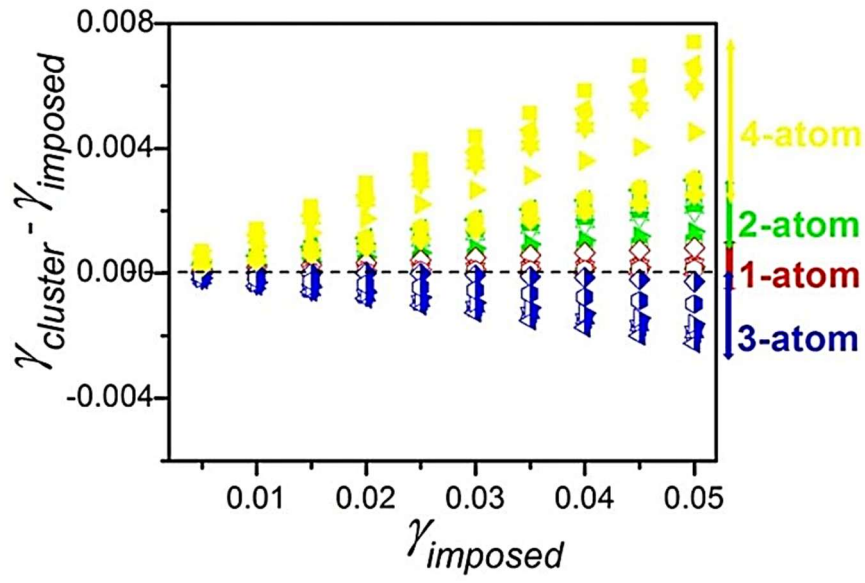
Figure 2-28: Difference in the shear strain in the cluster $\gamma_{cluster}$ to the imposed macroscopic shear strain $\gamma_{imposed}$ for different cluster connections present in 8 different metallic glasses. Taken from Ding et al. [88].

3. Materials and Methods

3.1 Sample Production

3.1.1 Alloying

All samples in this work are produced from high purity raw elements (purity > 99.95%). They contain a high amount of P (21 at%, translating to 5.8 - 8.7 wt%, depending on the composition), which in its elemental form is highly volatile, basically possessing no stable liquid phase under ambient pressure and a low evaporation temperature (554 K). Hence, special caution and a good alloying strategy is needed to safely introduce the elemental phosphorus into the alloy. A special procedure was developed and well-probed for Fe-P and Ni-P pre-alloys, which was then adapted for noble metals. For this alloying technique all metallic, nonvolatile components of the alloy (Pt, Pd, Cu, Ni) are molten in an arc-furnace under Ti-getter purified high purity Ar atmosphere (Ar. 5.0), to create a metallic precursors alloy. Master alloys of $Pt_{42.5}Cu_{27}Ni_{9.5}P_{21}$ and $Pd_{42.5}Cu_{27}Ni_{9.5}P_{21}$ are produced by inductively melting the high-purity metallic precursors alloy and the elemental phosphorous under a slight over-pressure (+ 0.1 mbar to ambient pressure) high-purity argon (Ar 6.0) atmosphere in a fused silica tube, priorly evacuated to at least 5×10^{-3} mbar. In the silica tube, the metallic precursor alloys are put on top of the elemental phosphorous and are heated inductively at the top until the metal starts to melt. The dropping and flow of the melt through gravity ensures a sealing of the area below, where the P is located, creating a sealed reaction chamber for P to dissolve in the metallic melt, hindering its evaporation. For this step it is important that the inner diameter of the silica tube is not significantly bigger than that of the metallic pre-alloy. In the current case an inner diameter of 12 mm was chosen, as the metallic pre-alloy features diameters of around 9 ± 2 mm. The hot metal above the reaction area absorbs the small amounts of evaporating phosphorous, limiting its loss. Images documenting the different steps are provided in Figure 3-1. After the alloying process, any loss of mass can be accounted for by P, as none of the metal should have evaporated at the overpressure and the temperatures used. By weighing of the samples after the process deviations in P-content can be assured to be below 0.5 at%. For these noble-metal and phosphorous containing alloys, it is reported in Ref. [140] that a fluxing treatment with B_2O_3 is possible to cleanse the melt of residual impurities that can act as nuclei for crystallization, thereby greatly increasing their ability to be undercooled and consequentially their ability to form a glass. Subsequently, the pre-alloys are heat-treated in dehydrated B_2O_3

for at least 16 hours at 1200 °C under high purity Ar atmosphere in a fused silica tube with a larger inner diameter of 16 mm according to the procedures described in Ref. [140].
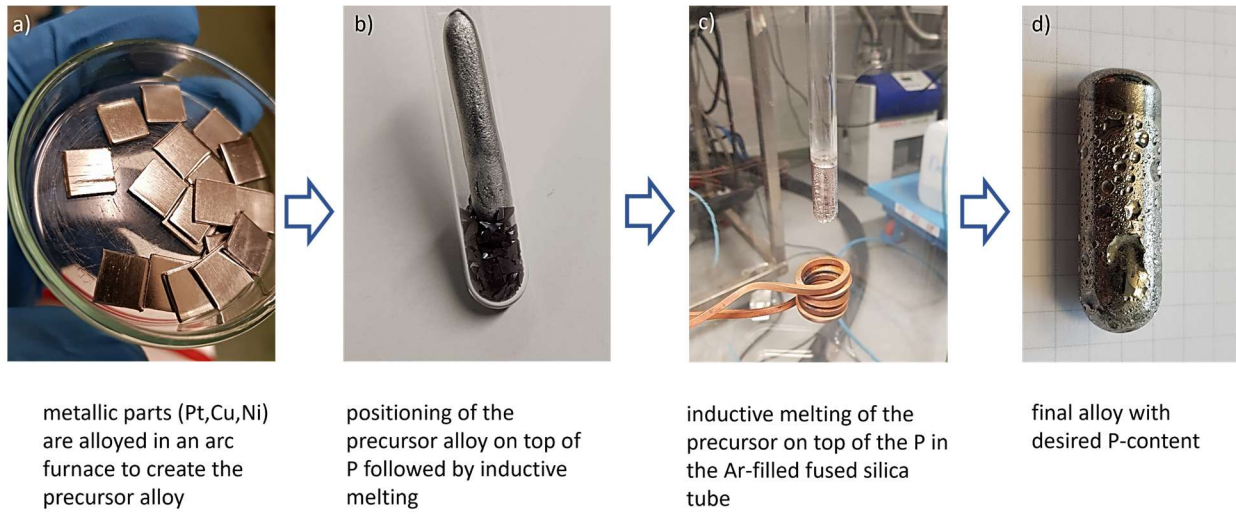
Figure 3-1: Schematic of the alloying procedure with P: Starting from the elemental metallic components (a) that are used to form the precursor alloy, which is then inductively alloyed on top of the volatile elemental P (b) in a sealed silica tube under argon atmosphere, preventing the loss of P during the alloying (c), leading to the final alloy with desired P-content (d)

Figure 3-2: Purified Master-alloy of $Pt_{42.5}Cu_{27}Ni_{9.5}P_{21}$ after the fluxing procedure with B_2O_3

Finally, the purified master-alloys are mixed in the ratio of the desired compositions; $Pt_{42.5-x}Pd_xCu_{27}Ni_{9.5}P_{21}$ where x is x =0, 2.5, 7.5, 12.5, 17.5, 20, 22.5, 30, 40, 42.5 at%. In the following the specific alloys will be termed by their Pt and Pd content, e.g., Pt22.5Pd20 for $Pt_{22.5}Pd_{20}Cu_{27}Ni_{9.5}P_{21}$. The solid mixture is then re-melted in an arc furnace under a high-purity argon atmosphere, to ensure homogeneity of the sample.

3.1.2 Casting Techniques

To achieve the final amorphous products in the desired geometry different casting techniques are needed. In the context of this works samples in the dimension of ribbons (~20 μm in thickness), 500 μm thick plates, 2 mm thick plates, and rods of 5 mm diameter were used.

Tilt Casting

The two latter geometries are produced by a tilt-casting process into a directly water-cooled Cu-mold after inductive heating in a ZrO_2 coated quartz crucible (compare Figure 3-3). This technique allows the melt to be cast without larger turbulences or shear forces comparable to e.g., suction casting. Unfortunately, this technique is not favorable for all geometries and bulk glass forming alloys for several reasons. Firstly, a high specific weight of the used alloys is needed to enable a good filling of the mold. Further, a low melting point of the used composition is needed, allowing sufficient overheating of the melt, which is generally important but even more as the inductive heating limits the absolute temperatures reachable. Also, the filling of smaller cavities becomes harder, when the mold is only filled by gravitational forces, mainly limiting this technique to casting diameters of 1 mm and above.

Suction Casting

Smaller sample dimensions, such as the 0.5 mm plates that are well suitable for X-ray diffraction studies, are produced using the suction casting technique. Here, the alloys are re-melted by an electric arc under a Ti-gettered high-purity argon atmosphere and subsequentially sucked into water-cooled copper molds in a custom-built suction casting device.
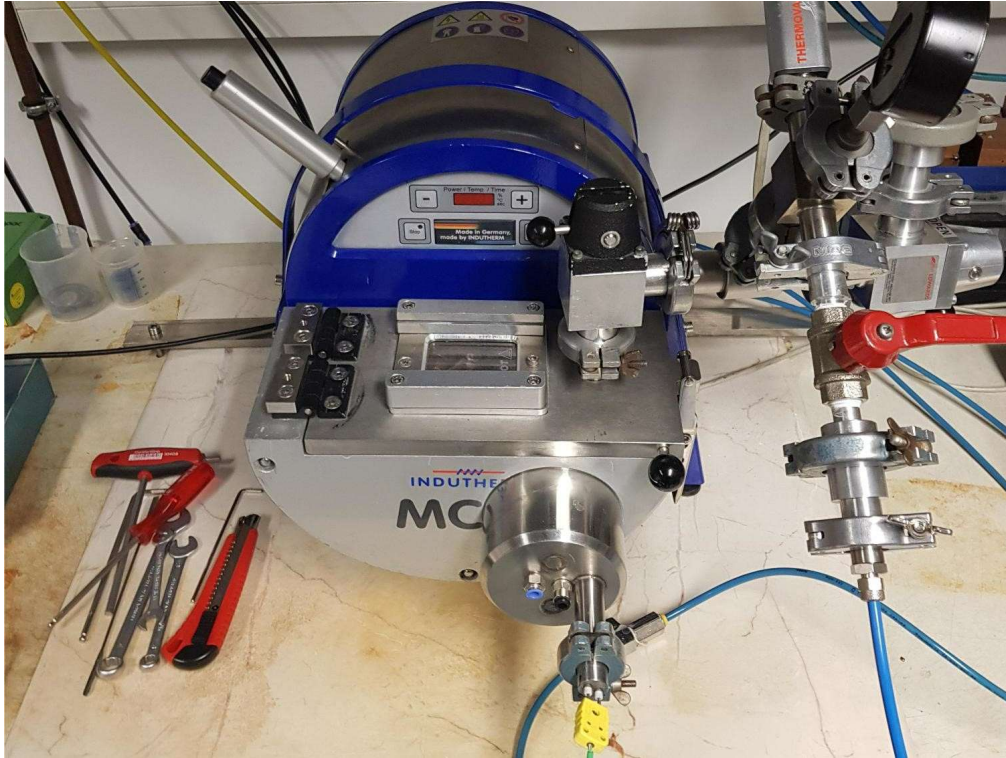
Figure 3-3: Modified MC15 tilt-casting device from Indutherm-Erwärmungsanlagen GmbH . An additional water-cooling system is attached to the vacuum chamber in the front. This feature allows direct water cooling of the Cu-molds.

Figure 3-4: 0.5 mm thick plate out of $Pt_{42.5}Cu_{27}Ni_{9.5}P_{21}$ with the 2 mm gate and cast-on section created through suction casting into an indirectly water-cooled Cu-mold.

Melt-spinning

Due to the low incident energies of around 8 keV, used in X-ray photon correlation spectroscopy (XPCS), small sample thicknesses of around 20 μm are needed to enable a measurement in transmission mode with sufficient signal-to-noise ratio. Hence, ribbon-shaped samples of all alloys are produced by a melt-spinning technique. The device consists out of a vacuum chamber with a quartz nozzle inserted in an inductive heating coil, which is located above a fast-spinning Cu-wheel. The alloy is put into the nozzle and is inductively heated well above its liquidus temperature. The nozzle itself is connected to an inert gas supply i.e. Ar, that allows a spraying of the liquid melt onto the Cu-wheel. The thin jet of molten metal is cooled extremely fast by the large thermal mass of the wheel, reaching cooling rates of up to 10^6 K s^{-1} [141]. The width can be controlled by the size of the nozzle, which in this case had an 8 mm opening. The thickness of the obtained ribbons can be controlled by the rotational velocity of the wheel. For the Pt-Pd-Cu-Ni-P based samples a rotational speed of 2700 min^{-1} and a maximum heating power of 40% was used to create ribbons of approximately 10-18 μm thickness. The heating time was adjusted to the amount of material (~2 g) in the nozzle to ensure a full melting and homogenization of the melt via visual observation.

3.2 Calorimetry

3.2.1 Differential Scanning Calorimetry

3.2.1.1 Temperature Scans

The significant changes in heat capacity between glass and liquid state as well as the release of heat during crystallization or latent heat needed during melting highly endorse the use of calorimetric techniques for the characterization of amorphous metals. Hence, calorimetry is used to quantify the thermophysical properties of the alloy system, regarding glass transition, crystallization and melting behavior. This means that the quantification of characteristic temperatures like glass transition T_g, crystallization T_x, melting T_m, and liquidus temperature T_l, but also specific isobaric heat capacities of liquid, crystal and glass and the respective changes in enthalpy and entropy involved in the transition between the different states is possible.

Per definition calorimetry focusses on the measurement of differences in heat in a material. The absolute heat Q cannot be measured directly, but changes in heat ΔQ can be tracked through changes in temperature ΔT being connected via the mass m and heat capacity c of the material:

$$\Delta Q = m\, c\, \Delta T \tag{3.1}$$

In the most simple variant, differential thermal analysis (DTA), the same temperature protocol is applied to a sample (S) in an inert crucible and an (often empty) reference (R) crucible, while the temperature difference ΔT_{SR} between both sides is tracked. Like that exothermal and endothermal processes as well as changes in the heat capacity of the sample can be tracked through a positive or negative difference in temperature compared to the reference.
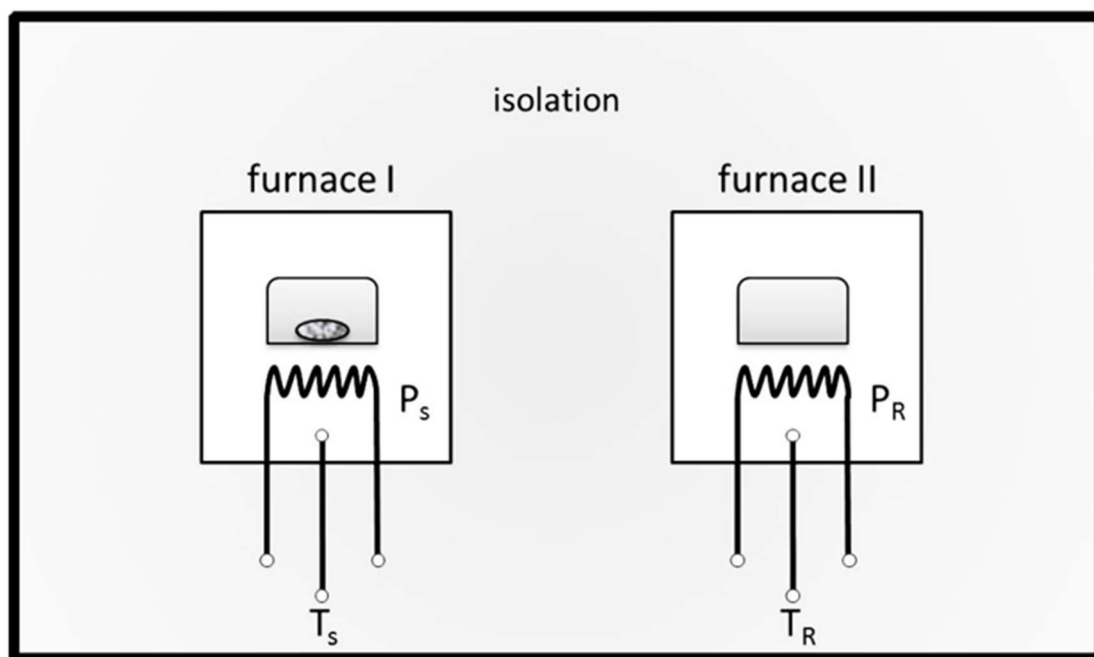
Figure 3-5: Schematic of a power-compensated differential scanning calorimeter (DSC) , consisting of two separate micro-furnaces, which can be heated individually by a heating power P and are controlled by the temperatures detected by thermocouples directly below the crucible. The left side contains the sample in its crucible, whereas the right side only contains an empty crucible, serving as a reference. Taken from Ref. [91].

In this work a differential scanning calorimeter (DSC) of the type DSC8500 from Perkin Elmer was used. This type of calorimeter applies the so called "power-compensation" method. This mode of operation differs significantly from "heat-flux" DSCs, that are widely spread in thermal analysis. Whereas the latter method is based on measurements of temperature differences alike DTA, the power-compensated DSC tries to eliminate the temperature differences by applying different heating power to sample and reference. Technically this is realized by thermally insulating the sample and reference side from each other and each side possessing its own

heating element and thermocouple. A sketch of the power-compensated DSC is provided in Figure 3-5.This allows to keep ΔT_{SR} constant over the course of the measurement, by reducing or rising the heating power of the sample side P_S. This allows a direct physical measurement of the difference in heating power ΔP_{SR} that is needed to ensure thermal equilibrium, which itself is proportional to the heat flow $dQ/dt = \dot{Q}$ into or out of the sample. This heat flow can be described through the derivative of Eq.(3.1):

$$\frac{dQ}{dt} = \dot{Q} = (m_S - m_R)(c_S - c_R)\frac{dT}{dt} \tag{3.2}$$

, where m_S is the mass and c_S the heat capacity of the sample and m_R is the mass and c_R the heat capacity of the reference, which is assumed to be zero. The used power-compensated DSC8500 can be operated in a temperature range from 183 K up to 983 K by using a three-stage intracooler. The maximum linear heating and cooling rates that can be applied are around 3 K s^{-1}. The lower limit is basically given by the sample mass that can be inserted into the calorimeter, ensuring a detectable measurement signal, as $\dot{Q}$ is directly proportional to the applied rate $\frac{dT}{dt} = \dot{T}$ (compare Eq. (3.2)). All measurements below 873 K are carried out in conventional aluminum crucibles, while measurements above this temperature, which include the melting of the samples, are carried out in graphite (C) crucibles. Calibrations of heat flow and temperature are conducted for each combination of applied rate and crucible type based on the melting of pure In and Zn. For the high temperature measurement in C crucibles also the melting event of Al is used. All measurements are carried out under a constant flow of high-purity Ar6.0 (99.9999 wt%) with a flow rate of 20 ml min^{-1}.

3.2.1.2 Interpretation of the Heat Flow Signal

Now the question arises how the measured heat flow is related to the thermophysical properties such as the isobaric heat capacity and enthalpy. To relate the changes in heat, one has to look at the definition of the enthalpy H:

$$H = U + pV \tag{3.3}$$

, where U is the internal energy and p is the pressure and V is the volume. By calculating the total differential, applying the assumption of isobaric conditions[18] (dp = 0) and the 1st law of thermodynamics:

$$
\begin{aligned}
dH &= dU + pdV + Vdp \\
dH &= dQ - pdV + pdV \\
dH &= dQ
\end{aligned} \tag{3.4}
$$

Hence, the measured heat flow $\dot{Q}$ normalized on the applied heating rate $\dot{T}$ can be directly related to the enthalpy release via integration in temperature space:

$$\Delta H = K \int_{T_1}^{T_2} \frac{\dot{Q}}{\dot{T}}\, dT\,, \tag{3.5}$$

, with K being a calibration constant, based on the heat flow calibration. Respectively, the specific isobaric heat capacity is proportional to the measurement signal, the heat flow $\dot{Q}$ can be calculated by:

$$c_p = K' \frac{\dot{Q} M}{m_s \dot{T}}\,, \tag{3.6}$$

,with M being the molar mass of the sample and K' being a constant. This constant is used to represent on the one hand the calibration but also the uncertainty resulting from the assumptions

---

[18] The isobaric assumption is mostly used for condensed matter like liquids and solids. In the case of gases, which are mainly encapsulated during measurement, isochor conditions are normally assumed, which leads to the heat flow being proportional to the isochor heat capacity c_v and its integration leading to information about the internal energy U of the measured system.

of a reference having no thermal mass (m_R and c_R being zero), which would actually result in an additional heat flow $\dot{Q}_0$. Hence, the actual heat flow of the sample would be more accurately described by:

$$\dot{Q}_S = m_S \, c_S \frac{dT}{dt} + \dot{Q}_0 \qquad\qquad (3.7)$$

The baseline subtracted heat flow curves[19] can then be evaluated via a tangent method and proper integration, as depicted in Figure 3-6. Here an amorphous sample is heated above the glass transition temperature, with its depicted temperatures of onset $T_{g,on}$ and end $T_{g,end}$ of the glass transition, followed by the increased heat capacity of the supercooled liquid and then the crystallization at the crystallization temperature T_x. At elevated temperatures the melting sets in, visible by an endothermic peak or set of peaks. The starting temperature of this event is the melting temperature T_m and the end temperature after which the sample is fully liquid is the liquidus temperature T_l. For a well reproducible determination of the crystallization enthalpy ΔH_x the integration is performed over the zero-baseline as it represents the crystalline state. The same is done to determine the enthalpy of fusion ΔH_f.

---

[19] In the case of measurements below the melting point always the second scan of the fully crystallized sample is used. If melting is involved the baseline has to be interpolated in the section of melting.
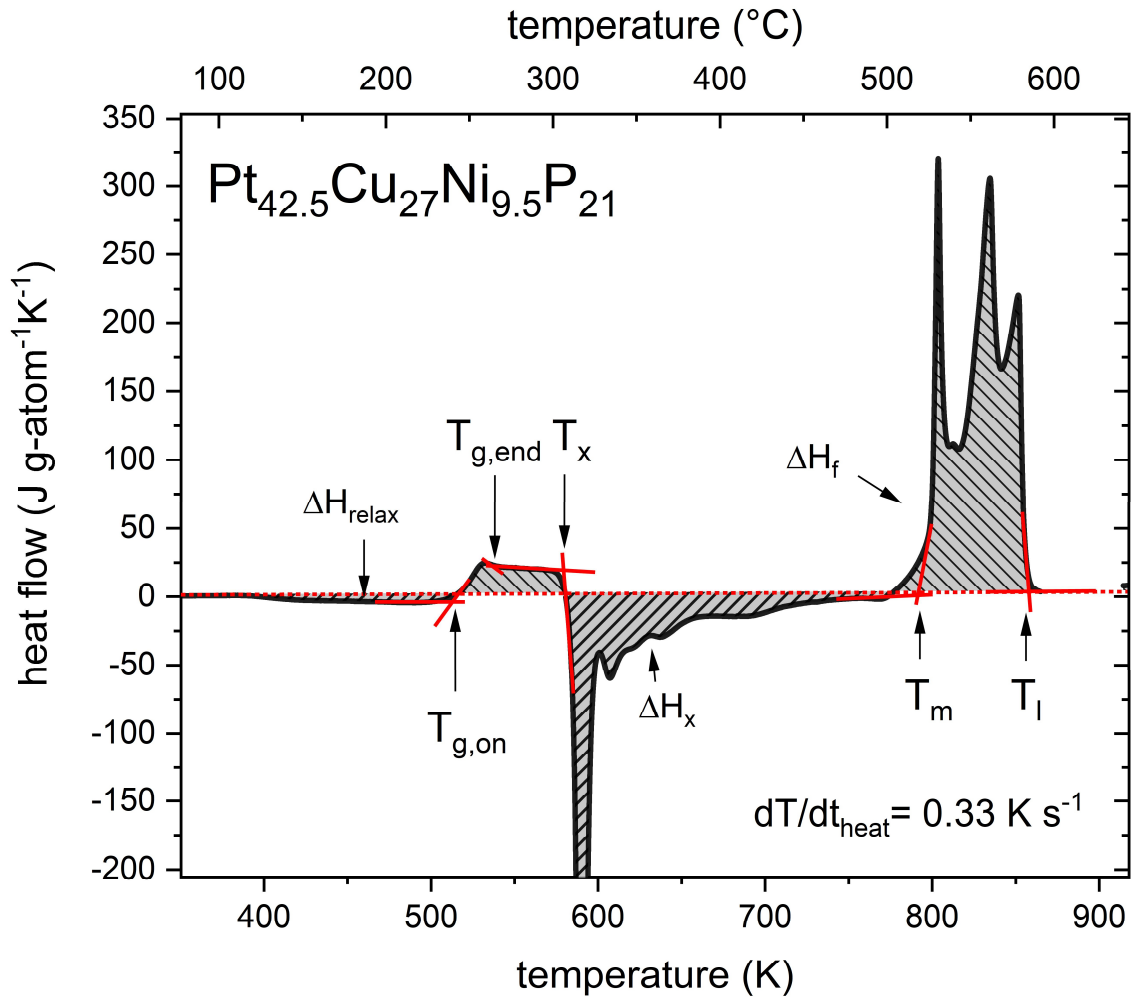
Figure 3-6: Depiction of characteristic heat flow curve of a DSC measurement and its characteristic temperatures and how they are determined through the tangent method as well as the enthalpies of relaxation, crystallization, and melting and the used baseline for their integration from the heat flow signal in this work. The dotted red line depicts the applied baseline and the full red lines are the tangents used.

3.2.2 Heat Capacity Measurements

For high-precision determination of the heat capacity it is necessary to account for the additional heat flow $\dot{Q}_0$ mentioned above, by using a reference measurement under the same experimental conditions for a material of known heat capacity. In this work a Sapphire disk with a diameter of 4 mm and a mass $m_{Sapphire} = 37.52$ g is used. This leads to the description of the heat flow of the sapphire:

$$\dot{Q}_{Sapphire} = m_{Sapphire}\, c_{Sapphire}\, \frac{dT}{dt} + \dot{Q}_0 \tag{3.8}$$

A combination of both Eq. (3.7) and Eq. (3.8) leads to a heating rate independent term for the heat capacity of the sample:

$$c_S = \frac{\dot{Q}_S - \dot{Q}_0}{\dot{Q}_{Sapphire} - \dot{Q}_0} \frac{m_{Sapphire}}{m_S} c_{Sapphire} \qquad (3.9)$$

Under isobaric conditions this leads to a specific isobaric heat capacity of the sample:

$$c_{p,S}(T) = \frac{\dot{Q}_S - \dot{Q}_0}{\dot{Q}_{Sapphire} - \dot{Q}_0} \frac{m_{Sapphire}}{m_S} \frac{M_S}{M_{Sapphire}} c_{p,Sapphire}(T), \qquad (3.10)$$

With $M_{Sapphire}$ = 20.392 g/mol. Consequently, the measurement of three different configurations is needed to accurately calculate the c_p of a sample at a given temperature: empty pans ($\dot{Q}_0$), reference sample (here sapphire, $\dot{Q}_{Sapphire}$) and the actual sample ($\dot{Q}_S$).
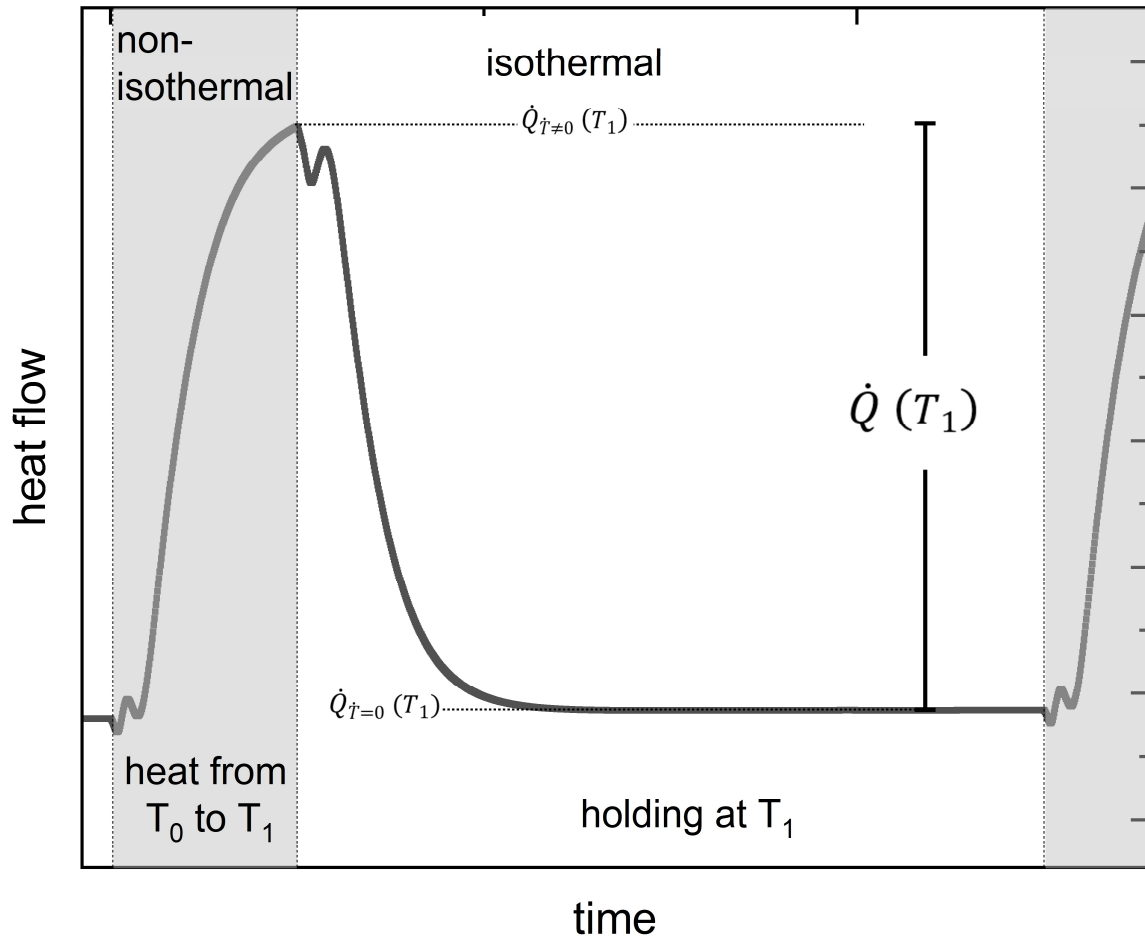
Figure 3-7: Schematic drawing of the resulting heat flow during the application of the thermal protocol of the step-method for high-precision measurements of the specific isobaric heat capacity.

Further elimination of baseline effects is provided by the accession of discrete temperatures compared to a continuous scan. A common mode is a so-called step-method. Here the samples are heated at a constant heating rate of 0.33 K s^{-1} to a temperature T_1, followed by an isothermal equilibration process step with a holding time t_{iso} = 120 s. During heating a non-isothermal heat flow $\dot{Q}_{\dot{T} \neq 0}$ (T_1) can be determined relating to the heat flow needed to heat the sample to the desired temperature T_1. Afterwards, during equilibration an isothermal heat flow $\dot{Q}_{\dot{T}=0}(T_1)$ is established, corresponding to the heat flow needed to maintain the temperature T_1 [58]. Finally the heat flow of the whole temperature step can be calculated by the difference of both heat flows, while the isothermal heat flow could be interpreted as a kind of baseline:

$$\dot{Q}\,(T_1) = \dot{Q}_{\dot{T} \neq 0}\,(T_1) - \dot{Q}_{\dot{T}=0}\,(T_1) \qquad\qquad (3.11)$$

The determination of both heat flows during the applied underlying heating protocol is schematically shown in Figure 3-7. Further a detailed drawing of the heating protocol and actual measured heat flows are depicted in Figure 3-8. It is important to note that the size of the sapphire or the reference material itself should somehow mimic that of the measured sample to create similar conditions for the heat transfer.

In the framework of this work heat capacities of the glassy, supercooled liquid, crystalline and liquid state are determined. The liquid state is measured in crucibles out of C, whereas Al crucibles are used for the other states that do not involve melting of the crystalline phase. Wherever possible Al crucibles are preferred as they possess the smallest thermal mass combined with good thermal conductivity, leading to the smallest thermal inertia. For practical purposes the empty pans are measured first, followed by the sapphire and then followed by the initially amorphous sample. After the crystallization of the initial amorphous samples during the heating run, the samples are heated closely below the onset of melting T_m to ensure a full crystallization. Afterwards the measurement program is repeated to record c_p for the crystalline state. The same samples are used for the determination of the liquid c_p above T_1, measured in C crucibles. For each alloy the measurement is repeated at least once with a shift of the temperature steps by 5 K.
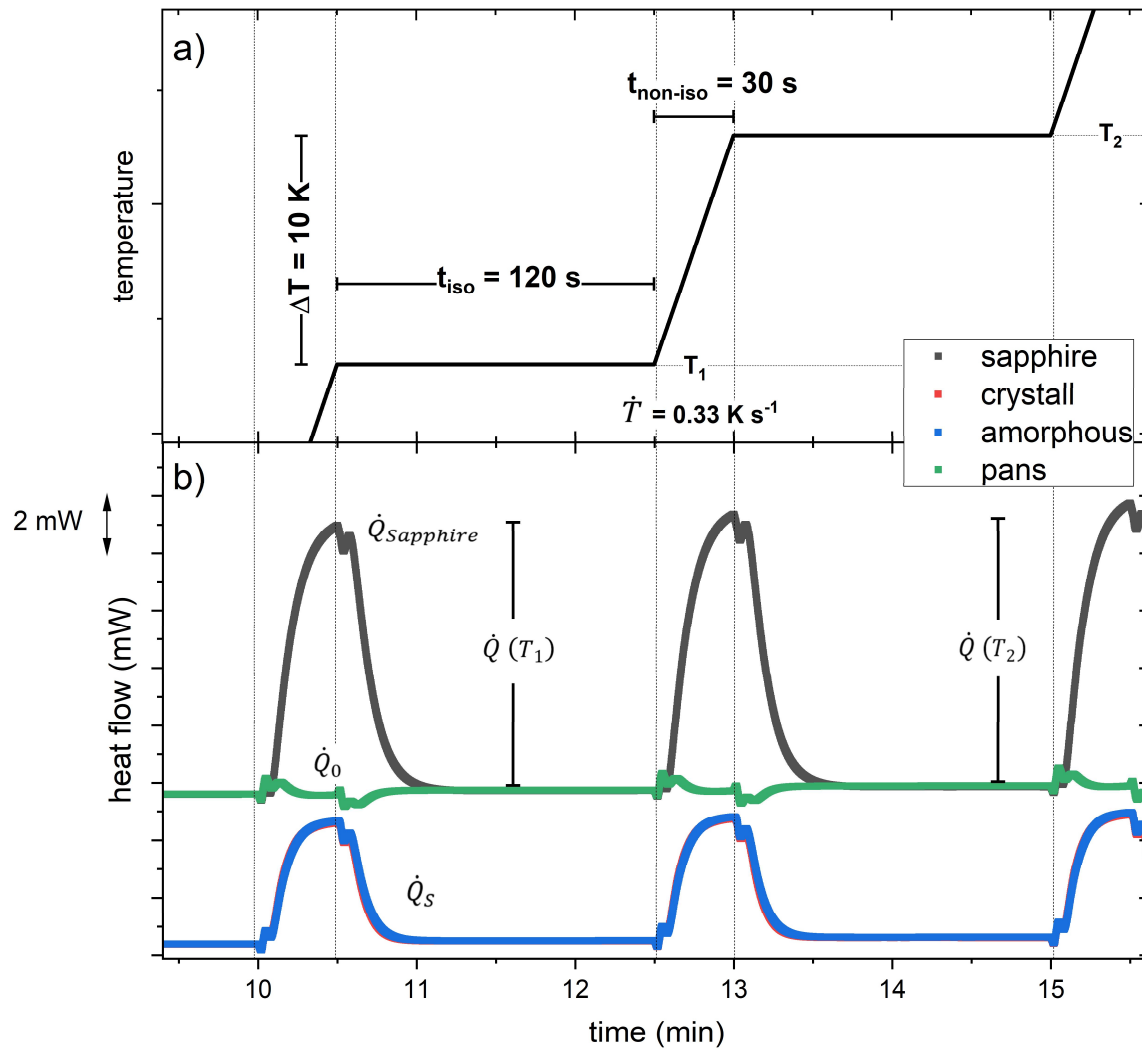
Figure 3-8: The underlying time-temperature profile and resulting heat flow during the step measurement for amorphous and crystalline sample, sapphire and empty pans. The heat flows are taken from actual measurements.

The discrete values of the specific isobaric heat capacities of the liquid and crystalline state are then fitted by Eq. (2.6) and Eq. (2.7)

3.2.3 T_g-shift Method

One method to assess the kinetics of the glass transition process, describing the transformation process from the glassy non-equilibrium back to the (metastable) equilibrium liquid state, is the so-called T_g-shift method. The observed glass transition temperature in a calorimetric measurement is highly dependent on the applied heating rate, as well as the thermal history of the sample and in particular the cooling rate it experienced leaving the liquid state, ultimately

described by the fictive temperature T_{fic}. A detailed review of the influence of the thermal history and the concept of the fictive temperature is found in sections 2.3.1.

Consequently, a well-defined thermal history i.e. fictive temperature is needed for a correct examination of the glass transition process. This well-defined state is created by heating the samples into the supercooled liquid state, followed by a defined cooling rate $\dot{T}_C$ that is equal to the heating rate $\dot{T}_H$ which is probed afterwards. For these conditions of similar heating and cooling ($\dot{T}_H = \dot{T}_C$) it was shown that the onset of the glass transition in heating $T_{g,on}$ is coinciding with the fictive temperature T_{fic} in cooling [142]. Based on the observed width of the glass transition in heating a transition time τ_{trans} can be defined for the specific fictive temperature that was created as:

$$\tau_{trans}(T_{fic}) = \tau_{trans}(T_{g,on}) = \frac{T_{g,end} - T_{g,on}}{\dot{T}_H} \tag{3.12}$$

This transition time describes the time the glass transition process takes under non-isothermal conditions and provides a timescale to the transition kinetics. It has to be underlined that it is an intrinsic property of the frozen-in non-equilibrium, which is the reason why it is influenced by thermal history. It is important to distinguish between transition time and the relaxation time of the SCL, which is an intrinsic property of the (metastable) equilibrium liquid. Hence, this property is only assessable above the kinetic glass transition temperature.

3.2.4 Modulated Differential Scanning Calorimetry

Modulated differential scanning calorimetry (MDSC) is an alternative operation mode of a conventional DSC, applicable mainly in heat-flux DSCs. In this method a modulation in temperature allows the separation of the heat flow into reversible and irreversible components, ultimately providing a tool to distinguish between thermodynamic and kinetic contributions during a relaxation process such as the glass transition phenomenon.

The first descriptions of this method were made in the early 90's by Reading et al. [143,144]. In MDSC the linear heating rate $\dot{T}_0$ is superimposed by a sinusoidal modulation of the temperature, where the absolute applied heating rate $\dot{T}_{absolute}$ can be described by:

$$\dot{T}_{absolute}(\text{t}) = \dot{T}_0 + A_T \omega cos(\omega t) \tag{3.13}$$

where A_T is the amplitude of the temperature modulation and ω is the angular frequency of the modulation which is connected to the period time P by

$$P = \frac{2\pi}{\omega} \tag{3.14}$$

The modulation of the temperature described by $\dot{T}_{absolute}(t)$ leads to a modulated heat flow signal $HF_{mod}(t)$. From the sliding average of $HF_{mod}(t)$[20], the total heat flow $HF_{tot}(T)$ is derived where T refers to the average temperature defined by $\dot{T}_0$.

According to the approach of reversing and non-reversing heat flow, described in Ref. [145], this resulting heat flow $HF_{tot}(T)$ can be split into a reversing heatflow $HF_{rev}(T)$ and a non-reversing heatflow $HF_{non-rev}(T)$:

$$HF_{tot}(T) = HF_{rev}(T) + HF_{non-rev}(T) \tag{3.15}$$

The course of these heat flows, illustrated in in the case of the $Pt_{42.5}Cu_{27}Ni_{9.5}P_{21}$ alloy, highlights their different trajectories and temperature dependencies. In particular, the $HF_{tot}(T)$ is resembling a conventional temperature scan at the respective linear heating rate $\dot{T}_0$, featuring a step at the kinetic glass transition event. Similar behavior can be observed for the HF_{rev}, but at higher temperatures. This effect is due to the fact that the reversing heat flow is not probing the kinetic glass transition, but the dynamic glass transition. Hence the observed step in the signal is not due to the applied linear rate, but its modulation frequency/period. While the kinetic glass transition describes the devitrification of the system and its recovery of the metastable equilibrium state, the step in the reversing heat flow describes the ability of the liquid [21], due to its intrinsic dynamic state i.e. atomic mobility, to "follow" the external perturbation given through the temperature modulation. This means the step in the heat flow corresponds to the

---

[20] A sliding time window of the length of one modulation period is used for a Fourier analysis of $HF_{mod}(t)$ to determine the average value and amplitude of it.

[21] Hence, the probing of this effect/property is only possible above the kinetic glass transition, as the metastable equilibrium of the liquid has to be established already.

temperature region, where the average relaxation time spectrum of the liquid $\tau_d(T)$ is in the order of the applied modulation period [146].

$$\tau_d = \frac{1}{\omega} = \frac{P}{2\pi} \tag{3.16}$$

For smaller modulation periods, the step in the reversing heat flow shifts to higher temperatures and $\tau_d(T)$ decreases. The temperature of the dynamic glass transition $T_{g,dyn}$, is defined as the inflection point of the curve, determined by peak fitting of the maximum of $\delta HF_{rev}(T)/\delta T$. A depiction of the fitting is depicted in Figure 6-4a).
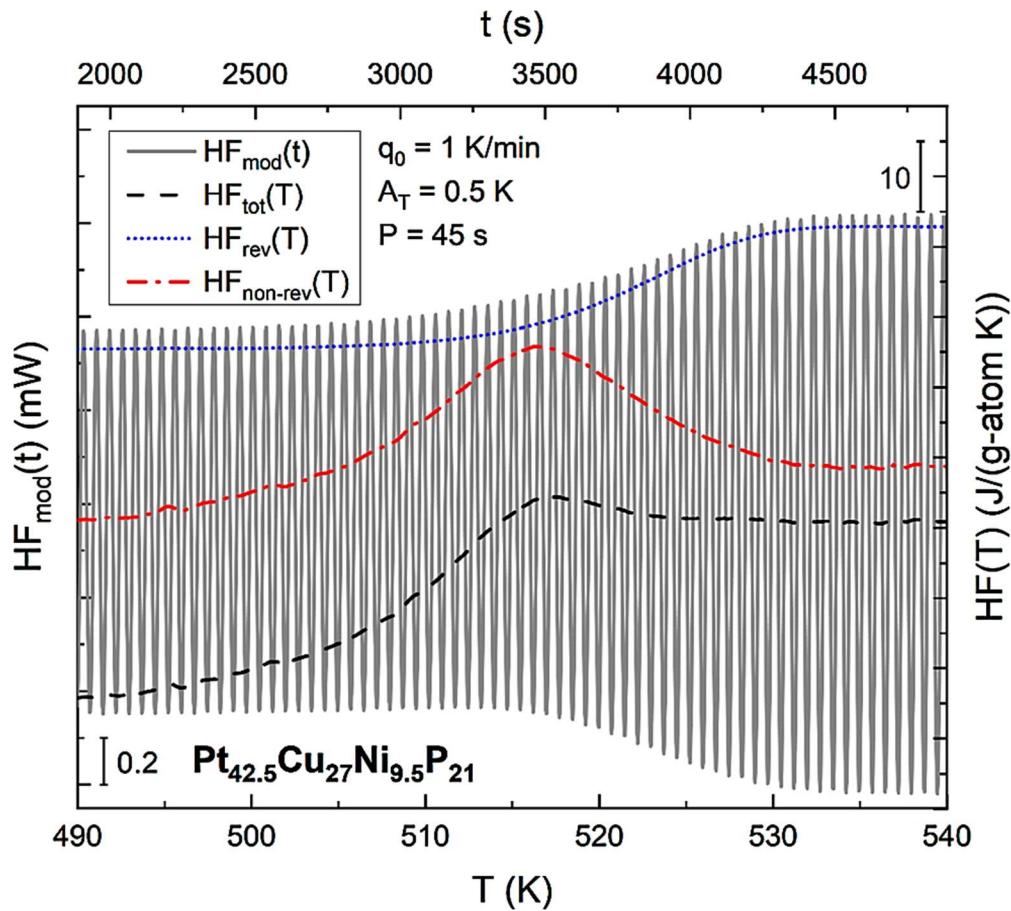
Figure 3-9: Modulated heat flow $HF_{mod}(t)$ induced by the sinusoidally modulated temperature during a heating scan of $Pt_{42.5}Cu_{27}Ni_{9.5}P_{21}$. The total heat flow $HF_{tot}(T)$ resembles a classical DSC scan at a linear heating rate, featuring the kinetic glass transition event due to the linear heating rate $\dot{T}_0$ (in the depiction it is noted as q_0) . The reversing heat flow $HF_{rev}(T)$ features the dynamic glass transition event, due to the underlying modulation period/frequency. The non-reversing heat flow $HF_{non-rev}(T)$ mathematically originates from difference between $HF_{tot}(T)$ and $HF_{rev}(T)$. Taken from Frey et al. [146]

It is important to note that there are several assumptions to be made that lead to the simplicity of the given formulas. In particular for MDSC high attention has to be paid to not severely violate these assumptions, as it can lead to serious misinterpretation of the measured signal. At first no structural changes should occur during one period of the sinusoidal modulation. Whereas this assumption is still valid for small changes in heat flow e.g. during the glass transition, it is strongly violated during crystallization or melting events. Even the glass transition of a highly relaxed glass, leading to a large enthalpy of recovery during heating, can lead to a violation of this assumption. A more in-depth explanation to the method is provided in Ref. [145].

In the framework of this work the MDSC measurements are performed with a Q100 DSC from TA instruments in Al pans. Heating and cooling temperature scans with an underlying rate of $\dot{T}_0 = 0.016$ K s^{-1} and a sinusoidal temperature modulation using an amplitude of 0.5 K are performed in the supercooled liquid state of the alloys. Modulation periods between 15 s and 120 s are applied. The resulting heat flow signal is analyzed in terms of the reversing-non-reversing approach, allowing to determine the period-dependent dynamic glass transition temperature for the applied modulation period from the inflection point of the reversing heat flow curve HF$_{rev}$(T).

3.3   X-ray Diffraction

3.3.1 Theoretical Background

The following subsection orients on the book "Underneath the Bragg Peaks" by T. Egami and S. J. L. Billinge, which is recommended for a more detailed and in-depth review of total scattering in non-crystalline materials, regarding theory, practical use, and data analysis.

The verification of the amorphous nature of a solid requires knowledge about its structure on the sub-nanometer length scale. One vital technique that can provide such information is X-ray diffraction (XRD). Whenever an ordered structural unit, e.g., a crystal is interfering with radiation that possesses a wavelength in the order of the average distance of these ordered structural unit, diffraction can occur. In the case of metallic systems possessing small interatomic distances in the order of Å, consequently radiation with a very small wavelength, as for example X-ray radiation is needed. One basic model to describe diffraction and the underlying principle of interference, was provided by X. Bragg [147]. Waves that hit an ordered

body, like a crystal lattice, are reflected/diffracted by different planes of it. This initial process can be described according to Huygens principle, which describes that all points of a wave front can be regarded as new sources of secondary waves. In practice this means that between each plane that is hit by the incident wave another secondary wave is originating. Afterwards, these new reflected waves can interfere with each other either in a constructive or destructive way, depending on their path difference, leading to a distinct motive that depends on the wavelength of the incoming wave, as well as the average distance between the lattice planes. From the requirement for constructive interference Bragg derived a law, which describes the maxima of intensity of the diffracted beams as a function of the wavelength of the radiation, the incident angle and the distance between the ordered particles, the lattice parameter. Hence, once an ordered system interacts with radiation with known wavelength and angle of incidence, information on its microscopic structure can be derived.

$$\mathrm{d} = \left(\frac{n\lambda}{2\,sin\,(\theta)} \right) \qquad\qquad (3.17)$$

, with d being the distance between the crystallographic planes, n being an integer describing the order of the scattered intensity, λ being the wavelength of the incident wave and 2θ being the scattering angle. This law marks the foundation of crystallography, which utilizes the translational symmetry of a crystal to fully describe the lattice and atomic positions by a small set of parameters such as the lattice constants and angles. At this point it shall be stressed, that a larger distance between the planes of the lattice leads to a smaller scattering angle, due to the reciprocal correlation. This fact is important to understand, when working with diffraction data, as the diffracted intensity that is experimentally assessed basically consists of a Fourier transform of the real space in the sample to the so called reciprocal space.

Even more important in the context of this work is to understand that not only a perfect crystalline lattice leads to diffraction, but any structural unit that is in the size of the wavelength. For metallic liquids, possessing structural units in the size of several Å this leads to broad diffraction peaks, originating from the large distribution of structural lengths, compared to the discrete length scales in a lattice that lead to Bragg peaks. To describe the scattering of real samples in more than one dimension the basic Bragg equation can be transferred towards a vectorial formulation by introducing the diffraction vector or wave-vector Q:

$$Q = k_{initial} - k_{final} \tag{3.18}$$

, where $k_{initial}$ is the wave-vector of the incoming beam and k_{final} is the wave-vector of the diffracted beam. In the case of elastic scattering $|k_{final}|$ and $|k_{initial}|$ are identical and the the magnitude of $|Q|$ can be derived by:

$$|Q| = \frac{4\pi \sin(\theta)}{\lambda} \tag{3.19}$$

From this equation also the need of high energy X-ray diffraction to gain insights into the structure of metallic glasses can basically be derived. From basic geometric limitations the scattering angle cannot be larger than 90°, leading to the detectable maximum wave-vector $Q_{max,\lambda}$:

$$Q_{max,\lambda} = \frac{4\pi}{\lambda} \tag{3.20}$$

, which leads to the need of small wavelength, i.e. large beam energies to cover large Q values. For laboratory scales, which commonly use Cu k-α radiation with a characteristic wavelength of 1.54 Å, this leads to a $Q_{max,\lambda}$ of around 8 Å^{-1}. In contrast it was shown that for amorphous metallic systems a $Q_{max,\lambda}$ of around 14 Å^{-1} is needed for a sufficiently good Fourier transform in real space. [148]. The implications of the detectable Q-range on the extractable information will be discussed in section 2.5.3 and in the following paragraphs.

Whereas Eq.(**3.17**) is basically providing the spatial information on where the beam is scattered, one major information that is missing is the scattered intensity I(Q) at a given position or more general wave-vector. Any transmitted scattering intensity I_T that is obtained from elastic scattering is composed of several components:

$$I_T = I_C + I_{IC} + I_{MC} + I_{BG} \tag{3.21}$$

, where I_c is the coherently scattered part of the intensity, I_{IC} is the incoherent scattered intensity, I_{MC} is the multiple-scattering intensity and I_{BG} is the intensity of photons scattered by the experimental background i.e. sample container, and oven. The incoherent scattering originates from Compton scattering. The contribution of multiple scattering stems from photons that are

scattered within the sample more than once, which has a higher probability when travelling through large sample volumes. The background scattering is of high importance and needs additionally to be recorded in the setup without a sample to be successfully subtracted. At last, the coherently scattered intensity is the intensity that is scattered from the structure with a well-defined phase relationship. With the goal to obtain structural data of a given system, this coherently scattered intensity is the contribution that is of interest. These scattered waves do have the well-defined phase relationship, that is needed for the processes of constructive and destructive interference, which is basically how the structural information is transmitted. This structural information is mainly contained in the so-called coherent scattering cross-section $d\sigma_C/d\Omega$, with $d\Omega$ being the solid angle between the detector and the origin of the scatterer/sample. The coherent scattering cross-section is proportional to the coherently scattered intensity:

$$I_C = A\ P\ C\ \left(\frac{d\sigma_C}{d\Omega}\right) \tag{3.22}$$

, where A is the sample absorption factor, depending on the sample geometry and the atomic composition, P is the electric polarization factor and C is a normalization factor, that scales the coherent scattering cross-section to an intensity per atom. The distribution of the coherent intensity as a function of the scattering vector Q can be described as:

$$I_C(Q) = \frac{\langle f(Q)\rangle^2}{N}\ |\Psi(Q)|^2 \tag{3.23}$$

, with $\langle f(Q)\rangle$ being the averaged atomic form factor of all N atoms in the sample[22], calculated by

$$\langle f(Q)\rangle = \frac{1}{N}\sum_i c_i f_i \tag{3.24}$$

where c_i is the concentration of the i-th element and f_i is the atomic form factor, which is a measure of the scattering intensity of the atoms involved. Further $\Psi(Q)$ is the sample scattering

---

[22] The angle brackets denote a compositional average over all constituents.

amplitude that contains the information of the distribution of the atoms in the form of the position of the ν-th atom R_ν

$$\Psi(Q) = \frac{1}{\langle f(Q) \rangle} \sum_\nu f_\nu \, exp\,(iQR_\nu) \tag{3.25}$$

, with f_ν being the atomic form factor of the ν-th atom.

Through this correlation the information of the atomic configuration is basically transferred onto the coherent intensity that can be caught by a detector. From the coherently scattered intensity the so-called total structure factor S(Q) can be derived, which basically describes a normalized scattering intensity:

$$S(Q) = 1 + \frac{I_C(Q) - \langle f(Q)^2 \rangle}{\langle f(Q) \rangle^2} \tag{3.26}$$

Through this normalization the total structure factor oscillates around a value of one. In the case of systems that lack long-range order i.e. liquids and glasses this oscillating decay towards unity is rather quick compared to crystalline systems. Regarding the multicomponent nature of the systems measured within this work it is important to understand how S(Q) is related to the different atomic species. If the system is composed out of n components the total structure factor is composed out of the weighted superposition of the (n+1)/2 partial structure factors S_{ij}[23], also called Faber-Ziman partial structure functions:

$$S(Q) = \sum_{i \le j} w_{ij} S_{ij}(Q) \tag{3.27}$$

with the weighting factors for each atomic pair w_{ij}

$$w_{ij} = \frac{c_i c_j f_i(Q) f_j(Q)}{\langle f(Q) \rangle^2} \tag{3.28}$$

---

[23] As we are looking at coherent scattering the signal is always based on a pair-correlation so the partial is originating by an atomic pair of species i and j, e.g. (Pt-Pt or Pt-Cu).

The partial Faber Ziman structure function $S_{ij}(Q)$ in their reported form, behave similar so the total structure function, as they also decay towards unity.

From the information contained in the total structure factor on the reciprocal length scale also information in real space as a function of the distance to the reference atom r can be derived through a Fourier transformation. Then the reduced pair distribution function can be calculated by:

$$G(r) = \frac{2}{\pi} \int_0^\infty Q[S(Q) - 1] \, sin(Qr) \, dQ \tag{3.29}$$

The reduced PDF is connected to the actual spatial distribution of the atomic pair density function $\rho(r)$ and the pair distribution function g(r) via :

$$G(r) = 4\pi r [\rho(r) - \rho_0] = 4\pi r \rho_0 [g(r) - 1] \tag{3.30}$$

here ρ_0 is the average number density. Per definition the reduced PDF describes the probability to find two atoms in the radial distance r. The fact that the amorphous systems can be assumed to be isotropic eases the description significantly, as otherwise the description in a generalized space coordinate such as the radius would not be possible. G(r) is oscillating around a value of 0, which would describe a totally disordered gaseous state. As G(r) is derived from S(Q), whose connection to partial structure factors in the case of multicomponent systems was discussed in the previous section, analogous superposition rules are necessarily also valid for G(r) of multicomponent systems:

$$G(r) = \sum_{i \leq j} w_{ij} G_{ij}(r) \tag{3.31}$$

3.3.2 Setups used at Synchrotron Radiation Facilities

X-ray diffraction experiments carried out in the context of this work were performed in several different setups in different beamlines of PETRAIII at the "Deutsches Elektronen Synchrotron" (DESY) in Hamburg. In all setups a transmission geometry is used, yet different furnaces, detectors, beam sizes and energies are used, depending on the beamline. An oversigh it listed in Table 3-1.

Table 3-1: Experimental setup details about the diffraction experiments carried out at PETRAIII

Beamline	Furnace	Energy (keV)	Beam size (mm²)	Resolution, pixel size	Detector
P02.1	Ceramic	60	0.8 x 0.8	2048 x 2048, 200 μm	Perkin Elmer XRD1621 CsI bonded detector
P02.1	THMS600	60	0.5 x 0.5		
P21.1	THMS600	100	0.5 x 0.5		
P21.1	TS1500	100	0.5 x 0.5		
P21.2	THMS600	70	0.5 x 0.5	2880 x 2880, 150 μm	VAREX XRD4343CT

In the experiments three different furnaces are used. For low temperature measurements from room temperature (RT) to 873 K the Linkam furnace type THMS600 was used. The THMS600 consists of a heating block out of Ag, that is surrounded by a water-cooled steel housing with inlets for purging with inert gases (i.e. Ar). The flat samples are glued to the Ag-block by applying a small amount of Cu-conductive paste. This ensures an optimal thermal contact between the block and the sample. However due to the direct contact it allows only measurements in the solid and deeply undercooled liquid state, where significant flow can be excluded.

For the melting of the samples or measurements above the liquidus temperature, two different furnaces were used. One setup is a custom-built ceramic furnace supplied by the experimental environment group of DESY. It uses thin quartz capillaries that are put into a resistive ceramic heater, allowing temperatures up to 1200 K(compare Figure 3-11). For the other setup a Linkam furnace of the type TMS1500 was used. This furnace is normally operated in a horizontal way. For the vertical usage, which is needed for the measurements with synchrotron radiation in transmission mode a custom-built setup was needed. In this case custom-built quartz capillaries that were inserted into a tungsten holder with a bore, which was placed in the furnace was used. Courtesy to this design goes to B. Adam and L. Ruschel. A depiction of the custom setup is shown in Figure 3-12, showing a rod-like sample being put into the quartz crucible, standing in the tungsten holder.

Figure 3-10: Linkam furnace THMS600 with the silver furnace within the chamber and the custom-built sample holder for the measurements in vertical position of the furnace. The side inlets and outlets are used for purge gas and a water-cooling of the chamber.
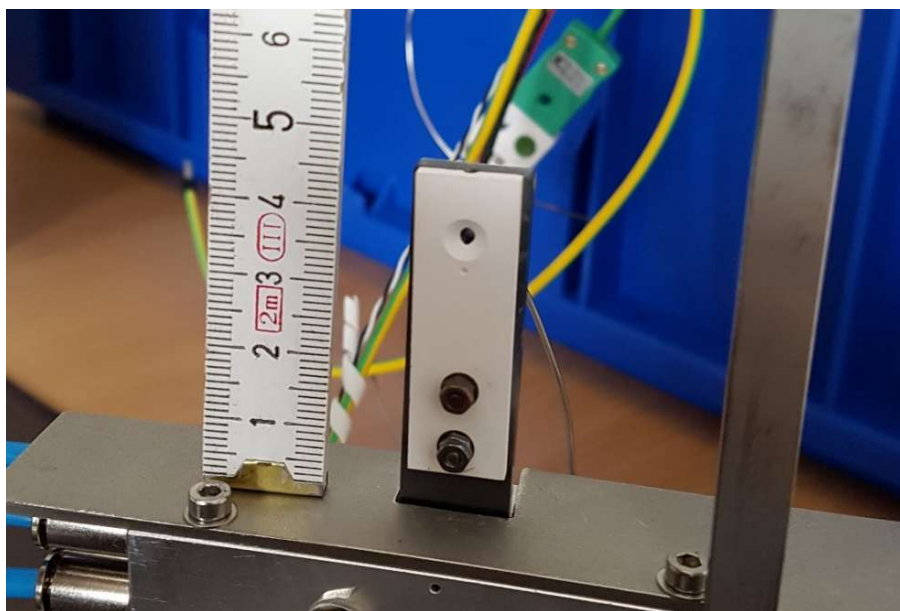
Figure 3-11: Ceramic furnace of the DESY sample environment group. Taken from the setup information of the Sample Environment Group of DESY [149].
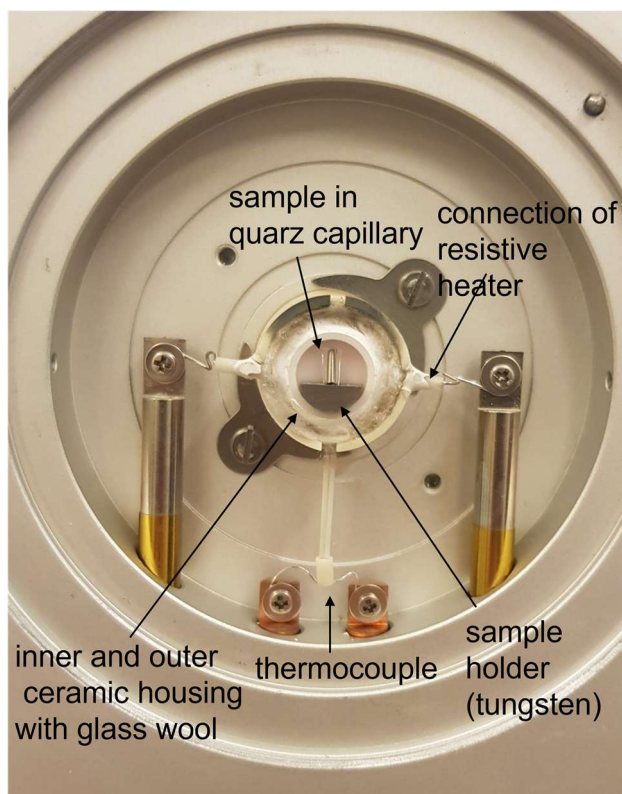
Figure 3-12: Linkam TMS1500 ceramic furnace in vertical mode . A custom-built setup out of a capillary and a tungsten sample holder is placed into the actual ceramic chamber.

The specific details of temperature range, applied heating and cooling rate are provided in each published article.

3.3.3 Data Handling

The intensity distributions I(Q), collected from the flat panel detectors were azimuthally integrated utilizing the program PyFAI integrate module and Fit2D using the option of pixel splitting. For each setup geometric calibrations of the point of normal incidence (PONI) were carried out with a calibrant (Ni, LaB_6 or CeO_2) being measured at the exact position of the sample. Further processing of the integrated raw intensity is carried out with the PDFgetX2 software [150].This processing includes an absorption corrected background subtraction, multiple scattering fluorescence and Compton scattering correction. The program PDFgetX2 is also used to calculate S(Q) and carry out the Fourier transformation to extract G(r). For the transformation an upper limit of the used Q-range of at least 14 Å^{-1} is used, which is needed to obtain the amount of detail in the second nearest neighbor distance (r_2) of the reduced pair distribution function (see Figure 3-13). For each curve an optimization algorithm is run that optimizes the correction parameters based on the minimization of oscillations on the low r side

of the first peak in G(r), where the probability of an atom being located should be zero. The applied correction procedure further facilitates the oscillating decay of S(Q) towards unity for large wave-vectors Q [151].

Further data handling was carried out utilizing OriginPro software to analyze the individual peaks of S(Q) and G(r) regarding height, position and width. For this the methodology of Wei et al. [151] is used as the discrete experimental datapoints are interpolated via a cubic-spline followed by a conventional peak integration procedure of OriginPro that is used to extract, peak height, peak position and the full-width at half maximum (FWHM).
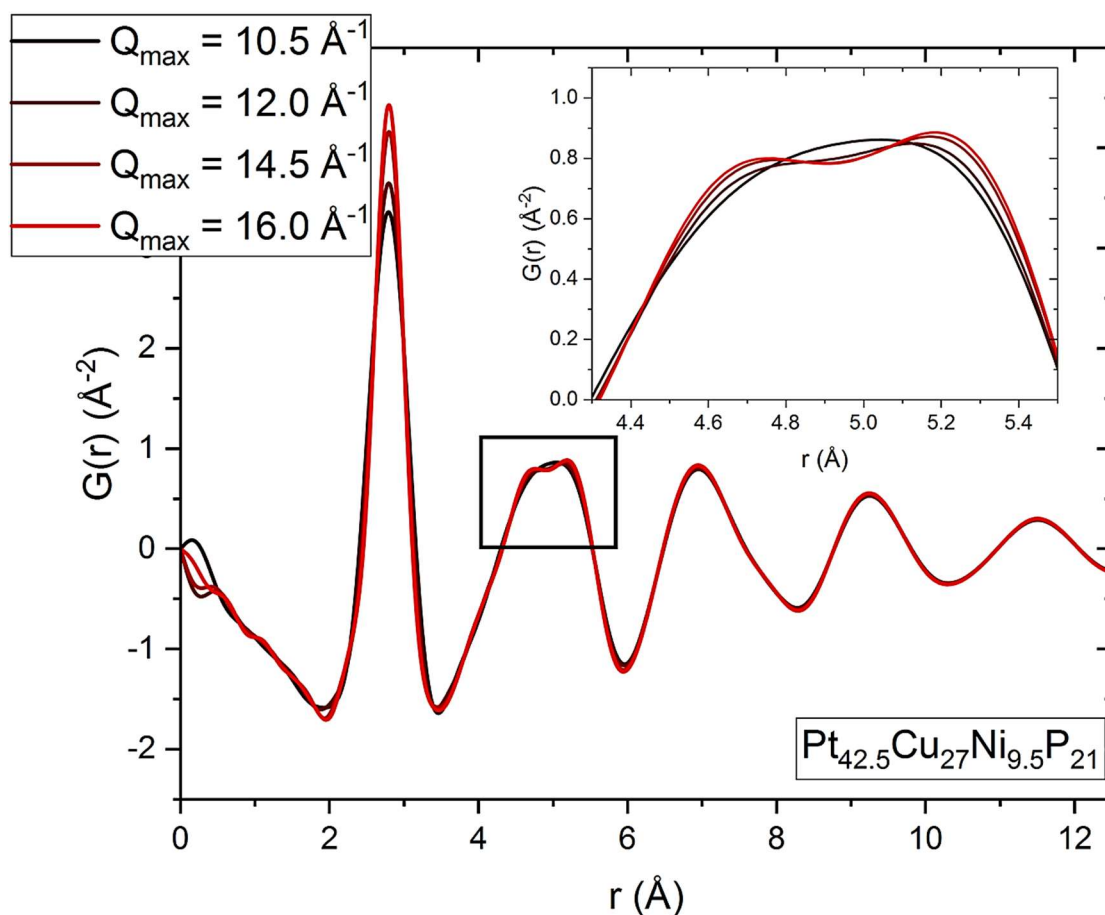
Figure 3-13: Influence of the used maximal Q-value during the Fourier transformation on the shape of the reduced pair distribution function. Taken from Ref. [152].

3.4 X-ray Photon Correlation Spectroscopy

3.4.1 Theoretical Background

The uniquely high coherence and flux of the radiation creatable at the newest generation synchrotron radiation also allows for new techniques[24]. The coherence of a radiation describes a well-defined phase relationship over the wavefront, yielding a direct relationship of the intensity of scattered particles to the distribution of scatterers that are interacting the incoming radiation in a specific volume. This local information on the illuminated volume of scatterers then leads to so-called speckle patterns. In comparison, this local information is not available during an incoherent scattering event, as only average sample properties that stem from the whole scattering volume are obtainable. In summary the obtainable speckle patterns are interference patterns that are related to the exact spatial arrangement of the scattering particle in a disordered system. Based on this idea Sutton et al. developed the new technique of X-ray photon correlation spectroscopy (XPCS) [153]. This technique basically utilizes the spatial information contained in the speckle-patterns to track the movement of the scatterers as a function of time. The idea is directly derived from the established method of dynamic light scattering (DLS), where analogously a highly coherent light source, a monochromatic laser is used. The main difference between both techniques is found in the applied wavelengths. Whereas in DLS the light source is operating in large wavelengths around the visible spectrum, XPCS is working with the very short wavelength of X-rays (here 8 keV, $\lambda = 1.55$ Å). These short wavelengths enable the tracking of the atomic motion in disordered systems. The typical timescales observable in XPCS are around 10^{-2} s up to 10^4 s, with the latter being limited by reasonable measurement time available at a synchrotron source.

In XPCS the aforementioned speckle patterns are recorded over time by a detector (here EIGER X4M) that is placed at a certain scattering angle 2θ with respect to the sample. Depending on the resulting wave-vector $Q = 4\pi/\lambda \sin(\theta)$ different spatial information ($d = 2\pi/Q$) is retrieved from the speckle patterns. For amorphous systems, commonly the wave-vector position of the

---

[24] As synchrotron radiation is based on spontaneous emission, it is actually a chaotic light source. Still, its coherence can be improved by creating a good match between the illuminated sample volume and the (small) coherence volume of the beam through a small beam aperture, combined by cutting out a narrow bandwidth of the radiation through suitable monochromators. Hence, all actions that have to taken to improve coherence go in hand with severe loss of intensity, which is the reason of the high flux of 3rd generation synchrotron sources being needed for XPCS.

first sharp diffraction peak Q_{FSDP} is chosen, as it provides the highest scattering intensity and represents the average interatomic distance. The speckle patterns obtained are then compared to each other by applying a two-times correlation function (TTCF) that basically compares the ensemble average of intensity over all detector pixels between two specific points in time t_1 and t_2:

$$G(Q, t_1, t_2) = \frac{< I(Q, t_1) \cdot I(Q, t_2) >_p}{< I(Q, t_1) >_p \cdot < I(Q, t_2) >_p}$$
(3.32)

Commonly, the TTCF are reported in a color-coded m x n matrix that reports the correlation between image m and n, that is often already converted into time instead of number of frames. In this depiction a full correlation is found on the bisecting line through the origin, that is decreasing on the orthogonal direction away from that line. Thus, the width of the colored region around the bisecting line is directly proportional to the observed decorrelation time. Further this depiction allows to distinguish between stationary and non-stationary dynamics. In the case of the SCL, the dynamics is stationary, leading to a constant width of the TTF, whereas in the glass, aging can be observed, which leads to a constant slow-down of dynamics, i.e. a broadening of the TTF. In the case of rejuvenation, an analogous narrowing of the TTF would observable.

Based on this TTCF intensity auto correlation functions $g_2(Q,t)$ can be calculated by averaging the TTCF over the whole measured temporal interval. The $g_2(Q,t)$ functions are associated to the intermediate scattering function, $f(Q,t)$, through the Siegert relation $g_2(Q, t) = 1 + \gamma \cdot |f(Q, t)|^2$ with γ being the experimental contrast. The $g_2(Q,t)$ functions were fitted using a Kohlrausch-Williams-Watts (KWW) function:

$$g_2(Q, t, T) = 1 + c(Q, T) \, exp(-2\left(\frac{t}{\tau(Q, T)}\right)^{\beta(Q,T)})$$
(3.33)

where $\tau(Q,T)$ is the structural relaxation time, $\beta(Q,T)$ is the shape parameter and $c(Q,T)$ is the product of the experimental contrast $\gamma_c(Q,T)$ and the square of the non-ergodicity factor $f_q(Q,T)$.
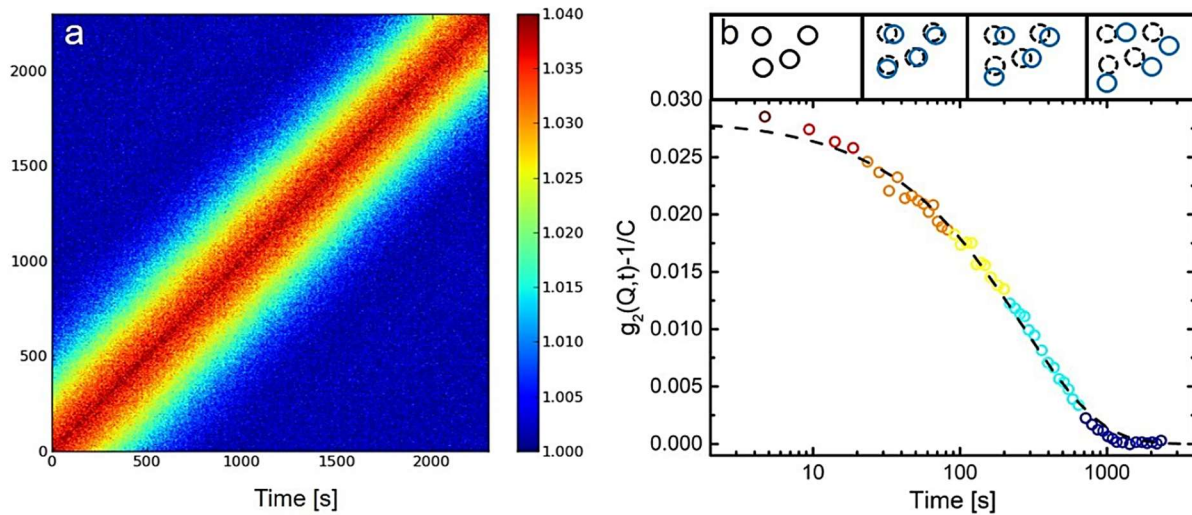
Figure 3-14: Ways to depict and understand data obtained by XPCS :Two-times-correlation function (TTCF) of a stationary dynamics (a) and a normalized intensity auto-correlation function $(g_2(Q,t)-1)/c$ with a schematical depiction of the motion of several exemplary atoms that lead to the decorrelation over time (b). For a better comparison and to underline the connection, the individual data points in b) are colored according to the color-code used in the TTCF of part a). The image is taken from Ref. [154].

3.4.2 Wave-vector-dependence of Dynamics

As aforementioned, the area detector used in XPCS does cover a certain scattering angle, that translates in a certain amount of different wave-vectors, being covered. Whereas in the past, metallic glasses and liquids were mainly measured at wave-vectors corresponding to the FSDP of the respective material, reflecting its average interatomic distance, as well as the highest scattering intensity, there is additional information to obtain from studying the wave-vector dependence of the relaxation event. First observations on the wave-vector dependence of the relaxation dynamics were made by De Gennes in 1959, based on neutron scattering experiments[155]. He observed a slowdown of the dynamics right around the structural first sharp diffraction peak in the total scattering function S(Q), combined with a change in the shape of its distribution. He described a change from a Gaussian distribution towards a Lorentzian distribution, which lead to the phenomenon being named "De Gennes narrowing". Experimental evidence of "De Gennes narrowing" was found in different kinds of liquids with different structures and seems to be a universal phenomenon of liquid systems, such as silica, water or hard sphere systems [156–158], but also polymeric systems or ionic glasses $[Ca(NO_3)_2]_{0.4}[KNO_3]_{0.6}$ (CKN) [159–162].

For metallic liquids this event is described in the frequency domain around or above the melting point, where the melt dynamics is fast enough for the neutron scattering methods [155,163]. Through the large timescale that can be covered by XPCS, together with the moveable large area detectors, the wave-vector dependence of the dynamics in deeply supercooled liquids can be investigated.

Especially the wave-vector dependence of the dynamics at wave-vectors smaller than the FSDP, connected to density fluctuations on length scales larger than the interparticle distance provides information of the underlying particle motion. At low Q the relaxation time can then by described by a power law[164]:

$$\tau(Q) = Q^{-\alpha} \qquad\qquad (3.34)$$

, where n is the respective exponent of the wave-vector dependence. For $\alpha = 2$ the transport mechanism of the particles follows the rules of Brownian motion, describing a purely diffusive nature of movement, typical for high temperature metallic liquids. In the case of a linear Q-dependence i.e. $\alpha = 1$, the transport mechanism is described by ballistic motion due to heterogeneous distributions of stress in the liquid that leads to a hopping rather than diffusive motion [165,166]. In the case of $\alpha = 0$ the relaxation time would become Q-independent. A constant value of $\tau(Q)$ at Q below the FSDP of S(Q), suggests the existence of a Q-independent (called Q_0) relaxation mode in agreement with the numerical simulations mentioned in Ref. [167]. It indicates the absence of concentration fluctuations on the probed length scale, i.e. above length scales larger than those connected to the FSDP. Its origin appears to be connected to the presence of independent locally fluctuating elastic moduli on the probed length scale and suggests the presence of a crossover to diffusive-like dynamics for these larger length scales [168].

3.5   Thermomechanical Characterization

3.5.1 Thermomechanical Analysis

The original description of the fragility concept by Angell was made based on the observation of shear viscosity. It assumes the direct connection of the macroscopic property of viscosity to the microscopic dynamics of the atoms in the liquid state. A conventional way to determine the viscosity, especially in the highly viscous regime right around the glass transition temperature, thermomechanical analysis (TMA), in a three-point beam bending setup is commonly used. It allows for a good accuracy in the range of rather high viscosities from 10^7 to 10^{13} Pa s[169]. In the method, a rectangular beam of the examined material is symmetrically bent under a static load. From the recording of the deflection of the mid-point u over time, the mid-point deflection rate $\dot{u}$ can be computed. It relates to the bending velocity v as just its negative value ($-\dot{u} = v$).
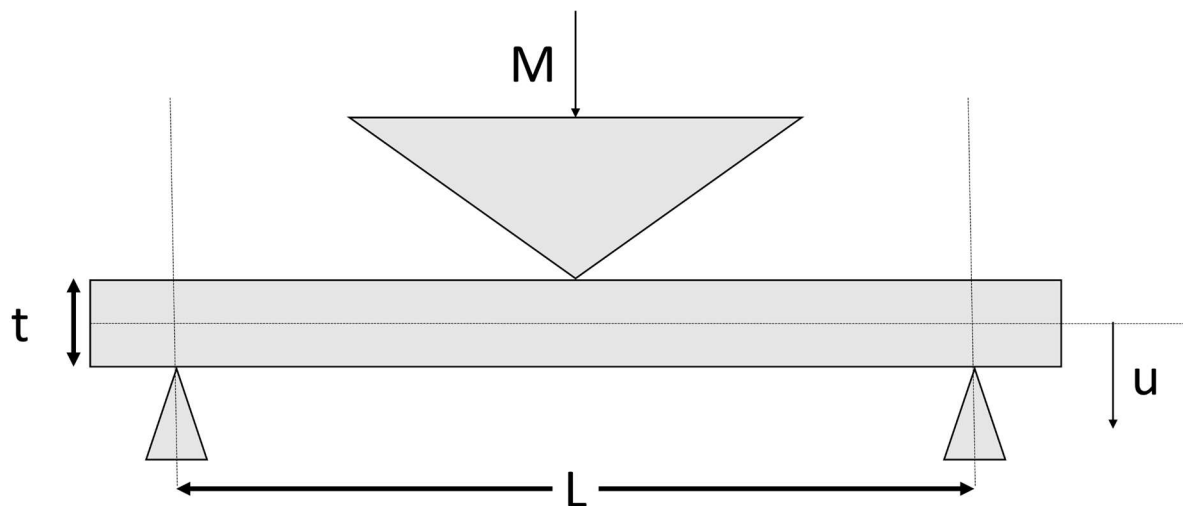
Figure 3-15: Schematic drawing of a three-point beam bending setup. A rectangular beam with the thickness t, is bent by the load M in the middle of two bearings with distance L, leading to a deflection u in the highlighted positive direction toward the ground.

The method to extract the viscosity from the bending velocity is based on analogies between elastic and viscous deformation, first described by Trouton in the early 1900's [170]. Around 60 years later, this concept was picked up by Hagy et al. to show an inverse proportionality between the deflection rate of the beam and viscosity [171]. In a three-point beam bending experiment that applied an external load M, viscosity can then be calculated by:

$$\eta(t) = -\frac{g \cdot L^3}{144 \, Iv} \cdot \left[M + \frac{\rho AL}{1.6} \right] \tag{3.35}$$

,where v is the mid-point deflection rate, L the distance between the two rigid supports of the beam-bending setup, I the cross-sectional moment of inertia of the beam, A the cross-sectional area of the beam, and ρ the volume density of the sample.

In this work a NETZSCH TMA 402 F3 thermomechanical analyzer is used with a static loading force of 10 N. The beams were cut with a diamond saw from X-ray-amorphous plates with the dimensions of $1.5 \times 13 \times 40$ mm. To optimize the signal-to-noise ratio the thickness of the beams was varied from 0.4 to 1.5 mm.
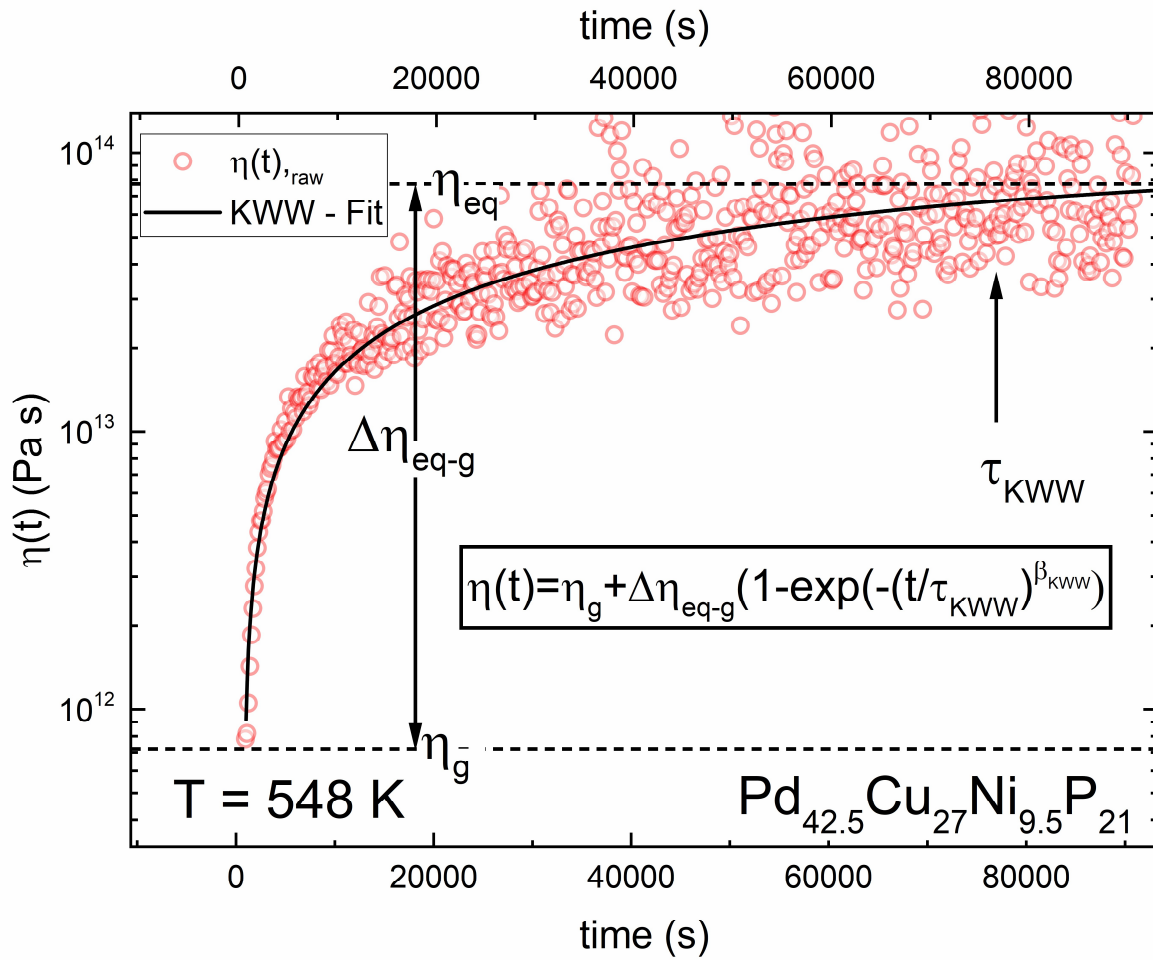
Figure 3-16: Isothermal viscosity measurement of $Pd_{42.5}Cu_{27}Ni_{9.5}P_{21}$ at 548 K obtained in three-point beam bending. The raw data is fitted by the Kohlrausch-Williams-Watts stretched exponential function to obtain the equilibrium viscosity η_{eq}.

The determination of viscosity was performed in continuous heating at heating rates of 0.33 K s^{-1} until the deflection limit of the machine was reached or the crystallization of the samples occurred. Furthermore a set of low-temperature viscosities was obtained in isothermal mode covering a temperature range of 533 K to 573 K, where the same heating rate of 0.33 K s^{-1} was used to reach the isothermal plateau. The isothermal data is fitted by a Kohlrausch-Williams-Watts stretched exponential function to obtain the equilibrium viscosity:

$$\eta(t) = \eta_g + \Delta\eta_{eq-g}\left(1 - exp\left(-\left(\frac{t}{\tau}\right)^\beta\right)\right)$$

(3.36)

,where η_g is the initial viscosity of the glassy state, $\Delta\eta_{eq-g}$ the difference between the equilibrium viscosity and the viscosity of the glass, τ the relaxation time and β the stretch exponent. The fitting procedure together with the raw data during an isothermal relaxation experiment is exemplary shown in Figure 3-16. The resulting curves can be found in the Supplementary information of Publication II [172].

3.6   Micromechanical Characterization

For the mechanical characterization of the Pt-Pd-Cu-Ni-P metallic glasses micromechanical techniques such as nanoindentation and micropillar compression tests were chosen. The choice of micromechanical testing originates from the effort to reduce sample volume and therefore cost of the noble-metal containing alloys, while ensuring the amount of tests needed to have adequate statistics. In the following the basic concepts of both methods shall be provided together with insights into the strain-rate sensitivity of metallic glasses.

3.6.1 Nanoindentation

Nanoindentation is a micromechanical technique used to determine the hardness of a material, by measuring the size of an indentation with a defined indenter geometry and force. The small penetration depth in this technique allows the probing of small sample geometries and a high number of repetitions. For metallic glasses, with their limitations in geometry due to the critical thickness and the large monetary and timely efforts needed for noble metal systems in particular this small sample volume and good statistics is highly advantageous efforts. In classical indentation techniques such as conventional hardness testing, the contact area and penetration depth are calculated from an optical measurement of the indentation size. This is not possible

in nanoindentation due to the small size of the indent. Instead, the indentation depth of the indenter is tracked, and the contact area is calculated from an area function, which is defined by the geometry of the indenter tip. The indenter tip is conventionally a three-sided Berkovich pyramid made out of diamond, which has a nominal geometric self-similarity [173]. However, knowledge of the exact shape of the tip and a characterization of it is paramount for this type of technique [174]. The mechanical hardness H of the material can then be characterized by:

$$H_{mech} = \frac{P_{max}}{A} \qquad (3.37)$$

With P_{max} being the maximum applied load and A being the contact area between indenter and the material.

During the experiment a load-displacement curve is recorded following a defined loading and unloading ramp. A typical load-displacement curve recorded for amorphous $Pt_{42.5}Cu_{27}Ni_{9.5}P_{21}$ is shown in Figure 3-17, showing a loading cycle with 100 mN that leads to elastic and plastic deformation, followed by an elastic unloading. During the loading cycle plastic deformation is occurring and discontinuities can be detected in the curve, labeled by the term serrations. These discontinuities are characteristic marks during a nanoindentation experiment and stem from energy-releasing events during the deformation process. While they are observed in different classes of materials, the physical reason behind it varies with the bonding character and underlying structure of the material. Whereas for crystalline materials the discontinuity is is connected to the activation and creation of dislocations [175], it is connected to shear localization and the activation of individual shear bands in amorphous metals [176]. The small volume probed allows a detailed study of the actual initiation event of the deformation. In particular the study of the temperature and strain rate dependence (compare section 2.6.2) of these serration events and the response of the material allows insights into its deformation behavior [177].
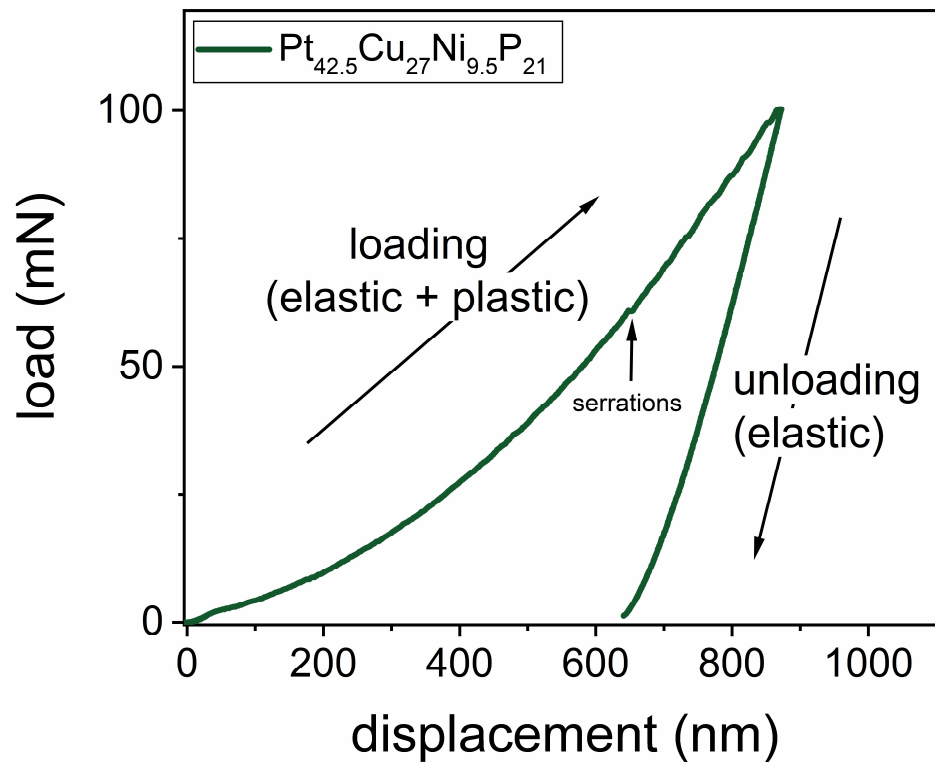
Figure 3-17: Load-displacement curve (P-h-curve) for a $Pt_{42.5}Cu_{27}Ni_{9.5}P_{21}$ metallic glass sample at room temperature , showing a loading and unloading cycle. During the loading cycle small discontinuities can be detected in the measurement signal, stemming from energy-releasing events, here called serrations, that are happening under the indenter tip.

In the context of the nanoindentation study of Publication III a Hysitron nano-indenter was utilized. The instrument allows indentation in load as well as displacement-controlled measurement protocols. The measurements were carried out at the University of North Texas, Denton.

4. Summary of Publications

4.1 General Overview

This subchapter provides a brief overview on the different publications that are summarized in this work, together with its main questions and the methodology used to provide an answer.

Table 4-1: Overview of general questions of the studies reported in the publications of the thesis, combined with the methodologies applied to solve the apparent scientific questions

Publication # Journal	Central questions	Methodology used
I Acta Materialia	• How does the Pt/Pd ratio influence the characteristic temperatures (T_g, T_x, T_m, T_l), heat capacities ($c_{p,l}$ $c_{p,x}$), enthalpy (ΔH_{l-x}) entropy (ΔS_{l-x}) and Gibbs free energy (ΔG_{l-x})? • Can the embrittlement at high Pd content be explained? • Is there a correlation of the changes in heat capacity to the structural information obtainable by High-energy synchrotron X-ray diffraction?	• Differential Scanning Calorimetry (DSC) in the glassy, crystalline, and undercooled and equilibrium liquid state • High-energy synchrotron X-ray diffraction (HE-XRD) in the glassy and supercooled liquid (SCL) state
II Communications Physics	• How does the dynamics of the deeply undercooled Pt-based liquid behave in comparison to the Pd-based liquid in the vicinity of the glass transition.	• X-ray photon correlation spectroscopy in the supercooled liquid state at different temperatures and wave-vectors (XPCS) • HE-XRD in the glassy and supercooled liquid state

	• How are the underlying structural changes compared to the dynamic slowdown close to the glass transition? • How do the structural differences in the Pt and Pd-based liquids influence the wave-vector dependence ("De Gennes narrowing") of the intermediate scattering function?	• Structural analysis via Fourier-transformation of HE-XRD data • Thermomechanical Analysis (TMA) in the glassy and supercooled liquid state • DSC in the glassy and SCL state
III Scientific Reports	• How do the changes in Pt/Pd content as well as thermal history/relaxation state influence the micromechanical performance, regarding microhardness, number of serrations, plasticity, and strain-rate sensitivity (SRS)? • Does the plasticity in micropillar compression correlate to the changes in SRS? • Is there a structural signature regarding the connecting schemes of clusters that fits the changes in plasticity? • Can the theory of cluster connecting schemes, stated in Publication IV be verified experimentally?	• Nanoindentation in the glassy state with different thermal histories • Micropillar compression in the glassy state with different thermal histories • HE-XRD in the glassy state with different thermal histories

IV Communications Physics	• Can the significant differences in thermophysical properties (heat capacity, melting enthalpy and tendency to embrittlement) of Pt-P compared to Pd-P liquids be explained by structural investigations?	• HE-XRD)in the glassy and SCL state on the series of Pt-Pd-Cu-Ni-P based metallic glass formers
V Physical Review Letters	• Is there experimental evidence on the wave-vector dependence of the intermediate scattering function in the deeply supercooled state?	• X-ray photon correlation spectroscopy (XPCS) in the supercooled liquid state at different temperatures and wave-vectors on two metallic liquids (Pd-Cu-Ni-P and Au-Cu-Si-Pd-Ag)

4.2 Publication I: "On the thermodynamics and its connection to structure in the Pt-Pd-Cu-Ni-P bulk metallic glass forming system"
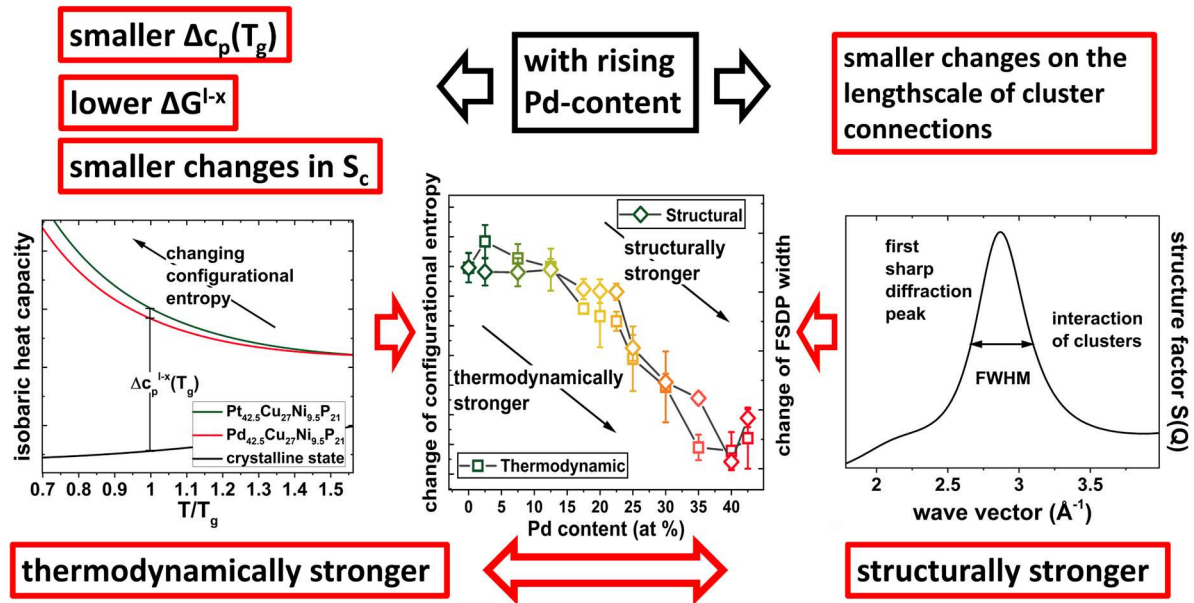
Figure 4-1: Graphical abstract of publication I "On the thermodynamics and its connection to structure in the Pt-Pd-Cu-Ni-P bulk metallic glass forming system" providing an overview of the main results regarding the connection of thermodynamics and structure.

In this work the thermodynamic properties of the glassy, liquid and crystalline states of the PtPdCuNiP series as a function of Pt/Pd ratio are examined. In more detail, the thermodynamic behavior i.e. the changes in heat capacity are empirically connected to structural features of the liquid state. The heat capacities of the glassy, liquid and crystalline phases as well as melting and crystallization enthalpies are assessed by differential scanning calorimetry and the thermodynamic functions of specific isobaric heat capacity, excess enthalpy and excess Gibbs free energy are calculated on the basis of these measurements.

The manuscript is split into a general assessment of the thermophysical properties i.e. glass transition, crystallization, melting and liquidus temperatures, together with the determination of melting and crystallization temperatures. The first central finding of the paper is that the glass transition temperature and thermal stability of the liquid state upon cooling increase almost linearly with rising Pd content of the alloys.

Thermodynamic properties for twelve alloys with different amounts of Pt/Pd are quantified utilizing calorimetry. Their structure is measured with high energy synchrotron X-ray diffraction. For all twelve alloys the thermophysical properties of the glassy and liquid state, as well as the crystallization and melting behavior are studied. Based on this, the difference in enthalpy and Gibbs free energy between liquid and crystalline mixture is determined. This allows a description of the thermodynamic fragility, the residual enthalpy of the glassy state as well as a lower estimate of the driving force for crystallization for each composition.

For the first time it is systematically shown that the driving force for crystallization is incrementally lowering in the $(Pt/Pd)_{42.5}Cu_{27}Ni_{9.5}P_{21}$ with rising Pd content, validating the extremely high thermodynamic stability of Pd-Cu-Ni-P based liquids against crystallization. Secondly, based on the dropping residual enthalpy in the glass with rising Pd content and its inherent connection to the free volume, our study provides a thermodynamic criterion of the often-described loss in mechanical ductility with increasing Pd content. Additionally, while kinetic fragility is reported to remain similar, the system is showing an unexpected thermodynamically stronger behavior towards the Pd-rich liquids. To shed further light on the liquid properties, structural data obtained by high-energy synchrotron diffraction experiments is used to compare the structural changes with temperature in the liquids. The width of the first sharp diffraction peak of the total structure factors is used to quantify the temperature induced changes on the length scale of cluster connections (medium range order). It is found to qualitatively mimic the trend of the thermodynamic fragility. Analogous to the small changes in excess entropy (thermodynamically strong), the Pd rich liquids also show smaller structural changes with respect to temperature, drawing the picture of a thermodynamically and structurally strong liquid.

In conclusion this work shows a connection of thermodynamic properties to structural features within this model system. Ultimately, the study provides a uniquely large description of thermodynamic and structural properties of the Pt/Pd-Cu-Ni-P system, while also motivating for future dynamic/kinetic studies to further understand the role of fragility in this perfect model system for metallic glasses. The current findings provide another milestone on the road to identify and understand the different roles of two topologically similar elements (Pt and Pd) in a metallic glass forming (Pt/Pd-Cu-Ni-P) alloy system and how the change of the structural motifs on the medium range order can influence thermodynamic properties such as entropy, enthalpy and heat capacity.

4.3 Publication II: "Disentangling structural and kinetic components of the α-relaxation in supercooled metallic liquids"
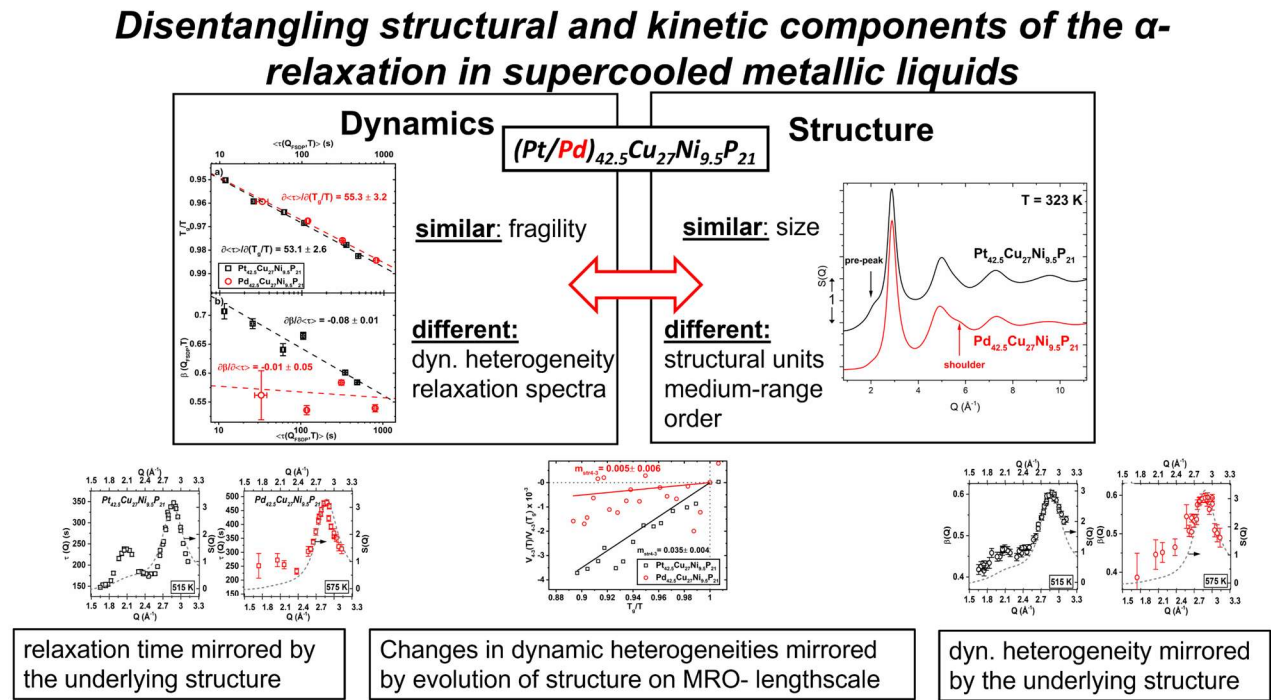
Figure 4-2: Graphical abstract of publication II "Disentangling structural and kinetic components of the α-relaxation in supercooled metallic liquids" providing an overview of the main results regarding the connection of dynamics and structure.

In this work goal the microscopic dynamics in the deeply supercooled liquid state of $Pt_{42.5}Cu_{27}Ni_{9.5}P_{21}$ in contrast to $Pd_{42.5}Cu_{27}Ni_{9.5}P_{21}$ are characterized with X-ray photon correlation spectroscopy. The initial aim was to investigate whether the similar fragility of both alloys obtained from viscosity and calorimetric measurements can be verified microscopically by XPCS. However, the detailed observations of the relaxation process in XPCS showed significant differences in both alloys with respect to the underlying distribution of relaxation times at similar temperatures with respect to T_g, as well as its wave-vector dependence. Both information are not at all or to that extent obtainable by conventional experiments that are used to probe the dynamics of a liquid (e.g. dynamical mechanical characterization (DMA).

Moreover, the underlying spectrum of relaxation times, can be derived out of the shape (parameter) of the relaxation time (compare section 2.3). In the case of $Pd_{42.5}Cu_{27}Ni_{9.5}P_{21}$ a

constantly wide distribution of relaxation times of the deeply supercooled liquid is observed when approaching the glass transition, similarly to a Zr-based system reported in literature [178]. In contrast, an initially sharper distribution that is broadening at lower temperatures is observed in a similar cooling protocol of $Pt_{42.5}Cu_{27}Ni_{9.5}P_{21}$. These changes in the heterogeneity of the dynamics i.e. the relaxation spectra are not reflected in the framework of the fragility concept. The kinetic fragility is commonly a successful concept to interpret the dynamics of liquids glass-formers [51]. Developed by A. C. Angell, this quantity describes the slowing down of the structural α-relaxation accompanying the vitrification and correlates with many glass properties [62,179,180]. With the degree of experimentally obtainable detail on the collective atomic motion and structure in supercooled metallic liquids, we show that the kinetic fragility alone is not able to fully describe the evolution of the α-relaxation process. Interestingly, the observed changes in the relaxation spectra fit well the thermally induced structural changes observed in in-situ X-ray diffraction during heating and cooling. Here, the Pt-liquid with its changing relaxation spectrum also undergoes much more significant structural changes, visible in the changes of shape and position of the first sharp diffraction peak, but also in the changes of the reduced pair distribution function on the length scale of medium range order. Interestingly, the latter was reported to correlate well with the fragility of the systems [96], and can therefore be interpreted as a "structural fragility". However, its general validity, even in metallic systems, is still up to debate and quite challenging especially in the Pt-Pd-P system (see Discussion section 6.3 "Structural fingerprints of Fragility"). Still the changes on the MRO length scale do mirror the changing shape of the intermediate scattering function i.e. the relaxation spectra, showing the connection between changing dynamics and the underlying structure of the liquid.

The structure-dynamics relationship in these model alloys was further established through an examination of the wave-vector dependence of the dynamics. It is found that the relaxation time and the heterogeneity parameter mimic the structure of the alloys. This means that the dynamics is directly related to both the topological order and the chemical short-range order of the liquid. In the Pt-liquid the structural pre-peak at low wave-vectors even leads to a slowing down of the structural α-relaxation process at the medium range order length scale beyond that of the first sharp diffraction peak. It marks the first time that a second peak in the relaxation time was experimentally observed in deeply undercooled metallic liquids.

It is believed that these results challenge some widely accepted concepts related to the underlying mechanisms that control the rheological behavior of supercooled liquids. Due to

their simple structure, metallic glass-formers are often considered as model systems to study the glass transition. These results may also serve as a guide for future numerical and experimental investigations and will be of interest for a large community of scientists.

4.4   Publication III: "Effect of composition and thermal history on Deformation Behavior and cluster connections in model Bulk Metallic Glasses"
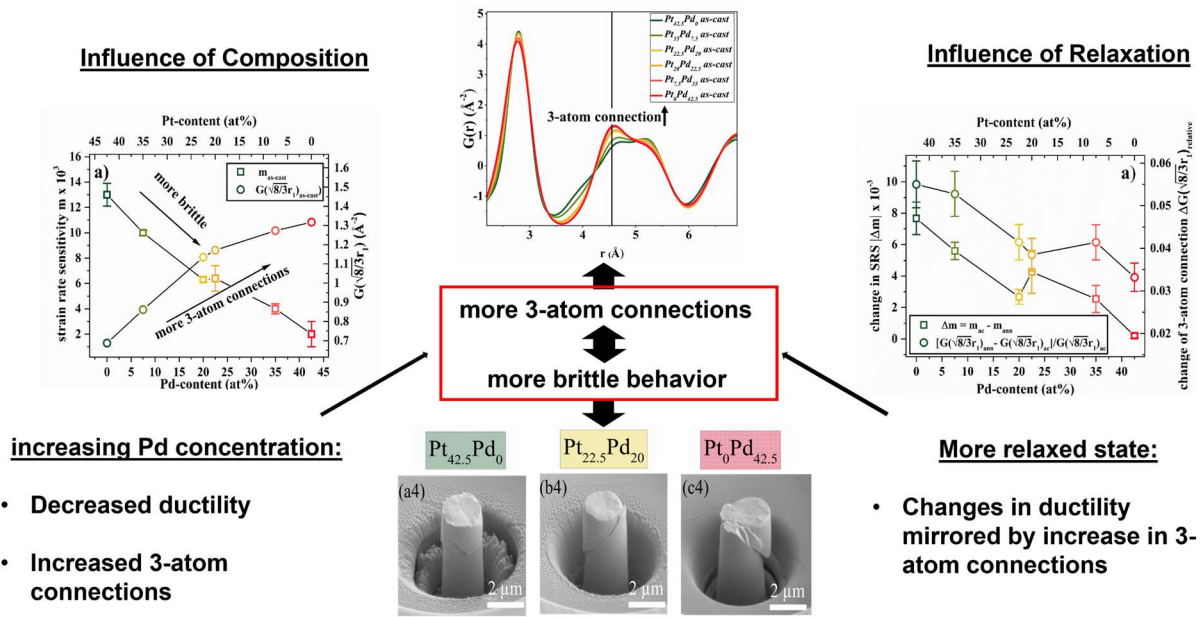
Figure 4-3: Graphical abstract of publication III "Effect of composition and thermal history on Deformation Behavior and cluster connections in model Bulk Metallic Glasses" providing an overview of the main results regarding the connection of micromechanical behavior and structure.

In this work the mechanical behavior of the series of Pt-Pd-Cu-Ni-P metallic glasses with different Pt/Pd content in the as-cast state and after severe relaxation through sub-T_g annealing (T_g-50 K for 24 h) are characterized. Based on less systematic studies on Pt-Pd-P based alloys [33] and the thermodynamic results of publication I [21], the working hypothesis/expectation is to observe an embrittlement with larger Pd content. To analyze the mechanical behavior, nanoindentation at different strain rates is used to characterize the number and length of serrations, micro hardness, elastic modulus and strain rate sensitivity (SRS), combined with micropillar compression experiments to characterize ductility. Furthermore, the structure of the glassy samples is tracked by high energy synchrotron X-ray diffraction (HE-XRD), to monitor the changes in the connecting schemes by analyzing the 2nd peak in the reduced pair distribution function G(r), according to simulations of Ding et al. [88].

In the nanoindentation study a growing number of serrations that also become larger with Pd content is observed. For the annealed samples only minor effects in the average serration length are observed, but their frequency was slightly decreased. The probing of different strain rates reveal a decreasing SRS with rising Pd content. For the annealed samples also a drop in SRS is observed compared to the as-cast samples, while the absolute changes are the highest for Pt-rich glasses. This severe changes in SRS can be seen as a fingerprint of the emerging embrittlement through the Pd substitution or annealing. A larger SRS is often attributed to the delay in shear band activation with increased strain rate, therefore easing multiple shear band formation, which is needed for macroscopic plastic flow [181]. Based on the cooperative shear model (CSM) of Johnson and Samwer also the volume of the shear transformation zone (STZ) is calculated for all compositions [120,123]. The STZ volume of the as-cast BMGs varies from ~ 2.5 to ~ 18 nm^3, increasing with Pd concentration. The smaller STZ volume for $Pt_{42.5}Pd_0$ enables the activation of greater numbers of flow units, leading to the nucleation of more shear bands and promoting more ductile behavior in contrast to $Pt_0Pd_{42.5}$ with its large STZ volume [182,183]. Similarly, an increase of STZ volume is seen for the annealed alloys. The addition of Pd and thermal annealing showed similar effects in terms of increasing STZ volume, with the effect of annealing being more significant on the Pt-rich side of the composition spread. The suggested embrittlement is further reassured by the micropillar compression tests. Here also a more brittle behavior can be seen with growing Pd content, as in $Pt_0Pd_{42.5}$ only a single major shear band is activated leading to a brittle fracture. In contrast, $Pt_{42.5}Pd_0$ shows multiple shear band that interact with each other, leading to a more homogeneous ductile deformation. These qualitative observations are in line with a growing average stress drop and elastic energy release with rising Pd content, being derived from the stress-strain curves. The magnitude of these stress drops is an implicit measure of the propensity of the system towards stable or unstable propagation of a shear band, with smaller stress drops facilitating a more stable deformation process [184]. Similarly, the larger release of elastic energy for the Pd-rich glasses indicates a more localized deformation that facilitates catastrophic shear banding. Additionally, a steady rise of hardness and yield strength is observed in nanoindentation and micropillar compression, scaling well with the increase in the glass transition temperature [185].

With the mechanical data supporting the hypothesis of the embrittlement towards large Pd contents and the availability of quantitative data, now the last step was to create a connection to the structure. For all samples that are used for the mechanical tests, high energy synchrotron X-ray diffraction patterns are produced. Based on a further analysis and the prior results of

Publication V [152], a change in the representative clusters and their interconnection was suggested in the Pt/Pd-Cu-Ni-P system. Specifically, three atom connections between clusters, being most rigid [88], were found to increase with Pd content. This unique combination of structural and mechanical data allows to establish a quantitative correlation between the intensity of the reduced PDF on the length scale of 3-atom connections and reduction in strain rate sensitivity (SRS) as a measure of ductility. The reduced pair distribution function (PDF) in the as-cast and relaxed states is used to quantify the changes in atomic connections. For the changing compositions a good correlation of the intensity of the PDF at the length scale of the 3-atom connections with the measured SRS is found, supporting the suggested connection of a brittle behavior (small SRS) and a larger occurrence of 3-atom connections from simulations. Regarding the annealing, compared to the compositional changes, only small effects on the structure are visible. Nevertheless, the small changes are the most significant on the length scale of 3-atom connections. While the mechanical and structural changes due to the annealing do not match on an absolute scale, a match is found, when comparing to the relative changes in the structure. This result could be related to the multi component nature of the examined systems, which leads to a superposition of all pair-correlations (an n-component system leads to n(n+1)/2 pair correlations). All partials are weighted by their atomic form factor (compare chapter 3.3), which leads only minor contributions of especially metal-phosphorous pair correlations. Therefore, the changes due to annealing might be only partially represented in the X-ray diffraction experiment and should stimulate further in-depth studies including neutron scattering or in-situ TEM investigations.

In conclusion, a possible structural origin of embrittlement is suggested in a systematic series of interrelated alloys, where Pt is systematically replaced by topologically equivalent Pd atoms. The current findings provide fundamental insights into the role of compositional changes and thermal history in metallic glass forming alloy systems and how both can be used to manipulate the structural motifs and tailor their mechanical properties.

4.5 Publication IV: "Signatures of structural differences in Pt–P- and Pd–P-based bulk glass-forming liquids"
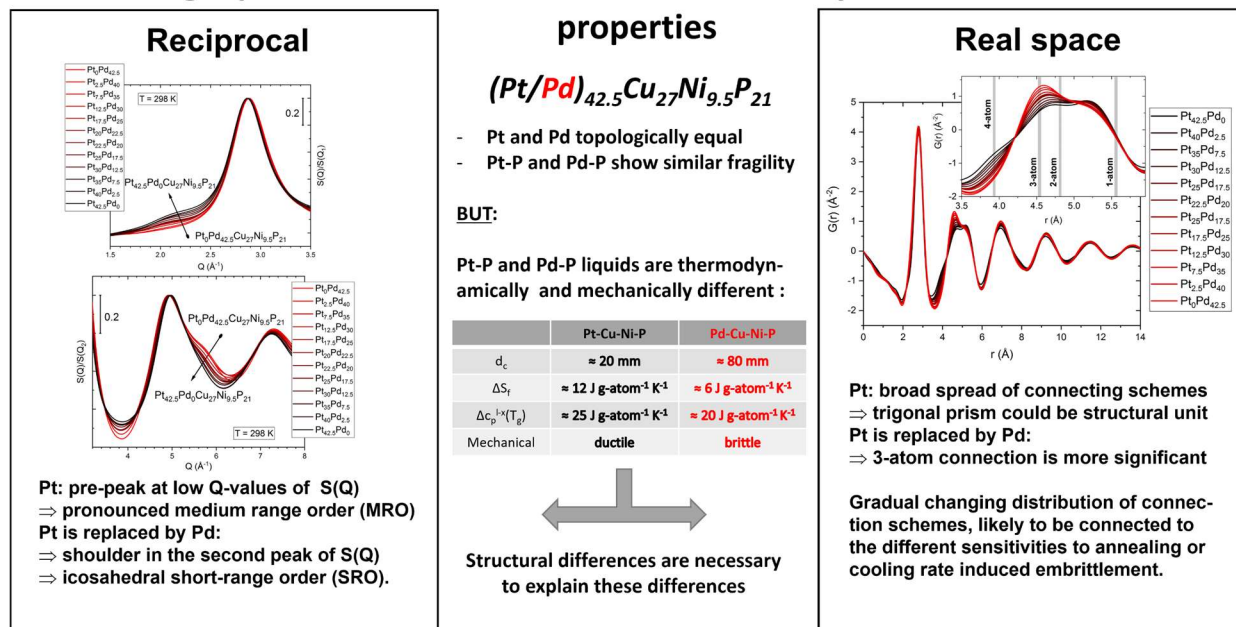
Figure 4-4: Graphical abstract of publication IV "Signatures of structural differences in Pt–P- and Pd–P-based bulk glass-forming liquids" providing an overview of the main results regarding the compositional dependence of the structure of Pt/Pd-Cu-Ni-P glass forming liquids.

In this initial work synchrotron X-ray scattering experiments are conducted to investigate the structure of Pt-P- and Pd-P-based liquids. All twelve alloys with different Pt/Pd ratios of the $Pt/Pd_{42.5-x}Cu_{27}Ni_{9.5}P_{21}$ alloy series are investigated at room-temperature and the $Pt_{42.5}Cu_{27}Ni_{9.5}P_{21}$ and $Pd_{43}Cu_{27}Ni_{10}P_{20}$ alloy are probed in a temperature range from room temperature up to a temperature of around 300 K above the liquidus.

From taking a closer look at the total structure factors S(Q) of the latter alloys already significant differences are revealed. On the one hand the total structure factor of $Pt_{42.5}Cu_{27}Ni_{9.5}P_{21}$ at room temperature displays a pre-peak on the low Q flank of the first sharp diffraction peak, suggesting the existence of a pronounced MRO. Whereas on the other hand the structure factor of $Pd_{43}Cu_{27}Ni_{10}P_{20}$ does not possess such a signature at this position, but instead a shoulder on the high Q flank of the second peak is detected, signifying icosahedral SRO. These structural signatures are indicative form the occurrence of different ratios and

distributions of representative structural units in both compositional families. Whereas the short-range ordered icosahedra dominate in Pd-P-based liquids, the Pt-P-based liquids may comprise out of a larger fraction of trigonal prisms. The structural information that is obtained by the compositions of $Pt/Pd_{42.5-x}Cu_{27}Ni_{9.5}P_{21}$, where Pt is gradually replaced by Pd does support this idea. At rising Pd contents, the pre-peak is gradually fading while the signature of the shoulder at the second diffraction peak is getting more intense.

From the additional high temperature measurements in the equilibrium liquid state further insight into the nature and origin of both structural features are derived. It is observed, that at elevated temperatures the pre-peak is disappearing, and the shoulder is getting less pronounced in the equilibrium liquid. In general, the smearing out of the diffraction signal at elevated temperatures is physically induced by the increased thermal atomic vibrations, the observed effects could be traced back to a kind of a (partial) breakup of the order on both the SRO and MRO length scale. Based on the rapid rise of the specific heat capacity and the large entropy of fusion and the loss of the pre-peak we conject the Pt-rich liquid to be rather disordered at high temperatures, undergoing significant ordering processes even on the MRO length scale during (under-) cooling. In contrast the Pd-rich liquid with its shallowly rising specific heat capacity upon cooling and the persistence of the shoulder at the second peak in the stable equilibrium suggest that it already contains a certain degree of SRO.

The diffraction data is also used to construct the reduced pair distribution function of all compositions, revealing the most significant differences in the splitting of its second peak. The splitting of the second peak, that in a first approximation corresponds to the average second nearest neighbor distances, reflects the different kind of cluster connections that occur in the system. For the Pt-P based liquids this second peak is rather broad, representing a wide distribution and variety of connecting schemes. From geometric considerations in Pt-P the 2-and 4-atom connections seem to be dominant, compared to the 3-atom connection, typical for icosahedral structural motifs, becoming more and more dominant upon replacing Pt by Pd. In simulations the 3-atom connection itself was shown to be rather stiff and tends to react brittle, compared to the more flexible 2- and 4-atom connections. This supports the findings of the different sensitivities towards annealing and cooling rate induced embrittlement between both alloys. On the one hand the ordered Pd-P liquids with predominant icosahedral short-range order that leads to features the more brittle 3-atom connections and undergoes less ordering during cooling, in comparison to the Pt-P liquids with a large variation of more flexible connecting schemes that establish during cooling, ultimately providing a more ductile glass.

Overall, these findings and considerations facilitated and motivated the other studies that led to the publications I-III of this work and provide an experimental basis for the structure-property relations within this class of amorphous metals.

4.6 Publication V: "Wave-Vector Dependence of the Dynamics in Supercooled Metallic Liquids"
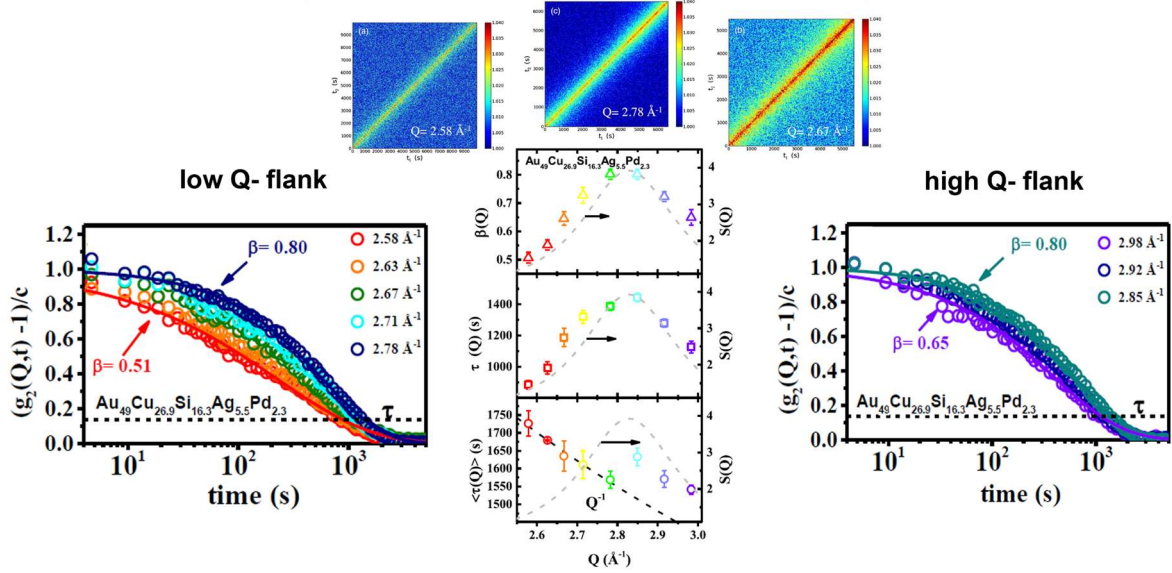
Figure 4-5: Graphical abstract of publication V "Wave-Vector Dependence of the Dynamics in Supercooled Metallic Liquids" providing an overview of the main results regarding the general dependence of the static structure of deeply undercooled metallic melts and their microscopic dynamics.

In this work we studied the wave-vector Q dependence of the dynamics in the deeply undercooled liquid. The effect itself, known as "De Gennes narrowing" and was originally proposed for simple liquids. To experimentally prove its existence also for deeply supercooled metallic liquids the method of X-ray photon correlation spectroscopy (XPCS) is utilized to probe two different metallic glass forming liquids ($Au_{49}Cu_{26.9}Si_{16.3}Ag_{5.5}Pd_{2.3}$ and $Pd_{42.5}Cu_{27}Ni_{9.5}P_{21}$) closely above the glass transition temperature.

From modelling of the decay of the intermediate scattering function the shape parameter β of the relaxation process and its relaxation τ time are obtained. In comparison to the static structure factor S(Q) it is found that the maximum in both parameters, β and τ are matching with the first sharp diffraction peak (FSDP) of S(Q). This slow-down around the average interparticle distance, represented by the FSDP, is connected to the "De Gennes narrowing". The strong decrease of the shape parameter instead suggests the existence of larger dynamical heterogeneities possibly related to medium-range-order domains fluctuations. Especially the

explicit wave-vector dependence of the dynamics in the low Q-range is substantial as it is connected to the mechanism of particle movement. While the probed Q-range does not allow to give exclusive evidence, our results suggest the existence of a rather ballistic-like mechanism of particle motion, which appears to be related to differences in the rigidity of the amorphous structure in the highly viscous liquid state close to the glass transition. The study provides a cornerstone for future studies on the evolution of the dynamics around and across the glass transition in a larger temperature range but also in a broader Q-range that will facilitate the understanding of the glass transition process and the phenomena.

5. Publications

In the following pages the five publications relevant for this cumulative work are reprinted.

5.1 Publication I

Full length article

On the thermodynamics and its connection to structure in the Pt-Pd-Cu-Ni-P bulk metallic glass forming system

Nico Neuber [a,*], Oliver Gross [b], Maximiliam Frey [a], Benedikt Bochtler [b], Alexander Kuball [b], Simon Hechler [b], Isabella Gallino [a], Ralf Busch [a]

[a] Chair of Metallic Materials, Saarland University, Campus C6.3, 66123 Saarbrücken, Germany
[b] Amorphous Metal Solution, Michellinstraße 9, 66424 Homburg, Germany

ABSTRACT

Contrary to basic hard sphere structure models, recent studies revealed, significant structural differences between Pt-Cu-Ni-P and Pd-Cu-Ni-P metallic glass-forming liquids with the same stoichiometry. To cover the compositional space between both systems, platinum is subsequently replaced by palladium in the composition $(Pt/Pd)_{42.5}Cu_{27}Ni_{9.5}P_{21}$. For this systematic set of alloys, the thermodynamic properties, such as isobaric heat capacity, enthalpy and Gibbs free energy are assessed. A systematic drop of the Gibbs free energy difference between crystal and liquid, providing a lower estimate of the driving force for crystallization was observed, underlining the high glass-forming ability of the Pd-rich systems. Contrary to kinetic fragility data, a change of the thermodynamic fragility can be observed, drawing the picture of an increasing thermodynamically strong behavior with rising Pd-content. Further, the temperature induced changes of the total structure factors S(Q) were monitored using high-energy synchrotron X-ray diffraction. Focus was laid on the changes on the medium-range length scale, by analyzing changes of the first sharp diffraction peak. Here a good correlation of the changes in peak-width and the thermodynamic fragility was found. From the determination of the excess enthalpy, large amounts of residual enthalpy in the glassy state were observed for the Pt-rich alloys, supporting the increased ductility of these alloys. The current findings further carve out the different roles of the topologically similar Pt and Pd in the Pt/Pd-Cu-Ni-P alloy system and how the change of the structural motifs on the medium range order is influencing thermal properties such as enthalpy and heat capacity.

1. Introduction

The ability of a metallic melt to evade crystallization and eventually forming a glass when being cooled below its melting point has its origin in thermodynamic, kinetic and structural features of the system [1–4]. This implies a low driving force towards crystallization, sluggish kinetics and a high interfacial energy between the liquid and crystalline phase.

The structural evolution with decreasing temperature involves the formation and expansion of short- (SRO) and eventually medium-range order (MRO). However, the exact nature of these ordering processes is not fully understood. Simple hard sphere structural models of bulk glass-forming liquids are based on the efficient packing of representative structural units (clusters) [5]. In these models, elements with atomic radii that differ by no more than 2 % are considered as topologically equivalent [6]. According to this definition, Pd-Cu-Ni-P and Pt-Cu-Ni-P are topologically identical systems and the alloy compositions with the highest glass-forming ability (GFA) are found in the same compositional range [7], making them ideal "case-study" systems. However, the discrepancy in GFA (factor of four in critical thickness, 80 mm for $Pd_{42.5}Cu_{30}Ni_{7.5}P_{20}$ [8], 20 mm for $Pt_{42.5}Cu_{27}Ni_{9.5}P_{21}$ [9]) can neither be explained by the structural models nor by the very similar temperature dependence of the viscosity in the supercooled liquid (kinetic fragility) [10,11].

The decisive reasons, explaining the large difference in GFA, are found in the thermodynamic properties of the liquid, namely the interfacial energy between the liquid and the crystalline state as well as the driving force for crystallization [12], commonly approximated by the Gibbs free energy difference between the liquid and the crystal. The Pd-P-based liquids feature a small difference in Gibbs free energy between liquid and crystalline phase, resulting

* Corresponding author.

in an extremely low driving force for crystallization. In the Pt-P-based liquids a relatively large driving force for crystallization, normally leading to small GFA, is observed. For Pt-P based liquids this is partially compensated by a high interfacial energy γ_{l-x} between the liquid and crystalline phase, which increases the critical radius for nucleation r* (r* $\propto \gamma_{l-x}^3$) and hampers the formation of critical nuclei, which leads to the high GFA in the Pt-based system [12].

The significant variation of the driving force for crystallization in both glass-forming liquids is reflected in the pronounced increase in the entropy of fusion (factor of two) if Pd is replaced by Pt. Although not entirely independent from the crystalline state, the striking change in the entropy of fusion suggests that, contrary to the predictions of structural models, pronounced structural differences between both liquid families must exist [11]. This is corroborated by structural investigations, indicating that the local representative structural units and their connection scheme varies, when Pd and Pt replace each other [13]. These structural differences, leading to different connecting schemes between the clusters, could also be responsible for the pronounced differences in sensitivity to cooling rate dependent and annealing induced embrittlement of Pt-P-based and Pd-P-based liquids reported by Kumar et al. [14,15], i.e. they might affect the topology of shear transformation zones and the formation of shear bands.

To systematically investigate the effect of the Pd/Pt concentration on thermo-physical properties, twelve alloy compositions with different Pt/Pd ratios ($Pt_{42.5-x}Pd_xCu_{27}Ni_{9.5}P_{21}$, x=0-42.5 at %) are examined in an intensive calorimetry-based study. The glass transition, crystallization and liquidus temperatures; the enthalpies of crystallization and melting, as well as the isobaric specific heat capacity of glassy, crystalline and liquid state are determined and used to calculate the thermodynamic functions of excess enthalpy, entropy and Gibbs free energy between liquid and crystalline state as a function of Pt and Pd content. Furthermore, non-isothermal high energy X-ray diffraction (HEXRD) structural data are used to connect the thermodynamic behavior to structural changes in the deeply supercooled state. The experiments yield a comprehensive data set of the thermodynamic and structural properties as a function of the Pt/Pd concentration.

2. Experimental

2.1. Sample synthesis

For sample preparation, master alloys of $Pt_{42.5}Cu_{27}Ni_{9.5}P_{21}$ and $Pd_{42.5}Cu_{27}Ni_{9.5}P_{21}$ are produced by melting the high-purity raw elements (purity > 99.95%) under high-purity argon (Ar 6.0) atmosphere in a fused silica tube. Subsequently, the pre-alloys are heat-treated in dehydrated B_2O_3 for at least 16 hours at 1200°C in a fused silica tube to remove impurities [16]. Afterwards, the master-alloys are mixed in the ratio of the desired compositions; $Pt_{42.5-x}Pd_xCu_{27}Ni_{9.5}P_{21}$ where x is x=0, 2.5, 7.5, 12.5, 17.5, 20, 22.5, 30, 40, 42.5 at%. In the following the specific alloys will be termed by their Pt and Pd content, e.g., *Pt22.5Pd20* for $Pt_{22.5}Pd_{20}Cu_{27}Ni_{9.5}P_{21}$. The solid mixture is then re-melted in an arc-melter under a high-purity argon atmosphere, to ensure a homogeneous sample. For both, the master-alloys and their derivatives, parts of the ingots are extracted for energy-dispersive X-ray analysis (EDX) measurements, to additionally monitor their composition and exclude experimental errors in compositional range.

The alloys are then inductively re-melted under a Ti-gettered high-purity argon atmosphere and subsequentially cast into water-cooled copper molds in a suction casting device to produce glassy plates with 0.5 mm thickness. The glassy state of the produced samples is initially confirmed by X-ray diffraction (XRD) with a PANalytical X'Pert Pro and later by synchrotron radiation based HEXRD at the P02.1 beamline with 60 keV at the Deutsche Elektro-

nensynchrotron (DESY) (for a more detailed experimental description see section 2.3).

2.2. Thermal analysis

Thermal analysis is carried out using a power-compensated Perkin Elmer Hyper-DSC 8500 with a three-stage intra-cooler under constant flow of 20 ml min^{-1} high purity Ar (Ar 6.0). For low temperature measurements up to a maximum temperature of 723 K, Al-pans are used. For examinations in higher temperature regions up to a maximum temperature of 973 K, including melting of the samples, graphite crucibles are utilized. For low temperature measurements, each sample is remeasured after crystallization, enabling to use the signal of the crystal as a baseline. Each melting curve is measured at least 5 times to account for experimental uncertainty.

For measurements of the isobaric specific heat capacity, a step-method using a sapphire standard as reference was applied, described in detail in Refs. [17,18]. In this method a heating rate of 0.33 Ks^{-1} with temperature steps of ΔT=10 K and equilibration times of Δt=120 s are chosen resulting in an effective heating rate of ~ 0.07 Ks^{-1}.

According to this protocol, the heat capacity of the glass and supercooled liquid (SCL) is determined in the first measurement run. Subsequently, the sample is heated to 750 K to ensure a full crystallization of the amorphous fraction. This allows a second measurement run to determine the heat capacity of the crystalline mixture. To increase the number of data points, especially in the metastable region of the SCL, identical measurements on a new sample are carried out with a temperature program shifted by 5 K. For assessments of the heat capacity in the liquid state, the exact same samples are moved into graphite crucibles. Here the analogous protocol is carried out in cooling, starting well above the liquidus temperatures of the respective alloys at 973 K, until crystallization is interfering.

The isobaric specific heat capacities of the respective states are then modeled by

$$c_p^l(T) = 3R + aT + bT^{-2}, \tag{1}$$

and

$$c_p^x(T) = 3R + cT + dT^2, \tag{2}$$

with R = 8.314 J mol^{-1} K^{-1} being the universal gas constant, a and b being fitting parameters of the liquid (l), and c and d being fitting parameters for the crystal (x) [19].

2.3. High-energy synchrotron X-ray diffraction

High energy in-situ X-ray scattering experiments are carried out at the high resolution beamline P02.1 at PETRA III at the Deutsches Elektronen Synchrotron (DESY) in Hamburg [20]. For the measurements in transition geometry X-ray radiation with a wavelength of 0.207 Å, corresponding to an energy of 60 keV, and a beam size of 0.8 × 0.8 mm^2 is used.

For the heating and cooling of the samples at a constant rate of 0.33 Ks^{-1} a ceramic heater is utilized. The samples are cut from amorphous plate-shaped samples to a dimension of 1×10×13 mm^3. They are placed in SiO$_2$ capillaries with a 1 mm diameter and a wall thickness of 0.01 mm. The sample is protected from oxidation by a constant flow of high purity Ar (Ar 5.0). Si-powder is used for a continuous temperature calibration of the furnace. A Perkin Elmer XRD1621 CsI bonded amorphous silicon detector (2048 pixels × 2048 pixels) records the diffraction pattern with an exposure time of 10 s, resulting in a temperature resolution of 3.3 K in the scans. The two-dimensional X-ray diffraction patterns are dark-subtracted and then integrated with the Fit2D data analysis

N. Neuber, O. Gross, M. Frey et al.

software [21]. Background subtraction of the SiO$_2$ capillaries and further processing is done with the PDFgetX2 software [22]. For determination of the background pattern, room-temperature measurements are used, assuming it to be constant upon temperature changes. The data are corrected for sample absorption, polarization, and multiple scattering. The total structure factor S(Q) is calculated as [23]

$$S(Q) = 1 + \frac{I_C(Q) - \langle f(Q)^2 \rangle}{\langle f(Q) \rangle^2}, \quad (3)$$

where $I_C(Q)$ is the coherently scattered intensity, f(Q) is the atomic form factor, and Q is the scattering vector. The angle brackets signify a compositional average over all constituents. It shall be noted that the total structure factor contains all the structural information and is composed of n(n+1)/2 partial structure factors [24],

$$S(Q) = \sum_{i \leq j} w_{ij} S_{ij}(Q), \quad (4)$$

where w_{ij} is the weighting factor expressed as

$$w_{ij} = \frac{c_i c_j f_i(Q) f_j(Q)}{\langle f(Q) \rangle^2} \quad (5)$$

where c_i and c_j are the molar concentration of element i and j. However, it must be pointed out that the main contribution to the scattering signal is provided by the elements with large scattering lengths e.g., Pt and Pd.

The S(Q) data is evaluated using OriginLab2020b. For the peak analysis the peak was interpolated using cubic splines, leading to an estimated uncertainty of 0.5 % based on Ref. [25]. The samples are heated with 0.33 Ks^{-1} to $T_{g,end}$+10 K well into the SCL region and then cooled by the same rate to room-temperature. The heat-treatment is used to create a well-defined enthalpic reference state and to exclude significant structural relaxation during the actual measurement. Afterward this heat treatment the actual measurement is performed in a second heating run with 0.33 Ks^{-1}, covering the glass transition and full SCL region until the sample crystallized.

3. Results

3.1. Characteristic Temperatures and Enthalpies

A first step of examining the thermo-physical properties of amorphous metals is the monitoring of their respective characteristic temperatures, which are the glass transition temperature and the onset of crystallization, together with the enthalpy that is released during the crystallization. In Fig. 1a) the heat flow curves of all twelve different Pt/Pd-Cu-Ni-P based alloys during a DSC heating scan with 0.33 Ks^{-1} obtained by differential scanning calorimetry are depicted. For each sample, the endothermal step of the glass transition is well visible. Here the initial glassy non-equilibrium state undergoes its transition to the metastable SCL state, detectable due to the increase in heat capacity generated by the change in configurations with temperature in the metastable liquid, as opposed to the glassy or crystalline state. The metastable plateau-like region of the SCL is then interrupted by a sudden exothermal event, the onset of crystallization. A clear shift of glass transition and onset of crystallization with increasing Pd content is observable. The growing length of the SCL region reflects an increasing resistance against crystallization with higher Pd content. In Fig. 2a) the evolution of the glass transition and onset of crystallization is depicted, showing a rather linear dependence with Pd content. Just the composition involving the least amount of Pt, *Pt2.5Pd40*, is posing an outlier by surpassing the *Pt0Pd42.5* alloy in thermal stability.
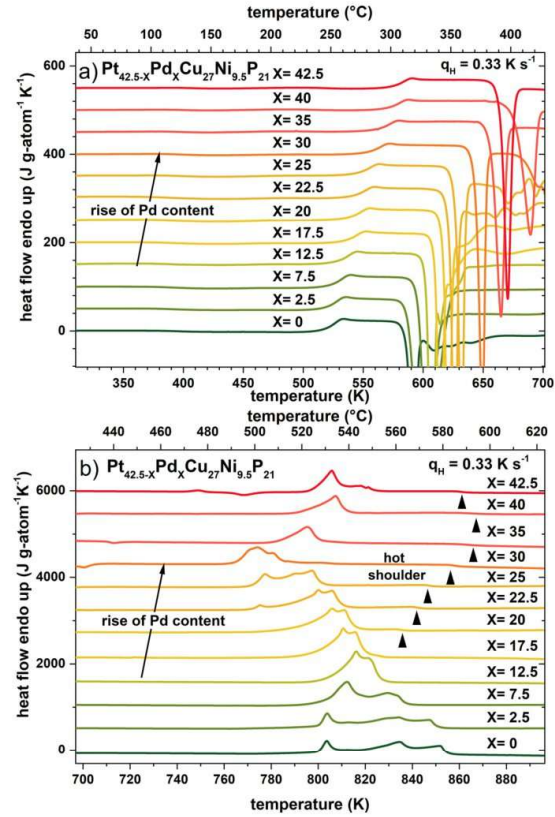
Fig. 1. a) DSC scan with 0.33 Ks^{-1} of Pt$_{42.5-X}$Pd$_X$Cu$_{27}$Ni$_{9.5}$P$_{21}$ with variations in Pd content (X) measured in Al pans up to 723 K giving a detailed view of the glass transition region as well as the crystallization event (exothermal peak). b) DSC scan with 0.33 Ks^{-1} of Pt$_{42.5-X}$Pd$_X$Cu$_{27}$Ni$_{9.5}$P$_{21}$ with variations in Pd content (X) measured in C crucibles up to 973 K depicting also the melting event (endothermal peak) of all alloys. The hot shoulder emerging at Pd contents $x \geq 17.5$ at% is labeled and marked with black triangles. The triangles highlight the end of the shoulder-like heat flow signal during melting, which is corresponding to the liquidus temperature for each alloy.

With changing Pd content the shape and area of the crystallization event change in the thermogram, i.e., the enthalpy of crystallization (Fig. 2a)) decreases significantly through the addition of Pd after a concentration of 22.5 at%. Beyond this concentration a drop of almost 50% can be observed comparing *Pt20Pd22.5* and *Pt7.5Pd35*. The detailed evolution of the enthalpy of crystallization as a function of composition is provided on the left axis of Fig. 2a).

When turning the focus on Fig. 1b) to higher temperatures beyond the crystallization event, the (endothermal) melting of the crystalline mixture can be observed. Here changes in the solidus and liquidus temperature and in the shape of the melting-event can be observed as well.

While the pure *Pt42.5Pd0* alloy is showing a (well-known) off-eutectic behavior with three distinct melting events [12], a merging of the events can be seen until a Pd content of 17.5 at% is reached. From there a high temperature shoulder of the melting peak, marked by an arrow in Fig. 1b) is evolving, leading to an increase of the liquidus temperature, while the melting peak is splitting up again to multiple events. Especially the onset of melting is shifted to lower temperatures as another peak is starting to
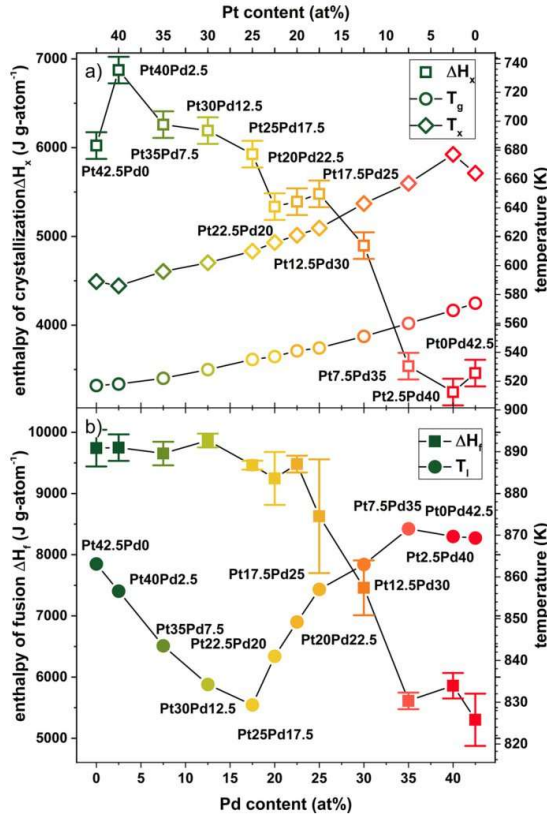
Fig. 2. a) Results of the low temperature DSC measurements of the glass transition temperature (open circle) and the onset of crystallization (open diamonds) and the enthalpy of crystallization (open rectangle) of $Pt_{42.5-x}Pd_xCu_{27}Ni_{9.5}P_{21}$ as a function of Pd content at a heating rate of 0.33 Ks^{-1}. b) Results of high temperature DSC measurements including enthalpies of fusion (filled rectangle) and liquidus temperatures (filled circles)) of $Pt_{42.5-x}Pd_xCu_{27}Ni_{9.5}P_{21}$ as a function of Pd content at a heating rate of 0.33 Ks^{-1}. The decrease in ΔH_f reflects the changes in entropy of fusion ΔS_f, which is the slope of the difference in Gibbs free energy at the liquidus temperature $\Delta G^{l-x}(T_l)$. Error bars of glass transition, crystallization and liquidus temperatures are in the size of the symbols and are therefore not shown.

establish at around 770 K. In the following the high temperature shoulder remains roughly at the same position for further addition of Pd, stabilizing the observed liquidus temperature. Between 17.5 and 30 at% the peaks mainly change their shape and position until they merge again at 35 at% Pd to a single main peak with a distinct shoulder. This evolution of the shape of the peak is briefly summarized in SI Fig. 1.

In contrast to the ongoing changes in shape, and magnitude of the melting peak, the enthalpy of fusion, remains relatively stable at around 9.5 kJ g-atom^{-1} until an amount of 22.5 at% of Pd is reached. From here a sudden drop to around 5.5 kJ g-atom^{-1} for alloys containing 35 at% or more Pd is observed. This progression of the enthalpy of fusion with rising Pd content is very similar to that observed for the enthalpy of crystallization, graphically summarized in Fig. 2a) and b). Compared to the, close to linear, dependence of the glass-transition and crystallization temperature the enthalpies rather show a sigmoidal trend, strictly shifting from "Pt-like" to "Pd-like" behavior. Further it seems notable that most significant changes occur on the Pd-rich side and not right in the

middle of the compositional range. Further the *Pt25Pd17.5* composition shows the minimum in the liquidus temperature as well as the smallest melting interval T_l-T_m, i.e., the composition closest to eutectic behavior is located on the Pt-rich side. for. Therefore, a possible change of the primary crystalline phases would rather be expected on the Pt-rich side than in the middle.

A detailed summary on the characteristic temperatures and enthalpies of all examined alloys is provided in Table 1. Here also the melting point of samples that are crystallized in the up-scan of initially amorphous samples with 0.33 Ks^{-1} is provided (for plot see SI Fig. 2). It shall be noted that due to the occurrence of several metastable crystalline phases in the alloy system the onset of melting is strongly depending on the thermal history/crystallization sequence (compare SI Fig. 3), similar to observations in Au-based BMGs during fast scanning calorimetry (FDSC) [26]. The narrowing of the temperature range of melting is further summarized in SI Fig. 2, depicting the evolution of the melting and liquidus temperature.

3.2. Isobaric specific heat capacity

In Fig. 3a)-d) the specific heat capacity in glassy, (supercooled) liquid, equilibrium liquid and crystalline state, measured by a step-method with a sapphire standard, is exemplarily depicted for four different Pt/Pd ratios. For reasons of space and clarity only the data of these alloys is shown in this figure, while an overview of all twelve alloys is provided in the SI-Fig. 4. Heat capacity data on the alloy *Pt42.5Pd0* was previously published in Ref. [10] The fits of the liquid (dashed line) and crystalline state (full line) are based on Eq. (1) and Eq. (2). The fitting parameters obtained for all twelve compositions are provided in Table 2. At low temperatures far away from the glass transition, but above the Debye-temperature, the specific heat capacity of the glassy and crystalline alloy are similar and at around 3 R ($\approx$ 25 J g-atom^{-1} K^{-1}) according to Dulong-Petits rule, typically observable in various metallic systems [17,27–29]. Independent of the glass transition temperature, the heat capacity of the glassy state begins to distinctively deviate from the crystal at around $\sim$430 K, which can be traced back to relaxation effects. Here the assumption of a stable thermodynamic state is not fulfilled within the observation window. Therefore, it should be noted that the described specific heat capacities of the glass above $\sim$430 K are unstable non-equilibrium values. This effect of relaxation becomes more eminent, when approaching the glass transition, where the glass fully relaxes to the supercooled liquid state. The respective jump in heat capacity at the glass transition temperature Δc_p^{l-x} (T_g(0.33 Ks^{-1})) for a heating rate of 0.33 Ks^{-1} is highlighted for each alloy. The lack of c_p-data between the deeply supercooled liquid and the liquidus temperature is caused by the limited thermal stability of the supercooled liquids and the resulting interference with crystallization.

3.3. Enthalpy

The determined functions of the isobaricspecific heat capacity of liquid and crystalline state allow a description of the enthalpy during undercooling for all observed liquids with respect to the crystalline state. The excess enthalpy between liquid and crystal $\Delta H^{l-x}(T)$ can be described by

$$\Delta H^{l-x}(T) = \Delta H_f + \int_{T_{fusion}}^{T} \Delta c_p^{l-x}(T')dT', \qquad (6)$$

with T_{fusion} being the temperature of fusion. The temperature of fusion defines the temperature at which the difference in Gibbs free energy between crystal and liquid ΔG^{l-x} would become zero. In this context the liquidus temperature is used as the temperature
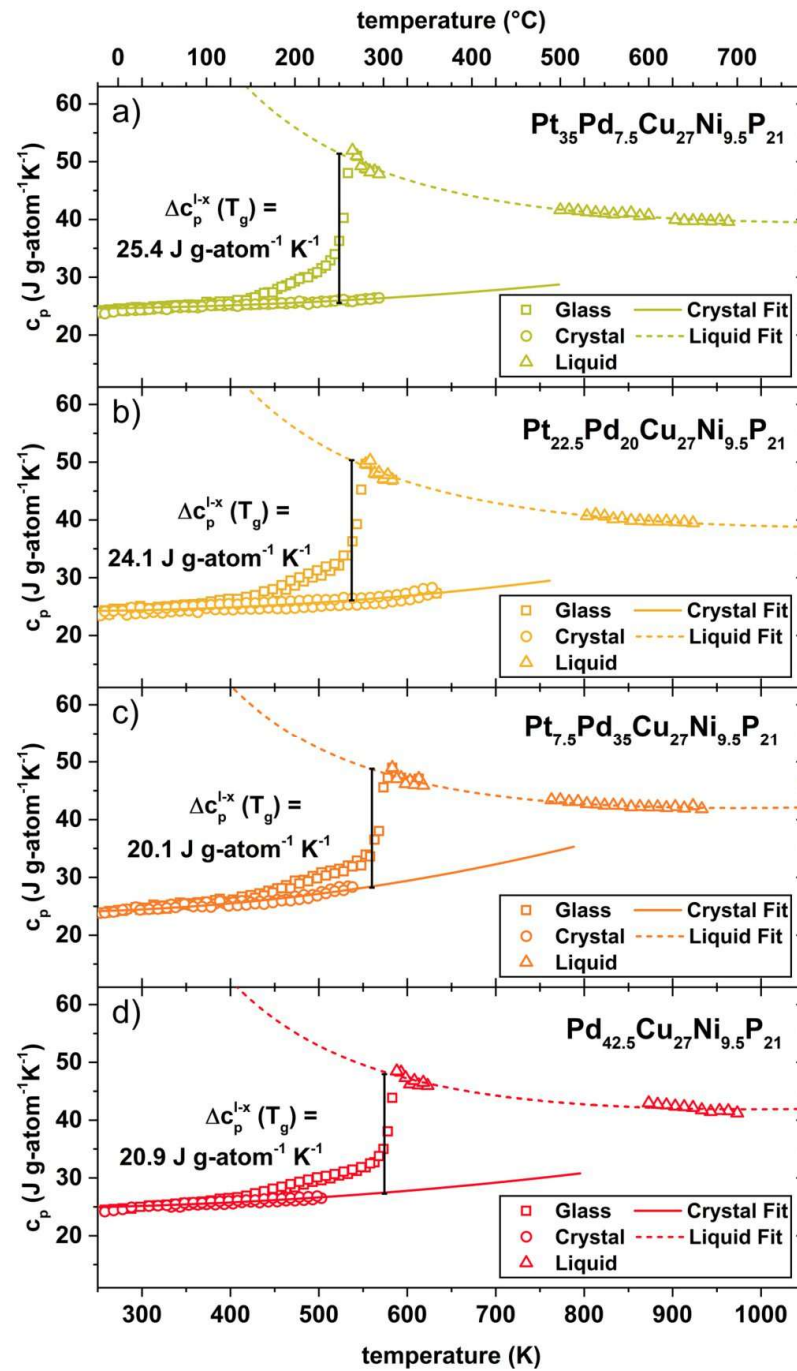
Fig. 3. Isobaric specific heat capacity of glassy c_p (open rectangle), liquid (open triangle) and crystalline state (open circle) for $Pt_{35}Pd_{7.5}Cu_{27}Ni_{9.5}P_{21}$ (light green), $Pt_{22.5}Pd_{20}Cu_{27}Ni_{9.5}P_{21}$ (yellow), $Pt_{7.5}Pd_{35}Cu_{27}Ni_{9.5}P_{21}$ (orange) and $Pt_0Pd_{42.5}Cu_{27}Ni_{9.5}P_{21}$ (red). The fits of crystalline states (full line) and liquid states (dashed line) are based on the Kubaschewski equations, compare Eq. (1) and 2. Additionally, the difference in the isobaric specific c heat capacity between liquid and crystalline state at the glass transition temperature Δc_p^{l-x} (T_g) at a heating rate of 0.33 Ks^{-1} is highlighted with a black bar for each alloy. (For interpretation of the references to colour in this figure legend, the reader is referred to the web version of this article.)

Table 1
Summary of characteristic temperatures and enthalpies extracted from DSC scans at a heating rate of 0.33 K s^{-1} of X-ray amorphous samples.

alloy	T_g (K)	T_x (K)	T_m (K)	T_l (K)	H_x (kJ g-atom^{-1})	ΔH_f (kJ g-atom^{-1})	ΔS_f (J g-atom^{-1} K^{-1}))
Pt42.5Pd0	517	589	799	863 ± 0.4	6 ± 0.2	9.7 ± 0.3	11.3 ± 0.3
Pt40Pd2.5	518	586	799	857 ± 0.2	6.9 ± 0.2	9.8 ± 0.2	11.4 ± 0.3
Pt35Pd7.5	522	596	801	844 ± 0.2	6.3 ± 0.2	9.7 ± 0.2	11.4 ± 0.2
Pt30Pd12.5	528	602	803	834 ± 0.6	6.2 ± 0.2	9.9 ± 0.1	11.8 ± 0.1
Pt25Pd17.5	535	610	798	829 ± 0.4	5.9 ± 0.2	9.5 ± 0.1	11.4 ± 0.1
Pt22.5Pd20	537	616	786	841 ± 1.2	5.3 ± 0.2	9.3 ± 0.4	11 ± 0.5
Pt20Pd22.5	541	621	771	849 ± 0.9	5.4 ± 0.2	9.5 ± 0.1	11.2 ± 0.2
Pt17.5Pd25	543	626	777	857 ± 2.7	5.5 ± 0.2	8.6 ± 0.9	10.1 ± 1.1
Pt12.5Pd30	551	643	765	862 ± 2.4	4.9 ± 0.2	7.5 ± 0.5	8.6 ± 0.5
Pt7.5Pd35	560	657	778	872 ± 3.5	3.5 ± 0.2	5.6 ± 0.1	6.4 ± 0.2
Pt2.5Pd40	569	677	790	870 ± 0.9	3.3 ± 0.2	5.9 ± 0.2	6.7 ± 0.2
Pt0Pd42.5	574	664	795	869 ± 2.1	3.5 ± 0.2	5.3 ± 0.4	6.1 ± 0.5

Table 2
Summary of the fitting parameters obtained by applying Eq. (1) and (2) to the specific heat capacity data.

alloy	a · 10^3 (J g-atom^{-1} K^{-2})	b · 10^{-6} (J K g-atom^{-1})	c · 10^3 (J g-atom^{-1} K^{-2})	d · 10^6 (J g-atom^{-1} K^{-3})
Pt42.5Pd0	11.5852 ± 0.4865	5.1317 ± 0.1748	−7.2702 ± 0.4197	16.5269 ± 0.8654
Pt40Pd2.5	8.898 ± 0.3475	5.9989 ± 0.1148	−4.1856 ± 0.709	12.6481 ± 1.4416
Pt35Pd7.5	8.6865 ± 0.2238	6.0151 ± 0.085	−4.3478 ± 0.286	12.0134 ± 0.6025
Pt30Pd12.5	9.6033 ± 0.2109	5.9562 ± 0.0837	−4.2551 ± 0.9987	12.0506 ± 2.0343
Pt25Pd17.5	12.7526 ± 0.2683	5.3118 ± 0.0911	−5.0686 ± 0.8625	14.1399 ± 1.671
Pt22.5Pd20	7.968 ± 0.2362	6.0837 ± 0.0855	−7.0333 ± 0.8697	17.082 ± 1.6396
Pt20Pd22.5	9.6053 ± 0.1791	5.8765 ± 0.0712	−3.8779 ± 0.3081	11.6243 ± 0.6424
Pt17.5Pd25	15.5827 ± 0.2856	4.737 ± 0.1064	−5.2054 ± 0.2286	15.5093 ± 0.4592
Pt12.5Pd30	4.5858 ± 0.1466	6.8645 ± 0.0584	−9.0089 ± 0.3869	25.4256 ± 0.7216
Pt7.5Pd35	11.7029 ± 0.2488	5.3953 ± 0.0948	−10.6974 ± 1.0505	30.2484 ± 2.3118
Pt2.5Pd40	9.4793 ± 0.2841	5.908 ± 0.1153	−6.5437 ± 0.5034	21.6794 ± 0.9928
Pt0Pd42.5	11.4358 ± 0.2719	5.5529 ± 0.1101	−3.317 ± 0.851	13.4045 ± 1.9733

of fusion, presuming thermodynamic equilibrium at this temperature. Since the present alloys do not show congruent melting, attention must be put to this assumption. For very off-eutectic systems, especially those showing a high temperature shoulder during melting, it can lead to underestimations of the excess enthalpy. Nevertheless, the liquidus temperature, T_l can be seen as a valid assumption, as it marks the first temperature boundary, below which a driving force for (partial) crystallization is eminent in multi-component systems.

In Fig. 4 the course of the excess enthalpies of the four exemplary alloys, already used in the depiction of the heat capacity data, is shown. In addition to the $\Delta H^{l-x}(T)$ curves a ± 3σ confidence interval, with σ being the standard deviation of the enthalpy of fusion, is shown. For each alloy resulting crystallization enthalpies ΔH_x of non-isothermal crystallization experiments at various rates between 0.025 Ks^{-1} and 3 Ks^{-1} are depicted. The variation of heating rates leads to different crystallization temperatures, which due to the difference in heat capacity Δc_p^{l-x} ultimately results in the different crystallization enthalpies, being consistent with the enthalpy changes that are calculated from integrating the specific heat capacities.

At the low-temperature branch of each $\Delta H^{l-x}(T)$ curve horizontal lines are added to describe the residual enthalpy ΔH_{res} ($\dot{T}$) of a glass that has initially left its metastable equilibrium at a cooling rate $\dot{T}$ =dT/dt at the fictive temperature $T_{fict}(\dot{T})$ [30]. The fictive temperature T_{fict} is defined as the temperature where the metastable equilibrium is left during cooling [30]. ΔH_{res} (T_{fict}) is a measure of the stored enthalpy in the glass assuming no further relaxation below T_{fict}. Hence, it is a first order approximation or upper limit, as in real systems relaxation is always present in the wider surroundings of the glass transition region (compare to the heat capacity of the glass in Fig. 3). The $\Delta H^{l-x}(T)$ curves of all twelve examined alloys can be found in SI Fig. 5.

4. Discussion

4.1. Residual enthalpy and connection to mechanical properties

Due to their similar phenomenology, the descriptions of volume or enthalpy as a function of temperature are often used in synonymous ways in glass science. This inherent connection of volume and enthalpy for supercooled liquids and glasses was often pursued experimentally and good correlations for the relative changes of both quantities were shown for glasses in general [31] and in particular for metallic glasses [32–35]. Hence, knowledge of the excess residual enthalpy in the glass allows inferences about the excess volume that is trapped in the glassy state, called free volume [36]. Free volume is of high significance for the glassy state as it is connected to manifold properties e.g. diffusion, viscosity and especially plastic flow [37–39]. The plastic flow in metallic glasses can be understood as the local redistribution of the free volume through shear-transition zones (STZs) [39]. A large amount of free volume facilitates ductility as it allows for the activation of multiple shear bands, instead of a single shear band that fatally runs through the sample. Further it does facilitate the shielding of crack tips, as high free volume leads to a plastic zone that is composed of a high number of easy moving shear bands [40]. Thus, the ductility of the glass is inherently connected to the amount of free volume of the glass, which is governed by its thermal history and chemical composition [14,41,42]. Within this context predictions of the mechanical properties based on the enthalpy curves can be made.

Regarding the mechanical properties Kumar et al. recently reported that Pt-based metallic glasses show much higher plasticity than their Pd-based peers, connecting the Pd content to the ductility [15]. Also structural considerations about the atomic connection schemes in Pt/Pd-based metallic glasses by Gross et al supported/suggested the embrittlement through additional Pd in these
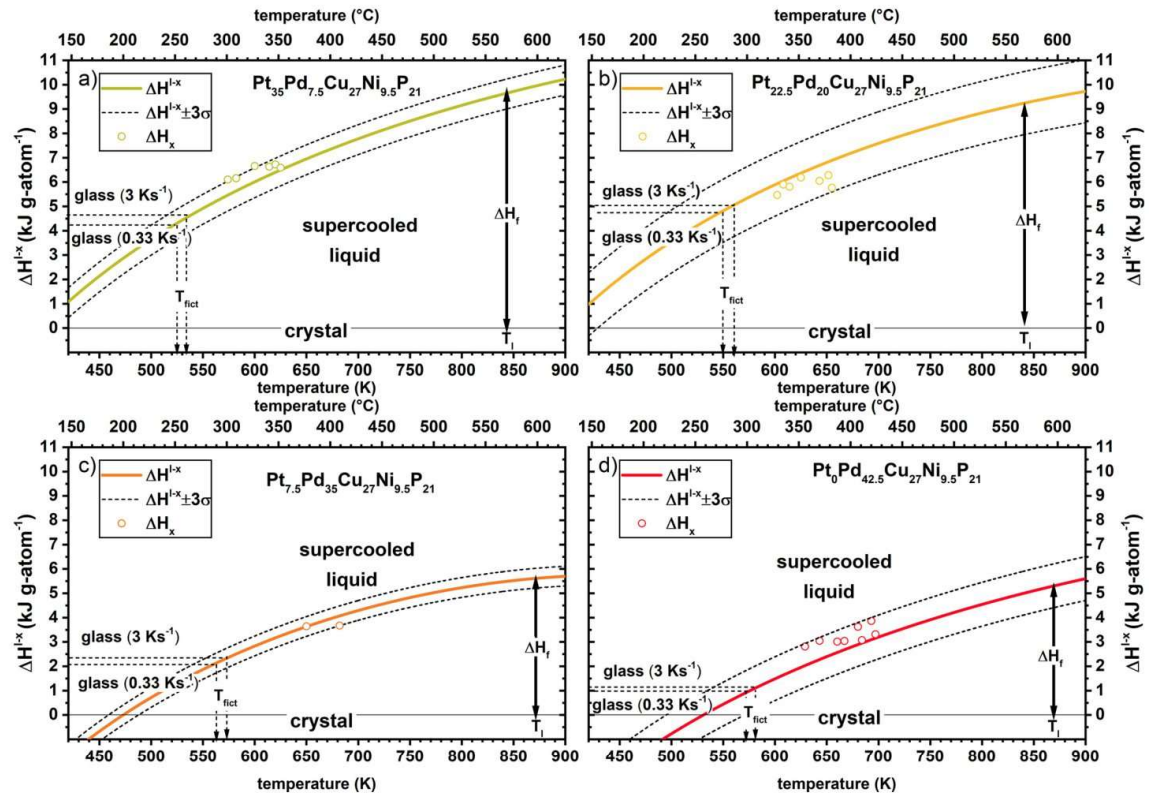
Fig. 4. Difference in excess enthalpy between liquid and crystalline state $\Delta H^{l-x}(T)$ for $Pt_{35}Pd_{7.5}Cu_{27}Ni_{9.5}P_{21}$ (light green), $Pt_{22.5}Pd_{20}Cu_{27}Ni_{9.5}P_{21}$ (yellow), $Pt_{7.5}Pd_{35}Cu_{27}Ni_{9.5}P_{21}$ (orange) and $Pt_0Pd_{42.5}Cu_{27}Ni_{9.5}P_{21}$ (red). A confidence interval of $\pm\,3\sigma$ (dashed line) is depicted to account for experimental uncertainty and crystallization enthalpies (open circles) from independent DSC measurements are inserted to support the validity of the calculation of the enthalpic curves based on measurements of the isobaric specific heat capacity and enthalpies of fusion (compare Fig. 2 and Fig. 3). Further the residual enthalpies for two different cooling rates, based on the respective fictive temperature are shown for each alloy by horizontal dashed lines. It estimates the amount of enthalpy that is stored in a glass that has left the metastable liquid at the given cooling rate. Error bars of the crystallization enthalpies are in the size of the symbols and are therefore not shown. (For interpretation of the references to colour in this figure legend, the reader is referred to the web version of this article.)

systems [13]. From our present results further predictions about the mechanical properties can be derived by reviewing the residual enthalpies ΔH_{res} in the glassy state. In Fig. 5a) ΔH_{res} for a cooling rate of 0.33 Ks^{-1} is shown as a function of Pd content. While the Pt-rich alloys feature a very high amount of ΔH_{res} with around 4 kJ g-atom^{-1}, a sudden drop at 30 at% Pd to about 2 or even 1 kJ g-atom^{-1} (*Pt0Pd42.5*) can be observed. Assuming the validity of the proportionality of excess enthalpy and free volume [34], this leads to a higher amount of free volume in the Pt-rich glasses in comparison to the Pd-based ones. This large amount of free volume can ease the nucleation of multiple shear bands, facilitating plastic flow and ultimately promote ductility for the alloys with large ΔH_{res}. Therefore, the enthalpy curves are in line with the idea that Pd decreases the ductility in the Pt/Pd-Cu-Ni-P system by lowering its free volume. It further agrees with the considerations regarding the mechanical properties based on structural data by Gross et al [13]. Here changes of atomic connection schemes in the Pt/Pd-Cu-Ni-P system were observed, suggesting a higher sensitivity towards embrittlement with rising Pd content [13]. Now, based on ΔH_{res} as a function of Pd content, a first estimate of the location of a ductile/brittle transition in compositional space can be made. Further does the sudden decrease of ΔH_{res} at around 30 at% Pd, depicted in Fig. 5a), suggest a rather sudden drop than a continuous de-

crease in the ductility, when consecutively replacing Pt by Pd in the alloys.

Nevertheless, the amount of ΔH_{res}, and hence the free volume does not only depend on the composition, but also on the cooling rate. The cooling rate of the liquid defines, at which temperature the metastable liquid is left (fictive temperature) and the glassy state is entered. Ultimately, fast cooling rates end up in a higher fictive temperature and slower cooling rates vice versa. The influence of the cooling rate on the ductility of a glass, described by the fictive temperature of the glass, was briefly examined by Kumar et al. showing the existence of a so called critical fictive temperature for embrittlement in different families of alloys [14]. In our study a Pt-based system can be seen exemplary for a low, and a Pd based system for a high critical fictive temperature, with respect to a standardized glass transition temperature. Consequently, Pt can sustain much lower cooling rates than the Pd-based system and still exhibit ductile behavior. From this the question arises if this cooling rate sensitivity is also mirrored in the enthalpic scenario.

To account for the enthalpic changes due to the cooling rate the residual enthalpy at a cooling rate of 3 Ks^{-1}is also depicted in Fig. 5a) and the absolute and relative changes with respect to a rate of 0.33 Ks^{-1} are shown in Fig 5b). Regarding the absolute num-

Fig. 5. a) Compositional dependence of the residual enthalpy that is frozen in at the glass transition temperature for the cooling rate of 0.33 Ks^{-1} (all alloys) and 3 Ks^{-1} (selected ones) with respect to the crystalli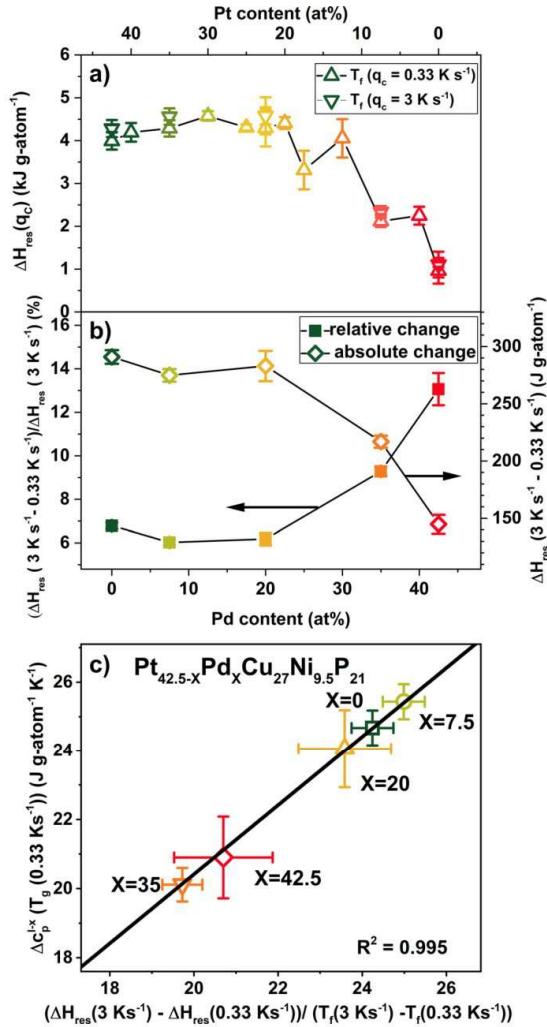ne mixture. The residual enthalpy is calculated based on the excess enthalpy at the fictive temperature at the specific cooling rate $\Delta H^{l-x}(T_f) = \Delta H_{res}(T_f)$.
b) Compositional dependence of relative (left axis) and absolute (right axis) change of residual enthalpy ΔH_{res} between glasses created at 0.33 Ks^{-1} and 3 Ks^{-1}. The change in ΔH_{res} is a measure of the cooling-rate dependence of the enthalpy that is stored in the glass at a given cooling rate. Whereas in absolute numbers this change is the highest in Pt-rich alloys and very low in *Pt0Pd42.5*, the relative trend is the complete opposite.
c) Scatter plot of the jump in specific heat capacity at the glass transition at a heating rate of 0.33 Ks^{-1} over the difference in residual enthalpy between cooling rates of 0.33 Ks^{-1} and 3 Ks^{-1} normalized by the respective change in fictive temperature. A very good correlation of both parameters is found resulting with an $R^2 \geq 0.995$.

ber, a steady decline of the enthalpic changes can be seen with rising Pd content, reflecting the overall trajectory of the residual enthalpy. It is a measure of the sensitivity of the residual enthalpy to different cooling rates as well as to annealing. At a first glance, a larger change of the residual enthalpy would mean a higher sensitivity to embrittlement. Although, as the total amount of residual

enthalpy/free volume should be decisive for the mechanical performance, a relative change of ΔH_{res} might be a more representative measure of the cooling rate sensitivity towards embrittlement. Regarding the relative changes to the residual enthalpy at 0.33 Ks^{-1} the Pd based glass shows a relative loss of 12% of its already low residual enthalpy, relating to its higher sensitivity to embrittlement. Nevertheless, for the accurate way to quantify the sensitivity to embrittlement of a glass, its critical fictive temperature or better the resulting critical residual enthalpy/free volume, would have to be known. It would allow to scale the enthalpic changes with this critical residual enthalpy, leading to the most physical way of quantifying the cooling rate sensitivity. The values for the residual enthalpies are summarized in Table 3.

Further, the sensitivity to changes of the enthalpy with different cooling rates should depend on the specific heat capacity of the liquid and scale well with the difference in c_p of crystal and liquid at the glass transition. This means, the higher the step of c_p at T_g, the higher should be the c_p of the supercooled liquid and the larger should be the change in enthalpy with changing cooling rate and the more pronounced should be the cooling rate sensitivity of the ductility. When nominating the difference in residual enthalpy on the change of the fictive temperature for the two exemplary rates, which incorporates the kinetic behavior, a scatter plot shows a good correlation with $\Delta c_p^{l-x}(T_g)$ with an R^2 value of 0.995, depicted in Fig. 5c). The good correlation of both quantities is not surprising, as $\Delta H_{res}/\Delta T_{fict}$ is somehow a linear approximation, as c_p is defined as the first derivative of H with respect to temperature at constant pressure $(\partial H/\partial T|_{p=const})$. Nevertheless, since the enthalpic curve is based on the combination of heat capacity and independent measurements of the heat of fusion it is a validation of the calculations and the used assumptions. At this point it shall be noted that $\Delta c_p^{l-x}(T_g)$ is connected to the thermodynamic fragility, discussed in detail later, which underlines the possible role of fragility regarding the mechanical properties. The given considerations underline the possibility to estimate the cooling rate sensitivity of the residual enthalpy, based on heat capacity data. It shall be remarked that the correlation of cooling rate sensitivity to the c_p is only robust, when the fictive temperature is showing similar cooling rate dependencies, which means similar kinetic fragilities.

4.2. Gibbs free energy and driving force for crystallization

Based on specific heat capacities and melting enthalpies a calculation of the difference in Gibbs free energy between the liquid and crystalline mixture ΔG^{l-x} is possible with

$$\Delta G^{l-x}(T) = \Delta H^{l-x}(T) - T \, \Delta S^{l-x}(T), \tag{7}$$

and

$$\Delta S^{l-x}(T) = \Delta S_f + \int_{T_f}^{T} \frac{\Delta c_p^{l-x}(T')}{T'} dT', \tag{8}$$

$$\Delta S_f = \frac{\Delta H_f}{T_l} \, . \tag{9}$$

where ΔS^{l-x} describes the excess entropy between liquid and crystalline state and ΔS_f is the entropy of fusion. The difference in Gibbs free energy between liquid and crystalline state allows a lower estimation of the driving force for crystallization in a multicomponent system [43]. Therefore it can be used to describe the thermodynamic contribution to the GFA of a liquid [2,3,44–46]. To relate it to the degree of undercooling ΔG^{l-x} is plotted as a function of temperature normalized to the liquidus temperature in Fig. 6a.

Table 3
Summary of the thermodynamic characteristics derived from the isobaric heat capacity data and melting analysis. The residual enthalpies are provided at fictive temperatures of different cooling rates. If not particularly marked T_g values correspond to a heating rate of 0.33 Ks^{-1}.

alloy	$\Delta c_p^{l-x}(T_g)$ (J g-atom^{-1} K^{-1})	$\Delta c_p^{l-x}/T_g$ (T_g) · 10^2(J g-atom^{-1} K^{-2})	ΔH_{res}(0.33 K s^{-1}) (J g-atom^{-1})	ΔH_{res}(3 K s^{-1}) (J g-atom^{-1})	$\Delta G^{l-x}(T_g)$ (J g-atom^{-1})	T_{rg}
Pt42.5Pd0	24.7 ± 0.5	4.79 ± 0.1	3990 ± 80	4280 ± 90	2720 ± 60	0.599
Pt40Pd2.5	25.7 ± 0.6	4.97 ± 0.11	4190 ± 90	/	2740 ± 60	0.604
Pt35Pd7.5	25.4 ± 0.5	4.86 ± 0.1	4290 ± 90	4560 ± 90	2620 ± 50	0.618
Pt30Pd12.5	25.3 ± 0.3	4.8 ± 0.05	4580 ± 50	/	2630 ± 30	0.633
Pt25Pd17.5	24.1 ± 0.2	4.52 ± 0.04	4310 ± 30	/	2410 ± 20	0.645
Pt22.5Pd20	24.1 ± 1.1	4.46 ± 0.21	4300 ± 200	4580 ± 210	2560 ± 120	0.639
Pt20Pd22.5	24 ± 0.3	4.43 ± 0.06	4410 ± 60	/	2500 ± 40	0.637
Pt17.5Pd25	22.7 ± 1.2	4.18 ± 0.22	3310 ± 170	/	2120 ± 110	0.634
Pt12.5Pd30	22.1 ± 1.3	3.99 ± 0.24	4050 ± 240	/	2150 ± 130	0.639
Pt7.5Pd35	20.1 ± 0.5	3.58 ± 0.09	2120 ± 50	2340 ± 60	1430 ± 30	0.642
Pt2.5Pd40	20.3 ± 0.7	3.56 ± 0.13	2250 ± 80	/	1430 ± 50	0.654
Pt0Pd42.5	20.9 ± 1.2	3.64 ± 0.21	960 ± 50	1110 ± 60	1050 ± 60	0.660
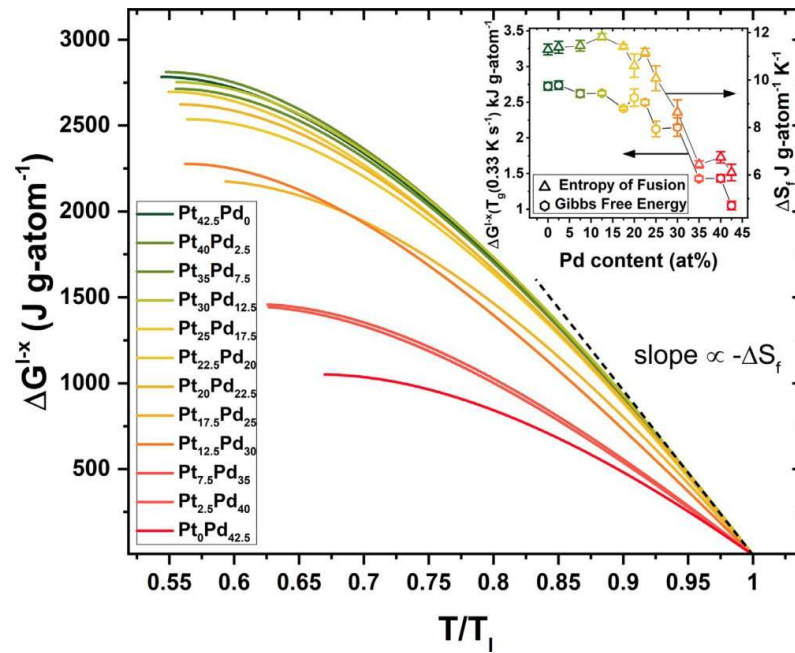
Fig. 6. Difference in Gibbs free energy between the supercooled liquid and the crystalline mixture ΔG^{l-x} for the Pt-Pd-Cu-Ni-P based bulk metallic glass-forming liquids over the by the liquidus temperature normalized temperature T/T_l. A consecutive decrease of the free energy curves with rising Pd-content is observed. The inset summarizes the value of the Gibbs free energy at the glass transition temperature for a cooling rate of 0.33 Ks^{-1} ΔG^{l-x} (T_g(0.33 Ks^{-1}), being a lower estimate for the maximum in driving force for crystallization that the liquid experiences before leaving its thermodynamic equilibrium. In addition, the entropy in fusion ΔS_f is shown on the right axis of the inset, showing the same trend as the Gibbs free energy. A dashed line is added to the curves to underline that the value of ΔS_f marks the slope of $\Delta G^{l-x}(T_l)$.

A decrease of the difference in Gibbs free energy is observed with increasing Pd content. For reasons of clarity a depiction of the Gibbs free energy at the glass transition temperature for 0.33 Ks^{-1} (fictive temperature) together with the entropy of fusion ΔS_f, is provided in the inset. For the total values of ΔS_f, the Pt-rich alloys trend to show a higher, whereas the Pd-rich alloys feature a lower value than expected by Richard's rule, which predicts an approximated ΔS_f of 8.78 J g-atom^{-1} K^{-1} ≈ R for metals [47], while elemental Pd and Pt are both known to follow Richards rule very well [47]. The entropy of fusion further represents the negative slope of the ΔG^{l-x} ($\partial \Delta G^{l-x}/\partial T|_{T=Tl}$ = -ΔS_f) curves at the liquidus temperature. The compositional dependence of ΔG^{l-x} is very similar to the changes of the enthalpy and entropy of fusion ΔS_f, in the system. This good agreement was shown in several systems

e.g. Au-based systems [48]. Therefore ΔS_f, can be used as an estimation of ΔG^{l-x} (T) (Turnbull approximation) assuming a linear course of ΔG^{l-x} (T) (physically relating to assumption of Δc_p^{l-x} = 0) [49] with undercooling. The ΔG^{l-x} (T) curves of *Pt42.5Pd0 and Pt0Pd42.5* are in good agreement to those reported for the same or similar compositions (*Pd$_{43}$Cu$_{27}$Ni$_{10}$P$_{20}$*) in Refs. [12,50].

Pt0Pd42.5 features one of the lowest driving forces for crystallization that was measured in any metallic system and can therefore be considered a thermodynamically very stable liquid against crystallization. Another parameter widely used to quantify the thermodynamic contribution to GFA is the so called reduced glass transition temperature T_{rg} = T_g/T_l [51,52]. T_{rg} is a measure for the temperature range between the first occurrence of a driving force for crystallization (here the liquidus temperature) and the

moment of kinetic arrest (T_g). The smaller this temperature span, which is critical for crystallization, the higher becomes T_{rg}. Hence, the higher T_{rg}, the better should be the glass forming ability. The values of T_{rg}, provided in Table 3 (also graphically depicted in SI Fig. 2), mirror the tendency of the driving forces well. Still one has to note that here the change of T_{rg} is actually not caused by the change of the liquidus temperature, as it is often observed [52], but rather by the increase of T_g with Pd content. This suggests some changes of merely the liquid state. The additional Pd must contribute to an internal slow-down of the liquid shifting the glass transition to higher temperatures, without significantly influencing the liquidus temperature.

4.3. Thermodynamic fragility and structural signatures

The rise of the glass transition temperature (Fig. 2, Tab. 1) within the alloy system already suggests a significant slowdown of the dynamics in the liquid state with rising Pd content. This leads to the question: Which thermodynamic property is the most appropriate to describe these changes? MD simulations suggest that structural redistribution and ordering processes of the deeply supercooled liquid lead to significant changes of the specific heat capacity with temperature close to the glass transition [53]. Therefore, the suggested dynamic slowdown of the liquid phase may also be reflected by the different temperature dependence of the specific heat capacity of the liquid during cooling. This idea ultimately traces back to the theory of Adam and Gibbs, assuming that the supercooled liquid is consisting of groups of atoms that form so called cooperatively rearranging regions (CRRs). Upon undercooling the liquid, CRRs grow in size and increase their degree of cooperativity. Hence, this process is consecutively reducing the number of available configurations within the system [54], resulting in a decrease of the configurational entropy S_c, accompanied by a rise of the specific heat capacity and being connected to the tremendous rise of viscosity and relaxation times when approaching the glass transition. In this framework Adam and Gibbs described the change in viscosity η, a kinetic/dynamic quantity, using a temperature dependent thermodynamic quantity, the configurational entropy $S_c(T)$ as

$$\eta(T) = \eta_0 \exp\left(\frac{C}{S_c(T)\,T} \right). \qquad (10)$$

where η_0 is the high temperature limit of viscosity and C is a constant that is proportional to the free energy barrier for a cooperative rearrangement [55]. Under the assumption of a neglectable difference in vibrational entropy between liquid and crystalline state, experimentally underpinned by recent studies of Fultz et al. [56], the excess entropy ΔS^{l-x} can be used instead of S_c to describe the entropic changes with temperature [57].

This connection between kinetic and thermodynamic properties allows to quantitatively determine a thermodynamic fragility [50,58]. A connection between the excess entropy and kinetic fragility concept was qualitatively made by Angell and his co-workers as early as 2001 [57,59]. Instead of relaxation time or viscosity, the change of configurational entropy/excess entropy around the glass transition is used to describe the (thermodynamic) fragility.

Due to the connection of ΔS^{l-x} to Δc_p^{l-x} ($d\Delta S^{l-x}/dT = \Delta c_p^{l-x}/T$, compare equ. 8) and taking into account the minor difference in the heat capacity of glass and crystal ($\Delta c_p^{l-x}(T_g) \approx \Delta c_p^{l-g}(T_g)$) [60], the difference in isobaric specific heat capacity between liquid and crystal $\Delta c_p^{l-x}(T_g)$ at the glass transition or rather the temperature nominated value $\Delta c_p^{l-x}(T_g)/T_g$ ($= d\Delta S^{l-x}/dT|_{T=T_g}$) can be used as a measure of thermodynamic fragility [50,57,58]. A larger c_p-step at the glass transition corresponds to a more rapidly increasing configurational entropy in the liquid upon cooling, corre-
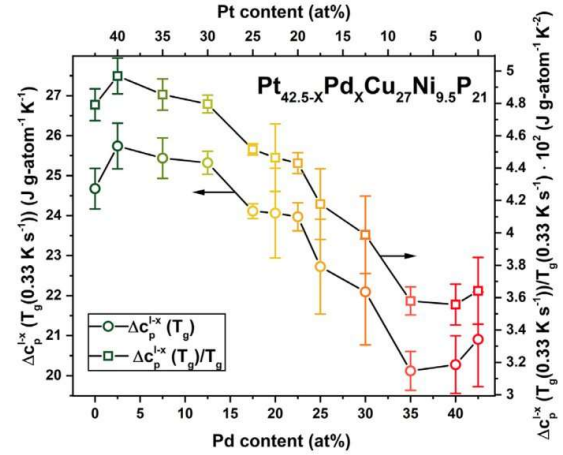
Fig. 7. Difference in isobaric specific heat capacity between liquid and crystal $\Delta c_p^{l-x}(T_g)$ as a function of Pd-content (left axis) together with the same difference being normalized by the glass transition temperature $\Delta c_p^{l-x}(T_g)/T_g$. This is a measure of the rate at which the configurational entropy of the liquid changes at the given temperature and ultimately reflects the thermodynamic fragility.

sponding to thermodynamically more fragile behavior. Vice versa, a smaller step is reflecting thermodynamically stronger behavior.

Both parameters $\Delta c_p^{l-x}(T_g)$ and $\Delta c_p^{l-x}(T_g)/T_g$, show the same development with changing Pt and Pd content in Fig. 7, which is not surprising due to the linear progression of the glass transition temperature with changing Pt/Pd ratio (compare Fig. 2a)). With growing Pd content the increase of the heat capacity in the liquid state during cooling becomes shallower, i.e., the decrease of excess entropy becomes smaller, which would be associated with a thermodynamically stronger liquid behavior.

When reviewing the kinetic fragility in literature, fragility parameters D^* of 15.3 for $Pt42.5Pd0$ [10] and D^* values of 14.0 [11] for $Pd_{43}Cu_{27}Ni_{10}P_{20}$ are reported. This is surprising, as both liquids should exhibit the thermodynamic signature of a similarly fragile metallic liquid. However, the current results have drawn the different picture of a thermodynamically stronger Pd-based liquid.

Nevertheless, the thermodynamically strong behavior agrees with the picture of the Pd-rich liquid that is thermodynamically close to the crystalline state, as suggested by the Gibbs free energy curves and the relatively low enthalpy and entropy of melting. This picture is further supported by structural investigations by Gross et al. [13], which suggested the occurrence of distinct structural motifs with different structural units and spatial arrangement in the Pt-P and Pd-P liquids. Regarding the structural units, the Pt-P liquid contains a larger fraction of trigonal prisms with a significant medium-range order (MRO), while the Pd-rich liquid features an almost perfect icosahedral short-range order (SRO). Concerning the spatial arrangement, the Pt-rich liquid shows a high diversity with 1-, 2- and even 4-atom connections of the individual clusters, whereas the more rigid 3-atom connection seems to prevail for the Pd-rich liquid. This high diversity of connection schemes of the structural units/clusters is further pointing towards the high degree of medium range order in the Pt based system [13]. Ultimately it is assumed that the thermodynamically strong behavior of the Pd rich alloys, deduced from the behavior of the excess heat capacity and change of excess entropy, is in high resemblance to the structural findings. Further it is hypothesized that the thermodynamic strong behavior is presumably associated to the described variations in the distribution of cluster connections.
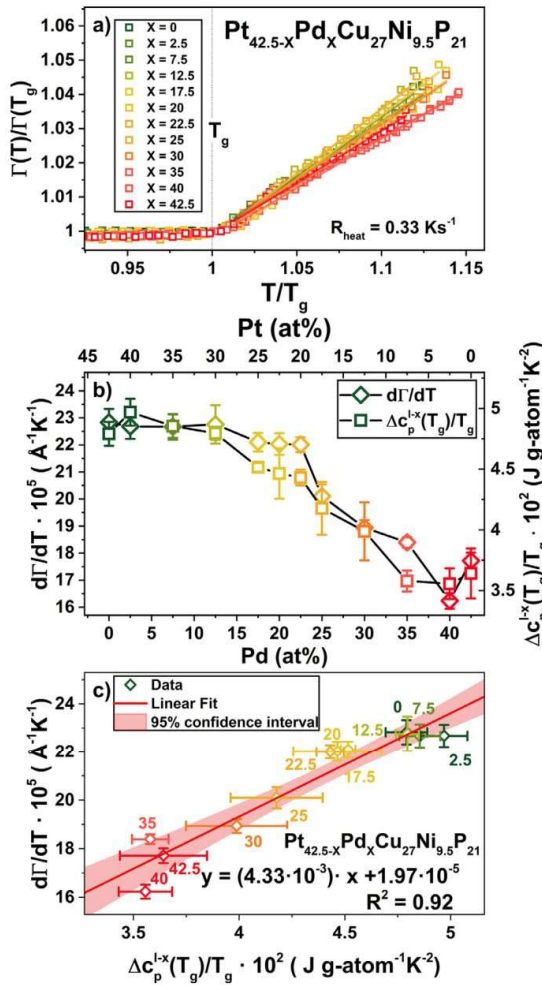
Fig. 8. a) Full width half maximum (FWHM) $\Gamma(T)$ of the FSDP of the total structure factor $S(Q)$ nominated on the FWHM at the respective glass transition temperature at 0.33 Ks^{-1} $\Gamma(T_g)$ for all Pt/Pd variations on a T_g-normalized temperature scale. The measurements are carried out on samples that were priorly cooled with 0.33 Ks^{-1} from the SCL state ($T_{g,end}$+10 K) to exclude structural relaxation during the main measurement. Whereas the FWHM remains constant in the glassy region it shows a significant increase above the glass transition (here $T/T_g > 1$). A strong variation in the slope of the curves in the SCL with composition can be detected in the SCL region. b) The change of FWHM of the FSDP of the total structure factor $S(Q)$ with temperature $d\Gamma/dT$ in the SCL region as a function of Pd content (left axis) and the change of the difference in isobaric specific heat capacity between liquid and crystal nominated on the glass transition temperature $\Delta c_p^{l-x}(T_g)/T_g$ as a function of Pd content (right axis). Both quantities are showing the same trend in compositional space. c) Scatter plot of the change in FWHM with temperature $d\Gamma/dT$ over the by T_g normalized difference in isobaric specific heat capacity between liquid and crystal $\Delta c_p^{l-x}(T_g)/T_g$. The latter describes the rate of loss of configurational entropy at the glass transition, ultimately being a measure of the thermodynamic fragility. A strong correlation of both quantities with an R^2-value of 0.92 was achieved, hinting towards at least a qualitative correlation within the system.

Following this argumentation, the evolution of the c_p-step at T_g and ultimately the thermodynamic fragility of the systems might be connected to the changes on the MRO length scale. In other words, the increasing c_p-step and slope of excess entropy upon substituting Pd by Pt might reflect the increasing diversity

of cluster connection schemes. To structurally assess these relevant length-scales in X-ray diffraction experiments, the first sharp diffraction peak (FSDP) comprises a large part of the corresponding information [61]. Nevertheless, when connecting to macroscopic properties it is important to pay attention, as due to their large scattering cross-section [62], the scattering data is dominated by the contribution of Pt and Pd atoms. Hence, all structural information is merely reflecting the behavior of these large noble metal atomic species, while the role of e.g., P cannot directly be probed by the used diffraction techniques.

Especially with the focus on the characteristics of specific heat capacity and the change in configurational entropy, the full width at half maximum (FWHM) Γ should be a good quantity representing the diversity in the connection schemes, and therefore in the MRO. Structural studies have shown that the FWHM of the FSDP correlates well with the correlation length over which the period of a repeated unit survives, underlining its connection to the medium range order in non-crystalline systems [63]. Further it was also used to characterize the relaxation state and increasing MRO in a metallic glass [64]. The FWHM itself is very sensitive to temperature changes and is broadening with increasing temperature due to the increasing atomic vibrations (Debye-Waller factors [65]). The atomic clusters themselves are representing the SRO of the system, whereas the interaction between the clusters and how they are interconnected is described by the MRO. The change of the FWHM of the FSDP corresponds to changes on the length scale of the MRO and therefore allow to quantify differences in the cluster connections. A large temperature sensitivity of the FWHM of the FSDP might resemble a high diversity of cluster connections (MRO) which should thermodynamically condense in a larger change in configurational entropy, thus a thermodynamically fragile behavior, as observed for the Pt-rich liquids.

For that reason, the FWHM Γ during heating is evaluated for the changing Pt/Pd content throughout the glassy and SCL state until crystallization sets in. To exclude structural relaxation effects during the heating, the samples were initially heated to a temperature $T_{g,end}$+10 K and then cooled at the same rate of 0.33 Ks^{-1} (see course of the FWHM in SI Fig. 6). In Fig. 8a) the normalized FWHM is shown on a temperature scale normalized by T_g. In the glassy state the FWHM features a shallow progression with temperature, leading to a slope of almost zero. It is followed by an abrupt rise in FWHM, as the system is entering the supercooled liquid state. Qualitatively the trend of the curves already shows high similarity to the progression of excess enthalpy or entropy during heating from the glassy state, when excluding relaxation effects. In the glassy state excess enthalpy and entropy are assumed to remain frozen in/constant until reentering the (supercooled) liquid state, where significant rearrangements, which can lead to enthalpic and entropic changes, are activated again. Above the glass transition temperature different slopes of the FWHM are already visible by eye. While the Pt-rich alloys feature a large increase of the peak width, this increase is less significant for the liquids that feature higher Pd contents.

In Fig. 8b), the linearly fitted slope of the FWHM above the glass transition temperature with respect to temperature, $d\Gamma/dT$ is depicted on the left axis, quantifying the graphical trend of Fig. 8a), of a decreasing $d\Gamma/dT$ with rising Pd content. This means the temperature induced changes in the peak width are becoming less prominent with increasing Pd content, well mirroring the trend of $\Delta c_p^{l-x}(T_g)/T_g$ with Pd content, which is added on the right axis of Fig. 8b). Considering $\Delta c_p^{l-x}(T_g)/T_g$ as a measure of the rate of change in excess entropy $\Delta S^{l-x}(T)$, the tendency of a less pronounced ordering process of the liquid with rising Pd content, is qualitatively mirrored by the smaller structural changes regarding the width of the FWHM. Therefore, the structure of the Pd based systems are showing smaller temperature induced changes, resem-

bling a structurally stronger behavior compared to the Pt-rich systems.

Ultimately, the scatter plot of Fig. 8c) proves the good qualitative congruence between the temperature induced changes of the FWHM $d\Gamma/dT$ and the changes in specific heat capacity at the glass transition temperature $\Delta c_p^{l-x}(T_g)/T_g$, which in the end serves as a measure of the thermodynamic fragility. Thus, it can be conjectured that the Pd based alloys behave thermodynamically and structurally stronger than the Pt based liquids, which is also in accordance with the findings based on the structural fragility concept of Wei et al. (compare Ref. [66]) for the $Pt_{42.5}Cu_{27}Ni_{9.5}P_{21}$ and $Pd_{43}Cu_{27}Ni_{10}P_{20}$ liquid [11].

Although, both Pt- and Pd-P liquid families feature significant differences in their thermodynamic properties, which are also being detectable by different structural signatures, the fact that both systems behave kinetically fragile leads to the fundamental question of the origin of the kinetic fragility and its underlying structural mechanisms in metallic liquids. Consequently, the Pt/Pd-P based liquids appear to be the ideal candidate for further research on the connection between thermodynamics, kinetics, and structure. To elucidate this fundamental issue additional work will be needed to further examine the dynamic and kinetic behavior of the Pd-rich liquids to shed light on their anomalous behavior. Especially methods like X-ray photon correlation spectroscopy (XPCS), which enable the resolution of the dynamics on the atomic scale, might be providing a new insight into the dynamics and kinetics of these metallic systems and can possibly guide to a resolution of this dilemma.

5. Conclusion

In summary, the study reports on thermodynamic properties of the glassy, liquid and crystalline phase of the Pt–Pd–Cu–Ni–P bulk metallic glass forming alloy system. The glass transition, crystallization and melting event is assessed regarding characteristic temperatures and enthalpies. Based on measurements of isobaric specific heat capacity, the alloy system is thermodynamically modelled to calculate the enthalpic behavior of liquid and glassy state with respect to the crystal and the driving forces for crystallization are estimated via calculations of the Gibbs free energy difference between crystal and liquid.

The often suggested and, in an earlier study structurally indicated, scenario of rising tendencies to embrittlement through Pd addition in the system was further underpinned through the thermodynamic considerations. Via monitoring of the residual enthalpy in the glassy state as a function of Pd content, a large amount of residual enthalpy was found for Pt-rich glasses compared to their Pd-rich peers. Under the assumptions of a direct correlation of free volume and residual enthalpy, the large free volume is assumed to facilitate multiple shear banding and ultimately promote ductility.

Furthermore, the Gibbs free energy curves of the liquid with respect to the crystalline state show a decreasing driving force for crystallization with increasing Pd content, resulting in an increasing thermodynamic stability of the liquid phase when replacing Pt with Pd. It systematically validates the surprisingly low driving force for similar Pd-based systems reported in literature.

Based on the behavior of the excess specific heat capacity with temperature, the change of the excess entropy around the glass transition was derived, suggesting a thermodynamically stronger behavior with increasing Pd content. This stands in a contrast to the reported kinetic fragilities, which would propose a constant or even more fragile behavior with growing Pd content. To resolve this discrepancy also the structural changes with temperature are examined with HEXRD. From this a good correlation between the excess heat capacity at the glass transition/rate of loss of configurational entropy with the change of the FWHM of the FSDP Γ in

the liquid state with respect to temperature $d\Gamma/dT$ is found. This further supports the picture drawn by the heat capacity data of a thermodynamically more fragile Pt system, that is undergoing more severe structural changes on the length scale of the FSDP during cooling and the rather strong Pd system that remains comparably stable/unchanged on these observed length scales. Finally, the findings can be seen as another milestone in the understanding of structural changes on the MRO length scale and their connection to thermodynamic parameters, such as excess heat capacity or configurational entropy, and ultimately thermodynamic fragility.

Declaration of Competing Interest

The authors declare that they have no known competing financial interests or personal relationships that could have appeared to influence the work reported in this paper.

Supplementary materials

Supplementary material associated with this article can be found, in the online version, at doi:10.1016/j.actamat.2021.117300.

References

[1] C.A. Angell, Formation of glasses from liquids and biopolymers, Sci. (80-.) 267 (1995) 1924–1935, doi:10.1002/hlca.19690520729.

[2] W.H. Busch, R. Schroers, J. Wang, T hermodynamics and kinetics of bulk metallic glass thermodynamics of supercooled, MRS Bull 32 (2007) 620–623.

[3] R. Busch, Thermophys. Prop. Bulk Met. Glass-Form. Liq. (2000) 39–42.

[4] R.W. Cahn, P. Haasen, E.J. Kramer, Glasses and amorphous materials, Mater. Sci. Technol. 9 (1991) 493.

[5] D.B. Miracle, A structural model for metallic glasses, Microsc. Microanal. 10 (2004) 786–787, doi:10.1038/nmat1219.

[6] D.B. Miracle, The efficient cluster packing model - An atomic structural model for metallic glasses, Acta Mater 54 (2006) 4317–4336, doi:10.1016/j.actamat. 2006.06.002.

[7] K.J. Laws, D.B. Miracle, M. Ferry, A predictive structural model for bulk metallic glasses, Nat. Commun. 6 (2015) 1–10, doi:10.1038/ncomms9123.

[8] N. Nishiyama, K. Takenaka, H. Miura, N. Saidoh, Y. Zeng, A. Inoue, The world's biggest glassy alloy ever made, Intermet. 30 (2012) 19–24.

[9] J. Schroers, W.L. Johnson, Highly processable bulk metallic glass-forming alloys in the Pt-Co-Ni-Cu-P system, Appl. Phys. Lett. 84 (2004) 3666–3668, doi:10. 1063/1.1738945.

[10] O. Gross, B. Bochtler, M. Stolpe, S. Hechler, W. Hembree, R. Busch, I. Gallino, The kinetic fragility of Pt-P- and Ni-P-based bulk glass-forming liquids and its thermodynamic and structural signature, Acta Mater 132 (2017) 118–127, doi:10.1016/j.actamat.2017.04.030.

[11] O. Gross, Precious metal based bulk glass-forming liquids: development, thermodynamics, kinetics and structure, Diss. Saarl. Univ. (2018), doi:10.22028/ D291-27993.

[12] O. Gross, S.S. Riegler, M. Stolpe, B. Bochtler, A. Kuball, S. Hechler, R. Busch, I. Gallino, On the high glass-forming ability of Pt-Cu-Ni/Co-P-based liquids, Acta Mater 141 (2017) 109–119, doi:10.1016/j.actamat.2017.09.013.

[13] O. Gross, N. Neuber, A. Kuball, B. Bochtler, S. Hechler, M. Frey, R. Busch, Signatures of structural differences in Pt–P- and Pd–P-based bulk glass-forming liquids, Commun. Phys. 2 (2019) 83, doi:10.1038/s42005-019-0180-2.

[14] G. Kumar, P. Neibecker, Y.H. Liu, J. Schroers, Critical fictive temperature for plasticity in metallic glasses, Nat. Commun. 4 (2013) 1536, doi:10.1038/ ncomms2546.

[15] G. Kumar, S. Prades-Rodel, A. Blatter, J. Schroers, Unusual brittle behavior of Pd-based bulk metallic glass, Scr. Mater. 65 (2011) 585–587, doi:10.1016/j. scriptamat.2011.06.029.

[16] L. Sun, Q. Wu, Y. Xu, W. Wang, Study on solidification behaviour of Pd40Ni40P20 alloy by fluxing method, Phys. B Condens. Matter. 240 (1997) 205–210.

[17] R. Busch, W. Liu, W.L. Johnson, Thermodynamics and kinetics of the Mg65Cu25Y10bulk metallic glass forming liquid, J. Appl. Phys. 83 (1998) 4134–4141, doi:10.1063/1.367167.

[18] B.A. Legg, J. Schroers, R. Busch, Thermodynamics, kinetics, and crystallization of Pt57.3Cu14.6Ni5.3P22.8 bulk metallic glass, Acta Mater 55 (2007) 1109–1116, doi:10.1016/j.actamat.2006.09.024.

[19] O. Kubaschewski, C.B. Alcock, P.J. Spencer, Materials thermochemistry, (1993) 363. https://doi.org/10.2170/physiolsci.RP009208.

[20] A.C. Dippel, H.P. Liermann, J.T. Delitz, P. Walter, H. Schulte-Schrepping, O.H. Seeck, H. Franz, Beamline P02.1 at PETRA III for high-resolution and high-energy powder diffraction, J. Synchrotron Radiat. 22 (2015) 675–687, doi:10.1107/S1600577515002222.

[21] A. Hammersley, Fit2d: an introduction and overview, Eur. Sychrotron Radi Facil. Int. Rep. ESRF97HA02T. 68 (1997).

[22] X. Qiu, J.W. Thompson, S.J.L. Billinge, PDFgetX2: a GUI-driven program to obtain the pair distribution function from X-ray powder diffraction data, J. Appl. Crystallogr. 37 (2004) 678, doi:10.1107/S0021889804011744.

[23] T. Egami, S.J.L. Billinge, Underneath the Bragg Peaks: Structural Analysis of Complex Materials, 2nd ed., 2012.

[24] T.E. Faber, J.M. Ziman, A theory of the electrical properties of liquid metals, Philos. Mag. 11 (1965) 153–173, doi:10.1080/14786436508211931.

[25] S. Wei, M. Stolpe, O. Gross, W. Hembree, S. Hechler, J. Bednarcik, R. Busch, P. Lucas, Structural evolution on medium-range-order during the fragile-strong transition in Ge15Te85, Acta Mater 129 (2017) 259–267, doi:10.1016/j.actamat. 2017.02.055.

[26] S. Pogatscher, D. Leutenegger, J.E.K. Schawe, P.J. Uggowitzer, J.F. Löffler, Solid-solid phase transitions via melting in metals, Nat. Commun. 7 (2016) 1–6, doi:10.1038/ncomms11113.

[27] M. Frey, R. Busch, W. Possart, I. Gallino, On the thermodynamics, kinetics, and sub-Tg relaxations of Mg-based bulk metallic glasses, Acta Mater 155 (2018) 117–127, doi:10.1016/j.actamat.2018.05.063.

[28] N. Neuber, O. Gross, M. Eisenbart, A. Heiss, U.E. Klotz, J.P. Best, M.N. Polyakov, J. Michler, R. Busch, I. Gallino, The role of Ga addition on the thermodynamics, kinetics, and tarnishing properties of the Au-Ag-Pd-Cu-Si bulk metallic glass forming system, Acta Mater 165 (2019) 315–326, doi:10.1016/j.actamat.2018.11. 052.

[29] A. Kuball, O. Gross, B. Bochtler, R. Busch, Sulfur-bearing metallic glasses: a new family of bulk glass-forming alloys, Scr. Mater. 146 (2018) 73–76, doi:10.1016/ j.scriptamat.2017.11.011.

[30] C.T. Moynihan, A.J. Easteal, M.A. De BOLT, J. Tucker, Dependence of the fictive temperature of glass on cooling Rate, J. Am. Ceram. Soc. 59 (1976) 12–16, doi:10.1111/j.1151-2916.1976.tb09376.x.

[31] A. van den Beukel, J. Sietsma, The glass transition as a free volume related kinetic phenomenon, Acta Metall. Mater. 38 (1990) 383–389, doi:10.1016/ 0956-7151(90)90142-4.

[32] Z. Evenson, R. Busch, Equilibrium viscosity, enthalpy recovery and free volume relaxation in a Zr44Ti11Ni10Cu10Be25 bulk metallic glass, Acta Mater 59 (2011) 4404–4415, doi:10.1016/j.actamat.2011.03.064.

[33] A. Slipenyuk, J. Eckert, Correlation between enthalpy change and free volume reduction during structural relaxation of Zr55Cu30Al10Ni 5 metallic glass, Scr. Mater. 50 (2004) 39–44, doi:10.1016/j.scriptamat.2003.09.038.

[34] O. Haruyama, Y. Nakayama, R. Wada, H. Tokunaga, J. Okada, T. Ishikawa, Y. Yokoyama, Volume and enthalpy relaxation in Zr55Cu30Ni5Al10 bulk metallic glass, Acta Mater 58 (2010) 1829–1836, doi:10.1016/j.actamat.2009.11.025.

[35] M.E. Launey, J.J. Kruzic, C. Li, R. Busch, Quantification of free volume differences in a Zr 44Ti 11Ni 10Cu 10Be 25bulk amorphous alloy, Appl. Phys. Lett. 91 (2007) 8–11, doi:10.1063/1.2766659.

[36] D. Turnbull, M.H. Cohen, Free-volume model of the amorphous phase: glass transition, J. Chem. Phys. 34 (1961) 120–125, doi:10.1063/1.1731549.

[37] G. Ruitenberg, P. De Hey, F. Sommer, J. Sietsma, Pressure dependence of the free volume in amorphous Pd40Ni40P20 and its implications for the diffusion process, Mater. Sci. Eng. A 226–228 (1997) 397–400, doi:10.1016/ s0921-5093(96)10651-1.

[38] W.L. Johnson, J. Lu, M.D. Demetriou, Deformation and flow in bulk metallic glasses and deeply undercooled glass forming liquids - A self consistent dynamic free volume model, Intermet. 10 (2002) 1039–1046, doi:10.1016/ S0966-9795(02)00160-7.

[39] C.A. Schuh, T.C. Hufnagel, U. Ramamurty, Mechanical behavior of amorphous alloys, Acta Mater 55 (2007) 4067–4109, doi:10.1016/j.actamat.2007.01.052.

[40] M.E. Launey, R. Busch, J.J. Kruzic, Effects of free volume changes and residual stresses on the fatigue and fracture behavior of a Zr-Ti-Ni-Cu-Be bulk metallic glass, Acta Mater 56 (2008) 500–510, doi:10.1016/j.actamat.2007.10.007.

[41] A.R. Yavari, Absence of thermal embrittlement in some FeB and FeSiB glassy alloys, Mater. Sci. Eng. 98 (1988) 491–493, doi:10.1016/0025-5416(88)90214-5.

[42] T.W. Wu, F. Spaepen, The relation between enbrittlement and structural relaxation of an amorphous metal, Philos. Mag. B Phys. Condens. Matter; Stat. Mech. Electron. Opt. Magn. Prop. 61 (1990) 739–750, doi:10.1080/ 13642819008219307.

[43] Z. Evenson, On the thermodynamic and kinetic properties of bulk glass forming metallic systems, Univ. Des Saarlandes, 2012 https://doi.org/doi:10.22028/D291-22851.

[44] R. Busch, E. Bakke, W.L. Johnson, On the glass forming ability of bulk metallic glasses, Mater. Sci. Forum. 235–238 (1997) 327–336, doi:10.4028/www. scientific.net/MSF.235-238.327.

[45] H.-R. Jiang, B. Bochtler, S.S. Riegler, X.-S. Wei, N. Neuber, M. Frey, I. Gallino, R. Busch, J. Shen, Thermodynamic and kinetic studies of the Cu–Zr–Al(–Sn) bulk metallic glass-forming system, J. Alloys Compd. (2020) 156126, doi:10. 1016/j.jallcom.2020.156126.

[46] M. Frey, R. Busch, W. Possart, I. Gallino, On the thermodynamics, kinetics, and sub-Tg relaxations of Mg-based bulk metallic glasses, Acta Mater 155 (2018) 117–127, doi:10.1016/j.actamat.2018.05.063.

[47] J.W. Richards, Relations between the melting points and the latent heats of fusion of the metals, J. Franklin Inst. 143 (1897) 379–383, doi:10.1016/ s0016-0032(97)90124-1.

[48] O. Gross, M. Eisenbart, L.Y. Schmitt, N. Neuber, L. Ciftci, U.E. Klotz, R. Busch, I. Gallino, Development of novel 18-karat, premium-white gold bulk metallic glasses with improved tarnishing resistance, Mater. Des. 140 (2018) 495–504, doi:10.1016/j.matdes.2017.12.007.

[49] D. Turnbull, Formation of crystal nuclei in liquid metals, J. Appl. Phys. 21 (1950) 1022–1028, doi:10.1063/1.1699435.

[50] I. Gallino, J. Schroers, R. Busch, Kinetic and thermodynamic studies of the fragility of bulk metallic glass forming liquids, J. Appl. Phys. 108 (2010) 063501, doi:10.1063/1.3480805.

[51] D. Turnbull, Under What Conditions Can A Glass Be Formed? Contemp. Phys. 10 (1969) 473–488, doi:10.1080/00107516908204405.

[52] Z.P. Lu, H. Tan, Y. Li, S.C. Ng, Correlation between reduced glass transition temperature and glass forming ability of bulk metallic glasses, Scr. Mater. 42 (2000) 667–673, doi:10.1016/S1359-6462(99)00417-0.

[53] J. Ding, Y.Q. Cheng, H. Sheng, E. Ma, Short-range structural signature of excess specific heat and fragility of metallic-glass-forming supercooled liquids, Phys. Rev. B - Condens. Matter Mater. Phys. 85 (2012) 1–5, doi:10.1103/PhysRevB.85. 060201.

[54] P.G. Debenedetti, Metastable liquids: Concepts and Principles, Princeton university press, 1996.

[55] G. Adam, J.H. Gibbs, On the temperature dependence of cooperative relaxation properties in glass-forming liquids, J. Chem. Phys. 43 (1965) 139–146, doi:10. 1063/1.1696442.

[56] H.L. Smith, C.W. Li, A. Hoff, G.R. Garrett, D.S. Kim, F.C. Yang, M.S. Lucas, T. Swan-Wood, J.Y.Y. Lin, M.B. Stone, D.L. Abernathy, M.D. Demetriou, B. Fultz, Separating the configurational and vibrational entropy contributions in metallic glasses, Nat. Phys. 13 (2017) 900–905, doi:10.1038/nphys4142.

[57] C.A. Angell, L.-.M. Martinez, A thermodynamic connection to the fragility of glass-forming liquids, Nat. 410 (2001) 663–667.

[58] I. Gallino, On the fragility of bulk metallic glass forming liquids, Entropy (2017) 19, doi:10.3390/e19090481.

[59] J. Ding, Y.Q. Cheng, H. Sheng, E. Ma, C.A. Angell, L.-.M. Martinez, A thermodynamic connection to the fragility of glass-forming liquids, Phys. Rev. B - Condens. Matter Mater. Phys. 85 (2012) 1–5, doi:10.1103/PhysRevB.85.060201.

[60] I. Gallino, O. Gross, G. Dalla Fontana, Z. Evenson, R. Busch, On the kinetic and thermodynamic fragility of the Pt60Cu16Co2P22 and Pt57.3Cu14.6Ni5.3P22.8 bulk metallic glasses, J. Alloys Compd. 615 (2015) S35–S39, doi:10.1016/j. jallcom.2013.12.006.

[61] D. Ma, A.D. Stoica, X.L. Wang, Power-law scaling and fractal nature of medium-range order in metallic glasses, Nat. Mater. 8 (2009) 30–34, doi:10.1038/ nmat2340.

[62] P.J. Brown, A.G. Fox, E.N. Maslen, M.A. O'Keefe, B.T.M. Willis, Intensity of diffracted intensities, Int. Tables Crystallogr. C (2006) 554–595, doi:10.1107/ 97809553602060000600.

[63] A.P. Sokolov, A. Kisliuk, M. Soltwisch, D. Quitmann, Medium-range order in glasses: comparison of Raman and diffraction measurements, Phys. Rev. Lett. 69 (1992) 1540–1543, doi:10.1103/PhysRevLett.69.1540.

[64] V.M. Giordano, B. Ruta, Unveiling the structural arrangements responsible for the atomic dynamics in metallic glasses during physical aging, Nat. Commun. 7 (2016), doi:10.1038/ncomms10344.

[65] I. Waller, Zur Frage der Einwirkung der Wärmebewegung auf die Interferenz von Röntgenstrahlen, Zeitschrift Für Phys 17 (1923) 398–408.

[66] S. Wei, M. Stolpe, O. Gross, Z. Evenson, I. Gallino, W. Hembree, J. Bednarcik, J.J. Kruzic, R. Busch, Linking structure to fragility in bulk metallic glass-forming liquids, Appl. Phys. Lett. 106 (2015) 10–15, doi:10.1063/1.4919590.

5.2 Publication II

Disentangling structural and kinetic components of the α-relaxation in supercooled metallic liquids

Nico Neuber [1]✉, Oliver Gross[1,2], Maximilian Frey [1], Benedikt Bochtler [1,2], Alexander Kuball[1,2], Simon Hechler[1,2], Fan Yang[3], Eloi Pineda [4], Fabian Westermeier[5], Michael Sprung[5], Florian Schäfer [6], Isabella Gallino [1], Ralf Busch [1] & Beatrice Ruta [7]✉

The particle motion associated to the α-relaxation in supercooled liquids is still challenging scientists due to its difficulty to be probed experimentally. By combining synchrotron techniques, we report the existence of microscopic structure-dynamics relationships in $Pt_{42.5}Cu_{27}Ni_{9.5}P_{21}$ and $Pd_{42.5}Cu_{27}Ni_{9.5}P_{21}$ liquids which allows us to disentangle structural and kinetic contributions to the α-process. While the two alloys show similar kinetic fragilities, their structural fragilities differ and correlate with the temperature dependence of the stretching parameter describing the decay of the density fluctuations. This implies that the evolution of dynamical heterogeneities in supercooled alloys is determined by the rigidity of the melt structure. We find also that the atomic motion not only reflects the topological order but also the chemical short-range order, which can lead to a surprising slowdown of the α-process at the mesoscopic length scale. These results will contribute to the comprehension of the glass transition, which is still missing.

[1] Chair of Metallic Materials, Saarland University, Campus C6.3, 66123 Saarbrücken, Germany. [2] Amorphous Metal Solutions GmbH, Michellinstraße 9, 66424 Homburg, Germany. [3] Institut für Materialphysik im Weltraum, Deutsches Zentrum für Luft- und Raumfahrt (DLR), 51170 Köln, Germany. [4] Department of Physics, Institute of Energy Technologies, Universitat Politècnica de Catalunya - BarcelonaTech, 08019 Barcelona, Spain. [5] Deutsches Elektronen-Synchrotron DESY, Notkestr. 85, 22607 Hamburg, Germany. [6] Chair of Materials Science and Methods, Saarland University Campus, D2 3, 66123 Saarbrücken, Germany. [7] Université Lyon, Université Claude Bernard Lyon 1, CNRS, Institut Lumière Matière, Campus LyonTech - La Doua, F-69622 Lyon, France. ✉email: nico.neuber@uni-saarland.de; beatrice.ruta@univ-lyon1.fr

ARTICLE

Despite decades of studies, glass formers keep fascinating scientists and are often considered as archetypes of complex systems[1–5]. Understanding glass formation and the microscopic mechanisms responsible for the extreme slowing down of the structural α-relaxation process in supercooled liquids, prior to the glass transition, is a challenging task due to the difficulty associated with the measurement of the atomic motion using experiments and numerical simulations. Despite these challenges, several common features have been identified in recent years: i) the glass transition is often considered as a dynamical process accompanied by weak structural changes[6], although indications for underlying increasing structural correlation lengths have been reported in the last ten years in numerical studies[7,8]; ii) during undercooling, the relaxation time of the α-process (or the viscosity) of glass formers increases over several orders of magnitude in a faster-than-exponential way, until the liquid eventually transforms in an out-of-equilibrium glass[9]; iii) the supercooled liquid is characterized by the emergence of dynamical heterogeneities, which result in a stretched exponential long time decay of the density fluctuations associated to the α-relaxation[3,10].

Usually, the evolution of the dynamics in supercooled liquids approaching the glass transition temperature, T_g, is described by the kinetic fragility, m, a parameter introduced for the first time by C. A. Angell[11]. The kinetic fragility quantifies the departure from an Arrhenius behavior of the shear viscosity – or the structural relaxation time, τ, upon cooling a liquid at T_g. Following this description, all those liquids exhibiting an Arrhenius-like evolution of the viscosity on cooling, often characterized by strong directional bonds, are called strong, while fragile liquids display a super Arrhenius behavior and are usually systems with nondirectional bonds or van der Waal interactions. In the last years, many correlations have been proposed between the kinetic fragility and several properties of both liquids and glasses, highlighting the importance of this parameter[12–14].

By combining state-of-the-art synchrotron techniques, X-ray Photon Correlation Spectroscopy (XPCS) and High Energy X-ray diffraction (HEXRD), we show here that the evolution of the atomic motion, and therefore of the structural α-relaxation process, on approaching the glass transition should be described not only by the kinetic fragility but also by the structural fragility of the liquid[15]. The latter parameter is related to the evolution of the structure on the length scale of medium-range order (MRO) and is found to evolve similarly to the degree of dynamical heterogeneities emerging during the cooling. The results of this work emphasize the importance of the subtle changes accompanying the vitrification process by showing that both the temperature and length scale dependence of the microscopic α-relaxation are correlated with the underlying structural changes.

Metallic liquids are ideal candidates for this study. Due to their simple metallic bond structure, they have only translational motion and, therefore, they can be considered as model systems to study the glass transition. The two metallic glass-forming liquids $Pt_{42.5}Cu_{27}Ni_{9.5}P_{21}$ and $Pd_{42.5}Cu_{27}Ni_{9.5}P_{21}$ were selected for this study for several more reasons. According to structural models of glass-forming liquids, based on the efficient packing of representative structural units (clusters)[16], elements with atomic radii that deviate no more than 2 % are considered as topologically equivalent[17], which is true for Pt and Pd in these two compositions. However, HEXRD experiments have revealed significant differences in their structures[18]. Based on these experiments, it is suggested that the structure of both liquids is dominated by two different structural motifs. While the $Pd_{42.5}Cu_{27}Ni_{9.5}P_{21}$ liquid consists mainly of icosahedral motifs, leading to a pronounced short-range order (SRO), the structure of the $Pt_{42.5}Cu_{27}Ni_{9.5}P_{21}$ shows a larger part of trigonal prisms, leading to a rather

pronounced MRO. This MRO is manifested in the appearance of a pre-peak in the low-Q range of the total structure factor S(Q), before the first sharp diffraction peak (FSDP), which is present in the Pt-based liquid but absent in the Pd-based one. In contrast, the Pd-based liquid shows a shoulder on the larger Q-side of the second sharp diffraction peak, associated to icosahedral SRO (see Supplementary Fig. 1). Despite these structural differences, both alloys show similar kinetic fragilities[19–21], whereas the excess heat capacity around the glass transition, as well as melting enthalpy and entropy are found to be much higher in the Pt-based liquid[21–23] than in the Pd-based alloy. This indicates that the Pt-based alloy is more fragile from the thermodynamic point of view. Furthermore, Pt-based glasses tend to show a more ductile mechanical performance than their Pd-based peers, which, in contrast, are more sensitive to cooling rate and annealing related embrittlement[24–27]. Finally, both systems have an excellent glass-forming ability (GFA), as described by the critical casting thickness d_c which is $d_c = 20$ mm for $Pt_{42.5}Cu_{27}Ni_{9.5}P_{21}$ and $d_c = 80$ mm for the $Pd_{42.5}Cu_{30}Ni_{7.5}P_{20}$[28,29]. Such exceptional resistance to crystallization allows us to perform dynamical measurements in the supercooled liquid phase. All these features make these two systems perfect candidates to study the connection between atomic motion and the inherent structures. Our work shows that the combination of state-of-the-art synchrotron techniques applied on metallic glass forming liquids, can elucidate the influence of the structure on the particle motion in the deeply supercooled liquid state close to the dynamic arrest during the glass transition and facilitate the distinction between kinetic and structural contributions to the α-relaxation process.

Results and Discussion

Collective particle motion in the supercooled liquid phase. Information on the dynamics can be obtained from the intermediate scattering function (ISF), f(Q,t), which describes the temporal evolution of the density-density correlation function normalized to the static structure factor. The long-time decay of the ISF provides therefore a direct measurement of the α-relaxation process at the probed length scale 2π/Q, with Q being the investigated wave-vector. It can be obtained in an XPCS measurement by the determination of the correlation function of the intensity fluctuations, $g_2(Q,t)$, generated by the scattering of coherent X-rays from the sample, being $g_2(Q,t) = 1 + \gamma \cdot |f(Q,t)|^2$. In this expression, γ is the experimental contrast[30]. In glass-formers, $g_2(Q,t)$ can be described by the Kohlrausch-Williams-Watts (KWW) function $g_2(Q,t) = 1 + c \cdot \exp[-2(t/\tau)^\beta]$ where $c = \gamma \ast f_q^2$ is the product between the experimental contrast and the square of the nonergodicity parameter, f_q, of the system, τ is the relaxation time, and β the shape parameter[30]. By definition, the shape parameter describes the degree of nonexponentiality of the ISF, which originates from the underlying distribution of relaxation times, and it can therefore be considered as a measure of the heterogeneous nature of the dynamics in the liquid phase.

Figure 1a, b show the temperature dependence of normalized $[g_2(Q,t)-1]/c$ functions measured at $Q_{FSDP} \approx 2.8$ Å^{-1}, corresponding to the position of the first sharp diffraction peak (FSDP) in the static profile. For both compositions, the data have been acquired in the supercooled liquid phase, cooling from about $(T_g + 25)$ K, with T_g $(Pt_{42.5}Cu_{27}Ni_{9.5}P_{21}) = 506$ K and T_g $(Pd_{42.5}Cu_{27}Ni_{9.5}P_{21}) = 566$ K for the applied cooling rate of 0.025 K s^{-1}. By decreasing the temperature by only ≈ 20 K, the decay of the curves clearly shifts by about two orders of magnitude towards longer times, indicating the rapid slow-down of α-relaxation process when approaching the glass transition. The corresponding relaxation times display a very similar evolution with temperature in both compositions. This is shown
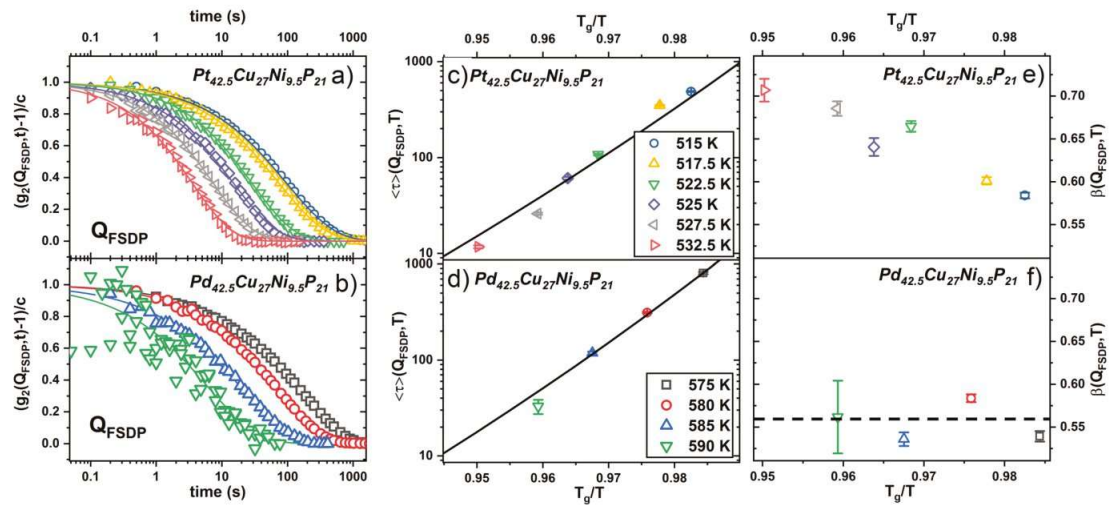
Fig. 1 Temperature dependence of the atomic dynamics in $Pt_{42.5}Cu_{27}Ni_{9.5}P_{21}$ and $Pd_{42.5}Cu_{27}Ni_{9.5}P_{21}$ supercooled liquids. a, b Normalized intensity autocorrelation functions measured at various temperatures for $Pt_{42.5}Cu_{27}Ni_{9.5}P_{21}$ (**a**), and $Pd_{42.5}Cu_{27}Ni_{9.5}P_{21}$ (**b**) at the wave vector Q of the first sharp diffraction peak ($Q_{FSDP} \approx 2.8$ Å^{-1} for both systems). **c, d** Mean relaxation time $<\tau(Q,T)>$ of the Pt- and Pd-based alloys measured at the position of the first sharp diffraction peak Q_{FSDP} at various temperatures T. The solid lines are fits to the Vogel-Fulcher-Tammann equation (see section "Collective particle motion in the supercooled liquid phase"). **e, f** Temperature dependence of the corresponding exponent of the Kohlrausch-William-Watts equation $\beta(Q,T)$ for $Pt_{42.5}Cu_{27}Ni_{9.5}P_{21}$ (**e**) and $Pd_{42.5}Cu_{27}Ni_{9.5}P_{21}$ (**f**). The dashed line is a guide to the eyes. Error bars indicate the standard error due to fitting of the experimental data using the Levenberg Marquardt algorithm.

in Fig. 1c, d, where we report the mean relaxation time $\langle \tau(Q) \rangle = \Gamma(\beta(Q)^{-1})\frac{\tau(Q)}{\beta(Q)}$, where Γ is the Gamma function[31]. In both systems, <$\tau(Q,T)$ > can be described by the Vogel-Fulcher-Tammann (VFT) equation with $<\tau(Q,T)> = \tau_0 \cdot \exp[(D^*T_0)/(T-T_0)]$ using the parameters obtained by macroscopic studies such as viscosity measurements, from Gross et al.[19] for the Pt-alloy and from new measurements (see Supplementary Fig. 2) for the Pd-alloy. This means that the temperature dependence of the microscopic relaxation times measured with XPCS agrees well with that of the corresponding macroscopic viscosity data.

In contrast to <$\tau(Q,T)$ >, the shape of the ISFs exhibits a different evolution with temperature in the two liquids. In both cases, the curves can be described by a stretched exponential decay with a KWW parameter $\beta(Q,T) < 1$, indicating the heterogeneous nature of the dynamics in the viscous liquid phase (Fig. 1e, f)[3]. However, for the Pd-liquid $\beta(Q_{FSDP},T)$ remains constant at a value of ≈ 0.55 within the probed temperature range, whereas for the Pt-liquid, $\beta(Q_{FSDP},T) \approx 0.7$ at high temperature and then clearly decreases by about 20% of its initial value during cooling. Similar temperature dependences of the KWW parameters have been observed also at length scales corresponding to few interatomic distances (see Supplementary Fig. 3).

The rapid decrease of $\beta(Q,T)$ on cooling in the Pt-based alloy implies the failure of the time-temperature superposition principle for this composition (see also Supplementary Fig. 4). This result contrasts with previous XPCS studies of metallic glass formers where $\beta(T)$ has been found T-independent in all measured supercooled liquids allowing to superpose all the correlation curves in a single master curve[32–34]. Although the relationship between macroscopic and microscopic dynamics is not straightforward, also most metallic glasses show a T-independent shape of the α-relaxation peak in mechanical experiments. The shape of such peak is in agreement with a KWW exponent of around 0.5[35–37]. This means that the satisfaction of the time-temperature-superposition (TTS)

principle is expected in many metallic glass-forming systems. Further detailed studies on the dynamic relaxation processes in metallic glasses can be found in literature[38–42].

Structural evolution in the supercooled liquid phase. The different temperature evolution of the dynamics in the two alloys can be explained by looking at the temperature dependence of the underlying structure. Figure 2 shows the temperature dependence of the peak intensity (a), full width at half maximum (FWHM) (b) and peak position (c) of the FSDP of the static structure factors S(Q) measured in both compositions with HEXRD (the corresponding diffraction spectra can be found in Supplementary Fig. 1, 5 and 6). All data are linearly fitted in the supercooled liquid state and rescaled to the T_g at the measured rate of 0.33 K s^{-1}. While the peak intensity displays a similar temperature dependence in both alloys (Fig. 2a), the FWHM and the peak position exhibit a steeper evolution with temperature in supercooled $Pt_{42.5}Cu_{27}Ni_{9.5}P_{21}$ (b) and c)). Structural studies have shown that the FWHM of the FSDP correlates well with the correlation length over which the period of a repeated unit persists, underlining its connection to the medium-range order in non-crystalline systems[43]. The more pronounced temperature dependence of FWHM$_{FSDP}$ of the Pt-liquid (Fig. 2b) thus provides evidence of the presence of a more pronounced reorganization of the MRO in the deeply undercooled Pt-liquid compared to the Pd-based one. This effect is accompanied by a more rapid evolution of the peak position with temperature (Fig. 2c) in the $Pt_{42.5}Cu_{27}Ni_{9.5}P_{21}$ supercooled liquid, confirming the presence of significant structural rearrangements during cooling. A recent study has furthermore evidenced that the slope of the increase in the liquid of the FWHM of the measured alloys is proportional to the growth rate of the excess entropy[23]. This suggests that the evolution of the FWHM across T_g is connected to the unfreezing of the glassy state and the reactivation of thermal vibrations. Earlier work on the thermal evolution of structure in a very similar Pd-Cu-Ni-P-based system can be found
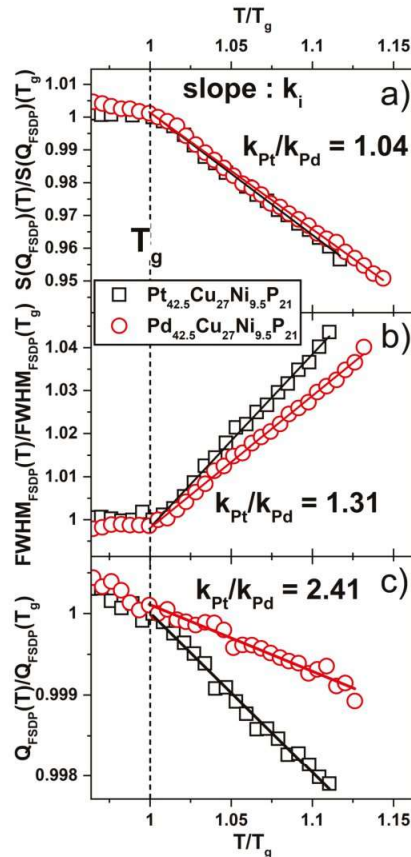
Fig. 2 Temperature dependence of the first sharp diffraction peak of $Pt_{42.5}Cu_{27}Ni_{9.5}P_{21}$ and $Pd_{42.5}Cu_{27}Ni_{9.5}P_{21}$ measured with synchrotron X-ray diffraction. Peak intensity of the total structure factor $S(Q_{FSDP})$ (**a**), full width at half maximum $FWHM_{FSDP}$ (**b**) and peak position (Q_{FSDP}) (**c**) of the first sharp diffraction peak as a function of temperature normalized by the glass transition temperature T/T_g for the Pt-based (black squares) and Pd-based (red circles) alloys. All data are normalized to the respective value of the glass transition. In all panels, k is the respective slope of a linear fit of the data in the liquid state of the Pt/Pd-based alloys (above the glass transition temperature T_g).

in various publications[44–46] with further works already pointing towards the relation between structure and fragility[47].

The larger tendency to temperature induced structural rearrangements at the MRO length scale in the $Pt_{42.5}Cu_{27}Ni_{9.5}P_{21}$ liquid is likely responsible for the temperature evolution of the KWW exponent describing the decay of the ISFs. At temperatures (much) higher than those probed in this work, the system is likely governed by diffusion with ISFs described by a single exponential decay (i.e., $\beta = 1$) and $\tau \sim Q^{-2}$. During cooling in the supercooled liquid phase, the viscosity increases (Supplementary Fig. 2), the dynamics slows down, and $\beta(T)$ decreases due to the formation of cages of atoms and the occurrence of dynamical heterogeneities. The relatively large value of $\beta \approx 0.7$ in the Pt-alloy at only 25 K above T_g, suggests that the cages can already break easier at this temperature leading to more homogeneous dynamics. During cooling, the liquid experiences a rapid slowdown of the dynamics which hinders the particle motion and cages break less frequently,

leading to an increased heterogeneity in the dynamics and thus to a lower value of β in the Pt-alloy. The low constant value of the shape parameter in the $Pd_{42.5}Cu_{27}Ni_{9.5}P_{21}$ and the absence of important structural reorganizations suggest instead that this supercooled liquid is already in a dynamically highly heterogeneous, stable state. In the Pd-liquid, the transition from diffusive dynamics by collective motion at high temperature to activated collective dynamics in the supercooled liquid phase, if present, probably occurs at temperatures much higher than those measured in the current experiment. This is in agreement with neutron studies in other Pd-based alloys which report non-exponential decays of the ISFs even in the high-temperature melt[48].

Kinetic and structural fragility. For a better quantitative comparison of the relaxation behavior of both liquids, Fig. 3a shows a fragility plot where we report the inverse temperature as a function of the mean relaxation time $<\tau(Q_{FSDP})>$. On the atomic level, both systems exhibit similar kinetic fragilities, m, with $m_{Pt} = 53.1 \pm 2.6$ and $m_{Pd} = 55.3 \pm 3.2$. Here, m is defined as the logarithms slope of the kinetic variable X (e.g. viscosity/relaxation time) at T_g via $m = d\log X/d(T_g/T)|_{T=T_g}$[9,11]. These values are in good agreement with those obtained from macroscopic measurements[19,49,50], using the relation $m = 16 + 590/D^*$, which gives $m_{Pt} = 54.5$ ($D^* = 15.3$) and $m_{Pd} = 57$ ($D^* = 14.5$) (compare Supplementary Table 1). This is a further confirmation of the agreement between the microscopic relaxation times and independent macroscopic measurements as shown also by Fig. 1.

Despite their similar kinetic fragility, the evolution of the α-relaxation process during cooling is not the same in the two systems, as seen by the different values and temperature dependencies of the KWW shape parameter. This difference seems to disappear on approaching T_g where both liquids reach a similar degree of nonexponentiality of the ISF (Fig. 3b). A similar behavior was observed in macroscopic measurements of ultra-phosphate liquids with different sodium content, which display different temperature evolutions of $\beta(T)$ merging all to a value of $\beta(T_g) \approx 0.5$[51]. We find that the rate of change of $\beta(Q_{FSDP},T)$ with $<\tau(Q_{FSDP},T)>$, i.e., the slope $d\beta/d\log(<\tau>)$, is about -0.08 for the Pt-based alloy. This value is comparable with the steepest slope observed for pure ultraphosphate ($d\beta/d\log(<\tau>) \sim -0.06$,[51]) where it has been attributed to a high degree of cooperativity in the 3D-network of PO_4 tetrahedra[51]. In our case, the steep evolution of $\beta(T)$ appears to be related to the tendency of the Pt-alloy to temperature induced structural rearrangements on the length-scale of MRO[15](see Fig. 2). In amorphous metallic systems, the MRO is in fact mainly associated to the FSDP which is representative of structural rearrangements occurring on length scales beyond $r > 6$ Å[52]. The evolution of the 3rd (r_3) and 4th peak (r_4) of the reduced pair-distribution function $G(r)$ provides therefore another tool to gain insights into the structural changes of the two liquids[15]. Figure 3c shows the temperature dependence of the relative change of the volume expansion $\Delta V_{4-3} = 4/3\pi(r_4^3 - r_3^3)$ of a shell between r_3 and r_4 with respect to the value at T_g. As it can be immediately deduced from Fig. 3c), the ratio $\Delta V_{4-3}/\Delta V_{4-3}(T_g)$ mirrors the behavior of $\beta(Q_{FSDP},T)$ suggesting a correlation between changes on the MRO length scale and the temperature evolution of the KWW parameter. Following Wei et al.[15], we can define a structural fragility, m_{str4-3}, from the slope of $\Delta V_{4-3}/\Delta V_{4-3}(T_g)$ and we find $m_{str4-3,Pt} = 0.035 \pm 0.004$ for the $Pt_{42.5}Cu_{27}Ni_{9.5}P_{21}$ and a basically temperature independent $m_{str4-3,Pd} \approx 0.005 \pm 0.006$ for the $Pd_{42.5}Cu_{27}Ni_{9.5}P_{21}$. Both values are in good agreement with those given in earlier works[15,50]. In the work of Wei et al. m_{str4-3} was found to correlate to the kinetic fragility of the liquid through the empirical expression $m =$

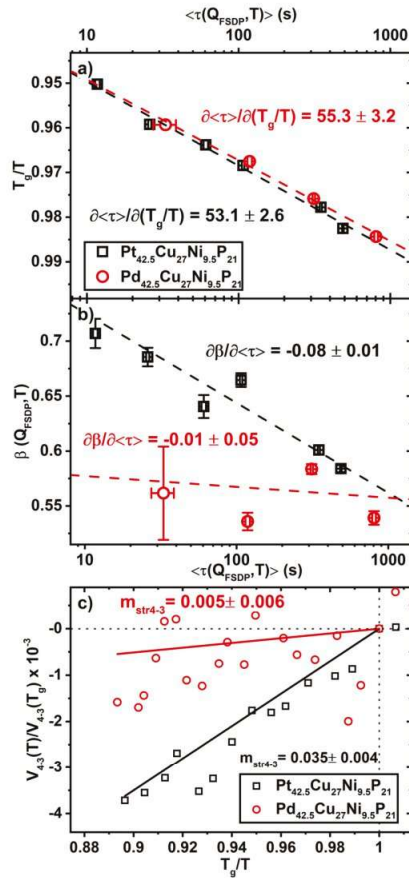   **ARTICLE**

Fig. 3 Temperature evolution of the dynamical parameters and of the structure on the medium-range order (MRO) length scale. a Glass transition temperature-scaled (for a cooling rate of 1.5 K min^{-1}) fragility plot of the mean relaxation time $<\tau(Q_{FSDP})>$ for $Pt_{42.5}Cu_{27}Ni_{9.5}P_{21}$ and $Pd_{42.5}Cu_{27}Ni_{9.5}P_{21}$ (black squares and red circles, respectively). Solid lines are linear fits on the logarithmic scale underlining the similar kinetic fragility of the two liquids. Note that the slope provided in the figure comes from the conventional definition of the kinetic fragility, m, where the axes are inverted. **b** Corresponding Kohlrausch-Williams-Watts exponent $\beta(Q_{FSDP},T)$ as a function of mean relaxation time $<\tau(Q_{FSDP})>$. The dashed lines are linear fits on the data on the logarithmic scale. **c** Evolution of normalized volume dilation of the fourth and third atomic shell from the reduced pair distribution function $V_{4-3}(T)/V_{4-3}(T_g)$ as a function of normalized inverse temperature T_g/T, where T_g is the glass transition temperature during heating with a rate of 0.33 K s^{-1}. A linear fit (full line in respective color) of the data is used to calculate the structural fragility parameter m_{str4-3} of the liquid phase. Error bars indicate the standard error due to fitting of the experimental data using the Levenberg Marquardt algorithm.

$((m_{str4-3} + 0.124)/2.95 \times 10^{-3})$[15]. While this relation is fulfilled for the Pt-liquid being $m_{Pt} = 53.9 \pm 1.3$ as well as numerous Zr-based liquids, it fails for the Pd-based alloy as it gives $m_{Pd} = 42.6 \pm 3.3$, which is significantly lower than the measured value. The failure of the proposed correlation for the Pd-based alloy, the temperature-independent KWW stretching exponent (Fig. 3b)) and the weak temperature evolution on the MRO length-scale

(Fig. 2), support the idea of a smaller tendency to structural rearrangements and thus of a rather strong structural behavior of the Pd-based alloy at the probed length scales, in agreement with the estimation obtained from the structural fragility. At this point it should be noted that further support for the structural strong behavior of the Pd-based liquid is provided by the behavior of the specific isobaric heat capacity c_p. During undercooling of the Pt-liquid, a more rapid rise of c_p can be observed compared to the Pd-based liquid[22,23]. This change of the liquid c_p is connected to the rate of the loss in the excess entropy, which itself is proportional to the configurational entropy of the liquid[13,21,53]. Within the framework of Adam and Gibbs[54], this behavior can be seen as the thermal signature of a faster growth of cooperatively rearranging regions in the Pt-liquid with ongoing undercooling. Thus, it further confirms the larger tendency of the Pt-liquid to structural changes indicated by the steep temperature dependence of the FSDP (Fig. 2), the evolution of the degree of dynamical heterogeneity $\beta(Q_{FSDP},T)$ (Fig. 3b)), and the fragile value of the structural fragility (Fig. 3c).

Wave-vector dependence of the dynamics. The different atomic dynamics of the two alloys is even more evident by looking at the wave-vector dependence of the relaxation time. As shown in Fig. 4a, $\tau(Q)$ displays two maxima for the $Pt_{42.5}Cu_{27}Ni_{9.5}P_{21}$ liquid at $Q_{PP} = 2.05$ Å^{-1} and $Q_{FSDP} = 2.8$ Å^{-1}. These values correspond to the position of the maximum of a structural pre-peak (Q_{PP}) and of the main FSDP observed in the corresponding static structure factor (dashed grey line). In contrast, $\tau(Q)$ exhibits only one maximum at Q_{FSDP} for $Pd_{42.5}Cu_{27}Ni_{9.5}P_{21}$, agreeing with the corresponding S(Q) (Fig. 4b). The increase of $\tau(Q)$ in correspondence with the different underlying structural motifs implies the existence of more stable configurations at the corresponding length scales. While the maximum at Q_{FSDP} is typical of glass formers, usually observed in high temperature liquids by neutron scattering (de Gennes narrowing[55,56]), the prominent increase of $\tau(Q)$ at Q_{PP} in the $Pt_{42.5}Cu_{27}Ni_{9.5}P_{21}$ is more surprising due to the very weak intensity of the pre-peak in the static profile.

A similar evolution with Q is observed also for $\beta(Q)$ in both supercooled liquids (Fig. 4c, d). For $Pt_{42.5}Cu_{27}Ni_{9.5}P_{21}$, however, the maximum at the prepeak is broader and less pronounced compared to that in $\tau(Q)$ (Fig. 4c). The larger values of $\beta(Q)$ in the Pt-alloy at the positions of the of structural maxima suggest more homogeneous dynamics at these length scales with respect to neighboring Q values. To better understand the observed behavior, we can distinguish two zones: the atomic scale, i.e., in the proximity of the FSDP for 2.5 Å^{-1} < Q < 3.2 Å^{-1}; and the intermediate regime at a length scale of few interatomic distances for 1.5 Å^{-1} < Q < 2.5 Å^{-1}.

We first concentrate on the atomic scale. Besides the experimental results reported for liquids at high temperature[55,56], a similar evolution of the collective relaxation time with Q has been observed also in numerical simulations of different glass formers close to the glass transition like, for instance, supercooled silica, water and hard spheres[57–59] where it has been described within the mode coupling theory. It should be noted that while in network glass formers $\beta(Q)$ is found constant with Q, only in hard spheres $\beta(Q)$ correlates also with the intensity evolution of the S(Q) and shows a maximum at the FSDP[58,60] as in our data. This suggests a stronger correlation between metallic glasses and hard spheres systems[61].

In the intermediate regime, the presence of a second peak in the relaxation time corresponds to an additional slow-down of the collective motion in correspondence with the weak structural pre-peak at a few interparticle distances. Similar behaviors on the
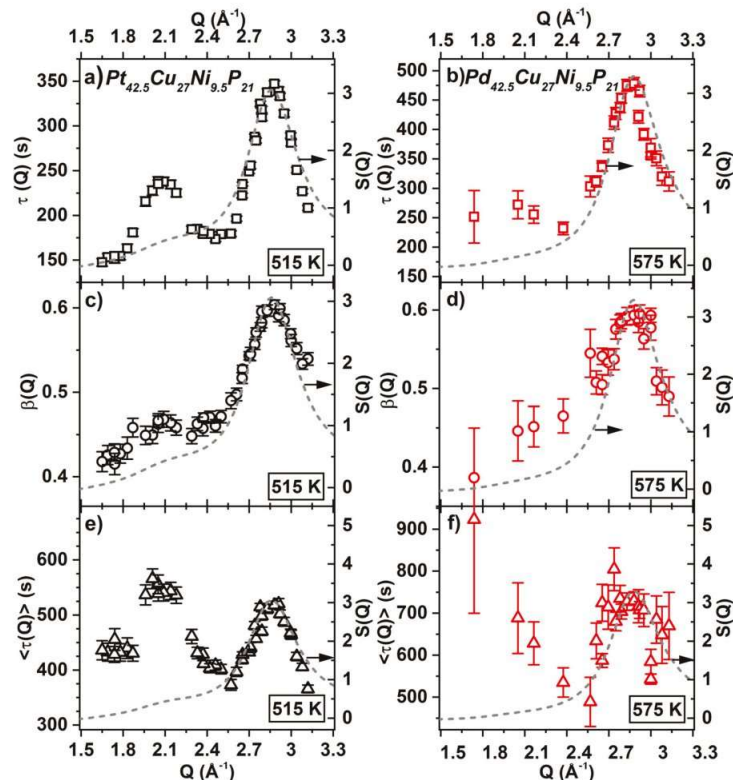
Fig. 4 Wave-vector dependence of the dynamics. Wave-vector- dependence of the Kohlrausch-Williams-Watts relaxation time (**a**, **b**), Kohlrausch-Williams-Watts exponent (**c**, **d**), and mean relaxation time (**e**, **f**) for the Pt-alloy at the temperature T = 515 K (left column, black) and the Pd-alloy at the temperature T = 575 K (right column, red). In all panels, the dashed grey lines represent the total structure factor S(Q) measured with synchrotron XRD. Error bars indicate the standard error due to fitting of the experimental data using the Levenberg Marquardt algorithm.

MRO length scale have been reported only in few other glass formers as silicates, ortho-terphenyl, polymeric systems and $[Ca(NO_3)_2]_{0.4}[KNO_3]_{0.6}$ (CKN)[62–65], where it has been associated to the underlying topological order. To the best of our knowledge, this is the first experimental observation in a metallic liquid. Furthermore, previous studies have been performed at much higher temperatures, close to the melting, where the collective motion is diffusive and $\tau(Q)$ evolves continuously with Q^{-2} at low Q values.

In order to account for the influence of the shape parameter on the observed relaxation times, Fig. 4e, f report the mean relaxation time for both compositions. A slow-down of the dynamics can be observed also in $<\tau(Q)>$ for the Pt-based alloy. Surprisingly, the dynamics at the pre-peak, Q_{PP}, is even slower than that at low Q values and at the FSDP, indicating the pronounced temporal durability of the medium-range structural features in this composition. Previous structural studies suggested that the scattering contribution of the pre-peak arises from Pt-Pt and Pt-Cu partial structure factors[18]. The presence of the pre-peak only in the Pt-based alloy shows that such structural feature is of chemical and thus electronic nature, rather than from a geometrical packing origin, as Pt and Pd can be assumed topologically equal but differ in their electronic structure. Thus, in this scenario, the slow-down of $<\tau(Q)>$ at Q_{pp} in the Pt-based alloy would not be related to a preferential fast diffusion path in a slow relaxing matrix as for silicate glasses or other non-metallic glass formers[63,66,67], but would originate from the presence of specific structural motifs that stems from chemical effects. The mechanism is similar to that of de Gennes narrowing at the FSDP usually observed in the frequency domain in high-temperature liquids[55], however, here the origin would not be due to geometrical constrains, but rather to strong chemical interactions which reduce the mobility at the mesoscopic scale.

A similar slow-down of the atomic motion in correspondence of a structural pre-peak has been reported for high-temperature binary alloys[68]. In such two-component systems, a full set of partial structure factors can be experimentally determined, and the presence of a pre-peak has been attributed to the preferential formation of non-equal pairs (as for instance Pt-Cu in our sample), which lead to an isolation of equal atoms and result in a spatial arrangement that can be described as a type of superstructure at the MRO length scale[69]. Although the same structural analysis cannot be done for the quaternary alloys studied here, the structural motifs and the role of the metal-metalloid interactions has been described by simulation studies[70]. The presence of different structural motifs in the two alloys[18], in particular of trigonal prisms in the Pt-based system, somehow leads to different connections between the atomic clusters and to the formation of some favored and temporally stable configurations on the length scales larger than the FSDP in the Pt-alloy.

Conclusion

In conclusion, our work scrutinizes the microscopic details controlling the evolution of the α-relaxation in supercooled metallic liquids in the vicinity of the glass transition. By comparing the evolution of the α-relaxation process and the structure of two similar supercooled liquids, we identify the different features describing the liquid dynamics. Although the two selected compositions would appear as identical in topological structural models[16], they present different structural motifs on the MRO and SRO length scales[18], which influence their relaxation dynamics. The kinetic fragility - described by the temperature evolution of the microscopic relaxation time - is insensitive to the composition and is similar for both alloys, in agreement with macroscopic studies[49,71]. In contrast, the two liquids have different structural fragilities which mirror the different temperature dependence of the $\beta(Q_{FSDP},T)$ parameter describing the heterogeneous nature of the dynamics. This means that the temperature evolution of dynamical heterogeneities in the supercooled liquid phase reflects the different tendencies of the two liquids to temperature-induced structural rearrangements at the MRO length scale. In the case of the $Pd_{42.5}Cu_{27}Ni_{9.5}P_{21}$ alloy, this structure-dynamic relationship results in a relatively weak temperature dependence of the structure and a constant value of $\beta(Q_{FSDP},T)$ in the probed temperature range. Differently, in the Pt-based alloy, the presence of structural rearrangements leads to a continuous evolution of the dynamical heterogeneities during the cooling, as signaled by the increased non-exponential shape of the decay of the density fluctuations on approaching T_g. This marked temperature dependence of $\beta(Q_{FSDP},T)$ in the Pt-based melt leads to the failure of the time-temperature superposition principle for the structural relaxation process (Supplementary Fig. 4), which contrasts with the usual law of invariance observed in previous studies on metallic glass formers at both microscopic[32–34] and macroscopic[35–37,72] scales. Interestingly, despite the different evolution of the dynamics during cooling, both alloys exhibit similar values of $\beta(Q,T)$ at the glass transition suggesting the existence of a common degree of heterogeneities in metallic liquids at the dynamical arrest.

In addition, we also find that the wave-vector dependence of the collective motion is influenced by the structure. In the $Pt_{42.5}Cu_{27}Ni_{9.5}P_{21}$ liquid, both $\tau(Q,T)$ and $\beta(Q,T)$ exhibit an unusual evolution with Q with two maxima, one at the position of the FSDP, the signature of the well-known increased stability at the interparticle distance, and an anomalous second one at the mesoscopic scale in correspondence with a weak pre-peak in the total structure factor. In contrast, only one maximum at Q_{FSDP} is observed in the Pd-alloy. This different dependence of the dynamics from the probed wave-vector is likely due to a more pronounced MRO in the Pt- than in the Pd-liquid, similarly to what was also reported in high-temperature binary alloys[68]. The different MRO in the two systems is likely related to stronger chemical and electronic interactions in the Pt-based alloy than in the Pd-liquid, which also result in the presence of different structural motifs at the level of the SRO. All together our results shed light on the influence of the structure on the particle motion and the different role played by kinetic and structural fragilities during the vitrification process.

Materials and Methods

Materials. The master alloys of $Pt_{42.5}Cu_{27}Ni_{9.5}P_{21}$ and $Pd_{42.5}Cu_{27}Ni_{9.5}P_{21}$ were produced by melting the pure metallic components (purity > 99.95 %) in an arc melter furnace under a Ti-gettered Ar-atmosphere (purity > 99.999%). Afterwards the elemental red P was alloyed inductively with the metallic components in a fused-silica tube under Ar-atmosphere. To control the P-content we use a fused silica tube in which the metals (arc-melted to a long "cigar") are put on top of the elemental red phosphorous (lump). Then an inductive coil is used to heat up the metal from top to bottom to carefully start the exothermic reaction. Only small amounts will not directly alloy with the hot metal in direct contact and evaporate. The small part of the P that initially evaporates is absorbed directly from the hot metal above it and cannot leave the reaction area. The result is an ingot with well-defined P content. By weighing of the ingots after its alloying with phosphorous and even assuming any loss in mass being attributed to P lost during the reaction, we can assure the P content to be in the limits of a derivation of less than 0.5 at% with this process.

The obtained alloy then underwent a fluxing treatment in dehydrated pure B_2O_3 for at least 6 h at 1473 K. This process was used to further purify the melt from possible oxides and impurities and enhances the glass-forming ability of the liquid even further[73]. Ribbons were prepared via melt-spinning by inductive melting of the master-alloy in a fused silica tube and injecting it onto a rotating copper wheel under high-purity Ar atmosphere in a custom-built melt-spinning device. The full amorphous nature of the sample has been confirmed by transmission electron microscopy and high-energy synchrotron x-ray diffraction.

X-ray photon correlation spectroscopy (XPCS). To probe the microscopic dynamics, X-ray photon correlation spectroscopy was performed at the Coherence Applications Beamline P10 at PETRA III at the *Deutsches Elektronen-Synchrotron* (DESY) in Hamburg during two different beamtimes of one week each. A partially coherent beam of $3 \times 2 \mu m^2$ (horizontal x vertical direction) at a photon energy of 8.2 keV and a photon flux on the sample of around 4×10^{10} photons s^{-1} was used on ribbons with a thickness of ~20 µm, mounted in a furnace under vacuum. Speckle patterns were collected with an EIGER X4M detector 1.8 m downstream of the sample at the end of a horizontally rotatable diffractometer arm, enabling measurements at different wavevectors Q. The low Q limit was set at ~1.6 Å^{-1} due to the weak scattering intensity at small angles, while the maximum angle that was reachable with the experimental setup was at 43°, corresponding to Q = 3.06 Å^{-1}, limiting thus the resolution of the FSDP on the high-Q flank. The wave-vector dependence of the dynamics was measured at different temperatures in the supercooled liquid phase. The exposure time per frame was adjusted to the observed timescales ranging from 0.1 s to 0.5 s. The overall measurement time was also adjusted at each temperature and wavevector position assuring the observation of a complete decorrelation of the signal, up to a maximum of ~10^4 s for the lowest measured temperature. The detector covers an angle of approximately 3° which corresponds to a ΔQ of about ~0.2 Å^{-1}. By binning the area of the detector, we could therefore probe up to 8 Qs simultaneously for each detector position.

Data were analyzed following the procedure reported by Chushkin et al.[74]. For each Q and temperature, we calculated the two times correlation function (TTCF) at two different times, t_1 and t_2:

$$G(Q, t_1, t_2) = \frac{<I(Q, t_1) \cdot I(Q, t_2)>_p}{<I(Q, t_1)>_p \cdot <I(Q, t_2)>_p}, \quad (1)$$

where $<...>_p$ represents the average over all detector pixels corresponding to the same Q-range.

Intensity auto correlation functions $g_2(Q,t)$ were calculated by averaging the TTCF over the whole measured temporal interval. The $g_2(Q,t)$ functions are directly related to the intermediate scattering function, $f(Q,t)$, through the Siegert relation $g_2(Q, t) = 1 + \gamma \cdot |f(Q,t)|^2$ with γ being the experimental contrast. The $g_2(Q,t)$ functions were modelled using a Kohlrausch-Williams-Watts (KWW) function:

$$g_2(Q, t, T) = 1 + c(Q, T) \exp\left(-2\left(\frac{t}{\tau(Q, T)}\right)^{\beta(Q,T)}\right), \quad (2)$$

where $\tau(Q,T)$ is the structural relaxation time, $\beta(Q,T)$ is the shape parameter and $c(Q,T)$ is the product of the experimental contrast $\gamma(Q,T)$ and the square of the non-ergodicity factor $f_q(Q,T)$.

The samples were first equilibrated at about T_g+30 K to remove their thermal history, and then slowly cooled with 5 K min^{-1} to the measurement temperatures. At each temperature, we waited about 10 min for temperature equilibration before starting the data acquisition. The amorphous structure was checked during the experiment and no signs of crystallization were observed, in agreement with the time-temperature-transformation diagrams reported in literature[22,75]. The temperature calibration of the furnace was checked by crystallizing additional samples and comparing the crystallization temperature T_x of the $Pt_{42.5}Cu_{27}Ni_{9.5}P_{21}$ and $Pd_{42.5}Cu_{27}Ni_{9.5}P_{21}$ samples at a constant heating rate of 5 K min^{-1} obtained in differential scanning calorimetry (DSC).

For the solute-rich metallic liquid $Pt_{42.5}Cu_{27}Ni_{9.5}P_{21}$, the main contributions to the pre-peak originate from the Pt-Pt and Pt-Cu partial structure factors, which, due to their high form factor, dominate the overall structure factor S(Q), while the signal of the Pd-based alloy is dominated by the Pd-Pd and Pd-Cu correlations (see Supplementary Information of Gross et al.[18] for further details).

During the XPCS experiments, we have particularly paid attention to crystallization effects. Thanks to the measurement of second-order correlation functions, such as the density-density correlation function, XPCS has a larger sensitivity to crystallization than any structural technique based on the detection of a static observable[76]. The presence of fluctuating crystalline contributions would dramatically alter the shape of the correlation functions, while the presence of static contributions due to nanocrystals in the XPCS spectra would lead to an increase in

ARTICLE

the baseline of the correlation functions, which has not been observed during the whole experiment.

Furthermore, the presence of nanocrystals in the as-cast sample would lead to stronger fringes of interference and zones of higher intensity in the speckle patterns recorded by the 4 Mpixel EIGER detector. During an atomic scale XPCS experiment on metallic glasses, the photon counting detector measures the weak scattered intensity, mainly originating from single photon events. Any stronger scattering event, as it would be occurring in the presence of nanocrystals would therefore be visible immediately, much in advance of being detected in a standard synchrotron XRD experiment with incoherent radiation.

The data reported in this work have been measured in two years during three different official XPCS beamtimes of 1 full week each, in European synchrotrons (DESY and ESRF).

High energy synchrotron X-ray scattering (HE-XRD). In-situ X-ray scattering experiments have been performed at the beamline P02.1 at PETRA III at the Deutsches Elektronen Synchrotron (DESY) in Hamburg[77]. For the measurements in transmission mode a wavelength of 0.207 Å (60 keV) and a beam size of 0.8×0.8 mm^2 was used. The samples were attached on a solid Ag-block of a THMS-600 LINKAM furnace using a Cu-paste and heated at a rate of 0.33 Ks^{-1} under a constant flow of high purity Ar (Ar 6.0). Prior to the measurements the samples were heated at 0.33 K s^{-1} to the supercooled liquid state ($T_{g,end} + 10$ K) and subsequently cooled from this point at the same rate of 0.33 Ks^{-1}. For the acquisition of the intensity patterns a Perkin Elmer XRD1621 CsI bonded amorphous silicon detector (2048 pixels × 2048 pixels) was used. The integration of the dark-subtracted, two-dimensional X-ray diffraction patterns was performed with the Fit2D data analysis software[78]. Further processing of the intensity data was realized with the PDFgetX2 software[79]. The background scattering was assumed to be constant with temperature and mainly originating from the setup. It was measured at room temperature and was subtracted from the integrated intensity data. For the corrections of the raw data, sample absorption, polarization and multiple scattering were considered. The total structure factor S(Q) was calculated as[80]

$$S(Q) = 1 + \frac{I_C(Q) - \langle f(Q)^2 \rangle}{\langle f(Q) \rangle^2}, \tag{3}$$

where $I_C(Q)$ is the coherently scattered intensity and f(Q) is the atomic form factor. The angle brackets denote a compositional average over all constituents. S(Q) contains all the structural information and is composed of n(n+1)/2 partial structure factors[81],

$$S(Q) = \sum_{i \leq j} w_{ij} S_{ij}(Q), \tag{4}$$

where w_{ij} is the weighting factor expressed as

$$w_{ij} = \frac{c_i c_j f_i(Q) f_j(Q)}{\langle f(Q) \rangle^2} \tag{5}$$

where c_i and c_j are the molar concentration of element i and j.

The Fourier transform of the total structure factor yields the reduced pair distribution function,

$$G(r) = \frac{2}{\pi} \int_0^\infty Q[S(Q) - 1] \sin(Qr) dQ, \tag{6}$$

where r is the distance to the reference atom. Each G(r) pattern was optimized using an optimization algorithm in PDFgetX2 as described by Wei et al.[82]. An upper limit of Q = 14.5 Å^{-1} was used here for the transformation. This Q_{max} ensures a successful evaluation of the data in real-space without the loss of significant structural details, as already observed by Ma et al. for even lower Q_{max}-values[52].

Thermomechanical analysis. To determine the kinetic fragility on a macroscopic experiment three-point beam bending (3PBB) was performed using a NETZSCH TMA 402 F3 thermomechanical analyzer under a static loading force of 10 N. The beams were cut out of fully X-ray-amorphous plates with the dimensions of 1.5 × 13 × 40 mm. For a good signal-to-noise ratio the thickness of the beams was varied from 0.4 to 1.5 mm. The viscosity η can be derived from the deflection rate ů(t), applying the equation[83]

$$\eta(t) = -\frac{g \cdot L^3}{144 I \dot{u}} \cdot \left[M + \frac{\rho A L}{1.6} \right], \tag{7}$$

with the applied load M and density ρ combined with the geometric information of the sample (cross-sectional area of the beam A, cross-sectional moment of inertia I and distance between the supporting edges of the machine L).

Isothermal measurements between 533 K and 573 K, as well as measurements with a constant heating rate of $q_h = 0.333$ Ks^{-1} were carried out. During the isothermal measurements the same heating rate of 0.333 Ks^{-1} was applied to reach the desired isothermal plateau temperature. A more detailed description of the technique and calculations to obtain the viscosity from the deflection rate can be found in literature[19,71].

The evolution of the equilibrium viscosities over temperature can be described with the empirical Vogel-Fulcher-Tammann (VFT) equation[11]

$$\eta(T) = \eta_0 \cdot \exp\left(\frac{D^* \cdot T_0}{T - T_0}\right), \tag{8}$$

with D* being the fragility parameter and T$_0$ being the VFT temperature, where viscosity would be diverging. The parameter η$_0$ corresponds to the lowest possible viscosity in the high-temperature liquid state.

The datasets generated and/or analyzed during the current study are available from the corresponding authors on reasonable request.

References

1. Donth, E. *The glass transition: relaxation dynamics in liquids and disordered materials*. 48 (Springer Science & Business Media, 2013).
2. Anderson, P. W. Through the Glass Lightly. *Sci.* **267**, 1615–1616 (1995).
3. Berthier, L. & Biroli, G. Theoretical perspective on the glass transition and amorphous materials. *Rev. Mod. Phys.* **83**, 587–645 (2011).
4. Ediger, M. D. & Harrowell, P. Perspective: Supercooled liquids and glasses. *J. Chem. Phys.* **137**, (2012).
5. Dyre, J. C. Colloquium: The glass transition and elastic models of glass-forming liquids. *Rev. Mod. Phys.* **78**, 953–972 (2006).
6. Chandler, D. & Garrahan, J. P. Dynamics on the way to forming glass: Bubbles in space-time. *Annu. Rev. Phys. Chem.* **61**, 191–217 (2010).
7. Tong, H. & Tanaka, H. Structural order as a genuine control parameter of dynamics in simple glass formers. *Nat. Commun.* **10**, 4–6 (2019).
8. Tanaka, H., Kawasaki, T., Shintani, H. & Watanabe, K. Critical-like behaviour of glass-forming liquids. *Nat. Mater.* **9**, 324–331 (2010).
9. Böhmer, R. et al. Nonexponential relaxations in strong and fragile glass formers. *J. Chem. Phys.* **99**, 4201–4209 (1993).
10. Ediger, M. D. Spatially Heterogeneous Dynamics in Supercooled Liquids. *Annu. Rev. Phys. Chem.* **51**, 99–128 (2000).
11. Angell, C. A. Formation of glasses from liquids and biopolymers. *Sci.* **267**, 1924–1935 (1995).
12. Scopigno, T., Ruocco, G., Sette, F. & Monaco, G. Is the Fragility of a Liquid Embedded in the Properties of Its Glass? *Sci.* **302**, 849–852 (2003).
13. Angell, C. A. & Martinez, L.-M. A thermodynamic connection to the fragility of glass-forming liquids. *Nature* **410**, 663–667 (2001).
14. Novikov, V. N. & Sokolov, A. P. Poisson's ratio and the fragility of glass-forming liquids. *Nature* **431**, 961–963 (2004).
15. Wei, S. et al. Linking structure to fragility in bulk metallic glass-forming liquids. *Appl. Phys. Lett.* **106**, 10–15 (2015).
16. Miracle, D. B. A structural model for metallic glasses. *Microsc. Microanal.* **10**, 786–787 (2004).
17. Miracle, D. B. The efficient cluster packing model - An atomic structural model for metallic glasses. *Acta Mater.* **54**, 4317–4336 (2006).
18. Gross, O. et al. Signatures of structural differences in Pt–P- and Pd–P-based bulk glass-forming liquids. *Commun. Phys.* **2**, (2019).
19. Gross, O. et al. The kinetic fragility of Pt-P- and Ni-P-based bulk glass-forming liquids and its thermodynamic and structural signature. *Acta Mater.* **132**, 118–127 (2017).
20. Kato, H. et al. Fragility and thermal stability of Pt- and Pd-based bulk glass forming liquids and their correlation with deformability. *Scr. Mater.* **54**, 2023–2027 (2006).
21. Gallino, I., Schroers, J. & Busch, R. Kinetic and thermodynamic studies of the fragility of bulk metallic glass forming liquids. *J. Appl. Phys.* **108**, 063501 (2010).
22. Gross, O. et al. On the high glass-forming ability of Pt-Cu-Ni/Co-P-based liquids. *Acta Mater.* **141**, 109–119 (2017).
23. Neuber, N. et al. On the thermodynamics and its connection to structure in the Pt-Pd-Cu-Ni-P bulk metallic glass forming system. *Acta Mater.* **220**, 117300 (2021).
24. Neuber, N. et al. Effect of composition and thermal history on deformation behavior and cluster connections in model bulk metallic glasses. *Sci. Rep.* **12**, 17133 (2022).
25. Schroers, J. & Johnson, W. L. Ductile bulk metallic glass. *Phys. Rev. Lett.* **93**, 255506 (2004).
26. Kumar, G., Neibecker, P., Liu, Y. H. & Schroers, J. Critical fictive temperature for plasticity in metallic glasses. *Nat. Commun.* **4**, 1536 (2013).
27. Kumar, G., Prades-Rodel, S., Blatter, A. & Schroers, J. Unusual brittle behavior of Pd-based bulk metallic glass. *Scr. Mater.* **65**, 585–587 (2011).
28. Schroers, J. & Johnson, W. L. Highly processable bulk metallic glass-forming alloys in the Pt-Co-Ni-Cu-P system. *Appl. Phys. Lett.* **84**, 3666–3668 (2004).

ARTICLE

29. Nishiyama, N. et al. The world's biggest glassy alloy ever made. *Intermetallics* **30**, 19–24 (2012).

30. Madsen, A., Fluerasu, A. & Ruta, B. Structural dynamics of materials probed by X-ray photon correlation spectroscopy. *Synchrotron Light Sources Free. Lasers Accel. Physics, Instrum. Sci. Appl.* 1989–2018, https://doi.org/10.1007/978-3-030-23201-6_29 (2020).

31. Boon, J. P. & Yip, S. *Molecular hydrodynamics* (Courier Corporation, 1991).

32. Amini, N. et al. Intrinsic relaxation in a supercooled ZrTiNiCuBe glass forming liquid. *Phys. Rev. Mater.* **5**, 1–8 (2021).

33. Ruta, B. et al. Atomic-scale relaxation dynamics and aging in a metallic glass probed by X-ray photon correlation spectroscopy. *Phys. Rev. Lett.* **109**, 1–5 (2012).

34. Hechler, S. et al. Microscopic evidence of the connection between liquid-liquid transition and dynamical crossover in an ultraviscous metallic glass former. *Phys. Rev. Mater.* **2**, 1–6 (2018).

35. Wang, L. M., Liu, R. & Wang, W. H. Relaxation time dispersions in glass forming metallic liquids and glasses. *J. Chem. Phys.* **128**, (2008).

36. Qiao, J. C. & Pelletier, J. M. Dynamic universal characteristic of the main (α) relaxation in bulk metallic glasses. *J. Alloy. Compd.* **589**, 263–270 (2014).

37. Yao, Z. F., Qiao, J. C., Pelletier, J. M. & Yao, Y. Characterization and modeling of dynamic relaxation of a Zr-based bulk metallic glass. *J. Alloy. Compd.* **690**, 212–220 (2017).

38. Wang, W. H. Dynamic relaxations and relaxation-property relationships in metallic glasses. *Prog. Mater. Sci.* **106**, 100561 (2019).

39. Qiao, J. C. et al. Structural heterogeneities and mechanical behavior of amorphous alloys. *Prog. Mater. Sci.* **104**, 250–329 (2019).

40. Zhang, L. T. et al. Dynamic mechanical relaxation and thermal creep of high-entropy La30Ce30Ni10Al20Co10 bulk metallic glass. *Sci. China Physics, Mech. Astron.* **64**, 296111 (2021).

41. Luo, P., Wen, P., Bai, H. Y., Ruta, B. & Wang, W. H. Relaxation Decoupling in Metallic Glasses at Low Temperatures. *Phys. Rev. Lett.* **118**, 1–6 (2017).

42. Wang, Z., Sun, B. A., Bai, H. Y. & Wang, W. H. Evolution of hidden localized flow during glass-to-liquid transition in metallic glass. *Nat. Commun.* **5**, 5823 (2014).

43. Sokolov, A. P., Kisliuk, A., Soltwisch, M. & Quitmann, D. Medium-range order in glasses: Comparison of Raman and diffraction measurements. *Phys. Rev. Lett.* **69**, 1540–1543 (1992).

44. Yavari, A. R. et al. Excess free volume in metallic glasses measured by X-ray diffraction. *Acta Mater.* **53**, 1611–1619 (2005).

45. Mattern, N. et al. Structural behavior of Pd40Cu30Ni10P20 bulk metallic glass below and above the glass transition. *Appl. Phys. Lett.* **82**, 2589–2591 (2003).

46. Georgarakis, K. et al. Variations in atomic structural features of a supercooled Pd-Ni-Cu-P glass forming liquid during in situ vitrification. *Acta Mater.* **59**, 708–716 (2011).

47. Louzguine-Luzgin, D. V. et al. Structural basis for supercooled liquid fragility established by synchrotron-radiation method and computer simulation. *J. Appl. Phys.* **110**, 0–6 (2011).

48. Meyer, A., Busch, R. & Schober, H. Time-temperature superposition of structural relaxation in a viscous metallic liquid. *Phys. Rev. Lett.* **83**, 5027–5029 (1999).

49. Frey, M. et al. Determining the fragility of bulk metallic glass forming liquids via modulated DSC. *J. Phys. Condens. Matter* **32**, 324004 (2020).

50. Gross, O. Precious metal based bulk glass-forming liquids: Development, thermodynamics, kinetics and structure. *Diss. Saarl. Univ.* https://doi.org/10.22028/D291-27993 (2018).

51. Fabian, R. & Sidebottom, D. L. Dynamic light scattering in network-forming sodium ultraphosphate liquids near the glass transition. *Phys. Rev. B - Condens. Matter Mater. Phys.* **80**, 1–7 (2009).

52. Ma, D., Stoica, A. D. & Wang, X. L. Power-law scaling and fractal nature of medium-range order in metallic glasses. *Nat. Mater.* **8**, 30–34 (2009).

53. Gallino, I. On the fragility of bulk metallic glass forming liquids. *Entropy* **19**, 483 (2017).

54. Adam, G. & Gibbs, J. H. On the temperature dependence of cooperative relaxation properties in glass-forming liquids. *J. Chem. Phys.* **43**, 139–146 (1965).

55. De Gennes, P. G. Liquid dynamics and inelastic scattering of neutrons. *Physica* **25**, 825–839 (1959).

56. Yang, F., Kordel, T., Holland-Moritz, D., Unruh, T. & Meyer, A. Structural relaxation as seen by quasielastic neutron scattering on viscous Zr-Ti-Cu-Ni-Be droplets. *J. Phys. Condens. Matter* **23**, (2011).

57. Fuchs, M., Hofacker, I. & Latz, A. Primary relaxation in a hard-sphere system. *Phys. Rev. A* **45**, 898–912 (1992).

58. Sciortino, F., Fabbian, L., Chen, S. H. & Tartaglia, P. Supercooled water and the kinetic glass transition. II. *Collective Dyn. Phys. Rev. E - Stat. Phys., Plasmas, Fluids, Relat. Interdiscip. Top.* **56**, 5397–5404 (1997).

59. Weysser, F., Puertas, A. M., Fuchs, M. & Voigtmann, T. Structural relaxation of polydisperse hard spheres: Comparison of the mode-coupling theory to a Langevin dynamics simulation. *Phys. Rev. E - Stat. Nonlinear, Soft Matter Phys.* **82**, 1–21 (2010).

60. Handle, P. H., Rovigatti, L. & Sciortino, F. Q-Independent Slow Dynamics in Atomic and Molecular Systems. *Phys. Rev. Lett.* **122**, 175501 (2019).

61. Poon, W. Colloids as Big Atoms. *Sci.* **304**, 830–831 (2004).

62. Colmenero, J. & Arbe, A. Recent progress on polymer dynamics by neutron scattering: From simple polymers to complex materials. *J. Polym. Sci. Part B Polym. Phys.* **51**, 87–113 (2013).

63. Ruta, B. et al. Revealing the fast atomic motion of network glasses. *Nat. Commun.* **5**, 3939 (2014).

64. Novikov, V. N., Schweizer, K. S. & Sokolov, A. P. Coherent neutron scattering and collective dynamics on mesoscale. *J. Chem. Phys.* **138**, 164508 (2013).

65. Tolle Albert. Neutron scattering studies of the model glass former ortho-terphenyl. *Rep. Prog. Phys.* **64**, 1473 (2001).

66. Horbach, J., Kob, W. & Binder, K. Dynamics of Sodium in Sodium Disilicate: Channel Relaxation and Sodium Diffusion. *Phys. Rev. Lett.* **88**, 4 (2002).

67. Meyer, A., Horbach, J., Kob, W., Kargl, F. & Schober, H. Channel formation and intermediate range order in sodium silicate melts and glasses. *Phys. Rev. Lett.* **93**, 1–4 (2004).

68. Voigtmann, T. et al. Atomic diffusion mechanisms in a binary metallic melt. *Epl* **82**, 1–6 (2008).

69. Nowak, B. et al. Partial structure factors reveal atomic dynamics in metallic alloy melts. *Phys. Rev. Mater.* **1**, 3–7 (2017).

70. Guan, P. F., Fujita, T., Hirata, A., Liu, Y. H. & Chen, M. W. Structural origins of the excellent glass forming ability of Pd 40Ni 40P 20. *Phys. Rev. Lett.* **108**, 1–5 (2012).

71. Neuber, N. et al. The role of Ga addition on the thermodynamics, kinetics, and tarnishing properties of the Au-Ag-Pd-Cu-Si bulk metallic glass forming system. *Acta Mater.* **165**, 315–326 (2019).

72. Soriano, D. et al. Relaxation dynamics of Pd-Ni-P metallic glass: Decoupling of anelastic and viscous processes. *J. Phys. Condens. Matter* **33**, (2021).

73. Kui, H. W., Greer, A. L. & Turnbull, D. Formation of bulk metallic glass by fluxing. *Appl. Phys. Lett.* **45**, 615–616 (1984).

74. Chushkin, Y., Caronna, C. & Madsen, A. A novel event correlation scheme for X-ray photon correlation spectroscopy. *J. Appl. Crystallogr.* **45**, 807–813 (2012).

75. Schroers, J., Wu, Y., Busch, R. & Johnson, W. L. Transition from nucleation controlled to growth controlled crystallization in Pd43Ni10Cu27P20 melts. *Acta Mater.* **49**, 2773–2781 (2001).

76. Giordano, V. M. & Ruta, B. Unveiling the structural arrangements responsible for the atomic dynamics in metallic glasses during physical aging. *Nat. Commun.* **7**, 164508 (2016).

77. Dippel, A. C. et al. Beamline P02.1 at PETRA III for high-resolution and high-energy powder diffraction. *J. Synchrotron Radiat.* **22**, 675–687 (2015).

78. Hammersley, A. P. {FIT2D}: An Introduction and Overview. *Eur. Sychrotron Radi Facil. Int. Rep. ESRF97HA02T* **68**, (1997).

79. Qiu, X., Thompson, J. W. & Billinge, S. J. L. PDFgetX2: A GUI-driven program to obtain the pair distribution function from X-ray powder diffraction data. *J. Appl. Crystallogr.* **37**, 678 (2004).

80. Egami, T. & Billinge, S. J. L. *Underneath the Bragg Peaks: structural analysis of complex materials. Pergamon Materials Series.* **7** (2003).

81. Faber, T. E. & Ziman, J. M. A theory of the electrical properties of liquid metals. *Philos. Mag.* **11**, 153–173 (1965).

82. Wei, S. et al. Structural evolution on medium-range-order during the fragile-strong transition in Ge15Te85. *Acta Mater.* **129**, 259–267 (2017).

83. Hagy, H. E. Experimental Evaluation of Beam-Bending Method of Determining Glass Viscosities in the Range 108 to 1015 Poises. *J. Am. Ceram. Soc.* **46**, 93–97 (1962).

Author contributions

N.N., R.B., O.G. and B.R. conceived the study. N.N. and M.F. prepared the samples. N.N., O.G., B.B., A.K., S.H., I.G., B.R., E. P., F. Y. and M.F. planned and conducted the synchrotron X-ray experiments with the help of F.W. and M.S. N.N. and B.R. analyzed the synchrotron data. N.N. and M.F. conducted and analyzed the thermo-mechanical

ARTICLE

and calorimetric experiments. F.S. prepared the samples for transmission electron microscopy. N.N. and B.R. wrote the paper with input from R.B., E.P., F.Y., I.G. and O.G. All authors proofread the article and contributed extensively to the discussion.

Competing interests
The authors declare no competing interests.

Additional information
Supplementary information The online version contains supplementary material available at https://doi.org/10.1038/s42005-022-01099-4.

Correspondence and requests for materials should be addressed to Nico Neuber or Beatrice Ruta.

Peer review information *Communications Physics* thanks Qiao Ji-Chao and the other, anonymous, reviewer(s) for their contribution to the peer review of this work. Peer reviewer reports are available.

Reprints and permission information is available at http://www.nature.com/reprints

Publisher's note Springer Nature remains neutral with regard to jurisdictional claims in published maps and institutional affiliations.

5.3 Publication III
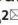
scientific reports

Check for updates

OPEN

Effect of composition and thermal history on deformation behavior and cluster connections in model bulk metallic glasses

Nico Neuber[1,5]✉, Maryam Sadeghilaridjani[2,5], Nandita Ghodki[2], Oliver Gross[1,3], Bastian Adam[1], Lucas Ruschel[1], Maximilian Frey[1], Saideep Muskeri[2], Malte Blankenburg[4], Isabella Gallino[1], Ralf Busch[1] & Sundeep Mukherjee[2]✉

The compositional dependence and influence of relaxation state on the deformation behavior of a Pt–Pd-based bulk metallic glasses model system was investigated, where platinum is systematically replaced by topologically equivalent palladium atoms. The hardness and modulus increased with rising Pd content as well as by annealing below the glass transition temperature. Decreasing strain-rate sensitivity and increasing serration length are observed in nano indentation with increase in Pd content as well as thermal relaxation. Micro-pillar compression for alloys with different Pt/Pd ratios validated the greater tendency for shear localization and brittle behavior of the Pd-rich alloys. Based on total scattering experiments with synchrotron X-ray radiation, a correlation between the increase in stiffer 3-atom cluster connections and reduction in strain-rate sensitivity, as a measure of ductility, with Pd content and thermal history is suggested.

Bulk metallic glasses (BMGs) are a relatively new class of metallic materials which have attracted considerable attention in structural applications over the past decades due to their outstanding mechanical properties such as high strength, large elastic limit, excellent irradiation, wear, and corrosion resistance in the glassy state and thermoplastic forming ability in the supercooled liquid state[1–4]. However, limited plasticity at room temperature in bulk form has restricted their widespread use[5,6]. Without dislocations and grain boundaries, BMGs show completely different deformation mechanism compared to conventional crystalline alloys[7]. Plastic deformation in metallic glasses tends to occur in the form of highly localized shear bands, which, depending on the mode of loading, may result in catastrophic failure[8,9]. Several different approaches have been introduced to enhance the plasticity of BMGs through altering of their chemistry and processing conditions such as ex-situ and in-situ fabrication of BMG matrix composites (BMGMCs)[10], metal coating confinement[11], heat treatment[12], ion radiation[13], and increase in Poisson's ratio[14]. These studies aimed to control and manipulate the processes of shear-band nucleation and propagation. Cold rolling at room temperature has been utilized to increase the intrinsic plasticity of BMGs by introducing microstructural inhomogeneities, leading to nucleation and branching of shear bands upon deformation[15]. Ti-based BMG composites with volume fraction of the glassy phase in the range of 20–70% exhibited ~ 5% tensile ductility, which is comparable to conventional polycrystalline titanium alloys[10]. In another study, the plasticity of Zr-based BMGs was improved with the addition of quasicrystals in the glassy matrix[16]. In case of $Nd_{60}Al_{10}Ni_{10}Cu_{20-x}Fe_x$ BMGs, compositional adjustments with the addition of Fe changed the deformation behavior from inhomogeneous to homogeneous plastic flow[17]. The effect of strain rate and temperature on deformation behavior of various BMGs has also been reported[18–24]. However, there are few studies on systematic series of interrelated glass-forming alloys[20] and limited understanding on the effect of chemistry and local atomic structure on deformation behavior of BMGs. This is critical in the rational design of new classes of BMGs with superior mechanical properties.

Glass formation is often limited to a narrow region in compositional space for metallic systems[25]. In the case of Pd-P- and Pt-P-based liquids, the high glass-forming ability (GFA)[26], similarity of phase diagrams[27,28], and

[1]Chair of Metallic Materials, Saarland University, Campus C6.3, 66123 Saarbrücken, Germany. [2]Department of Materials Science and Engineering, University of North Texas, Denton, TX 76203, USA. [3]Amorphous Metal Solutions GmbH, 66424 Homburg, Germany. [4]Deutsches Elektronen-Synchrotron DESY, Notkestr. 85, 22607 Hamburg, Germany. [5]These authors contributed equally: Nico Neuber and Maryam Sadeghilaridjani. ✉email: nico.neuber@uni-saarland.de; sundeep.mukherjee@unt.edu
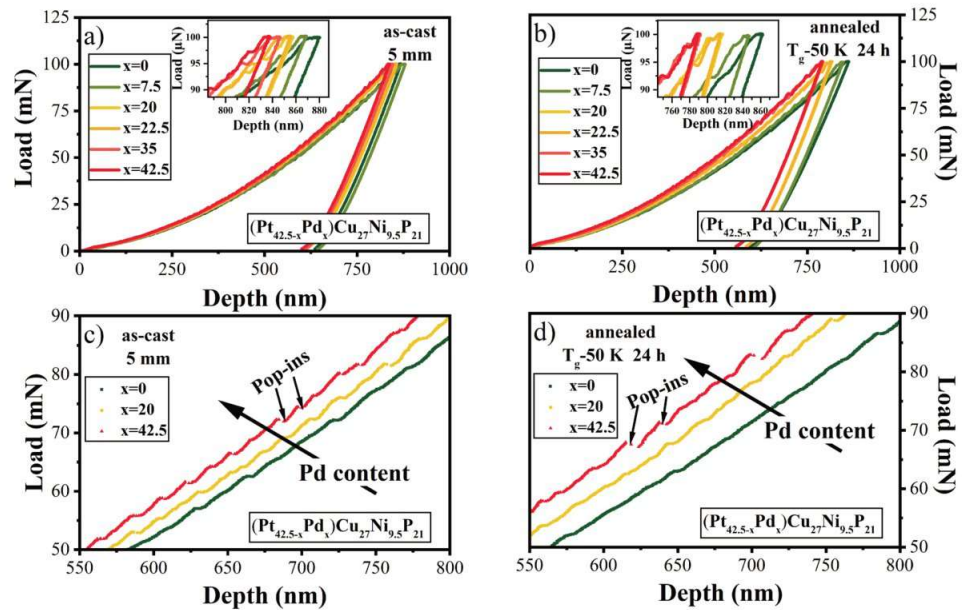
Figure 1. Nano-indentation load-depth plots for $Pt_{42.5-x}Pd_xCu_{27}Ni_{9.5}P_{21}$ bulk metallic glasses as a function of Pd content (i.e., x = 0,7.5, 20, 22.5, 35, 42.5); (**a**) in the as-cast state of a 5 mm rod and (**b**) after isothermal annealing at T_g-50 K for 24 h; The insets in parts (**a**) and (**b**) show the zoomed in view of the loading curves; (**c**) and (**d**) show serrated behavior for $Pd_{42.5}Cu_{27}Ni_{9.5}P_{21}$ (x = 42.5) with large displacement bursts (pop-ins) and relatively smooth curve for $Pt_{42.5}Cu_{27}Ni_{9.5}P_{21}$ (x = 0) in the as-cast and annealed states.

topological equivalency of Pt and Pd[29,30] make them model alloys for obtaining a systematic series of interrelated alloys. This idea is further supported by their similar temperature dependence of equilibrium viscosity (fragility) in the deeply supercooled liquid state[31–34]. However, their GFA varies by a factor of four[35,36] and they have significantly different entropies of fusion, ΔS_f[31,34,37,38]. The larger ΔS_f and more rapidly ascending heat capacity upon cooling for the Pt-P-based liquids stand out from those of the Pd-P-based liquids, indicating different atomic ordering processes upon undercooling[37,38]. The high GFA of Pd-P-based liquids originates from an extremely low driving force for crystallization, whereas the Pt-P-based liquids are stabilized by a high interfacial energy between the liquid and the crystal[33,37], which points to unique structural differences between the two systems.

Here, the influence of compositionally and thermally induced change in the distribution of dominant polyhedra and the associated variation in connection schemes in Pt–Pd-based BMGs on their deformation behavior is evaluated. Nanoindentation and micro-pillar compression are used for the mechanical characterization[4,39–45]. With gradual replacement of Pt by Pd, significant changes are noted in hardness and modulus, strain rate sensitivity, shear transformation zone volume, and serrated flow behavior. The evolution in mechanical properties is discussed in terms of their internal structure differences. Embrittlement effects, resembling those induced by changes in composition, are observed by annealing below the glass transition temperature (T_g). Further, synchrotron studies reveal that changes in mechanical properties are mirrored by the structural signatures in terms of the varying connection schemes, providing valuable insights into structure–property correlations in metallic glasses.

Results

Serration behavior, hardness, and modulus. Figure 1a) and b) show the representative nano-indentation load-depth curves for $Pt_{42.5-x}Pd_xCu_{27}Ni_{9.5}P_{21}$ amorphous alloys as a function of Pd-content (x = 0–42.5) in the as-cast and annealed states. The reduction in indentation depth h with increase in Pd content for both, the as-cast and annealed states (insets of Fig. 1a, b), suggests a rise in hardness value with increase in Pd content. Also, the degree of serrations, which is associated with shear strain accommodation[17,46–48], increases with Pd content as shown in the zoomed in regions of the loading curves in Figs. 1c, d. The loading curve appears relatively smooth for the Pd-free alloy in contrast to large displacement bursts or "pop-ins" seen for the Pd-rich BMGs[48]. Comparably, a decrease of serrated flow was reported in a prior study with increase in Fe content for $Nd_{60}Al_{10}Ni_{10}Cu_{20-x}Fe_x$ BMGs[17].

For quantitative analysis, the average serration length and serration frequency were calculated from the load–displacement curves. Figure 2a, b show the distribution of displacement bursts in the loading curves for $Pt_{42.5-x}Pd_xCu_{27}Ni_{9.5}P_{21}$ amorphous alloys as a function of Pd content from 0 to 42.5 at. % in the (a) as-cast and (b) annealed state. The spread of the minimum and maximum serration length broadens with increase in Pd content.
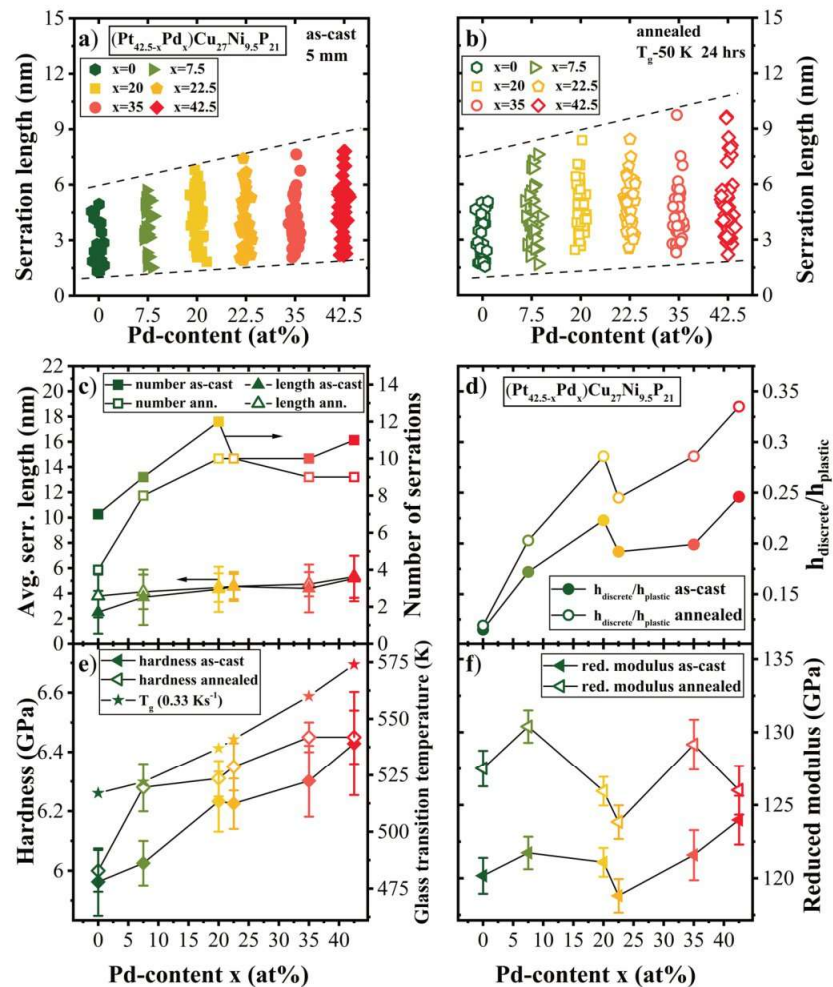
Figure 2. (**a**) and (**b**) Distribution of serration lengths for $Pt_{42.5-x}Pd_xCu_{27}Ni_{9.5}P_{21}$ bulk metallic glasses as a function of Pd content (i.e., x = 0, 7.5, 20, 22.5, 35, 42.5) in as-cast and annealed states; (**c**) average serration length and serration frequency, (**d**) plasticity ratio, (**e**) hardness and glass transition temperature, and (**f**) reduced modulus for $Pt_{42.5-x}Pd_xCu_{27}Ni_{9.5}P_{21}$ amorphous alloys as a function of Pd content from 0 to 42.5 at.% in the as-cast and annealed state (T_g-50 K for 24 h). An increase in magnitude and frequency of serration as well as hardness and modulus with increasing Pd content is seen. Annealing of the samples leads to similar increase in hardness and modulus.

Compared to the as-cast state, the annealed samples show a slightly broader distribution in serration length over the whole compositional range. Figure 2c shows the average serration length of both states summarized together with the number of serrations as a function of Pd content. For the as-cast state, the average serration length increases from 2.5 to 5 nm and the number of serrations increases from 5 to 15 over the load range studied with increase in Pd content from 0 to 42.5 at.%. Annealing of the samples did not lead to a significant change in average serration length or the number of serrations for all the compositions. The discrete plasticity ratio, $h_{discrete}/h_{plastic}$, is depicted in Fig. 2d), showing a similar trend as the number of serrations with change in composition. This parameter helps in determining the contribution of serrated flow on the total plastic deformation. It was estimated from the sum of each individual pop-in ($h_{discrete} = \Sigma h_{pop-in}$) divided by the residual indentation depth after releasing the load ($h_{plastic}$). The discrete plasticity ratio continuously increased with addition of Pd from 0.115 to 0.246 for the as-cast samples and from 0.119 to 0.335 for the annealed samples. In summary, annealing and Pd addition led to higher discrete plasticity ratio and decreased residual indentation depth.

The hardness (H) and reduced modulus (E) determined from load-depth curves are shown in Fig. 2e, f, respectively. The average hardness increased from ~ 5.9 GPa for $Pt_{42.5}Pd_0$ (x = 0) to ~ 6.5 GPa for $Pt_0Pd_{42.5}$, following

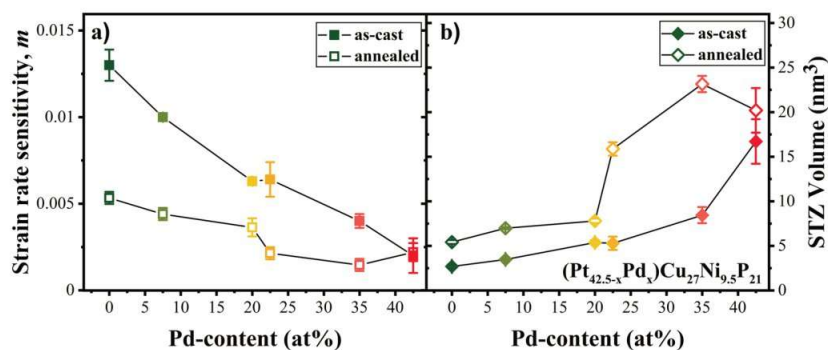**Figure 3.** (**a**) Strain rate sensitivity, *m*, as a function of Pd content for the as-cast and annealed state obtained from linear fitting of hardness versus logarithm of strain rate (shown in Supplementary Information Fig. S1); (**b**) STZ volume versus Pd concentration for as-cast and annealed state, showing the lowest STZ volume for $Pt_{42.5}Pd_0$ alloy supporting its more homogeneous plastic flow.

the same trend as the glass transition, which is also plotted on the right axis of Fig. 2e). Annealing led to a slight increase in hardness, which may be attributed to the reduction in free volume and denser packing. Increase in modulus with higher Pd content and with annealing was observed indicating higher stiffness for alloys with higher Pd content as well as after thermal annealing that leads to relaxation. With decreasing free volume or increasing ordering, the average inter-atomic distance decreases, resulting in increased material stiffness or elastic modulus[48].

Strain Rate Sensitivity and Shear Transformation Zone Volume. For all the examined $Pt_{42.5-x}Pd_xCu_{27}Ni_{9.5}P_{21}$ amorphous alloys, hardening was observed with increasing applied strain rate, described by a positive strain-rate sensitivity (SRS). The hardness values as a function of strain rate at a depth of 1000 nm for the $Pt_{42.5-x}Pd_xCu_{27}Ni_{9.5}P_{21}$ amorphous alloys are shown in Supplementary Information Fig. S1 on a double logarithmic scale. The strain rate sensitivity, *m*, was calculated from the slope of linear fitting [41] (see SI Fig. S1) and is reported in Fig. 3a) as a function of Pd content. Similar positive SRS in the range of 0.006–0.036 has been reported for various bulk metallic glasses[21,49–51] and may be attributed to the delay in shear band activation with increasing strain rate. A higher value of SRS indicates greater resistance to localized plastic deformation and is therefore associated with more ductile deformation behavior[52]. The $Pt_{42.5}Pd_0$ alloy showed almost an order of magnitude larger *m* value in comparison to the $Pt_0Pd_{42.5}$ alloy[53]. This is in line with the smooth load-depth curves for the Pt-rich glasses in contrast to more serrated behavior seen for the Pd-rich glasses (Figs. 1 and 2).

Structural relaxation due to thermal annealing led to a decrease in SRS for the entire compositional spread. However, hardness for the Pd-rich glasses was fairly insensitive to shear rate, while a significant drop in SRS of ~ 50% between the annealed and as-cast state was observed for the Pt-rich glasses. Comparing the effect of Pd addition and using SRS as a measure of ductility, the 24 h annealing at T_g-50 K for the $Pt_{42.5}Pd_0$ glass had a similar effect as substitution of ~ 50% of Pt by Pd.

During plastic deformation of a metallic glass, clusters of atoms undergo cooperative shear displacement in response to external applied stress, accommodating the plastic strain over a region known as shear transformation zone (STZ). A shear band is nucleated from the local accumulation of STZs and STZ volume provides estimation of the number of atoms involved in shear transformation in a metallic glass[54]. STZ volume for all the $Pt_{42.5-x}Pd_xCu_{27}Ni_{9.5}P_{21}$ BMGs was calculated based on Johnson–Samwer cooperative shearing model (CSM)[21] and shown in Fig. 3b) for the as-cast and annealed state. The STZ volume of the as-cast BMGs varies from ~ 2.5 to ~ 18 nm³, increasing with Pd concentration. The smaller STZ volume for $Pt_{42.5}Pd_0$ enables the activation of greater number of flow units, leading to the nucleation of more shear bands and promoting more ductile behavior in contrast to $Pt_0Pd_{42.5}$ with its large STZ volume[6,55]. Similarly, larger STZ volume is seen for the annealed alloys in the range of 6 nm³ to 23 nm³. Addition of Pd and thermal annealing showed similar effect in terms of increasing STZ volume, with the effect of annealing being more significant on the Pd-rich side of the composition spread.

Stress–strain and deformation behavior. Engineering stress–strain response obtained from micro-pillar compression for $Pt_{42.5-x}Pd_xCu_{27}Ni_{9.5}P_{21}$ (x = 0, 20, and 42.5) alloys are shown in Fig. 4a–c. Stresses and strains were calculated with consideration of taper correction. At least three micro-pillars were tested for each alloy as shown. The experiments were stopped at a strain of ~ 10% to examine the post-deformation morphologies of the micropillars. For all three alloys, the stress initially increases linearly with strain followed by numerous serrations or stress drops. The stress drops were elastic-like with the slope of the straight portion in between the drops approximately equal to the slope of the initial elastic deformation. Elastic unloading before the elastic reloading process was due to the readjustment of the indenter position to ensure steady displacement rate. The average value of yield strength was determined from the stress at the first serration to be ~ 0.95 GPa, ~ 1.05 GPa, and ~ 1.25 GPa
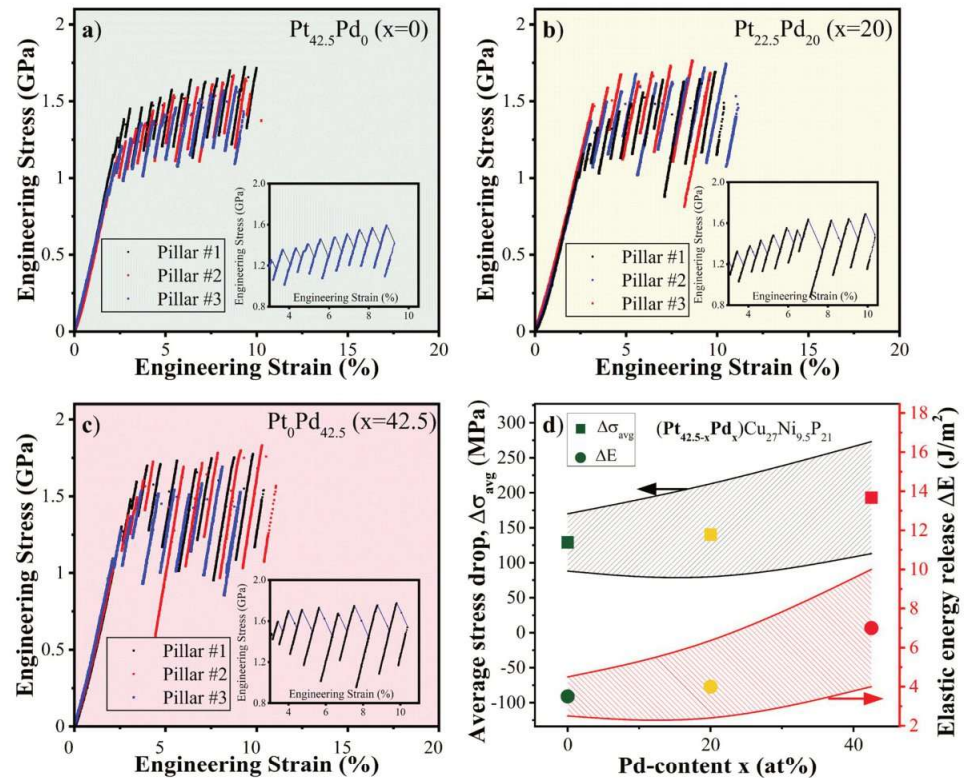
Figure 4. Engineering stress–strain curves for: (**a**) $Pt_{42.5}Pd_0$, (**b**) $Pt_{22.5}Pd_{20}$, and (**c**) $Pt_0Pd_{42.5}$ alloys in the as-cast state. Three pillars were tested for each alloy as shown. The insets show zoomed-in view of the serrations for each alloy; (**d**) Average value of the magnitude of stress-drop and stored elastic energy as a function of Pd content showing larger stress drop with higher elastic energy released for alloys with higher Pd content.

for $Pt_{42.5}Pd_0$, $Pt_{22.5}Pd_{20}$, and $Pt_0Pd_{42.5}$ alloys, respectively. The stress drops in stress–strain curves for all alloys were attributed to the nucleation and propagation of shear bands[56]. The amplitude of stress drops increased while its frequency decreased with increase in Pd content. In the insets of Fig. 4a–c, representative engineering stress–strain curves are shown to highlight the flow serrations while excluding the initial elastic loading segment (~ 2%). The size of stress drops ($\Delta\sigma$) was measured from the stress–strain curves and the average value for each alloy is shown in Fig. 4d. The average magnitude of stress drop measured for $Pt_{42.5}Pd_0$ (~ 130 MPa) was ~ 7% and 35% lower in comparison to stress drops in $Pt_{22.5}Pd_{20}$ (~ 140 MPa) and $Pt_0Pd_{42.5}$ (~ 200 MPa), respectively. The magnitude of stress drop is an indirect measure of the tendency of the alloy towards stable or unstable shear band propagation. A smaller stress drop indicates relatively more stable deformation process[57], in agreement with the observed homogeneous deformation behavior of $Pt_{42.5}Pd_0$ in nano-indentation experiments. In previous studies, brittle-natured Mg- and Au-based BMG micropillars exhibited smaller numbers of strain bursts during micro-compression in contrast to numerous strain bursts for ductile Zr-based BMG micropillars[58]. Individual serration events correspond to the accumulation and release of elastic energy in order to bypass the energy barrier for shear band formation[59]. The stored/released elastic energy within a single stress drop is calculated as[60]:

$$\Delta E = \frac{1}{2}\Delta\sigma\varepsilon_e\pi\left(\frac{d}{2}\right)^2 h \tag{3}$$

where d and h are the diameter and height of the pillar ($h = 2d$) and ε_e is the elastic strain. The area of the shear plane A may be calculated as $A = \pi[d/(2\sin\theta)]^2$, where θ is the angle between shear plane and the loading axis. The elastic energy release for each shear plane is measured according to $\Delta E/A = \varepsilon_e\Delta\sigma\sin^2\theta$ and shown in Fig. 4d for the studied bulk metallic glasses. The stored elastic energy increased with increase in Pd content. More energy released during the stress drops may increase the local temperature leading to quicker shear band sliding and more localized deformation[9]. Further, the larger standard deviation in stored elastic energy, depicted by the larger separation between the solid lines in Fig. 4d, indicates more heterogeneous distribution of stored elastic energy in the Pd-rich alloys. In-situ SEM images of the micro-pillars at the strains of 0%, 5%, and 10% are shown in Fig. 5 a1–a3, b1–b3, c1–5c3 for $Pt_{42.5}Pd_0$, $Pt_{22.5}Pd_{20}$, and $Pt_0Pd_{42.5}$ BMGs, respectively. Figure 5a4, b4, c4 show the
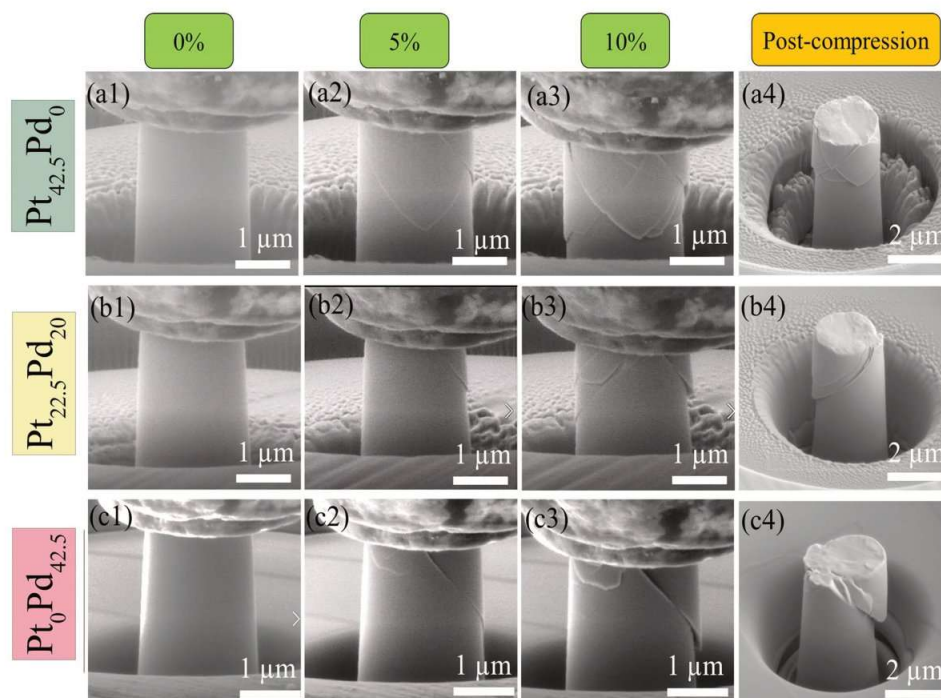
Figure 5. In-situ SEM image at strain of 0%, 5%, and 10% for micro-pillars of (**a1–a3**) $Pt_{42.5}Pd_0$, (**b1–b3**) $Pt_{22.5}Pd_{20}$, and (**c1–c3**) $Pt_0Pd_{42.5}$ amorphous alloys; post compression SEM images for (**a4**) $Pt_{42.5}Pd_0$, (**b4**) $Pt_{22.5}Pd_{20}$, and (**c4**) $Pt_0Pd_{42.5}$ alloys indicating multiple shear band formation for $Pt_{42.5}Pd_0$ in contrast to one major shear band for $Pt_0Pd_{42.5}$ alloy.

post-compression images for $Pt_{42.5}Pd_0$, $Pt_{22.5}Pd_{20}$, and $Pt_0Pd_{42.5}$ alloys, respectively. Multiple intersecting shear bands are seen for $Pt_{42.5}Pd_0$ micro-pillars during compression test (Fig. 5a1–a4) and pronounced interaction of the shear bands indicates more homogeneous plastic deformation for $Pt_{42.5}Pd_0$. The density of shear bands decreased for $Pt_{22.5}Pd_{20}$ (Fig. 5b1–b4) and the micro-pillars for $Pt_0Pd_{42.5}$ alloy failed primarily by a single major shear band (Fig. 5c1–c4), indicating highly localized deformation. Activation of multiple shear bands promotes plasticity accommodation in case of $Pt_{42.5}Pd_0$, resulting in overall higher ductility as compared to the Pd-rich alloys. Higher fractions of more closely spaced shear bands lead to greater plasticity in amorphous alloys as plastic flow may begin easily on preexisting shear bands leading to larger distribution of shear rather than catastrophic failure[54]. Also, the presence of more shear bands helps in dissipating the energy of primary shear bands during plastic deformation[61]. The number of serrations seen in the stress–strain curves in Fig. 5 is significantly higher compared to the number of observed shear bands in the SEM images of the micro-pillars, which may be attributed to the formation and propagation of new shear bands as well as the interaction, pinning, and reactivation of the preexisting ones[62].

High energy X-ray diffraction. Synchrotron diffraction experiments were performed for the annealed (T_g-50 K for 24 h) and as-cast samples (5 mm rods) and the reduced pair-distribution function (PDF) for six chosen alloys are shown in Fig. 6a. The differences in structure with changing Pt/Pd content become evident similar to previous report[26]. The main difference is in the 2nd peak of G(r), which describes the 2nd coordination shell and provides information about the interconnectivity of clusters, namely how many atoms are shared by adjacent clusters[63]. Detailed justification on the structural differences as a function of Pd content that can be derived from diffraction data is discussed in prior work[26]. An enlarged view of this region is shown in Fig. 6b. The distances referring to the different cluster connection schemes are highlighted by vertical lines in the plot, marking the distances, where adjacent clusters share one (2 r_1), two ($\sqrt{2}\,r_1$), three ($\sqrt{8/3}\,r_1$) or four atoms ($\sqrt{3}\,r_1$) [63]. The width of the lines is used to account for the slight shift of r_1 with composition. With increasing Pd-content, a peak at ~4.5 Å evolves, which is related to the 3-atom connection (meaning that adjacent clusters share 3 atoms), while the shoulder at 5.3 Å decreases.

Due to the small changes, a differential plot is used to compare the as-cast with the annealed state as shown in Fig. 6c. In the differential plot of Fig. 6c, the PDFs of the annealed samples (dashed lines) are more pronounced at the length scale corresponding to 3-atom connections. Further, annealing leads to a decrease in intensity of
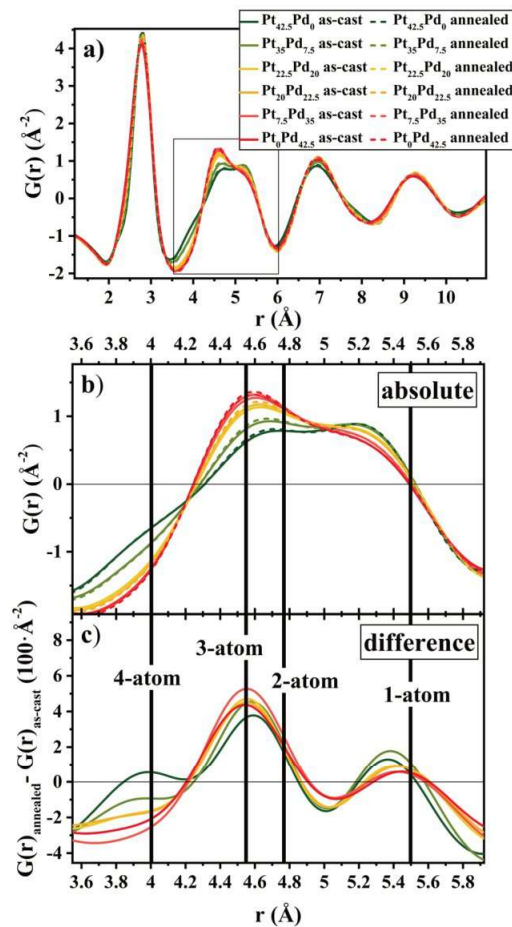
Figure 6. (a) The reduced pair distribution function G(r) for $Pt_{42.5-x}Pd_xCu_{27}Ni_{9.5}P_{21}$ BMGs, where x = 0, 7.5, 20, 22.5, 35, and 42.5 at 298 K in the as-cast state (full lines) and after annealing for 24 h at T_g-50 K (dashed lines). (b) Magnified view of the box in a), featuring the second peak of G(r) for all alloys in annealed and as-cast state. The second peak of G(r) corresponds to the second nearest neighbor distances, therefore bearing information of the cluster connection schemes. (c) Difference in the reduced pair distribution function between annealed and as-cast state. A large change on the length scale of 4.55 Å is seen, corresponding to a distance of $\sqrt{8/3}\, r_1$. The vertical lines in (b) and (c) represent the most likely second nearest neighbor distances if adjacent clusters share one ($2\, r_1$), two ($\sqrt{2}\, r_1$), three ($\sqrt{8/3}\, r_1$) or four atoms ($\sqrt{3}\, r_1$).

G(r) corresponding to the length scale of 4-atom connections, while the intensities on the spatial length of 2- and 1-atom connections remain rather unchanged.

Discussion

Changes in composition by the gradual replacement of Pt with Pd atoms as well as thermal history showed a significant effect on the deformation behavior of $Pt_{42.5-x}Pd_xCu_{27}Ni_{9.5}P_{21}$ bulk metallic glasses. For the Pt-rich alloys, relatively more ductile behavior was observed, characterized by smoother load-depth curves in nanoindentation (Fig. 1), high value of SRS (Fig. 3), and multiple intersecting shear bands formed in micro-pillar compression tests (Fig. 5). In contrast, the Pd-rich alloys showed more brittle characteristics. Amorphous alloys in which plastic flow is driven by the activation of a small number of large shear bands show large values of $h_{discrete}/h_{plastic}$[20]. This suggests that Pd addition influences the nucleation and propagation of shear bands. Further, higher numbers of large displacement bursts (or pop-ins) for the alloys with higher Pd content correspond to greater shear displacement within the shear band and more localized deformation behavior[54,61]. Annealing led to pronounced increase in the discrete plasticity ratio (Fig. 2d) as well as the magnitude of displacement bursts for each alloy (Fig. 2b).

Relatively more ductile behavior of the Pt-rich alloys results from easier nucleation of smaller STZs, leading to more homogeneous plastic flow. Alloys with higher Pd content were characterized by lower strain rate sensitivity and higher STZ volume, indicating a propensity for brittle deformation.

A greater tendency towards cooling rate dependent embrittlement was previously described within the framework of critical fictive temperature for $Pd_{43}Cu_{27}Ni_{10}P_{20}$ BMG in comparison to $Pt_{57.5}Cu_{14.7}Ni_{5.3}P_{22.5}$ BMG[64]. However, a systematic study on the role of Pt and Pd is lacking. The current work provides quantitative assessment of the change in deformation behavior with the substitution of Pt by Pd for a set of alloys with the same stoichiometry.

Previous high energy synchrotron diffraction experiments suggested the presence of different dominant atomic clusters, trigonal prisms and icosahedrons, together with changing connection schemes and ratios within these clusters as a function of Pt and Pd content[26]. Simulations of Ding et al. showed that the different connection schemes respond differently to external strains, which can ultimately have a large effect on the mechanical behavior of the glass, when they rearrange with changes in composition or thermal history. Based on these simulations, 3-atom connections (face sharing), whose signature in G(r) increases with Pd content, are the only connecting scheme that leads to a smaller local elastic strain compared to the macroscopic deformation. In contrast, 1-atom connections (vertex sharing) show local elastic deformations similar to the macroscopic deformation, while 2-atom (edge sharing) and 4-atom connections (squashed tetrahedra sharing) show higher local elastic strain compared to the macroscopic strain. Ultimately this means that the face sharing 3-atom connections tend to form a relatively stiffer structure and can therefore, be associated with more brittle deformation behavior[63]. This supports the current experimental observations of brittle deformation behavior with increasing Pd-content, characterized by small strain rate sensitivity, more serrated flow, and more localized deformation[26].

For a more quantitative analysis the structural features, namely the significance of 3-atom connection schemes of a specific composition in the series of interrelated alloys is correlated with its mechanical behavior in terms of SRS, with a high SRS indicative of more ductile behavior. Hence, the change in SRS with Pd content is directly compared with the value of PDF for 3-atom connections $G(r = \sqrt{8/3}\, r_1)$, used to quantify the significance of 3-atom connections. The distribution of the connecting schemes may be described by a Gaussian function[65]. As a result, changes in intensity of $G(r = \sqrt{8/3}\, r_1)$ may also be caused by broadening of the neighboring 2-atom and 4-atom connections. For this parameter to be significant, we assume no significant changes in the width of Gaussian distribution of each connecting scheme. Figure 7a shows a consistent decrease of SRS (m) with rising $G(r = \sqrt{8/3}\, r_1)$. The increasing number of 3-atom connections with increasing Pd content may be attributed to a change in the dominant structural motifs occurring in the Pt-rich (trigonal prisms) and Pd-rich (icosahedra) subsystems. Even though, Pt and Pd are considered topologically equivalent in structural models, the differences in their electronic configurations (Pt: ($[Xe]4f^{14}5d^{9}6s$) and Pd: ($[Kr]4d^{10}$)) as well as minor changes in their enthalpy of mixing with Ni (Pd–Ni 0 kJ, Pt-Ni-5 kJ (at equiatomic composition) might cause these changes in cluster distribution. Ultimately, this difference in chemistry of the topologically similar Pt and Pd atoms might lead to the different topology of the clusters and consequently their interconnection[66]. To further support our interpretation of increasing 3-atom connection with increasing Pd content and therefore increasing number of icosahedra, while decreasing the number of trigonal prisms one has to consider the geometry of these structural units. A perfect icosahedron has 20 triangular faces, which can be shared by adjacent clusters. Although, this may not be the exclusive connection scheme present in Pd-rich systems, the large number of triangular faces may lead to dominance of 3-atom connections. It has been suggested by Gaskell that trigonal prisms often connect via two atoms and 4 atoms, whereas 3-atom connections get less probable[67]. Ultimately, the replacement of Pd atoms by Pt atoms will lead to a change in the ratio between icosahedra and trigonal prisms and therefore alter the distribution of the connection schemes. These changes in the distribution of cluster connections are visible in the second peak of the reduced pair distribution function (Fig. 6). In summary, with increasing Pt content, the fraction of 3-atom connection decreases and the other connection schemes gain importance, which is a consequence of the reduction of the icosahedral SRO. A more detailed justification and discussion of the structural changes with Pt/Pd content is provided in our earlier work[26] as well as its respective Peer Review File[66]. Figure 7b is showing the correlation between SRS and the frequency of finding an atom at the distance of the 3-atom connections $G(r = \sqrt{8/3}\, r_1)$ (R^2 equal to 0.99), clearly supports our working hypothesis of an increasing icosahedral SRO with increasing Pd-content resulting in a macroscopically and microscopically more brittle mechanical behavior.

To quantify the structural changes from annealing, the difference in reduced PDF on the length scale of 3-atom connections, $G(\sqrt{8/3}\, r_1)$, is determined as function of Pd-content (Fig. 8). To account for the scaling of the different atomic form factors with composition, the changes are calculated with respect to their as-cast reference value $G(\sqrt{8/3}\, r_1)_{ac}$ leading to a relative change, $G(\sqrt{8/3}\, r_1)_{relative} = [\, G(\sqrt{8/3}\, r_1)_{rel} - G(\sqrt{8/3}\, r_1)_{ac}]/G(\sqrt{8/3}\, r_1)_{ac}$.

The change in SRS (Δm) after the annealing (left axis) is shown relative to the change in reduced PDF (right axis) in Fig. 8a, both showing a similar trend with variation in Pd-content. For the initially ductile Pt-rich glasses, annealing leads to the highest relative increase in the intensity of G(r) at the length scale of 3-atom connections accompanied by the largest change in SRS. This indicates that the largest drop in ductility is mirrored by the largest relative change in the probability of atoms being located at the length scale, geometrically predicted, for 3-atom connections. Vice versa, the Pd-rich alloys show almost no change in their SRS, which is consistent with minor changes in $G(\sqrt{8/3}\, r_1)$. The scatter plot of Δm versus $\Delta G(\sqrt{8/3}\, r_1)_{relative}$ in Fig. 8b shows the quantitative correlation between the changes in intensity at the length scale of $G(\sqrt{8/3}\, r_1)$, interpreted as the signature of 3-atom connections, and SRS, being used to describe the ductility of the material. Interestingly, the simulations of Ding et al. showed that structural ordering during cooling leads to an increase in the stiffer 3-atom connections[63]. To a certain degree isothermal annealing resembles the effects of slow cooling, as the system also undergoes structural relaxation and ordering to an enthalpically lower state leading to a lower fictive temperature. Therefore, further resemblance between experimental data and the reported simulations is given.
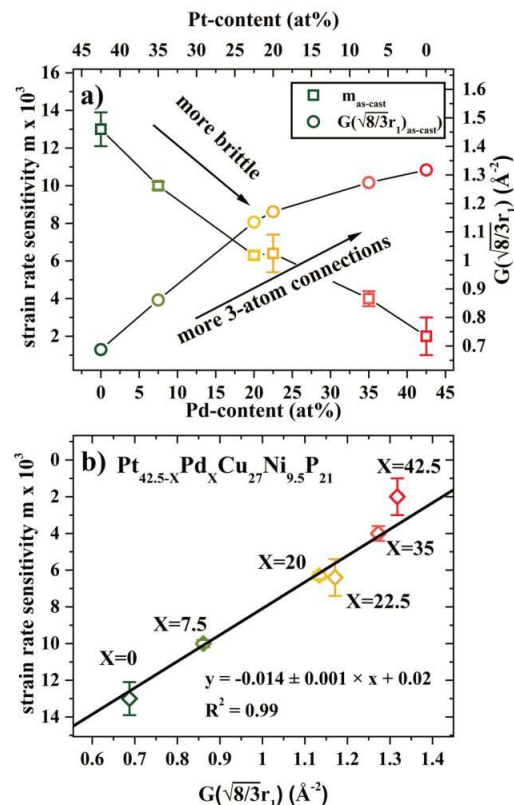
Figure 7. (**a**) Strain rate sensitivity m for as-cast state as a function of Pd-content (left axis, open squares) and absolute value of reduced pair distribution function at the length scale of 3-atom connections $G(\sqrt{8/3}\ r_1)$ in the as-cast state as a function of Pd-content (right axis, open circles). A decrease in SRS with increase in Pd content, associated with more brittle behavior, is observed. More rigid 3-atom connections in the reduced pair distribution function are observed with increase in Pd content, which is also characteristic of relatively brittle behavior. (**b**) Scatter plot of $m_{as-cast}$ and $G(\sqrt{8/3}\ r_1)_{as-cast}$ showing the correlation of decreasing strain-rate sensitivity with increasing fraction of 3-atom cluster connections.

The experimental results indicate that the absolute structural changes facilitated by compositional variation, when platinum is systematically replaced by topologically equivalent palladium atoms, are much more significant than those due to annealing. In contrast, the absolute changes in ductility/SRS with composition or due to annealing are comparable in magnitude. This indicates, that while the distinctiveness of 3-atom connections might play a significant role in the mechanical properties of metallic glasses, they do not directly allow a prediction of ductility. Ultimately, the deformation process of multicomponent metallic glasses with respect to chemical and thermal changes are of course too complex to be solved by a single parameter. Still, this does not come as a surprise as there are with a probability bordering on certainty further (structural) mechanisms and effects in combination with the limitations of structural data of multi-component systems obtained in a total scattering diffraction experiment. In total scattering, the atomic pairs with the highest atomic form factor/strongest scattering ability, dominate the reduced pair distribution function, which is a superposition of all atomic pairs involved. For the investigated systems, this means that only noble-noble metal interactions are probed with minor contributions of noble metal-Cu and Cu-Cu partials, whereas any pair associated with P remains unaccounted. Still, for the Pt/Pd–Pt/Pd partials, the increase in 3-atom connections with Pd-content and with relaxation shows good quantitative agreement, which is in line with simulations. This work may stimulate further investigations on the relation between local structure and mechanical performance of metallic glasses.

Conclusions

In summary, the plastic deformation mechanism of interrelated $Pt_{42.5-x}Pd_xCu_{27}Ni_{9.5}P_{21}$ bulk metallic glasses was studied, where platinum was systematically replaced by topologically equivalent palladium atoms. Increase in Pd content resulted in increasing hardness and yield strength and a drop in strain rate sensitivity. The Pt-rich
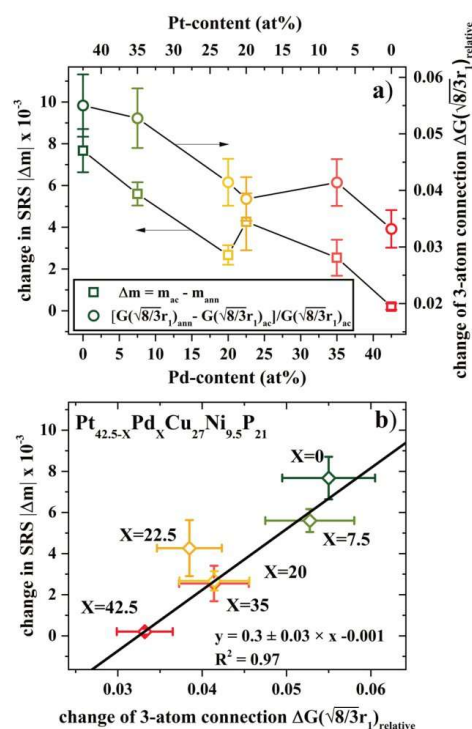
Figure 8. (**a**) Change in strain rate sensitivity (Δm) after annealing for 24 h at T_g-50 K in reference to the as-cast state as a function of Pd-content (left axis, open squares) and relative change of reduced pair distribution function at the length scale of 3-atom connections $\Delta G(\sqrt{8/3}\, r_1)_{relative}$ after annealing for 24 h at T_g-50 K in reference to the as-cast state as a function of Pd-content (right axis, open circles). (**b**) Scatter plot of Δm and $\Delta G(\sqrt{8/3}\, r_1)_{relative}$ showing the correlation of change in strain-rate sensitivity with increasing fraction of 3-atom cluster connections.

bulk metallic glasses showed higher strain rate sensitivity, lower discrete plasticity ratio in nano-indentation experiments, smaller stress-drops, and multiple shear band formation in micro-pillar compression, indicating more homogeneous flow compared to the Pd-rich alloys. Similar to the addition of Pd, embrittling effects were observed after sub-T_g annealing (T_g-50 K for 24 h) of the samples, both effects might be connected to a similarly increasing trend in the reduced pair distribution function on the length scale of rigid 3-atom cluster connections. This present systematic study helps to further shed light on the interrelation of structure and mechanical properties in metallic glasses through alloying and heat treatment.

Materials and methods

Sample preparation. $Pt_{42.5-x}Pd_xCu_{27}Ni_{9.5}P_{21}$ (x = 0 and 42.5) master alloys were synthesized by arc melting the mixture of pure elements (Pt, Pd, Cu, and Ni with purity of > 99.95%) under a Ti-gettered high purity argon atmosphere. Each ingot was flipped and re-melted for at least four times to ensure homogeneity in composition. Subsequently, the pre-alloys were placed on top of P in a fused quartz tube and heated inductively followed by a fluxing process in dehydrated B_2O_3 for at least 20 h at 1200 °C in a fused silica tube to remove impurities. Afterwards, the master-alloys are mixed in the ratio of the final composition; $Pt_{42.5-x}Pd_xCu_{27}Ni_{9.5}P_{21}$, where x is x = 0, 2.5, 7.5, 12.5, 17.5, 20, 22.5, 30, 35, 40, 42.5 at %. This solid mixture is then re-melted in an arc-melter under a Ti-gettered high-purity argon atmosphere to ensure a homogeneous sample.

Amorphous samples were prepared by inductive re-melting of the ingots and tilt- casting in a water-cooled copper mold with 5 mm diameter under argon atmosphere (Ar 6.0). Few select compositions with Pd content x = 0, 7.5, 20, 22.5, 35, 42.5 at % samples were annealed in a Perkin Elmer DSC 8000 at T_g-50 K for a duration of 24 h under a high purity Ar (Ar 6.0) atmosphere. All samples, annealed and as-cast, were polished to mirror surface finish for nano-mechanical characterization. Chemical compositions of the alloys were confirmed using

scanning electron microscopy (SEM, FEI, Hillsboro, OR, USA) equipped with energy dispersive spectroscopy (EDS).

Nano-indentation. Nano-indentation was done using a TI-Premier Triboindenter (Bruker, Minneapolis, MN, USA) with a diamond Berkovich tip at room temperature, a peak load of 100 mN, and a loading and unloading rate of 20 mN/s. The hardness and modulus were determined using Oliver and Pharr method[68]. Strain rate sensitivity (SRS) was calculated by nano-indentation in displacement-control mode with applied strain rates of 4.0×10^{-2} s^{-1}, 1.2×10^{-1} s^{-1}, 4.0×10^{-1} s^{-1}. An average of sixteen indents were performed to obtain the average and standard deviation. Distance between adjacent indents was more than 100 μm to avoid overlap of their plastic zones. All tests were performed in the center of the samples in order to avoid the influence of cooling rate on local structural state. Thermal drift rate was measured and maintained below 0.05 nm/s for all tests.

Micro-pillar compression. For micro-pillar compression tests, pillars ~ 5 μm in height and ~ 2.5 μm in diameter were milled in select alloys, namely $Pt_{42.5-x}Pd_xCu_{27}Ni_{9.5}P_{21}$ (x = 0, 20, and 42.5), using FEI Nova NanoLab 200 FIB-SEM using Ga ion beam, with current ranging from 5 nA to 10 pA. The top and bottom diameter of the micro-pillars were measured, and the taper angle was determined to be ~ 2°, which was considered for further analysis. PI88 SEM Picoindenter (Bruker, Minneapolis, MN, USA) with a 5 μm diameter flat diamond punch was used for the micro-pillar compression tests. Tests were performed in displacement-control mode at a strain rate of 6×10^{-3} s^{-1}. The recorded load versus displacement was converted to engineering stress–strain curves using the micro-pillar dimensions. A minimum of three micro-pillars were milled for each alloy to determine the standard deviation.

High-energy synchrotron X-ray diffraction. High-energy synchrotron radiation experiments were performed at beamline P21.2 at PETRAIII at Deutsches Elektronensynchrotron (DESY) synchrotron facility. Measurements were carried out in transmission geometry at a radiation energy of 70 keV (λ = 0.1771 Å) with a beam size of 0.5 × 0.5 mm. Disc-shaped samples were cut from 5 mm rods and were irradiated in the middle of the sample. A VAREX XRD4343CT detector with a pixel size of 150 × 150 μm and a resolution of 2880 × 2880 pixels was used for the recording of the patterns with a summed exposure time of 5 s. For the measurements, a set of five pictures was averaged, leading to a summed total exposure time of 25 s. The two-dimensional X-ray diffraction patterns were integrated using pyFAI integrate. For further processing, like background subtraction, corrections for sample absorption, polarization and multiple scattering PDFgetX2 software was used[69].

The total structure factor S(Q) was calculated as[70]

$$S(Q) = 1 + \frac{I_C(Q) - \overline{f(Q)^2}}{\overline{f(Q)}^2}, \tag{1}$$

where $I_C(Q)$ is the coherently scattered intensity, f(Q) the atomic form factor, and Q is the scattering vector. The angle brackets denote a compositional average over all constituents.

To obtain the reduced pair distribution function, G(r), a Fourier transformation of the total structure factor leads to:

$$G(r) = \frac{2}{\pi} \int_0^\infty Q[S(Q) - 1] \sin(Qr) dQ, \tag{2}$$

where r is the distance to the reference atom. Each G(r) pattern was optimized using an optimization algorithm in PDFgetX2 as described by Wei et al.[71] with a maximum Q-range (Q_{max}) for the Fourier transformation of S(Q) of 15 Å^{-1}. This value is sufficient to obtain the needed degree of details in G(r) for metallic glasses, as shown in prior studies[26,72].

Data availability
The datasets generated during and/or analyzed during the current study are available from the corresponding authors on reasonable request.

References
 1. Greer, A. L. & Editors, G. Bulk metallic glasses: At the cutting edge of metals research. *MRS Bull.* **32**, 611–619 (2007).
 2. Kruzic, J. J. Bulk metallic glasses as structural materials: A review. *Adv. Eng. Mater.* **18**, 1308–1331 (2016).
 3. Schroers, J., Pham, Q. & Desai, A. 04147602.Pdf. **16**, 240–247 (2007).
 4. Sadeghilaridjani, M. *et al.* Small-scale mechanical behavior of ion-irradiated bulk metallic glass. *Jom* **72**, 123–129 (2020).
 5. Schroers, J. & Johnson, W. L. Ductile bulk metallic glass. *Phys. Rev. Lett.* **93**, 255506 (2004).
 6. Kim, S. Y., Oh, H. S. & Park, E. S. A hidden variable in shear transformation zone volume versus Poisson's ratio relation in metallic glasses. *APL Mater.* **5**, 106105 (2017).
 7. Telford, M. The case for bulk metallic glass. *Mater. Today* **7**, 36–43 (2004).
 8. Huang, L., Hu, X., Guo, T. & Li, S. Investigation of mechanical properties and plastic deformation behavior of (TiuriIMetallic glasses by nanoindentation. *Adv. Mater. Sci. Eng.* **2014**, 2–7 (2014).
 9. Wang, Y. T. *et al.* Optimum shear stability at intermittent-to-smooth transition of plastic flow in metallic glasses at cryogenic temperatures. *Materialia* **9**, 100559 (2020).

10. Hofmann, D. C. *et al.* Development of tough, low-density titanium-based bulk metallic glass matrix composites with tensile ductility. *Proc. Natl. Acad. Sci. USA* **105**, 20136–20140 (2008).

11. Li, H., Li, L., Fan, C., Choo, H. & Liaw, P. K. Nanocrystalline coating enhanced ductility in a Zr-based bulk metallic glass. *J. Mater. Res.* **22**, 508–513 (2007).

12. Van Steenberge, N. *et al.* Microstructural inhomogeneities introduced in a Zr-based bulk metallic glass upon low-temperature annealing. *Mater. Sci. Eng. A* **491**, 124–130 (2008).

13. Raghavan, R. *et al.* Ion irradiation enhances the mechanical performance of metallic glasses. *Scr. Mater.* **62**, 462–465 (2010).

14. Greaves, G. N., Greer, A. L., Lakes, R. S. & Rouxel, T. Poisson's ratio and modern materials. *Nat. Mater.* **10**, 823–837 (2011).

15. Lee, M. H. *et al.* Improved plasticity of bulk metallic glasses upon cold rolling. *Scr. Mater.* **62**, 678–681 (2010).

16. Liu, B. C., Zhang, Q. D., Wang, H. J., Li, X. Y. & Zu, F. Q. Significantly improved plasticity of bulk metallic glasses by introducing quasicrystal within high energy glass matrix. *Intermetallics* **111**, 106504 (2019).

17. Wei, B. C. *et al.* Serrated plastic flow during nanoindentation in Nd-based bulk metallic glasses. *Intermetallics* **12**, 1239–1243 (2004).

18. Burgess, T., Laws, K. J. & Ferry, M. Effect of loading rate on the serrated flow of a bulk metallic glass during nanoindentation. *Acta Mater.* **56**, 4829–4835 (2008).

19. Schuh, C. A., Nieh, T. G. & Kawamura, Y. Rate dependence of serrated flow during nanoindentation of a bulk metallic glass. *J. Mater. Res.* **17**, 1651–1654 (2002).

20. Limbach, R., Kosiba, K., Pauly, S., Kühn, U. & Wondraczek, L. Serrated flow of CuZr-based bulk metallic glasses probed by nanoindentation: Role of the activation barrier, size and distribution of shear transformation zones. *J. Non. Cryst. Solids* **459**, 130–141 (2017).

21. Pan, D., Inoue, A., Sakurai, T. & Chen, M. W. Experimental characterization of shear transformation zones for plastic flow of bulk metallic glasses. *Proc. Natl. Acad. Sci. USA* **105**, 14769–14772 (2008).

22. Qian, X. *et al.* Dependence of shear yield strain and shear transformation zone on the glass transition temperature in thin film metallic glasses. *J. Alloys Compd.* **652**, 191–199 (2015).

23. Zhao, X. N. *et al.* Dependence of room-temperature nanoindentation creep behavior and shear transformation zone on the glass transition temperature in bulk metallic glasses. *J. Non. Cryst. Solids* **445–446**, 19–29 (2016).

24. Ma, Y., Peng, G. J., Debela, T. T. & Zhang, T. H. Nanoindentation study on the characteristic of shear transformation zone volume in metallic glassy films. *Scr. Mater.* **108**, 52–55 (2015).

25. Na, J. H. *et al.* Compositional landscape for glass formation in metal alloys. *Proc. Natl. Acad. Sci.* **111**, 9031–9036 (2014).

26. Gross, O. *et al.* Signatures of structural differences in Pt–P- and Pd–P-based bulk glass-forming liquids. *Commun. Phys.* **2**, 83 (2019).

27. Takeuchi, A. *et al.* Pd20Pt20Cu20Ni20P20 high-entropy alloy as a bulk metallic glass in the centimeter. *Intermetallics* **19**, 1546–1554 (2011).

28. Kumar, G., Prades-Rodel, S., Blatter, A. & Schroers, J. Unusual brittle behavior of Pd-based bulk metallic glass. *Scr. Mater.* **65**, 585–587 (2011).

29. Miracle, D. B. A structural model for metallic glasses. *Microsc. Microanal.* **10**, 786–787 (2004).

30. Laws, K. J., Miracle, D. B. & Ferry, M. A predictive structural model for bulk metallic glasses. *Nat. Commun.* **6**, 1–10 (2015).

31. Gross, O. *et al.* The kinetic fragility of Pt-P- and Ni-P-based bulk glass-forming liquids and its thermodynamic and structural signature. *Acta Mater.* **132**, 118–127 (2017).

32. Kato, H. *et al.* Fragility and thermal stability of Pt- and Pd-based bulk glass forming liquids and their correlation with deformability. *Scr. Mater.* **54**, 2023–2027 (2006).

33. Gross, O. Precious metal based bulk metallic glass-forming liquids: Development, thermodynamics, kinetics and structure. *Diss. Saarl. Univ.* https://doi.org/10.22028/D291-27993 (2018).

34. Gallino, I., Schroers, J. & Busch, R. Kinetic and thermodynamic studies of the fragility of bulk metallic glass forming liquids. *J. Appl. Phys.* **108**, 063501 (2010).

35. Schroers, J. & Johnson, W. L. Highly processable bulk metallic glass-forming alloys in the Pt–Co–Ni–Cu–P system. *Appl. Phys. Lett.* **84**, 3666 (2004).

36. Nishiyama, N. *et al.* The world's biggest glassy alloy ever made. *Intermetallics* **30**, 19–24 (2012).

37. Gross, O. *et al.* On the high glass-forming ability of Pt-Cu-Ni/Co-P-based liquids. *Acta Mater.* **141**, 109–119 (2017).

38. Neuber, N. *et al.* On the thermodynamics and its connection to structure in the Pt-Pd-Cu-Ni-P bulk metallic glass forming system. *Acta Mater.* **220**, 117300 (2021).

39. Mridha, S., Sadeghilaridjani, M. & Mukherjee, S. Activation volume and energy for dislocation nucleation in multi-principal element alloys. *Metals* **9**, 27–33 (2019).

40. Sadeghilaridjani, M. & Mukherjee, S. Strain gradient plasticity in multiprincipal element alloys. *Jom* **71**, 3466–3472 (2019).

41. Sadeghilaridjani, M., Muskeri, S., Hassannaeimi, V., Pole, M. & Mukherjee, S. Strain rate sensitivity of a novel refractory high entropy alloy: Intrinsic versus extrinsic effects. *Mater. Sci. Eng. A* **766**, 138326 (2019).

42. Sadeghilaridjani, M., Muskeri, S., Pole, M. & Mukherjee, S. High-temperature nano-indentation creep of reduced activity high entropy alloys based on 4–5–6 elemental palette. *Entropy* **22**, 230 (2020).

43. Sadeghilaridjani, M. & Mukherjee, S. High-temperature nano-indentation creep behavior of multi-principal element alloys under static and dynamic loads. *Metals* **10**, 250 (2020).

44. Tönnies, D., Maaß, R. & Volkert, C. A. Room temperature homogeneous ductility of micrometer-sized metallic glass. *Adv. Mater.* **26**, 5715–5721 (2014).

45. Shimanek, J., Rizzardi, Q., Sparks, G., Derlet, P. M. & Maa, R. Scale-dependent pop-ins in nanoindentation and scale-free plastic fluctuations in microcompression. *J. Mater. Res.* **35**, 196–205 (2020).

46. Schuh, C. A. & Nieh, T. G. A nanoindentation study of serrated flow in bulk metallic glasses. *Acta Mater.* **51**, 87–99 (2003).

47. Bhowmick, R., Raghavan, R., Chattopadhyay, K. & Ramamurty, U. Plastic flow softening in a bulk metallic glass. *Acta Mater.* **54**, 4221–4228 (2006).

48. Cheng, L., Jiao, Z. M., Ma, S. G., Qiao, J. W. & Wang, Z. H. Serrated flow behaviors of a Zr-based bulk metallic glass by nanoindentation. *J. Appl. Phys.* **115**, 084907 (2014).

49. Li, M. Effect of annealing on strain rate sensitivity of metallic glass under nanoindentation. *Metals* **10**, 1–10 (2020).

50. Boltynjuk, E. V. *et al.* Enhanced strain rate sensitivity of Zr-based bulk metallic glasses subjected to high pressure torsion. *J. Alloys Compd.* **747**, 595–602 (2018).

51. Li, M. C., Jiang, M. Q., Jiang, F., He, L. & Sun, J. Testing effects on hardness of a Zr-based metallic glass under nanoindentation. *Scr. Mater.* **138**, 120–123 (2017).

52. Bhattacharyya, A., Singh, G., Eswar Prasad, K., Narasimhan, R. & Ramamurty, U. On the strain rate sensitivity of plastic flow in metallic glasses. *Mater. Sci. Eng. A* **625**, 245–251 (2015).

53. Spaepen, F. A microscopic mechanism for steady state inhomogeneous flow in metallic glasses. *Acta Metall.* **25**, 407–415 (1977).

54. Greer, A. L., Cheng, Y. Q. & Ma, E. Shear bands in metallic glasses. *Mater. Sci. Eng. R Rep.* **74**, 71–132 (2013).

55. Liu, S. T., Wang, Z., Peng, H. L., Yu, H. B. & Wang, W. H. The activation energy and volume of flow units of metallic glasses. *Scr. Mater.* **67**, 9–12 (2012).

56. Shi, Y. & Falk, M. L. Stress-induced structural transformation and shear banding during simulated nanoindentation of a metallic glass. *Acta Mater.* **55**, 4317–4324 (2007).
57. Ye, J. C., Lu, J., Yang, Y. & Liaw, P. K. Study of the intrinsic ductile to brittle transition mechanism of metallic glasses. *Acta Mater.* **57**, 6037–6046 (2009).
58. Lai, Y. H., Chen, H. M., Lee, C. J., Huang, J. C. & Jang, J. S. C. Strain burst speeds in metallic glass micropillars. *Intermetallics* **18**, 1893–1897 (2010).
59. Gan, K., Zhu, S., Jiang, S. & Huang, Y. Study on stochastic nature of plasticity of Cu/Zr metallic glass micropillars. *J. Alloys Compd.* **831**, 154719 (2020).
60. Dubach, A., Raghavan, R., Löffler, J. F., Michler, J. & Ramamurty, U. Micropillar compression studies on a bulk metallic glass in different structural states. *Scr. Mater.* **60**, 567–570 (2009).
61. Liu, S. *et al.* Deformation-enhanced hierarchical multiscale structure heterogeneity in a Pd-Si bulk metallic glass. *Acta Mater.* **200**, 42–55 (2020).
62. Best, J. P. *et al.* Relating fracture toughness to micro-pillar compression response for a laser powder bed additive manufactured bulk metallic glass. *Mater. Sci. Eng. A* **770**, 138535 (2020).
63. Ding, J., Ma, E., Asta, M. & Ritchie, R. O. Second-nearest-neighbor correlations from connection of atomic packing motifs in metallic glasses and liquids. *Sci. Rep.* **5**, 1–9 (2015).
64. Kumar, G., Neibecker, P., Liu, Y. H. & Schroers, J. Critical fictive temperature for plasticity in metallic glasses. *Nat. Commun.* **4**, 1536 (2013).
65. Pan, S. P., Qin, J. Y., Wang, W. M. & Gu, T. K. Origin of splitting of the second peak in the pair-distribution function for metallic glasses. *Phys. Rev. B Condens. Matter. Mater. Phys.* **84**, 092201 (2011).
66. Gross, O. *et al.* Peer review file to signatures of structural differences in Pt–P- and Pd–P-based bulk glass-forming liquids. *Commun. Phys.* https://doi.org/10.1038/s42005-019-0180-2 (2019).
67. Gaskell, P. H. A new structural model for transition metal–metalloid glasses. *Nature* **276**, 484–485 (1978).
68. Oliver, W. C. & Pharr, G. M. Measurement of hardness and elastic modulus by instrumented indentation: Advances in understanding and refinements to methodology. *J. Mater. Res.* **19**, 3–20 (2004).
69. Qiu, X., Thompson, J. W. & Billinge, S. J. L. PDFgetX2: A GUI-driven program to obtain the pair distribution function from X-ray powder diffraction data. *J. Appl. Crystallogr.* **37**, 678 (2004).
70. Egami, T. & Billinge, S. J. L. *Underneath the Bragg Peaks Structural Analysis of Complex Materials*. (2012).
71. Wei, S. *et al.* Structural evolution on medium-range-order during the fragile-strong transition in Ge15Te85. *Acta Mater.* **129**, 259–267 (2017).
72. Ma, D., Stoica, A. D. & Wang, X. L. Power-law scaling and fractal nature of medium-range order in metallic glasses. *Nat. Mater.* **8**, 30–34 (2009).

Author contributions

N.N., R.B., O.G., M.S. and Su.M. conceived the study. N.N. prepared the samples. N.N., B.A, L.R. and M.F. planned and conducted the synchrotron X-ray experiments with the help of M.B. N.N. analyzed the synchrotron data. N.G., Sa.M. and M.S. conducted and analyzed the nanoindentation and micropillar mechanical experiments. N.N. prepared the figures with help of N.G. . N.N. and M.S. analyzed the data and wrote the paper with input from R.B., Su.M., I.G. and O.G. All authors proofread the article and contributed extensively to the discussion.

Competing interests

The authors declare no competing interests.

Additional information

Supplementary Information The online version contains supplementary material available at https://doi.org/10.1038/s41598-022-20938-6.

Correspondence and requests for materials should be addressed to N.N. or S.M.

Reprints and permissions information is available at www.nature.com/reprints.

Publisher's note Springer Nature remains neutral with regard to jurisdictional claims in published maps and institutional affiliations.
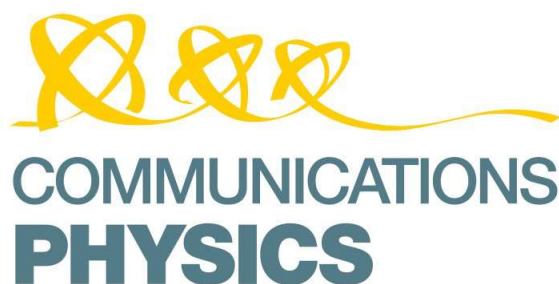
5.4 Publication IV

Signatures of structural differences in Pt–P- and Pd–P-based bulk glass-forming liquids

Oliver Gross[1], Nico Neuber [1], Alexander Kuball[1], Benedikt Bochtler [1], Simon Hechler[1], Maximilian Frey[1] & Ralf Busch[1]

The structural differences between the compositionally related Pt–P- and Pd–P-based bulk glass-forming liquids are investigated in synchrotron X-ray scattering experiments. Although Pt and Pd are considered to be topologically equivalent in structural models, we show that drastic changes in the total structure factor and in the reduced pair distribution function are observed upon gradual substitution. These variations indicate the existence of significant structural differences on the short- (SRO) and medium-range order (MRO) length scale. The structural data suggest that the distribution of the dominant polyhedra and the distribution of their connection schemes gradually change from Pt–P- to Pd–P-based alloys, which is likely connected to the different sensitivities to annealing or cooling rate induced embrittlement. The evolution of the total structure factor and the reduced pair distribution function with increasing temperature indicate the (partial) dissolution of both, the MRO and the SRO, which reflects the thermodynamic properties of the liquids.

[1] Chair of Metallic Materials, Saarland University, Campus C6.3, 66123 Saarbrücken, Germany. Correspondence and requests for materials should be addressed to O.G. (email: oliver.gross@uni-saarland.de)

Pt–P- and Pd–P-based bulk metallic glass (BMG) forming liquids feature a high glass-forming ability (GFA), which is reflected by their critical casting thicknesses (d_c) usually exceeding 1.5 cm[1–3]. The compositional similarities (e.g., $Pt_{42.5}Cu_{27}Ni_{9.5}P_{21}$ and $Pd_{43}Cu_{27}Ni_{10}P_{20}$), the interchangeability of Pt and Pd without losing the bulk GFA[4,5], the topological equivalence of Pt and Pd[6,7], and the similar kinetic fragility[8–11] suggest a close connection between Pt–P- and Pd–P-based liquids. However, the d_c of the alloy with the highest GFA in both systems varies by a factor of four from $d_c = 20$ mm for $Pt_{42.5}Cu_{27}Ni_{9.5}P_{21}$ to $d_c = 80$ mm for the $Pd_{42.5}Cu_{30}Ni_{7.5}P_{20}$ alloy[1,2]. This difference is attributed to the fact that the GFA of Pt–P-based BMG forming liquids originates from a high interfacial energy, compensating a high driving force for crystallization and a kinetically fragile behavior[12,13]. In contrast, the Pd–P-based liquids are rather stabilized by an extremely low-driving force for crystallization[12], which can be approximated by the entropy of fusion ΔS_f. ΔS_f represents the negative slope of the Gibbs free energy difference between the liquid and the crystal at the liquidus temperature. Although not independent from the crystalline state, the large variation in ΔS_f of about a factor of two ($\Delta S_f(Pt_{42.5}Cu_{27}Ni_{9.5}P_{21}) = 12$ Jg-atom^{-1} K^{-1}, $\Delta S_f(Pd_{43}Cu_{27}Ni_{10}P_{20}) = 5.8$ Jg-atom^{-1} K^{-1} [8,11,12]) between Pt–P- and Pd–P-based alloys can probably not solely be traced back to different entropic states of the crystalline mixtures. It rather suggests that the two liquids possess different structural states in the equilibrium liquid. This hypothesis is supported by the observation of a rapidly ascending specific heat capacity in the liquid state (c_p^l) upon undercooling the Pt–P-based liquids whereas that of the Pd–P-based alloy compositions ascends more slowly[12] (see also Supplementary Fig. 1). The excess heat capacity $\Delta c_p^{l-x}(T)$, representing the difference between the specific heat capacity of the liquid and the crystalline state, is connected to the rate of loss in the excess entropy $\Delta S_{l-x}(T)$. As $\Delta S_{l-x}(T)$ is proportional to the configurational part of the entropy of the liquid[14], the rate of change in $\Delta S_{l-x}(T)$ indicates a more pronounced ordering process in Pt–P-based liquids upon undercooling. The connection between the ascending specific heat capacity and structural ordering has been shown in computer simulations[15]. These observations draw the picture of rather disordered Pt–P-based liquids at high temperatures, undergoing a rapid ordering upon approaching the glass transition. On the other hand, a large degree of local order is likely already present at high temperatures in the equilibrium liquid of the Pd–P-based compositions, reflected by the small entropy of fusion. Moreover, the existence of structural differences is suggested by the varying sensitivity to cooling rate induced and annealing induced embrittlement[5,16]. Kumar et al.[5,16] reported that the bending ductility of Pd–P-based glasses strongly depends on the cooling rate and the annealing protocol whereas the Pt–P-based glasses always showed plasticity. The partial replacement of Pd by Pt reduced the sensitivity of the alloys to cooling rate induced embrittlement[5]. These observations are attributed to different critical fictive temperatures ($T_f^{critical}$)[16]. The fictive temperature T_f is defined as the glass transition upon cooling and therefore depends on the applied cooling rate[17]. T_f of a glass can also be changed by annealing or rejuvenation[18,19]. However, $T_f^{critical}$ is an inherent property of the alloy composition and should be connected to the structure of the glass. If a glass possesses a T_f below the $T_f^{critical}$, it will fracture without plastic deformation[16].

In order to find implications of structural differences in the two systems that might explain the different thermodynamic and mechanical properties as well as the variation in the GFA, synchrotron X-ray scattering experiments in the glass, the supercooled liquid and the equilibrium liquid are conducted on $Pt_{42.5}Cu_{27}Ni_{9.5}P_{21}$ and $Pd_{43}Cu_{27}Ni_{10}P_{20}$. Moreover, Pt is stepwise replaced by Pd and the total structure factor as well as the reduced pair distribution function (PDF) are determined at ambient temperature, revealing the compositionally induced structural changes. The experiments on theses multicomponent bulk glass-forming liquids can be considered as a top-down approach, complementing the computational modeling of less complex metallic liquids.

Results

The total structure factor at constant temperature. Figure 1 shows the total structure factor $S(Q)$ of the $Pt_{42.5}Cu_{27}Ni_{9.5}P_{21}$ and the $Pd_{43}Cu_{27}Ni_{10}P_{20}$ alloy composition at 323 K. The $S(Q)$ of the $Pt_{42.5}Cu_{27}Ni_{9.5}P_{21}$ glass exhibits a pronounced prepeak at ~2.1 Å^{-1}, preceding the first sharp diffraction peak (FSDP), whereas the shoulder of the second diffraction peak towards higher Q-values is more pronounced for the $Pd_{43}Cu_{27}Ni_{10}P_{20}$ alloy composition. In order to investigate the compositional effect on these two features, Pt in the $Pt_{42.5}Cu_{27}Ni_{9.5}P_{21}$ alloy is gradually replaced by Pd, following the compositions displayed in Fig. 2. As shown in Fig. 2a, b, the intensity of the prepeak fades with decreasing Pt content and the shoulder at the second peak gains intensity. It should be noted that the samples used for the diffraction experiments at 298 K were cut from plates with the same dimension. Hence, they experienced similar cooling rates and the observed variations in $S(Q)$ do not originate from differences in the thermal history.

The total structure factor as a function of temperature. The temperature-induced evolution of the total structure factor is shown for the $Pt_{42.5}Cu_{27}Ni_{9.5}P_{21}$ and the $Pd_{43}Cu_{27}Ni_{10}P_{20}$ composition in Fig. 3. Figure 3a, c display the low and Fig. 3b, d the high Q-region. The data at low temperatures were obtained upon heating a glassy sample (blue) and those at high temperature upon cooling the liquid from 1153 K (red). The temperature interval in-between the high and low temperature data is obscured by crystallization. The arrows indicate the evolution of the peak maxima and minima with decreasing temperature. For both alloy compositions it is observed that the peak intensities increase, and widths decrease which is on the one hand attributed to an increasing structural order and on the other hand to the decreasing atomic vibrations (Debye–Waller factor). The opposing movement of the first and second diffraction peak results in a virtually temperature invariant minimum in-between the two
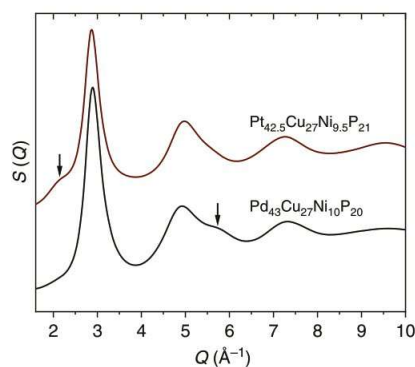
Fig. 1 Total structure factor $S(Q)$ of as-cast $Pt_{42.5}Cu_{27}Ni_{9.5}P_{21}$ and $Pd_{43}Cu_{27}Ni_{10}P_{20}$ at 323 K. At low Q-values (~2.1 Å^{-1}) only $Pt_{42.5}Cu_{27}Ni_{9.5}P_{21}$ exhibits a prepeak. The shoulder at the second peak (~5.7 Å^{-1}) is distinctly more pronounced for the $Pd_{43}Cu_{27}Ni_{10}P_{20}$ alloy composition

ARTICLE

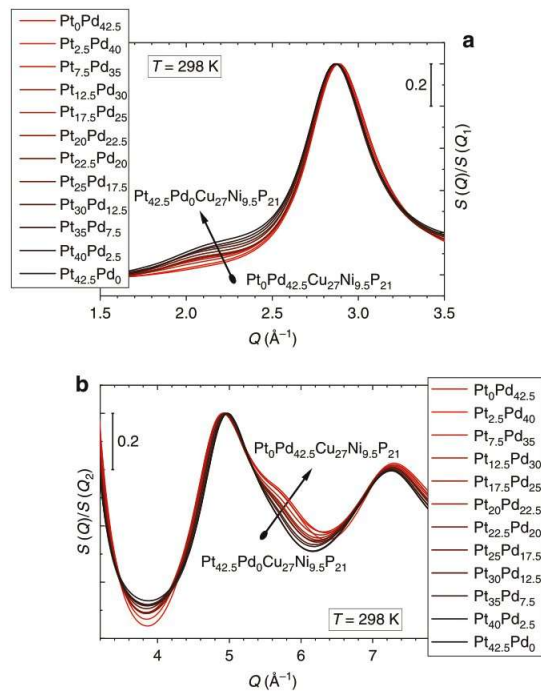**Fig. 2** Total structure factor $S(Q)$ of as-cast $Pt_{42.5-x}Pd_xCu_{27}Ni_{9.5}P_{21}$ samples, where $x = 0, 2.5, 7.5, 12.5, 17.5, 20, 22.5, 25, 30, 35, 40$, and 42.5. **a**, **b** The dependence of the prepeak at ~2.1 Å^{-1} and the shoulder at ~5.7 Å^{-1} on the Pt-to-Pd ratio. With increasing Pd concentration, the prepeak in the low Q-range diminishes whereas the characteristic at 5.7 Å^{-1} gets more pronounced. In **a**, **b**, $S(Q)$ is normalized to the peak height of the first and second sharp diffraction peak $S(Q_1)$ and $S(Q_2)$, respectively. The diffraction experiments were conducted at 298 K. All samples experienced similar cooling rates as they were cut from plates of the same dimension

peaks. The insets in Fig. 3a, c magnify the low Q-region of $S(Q)$. In the case of the $Pt_{42.5}Cu_{27}Ni_{9.5}P_{21}$ liquid, the intensity of the prepeak decreases upon heating and vanishes in the equilibrium liquid (see also Supplementary Fig. 2). For the $Pd_{43}Cu_{27}Ni_{10}P_{20}$ liquid, a comparable feature is not detected in the low Q-region. Instead, the shoulder at the second peak gets more pronounced as the temperature decreases.

The reduced PDF. In order to further investigate the structural differences in the two alloy families, the reduced PDF is calculated according to Eq. 4. Figure 4 shows the temperature-induced evolution of $G(r)$ of $Pt_{42.5}Cu_{27}Ni_{9.5}P_{21}$ and $Pd_{43}Cu_{27}Ni_{10}P_{20}$ in the same temperature interval as indicated in Fig. 3. The arrows indicate the shifts of the peak maxima and minima with decreasing temperature. As commonly observed in metallic liquids, the first peak position, which is assumed to reflect the average, weighted nearest neighbor distance, shifts towards higher values with decreasing temperature. This intuitively physically unlikely behavior has been attributed to an increasing coordination number (CN) upon cooling[20,21]. However, Ding et al.[22] argued that the anomalous peak shift might originate from the asymmetry of the peak shape. If the skewness is considered, the mean bond length is found to increase with increasing temperature[23].
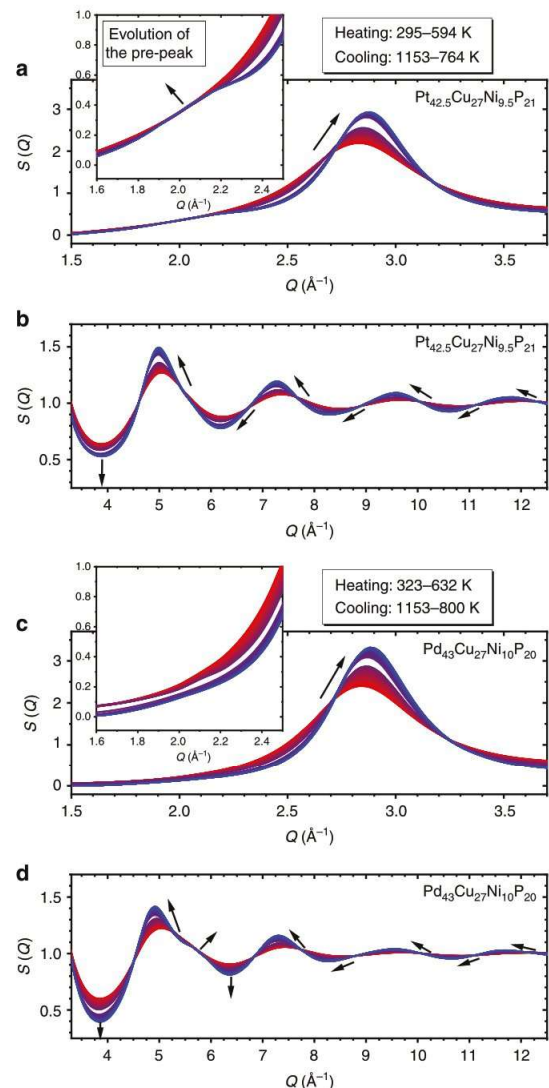
Fig. 3 Temperature-induced change of the total structure factor $S(Q)$. **a**, **b**, **c**, **d** The total structure factor of $Pt_{42.5}Cu_{27}Ni_{9.5}P_{21}$ and $Pd_{43}Cu_{27}Ni_{10}P_{20}$ as a function of temperature. The high temperature data (red) were collected upon cooling from 1153 K and those at low temperatures (blue) upon heating from the glassy state. **a**, **c** show the low Q-range and the insets magnify the region where the prepeak in $Pt_{42.5}Cu_{27}Ni_{9.5}P_{21}$ evolves with decreasing temperature. **b**, **d** show the oscillation of $S(Q)$ at high Q-values. The second peak of $S(Q)$ of both alloys is magnified in Supplementary Fig. 3. The arrows illustrate the evolution of the peak maxima and minima with decreasing temperature

The first peak position of $Pt_{42.5}Cu_{27}Ni_{9.5}P_{21}$ and $Pd_{43}Cu_{27}Ni_{10}P_{20}$ at 298 K is located at 2.79 and 2.77 Å. As $G(r)$ of the two alloy compositions is dominated by the Pt–Pt and the Pd–Pd partial PDFs (see Supplementary Figs. 4 and 5 and Supplementary Note 1), the first peak position represents in a first approximation the distance between two Pt and two Pd atoms, possessing an atomic radius of 1.39 and 1.40 Å[7]. The most
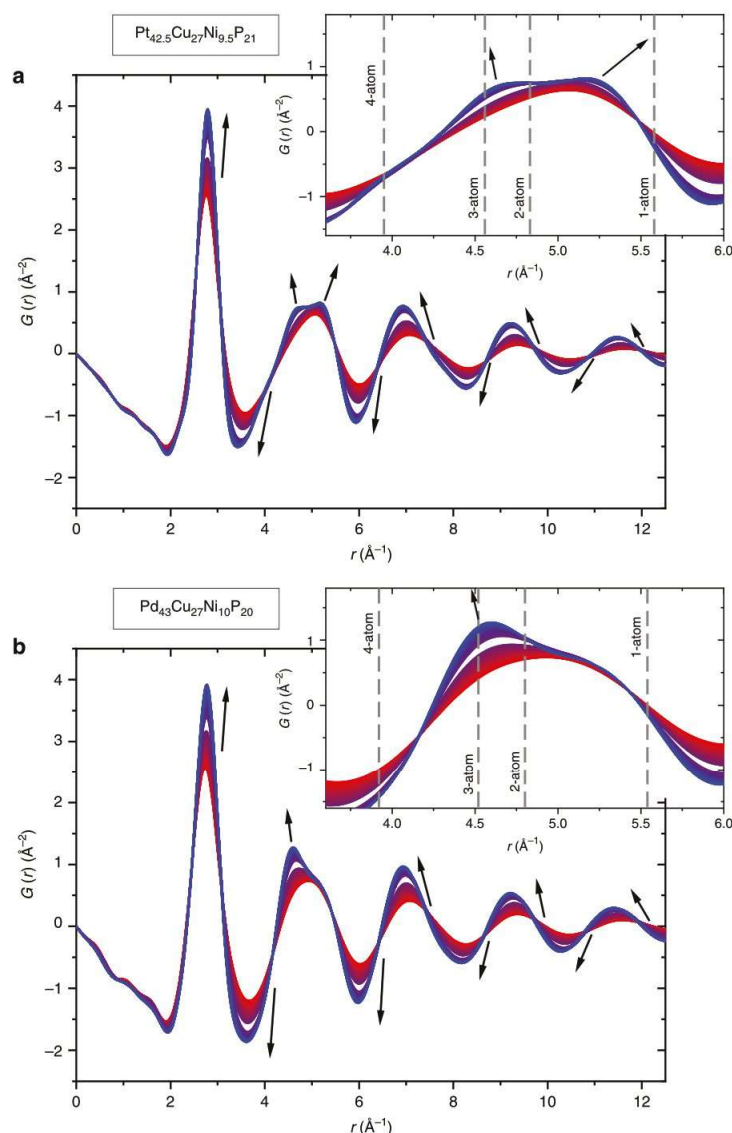
Fig. 4 Reduced pair distribution function $G(r)$ of **a** $Pt_{42.5}Cu_{27}Ni_{9.5}P_{21}$ and **b** $Pd_{43}Cu_{27}Ni_{10}P_{20}$ as a function of temperature. The high temperature data (red) were collected upon cooling from 1153 K and those at low temperatures (blue) upon heating from the glassy state. The arrows indicate the evolution of the peak maxima and minima with decreasing temperature. The insets magnify the second peak, corresponding to the second nearest neighbor distances. The vertical lines in the inset mark the most probable second nearest neighbor distances if adjacent clusters share one, two, three, or four atoms, calculated from the first peak position

distinct difference in $G(r)$ of the two alloys is observed at the second peak, reflecting the distances in the second nearest neighbor shell. In both cases, the second peak changes its shape and sharpens with decreasing temperature. The insets in Fig. 4, magnifying the temperature-induced evolution of the second peak, show that two peak maxima evolve for the $Pt_{42.5}Cu_{27}-Ni_{9.5}P_{21}$ liquid, whereas a single maximum with a pronounced shoulder on the high-r side forms for the $Pd_{43}Cu_{27}Ni_{10}P_{20}$ alloy composition. The compositional variation of $G(r)$ on the Pt–Pd axis at ambient temperature is shown in Fig. 5. Again, the changes

at the second peak of $G(r)$ upon substitution of Pd by Pt are obvious and are magnified in the inset of Fig. 5. The vertical lines in the insets of Figs. 4a, b and 5 are referred to in the discussion section.

Discussion

Although Pt and Pd atoms are considered to be topologically equivalent in structural models[6,7], the variations observed in $S(Q)$ and $G(r)$ suggest major structural differences. As the FSDP in

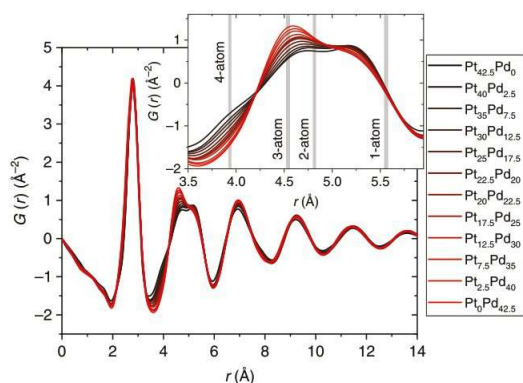   **ARTICLE**

Fig. 5 Compositional variation of the reduced pair distribution function $G(r)$ of Pt/Pd-P-based glasses at 298 K. The inset magnifies the second peak corresponding to the second nearest neighbor distances. The gray areas in the inset mark the most probable second nearest neighbor distances if adjacent clusters share one, two, three, or four atoms calculated from the first peak positions

$S(Q)$ already contains information on the medium-range order (MRO) of the liquid[24], the presence of a prepeak indicates a distinctly pronounced MRO[25] and is observed in various liquids[26–32]. Cheng et al.[25] concluded from experimental observations that the detection of a prepeak in $S(Q)$ is likely if the concentration of solutes is low (solute-lean composition) and if the solute specie possesses a high atomic form factor ("strong scatterer"). The type of MRO that results from these two statements is based on the avoidance of solute–solute bindings. Solute atoms, being the center of the representative cluster, form a sublattice-like structure that becomes visible as a prepeak in $S(Q)$ if the weighting factor of the solute–solute partial structure factor is sufficiently large[25]. Such a prepeak is detected in binary Zr–Pt liquids (solute-lean, e.g., $Zr_{80}Pt_{20}$)[27,33]. It originates from the spatial arrangement of the Pt-centered clusters and hence from the noble metal–noble metal correlations[27,33]. As reported by Mauro et al.[34], the prepeak at low Q-values vanishes if Pt is replaced by Pd. It was noticed that this observation is not equatable to the dissolution of the MRO as the lower atomic form factor of Pd in comparison to Pt might solely reduce the detectability of the prepeak (see Eqs. 2 and 3 in "Methods")[34].

Based on the discussion above, the type of MRO prevailing in $Pt_{42.5}Cu_{27}Ni_{9.5}P_{21}$ might be different as the composition can be considered as solute rich[35]. The existence of a prepeak for a solute-rich glass has previously been reported in the $Ce_{55}Al_{45}$ alloy composition[36]. Despite from the type of MRO prevailing in $Pt_{42.5}Cu_{27}Ni_{9.5}P_{21}$, the question arises if the disappearance of the prepeak in $Pd_{43}Cu_{27}Ni_{10}P_{20}$ only results from the variation of the atomic form factors of Pd and Pt. In the following section, possible origins of the prepeak are discussed, suggesting that the varying atomic form factor should not result in the disappearance of the prepeak.

The $S(Q)$ of the $Pt_{42.5}Cu_{27}Ni_{9.5}P_{21}$ is dominated by the Pt–Pt and Pt–Cu partial structure factors (Supplementary Fig. 4) and the prepeak most probably originates from one of the two partials. In a previous study, the authors observed that other Pt-P-based alloy compositions with a larger Pt and lower Cu content (i.e., $Pt_{60}Cu_{16}Co_2P_{22}$ and $Pt_{57.3}Cu_{14.6}Ni_{5.3}P_{22.8}$)[8] do not feature a prepeak at low Q-values. If the prepeak arises from the Pt–Cu partial, an increasing Pt and a decreasing Cu content would increase the significance of the Pt–Pt partial structure factor,

making the Pt–Cu correlations less dominant. Another possibility is that the MRO results from the Pt–Pt correlations as the Pt atoms in $Pt_{42.5}Cu_{27}Ni_{9.5}P_{21}$ are on average more often separated by a distance larger than the first coordination shell due to the larger amount of Cu, Ni, and P atoms. In the case of higher Pt-concentrations, the Pt atoms are less diluted, and they are more frequently nearest neighbors to each others, reducing the significance of the MRO. As the dominant partial structure factors in $Pd_{43}Cu_{27}Ni_{10}P_{20}$ and $Pd_{42.5}Cu_{27}Ni_{9.5}P_{21}$ are Pd–Pd and Pd–Cu, equivalent to Pt–Pt and Pt–Cu in $Pt_{42.5}Cu_{27}Ni_{9.5}P_{21}$ (Supplementary Figs. 4 and 5), the disappearance of the prepeak (Figs. 1 and 2) and the evolving shoulder at the second peak are most likely not traced back to the changing form factor as suggested for the Zr–Pd liquids. The varying signatures in $S(Q)$ rather suggest that the distribution of the local representative structural units (cluster types) and their spatial arrangements in Pt–P- and Pd–P-based liquids vary as discussed in more detail in the following.

The existence of a shoulder at the second peak of $S(Q)$ has been attributed to icosahedral short-range order (SRO). In the case of perfect icosahedral SRO, the ratio between the first two peak positions Q_2/Q_1 and the ratio between the first peak position and the location of the shoulder $Q_{shoulder}/Q_1$ is 1.71 and 2.04[37,38]. The location of the shoulder of the second peak of $S(Q)$ of $Pd_{43}Cu_{27}Ni_{10}P_{20}$ is determined by fitting, using a two Gaussian function. Q_2/Q_1 and $Q_1/Q_{shoulder}$ for the $Pd_{43}Cu_{27}Ni_{10}P_{20}$ composition are 1.71 and 1.96, which is in good agreement with the expected values, indicating a little distortion of the icosahedral SRO[37]. In the $Pd_{40}Ni_{40}P_{20}$ BMG forming liquid, tricapped trigonal prisms coexisting with Ni-centered icosahedra are found as representative structural units, supporting the idea of an at least partially icosahedral SRO in $Pd_{43}Cu_{27}Ni_{10}P_{20}$ and $Pd_{42.5}Cu_{27}Ni_{9.5}P_{21}$[39]. Moreover, Park et al.[40] determined a CN of 11.4 in $Pd_{40}Ni_{40}P_{20}$ and 12.6 in $Pd_{40}Cu_{30}Ni_{10}P_{20}$ around the Ni atoms, which are close to values of a perfect icosahedron ($CN = 12$). From a topological point of view, the ratios between the atomic radii of Pt (139 pm[7]), Pd (140 pm[7]), and Cu(/Ni) (126 pm[7]) suggest icosahedral SRO around the Cu(/Ni) atoms in both liquids[41]. The more pronounced shoulder at the second peak of S (Q) in the $Pd_{43}Cu_{27}Ni_{10}P_{20}$ and the $Pd_{42.5}Cu_{27}Ni_{9.5}P_{21}$ liquid might therefore indicate a larger fraction of icosahedral SRO. In the case of the $Pt_{42.5}Cu_{27}Ni_{9.5}P_{21}$ alloy composition, the existence of a comparable shoulder in $S(Q)$ can only be guessed (see Fig. 1). Following the simulations of Guan et al.[39] on the compositional induced structural changes in the Pd-Ni-P system, the substitution of Pd by Pt might change the ratio between the two structural units, the trigonal prism, and the icosahedron.

As Fig. 3 reveals, a change in temperature influences both the MRO as well as the SRO. At temperatures above the liquidus temperature $(T_l(Pt_{42.5}Cu_{27}Ni_{9.5}P_{21}) = 874$ K[8], $T_l(Pd_{43}Cu_{27}Ni_{10}P_{20}) = 866$ K[12]), the prepeak in $Pt_{42.5}Cu_{27}Ni_{9.5}P_{21}$ vanishes and the shoulder at the second peak in $S(Q)$ of $Pd_{43}Cu_{27}Ni_{10}P_{20}$ becomes less prominent (Fig. 3). The disappearance of the prepeak in $Pt_{42.5}Cu_{27}Ni_{9.5}P_{21}$ in the equilibrium liquid state, together with the large ΔS_f and the rapidly ascending c_p^l upon cooling (Supplementary Fig. 1), suggest a significant reduction or the entire dissolution of the MRO. In the case of the (at least partially) icosahedral SRO in $Pd_{43}Cu_{27}Ni_{10}P_{20}$ it is well known that this type of SRO prevails in many metallic glass-forming liquids (even above T_l) and gets more pronounced as the glass transition is approached upon cooling[42–45]. Once more it should be emphasized that the reduced significance of both characteristics upon heating is on the one hand traced back to the dissolution of atomic order and on the other hand affected by the increasing atomic vibrations, diminishing the peak intensity[46]. However, in the case of the prepeak it has been observed in other metallic liquids that it remains visible even hundreds of Kelvin above

ARTICLE

T_l[29,33], supporting the idea of the dissolution of atomic order in $Pt_{42.5}Cu_{27}Ni_{9.5}P_{21}$ in the equilibrium liquid.

The splitting of the second peak of the pair PDF (Figs. 4a, b and 5) reflecting the variety in the second nearest neighbor distances, has been observed in different metallic liquids[47–49]. In computer simulations it is suggested that the peak splitting originates from the uneven distribution of different types of cluster connections[49,50]. The local representative structural units may share one, two, three, and four atoms[49,50] and the most probable position of the second nearest neighbor for each cluster connection scheme according to these simulations can be calculated from the average bond length as $2\, r_1$ (1-atom connection), $\sqrt{3}\, r_1$ (2-atom connection), $\sqrt{8/3}\, r_1$ (3-atom connection), and $\sqrt{2}\, r_1$ (4-atom connection)[49,51]. As value for r_1, the first peak position of the reduced PDF is chosen, mainly representing the noble metal–noble metal correlations. The obtained positions for the second nearest neighbor are depicted as vertical dashed lines in the inset in Fig. 4a, b. For topological reasons the more atoms the clusters share the smaller is the second nearest neighbor distance. The effect of the Pt/Pd concentration on the shape of the second peak at ambient temperature is magnified in the inset in Fig. 5. The calculated second nearest neighbor positions indicate that the distribution of connection schemes gradually changes as Pt is replaced by Pd. In the Pd–P-based glass, the peak at ~4.5 Å seems to result from central atoms whose clusters are connected via face sharing (3-atom connection). As can be seen in Fig. 5, face sharing becomes less dominant upon substituting Pd by Pt. Instead the 1-atom and 2-atom connection schemes gain importance. The evolving shoulder at ~3.9 Å suggests that even the 4-atom connection scheme is facilitated by the replacement of Pd. Although these cluster connection schemes are thought to already exist in the high temperature liquid and the peak splitting is smeared out by the thermal vibrations, the structural ordering occurring during cooling also affects the distribution of the cluster connection schemes[49]. Therefore, the sharpening of the features of the second peak observed in Fig. 4 is again attributed to the decreasing atomic vibrations and to the growing portion of certain cluster connection schemes at the expense of others, increasing the packing density of the liquid[49,50]. In the case of $Pd_{43}Cu_{27}Ni_{10}P_{20}$, the 3-atom cluster connections seem to prevail, and its fraction increases upon cooling whereas the structural data of $Pt_{42.5}Cu_{27}Ni_{9.5}P_{21}$ suggest a larger diversity of cluster connection schemes. Against the background of an at least partially icosahedral SRO in $Pd_{43}Cu_{27}Ni_{10}P_{20}$ (suggested by the shoulder at the second peak of $S(Q)$), the existence of a variety of the 3-atom connections is reasonable as each (perfect) icosahedral cluster features 20 triangular faces, which adjacent clusters may share. In contrast, the representative structural units in $Pt_{42.5}Cu_{27}Ni_{9.5}P_{21}$ might comprise a large fraction of trigonal prisms that connect via edge sharing (2-atom connection) as suggest by Gaskell for metal–metalloid glasses[52]. A distinct diversity of cluster connection schemes in the $Pt_{42.5}Cu_{27}Ni_{9.5}P_{21}$ liquid including a larger portion of the more flexible 1-, 2-, and 4-atom connections would result in a higher configurational entropy of the liquid, contributing to, and agreeing with the experimentally measured, high ΔS_f of the Pt–P-based liquids.

Following the argumentation of Guan et al.[39], the coexistence of two structural units, the trigonal prism and the icosahedron, might be responsible for the good GFA in both systems. However, our structural investigations indicate that the ratio between both structural motifs changes upon substituting Pd by Pt. In the case of the Pd–P-based liquids, the icosahedral SRO is more dominant, leading to an increase of the 3-atom connections. In contrast, the prevalence of the trigonal prisms in the Pt–P-based liquids results in a broader distribution of the connection schemes.

Although the experimental findings discussed above are in striking accordance with the simulations performed by Ding et al.[49], it should be noted that the shape of the second peak in $G(r)$ of complex, multicomponent metallic liquids is also affected by the number of small atoms in the first coordination shell that may be involved in the cluster connection. As the partial reduced PDFs are not accessible in the conducted experiments, the contribution of the atoms possessing a much smaller atomic form factor than the noble metals has to remain unclear. Therefore, this study should be considered as top-down approach building a bridge between the experimental and computational material science on metallic glasses and relating the structural features of these bulk glass-forming metallic liquids to their thermodynamic and mechanical properties.

At this point one might speculate that the different distribution of the cluster connection schemes is related to the different sensitivity to annealing or cooling rate induced embrittlement of the two alloy families. When the sensitivity to embrittlement becomes more pronounced as Pt is partially replaced by Pd[5], it might be a consequence of the increase of 3-atom connections in the Pd–P-based glasses. Interestingly, Ding et al.[49] reported in their simulations that the various cluster connection schemes react differently on external stresses. Clusters that are connected via 2- and 4-atom are more flexible as their local deformation exceeds that of the macroscopic strain, whereas clusters sharing 1-atom experience an almost identical strain. In contrast, the local strain of clusters with 3-atom connections is the smallest and remains below the microscopically imposed shear strain[49]. In other words, the simulations suggest that 3-atom connections are stiffer than the other connection schemes. Hence, the fraction of 3-atom connections, which increases upon increasing the Pd concentration or which should increase upon annealing and upon reducing the cooling rate, might exceed a critical value if the fictive temperature of the glass (defined as the glass transition upon cooling) falls below the critical fictive temperature T_f^{crit} (fictive temperature of the glass below which the sample embrittles)[16]. T_f^{crit} is also connected to an alloy specific critical value in the configurational entropy. Although the macroscopic G/B ratio (G = shear modulus, B = bulk modulus) for both alloy classes remains below the critical value of 0.41[5,53] at which the transition from a ductile to brittle behavior is suggested[54], the locally increasing stiffness through the ascending portion of 3-atom connections in $Pd_{43}Cu_{27}Ni_{10}P_{20}$ and $Pd_{42.5}Cu_{27}Ni_{9.5}P_{21}$ might hamper the formation of multiple shear bands and increase the sensitivity to crack initiation and propagation.

In summary, the conducted synchrotron X-ray scattering experiments on the Pt–P- and Pd–P-based liquids suggest the existence of major structural differences in the two compositionally related alloy families. The comparison of the total structure factor of $Pt_{42.5}Cu_{27}Ni_{9.5}P_{21}$ and $Pd_{43}Cu_{27}Ni_{10}P_{20}$ indicate that significant structural differences exist. The total structure factor of the $Pt_{42.5}Cu_{27}Ni_{9.5}P_{21}$ glass exhibits a distinct prepeak preceding the FSDP, implying the existence of a pronounced MRO. In contrast, the $Pd_{43}Cu_{27}Ni_{10}P_{20}$ glass does not show a comparable feature, however, a shoulder at the second peak is observed, indicating at least partially icosahedral SRO. Both structural signatures suggest that the distribution of the representative structural units and their spatial arrangement in both families vary. In Pd–P-based liquids icosahedral SRO dominates, whereas the Pt–P-based liquids contain a larger fraction of trigonal prisms. Upon gradually replacing Pt by Pd, the prepeak fades and the shoulder at the second peak gains intensity, suggesting that the ratio between icosahedra and trigonal prisms is changing. When approaching the equilibrium liquid state upon heating, the prepeak vanishes, and the shoulder gets less pronounced which is on the one hand attributed the

increasing atomic vibrations and on the other hand to the dissolution of atomic SRO and MRO. The disappearance of the prepeak in combination with the rapidly descending specific heat capacity of the liquid with increasing temperature and the large entropy of fusion draws the picture of a rather disordered $Pt_{42.5}Cu_{27}Ni_{9.5}P_{21}$ liquid at high temperatures. This disordered liquid experiences a rapid ordering process involving the formation of MRO upon approaching the glass transition. The low entropy of fusion and the shallowly ascending specific heat capacity of the liquid upon cooling suggest that the structure of the $Pd_{43}Cu_{27}Ni_{10}P_{20}$ liquid in the stable equilibrium already comprises a certain degree of SRO. The appearance of the second peak in the reduced PDF suggests that Pt–P- and Pd–P-based liquids possess different distributions of cluster connection schemes, resulting from the varying ratio between the two representative structural units. Pt–P-based liquids feature a broad distribution of cluster connection schemes, comprising the more flexible 2- and 4-atom connections, whereas the stiffer 3-atom connections prevail in the Pd–P-based liquids, originating from the more dominant icosahedral SRO. The varying distribution of connection schemes contribute to the large difference in the entropy of fusion and are likely to be associated to the different sensitivity to annealing or cooling rate induced embrittlement, with the Pd–P-based alloys being more prone to embrittlement.

Methods

Sample preparation. In a first step, a prealloy is produced from the high-purity elements (purity > 99.95 wt%), Pt/Pd, Cu, and Ni. The elements are alloyed in an arc-furnace under a Ti-gettered high-purity Ar atmosphere. The prealloy is molten several times to ensure a homogeneous distribution of the elements. Subsequently, the prealloy is placed on top of the red P pieces in a fused silica tube of 1-m length, with an inner diameter of 12 mm and a wall thickness of 1.5 mm and heated inductively under high-purity Ar. A fluxing process is conducted by heating the alloys with dehydrated B_2O_3 up to 1473 K in a 1-m-long fused silica tube with an inner diameter of 16 mm and a wall thickness of 1.5 mm. The alloys are held at this temperature for at least 6 h. If the overall mass loss during the complete alloying process is attributed to the loss of P, a maximum deviation of 0.5 at% P is estimated. In general, the preparation process is similar to the one of S-containing BMGs, described in detail in references[55,56]. Amorphous samples are produced from the purified alloys by casting them in water cooled copper molds using a custom build suction casting device. The alloy compositions containing Pt and Pd are obtained by mixing appropriate masses of the $Pt_{42.5}Cu_{27}Ni_{9.5}P_{21}$ and $Pd_{42.5}Cu_{27}Ni_{9.5}P_{21}$ alloy compositions. The $Pt_{42.5}Cu_{27}Ni_{9.5}P_{21}$ and $Pd_{43}Cu_{27}Ni_{10}P_{20}$ samples that are heated to the equilibrium liquid and cooled at 0.333 K/s are cast as rods with a diameter of ~1.1 mm. In order to fit into SiO_2 capillaries for the synchrotron X-ray experiments, the diameter of the rods is reduced by grinding. The samples for measurements at ambient temperature are cut from amorphous plate-shaped samples with a dimension of $1 \times 10 \times 13$ mm^3.

Synchrotron X-ray scattering experiments. The X-ray scattering experiments are carried out at the high resolution beamline P02.1 at PETRA III at the Deutsches Elektronen Synchrotron (DESY) in Hamburg[57]. A wavelength of 0.207 Å (60 keV) and a beam size of 0.5×0.5 mm^2 is used. The samples are positioned in SiO_2 capillaries with a diameter of 1 mm and a wall thickness of 0.01 mm and placed in a ceramic heater and heated at a rate of 0.333 K/s under a constant flow of high-purity Ar. The temperature calibration of the furnace is performed using Si powder. The measurements are carried out in transmission mode using a Perkin Elmer XRD1621 CsI bonded amorphous silicon detector (2048 pixels × 2048 pixels). The dark-subtracted, two-dimensional X-ray diffraction patterns are integrated using the Fit2D data analysis software[58]. The data are further processed using the PDFgetX2 software[59]. The background is measured at room temperature, assumed to be constant upon heating and cooling and subtracted from the integrated intensity data. The data are corrected for sample absorption, polarization, and multiple scattering. The total structure factor $S(Q)$ is calculated as[46]

$$S(Q) = 1 + \frac{I_C(Q) - f(Q)^2}{f(Q)^2}, \tag{1}$$

where $I_C(Q)$ is the coherently scattered intensity and $f(Q)$ is the atomic form factor, and Q is the scattering vector. The angle brackets denote a compositional average over all constituents. $S(Q)$ contains all the structural information and is composed of $n(n + 1)/2$ partial structure factors[60],

$$S(Q) = \sum_{i \leq j} w_{ij} S_{ij}(Q) \tag{2}$$

where w_{ij} is the weighting factor expressed as

$$w_{ij} = \frac{c_i c_j f_i(Q) f_j(Q)}{f(Q)^2} \tag{3}$$

where c_i and c_j are the molar concentration of element i and j. The Fourier transform of the total structure factor yields the reduced PDF,

$$G(r) = \frac{2}{\pi} \int_0^\infty Q[S(Q) - 1] \sin(Qr) dQ \tag{4}$$

where r is the distance to the reference atom. Each $G(r)$ pattern was optimized using an optimization algorithm in PDFgetX2 as described by Wei et al.[61]. As shown in Supplementary Fig. 6, the splitting of the second peak in $G(r)$, which is discussed in the main text, only becomes apparent if the maximum Q-range (Q_{max}) for the Fourier transformation of $S(Q)$ is beyond 12 Å^{-1}. In contrast, the third and fourth peak in $G(r)$ remain rather unaffected if Q_{max} is varied within 10.5 and 16 Å^{-1} as already observed by Ma et al.[24] for even lower Q_{max}-values.

Data availability

Raw data were generated at DESY (Hamburg, Germany) at the PETRA III (P02.1 beamline). Derived data supporting the findings of this study are available from the corresponding author on reasonable request.

References

1. Schroers, J. & Johnson, W. L. Highly processable bulk metallic glass-forming alloys in the Pt–Co–Ni–Cu–P system. *Appl. Phys. Lett.* **84**, 3666 (2004).
2. Nishiyama, N. et al. The world's biggest glassy alloy ever made. *Intermetallics* **30**, 19–24 (2012).
3. Na, J. H. et al. Bulk platinum-copper-phosphorus glasses bearing boron, silver, and gold. US10036087B2 (2018).
4. Takeuchi, A. et al. $Pd_{20}Pt_{20}Cu_{20}Ni_{20}P_{20}$ high-entropy alloy as a bulk metallic glass in the centimeter. *Intermetallics* **19**, 1546–1554 (2011).
5. Kumar, G., Prades-Rodel, S., Blatter, A. & Schroers, J. Unusual brittle behavior of Pd-based bulk metallic glass. *Scr. Mater.* **65**, 585–587 (2011).
6. Miracle, D. B. A structural model for metallic glasses. *Nat. Mater.* **3**, 697–702 (2004).
7. Laws, K. J., Miracle, D. B. & Ferry, M. A predictive structural model for bulk metallic glasses. *Nat. Commun.* **6**, 8123 (2015).
8. Gross, O. et al. The kinetic fragility of Pt–P- and Ni–P-based bulk glass-forming liquids and its thermodynamic and structural signature. *Acta Mater.* **132**, 118–127 (2017).
9. Gallino, I., Gross, O., Dalla Fontana, G., Evenson, Z. & Busch, R. On the kinetic and thermodynamic fragility of the $Pt_{60}Cu_{16}Co_2P_{22}$ and $Pt_{57.3}Cu_{14.6}Ni_{5.3}P_{22.8}$ bulk metallic glasses. *J. Alloy. Compd.* **615**, S35–S39 (2014).
10. Kato, H. et al. Fragility and thermal stability of Pt- and Pd-based bulk glass forming liquids and their correlation with deformability. *Scr. Mater.* **54**, 2023–2027 (2006).
11. Gallino, I., Schroers, J. & Busch, R. Kinetic and thermodynamic studies of the fragility of bulk metallic glass forming liquids. *J. Appl. Phys.* **108**, 063501 (2010).
12. Gross, O. et al. On the high glass-forming ability of Pt-Cu-Ni/Co-P-based liquids. *Acta Mater.* **141**, 109–119 (2017).
13. Legg, B. A., Schroers, J. & Busch, R. Thermodynamics, kinetics, and crystallization of $Pt_{57.3}Cu_{14.6}Ni_{5.3}P_{22.8}$ bulk metallic glass. *Acta Mater.* **55**, 1109–1116 (2007).
14. Martinez, L.-M. & Angell, C. A. A thermodynamic connection to fragility of glass-forming liquids. *Nature* **410**, 663–667 (2001).
15. Ding, J., Cheng, Y. Q., Sheng, H. & Ma, E. Short-range structural signature of excess specific heat and fragility of metallic-glass-forming supercooled liquids. *Phys. Rev. B* **85**, 1–5 (2012).
16. Kumar, G., Neibecker, P., Liu, Y. H. & Schroers, J. Critical fictive temperature for plasticity in metallic glasses. *Nat. Commun.* **4**, 1536 (2013).
17. Angell, C. A. Glass transition. *Encycl. Mater. Sci. Technol.* **4**, 3565–3575 (2001).
18. Pan, J. et al. Extreme rejuvenation and softening in a bulk metallic glass. *Nat. Commun.* **9**, 560 (2018).
19. Ketkaew, J. et al. Mechanical glass transition revealed by the fracture toughness of metallic glasses. *Nat. Commun.* **9**, 3271 (2018).
20. Lou, H. et al. Negative expansions of interatomic distances in metallic melts. *Proc. Natl Acad. Sci. USA* **110**, 10068–10072 (2013).

ARTICLE

21. Gangopadhyay, A. K. et al. Anomalous thermal contraction of the first coordination shell in metallic alloy liquids. *J. Chem. Phys.* **140**, 044505 (2014).
22. Ding, J. et al. Temperature effects on atomic pair distribution functions of melts. *J. Chem. Phys.* **140**, 064501 (2014).
23. Sukhomlinov, S. V. & Müser, M. H. Determination of accurate, mean bond lengths from radial distribution functions. *J. Chem. Phys.* **146**, 024506 (2017).
24. Ma, D., Stoica, A. D. & Wang, X.-L. Power-law scaling and fractal nature of medium-range order in metallic glasses. *Nat. Mater.* **8**, 30–34 (2009).
25. Cheng, Y. Q. & Ma, E. Atomic-level structure and structure-property relationship in metallic glasses. *Prog. Mater. Sci.* **56**, 379–473 (2011).
26. Nakamura, T. et al. Structural study in amorphous Zr-noble metal (Pd, Pt and Au) alloys. *J. Non-Cryst. Solids* **312–314**, 517–521 (2002).
27. Sordelet, D. J. et al. Structure of Zr x Pt100-x metallic glasses. *Metall. Mater. Trans. A* **39**, 1908–1916 (2008).
28. Bondi, K. S. et al. Effects of microalloying with 3d transition metals on glass formation in AlYFe alloys. *J. Non-Cryst. Solids* **353**, 4723–4731 (2007).
29. Hoyer, W. & Jödicke, R. Short-range and medium-range order in liquid Au–Ge alloys. *J. Non-Cryst. Solids* **192–193**, 102–105 (1995).
30. Wang, L., Wang, Y. Q., Peng, C. & Zhang, Y. Medium-range structural order in liquid $Ni_{20}Al_{80}$ alloy: experimental and molecular dynamics studies. *Phys. Lett. A* **350**, 405–409 (2006).
31. Bai, Y. W. et al. Heredity of medium-range order structure from melts to amorphous solids. *J. Appl. Phys.* **112**, 083524 (2012).
32. Khan, S. A., Wang, X. D., Cao, Q. P., Zhang, D. X. & Jiang, J. Z. Structural signature in Au-based amorphous alloys. *Acta Mater.* **140**, 31–38 (2017).
33. Mauro, N. A. et al. Short- and medium-range order in $Zr_{80}Pt_{20}$ liquids. *Phys. Rev. B* **83**, 1–8 (2011).
34. Mauro, N. A. & Kelton, K. F. Medium range order in Zr-noble metal eutectic liquids. *J. Non-Cryst. Solids* **358**, 3057–3059 (2012).
35. Sheng, H. W., Luo, W. K., Alamgir, F. M., Bai, J. M. & Ma, E. Atomic packing and short-to-medium-range order in metallic glasses. *Nature* **439**, 419–425 (2006).
36. Sheng, H. W. et al. Polymorphism in a metallic glass. *Nat. Mater.* **6**, 192–197 (2007).
37. Kelton, K. F. et al. First x-ray scattering studies on electrostatically levitated metallic liquids: demonstrated influence of local icosahedral order on the nucleation barrier. *Phys. Rev. Lett.* **90**, 195504 (2003).
38. Sachdev, S. & Nelson, D. R. Theory of the structure factor of metallic glasses. *Phys. Rev. Lett.* **53**, 1947–1950 (1984).
39. Guan, P. F., Fujita, T., Hirata, A., Liu, Y. H. & Chen, M. W. Structural origins of the excellent glass forming ability of $Pd_{40}Ni_{40}P_{20}$. *Phys. Rev. Lett.* **108**, 1–5 (2012).
40. Park, C., Saito, M., Waseda, Y., Nishiyama, N. & Inoue, A. Structural study of Pd-based amorphous alloys with wide supercooled liquid region by anomalous X-ray scattering. *Mater. Trans. JIM* **40**, 491–497 (1999).
41. Miracle, D. B. The efficient cluster packing model—an atomic structural model for metallic glasses. *Acta Mater.* **54**, 4317–4336 (2006).
42. Holland-Moritz, D. et al. Short-range order in undercooled metallic liquids. *Mater. Sci. Eng. A* **375–377**, 98–103 (2004).
43. Schenk, T., Holland-Moritz, D., Simonet, V., Bellissent, R. & Herlach, D. M. Icosahedral short-range order in deeply undercooled metallic melts. *Phys. Rev. Lett.* **89**, 1–4 (2002).
44. Cheng, Y. Q., Ma, E. & Sheng, H. W. Alloying strongly influences the structure, dynamics, and glass forming ability of metallic supercooled liquids. *Appl. Phys. Lett.* **93**, 111913 (2008).
45. Cheng, Y. Q., Sheng, H. W. & Ma, E. Relationship between structure, dynamics, and mechanical properties in metallic glass-forming alloys. *Phys. Rev. B* **78**, 1–7 (2008).
46. Egami, T. & Billinge, S. J. L. *Underneath the Bragg Peaks Structural Analysis of Complex Materials*. Volume 16 (Pergamon, 2012).
47. Liu, X. J. et al. Metallic liquids and glasses: atomic order and global packing. *Phys. Rev. Lett.* **105**, 1–4 (2010).
48. Fang, X. W. et al. Spatially resolved distribution function and the medium-range order in metallic liquid and glass. *Sci. Rep.* **1**, 19–21 (2011).
49. Ding, J., Ma, E., Asta, M. & Ritchie, R. O. Second-nearest-neighbor correlations from connection of atomic packing motifs in metallic glasses and liquids. *Sci. Rep.* **5**, 1–9 (2015). https://doi.org/10.1038/srep17429.

50. Pan, S. P., Qin, J. Y., Wang, W. M. & Gu, T. K. Origin of splitting of the second peak in the pair-distribution function for metallic glasses. *Phys. Rev. B* **84**, 092201 (2011).
51. Bennett, C. H. Serially deposited amorphous aggregates of hard spheres. *J. Appl. Phys.* **43**, 2727–2734 (1972).
52. Gaskell, P. H. A new structural model for transition metal–metalloid glasses. *Nature* **276**, 484–485 (1978).
53. Schroers, J. & Johnson, W. L. Ductile bulk metallic glass. *Phys. Rev. Lett.* **93**, 255506 (2004).
54. Lewandowski, J. J., Wang, W. H. & Greer, A. L. Intrinsic plasticity or brittleness of metallic glasses. *Philos. Mag. Lett.* **85**, 77–87 (2005).
55. Kuball, A. et al. On the bulk glass formation in the ternary Pd–Ni–S system. *Acta Mater.* **158**, 13–22 (2018).
56. Kuball, A., Gross, O., Bochtler, B. & Busch, R. Sulfur-bearing metallic glasses: a new family of bulk glass-forming alloys. *Scr. Mater.* **146**, 73–76 (2018).
57. Dippel, A. C. et al. Beamline P02.1 at PETRA III for high-resolution and high-energy powder diffraction. *J. Synchrotron Radiat.* **22**, 675–687 (2015).
58. Hammersley, A. P. FIT2D: an introduction and overview. *ESRF Intern. Rep.* ESRF97HA02T 1–33 (1997).
59. Qiu, X., Thompson, J. W. & Billinge, S. J. L. PDFgetX2: a GUI-driven program to obtain the pair distribution function from X-ray powder diffraction data. *J. Appl. Crystallogr* **37**, 678 (2004).
60. Faber, T. E. & Ziman, J. M. A theory of the electrical properties of liquid metals. *Philos. Mag.* **11**, 153–173 (1964).
61. Wei, S. et al. Structural evolution on medium-range-order during the fragile-strong transition in $Ge_{15}Te_{85}$. *Acta Mater.* **129**, 259–267 (2017).

Author contributions

O.G. and R.B. conceived the study. N.N., A.K. and O.G. prepared the samples. O.G., N.N., A.K., B.B., S.H. and M.F. planned and conducted the synchrotron X-ray experiments. O.G. analyzed the data and wrote the paper with input from R.B., N.N., A.K., B.B., S.H. and M.F. All authors contributed extensively to the discussion.

5.5 Publication V

Wave-Vector Dependence of the Dynamics in Supercooled Metallic Liquids

B. Ruta[1,2,,*] S. Hechler,[1,3] N. Neuber,[3] D. Orsi,[4] L. Cristofolini,[4] O. Gross,[3] B. Bochtler,[3] M. Frey,[3] A. Kuball,[3]
S. S. Riegler,[3] M. Stolpe,[3] Z. Evenson,[5] C. Gutt,[6] F. Westermeier,[7] R. Busch,[3] and I. Gallino[3]

[1]*Univ Lyon, Université Claude Bernard Lyon 1, CNRS, Institut Lumière Matière, F-69622 Villeurbanne, France*
[2]*ESRF—The European Synchrotron, CS40220, 38043 Grenoble, France*
[3]*Chair of Metallic Materials, Department of Materials Science and Engineering, Saarland University,
Campus C6.3, 66123 Saarbrücken, Germany*
[4]*Dipartimento di Scienze Matematiche Fisiche ed Informatiche, Università degli Studi di Parma, Parma, Italy*
[5]*Heinz Maier-Leibnitz Zentrum (MLZ) and Physik Department, Technische Universität München,
Lichtenbergstrasse 1, 85748 Garching, Germany*
[6]*Department Physik, Universität Siegen, D-57072 Siegen, Germany*
[7]*Deutsches Elektronen Synchrotron DESY, D-22607 Hamburg, Germany*

We present a detailed investigation of the wave-vector dependence of collective atomic motion in $Au_{49}Cu_{26.9}Si_{16.3}Ag_{5.5}Pd_{2.3}$ and $Pd_{42.5}Cu_{27}Ni_{9.5}P_{21}$ supercooled liquids close to the glass transition temperature. Using x-ray photon correlation spectroscopy in a previously uncovered spatial range of only a few interatomic distances, we show that the microscopic structural relaxation process mimics the structure and presents a marked slowing down at the main average interparticle distance. This behavior is accompanied by dramatic changes in the shape of the intermediate scattering functions, which suggest the presence of large dynamical heterogeneities at length scales corresponding to a few particle diameters. A ballisticlike mechanism of particle motion seems to govern the structural relaxation of the two systems in the highly viscous phase, likely associated with hopping of caged particles in agreement with theoretical studies.

The dynamics of glass formers still attracts large interest in the scientific community as it is often considered the key to understanding the glass transition [1–5]. Considerable effort has been devoted to the comprehension of the enormous increase in viscosity, or structural relaxation time τ upon cooling toward the glass transition temperature T_g [5–7]. However, little is still known on the microscopic mechanisms responsible for such a tremendous slowdown of viscous flow as the majority of previous studies employ macroscopic approaches. One major obstacle to overcome is the difficulty in probing the ultraslow dynamics of glass formers close to T_g at the relevant length scale involving interparticle interactions with both experiments and simulations.

The collective atomic motion of glass formers can be described by the intermediate scattering function (ISF) $f(Q,t)$, which monitors the temporal evolution of the normalized density-density correlation function over a spatial scale $2\pi/Q$ defined by the probed wave-vector Q. The long time decay of the ISF corresponds to the structural relaxation process and it can be modeled by the Kohlrausch-Williams-Watts (KWW) function $f(Q,t) = f_Q \exp[-(t/\tau)^{\beta}]$, with the structural relaxation time $\tau(Q)$, the shape parameter $\beta(Q)$, and the nonergodicity parameter f_Q [3,8].

Studies on metallic glass formers report the existence of an anomalous dynamical crossover at the glass transition [9,10]. Above T_g, the structural relaxation process decays in a stretched exponential way with $\beta < 1$. Similar decays have been attributed largely to the emergence of dynamical heterogeneities on approaching T_g [3,11]. As soon as the material vitrifies, the shape of the long-time decay of the ISF changes abruptly to a highly compressed form ($\beta > 1$). Numerical simulations associate these compressed ISFs to an increasing number of connected icosahedral clusters on approaching T_g [12].

At high temperatures, liquids undergo Brownian motion and $\tau(Q) \approx Q^{-2}$. Theoretical studies suggest a gradual weakening of this Q dependence in supercooled liquids, due to a change in the transport mechanism from purely diffusive at high temperatures, to a combination of diffusion and hopping of caged particles on approaching T_g [13]. Differently, numerical simulations show that the relaxation dynamics depends on the rigidity of the amorphous structure being Q independent in network glass formers, while keeping a diffusive nature in more fragile systems [14]. This peculiar Q-independent dynamics occurs for few interparticle distances and it has been observed also in polymeric materials and DNA-based transient networks [15–17]. Its origin appears associated to the presence of independent locally fluctuating elastic moduli on the probed length scale [15,16] and suggests the presence of a crossover to a diffusivelike dynamics at larger length scales [15,17].

A deeper understanding of the dynamics requires the experimental knowledge of the Q dependence of the ISF in liquids and glasses. Such information is challenging to obtain. Experiments below T_g are currently strongly impeded by the evolution of the dynamics due to physical aging, which makes it extremely difficult to compare data acquired separately at different Q's [10,18]. The dynamics of supercooled liquids is also difficult to probe due to the relatively fast relaxation times and the weak scattering signal at the atomic scale. Because of these technical constraints, often only a single Q at the maximum of the static structure factor $S(Q)$ [10,19] has been studied, providing limited information on the microscopic mechanism responsible for the dynamics in supercooled liquids.

Here, we make use of recent experimental improvements in x-ray photon correlation spectroscopy (XPCS) [19], and probe the Q dependence of the relaxation dynamics at interatomic distances in two highly viscous metallic glass formers just a few degrees above the calorimetric T_g, i.e., in a previously unexplored range. The investigated systems are alloys of $Au_{49}Cu_{26.9}Si_{16.3}Ag_{5.5}Pd_{2.3}$ and $Pd_{42.5}Cu_{27}Ni_{9.5}P_{21}$ ($T_g = 574$ K). When slowly cooled with isothermal steps of 0.5 K and a cooling rate of 0.1 K min^{-1} from the supercooled liquid, the T_g of the $Au_{49}Cu_{26.9}Si_{16.3}Ag_{5.5}Pd_{2.3}$ is lowered by more than 30 K [20,21], and the system exhibits a fragile-to-strong liquid-liquid transition at 389 K. In this work, we have investigated the dynamics in the low temperature strong phase ($T_g = 380$ K [20]). For both studied materials, we measured the ISFs at different Q's around their respective maxima Q_m of the $S(Q)$ ($Q_{m,Au-alloy} = 2.80$ and $Q_{m,Pd-alloy} = 2.87$ Å^{-1}) and in the highly viscous state ($T_{Au-alloy} = 385.5$, $T_{Pd-alloy} = 580$ K).

The $Au_{49}Cu_{26.9}Si_{16.3}Ag_{5.5}Pd_{2.3}$ was measured at beam line ID10 at ESRF, France, and the $Pd_{42.5}Cu_{27}Ni_{9.5}P_{21}$ at beam line P10 at PETRA III, Germany (see also Supplemental Material [22]). XPCS provides information on the microscopic dynamics by monitoring the temporal evolution of the intensity fluctuations $g_2(Q,t)$, which are related to the ISF through the Siegert relation $g_2(Q,t) = 1 + \gamma \cdot |f(Q,t)|^2$, with γ the experimental contrast [19,23]. Despite the multicomponent nature of the probed alloys, in both cases, XPCS mainly measures the average dynamics coming from the noble-noble atoms correlation which dominates the scattered signal [22,24,25].

Figure 1 illustrates the two times correlation functions (TTCFs) measured in the $Au_{49}Cu_{26.9}Si_{16.3}Ag_{5.5}Pd_{2.3}$ at the low Q side of the maximum of the $S(Q)$ [Fig. 1(a)], over its flank [Fig. 1(b)], and at the maximum [Fig. 1(c)]. TTCF are a time-resolved version of the standard $g_2(Q,t)$. The width of the yellow-reddish intensity along the main diagonal is proportional to $\tau(Q)$. At all Q's, the intensity profile remains constant with time, which is a signature of the stationary dynamics of supercooled liquids. The lower
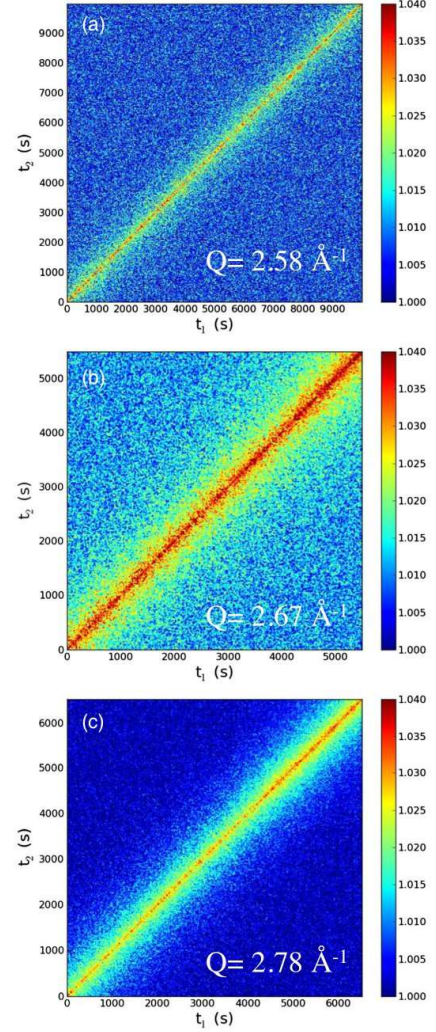

FIG. 1. TTCF at 385.5 K in $Au_{49}Cu_{26.9}Si_{16.3}Ag_{5.5}Pd_{2.3}$ for three different Q's [2.58 (a), 2.67 (b), and 2.78 Å^{-1} (c)].

intensity at low Q [Fig. 1(a)] is a consequence of the lower scattered signal far from Q_m, while the small intensity fluctuations along the diagonal contour are due to the heterogeneous nature of the dynamics in supercooled liquids, which results in a distribution of microscopic distinct relaxations [11].

Figure 2 shows normalized $g_2(Q,t)$ measured at different Q's together with the KWW fits $g_2(Q,t) = 1 + c \exp[-2(t/\tau)^\beta]$, with c the product between f_Q and the contrast. In the probed Q range, c is found constant and the data have been normalized for clarity. Figures 2(a) and 2(b) show normalized $g_2(Q,t)$ of the
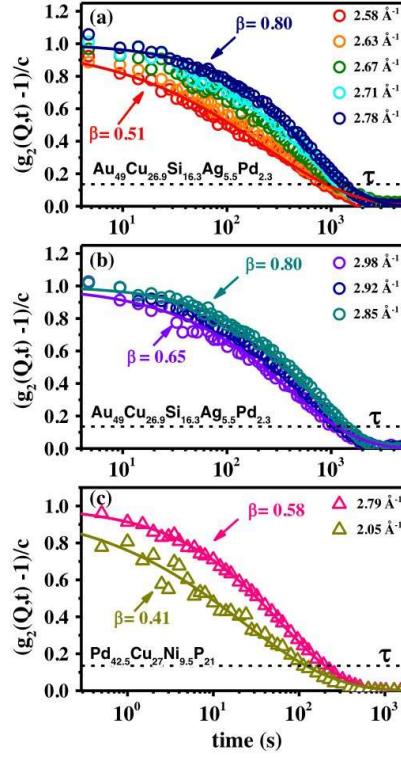
FIG. 2. Normalized intensity autocorrelation functions for the low (a) and the high (b) Q side of the main maximum of the $S(Q)$ in $Au_{49}Cu_{26.9}Si_{16.3}Ag_{5.5}Pd_{2.3}$ at $T = 385.5$ K, and (c) at the smallest probed Q and at the $Q_{m,Pd-alloy}$ for $Pd_{42.5}Cu_{27}Ni_{9.5}P_{21}$ at $T = 580$ K.

$Au_{49}Cu_{26.9}Si_{16.3}Ag_{5.5}Pd_{2.3}$ corresponding to the low and the high Q side of the $S(Q)$, respectively. The correlation functions visibly have distinct shapes with Q, and become more stretched at low [Fig. 2(a)] and high (Fig. 2(b)] Q's with respect to the shape at the maximum of the $S(Q)$. This effect is remarkable as $\beta(Q)$ decreases by almost 40% of its value, from $\beta(Q) = 0.80 \pm 0.02$ at 2.78 to 0.51 ± 0.02 at 2.58 Å^{-1}, i.e., in a very tiny Q range covering only 0.2 Å^{-1} [Fig. 2(a)]. Changes in $\beta(Q)$ are visible also in the $Pd_{42.5}Cu_{27}Ni_{9.5}P_{21}$ [Fig. 2(c)]. Here, the evolution of $\beta(Q)$ is weaker as it decreases to $\approx 30\%$ of its maximum value on a Q range which is ≈ 3 times larger than the one explored for the $Au_{49}Cu_{26.9}Si_{16.3}Ag_{5.5}Pd_{2.3}$.

The structural relaxation times and shape parameters measured at all Q's are reported in Fig. 3 for both $Au_{49}Cu_{26.9}Si_{16.3}Ag_{5.5}Pd_{2.3}$ (left column) and $Pd_{42.5}Cu_{27}Ni_{9.5}P_{21}$ alloys (right column) and compared with the $S(Q)$ measured with x-ray diffraction [25,26]. Both $\tau(Q)$ and $\beta(Q)$ mimic the $S(Q)$, showing a significant slowdown of the dynamics at Q_m accompanied by a

simultaneous increase in $\beta(Q)$ [panels (a)–(b) and (d)–(e)]. The evolution of $\tau(Q)$ is a signature of the de Gennes narrowing usually observed in the frequency domain in high temperature liquids [27–37]. It implies that the most probable and stable interatomic configurations are those probed at $Q \approx Q_m$, which need a high degree of cooperative motion to change the atomic arrangements. Interestingly, while the $S(Q)$ changes by almost a factor of 2 in the $Au_{49}Cu_{26.9}Si_{16.3}Ag_{5.5}Pd_{2.3}$, the relative change in τ is considerably smaller. This difference is even stronger in the $Pd_{42.5}Cu_{27}Ni_{9.5}P_{21}$. Similar trends have been reported for other viscous liquids [37–39] and are likely due to the occurrence of complex mechanisms of particle motion [30]. We note that although both samples have been measured close to their T_g, their dynamics differ by almost an order of magnitude, being of $\approx 10^4$ s in the $Au_{49}Cu_{26.9}Si_{16.3}Ag_{5.5}Pd_{2.3}$. This remarkable highly viscous state is a consequence of the applied thermal protocol [20,21].

Considering the heterogeneous scenario for supercooled liquids, i.e., the existence of groups of particles relaxing with different times with respect to neighboring particles, the $g_2(Q,t)$ can be viewed as a measure of the average dynamics with $\beta(Q)$ describing the degree of such a distribution of microscopic relaxation processes [11,40]. The decrease of $\beta(Q)$ for Q values smaller than that of the main peak in $S(Q)$ implies the occurrence of larger dynamical heterogeneities consistent with the notion of medium-range-order domain fluctuations. The smaller measured Q values correspond generally to length scales comparable to the typical size of icosahedra clusters whose occurrence in the Pd-based alloy has been confirmed by structural studies [25,41]. The dynamics of such clusters was recently identified to strongly dominate the evolution of the ISFs in supercooled metallic liquids [12]. This behavior contrasts dramatically with that observed in metallic glasses. Below T_g, not only is the dynamics characterized by a compressed decay of the ISFs (i.e., $\beta > 1$) and aging [10], but $\beta(Q)$ remains constant, at least in the same Q range as probed here [18].

To evaluate the mechanism of particle motion we include the influence of $\beta(Q)$ on the dynamics by considering the mean relaxation time $\langle \tau(Q) \rangle = \Gamma\{[1/[\beta(Q)]\}\{[\tau(Q)]/[\beta(Q)]\}$, where Γ is the Gamma function [30]. Differently from $\tau(Q)$, $\langle \tau(Q) \rangle$ decreases with increasing Q in both supercooled liquids before to evolve to a more flattened regime at larger Q values [Figs. 3(c) and 3(f)]. The low Q's regime is compatible with a $1/Q$, ballisticlike atomic motion suggesting the existence of a mechanism of hopping of caged particles in these ultraviscous liquids [42] as in the case of some concentrated colloidal suspensions [43], gels [44,45], and in numerical simulations of ortho-terphenyl [46]. Interestingly, the crossover between the two regimes occurs at different Q's in the two alloys. In the
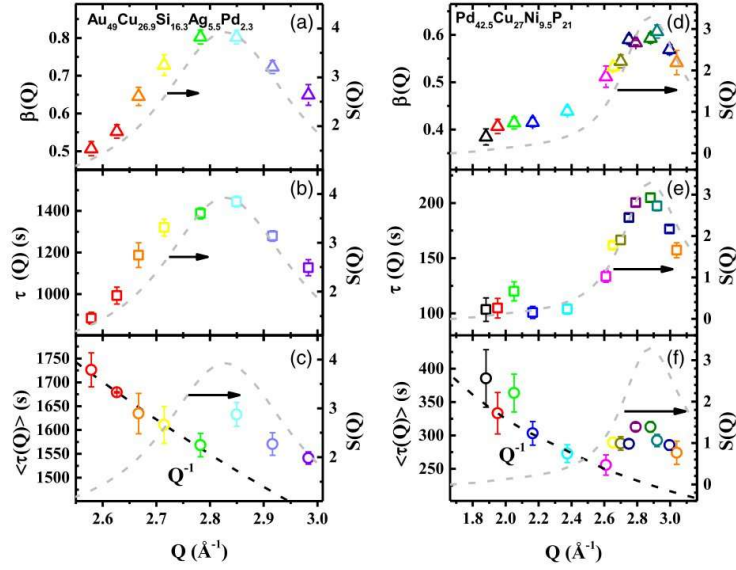
FIG. 3. $\beta(Q)$ (a),(d), $\tau(Q)$ (b),(e), and average relaxation time $\langle\tau(Q)\rangle$ (c),(f) for $Au_{49}Cu_{26.9}Si_{16.3}Ag_{5.5}Pd_{2.3}$ (left column) and $Pd_{42.5}Cu_{27}Ni_{9.5}P_{21}$ (right column). The colors of the Au-based alloy correspond to the curves in Fig. 2. The dashed black lines in [(c) and (f)] show a ballistic-like dynamics. In all panels, the dashed gray line is the corresponding $S(Q)$.

$Au_{49}Cu_{26.9}Si_{16.3}Ag_{5.5}Pd_{2.3}$, the ballisticlike regime persists up to $Q \approx Q_m$, while in the $Pd_{42.5}Cu_{27}Ni_{9.5}P_{21}$ it ends in correspondence of the onset of the main structural peak in the $S(Q)$. Such a difference is likely due to the huge reduction in $\beta(Q)$ at low Q's for the $Au_{49}Cu_{26.9}Si_{16.3}Ag_{5.5}Pd_{2.3}$, of about 40% of its value at Q_m [Fig. 3(a)], which dominates the $\langle\tau(Q)\rangle$ evolution. In the very same Q range, $\beta(Q)$ of $Pd_{42.5}Cu_{27}Ni_{9.5}P_{21}$ decreases to only 15% of its value at Q_m [Fig. 3(d)]. In this range, $\langle\tau(Q)\rangle$ is mainly controlled by the Q dependence of the relaxation time and decreases with lower Q, mirroring the evolution of the $S(Q)$. The distinct crossovers between the two dynamical regimes could be associated with the different structural detail of the two alloys and, in particular, to the stiffer nature of the Pd-based alloy [25] with respect to the microscopically softer structure of the $Au_{49}Cu_{26.9}Si_{16.3}Ag_{5.5}Pd_{2.3}$ [26].

We note that in the $Au_{49}Cu_{26.9}Si_{16.3}Ag_{5.5}Pd_{2.3}$ alloy the evolution of $\langle\tau(Q)\rangle$ comes from the marked Q dependence of both $\beta(Q)$ and $\tau(Q)$ in the probed Q range, confirmed by the distinct corresponding ISFs [Fig. 2(a)]. In stark contrast, the subquadratic dependence of $\langle\tau(Q)\rangle$ in $Pd_{42.5}Cu_{27}Ni_{9.5}P_{21}$ occurs in a Q range, where the corresponding KWW parameters are almost constant with Q's [Figs. 3(d) and 3(e)]. The slightly decreases of $\beta(Q)$ at low Q's is then likely to be the reason of the still marked Q dependence of the mean relaxation time in this range. Whether such dependence is real or not is, however, difficult to establish. As shown in Fig. 4, the decay of the corresponding ISFs almost overlap with Q, with the

relaxation time basically constant at low Q's, i.e., far from the structural contribution (inset of Fig. 4). Furthermore, the scattering of the data at short times introduces some noise in the evaluation of $\beta(Q)$ and $\tau(Q)$, which could affect the probed Q dependencies. This lower signal to noise ratio (SNR) in the $Pd_{42.5}Cu_{27}Ni_{9.5}P_{21}$ data at small Q's is due to the limited capabilities of the XPCS technique at synchrotrons of the 3rd generation and the relatively fast dynamics of this liquid, which is almost a factor 5 faster than in the Au-based alloy (see also Supplemental
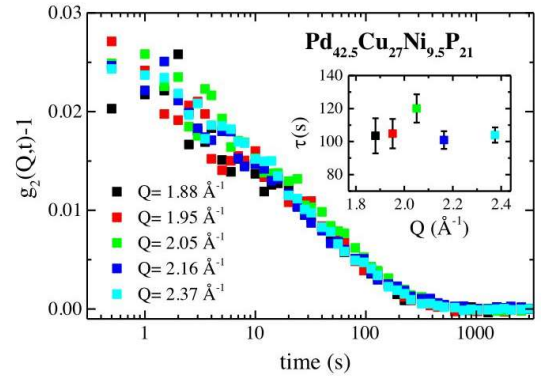

FIG. 4.   Intensity autocorrelation functions measured at the small Q's in the $Pd_{42.5}Cu_{27}Ni_{9.5}P_{21}$ at $T = 580$ K. The inset shows the corresponding $\tau(Q)$.

Material [22]). Hence, measurements with improved statistics or in a broader Q range will be necessary to confirm the observed subquadratic collective dynamics, or instead point to a Q-independent relaxation mode between the hydrodynamics limit and the interparticle distance [14], being the hydrodynamic limit around few μm for the Pd alloy [47].

In conclusion, we reported a detailed investigation of the atomic motion in highly viscous alloys close to T_g. Both $\tau(Q)$ and $\beta(Q)$ mirror the evolution of the $S(Q)$. While the slow down of the dynamics is due to the well-known de Gennes narrowing [29], the substantial decrease of $\beta(Q)$ at small Q's suggests the occurrence of large dynamical heterogeneities possibly related to medium-range-order domain fluctuations. A similar but smaller $\beta(Q)$ evolution is predicted by the mode coupling theory for hard spheres [48,49], and has been reported also in high temperature polymeric liquids [30] and in simulations of supercooled water [50]. In our case, the collective motion of both liquids follows a subquadratic dependence from the probed wave vector, suggesting the occurrence of a complex mechanism of diffusion and hopping responsible for the particle motion [42].

The dynamics of metallic glass formers across T_g has been often compared to that of nanoparticles probes in supercooled molecular and polymeric liquids [51,52]. In both cases, the glass transition is accompanied by the emergence of compressed ISFs and distinct aging regimes. This analogy does not extend to the Q dependence of the dynamics. While the dynamics of nanoparticle probes evolve from diffusive with stretched ISFs to ballisticlike with compressed ISFs on approaching the glassy state, our results show the existence of a distinct mechanism of particle motion, which appears related to the details of the amorphous structure in the viscous phase. This different dynamics contrasts also with the diffusive dynamics observed in Lennard Jones systems which are often considered similar to metallic alloys [14]. Studies of the dynamics across T_g and in a broader Q range will definitely help to elucidate the nature of the glass transition. This will soon be possible thanks to the current upgrade of coherent x-ray sources [53,54].

*Corresponding author.
 beatrice.ruta@univ-lyon1.fr

[1] Y.-Q. Cheng and E. Ma, Prog. Mater. Sci. **56**, 379 (2011).

[2] L. Berthier and G. Biroli, Rev. Mod. Phys. **83**, 587 (2011).

[3] A. Cavagna, Phys. Rep. **476**, 51 (2009).

[4] J. C. Dyre, Rev. Mod. Phys. **78**, 953 (2006).

[5] K. L. Ngai, *Relaxation and Diffusion in Complex Systems* (Springer-Verlag, New York, 2011).

[6] C. A. Angell, K. L. Ngai, G. B. McKenna, P. F. McMillan, and S. W. Martin, J. Appl. Phys. **88**, 3113 (2000).

[7] X. Monnier, D. Cangialosi, B. Ruta, R. Busch, and I. Gallino, Sci. Adv. **6**, eaay1454 (2020).

[8] B. Ruta, G. Baldi, F. Scarponi, D. Fioretto, V. M. Giordano, and G. Monaco, J. Chem. Phys. **137**, 214502 (2012).

[9] B. Ruta, Y. Chushkin, G. Monaco, L. Cipelletti, E. Pineda, P. Bruna, V. M. Giordano, and M. Gonzalez-Silveira, Phys. Rev. Lett. **109**, 165701 (2012).

[10] B. Ruta, E. Pineda, and Z. Evenson, J. Phys. Condens. Matter **29**, 503002 (2017).

[11] *Dynamical Heterogeneities in Glasses, Colloids and Granular Media*, edited by L. Berthier, G. Biroli, J. P. Bouchaud, L. Cipelletti, and W. Van Saarloos (Oxford University Press, Oxford, 2011).

[12] Z. W. Wu, W. Kob, W. H. Wang, and L. Xu, Nat. Commun. **9**, 5334 (2018).

[13] S. M. Bhattacharyya, B. Bagchi, and P. G. Wolynes, J. Chem. Phys. **132**, 104503 (2010).

[14] P. H. Handle, L. Rovigatti, and F. Sciortino, Phys. Rev. Lett. **122**, 175501 (2019).

[15] G. Nava, M. Rossi, S. Biffi, F. Sciortino, and T. Bellini, Phys. Rev. Lett. **119**, 078002 (2017).

[16] L. Rovigatti, G. Nava, T. Bellini, and F. Sciortino, Macromolecules **51**, 1232 (2018).

[17] N. Nemoto, A. Koike, and K. Osaki, Macromolecules **29**, 1445 (1996).

[18] B. Ruta, G. Baldi, G. Monaco, and Y. Chushkin, J. Chem. Phys. **138**, 054508 (2013).

[19] A. Madsen, A. Fluerasu, and B. Ruta, in *Synchrotron Light Sources and Free-Electron Lasers* (Springer International Publishing, Cham, 2015), pp. 1617–1641, https://doi.org/10 .1007/978-3-319-14394-1_29.

[20] S. Hechler, B. Ruta, M. Stolpe, E. Pineda, Z. Evenson, O. Gross, A. Bernasconi, R. Busch, and I. Gallino, Phys. Rev. Mater. **2**, 085603 (2018).

[21] I. Gallino, D. Cangialosi, Z. Evenson, L. Schmitt, S. Hechler, M. Stolpe, and B. Ruta, Acta Mater. **144**, 400 (2018).

[22] See Supplemental Material at http://link.aps.org/ supplemental/10.1103/PhysRevLett.125.055701 for further technical details, which includes Refs. [19–21,23–25].

[23] Y. Chushkin, C. Caronna, and A. Madsen, J. Appl. Crystallogr. **45**, 807 (2012).

[24] Z. Evenson, T. Koschine, S. Wei, O. Gross, J. Bednarcik, I. Gallino, J. J. Kruzic, K. Rätzke, F. Faupel, and R. Busch, Scr. Mater. **103**, 14 (2015).

[25] O. Gross, N. Neuber, R. Busch, A. Kuball, B. Bochtler, S. Hechler, and M. Frey, Commun. Phys. **2**, 83 (2019).

[26] Z. Evenson, T. Koschine, S. Wei, O. Gross, J. Bednarcik, I. Gallino, J. J. Kruzic, K. Rätzke, F. Faupel, and R. Busch, Scr. Mater. **103**, 14 (2015).

[27] F. Demmel, A. Diepold, H. Aschauer, and C. Morkel, Phys. Rev. B **73**, 104207 (2006).

[28] F. Demmel, P. Fouquet, W. Häussler, and C. Morkel, Phys. Rev. E **73**, 032202 (2006).

[29] P. G. De Gennes, Physica (N.Y.) **25**, 825 (1959), https://inis.iaea.org/search/search.aspx?orig_q=RN:49031303.

[30] A. Arbe and J. Colmenero, Phys. Rev. E **80**, 041805 (2009).

[31] R. Pérez-Aparicio, A. Arbe, F. Alvarez, J. Colmenero, and L. Willner, Macromolecules **42**, 8271 (2009).

[32] M. Tyagi, A. Arbe, F. Alvarez, J. Colmenero, and M. A. González, J. Chem. Phys. **129**, 224903 (2008).

[33] M. Krutyeva, J. Martin, A. Arbe, J. Colmenero, C. Mijangos, G. J. Schneider, T. Unruh, Y. Su, and D. Richter, J. Chem. Phys. **131**, 174901 (2009).

[34] M. Brodeck, F. Alvarez, A. Arbe, F. Juranyi, T. Unruh, O. Holderer, J. Colmenero, and D. Richter, J. Chem. Phys. **130**, 094908 (2009).

[35] A. Tölle, J. Wuttke, and H. Schober, Eur. Phys. J. B **5**, 231 (1998).

[36] F. Mezei, W. Knaak, and B. Farago, Phys. Rev. Lett. **58**, 571 (1987).

[37] V. N. Novikov, K. S. Schweizer, and A. P. Sokolov, J. Chem. Phys. **138**, 164508 (2013).

[38] J. Colmenero, F. Alvarez, Y. Khairy, and A. Arbe, J. Chem. Phys. **139**, 044906 (2013).

[39] B. Ruta, G. Baldi, Y. Chushkin, B. Ruffle, L. Cristofolini, A. Fontana, M. Zanatta, and F. Nazzani, Nat. Commun. **5**, 3939 (2014).

[40] R. Richert, J. Phys. Condens. Matter **14**, R703 (2002).

[41] P. F. Guan, T. Fujita, A. Hirata, Y. H. Liu, and M. W. Chen, Phys. Rev. Lett. **108**, 175501 (2012).

[42] S. M. Bhattacharyya, B. Bagchi, and P. G. Wolynes, J. Chem. Phys. **132**, 104503 (2010).

[43] F. Augusto de Melo Marques, R. Angelini, E. Zaccarelli, B. Farago, B. Ruta, G. Ruocco, and B. Ruzicka, Soft Matter **11**, 466 (2015).

[44] D. Orsi, B. Ruta, Y. Chushkin, A. Pucci, G. Ruggeri, G. Baldi, T. Rimoldi, and L. Cristofolini, Phys. Rev. E **89**, 042308 (2014).

[45] B. Ruta, O. Czakkel, Y. Chushkin, F. Pignon, R. Nervo, F. Zontone, and M. Rinaudo, Soft Matter **10**, 4547 (2014).

[46] A. Rinaldi, F. Sciortino, and P. Tartaglia, Phys. Rev. E **63**, 061210 (2001).

[47] W. H. Wang, Prog. Mater. Sci. **57**, 487 (2012).

[48] M. Fuchs, I. Hofacker, and A. Latz, Phys. Rev. A **45**, 898 (1992).

[49] F. Weysser, A. M. Puertas, M. Fuchs, and T. Voigtmann, Phys. Rev. E **82**, 011504 (2010).

[50] F. Sciortino, L. Fabbian, S. H. Chen, and P. Tartaglia, Phys. Rev. E **56**, 5397 (1997).

[51] H. Guo, G. Bourret, M. K. Corbierre, S. Rucareanu, R. B. Lennox, K. Laaziri, L. Piche, M. Sutton, J. L. Harden, and R. L. Leheny, Phys. Rev. Lett. **102**, 075702 (2009).

[52] C. Caronna, Y. Chushkin, A. Madsen, and A. Cupane, Phys. Rev. Lett. **100**, 055702 (2008).

[53] O. G. Shpyrko, J. Synchrotron Radiat. **21**, 1057 (2014).

[54] V. Favre-Nicolin, Y. Chushkin, P. Cloetens, J. C. da Silva, S. Leake, B. Ruta, and F. Zontone, Synchrotron Radiat. News **30**, 13 (2017).

6. Results and Discussion

In the following section, the main findings of the publications are subsumed and critically discussed in the context of further unpublished results and other literature references. It shall provide some deeper insights and more detailed understanding of the interconnection between kinetic, dynamic, thermodynamic, and mechanical properties with the underlying structure of the metallic glass. The section focusses on the concept of fragility and will try to discuss its many faces and what the changes of fragility could be based on structurally and what it is implying to mechanical properties. The color-coding of the compositions is ranging from green over yellow to red with increasing Pd and decreasing Pt content, similar to that used in the Publications I and III[25].

6.1   Kinetic and Dynamic Fragility

6.1.1 Rate Dependence of the Glass Transition

The characterization and classification of glass-forming liquids, especially in the deeply undercooled state well below the melting point, has been an ongoing research topic in condensed matter physics for many decades [3,51,121,186]. A well-known scheme to classify the slowdown behavior of liquids below their melting point is the so-called fragility concept established by Austen Angell [51,52](see 2.5.4.2). His original definition, based on shear viscosity, was later extended to include the temperature dependence of other dynamic quantities such as relaxation time. Due to the similar temperature dependence of e.g. transition kinetics and liquid dynamics, the original description of fragility is often used synonymously, to describe either kinetics or dynamics [187]. In the following section, we aim to distinguish precisely between both phenomena. Therefore, the term "dynamics" is used to describe intrinsic properties of the (metastable) equilibrium liquid and the α-relaxation process. It is connected to the dynamic glass transition process, i.e., the frequency dependence of the α-relaxation time of the undercooled system. In contrast; the concept of "transition kinetics" is used to describe the glass transition process (devitrification) of a glassy non-equilibrium system back to its (metastable) equilibrium liquid state and vice versa) i.e., the rate dependence of the kinetic glass

---

[25] In Publication II and IV a similar coding ranging from black to red was used instead.

transition[26] [188,189]. The connection and similar temperature dependence of the dynamic glass transition and the kinetic glass transition is summarized by the Frenkel-Kobeko-Rainer (FKR) equation, stating the proportionality between the cooling rate q_c and the dynamic relaxation time τ_d [188,190]. With these considerations in mind, the aim of this section is to present the fragility of twelve $Pt_{42.5-x}Pd_xCu_{27}Ni_{9.5}P_{21}$ alloys based on studies of the rate and frequency dependence of the kinetic and dynamic glass transition.
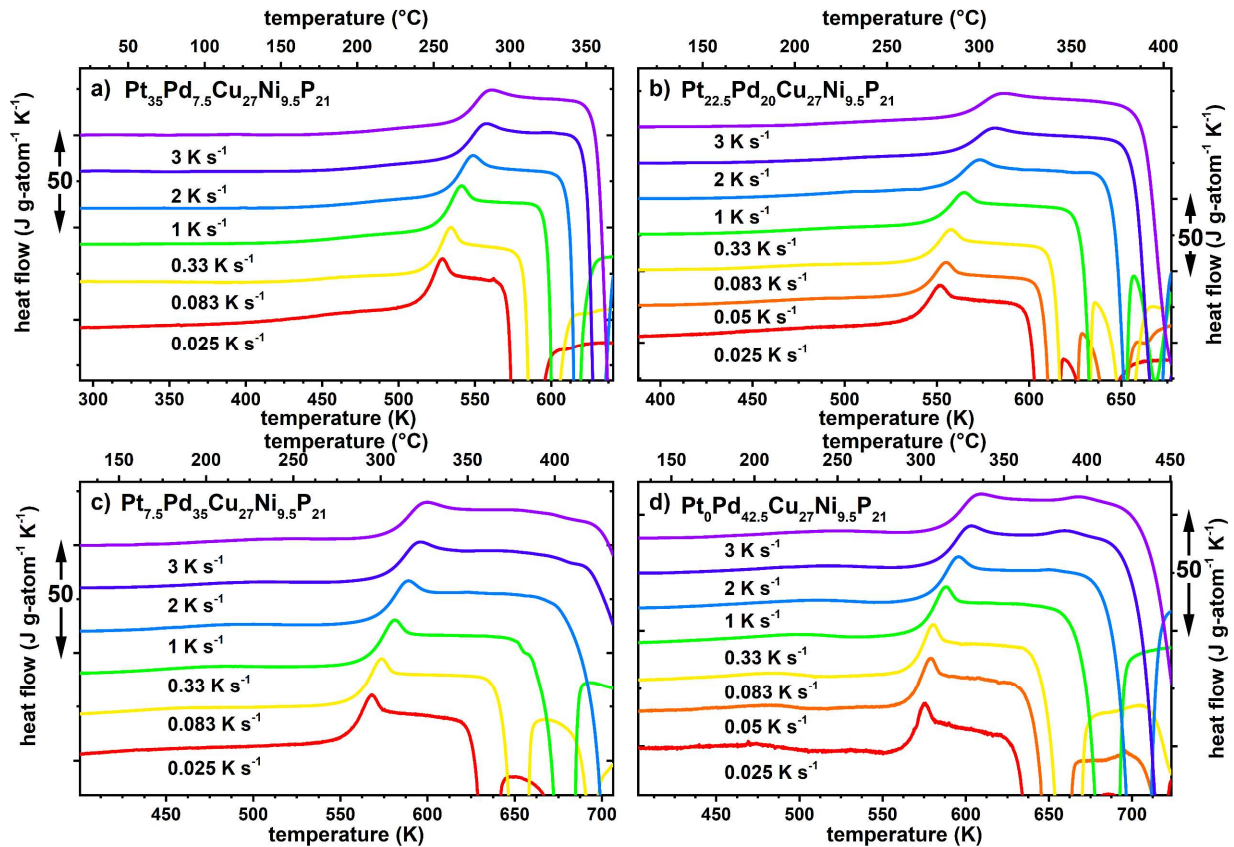
Figure 6-1: Thermograms of standard-treated samples with the composition $Pt_{42.5-x}Pd_xCu_{27}Ni_{9.5}P_{21}$ with a) x = 7.5, b) x = 20, c) x = 35 and d) for x = 42.5 for different heating rates spanning from 0.025 to 3 K s-1. Standard treated refers to an initial cooling protocol outgoing from the supercooled liquid ($T_{g,end}$ + 15 K) with a cooling rate identical to the applied heating rate in the scan ($q_h = q_c$).

To study the rate dependence of the kinetic glass transition, four compositions $Pt_{42.5-x}Pd_xCu_{27}Ni_{9.5}P_{21}$ with X = 7.5, 20, 35, and 42.5 at% are representatively chosen for the calorimetric study. Each alloy is probed with different heating rates from 0.025 to 3 K min^{-1}

---

[26] The kinetic glass transition is often also named as the thermal glass transition.

according to the protocol described in the section 3.2.3 as well as Ref. [191]. Fig. 1 summarizes the raw curves for the four alloys measured in this work, while the data for the alloy $Pt_{42.5}Pd_0Cu_{27}Ni_{9.5}P_{21}$ can be found in Ref. [36]. With increasing heating rate, a clear shift of the onsets of glass transition and crystallization event to higher temperatures can be observed[27]. Based on the width of the glass transition region $T_{g,end}$-$T_{g,on}$ and the applied rate q_h, Eq. (3.12) yields a timescale of the transition event from the glassy non-equilibrium state back to the supercooled liquid state. To ease the distinction between the different timescales used in this work, according to the nomenclature established in Ref. [36], this time is labeled transition time, τ_{trans}, as it describes the transition event from glassy non-equilibrium to the metastable equilibrium of the supercooled liquid state.

The resulting transition times for the compositions $Pt_{42.5-x}Pd_xCu_{27}Ni_{9.5}P_{21}$ with x = 0, 7.5, 20, 35, and 42.5 at% are summarized on a logarithmic scale as a function of inverse temperature in panels (a)-(e) of Fig. 2. For each composition, the data is fitted with the empirical Vogel-Fulcher-Tamann (VFT) equation in the time domain (compare eq. (2.27))

$$\tau(T) = \tau_0 \cdot exp\left(\frac{D^* \cdot T_0}{T - T_0}\right) , \qquad (6.1)$$

The pre-exponential factor τ_0 corresponds to the fastest possible relaxation time in the high temperature limit (T→∞) of the liquid state.

For the terminal compositions with x = 0 and x = 42.5 the pre-exponential factor τ_0 is calculated based on viscosity measurements and derived VFT- parameters of Refs. [36,172] and the newly determined proportionality factor $G_{\tau-\eta}$. The underlying methodology was applied and is discussed in detail in Ref. [28], being based on a Maxwell-type equation (compare eq. (2.30)):

$$\eta(T) = G_{\tau-\eta}\,\tau(T) \qquad (6.2)$$

---

[27] For the given conditions of similar heating and cooling ($\dot{T}_H = \dot{T}_C$) the onset of the glass transition in heating $T_{g,on}$ is coinciding with the fictive temperature T_{fic} in cooling.
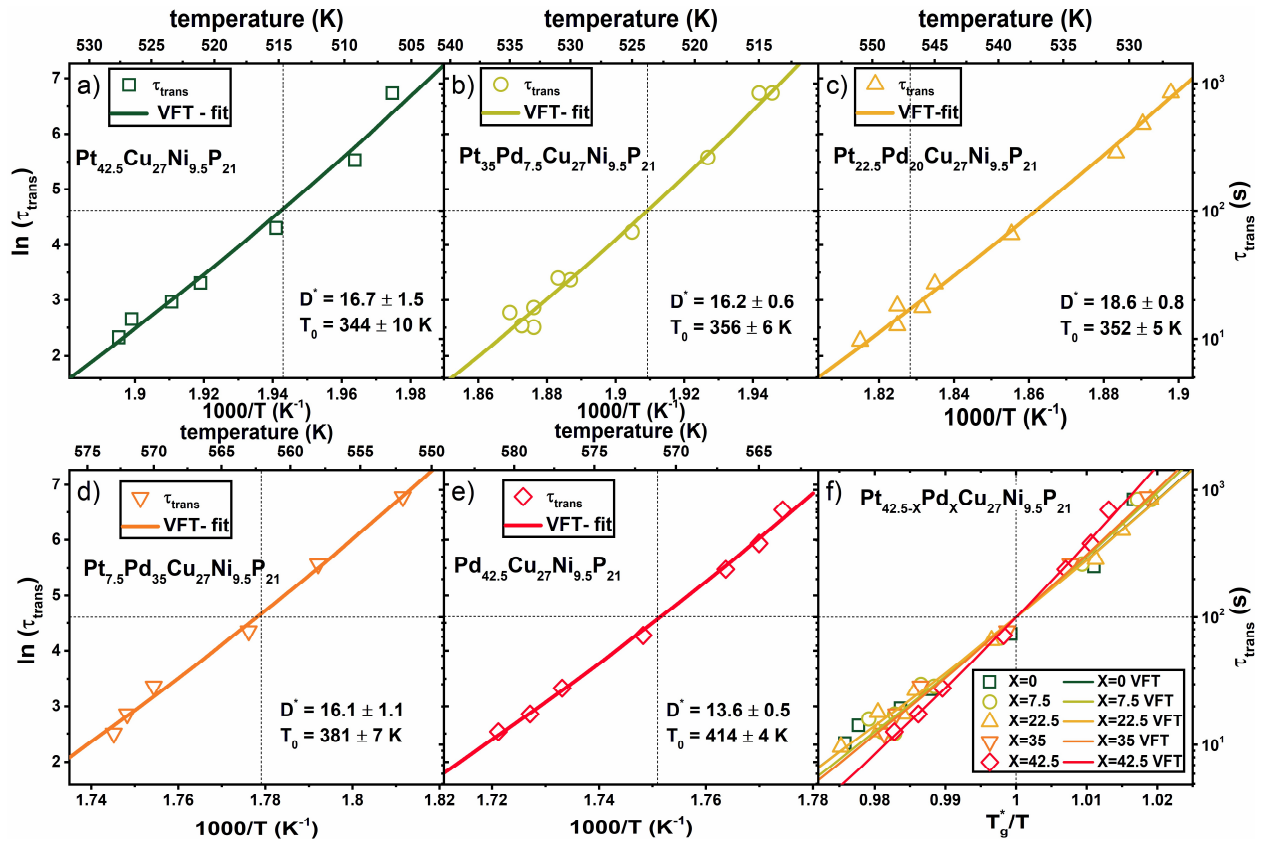
Figure 6-2: Natural logarithm of the transition times as a function of inverse temperature obtained by the measurements of the shift of the thermal glass transition for the compositions $Pt_{42.5-x}Pd_xCu_{27}Ni_{9.5}P_{21}$ with a) x = 0, b) x = 7.5, c) x = 20, d) x = 35 and e) x = 42.5. In each dataset a respective VFT-Fit and the resulting fitting parameters are provided. In part f) all transition times and respective VFT-fits are shown on a T_g^*-nominated inverse temperature scale in an Angell-plot for better graphical illustration of the fragility.

The intermediate τ_0 values are calculated based on interpolated proportionality factors $G_{\tau-\eta}$, that are weighted with the respective Pt and Pd content [$G_{\tau-\eta} = $ (Pt-content/42.5)·$G_{\tau-\eta}$($Pt_{42.5}Pd_0$) + (Pd-content/42.5)·$G_{\tau-\eta}$($Pt_0Pd_{42.5}$)]. An overview of the used constants and resulting fitting parameters is provided in Table 6-2. For a better graphical comparison, the data are normalized by T_g^*, which per convention is the temperature, where a transition time of 100 s is found (Figure 6-2f)). From this so-called Angell-plot, one can directly read off that the Pd-alloy is the kinetically most fragile liquid within the system.
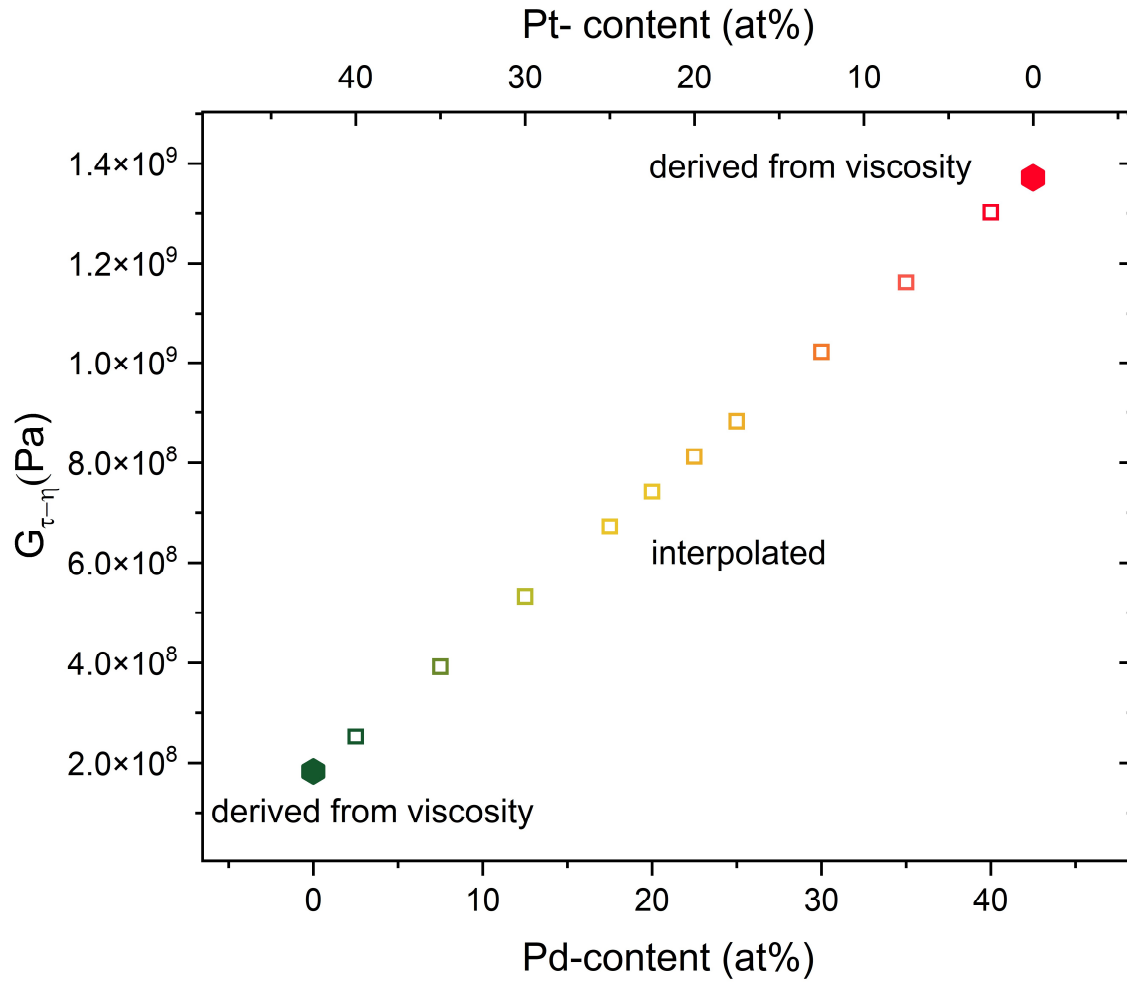
Figure 6-3: Proportionality factor $G_{\tau-\eta}$ for the transition times from $T_{g\text{-shift}}$ measurements as a function of Pd-content for the $Pt_{42.5-x}Pd_xCu_{27}Ni_{9.5}P_{21}$ system . The boundary compositions with x = 0 and x = 42.5 is calculated from viscosity measurements according to Ref. [146]

Table 6-1: Summary of VFT fitting parameters and constants used for the fitting of dynamic data from MDSC measurements. The τ_0 parameter is fixed in the fits. The error describes the fitting error.

Pt content (at%)	Pd content (at%)	$G_{\tau,d\text{-}\eta}$ (MDSC) (Pa)	τ_0 (MDSC) (s)	D* (MDSC)	T_0 (MDSC) (K)
42.5	0	3.74×10^8	1.07×10^{-13}	15.6 ± 0.4	352 ± 3
40	2.5	4.65×10^8	8.60×10^{-14}	15.4 ± 0.4	356 ± 3
35	7.5	6.47×10^8	6.18×10^{-14}	16.1 ± 0.4	355 ± 3
30	12.5	8.29×10^8	4.83×10^{-14}	17.0 ± 0.5	353 ± 4
25	17.5	1.01×10^9	3.96×10^{-14}	17.2 ± 0.3	357 ± 2
22.5	20	1.10×10^9	3.63×10^{-14}	16.9 ± 0.9	362 ± 6
20	22.5	1.19×10^9	3.35×10^{-14}	17.3 ± 0.4	362 ± 3
17.5	25	1.28×10^9	3.12×10^{-14}	16.2 ± 0.7	372 ± 5
12.5	30	1.47×10^9	2.73×10^{-14}	15.9 ± 0.3	381 ± 2
7.5	35	1.65×10^9	2.43×10^{-14}	15.1 ± 0.3	393 ± 2
2.5	40	1.83×10^9	2.19×10^{-14}	14.0 ± 0.3	408 ± 3
0	42.5	1.92×10^9	2.08×10^{-14}	14.8 ± 0.3	404 ± 2

Table 6-2: Summary of VFT fitting parameters and constants used for the fitting of kinetic data from T_g-shift measurements. The τ_0 parameter is fixed in the fits. The error describes the fitting error.

Pt content (at%)	Pd content (at%)	$G_{\tau,t\text{-}\eta}$ (T_g-shift) (Pa)	τ_0 (T_g-shift) (s)	D* (T_g-shift)	T_0 (T_g-shift) (K)
42.5	0	1.82×10^8	2.19×10^{-13}	16.7 ± 1.5	344 ± 10
40	2.5	2.52×10^8	1.58×10^{-13}	/	/
35	7.5	3.92×10^8	1.02×10^{-13}	16.3 ± 0.8	356 ± 6
30	12.5	5.32×10^8	7.51×10^{-14}	/	/
25	17.5	6.72×10^8	5.95×10^{-14}	/	/
22.5	20	7.42×10^8	5.39×10^{-14}	18.6 ± 0.8	352 ± 5
20	22.5	8.12×10^8	4.92×10^{-14}	/	/
17.5	25	8.82×10^8	4.53×10^{-14}	/	/
12.5	30	1.02×10^9	3.91×10^{-14}	/	/
7.5	35	1.16×10^9	3.44×10^{-14}	16.9 ± 0.9	381 ± 7
2.5	40	1.30×10^9	3.07×10^{-14}	/	/
0	42.5	1.37×10^9	2.92×10^{-14}	13.6 ± 0.5	414 ± 4

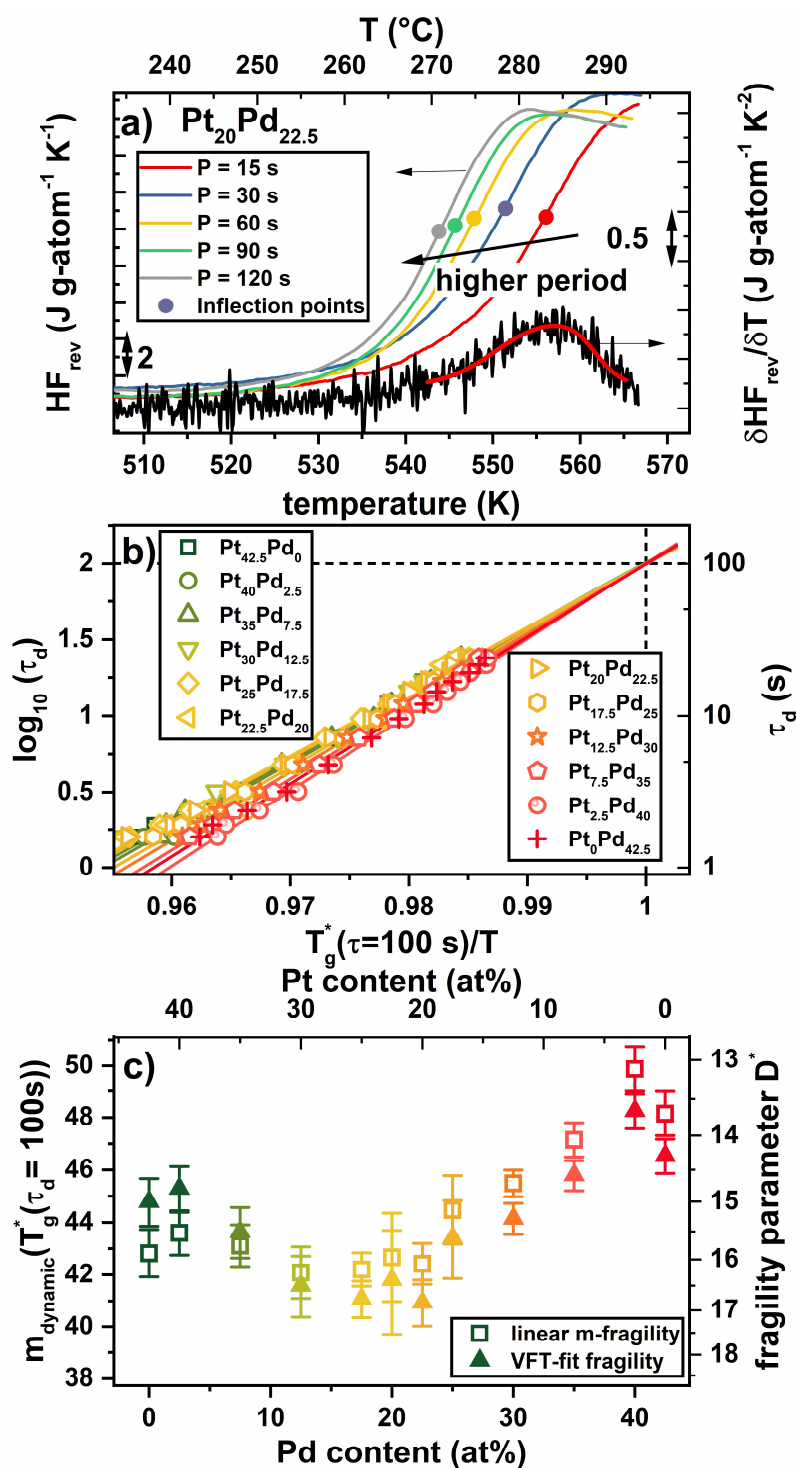## 6.1.2 Frequency Dependence of the Dynamic Glass Transition

Figure 6-4: Results of the modulated DSC measurements :

a) Reversing heat flow obtained by modulated scanning calorimetry at 0.05 K s⁻¹ with different modulation periods P for the alloy $Pt_{20}Pd_{22.5}Cu_{27}Ni_{9.5}P_{21}$. The point of inflection, corresponds to the peak of the derivative of the reversing heat flow with respect to temperature, marking the dynamic glass

transition is highlighted by a point in each curve. To illustrate this the derivative for the measurement with a period of $P = 15$ s is shown in black. Smaller modulation periods lead to a shift of the dynamic glass transition to higher temperatures.

b) Logarithmic plot of the dynamic relaxation time obtained by MDSC measurements as a function of T_g^* ($\equiv T(\tau = 100$ s$)$) nominated inverse temperature for all twelve alloys with the compositions $Pt_{42.5-x}Pd_xCu_{27}Ni_{9.5}P_{21}$ from $X = 0$ to 42.5.

c) m-fragility parameter as a function of Pd-content obtained from linear fits of the dynamic relaxation times from MDSC measurements on the left axis, combined with the D^* fragility parameter obtained by VFT-fitting of the same data.

For quantification of liquid dynamics, MDSC measurements are used to determine the dynamic glass transition temperature $T_{g,dyn}$ as a function of applied modulation period P or frequency f ($f = 1/P$). The influence of the modulation period on the reversing heat flow is depicted in Figure 6-4a). Longer modulation periods lead to a shift of $T_{g,dyn}$ to lower temperatures, reflecting the reduced mobility of the atoms in the liquid with lower temperature and its decreasing ability to react on the external perturbation through the modulation of temperature. The dynamic relaxation times τ_d, which represent the average of the relaxation time spectrum of the liquid at the respective dynamic glass transition temperature for the applied period time P are calculated by

$$\tau_d = \frac{P}{2\pi} \qquad (6.3)$$

To report the results of all twelve examined alloys a normalization on T_g^*, similar to the one used in Figure 6-2f) is chosen, showing the different fragilities of the probed liquids in Figure 6-4b). The data of $Pt_{42.5}Cu_{27}Ni_{9.5}P_{21}$ are taken from Ref. [146]. The data for each alloy are linearly fitted on the logarithmic scale over the normalized inverse temperature, to obtain the classical m-fragility values [192]. All data points are per definition fixed at the point of T_g^* and 100 s. The resulting m-fragilities are summarized in Figure 6-4c) as a function of the respective Pd/Pt content of the liquid. Intermediate compositions with similar Pt and Pd contents show the smallest m-fragility, which means they show the dynamically strongest behavior. For reasons of comparability the data are also fitted with the VFT equation, with the pre-exponential parameter τ_0 being determined similar to that of the kinetic data and according to the methodology of Ref. [146]. An overview on the used constants and resulting fitting parameters

is provided in Table 1. The obtained fragility parameters D^* are also added on the right ordinate with reciprocal spacing of Figure 6-4c), showing the exact same compositional trend as the m-fragility. This further proves the validity of the used methodology of using the VFT-fit in the time domain based on the determination of the pre-exponential τ_0 from viscosity measurements. A detailed discussion on this topic can be found in Ref. [146].
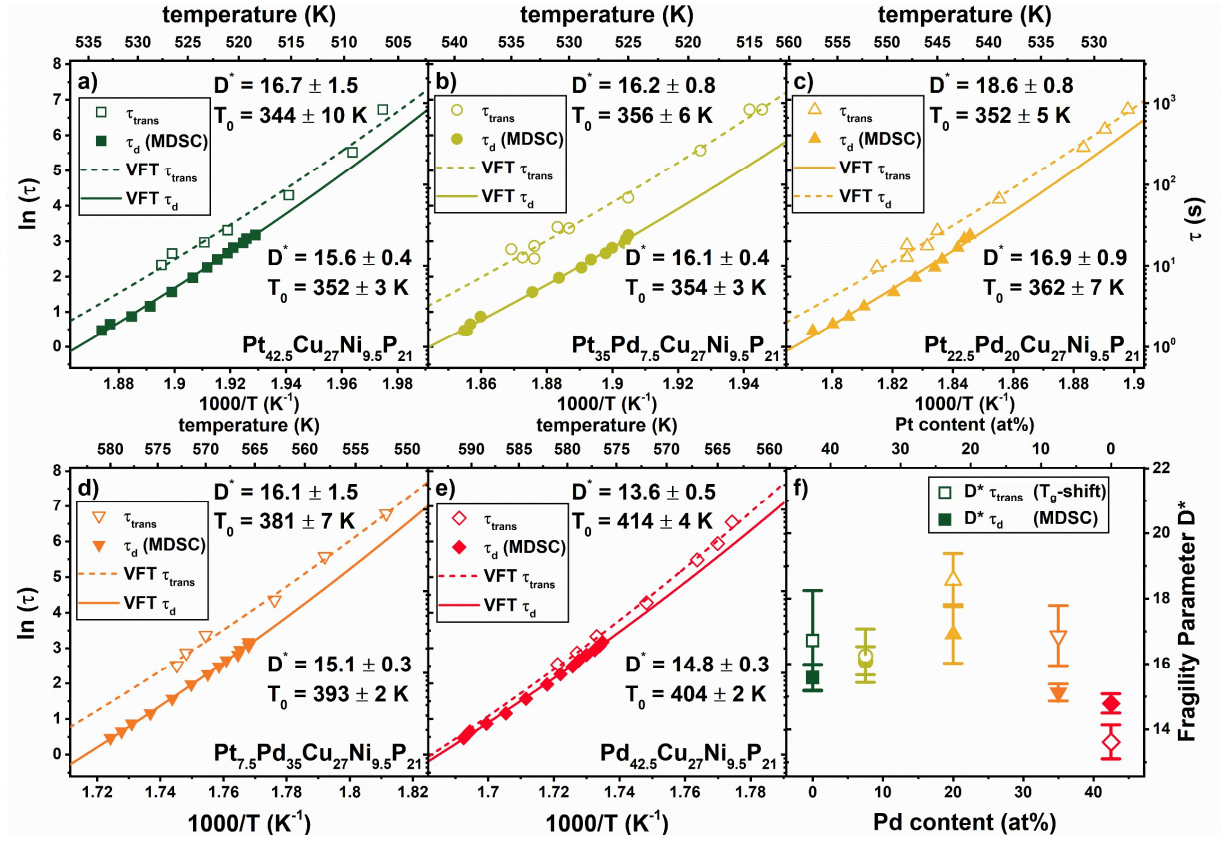

Figure 6-5: Transition and dynamic relaxation times over inverse temperature for the compositions $Pt_{42.5-x}Pd_xCu_{27}Ni_{9.5}P_{21}$ with a) x = 0, b) x = 7.5, c) x = 20, d) x = 35 and e) x = 42.5 with their respective VFT-fits. In section f) the resulting fragility parameters D^* are compared as a function of Pd content.

To compare kinetic and dynamic behavior, both sets of data are depicted in Figure 6-5a)-e) for five alloys with x = 0, 7.5, 20, 35, and 42.5. A clear offset in all alloys can be observed, with the data from dynamics being found to be faster in comparison to the kinetic data. Similar observations of a temporal offset between vitrification/devitrification kinetics and dynamics of the supercooled liquid have been reported in literature [193,194]. Still, the temperature dependence of both processes, described by the fragility parameters in Figure 6-5f), seems to be similar within the error of measurement. The larger timescale of vitrification kinetics compared to dynamics is somewhat expectable. If we take a closer look at the devitrification of a liquid, being the process of regaining equilibrium, it must be connected to the changes of the

equilibrium dynamics. Therefore, one can argue that the devitrification process itself is not expected to be faster than the atomic mobility of the equilibrium system itself at the same temperature in the end. Although both quantities of kinetic and dynamic fragility seem to be identical in their value - underlining their intrinsic connection. It is important to clearly differentiate between them as they ultimately describe different processes.

6.1.3 Description of Fragility in the Viscosity Domain: Creating a Master Curve for Kinetic and Dynamic Behavior

Finally, the similar temperature dependence of the probed relaxation times allows to create a master curve that fits the different observed timescales onto the viscosity domain according to eq. (6.2). In Figure 6-6 the relaxation and transitions times obtained from XPCS, $T_{g\text{-shift}}$ and MDSC measurements are converted into equilibrium viscosity values through their individual proportionality constants $G_{\tau\text{-}\eta}$ for the two boundary compositions of $Pt_{42.5}Cu_{27}Ni_{9.5}P_{21}$ and $Pd_{42.5}Cu_{27}Ni_{9.5}P_{21}$. It shall be noted that the calculation of $G_{\tau\text{-}\eta}$ is based on the VFT-fit obtained through the viscosity measurements. Hence, the actual viscosity data and the respective VFT-fits based on the viscosity measurements are depicted. The construction of such a master curve into the viscosity domain demonstrates the similar temperature dependence of all probed processes with the different techniques. The combination of all the shown techniques further allows to cover a large temperature range and dynamic phenomena of around 5 orders of magnitude.

Further it implies the universality of the measured activation energies for the different methods used to probe the system. This means that it does not matter whether the devitrification, connected to the complete change of the relaxation spectrum or simply an average or somehow weighted portion of the relaxation spectrum is probed at different temperatures. All may yield a good description of the dynamic/kinetic behavior of the system. In particular the good measurement statistics during the XPCS experiment of the Pt-based system allowed to probe the relaxation time on different length scales by measuring at the different wave-vector positions (main peak and pre-peak data is already in the master curve). This particular data from XPCS is shown in Figure 6-7, combined with an inset that shows the variation in the τ_0 VFT-parameter as well as the measured structure factor, which is proportional to the scattered intensity, as a function of the probed wave-vector. All data from the different length scales can be well described by the macroscopic fragility parameters from the viscosity measurements.
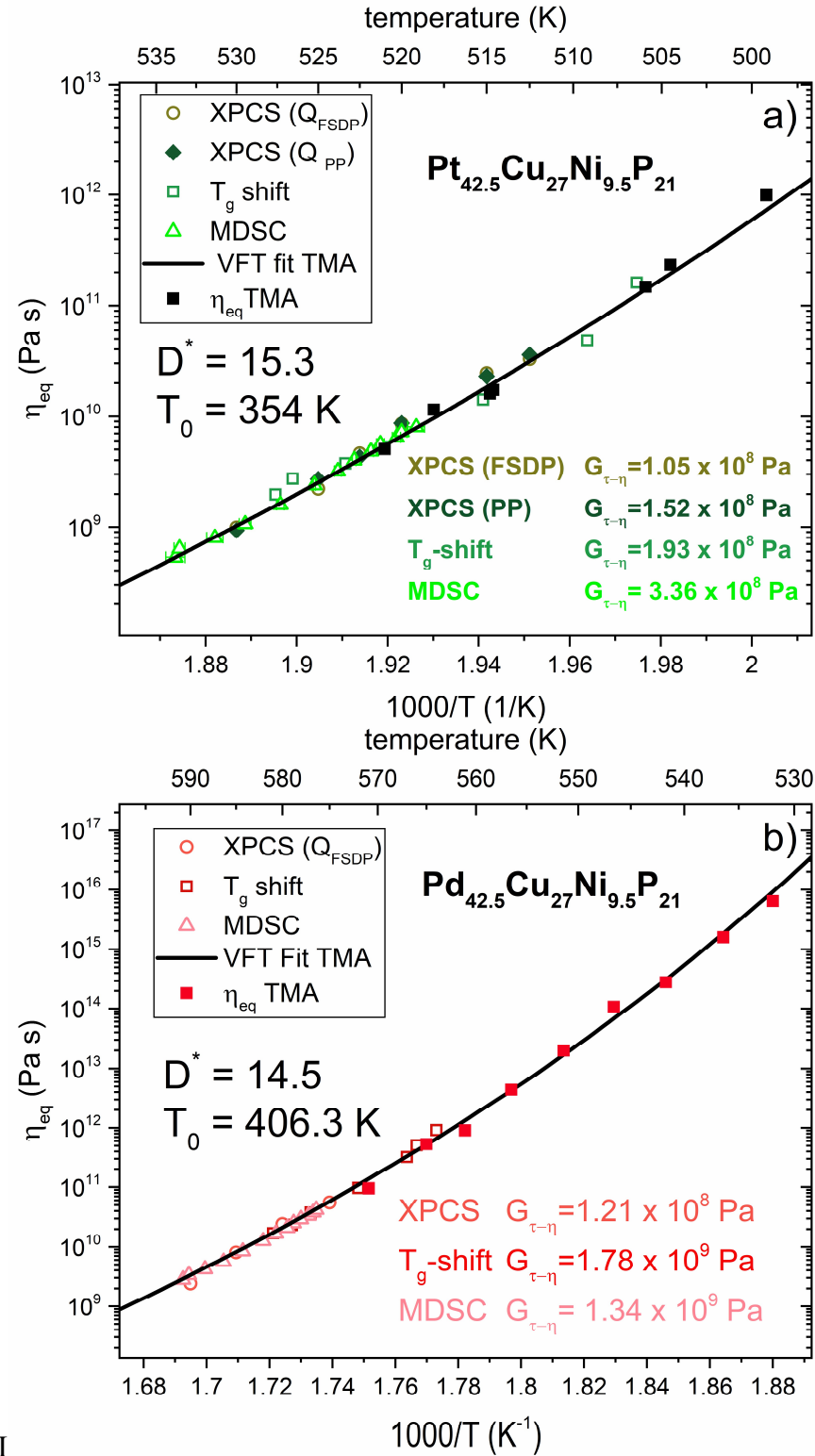
Figure 6-6: Equilibrium viscosities as a function of inverse temperature determined from relaxation and transition times from different techniques for a) Pt$_{42.5}$Cu$_{27}$Ni$_{9.5}$P$_{21}$ and b) Pd$_{42.5}$Cu$_{27}$Ni$_{9.5}$P$_{21}$. The kinetic data from T$_g$-shift measurements are combined with dynamic data of MDSC, XPCS [172] and actual viscosity measurement from 3-point beam bending in TMA (Refs. [36] and [172]). The method-specific proportionality factors lead to a good agreement of the data with the temperature dependence and fragility parameters determined from the VFT-fitting of the TMA data.

The basic fact that these similar activation energies are observable on the different length scales can be explained by several reasons. The most simple would be the limited variation of length scale as well as the limited amount of data, being not sufficient to maybe describe the minuscule variations in the activation energies mirroring the heterogeneity of the deeply supercooled liquid [103,195]. However, if the measurements do indeed point towards the uniformity of the activation energy spectrum this could somehow hint towards the often described fractal nature of the structure of these deeply undercooled liquids[196].
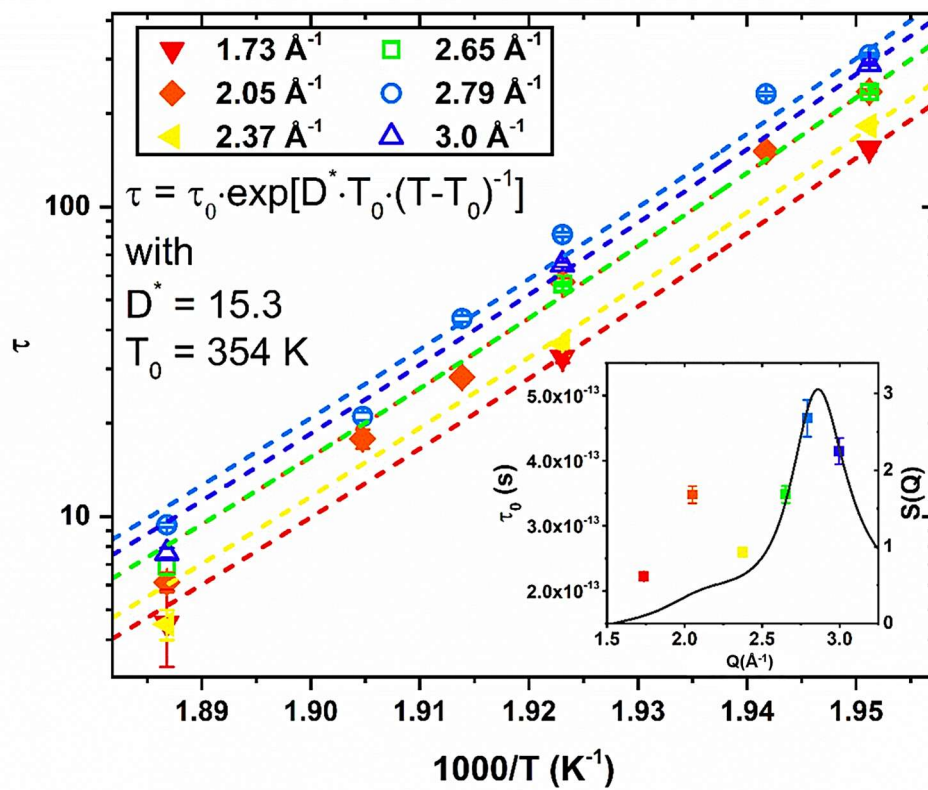

Figure 6-7: Relaxation times over inverse temperature of Pt-liquid at various wave-vectors . The dashed lines represent VFT fits using D* and T_0 parameters obtained from macroscopic viscosity measurements from Ref. [36], keeping τ_0 , the minimal relaxation time at infinite temperature, an open fitting parameter. At all wave-vectors the system is showing a good agreement to the macroscopic fragility parameter. The variation of τ_0 as a function of Q is provided in the inset. τ_0 is following the profile of the total structure S(Q), which is also included in the inset.

6.2   Thermodynamic Fragility

Over the years the fragility model was further extended from its purely kinetic and dynamic point of view to also include thermodynamic aspects. Based on the Adam-Gibbs model, a concept of thermodynamic fragility was derived. The model allows to relate viscosity, a dynamic property, to the configurational entropy of the liquid, which is itself a thermodynamic property [62,197]. A more detailed description is provided in section 2.2.2..

Taking a closer look at the thermodynamics of the PtPdCuNiP system, a smaller jump of the specific heat capacity at the glass transition in conjunction with a shallower change of the configurational entropy during cooling with rising Pd content is reported in Publication I, suggesting an increasingly strong behavior for compositions with higher Pd-content [21]. In the context of the reported fragile behavior of $Pd_{42.5}Cu_{27}Ni_{9.5}P_{21}$ and compositionally close alloys (e.g. $Pd_{43}Cu_{27}Ni_{10}P_{20}$) [198–200], this finding was already unexpected and seemingly contradictive and partially motivated the detailed study of the kinetic and dynamic fragility. The kinetic/dynamic fragilities now available allow for a detailed comparison. Hence, the inverse fragility parameter $1/D^*$ and the difference in heat capacity between the liquid and the crystalline mixture at the glass transition, normalized to the glass transition temperature $\Delta c_p^{l-x}(T_g)/T_g$ are reported as a function of Pd/Pt content in Figure 6-8a). The quantity $\Delta c_p^{l-x}(T_g)/T_g$ describes the rate of change of the excess entropy ΔS^{l-x} ($d\Delta S^{l-x}/dT \mid_{T=Tg} = \Delta c_p^{l-x}/T_g$, compare eq. (2.32)), which itself is assumed proportional to the change of configurational entropy. Therefore it can be used as a measure of the thermodynamic fragility [36]. A detailed reasoning and argumentation on the connection between excess entropy and configurational entropy can be found in Refs. [21,36]. Due to its different mathematical definition (higher values imply more fragile behavior), the fragility parameter D^* is plotted on a reciprocal scale.
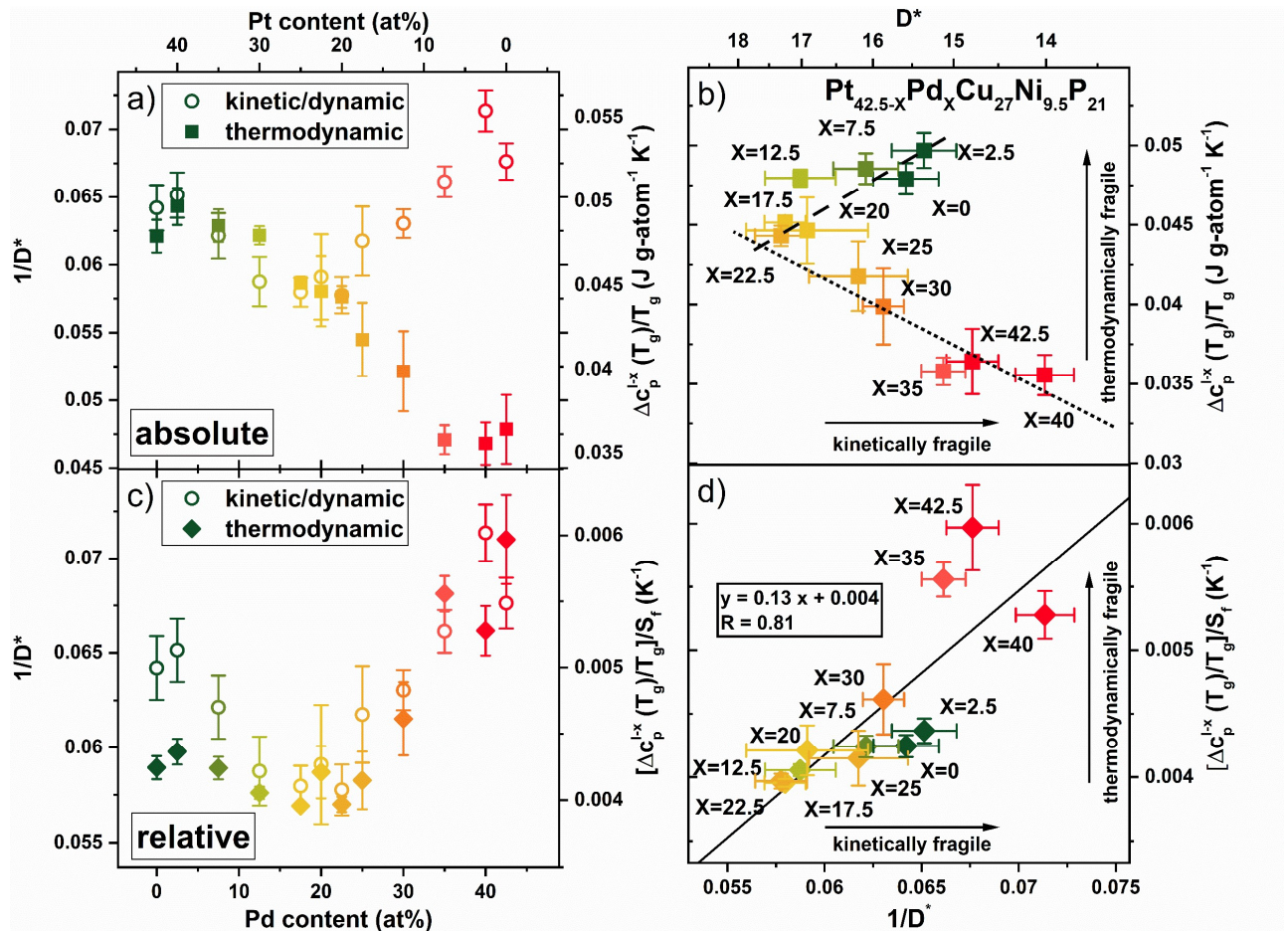
Figure 6-8: Comparison of kinetic/dynamic fragility with thermodynamic properties :

a) Inverse fragility parameter $1/D^*$ (left axis) as a measure of kinetic fragility and T_g-normalized jump in heat capacity at T_g as a total measure of the change in configurational entropy (right axis) as a function of Pd/Pt content of the $Pt_{42.5-x}Pd_xCu_{27}Ni_{9.5}P_{21}$ liquids

b) Scatter Plot of the T_g-normalized jump in heat capacity at T_g over the inverse of the kinetic fragility parameter D^* of the different $Pt_{42.5-x}Pd_xCu_{27}Ni_{9.5}P_{21}$ liquids. A good correlation of the absolute change in configurational entropy and kinetic fragility is found until a Pd content of ~20 at%. At higher Pd contents an inverse trend of kinetically more fragile and smaller entropic changes are observed.

c) Inverse fragility parameter $1/D^*$ (left axis) as a measure of kinetic fragility and T_g-normalized jump in heat capacity at T_g normalized on the entropy of fusion as a measure of the relative change in configurational entropy (right axis) as a function of Pd/Pt content of the $Pt_{42.5-x}Pd_xCu_{27}Ni_{9.5}P_{21}$ liquids

d) Scatter Plot of the T_g-normalized jump in heat capacity at T_g normalized to the entropy of fusion over the inverse of the kinetic fragility parameter D^* of the different $Pt_{42.5-x}Pd_xCu_{27}Ni_{9.5}P_{21}$ liquids. A better correlation of relative changes of entropy and kinetic fragility is found in comparison to the absolute changes.

In Figure 6-8a) a diverging trend, starting at the intermediate compositions becomes obvious. For a better comparison of the kinetic/dynamic and thermodynamic data, a scatter plot of both quantities is provided in Figure 6-8b). Here, the $\Delta c_p^{l-x}/T_g$ is plotted as a function of $1/D^*$, so a more fragile behavior in both parameters is oriented in positive direction of abscissa and ordinate. For the scattering plot, a good agreement between both quantities is given if the data can be fitted by a linear function with a positive slope. Until the intermediate concentration of 20 at% Pd the dashed line shows that the trend of the thermodynamic data towards a smaller $\Delta c_p^{l-x}(T_g)/T_g$, reflecting to a stronger behavior, agrees to the kinetic/dynamic behavior. In contrast, beyond the 20 at% of Pd an increasingly more fragile behavior is observed, while the system becomes thermodynamically stronger. Here the behavior can be described by the dotted line with a negative slope, underlining the unexpected trend in the scatter plot. Now the question arises whether the thermodynamic or kinetic/dynamic estimations of fragility are containing errors or are misinterpreted. With the kinetic and dynamic fragility data being obtained by two independent measurements, while also being in line with the reported fragile behavior of the Pt and Pd-rich systems [36,197–201], we assume the determined kinetic/dynamic fragility to be accurate and least prone to error. Additionally, since the original fragility concept is based on dynamic and kinetic properties, we want to use these data as a base for the following discussion. In this context, the apparent anomalous thermodynamic behavior of the Pd-rich liquids needs to be resolved.

The first possible resolution for the failure of the correlation between thermodynamics and kinetics could be found in the inadequacy of the assumption of the changes in excess entropy being representative for the changes in configurational entropy. The main flaw in this assumption could stem from different contributions of the vibrational entropy of liquid and crystal. As we observe a stronger than expected behavior in the Pd-based system, the actual change in configurational entropy would have to be bigger than observed. Hence, the vibrational entropy in the crystalline state would have to be significantly bigger than in the liquid, for the contribution of the configurational entropy to the excess entropy to be underestimated. However, this would have to stand in a clear contradiction to recent studies by Fultz et al., that revealed similar vibrational entropies in the crystalline and liquid state for Zr-based metallic glasses [60]. Based on their findings the excess entropy between the liquid and crystalline state is dominated by the configurational entropy of the liquid. For an actual scientific proof in the current case a large set of inelastic neutron scattering (INS) experiments would be needed to quantify the vibrational entropies of the liquid and crystalline states.

One thing that stands out in the Pt/Pd system is the fact that the melting enthalpies and entropies are changing tremendously with Pt/Pd content (compare Figure 6-9). The Pd-rich alloys possess a much smaller entropy of fusion of 6.1 J g-atom^{-1} K^{-1} compared to the Pt-rich alloys of 11.3 J g-atom^{-1} K^{-1}. In units of the gas constant, R, the Pd alloy has an entropy of fusion of ~0.73 R and the Pt alloy an entropy of fusion of ~1.36 R, , which is suggesting that the enthalpy and entropy of the Pd-rich liquids are much smaller than those of the Pt-rich liquids (compare Figure 6-9 and Ref. [21]). According to Richard's rule, pure metals are assumed to have melting entropies of around 9.2 J g-atom^{-1} K^{-1} (= 1.2 R) [202,203], which means that Pt shows slightly higher values, whereas for the Pd-rich liquids it seems to be outstandingly small. Therefore, if these significant changes can be traced back to different absolute entropic levels of the liquid state, normalizations are needed to account for it. The idea of different entropic levels is further supported by presumable structural differences of their liquid states suggested by an earlier X-ray diffraction study [204]. It proposed the occurrence of different structural motifs, trigonal prisms in Pt and a larger fraction of icosahedra in Pd, with the latter leading to a strong icosahedral short-range order, fitting the picture of a significantly small entropic level of the Pd-rich liquid. All this suggests the necessity of a normalization of the enthalpic $(dH^{l-x}/dT|_{T=Tg} = \Delta c_p^{l-g}(T_g))$ and entropic $(dS^{l-x}/dT|_{T=Tg} = \Delta c_p^{l-g}(T_g)/T_g)$ changes.

In the context of thermodynamic fragility, similar normalizations on entropy and enthalpy are reported in literature. There, the necessity of normalization was obtained from random first order transition theory (RFOT) that was used to derive the thermodynamic equivalent of kinetic fragility [205,206]. Also, in separate attempts to describe the thermodynamic fingerprint of fragility, normalizations on the entropy of fusion are utilized, leading to a so called reduced excess entropy [199,207]. Hence, the relative changes of configurational entropy are rather to be used for a correlation with kinetic fragility.

One approach can be found in a normalization of the entropic changes $\Delta c_p^{l-x}(T_g)/T_g$ to the absolute value of the entropy of fusion $S_f (= H_f / T_{liq})$[28]. This allows a description of the relative instead of the absolute changes in entropy. However, to correctly utilize the entropy of fusion, assumptions need to be made. Most importantly, the entropic levels of the crystalline mixtures

---

[28] It should be noted that the use of the liquidus temperature to derive the entropy of fusion, implies the assumption of thermodynamic equilibrium ($\Delta G^{l-x} = 0$) between the liquid and crystalline phases of the system. However, especially in off-eutectic systems it has to be remembered that this assumption can be worse compared to near-eutectic systems with small melting intervals ($T_{liq}-T_{solidus}$).

with changing Pt and Pd content need to be similar. To review the validity of this assumption it is needed to look at the contributions to the total entropy of the liquid compared to the crystalline mixture. It can be split into a vibrational S_{vib} and a configurational part S_{conf}. With the alloys possessing similar liquidus temperatures [21], the difference in the vibrational term can be assumed similar in a first approximation. Nevertheless, the configurational entropy of the crystalline mixtures may differ. In a first order approximation, the configurational entropy of the crystal is determined by the entropy of mixing and thus mostly influenced by the number of components and its relative ratios. Taking a closer look at the terminal compositions, both possess the same number of components (four) in similar ratios, which should lead to similar configurational contributions due to the entropy of mixing. Still, it must be noted that in the complex multicomponent systems at hand the final crystallization product is consisting of a multi-phase crystalline mixture.
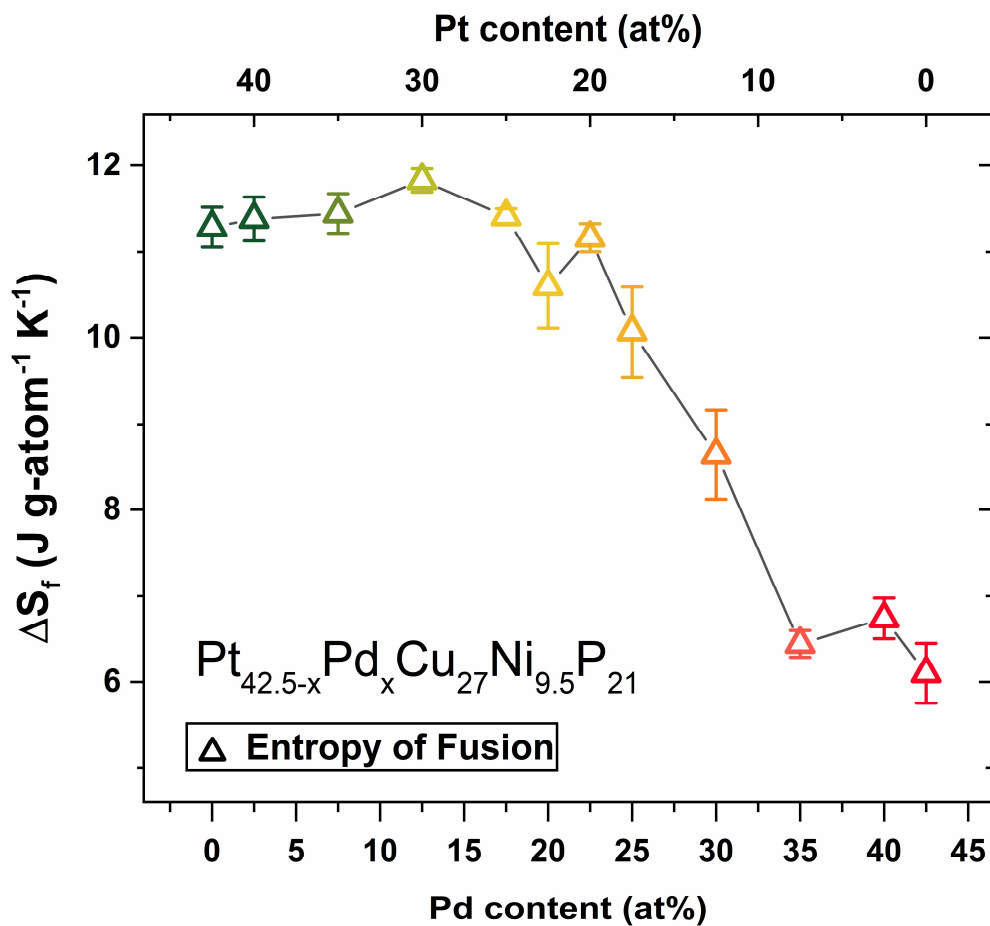

Figure 6-9: Entropy of fusion as a function of Pd content for $Pt_{42.5-x}Pd_xCu_{27}Ni_{9.5}P_{21}$. Data reproduced from Publication I [21].

Based on the provided arguments, we see its use as the best option in the attempt to have a reference state to compare the absolute entropic states of the liquids. Finally, the inclusion of the entropy of fusion considers the tremendous change of the melting entropies (and enthalpies) of the systems, which probably cannot solely be explained by a change of entropy in the crystalline mixtures, but rather by a different entropic level of the liquids. The normalization on the entropies of fusion seems to resolve the mismatch at higher Pd contents and leads to an improved matching trend to the kinetic fragility, depicted in Figure 6-8c) and d). The normalization to the entropy of fusion (Figure 6-8c) now leads to a good match of the trend of kinetic/dynamic and thermodynamic fragility on the Pd rich side as well based on the aforementioned derivations of RFOT theory from Refs. [205,206]. The Pd-rich liquids shows small entropic changes on an absolute scale, but significant changes compared to the already small configurational entropy at the melting point reflecting its kinetically fragile behavior.

6.3   Structural Fingerprints of Fragility

Based on these entropic considerations, large efforts were made to identify a structural fingerprint or signature of fragility in metallic liquids. Numerous studies investigated the temperature evolution of structure in the supercooled liquid state by utilizing high-energy synchrotron diffraction [50,54,79,96,208–211]. For deeply undercooled multicomponent BMG forming liquids, it was shown that structural changes on the medium-range order length-scale (> 8 Å) seem to mirror well the kinetic fragility determined through macroscopic experiments (compare section 2.5.4) [96]. Especially the volume dilation of the 3rd and 4th coordination shell, scaling between 8 and 12 Å, showed strong correlations with kinetic fragility. Nevertheless, detailed knowledge on the microscopic mechanisms that could be summarized to a microscopic structural signature of fragility in metallic melts is still missing. Due to the high complexity of such multicomponent systems, systematic variations of the composition can be a vital tool for case studies. In the following, the structural signature of fragility is evaluated for all alloys in the context of the structural fragility parameter, $m_{str}^{V4\text{-}3}$, proposed by Wei et al. [96].

6.3.1 Structural Fragility Parameter of SCL upon heating

Figure 6-10a) shows the volume dilatation $\varepsilon_{4\text{-}3}$ for a selected number of alloys in the supercooled liquid region upon heating. The solid lines are obtained by linear fitting, averaged from at least three measurements for each alloy obtained in the Linkam THMS600 furnace as well as in the ceramic furnace during different beamtimes (compare section 3.3.2). For reasons of clarity, only data points from a single measurement run, are shown for each selected composition. A variation in slope is seen, with decreasing steepness for increasing Pd contents. The respective results of the averaged structural fragility $m_{str}^{V4\text{-}3}$ are summarized as a function of Pd/Pt content in Fig. 5b). The quantitative correlation between the kinetic m-fragility parameter $m_{kinetic,calc}$ and $m_{str}^{V4\text{-}3}$ described in eq. (2.41), can be read off from the right ordinate of Figure 6-10b). A small value of $m_{str}^{V4\text{-}3}$ means almost no dilation between the 3rd and 4th shell and is connected to a strong behavior and vice versa for fragile liquids. Up to a concentration of about 20 at% Pd, a clear trend towards a smaller $m_{str}^{V4\text{-}3}$ can be observed, suggesting an increasingly strong behavior. At higher Pd contents, the value of $m_{str}^{V4\text{-}3}$ remains almost constant at values around 0.015 and 0.02, with a slight drop to 0.013 for the terminal composition $Pd_{42.5}Cu_{27}Ni_{9.5}P_{21}$, exhibiting the strongest structural fragility behavior.
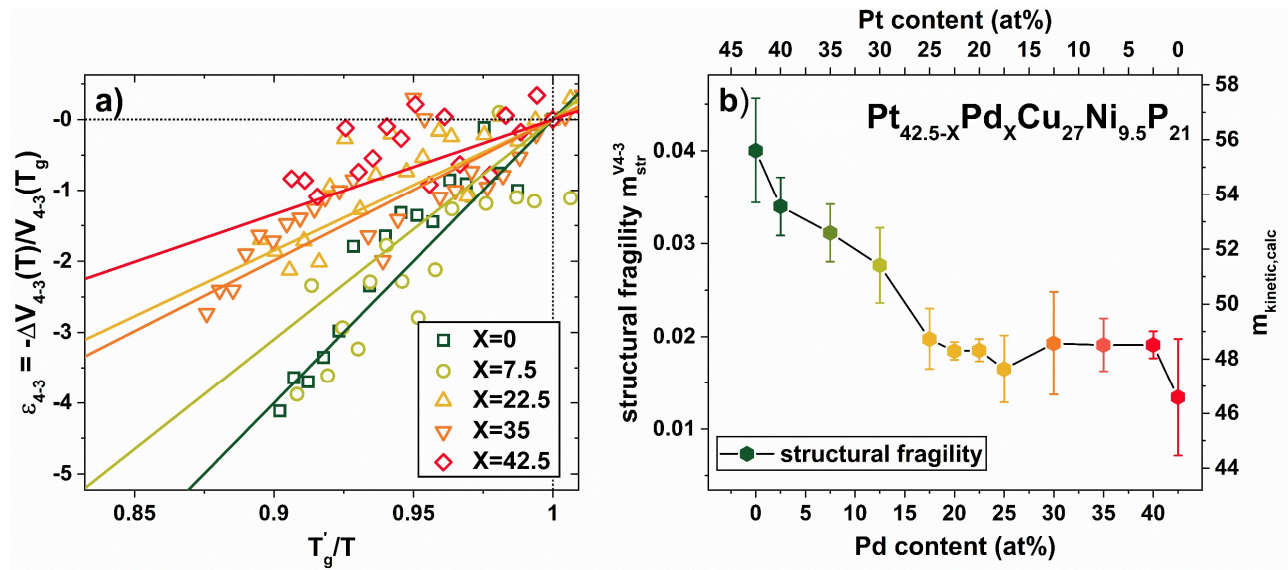
Figure 6-10: The structural fragility model of Wei for $Pt_{42.5-x}Pd_xCu_{27}Ni_{9.5}P_{21}$ liquids :

a) Structural evolution of the $Pt_{42.5-x}Pd_xCu_{27}Ni_{9.5}P_{21}$ liquids with different Pt/Pd contents just above T_g represented by the volume dilation ε_{4-3}, reflecting the change of the local volume V_{4-3} between r_3 and r_4 of the reduced pair distribution function $G(r)$. The lines are based on the average slope from linear fits of all data of the respective alloys, corresponding to the structural fragility parameter m_{str}.

b) Structural Fragility m_{str} as a function of Pd content. All data points are averages of at least three measurements. Based on the empirical correlation of Wei et al. [96] ($m_{kinetic,calc} = (m_{str}^{V4-3}+0.124)/2.95\times10^{-3})$) also the expected kinetic fragility is depicted on the right ordinate.

To investigate the agreement between the structural fragilities are plotted over the inverse kinetic fragility parameter $1/D^*$ determined in the previous sections and the Publications I and II, the empiric correlation of Wei et al.[29] (solid line) and the data from Ref. [96] (compare Figure 2-21) is added and the data of the structural fragility is added. On the Pt-rich side (green to yellow) a good agreement to the correlation is found. However, on the Pd-rich side a failure of the correlation is observed[30]. Here the structural data, with its smaller changes on the MRO length scale suggests a much stronger behavior in comparison to that observed in the kinetic and dynamic measurements. So, the question arises, how this apparent structural strong

---

[29] The original data was plotted with the m-fragilities. Here the actual D^* values from Ref. [96] are used and the correlation is recalculated with $1/D^*$.

[30] It should be noted that the original correlation of Wei et al. in Ref. [96] was established without a Pd-containing system.

behavior in the Pd-rich systems, which is deduced from the small volume dilatations on the MRO length scale, can be understood in light of the fragile appearance observed in its kinetic/dynamic and thermodynamic behavior. Such fragile behavior should rather be reflected by significant changes on the MRO length scale.
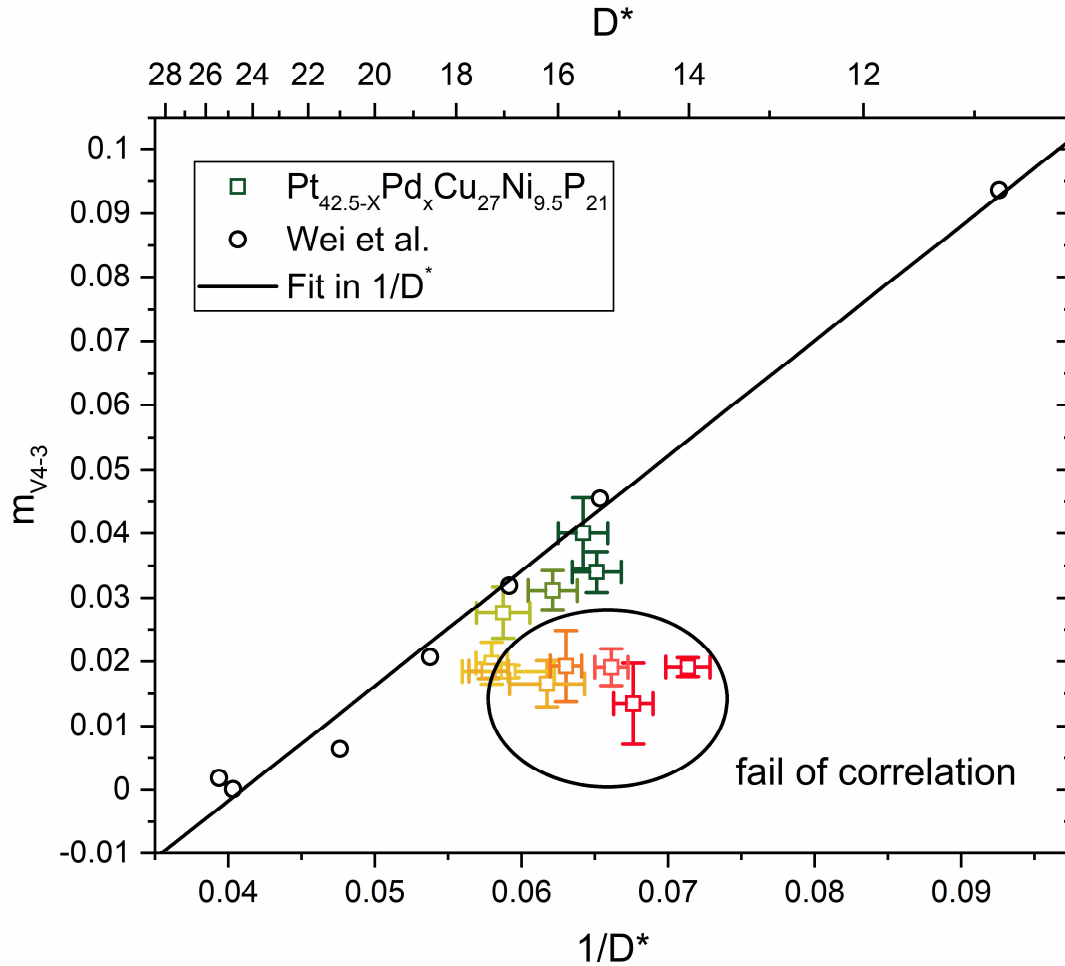

Figure 6-11: Empirical connection of the inverse of the kinetic fragility parameter $1/D^*$ and the structural fragility parameter . Reproduced after Wei et al. [96] with the addition of the fragilities determined for the $Pt_{42.5-x}Pd_xCu_{27}Ni_{9.5}P_{21}$ liquids.

6.3.2 Structural Changes on Different Length Scales

To better understand the apparent misfit of the structural fragility model of Wei et al. for the Pd-rich liquids, a closer and more detailed look on the thermal evolution of structure in the Pt/Pd-Cu-Ni-P systems at different length scales is needed. This is of particular interest as, the topologically equal sub-systems of Pt-rich on the one side and Pd-rich alloys on the other side seem to feature significant differences in their structure. While for the Pt-rich systems a significant degree of medium-range order (MRO) is suggested, manifested mainly in a

structural pre-peak to the first sharp diffraction peak (FSDP) in the total structure factor $S(Q)$ [41], the Pd-rich systems seem to possess a pronounced icosahedral short-range order (SRO) [204]. Ultimately, as mentioned above, previous studies by our group suggest the existence of different dominant structural motifs. The experimental data indicate that for Pt-rich compositions, trigonal prisms are the most prominent structural motifs, and with rising Pd content the number of icosahedra is growing, ultimately becoming the dominant structural unit. The trigonal prisms in the Pt-rich alloys can be seen as the key to form a repeating unit on scattering lengths larger than the FSDP, therefore increasing the degree of MRO significantly. A more detailed discussion on the structure can be found in Publication IV [204]. The goal of this subchapter is to monitor the structure and the thermally induced structural changes in the Pt-Pd-Cu-Ni-P system for peculiarities that might relate to the unexpectedly small changes on the MRO length scale of the Pd-rich systems.

6.3.2.1   Structural analysis in Reciprocal Space:

6.3.2.1.1   Analysis of the FSDP at Room Temperature

The simplest approach to analyze the structure is the monitoring of the first sharp diffraction peak. Following the work of Ma et al [196], already a significant amount of information on the MRO is contained in the FSDP [212]. Therefore, the focus of the structural analysis in reciprocal space is put on the FSDP.
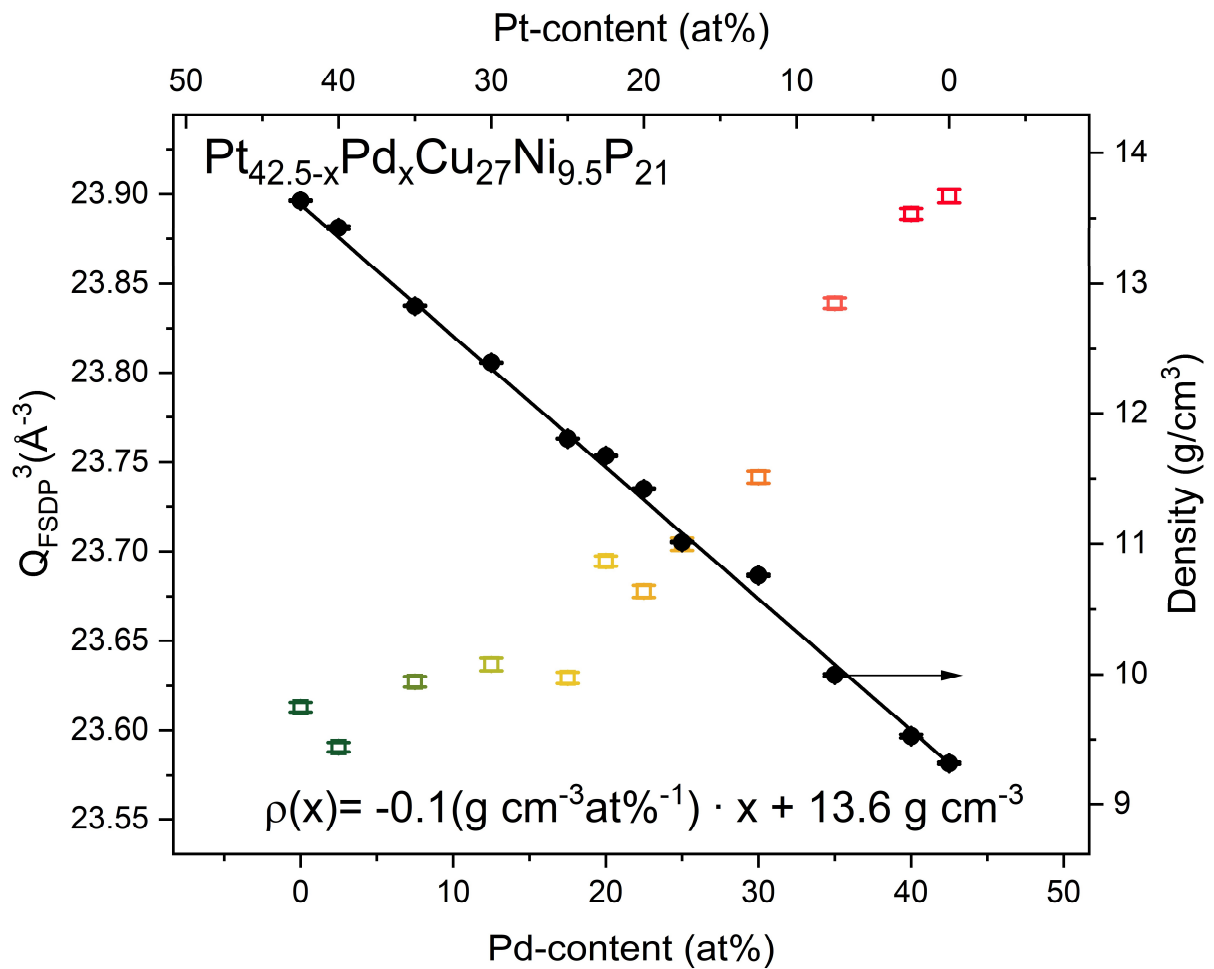

Figure 6-12: Comparison of macroscopic and microscopic density in $Pt_{42.5-x}Pd_xCu_{27}Ni_{9.5}P_{21}$. Average atomic density of the glassy state at room temperature derived from the cube of the position of the first sharp diffraction peak Q_1^3 as a function of Pt/Pd content in $Pt_{42.5-x}Pd_xCu_{27}Ni_{9.5}P_{21}$ in colored open squares. The error bars of the FSDP position correspond to the standard deviation during ten consecutive diffractograms. The diffraction data is combined with macroscopic density measurements in black full circles applying the Archimedean method. The error bars of the density measurements reflect the standard deviation of five consecutive measurements.

In a first attempt, the evolution of the peak position of the FSDP as a function of composition can be analyzed. It allows to study the changes of the average distance between the atomic ensembles. Analogous to considerations by Yavari et al. [92] and eq. (2.36) the cube of the position of the FSDP describes an atomic density. In Figure 6-13, the changes of Q_{FSDP}^3 with changing Pt/Pd content is depicted together with the measured macroscopic density at room temperature of the same alloys. The density was measured using the Archimedes method. Whereas the density is declining with growing Pd content, which can be traced back to the smaller atomic weight of Pd compared to Pt, the atomic density remains quite similar on the Pt-rich side and then increases with Pd. This suggests, especially considering the similar topological size of the Pt and Pd atoms, that the Pd-rich systems are denser packed from an atomistic point of view, while showing a smaller mass-density.

To clearly investigate the effect of packing the packing fraction φ is calculated by [213]:

$$\varphi = V_{atomic}\, n$$

$$(6.4)$$

with V_{atomic} being the weighted mean atomic volume[31] and n being the number density, which is calculated by:

$$n = \frac{\rho\, N_A}{M}$$

$$(6.5)$$

When comparing the actual packing fraction as a function of composition a similar picture to the atomic density from the diffraction data is revealed. The packing fraction rises substantially with increasing Pd-content. The packing fraction is becoming close to that of a bcc crystal, which has a packing fraction of around 68 %. This effective packing is partially represented by the location of the FSDP and aligns with the outstanding glass forming ability of the Pd-rich systems. The high packing fraction also fits the observed small free volume of the glassy state derived from enthalpic considerations of Publication I [21], together with the small driving force towards crystallization.

---

[31] For the atomic radii the values of the ECM model are used, shown in Table 2-1.

Table 6-3: Results from density measurements and molar mass calculation and the related results of average atomic volume and packing fractions assuming the atomic radii from the ECM model.

Pt	Pd	density	molar mass	number density	avg .atomic volume[32]	packing fraction	Q_1
at%	at%	g cm^{-3}	g mol^{-1}	x10^{22} cm^{-3}	Å^3	/	Å^{-1}
42.5	0	13.63	112.146	7.32	8.89	0.65	2.8689
40	2.5	13.43	109.93	7.35	8.89	0.65	2.8680
35	7.5	12.82	105.497	7.32	8.91	0.65	2.8695
30	12.5	12.39	101.064	7.38	8.92	0.66	2.8699
25	17.5	11.81	96.631	7.36	8.93	0.66	2.8696
22.5	20	11.68	94.415	7.45	8.94	0.67	2.8722
20	22.5	11.42	92.198	7.46	8.94	0.67	2.8715
17.5	25	11.01	89.982	7.37	8.95	0.66	2.8726
12.5	30	10.76	85.549	7.57	8.96	0.68	2.8741
7.5	35	10.00	81.116	7.42	8.97	0.67	2.8780
2.5	40	9.53	76.683	7.48	8.98	0.67	2.8800
0	42.5	9.32	74.467	7.54	8.99	0.68	2.8805

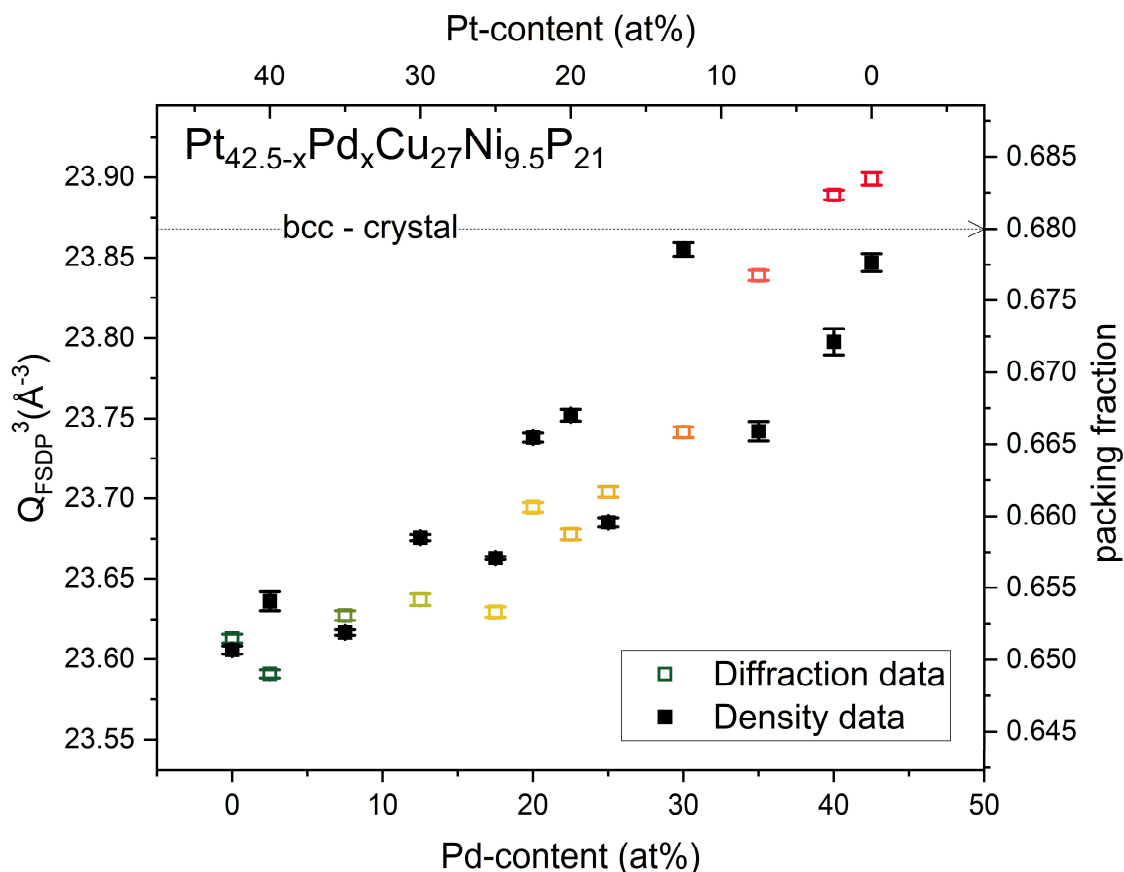[32] based on the average atomic size derived from the ECM model radii, shown in Table 2-1.

Figure 6-13: Packing density at room temperature based on X-ray diffraction experiments .
Average atomic density derived from the cube of the position of the first sharp diffraction peak Q_1^3 as a
function of Pt/Pd content in $Pt_{42.5-x}Pd_xCu_{27}Ni_{9.5}P_{21}$ and the packing fraction derived from the atomic radii
of the ECP model and the measured density from Archimedes method. The error bars of the FSDP
position correspond to the standard deviation during ten consecutive diffractograms. The error bars of
the density measurements reflect the standard deviation of five consecutive measurements.

6.3.2.1.2   Thermal and Compositional Evolution of the FSDP

More information can be gained when studying the evolution of the FSDP as a function of
temperature. In the following, all samples shown have undergone a standardizing treatment of
being heated with 0.33 K s^{-1} into the SCL at a temperature of $T_{g,end}$ + 15 K followed by a
controlled cooling with the same rate down to 50 °C. This treatment creates an equal thermal
history for all samples, while also limiting relaxation events during the second heating, similar
to the treatment for the T_g-shift method (compare section 3.2.3). In Figure 6-14 the evolution
of the FSDP during this heating protocol is shown for the $Pt_{42.5}Cu_{27}Ni_{9.5}P_{21}$ composition. The
depiction demonstrates well the different sensitivity of the parameters describing the evolution
of the shape of the peak. Especially the variation in the differences between the initial fast

quenched as-cast state (0.5 mm thickness translate to an estimated cooling rate of ~4000 K s^{-1} [6]) and the slowly cooled one are significant. Whereas the peak position remains almost unchanged between the different relaxation states of the glasses, the peak height S(Q) and the full-width at half maximum FWHM(Q$_1$) are significantly influenced by it (changes of ~ 2.5%). During heating, a change in slope can be observed in all three quantities, when the glassy state is left and the supercooled liquid state is reached.

In the first heating run, the structural relaxation is visible in all quantities, but to a different degree. The reduction in enthalpy and free volume during the relaxation leads to a densification that results in a shift of Q$_1$ towards higher values. It also results in a higher degree of order that is visible in a growth of S(Q$_1$) and a sharpening of the peak, leading to a decrease in FWHM(Q$_1$). For a better understanding, the calorimetric trace of both the 1st heating (as-cast state) and 2nd heating ("standardized" state) is shown in Figure 6-15, highlighting the different behavior below the glass transition temperature. In particular, this different behavior is characterized by the structural relaxation of the fast quenched as-cast sample marked by a shaded area in Figure 6-15.
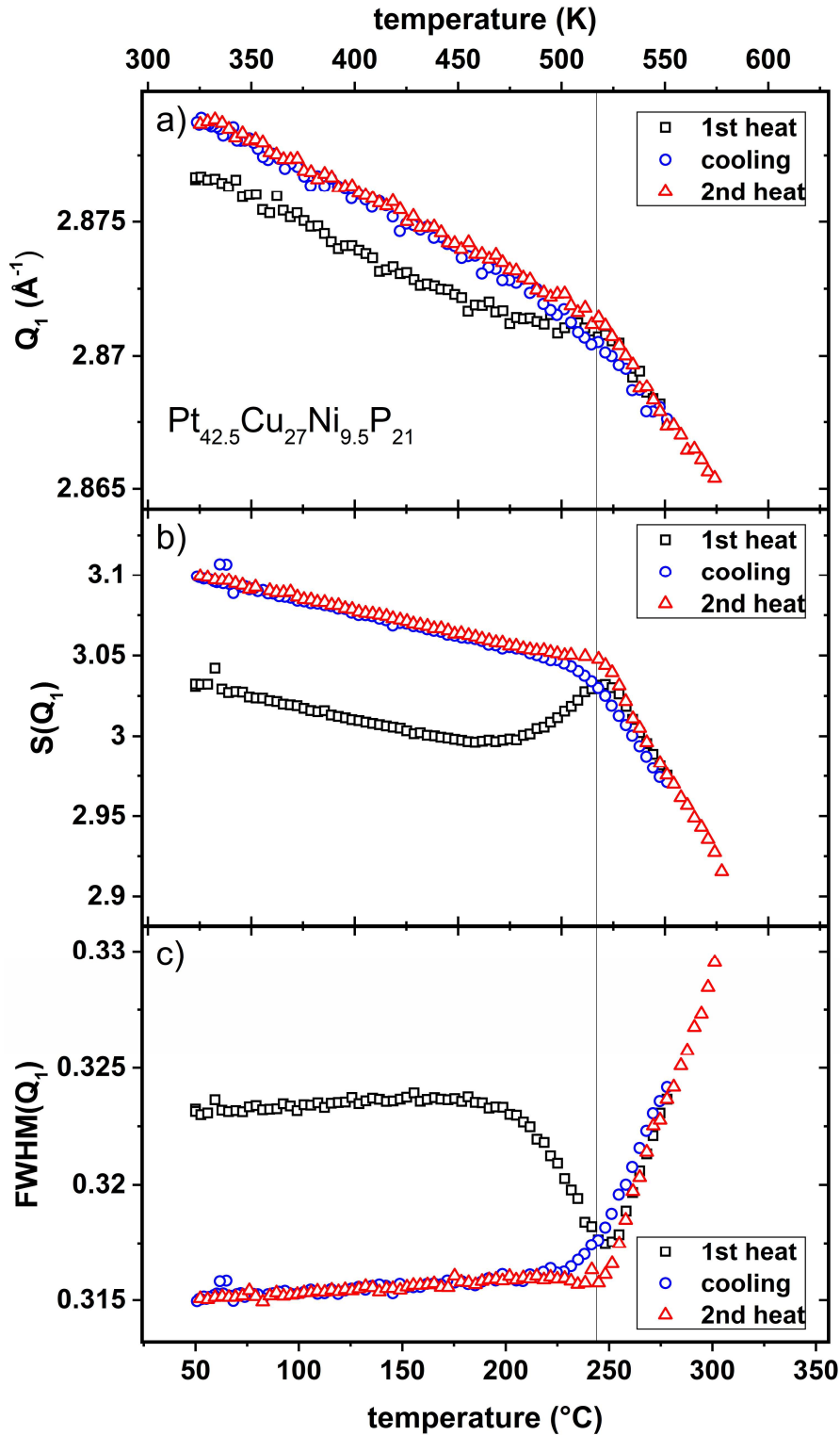
Figure 6-14: Evolution of the first sharp diffraction peak during heating and cooling with 0.33 K s^{-1} in an in-situ high energy synchrotron X-ray diffraction experiment of $Pt_{42.5}Cu_{27}Ni_{9.5}P_{21}$. The shape of the peak is described using the different parameters of a) peak position Q_1, peak height $S(Q_1)$ and full-width at half maximum $FWHM(Q_1)$. An initial heating into the SCL to $T_{g,end}$ +15 K (black) is used to erase the thermal history of the casting (0.5 mm plate), followed by a controlled cooling to 50 °C and a consecutive 2nd heating, until the sample crystallized.
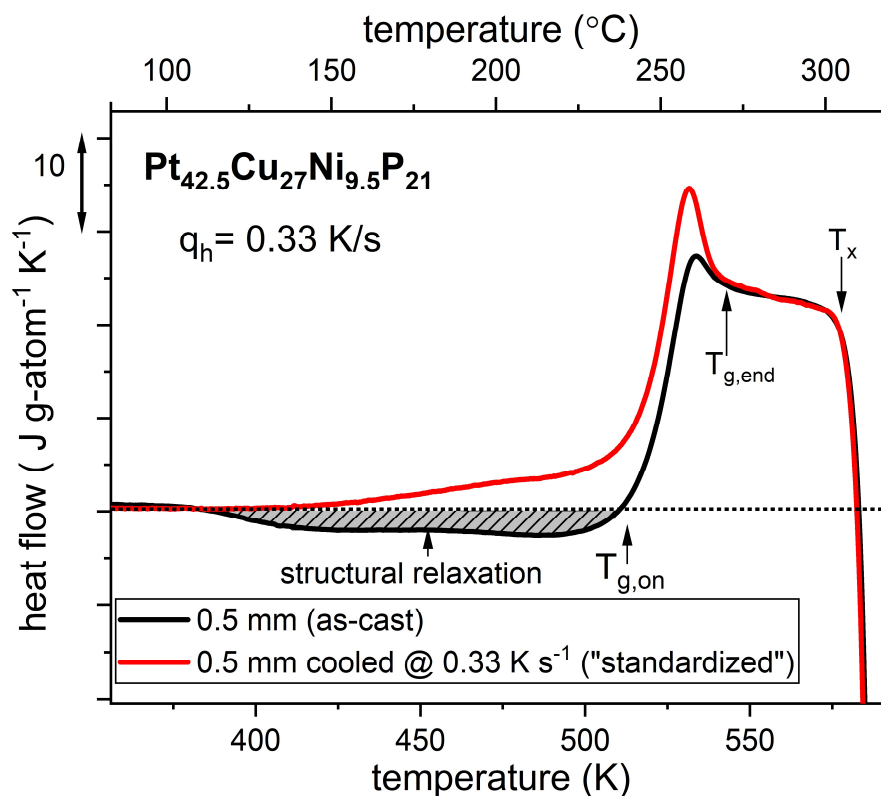
Figure 6-15: Heat flow of 0.5 mm plates of $Pt_{42.5}Cu_{27}Ni_{9.5}P_{21}$ at a heating rate of 0.33 K s^{-1} obtained from differential scanning calorimetry comparing the as-cast and "standardized" state, which was obtained through a defined cooling with -0.33 K s^{-1} from the SCL ($T_{g,end}$+15 K). The shown curves mimic the heating protocol used in the synchrotron study in Figure 6-14. Both states differ significantly in the amount of structural relaxation before the onset of the glass transition (grey area), as well as the enthalpic overshoot before $T_{g,end}$ is reached. For reasons of clarity the cooling curve is left out. The dotted line marks the baseline of zero heat flow, indicating the difference between endo and exothermal processes

For a better understanding, the enthalpic difference between the two states is calculated by integrating the DSC-traces of Figure 6-15. The resulting enthalpic trajectories of both states during heating are depicted in Figure 6-16, combined with the excess enthalpy between the liquid and crystalline state determined from the thermodynamic analysis of Publication I [21]. The excess enthalpy is used to align the integrated heat flow curves in the supercooled liquid state, providing the integration constant that creates the enthalpic offset between both states. The enthalpic description shows nicely the different states of as-cast and standardized sample, as well as the amount of enthalpy relaxation that is occurring during heating. While the exothermal signature of the relaxation is well visible in the structural signal of Figure 6-14, particularly regarding the FWHM, the endothermal signatures in the second heating below the glass transition (starting at around 430 K) are not. The endothermal signatures are possibly related to a β-relaxation process [214–216]. However, together with the enthalpic overshoot or

enthalpy recovery before the equilibration [64], they remain invisible in the structural data. This missing signature could be related to the nature of the relaxation process itself. The β-relaxation process is often associated with the remaining mobility of the smallest and the most mobile atomic species in the glassy system, indicated by similar activation energies of the the β-relaxation process and the hopping of the smallest atoms [217]. In the case of the underlying system, this would be the P atoms, which remain almost invisible in X-ray studies compared with the other constituents (compare Figure 6-30). Thus, assuming that the endothermal process is governed by the motion of the P atoms, suggested for similar Pd-Cu-Ni-P compositions in Ref. [217] it should not be detectable in the structural data (compare to the small impact of the P-containing pair correlations in Figure 6-30).
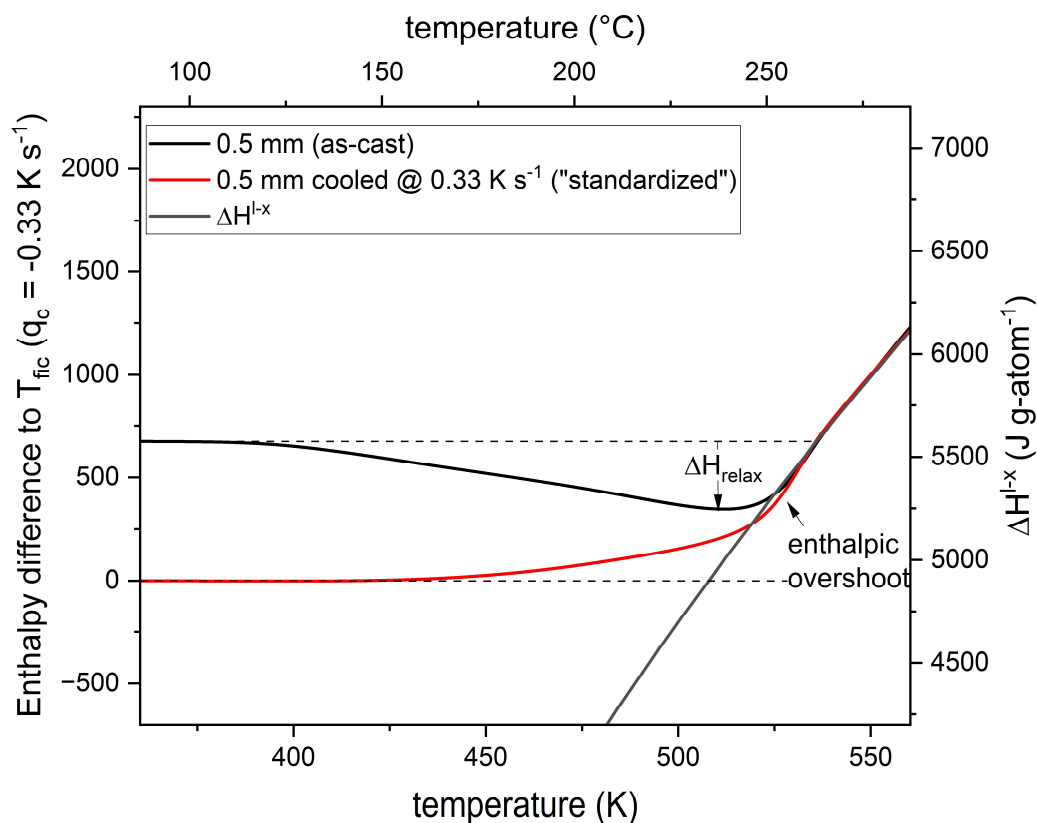
Figure 6-16: Enthalpy of 0.5 mm plates of $Pt_{42.5}Cu_{27}Ni_{9.5}P_{21}$ at a heating rate of 0.33 K s^{-1} obtained from differential scanning calorimetry comparing the as-cast and "standard-treated" state , which was obtained through a defined cooling with -0.33 K s^{-1} from the SCL ($T_{g,end}$+15 K). The shown curves mimic the heating protocol used in the synchrotron study in Figure 6-14. Both states differ significantly in the amount of structural relaxation before the onset of the glass transition (grey area), as well as the enthalpic overshoot before $T_{g,end}$ is reached. For reasons of clarity the cooling curve is left out.

Further comparison of the structural state (the FWHM of the FSDP) created by different cooling or annealing with its enthalpic signature obtained in calorimetry can be found in the Appendix for $Pt_{42.5}Cu_{27}Ni_{9.5}P_{21}$ in Figure 8-5 and Figure 8-6.
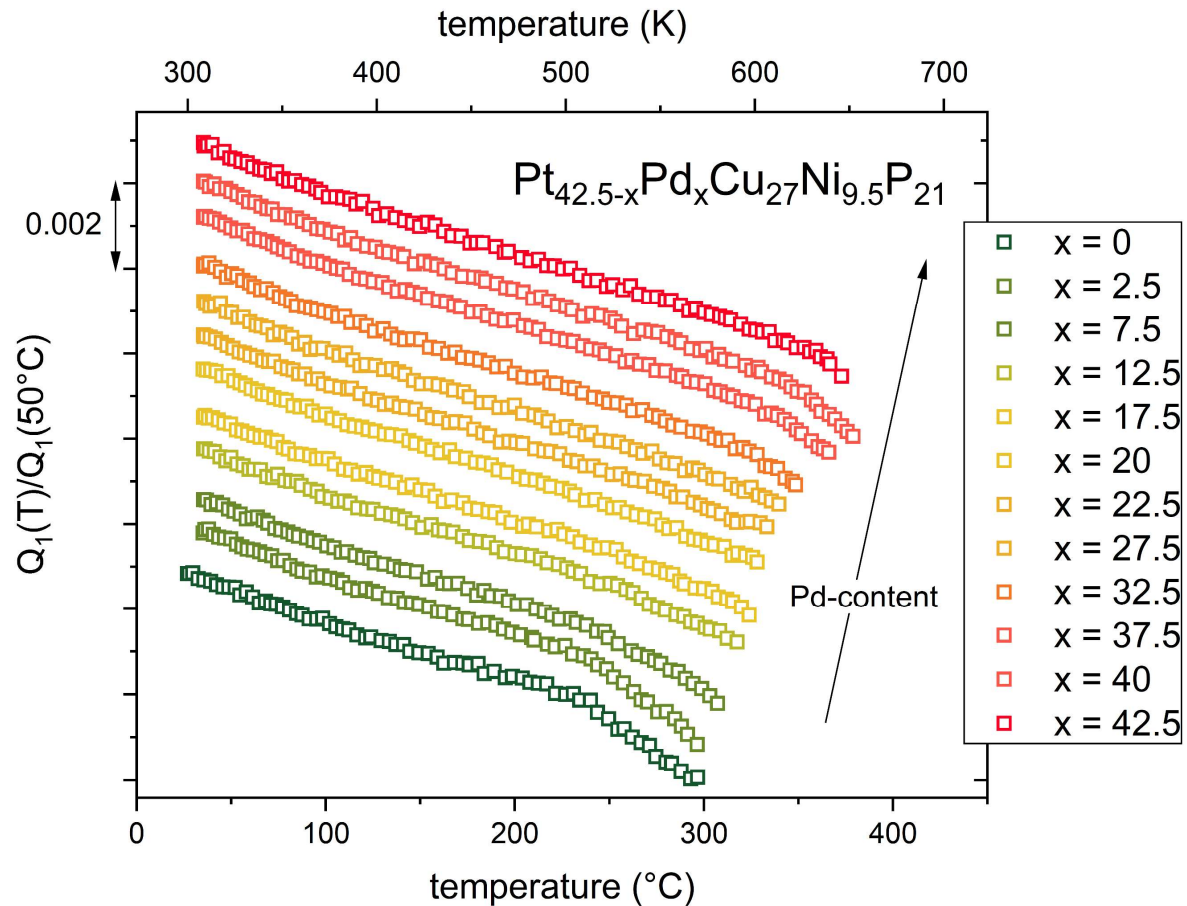
6.3.2.1.3   Thermal Evolution of the Peak Position of the FSDP

Figure 6-17: Relative change of the position of the FSDP of the total structure factor S(Q) as a function of temperature for $Pt_{42.5-x}Pd_xCu_{27}Ni_{9.5}P_{21}$ upon heating with 0.33 K s^{-1}. For all compositions the glassy state created after being cooled by 0.33 K s^{-1} from the supercooled liquid state ("standardized") at a temperature of 50 °C is used as a reference state

In the following section, the thermal evolution of the FSDP for all different Pt/Pd compositions is examined, in particular focusing on the glassy and supercooled liquid state. All following data is recorded from samples in the standardized state that was initially cooled at the same rate that is used to probe it (0.33 K s^{-1}), eliminating relaxation effects (compare 2nd heating of Figure 6-14). For a better comparison, a normalization on the initial state at 323 K/50°C is used. The evolution of the first peak positions, depicted in Figure 6-17, shows a bending at the glass transition temperature for the Pt-rich compositions (compare Figure 6-14). This bending is

typically observed for metallic glasses when they are undergoing the glass transition [92,151,218,219]. However, the difference between the slope in the liquid and glassy state becomes less significant with increasing Pd content, with slight outliers in the compositions with 37.5 and 40 at% Pd. A similar phenomenology, of similar slopes of the glassy and liquid states, has been reported in literature for similar Pd-Cu-Ni-P compositions [37,220]
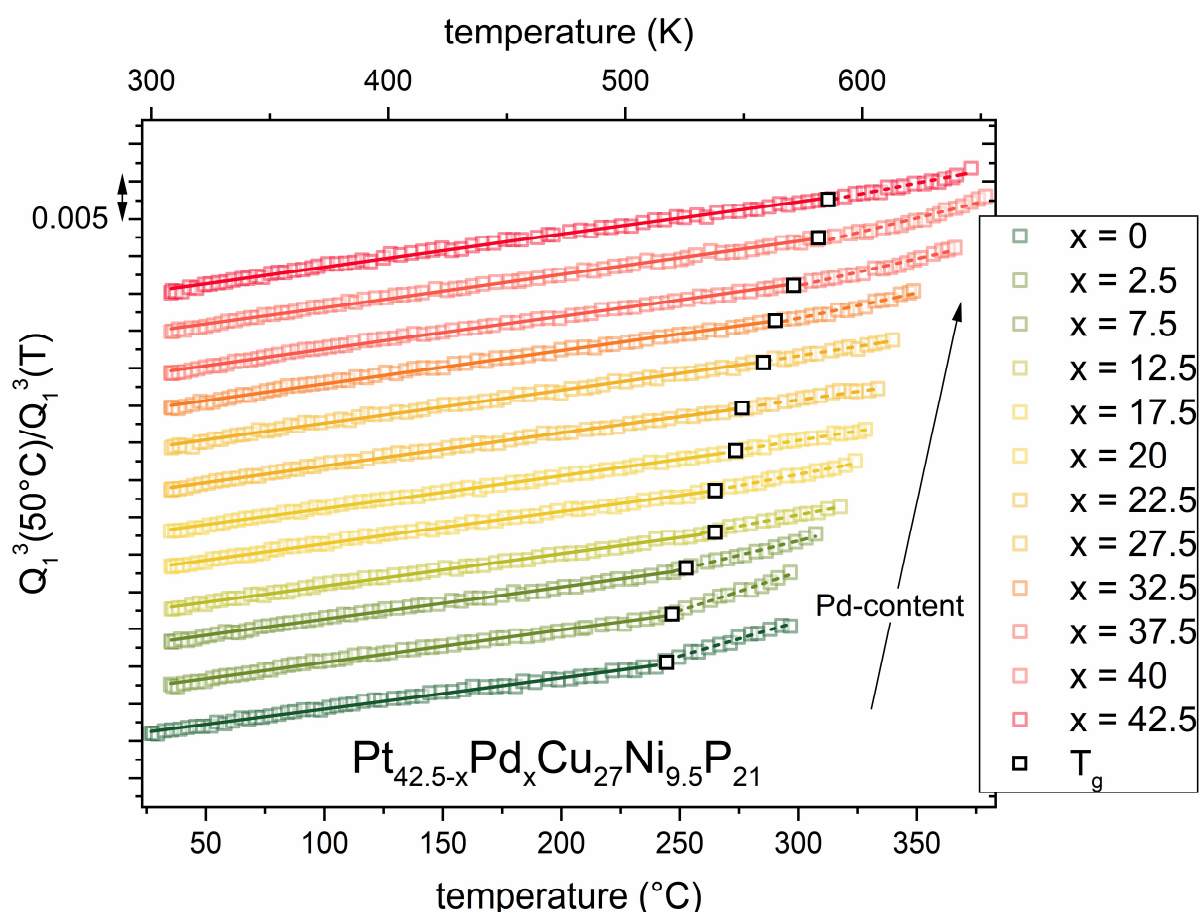

Figure 6-18: Relative change of the inverse cube of the position of the FSDP of the total structure factor $S(Q)$ as a function of temperature for $Pt_{42.5-x}Pd_xCu_{27}Ni_{9.5}P_{21}$ upon heating with 0.33 K s^{-1}. For all compositions the glassy state created after being cooled by 0.33 K s^{-1} from the supercooled liquid state ("standardized") at a temperature of 50 °C is used as a reference state

A more graphical interpretation can be derived from the temperature dependence of the inverse cube of the position of the FSDP. In a first approximation it allows a determination of the thermal expansion coefficient based on eq. (2.36) [92]. For a better distinction between the glassy and liquid data the glass transition temperature and the linear fits of the glassy and liquid state are shown for each composition in Figure 6-18. The results of the linear fits of the glassy

state (a), the supercooled liquid state (b) and the ratio out of both slopes (c) are summarized in Figure 6-19.

In the glassy state, a slight increase of the thermal expansion coefficient from the XRD experiment $\alpha_{th,XRD}$ is observed, reaching a plateau at $\sim 4.4 \ 10^{-5} \ K^{-1}$. The value of the thermal expansion of the $Pt_{42.5}Cu_{27}Ni_{9.5}P_{21}$ determined from the diffraction data $\alpha_{th,XRD} = 4.18 \ 10^{-5} \ K^{1}$ is in reasonable agreement with the value of α_{th} obtained through dilatometry $\alpha_{th,Dil} = 3.95 \ 10^{5} \ K^{1}$ [78] Further similar values of $\alpha_{th,XRD} = 4.21 \ 10^{-5} \ K^{-1}$ are reported for the compositionally similar $Pd_{43}Cu_{27}Ni_{10}P_{20}$ composition [220]. With respect to the slope in the liquid state, a different trend is observed. The smallest changes are located in the intermediate composition with almost equal Pt/Pd. However, the evolution of Q_1 in the SCL cannot be interpreted as reliable thermal expansion coefficients, as the assumption of a static system [92], that is not undergoing structural changes may not be valid in the SCL region anymore. To account for the relative changes, the ratio out of both slopes of Q_1 in the glassy and the SCL state are depicted in Figure 6-19. The V-like shape of this ratio as a function of Pd content is partially reminiscent of the course of the fragility over Pt/Pd content (compare Figure 6-8).
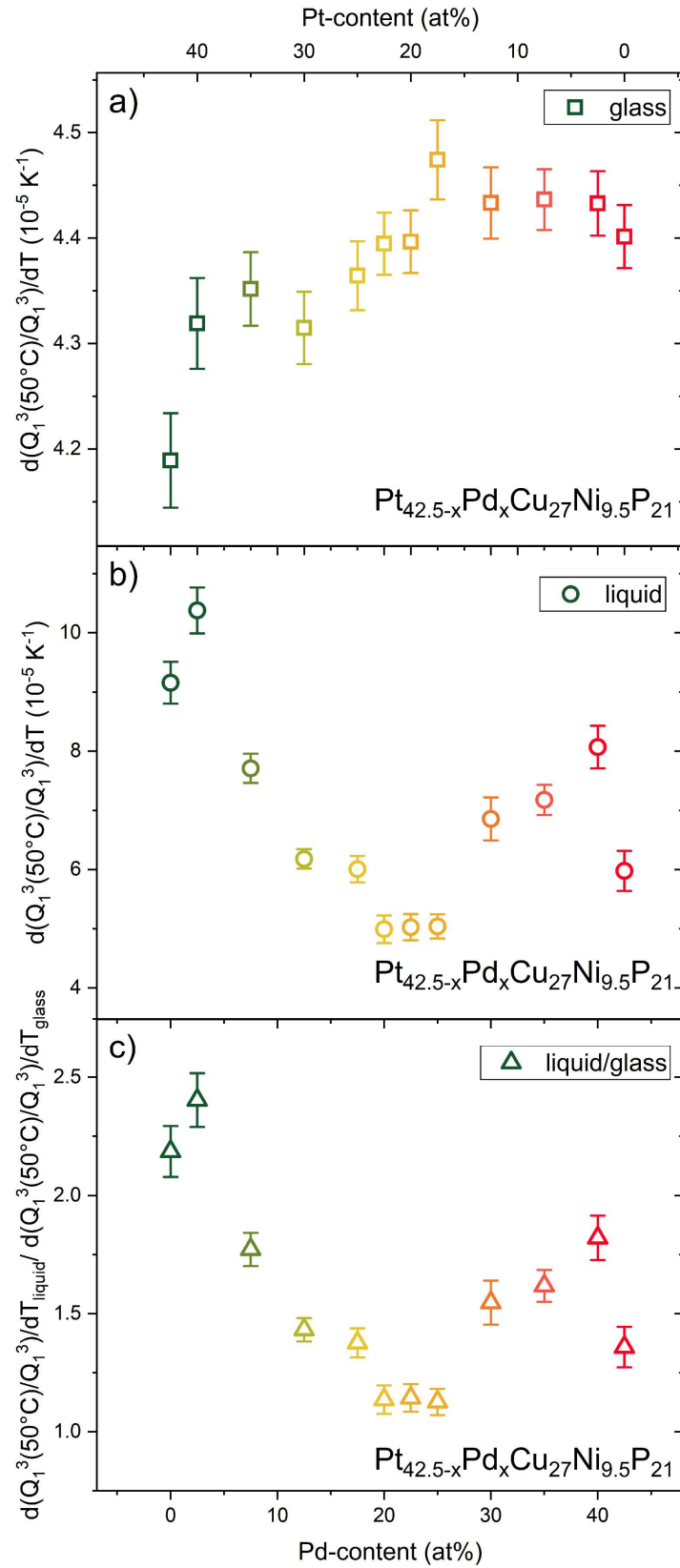
Figure 6-19: Linear fit of the relative change of the inverse cube of the position of the FSDP of the total structure factor S(Q) as a function of temperature for $Pt_{42.5-x}Pd_xCu_{27}Ni_{9.5}P_{21}$ upon heating with 0.33 K s^{-1} in the glassy state (a) and the liquid state (b). The ratio between both slopes, shown in c) describes the change of slope associated with the glass transition

6.3.2.1.4 Thermal Evolution of the Peak Height of the FSDP

Another metric of the FSDP to consider is the change of the peak height $S(Q_1)$ with temperature, depicted in Figure 6-20. $S(Q)$ can be considered as an indicator of the degree of order present in the system, as an infinite value of $S(Q)$ is considered in the case of a crystalline perfectly long-range ordered system creating a Bragg-peak. On the other hand, when $S(Q)$ would strive towards unity if no structural order would be observable in a system. Hence, the decrease in $S(Q)$ can be related to a growing disorder of the system [93]. Different to the peak position the typical change of slope is observed at T_g for all compositions.

During heating of the already standardized glassy state no significant relaxation is observed and just a small decrease in the peak height is expected (compare to the difference of relaxed vs. unrelaxed state in Figure 6-14). This negative slope is gradually becoming steeper for higher Pd contents revealing a linear trend, which is summarized in Figure 6-21a). In contrast, for the supercooled liquid state above T_g a much faster decrease of the peak size can be observed. This fact is connected to the regained degrees of motion of the liquid that allow more significant rearrangement and go in hand with a decrease of order during heating. Interestingly the steepest slopes are here observed in the intermediate section of the compositional Pt-Pd axis. When just comparing the ratio between the slopes $dS(Q_1)/dT$ of the glassy and liquid state a similar picture is drawn, with the intermediate compositions possessing a more than 6 times steeper slope in the SCL state compared to the glassy state. However, this if the changes of $S(Q)$ are actually related to the order that is lost in the system during heating or the amount of order that is created during cooling, assuming the changes of $S(Q)$ give us an indication on the order of the system, we would rather expect a different picture. As the intermediate compositions e.g. $Pt_{22.5}Pd_{20}$ feature the strongest behavior, their relative change in order should behave similarly if a correlation would be present (compare Figure 6-4 and Figure 6-5).
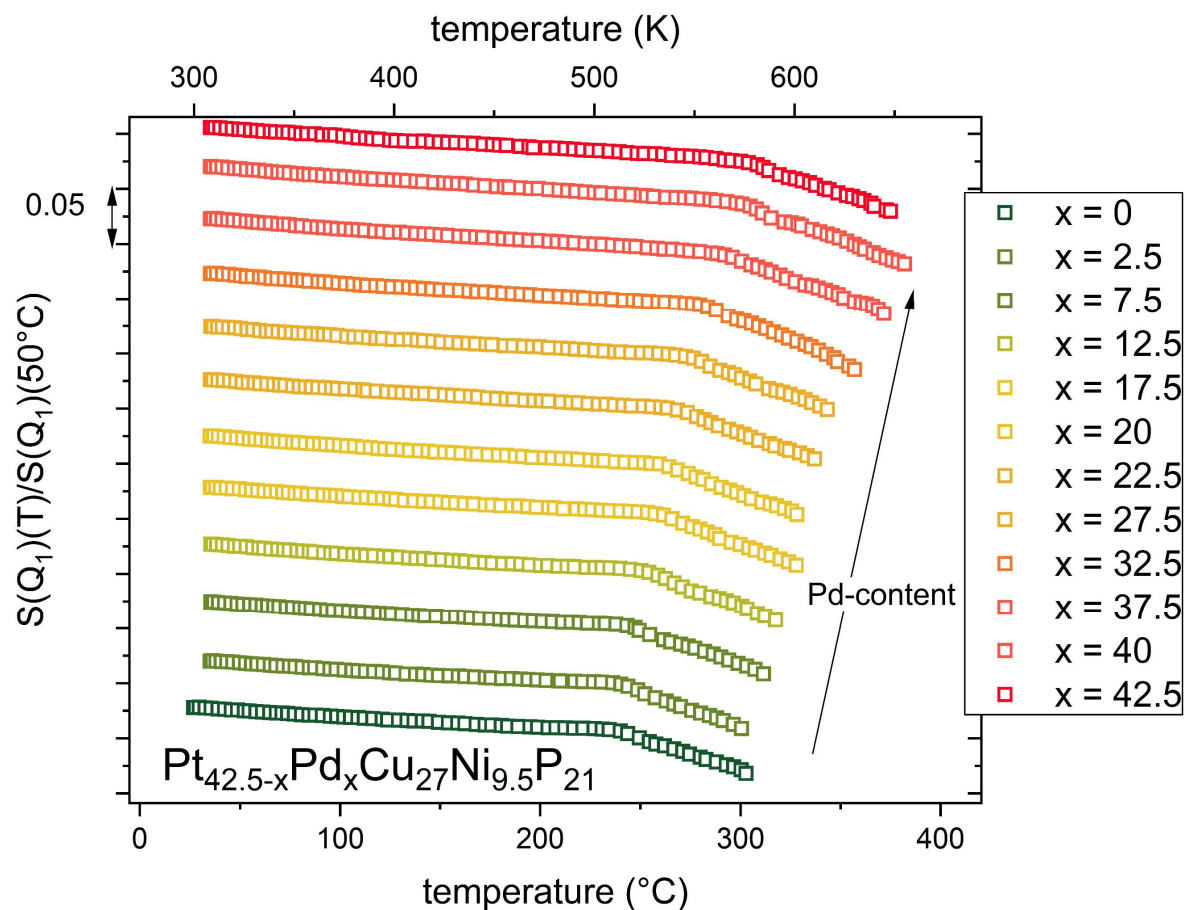
Figure 6-20: Relative change of the peak height of the FSDP of the total structure factor S(Q) as a function of temperature for $Pt_{42.5-x}Pd_xCu_{27}Ni_{9.5}P_{21}$ upon heating with 0.33 K s^{-1}. For all compositions the glassy state created after being cooled by 0.33 K s^{-1} from the supercooled liquid state ("standardized") at a temperature of 50 °C is used as a reference state
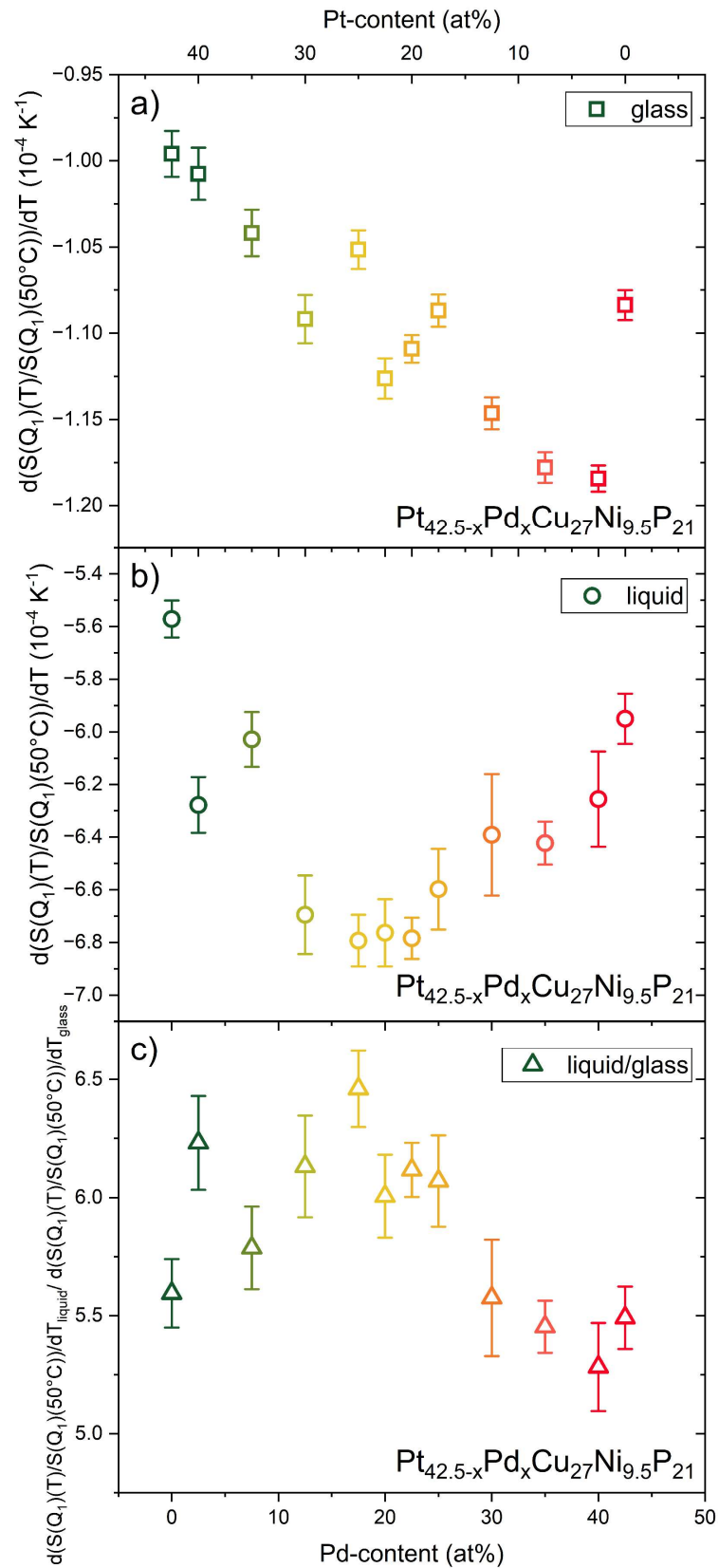
Figure 6-21: Results of the slope obtained by linear fitting of the relative change of the height of the FSDP of the total structure factor S(Q) as a function of temperature for $Pt_{42.5-x}Pd_xCu_{27}Ni_{9.5}P_{21}$ upon heating with 0.33 K s^{-1} in the glassy state (a) and the liquid state (b). The ratio between both slopes, shown in c) describes the change of slope associated with the glass transition

During heating of the already standardized glassy state no significant relaxation is observed and just a small decrease in the peak height is expected (compare to the difference of relaxed vs. unrelaxed state in Figure 6-14). This negative slope is gradually becoming steeper for higher Pd contents revealing a linear trend, which is summarized in Figure 6-21a). In contrast, for the supercooled liquid state above T_g a much faster decrease of the peak size can be observed. This fact is connected to the regained degrees of motion of the liquid that allow more significant rearrangement and go in hand with a decrease of order during heating. Interestingly the steepest slopes are here observed in the intermediate section of the compositional Pt-Pd axis. When just comparing the ratio between the slopes $dS(Q_1)/dT$ of the glassy and liquid state a similar picture is drawn, with the intermediate compositions possessing a more than 6 times steeper slope in the SCL state compared to the glassy state. However, this if the changes of S(Q) are related to the order that is lost in the system during heating or the amount of order that is created during cooling, assuming the changes of S(Q) give us an indication on the order of the system, we would rather expect a different picture. As the intermediate compositions e.g. $Pt_{22.5}Pd_{20}$ feature the strongest behavior, their relative change in order should behave similarly if a correlation would be present (compare Figure 6-4 and Figure 6-5).

6.3.2.1.5   Thermal Evolution of the Peak Width of the FSDP

The third quantity that can be used to describe the shape of the peak is the width of the peak, namely the FSDP. In Figure 6-22 the change in the FWHM is shown during heating of priorly standardized samples with varying Pt and Pd content. Here almost no change in slope is visible in the glassy state, being in line with an assumable isoconfigurational of the well relaxed glass below the glass transition. It is followed with a strong bending at the glass transition temperature showing a significant change of slope. The course of the curves schematically resembles the course of the enthalpy or entropy assumed for the same temperature range. The curves are evaluated by linear fits of the glassy and the supercooled liquid state, with the results being summarized in Figure 6-23. The evaluation of the linear fits for the glass state shows a linear trend with increasing Pd content similar to the peak height or position. The liquid state however shows a plateauing behavior on the Pt-rich side, followed by a decrease in the slope on the Pd-rich side. The ratio between the slopes of liquid and glassy state is dominated by the liquid trend, as here the changes of slope during the unfreezing of the glass are in the range 38-20.
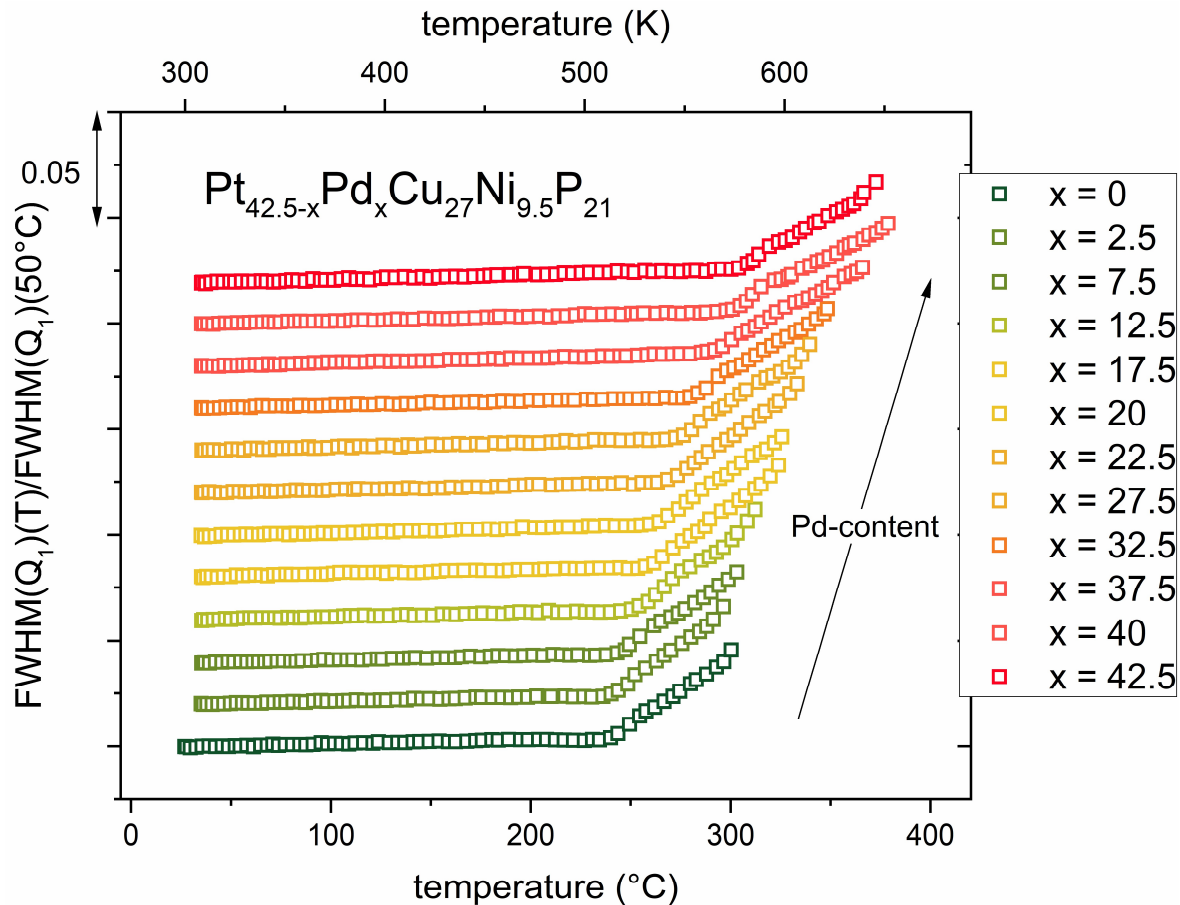
Figure 6-22: Relative change of the full width at half maximum (FWHM) of the FSDP of the total structure factor S(Q) as a function of temperature for $Pt_{42.5-x}Pd_xCu_{27}Ni_{9.5}P_{21}$ upon heating with 0.33 K s^{-1}. For all compositions the glassy state created after being cooled by 0.33 K s^{-1} from the supercooled liquid state ("standardized") at a temperature of 50 °C is used as a reference state

However this behavior mimics quite well the results from our thermodynamic analysis, regarding the change of the configurational entropy, which was assumed by the T_g-normalized jump of the heat capacity at the glass transition temperature $c_p^{l-x}(T_g)/T_g$. It seems as if the changes in the FWHM are closely connected to the changes in configurational entropy. In the end we assume that this is closely connected to the changes of the dominant structural motifs, away from the MRO-promoting trigonal prisms towards the higher number of icosahedra that lead to a very stable icosahedral SRO [21,152]. The topic is briefly discussed in Publication I, with an adapted plot being shown in Figure 6-24.
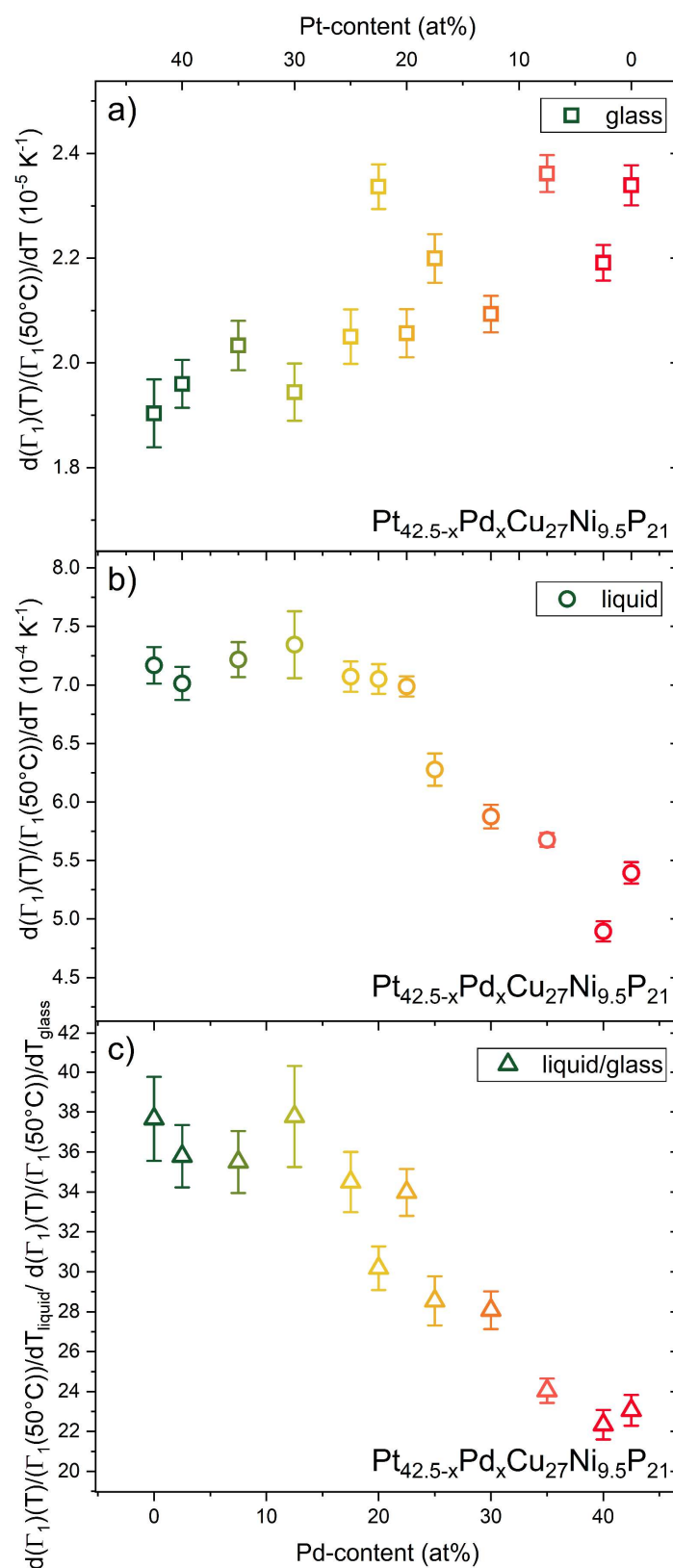
Figure 6-23: Linear fit of the relative change of the full-width at half maximum of the FSDP of the total structure factor S(Q) as a function of temperature for $Pt_{42.5-x}Pd_xCu_{27}Ni_{9.5}P_{21}$ upon heating with 0.33 K s^{-1} in the glassy state (a) and the liquid state (b). The ratio between both slopes, shown in c) describes the change of slope associated with the glass transition.
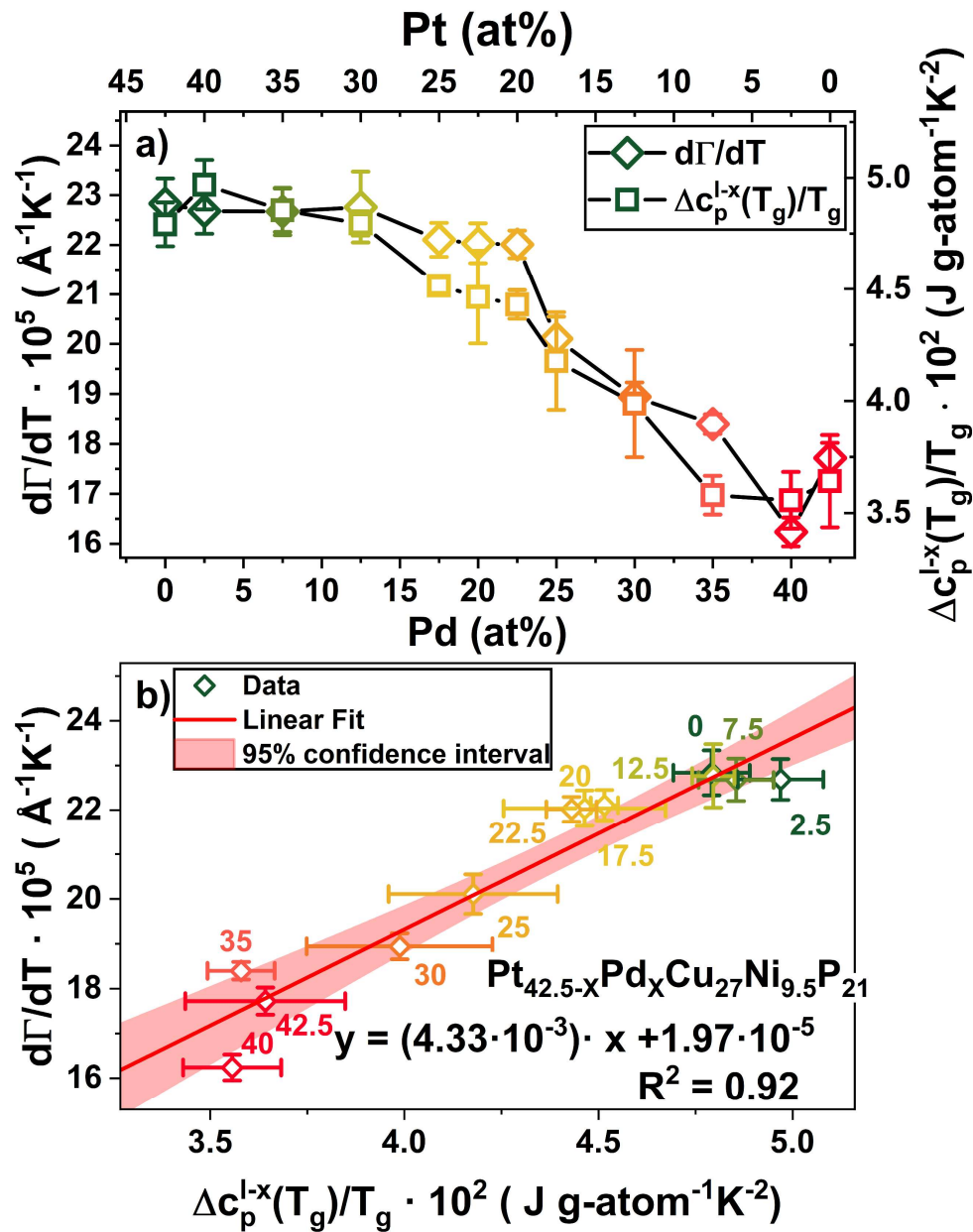
Figure 6-24: Comparison of the changes in FWHM of the FSDP and thermodynamic data:

a) First derivative of the full width at half maximum (FWHM) of the FSDP of the total structure factor $S(Q)$ with respect to temperature $d\Gamma/dT$ for the different $Pt_{42.5-x}Pd_xCu_{27}Ni_{9.5}P_{21}$ upon heating with 0.33 K s (left axis) and the difference in specific isobaric heat capacity between liquid and crystal normalized by the glass transition temperature $\Delta c_p^{l-x}(T_g)/T_g$ for the different $Pt_{42.5-x}Pd_xCu_{27}Ni_{9.5}P_{21}$ upon heating with 0.33 K s (right axis).

b) Scatter plot of the change in FWHM with temperature $d\Gamma/dT$ over the by T_g normalized difference in specific isobaric heat capacity between liquid and crystal $\Delta c_p^{l-x}(T_g)/T_g$. The latter describes the rate of loss of configurational entropy at the glass transition, ultimately being a measure of the thermodynamic fragility. A strong correlation of both quantities with an R^2-value of 0.92 was achieved, hinting towards at least a qualitative correlation within the system. Adapted from Ref. [21]

6.3.2.2 Structural Analysis in Real Space

6.3.2.2.1 Changes on Different Length Scales

Based on the aforementioned change of type and especially size of the dominant structural motifs, it could be possible that the dominant length scale of structural rearrangements is also changing with Pd-content. If this would be the case, the failure to use the changes in MRO to describe the fragility of the system could be traced back to the dominance of such a significant SRO in the liquid. One way get actual special information is the transformation of S(Q) to the reduced pair distribution function G(r), briefly described in section 3.3.1. It allows to directly compare structural changes on the different length scales of nearest neighbors and higher orders of surroundings.

All S(Q) data used in the prior correlations is transformed into G(r). The focus of this part of the work is the supercooled liquid state and the glassy state is put out of the focus. To determine the thermally induced changes on the different length scales, the first four peak positions r_i with $i = 1, 2.1, 2.2, 3, 4$ of G(r) are analyzed for the supercooled liquid region. It shall be noted that the 2nd peak of G(r), also representing the connection of neighboring clusters [88], splits up into two distinguishable sub-peaks, indicated by 2.1 and 2.2. To quantify the thermal expansion of each shell, normalized to the glass transition temperature, the slope $m_{ri} = dr_i/(dT/T_g)$ is determined by linear fitting of the data in the supercooled liquid above the glass transition, until the onset of crystallization.
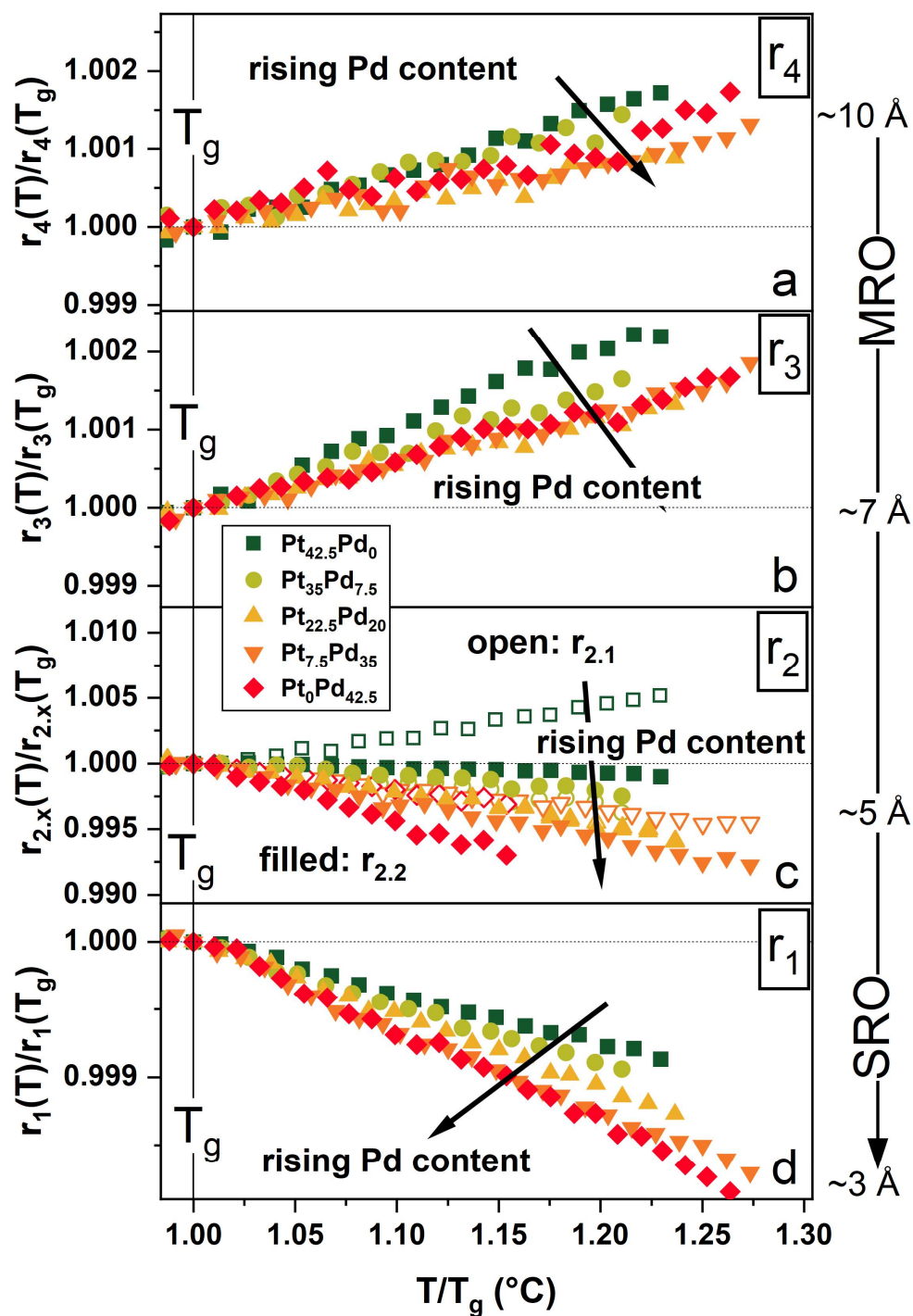
Figure 6-25: Relative change of the peak positions of the reduced pair distribution function of a) r_4, b) r_3, c) $r_{2.1}$ and $r_{2.2}$ and d) r_1 on a T_g-scaled temperature axis for five chosen alloys of $Pt_{42.5x}Pd_xCu_{27}Ni_{9.5}P_{21}$ with x = 0, 7.5, 20, 35 42.5. While the biggest absolute relative changes are observed for Pt-rich alloys on the length scales of r_3 and r_4 the opposite is the case on the smallest length scales of r_2 and r_1. The black arrows within the figures indicate the changes with rising Pd-content. The large arrow on the side of the figure underlines the changes of the representative length scale from around 3 Å at the FSDP up to around 10 Å at the 4th peak position.

In Figure 6-25a)-d) the resulting linear thermal expansions of the different atomic shells m_{ri} are depicted as a function of Pd content. The error bars represent the standard deviation of the fitting results of at least three independent measurements. The changing temperature dependence of the peak positions in the SCL on the different length scales with different Pt/Pd content is graphically summarized in Figure 6-25 e)-h), where the relative changes of the peak positions for five representative alloys are shown on a T_g normalized scale. Here it becomes obvious that with an increasing amount of Pd the changes on the 3rd and 4th shell decrease by a factor of three, until a Pd content of 20 at% is reached. On the Pd-rich side then the changes remain on a similarly low level. In contrast, on the smaller length scales of r_1 and r_2 an opposite behavior is revealed. On the first and second shell the thermal expansion is growing with rising Pd ratio, until a Pd content of around 20 at% is reached. For the Pd rich alloys the absolute changes are the biggest but remain constant with composition. For the Pt-rich alloys, the most significant thermally induced structural changes are happening on the 3rd and 4th shell, corresponding to a length scale of 6 - 10 Å, associated to MRO. In contrast, the Pd-rich compositions feature the most significant changes at the 1st peak of G(r), associated to the nearest neighborhood of atoms in the clusters and therefore SRO. When referring to the structural fragility model proposed by Wei et al. this agrees well with their observations: While for fragile systems, large changes on the MRO length scale are observed, strong systems show larger changes on the length scale of SRO, while almost no expansion on the MRO length scale is observed. So, in terms of the structural fragility model of Wei et al., the Pd-rich compositions meet all criteria of a strong system, whereas in terms of kinetics, dynamics, and thermodynamics, they are characterized by increasingly fragile behavior.
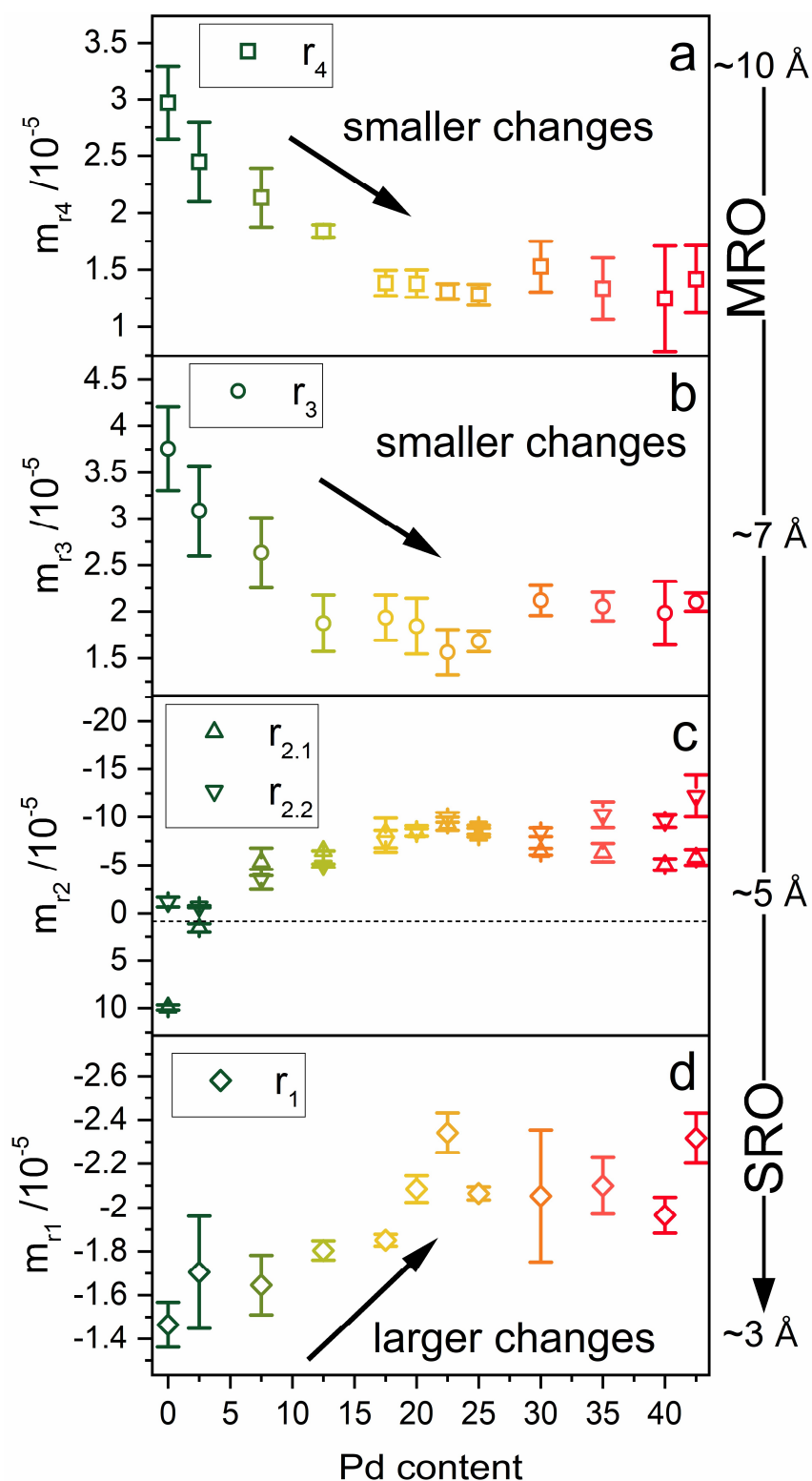
Figure 6-26: Slopes m_{ri} of linear fitted change of the different peak positions of the reduced pair distribution function a) r_4, b) r_3 , c) $r_{2.1}$ and $r_{2.2}$ and d) r_1 of the reduced pair distribution function $G(r)$ with respect to temperature in the supercooled liquid above the glass transition measured in heating at a rate of 0.33 K s^{-1} as a function of Pd-content. The black arrows within the figures indicate the changes with rising Pd-content. The large arrow on the side of the figure underlines the changes of the representative length scale from around 3 Å at the FSDP up to around 10 Å at the 4th peak position.

6.3.3 Structural Fragility Parameter of the Liquid upon Cooling

The excellent glass-forming ability of Pd-rich liquids with Pd contents above 35 at% allows X-ray diffraction data to be recorded during cooling from above the liquidus temperature to below the glass transition temperature without the interference of crystallization. The high temperature measurements were carried out in the ceramic furnace ($Pd_{42.5}Cu_{27}Ni_{9.5}P_{21}$) and the Linkam TMS1500 furnace ($Pt_{2.5}Pd_{40}Cu_{27}Ni_{9.5}P_{21}$ and $Pt_{7.5}Pd_{35}Cu_{27}Ni_{9.5}P_{21}$) (compare section 3.3.2). Based on these measurements the volume dilation between the 3rd and 4th shell ε_{4-3} is reported on a T_g-normalized inverse temperature scale in Figure 6-27a)-c) for these three alloys featuring the highest Pd content. In the high temperature range, a much steeper slope is observed for all three alloys followed by a marked flattening of the slope around $T_g/T \sim 0.8$. While the low temperature data is fitting the determined structural fragilities from the former experiments upon heating (compare Figure 6-10a)), the much steeper slope at higher temperatures is correlating to the expected more fragile behavior of the kinetic and dynamic experiments, visible in the depiction of all structural fragilities together with the classical kinetic and dynamic ones.

On the first glance these apparent changes in structure might suggest the occurrence of a dynamic crossover, often associated with a liquid-liquid phase transition (LLPT), reported in numerous metallic and non-metallic liquids [151,221–227], where the change from a fragile high temperature phase to a strong low temperature phase is observed. However, it does not seem to be the answer to the observed behavior in this case for several reasons. The strongest argument against such a LLPT is the fact that all fragility values, kinetic/dynamic and thermodynamic, showed the fragile behavior already in the temperature region, where the structurally strong behavior was observed. If the system would be changing its behavior due to a LLPT it should behave similarly regarding its fragility if the same material of the same state is probed[33]. The argument that both the kinetically fragile and structurally strong behavior was observed in samples with the same thermal history also rejects a possible undercooling of the fragile liquid, suppressing the LLPT during cooling. From this, the structural measurement upon heating should not show a strong behavior during the same thermal treatment as during a DSC scan. Another strong indicator is the fact that even the relaxation times on the atomic scale,

---

[33] The same state is referring here to the similar thermal history of samples e.g. casting geometry and a similar thermal protocol during the actual measurement.

determined by XPCS in Publication II show the clear fragile behavior of the Pd-rich system, supporting the other techniques. Still, the reported changes in the relaxation spectra or rather their invariance with temperature were connected to the "strong" behavior of the structural fragility parameter derived from the small changes on the MRO length scale.
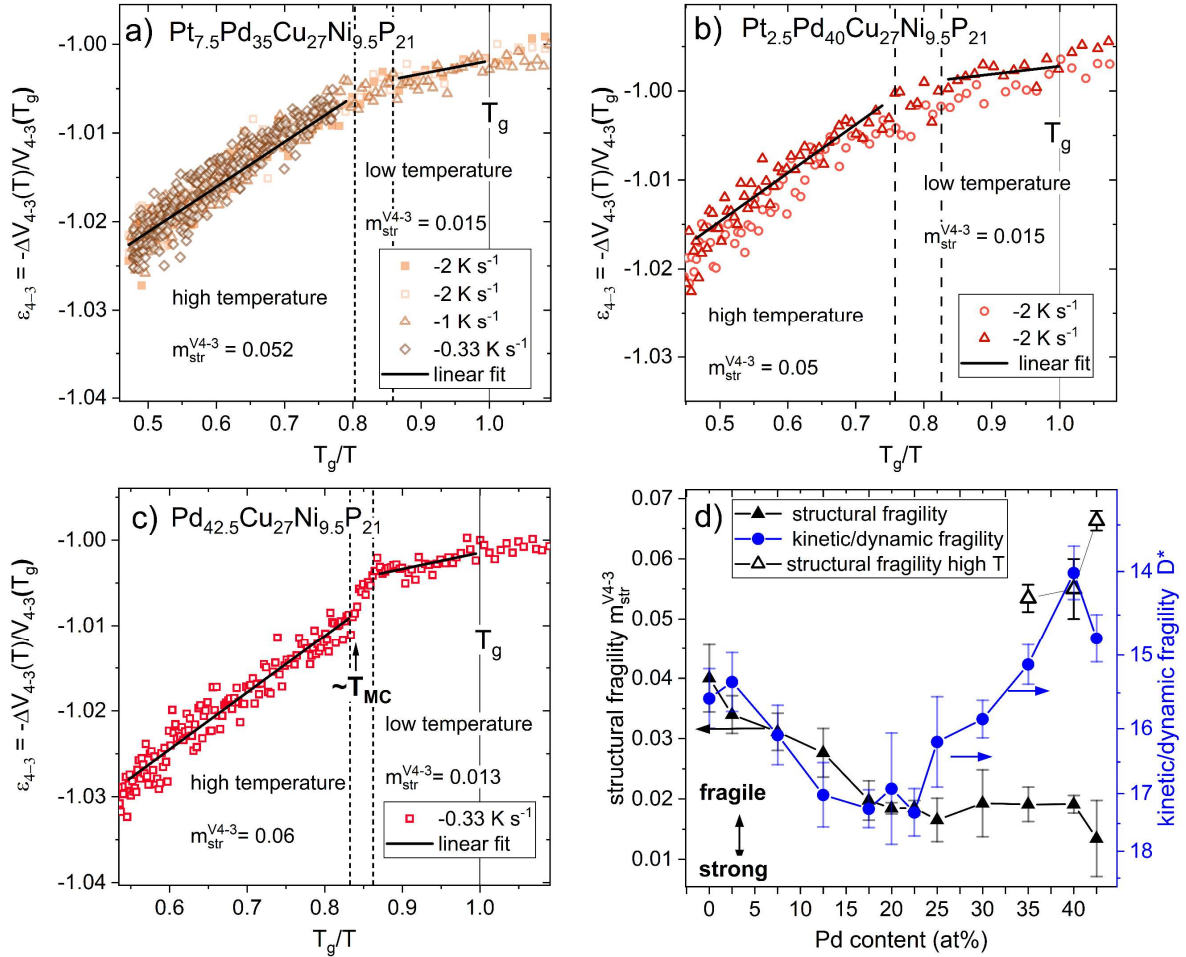

Figure 6-27: a) Volume dilation ε_{4-3} of a) $Pt_{7.5}Pd_{35}Cu_{27}Ni_{9.5}P_{21}$ b) $Pt_{2.5}Pd_{40}Cu_{27}Ni_{9.5}P_{21}$ and c) $Pd_{42.5}Cu_{27}Ni_{9.5}P_{21}$ during cooling with various cooling rates, reflecting the change of the local volume V_{4-3} between r_3 and r_4 of the reduced pair distribution function G(r). Individual linear fits of the high temperature and low temperature region are used to determine m_{str}^{V4-3}.

d) Structural Fragility m_{str} as a function of Pd content. All data points are averages of at least three measurements. Based on the empirical correlation (see Figure 6-11) also the expected kinetic fragility D^* is depicted on the right ordinate. The resulting structural fragility parameters of the high temperature liquid, obtained from the data of a)-c) are added as open symbols, in this case the error bars correspond to the standard deviation between the depicted measurements at variating rates.

In Figure 6-28 the additional high-temperature data is added to the correlation plot of fragility and structural fragility underlining how the high-temperature data is narrowing the original

correlation curve. The high temperature data seems to reasonably fit the correlation. At this point it needs to be noted, that the original set of data that was used for the correlation is only featuring one composition at the very fragile spectrum of alloys, with a fragility parameter $D^* \sim 10$ (see the open dotted data point on the upper right corner of Figure 6-28). Hence, the actual slope of the correlation curve might be a bit larger as it is not that strongly supported by experimental data in the fragile regime with $D^* < 10$.
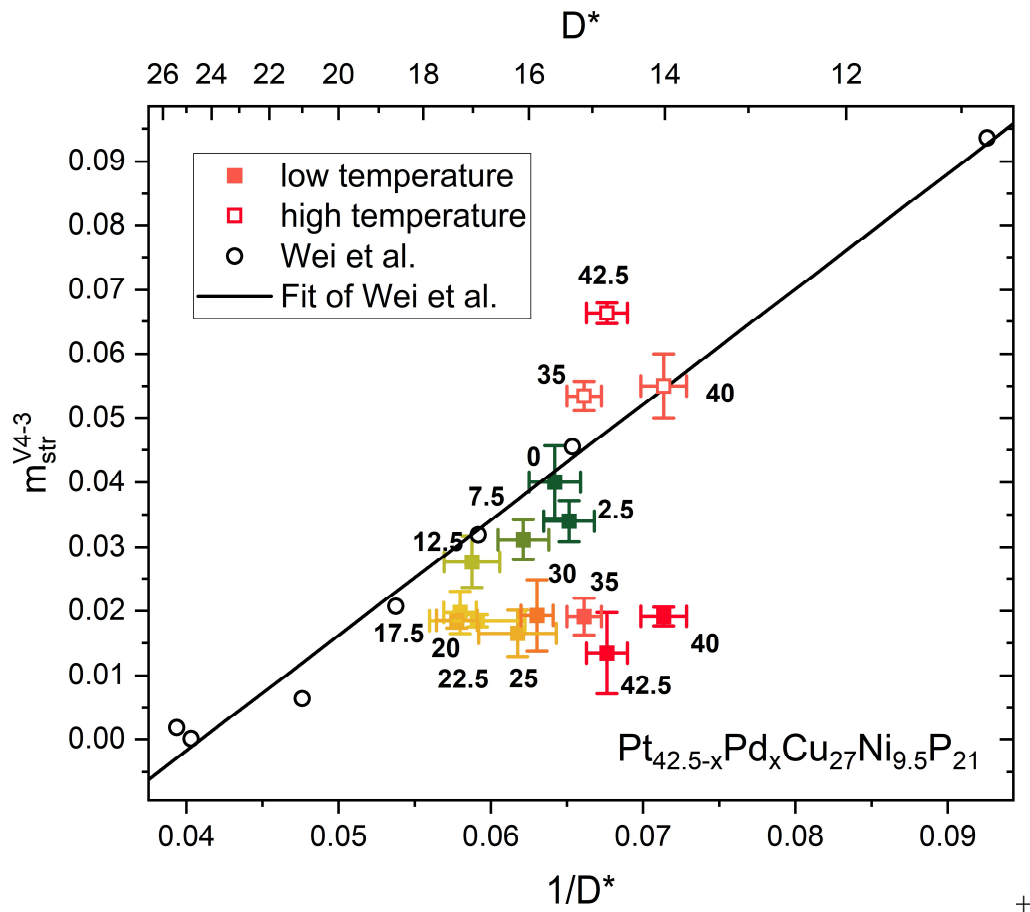

Figure 6-28: High and low temperature results of the structural fragility model within the correlation established by Wei et al.[96]

To support this quite unique behavior of the liquids also the correlation length ξ of the $Pd_{42.5}Cu_{27}Ni_{9.5}P_{21}$ measurement is determined. This method shall provide another metric to get further insights into the phenomenon observed during continuous cooling. The changes of the fitted decay function at different states and temperatures is exemplarily shown in the Appendix in Figure 8-7.
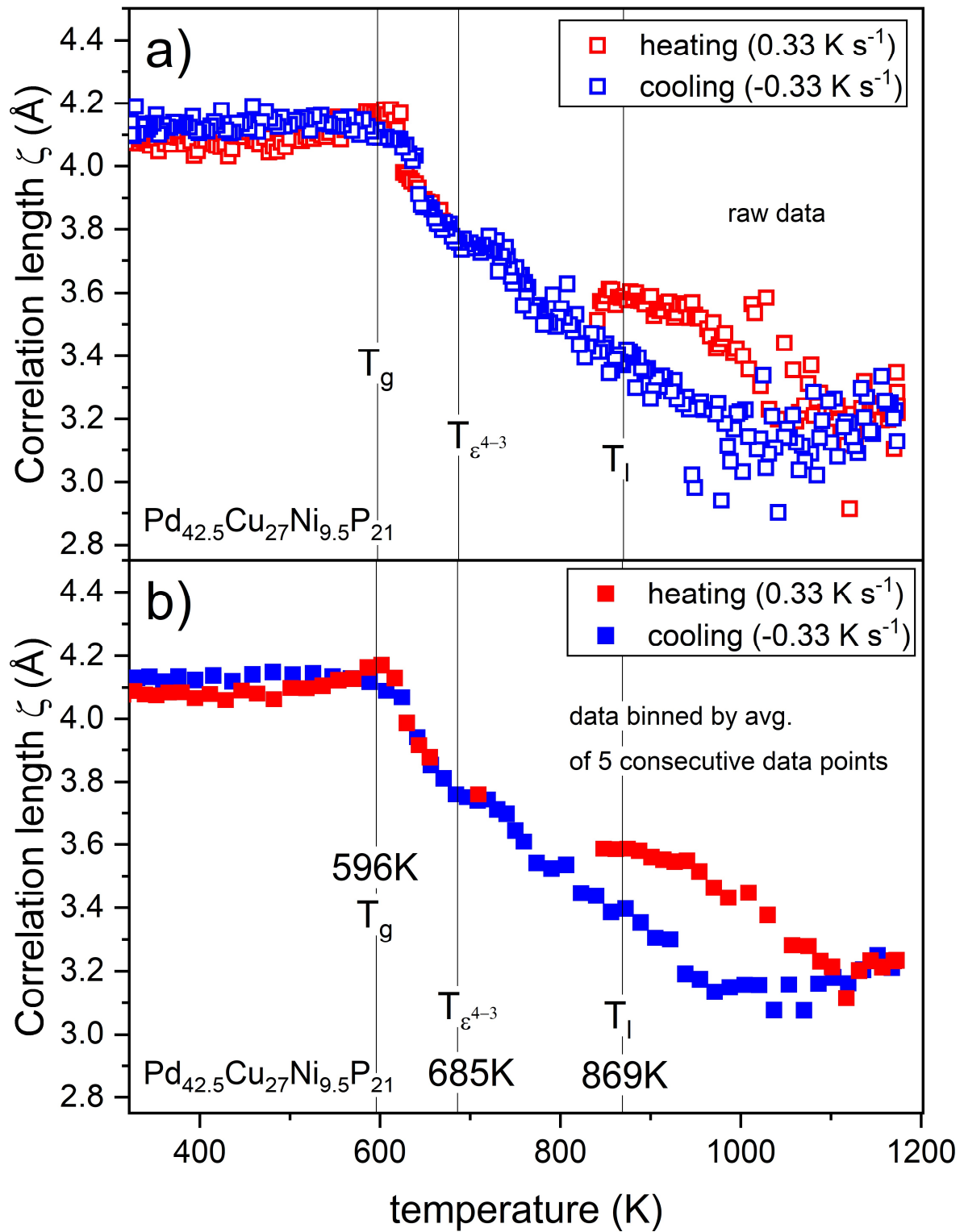
Figure 6-29: Correlation length obtained from the Ornstein-Zernike analysis from the G(r) of $Pd_{42.5}Cu_{27}Ni_{9.5}P_{21}$ during heating and cooling at a constant rate of 0.33 K s^{-1}. For a better orientation the liquidus temperature T_l is included as well as the glass transition temperature T_g and the temperature, where the changing behavior of ε_{4-3} was observed, here labeled by $T_{\varepsilon4-3}$ (compare Figure 6-27). Due to the noise in the raw data (section a)) the data was binned by an average of five consecutive data points.

The changes of the correlation length ξ during heating and cooling of $Pd_{42.5}Cu_{27}Ni_{9.5}P_{21}$ are depicted in Figure 6-29. During heating of the glassy state the correlation length remains relatively constant followed by an increase during the structural relaxation, where the system begins to order analogous to the observations of the FWHM of the FSDP (see Figure 6-14). After the glass transition the system abruptly changes by a strong decrease of the correlation length, which then is cut-off by crystallization of the sample. The evaluation of the correlation length then only makes sense once the sharp diffraction peaks are vanishing during the melting procedure. During heating in the equilibrium liquid above T_l the correlation length is still changing and the offset between the heating and cooling curve still suggests that the system is not fully equilibrated. This might be related to residual crystalline parts that still need to be dissolved in the liquid, also affecting the ability of the system to undercool dramatically [228]. At around 1100 K the system seems to remain on a constant level of correlation length at around 3.25 Å in heating and cooling, which is seemingly the equilibrium value of the liquid state. During cooling already an increase of the correlation length can be observed above at about 80 K above the liquidus temperature. The increase is rather linear until a step-like change is observed at a similar temperature to the bending observed in ε_{4-3} at the $T_{\varepsilon4-3}$. Interestingly, similar bending was observed in the Zr-based alloy Vitreloy 106a (Vit 106a) by Stolpe. However, in this case a strong thermal signature was accompanied by fitting dynamic and kinetic experiments that suggested a LLPT. A comparison of both data sets is provided in the Appendix Figure 8-9. A possible resolution of this behavior on the Pd-rich side of the observed alloys will be discussed in the following chapter.

6.3.4 Possible Resolutions of the Structurally Strong Behavior

6.3.4.1 Complexity of Pair-distribution Functions in Multi-component Systems

A possible explanation of the failure of the model on the Pd rich side could be found in the nature of the reduced total PDF from which the structural information is derived. In n-component systems G(r) consists of the weighted superposition of n(n+1)/2 partial PDFs, each scaled by their scattering contribution, i.e., the atomic form factor and the relative amount of atoms (compare eq. (3.28)). In the case of the intermediate compositions that are composed out of five components, the coherently scattered signal originates from the superposition of 15 different partial contributions. For a better understanding, the wave-vector dependent weighting factors of five different compositions are shown in Figure 6-30. To better distinguish between

the different contributions the data is also reported on a logarithmic scale on the right part of Figure 6-30. From the depiction it can be observed that for the present systems the scattering signal is dominated by noble metal - noble metal pair correlations together with minor contribution of noble metal - Cu and Ni partials[34], also highlighted in Ref. [204]. For a better comparison the Pt-Pt, Pd-Pd and Pt-Pd contributions are grouped, being considered the noble metal - noble metal pair correlations, adding up between 35 % to above 50 % contribution with rising Pt content. Secondly, the pair correlations of the noble metals with Cu and Ni each (Pt/Pd-Cu/Ni) is grouped, accounting for 30 % up to nearly 40 % with rising Pd content. In summary, both of these noble-metal related contributions add up to the vast majority of the scattering signal with ~75 % to 85 % with rising Pt content. A graphic representation of the data is provided in Figure 6-31. For a fair comparison it has to be noted, that especially on the Pd-rich side the contribution of the Pt/Pd-Cu/Ni atomic pairs contributes almost as equally to the scattering signal as the noble metal – noble metal contribution, as Pd atoms are scattering much weaker compared to Pt atoms.

---

[34] The Ni-related contributions are rather small compare to the Cu ones. While both atomic species feature similar atomic form factors the difference is due to the smaller amount of Ni in the samples (Cu-Ni-ratio of ~ 3:1). However, due to their similar topological role both elements are added in this consideration.
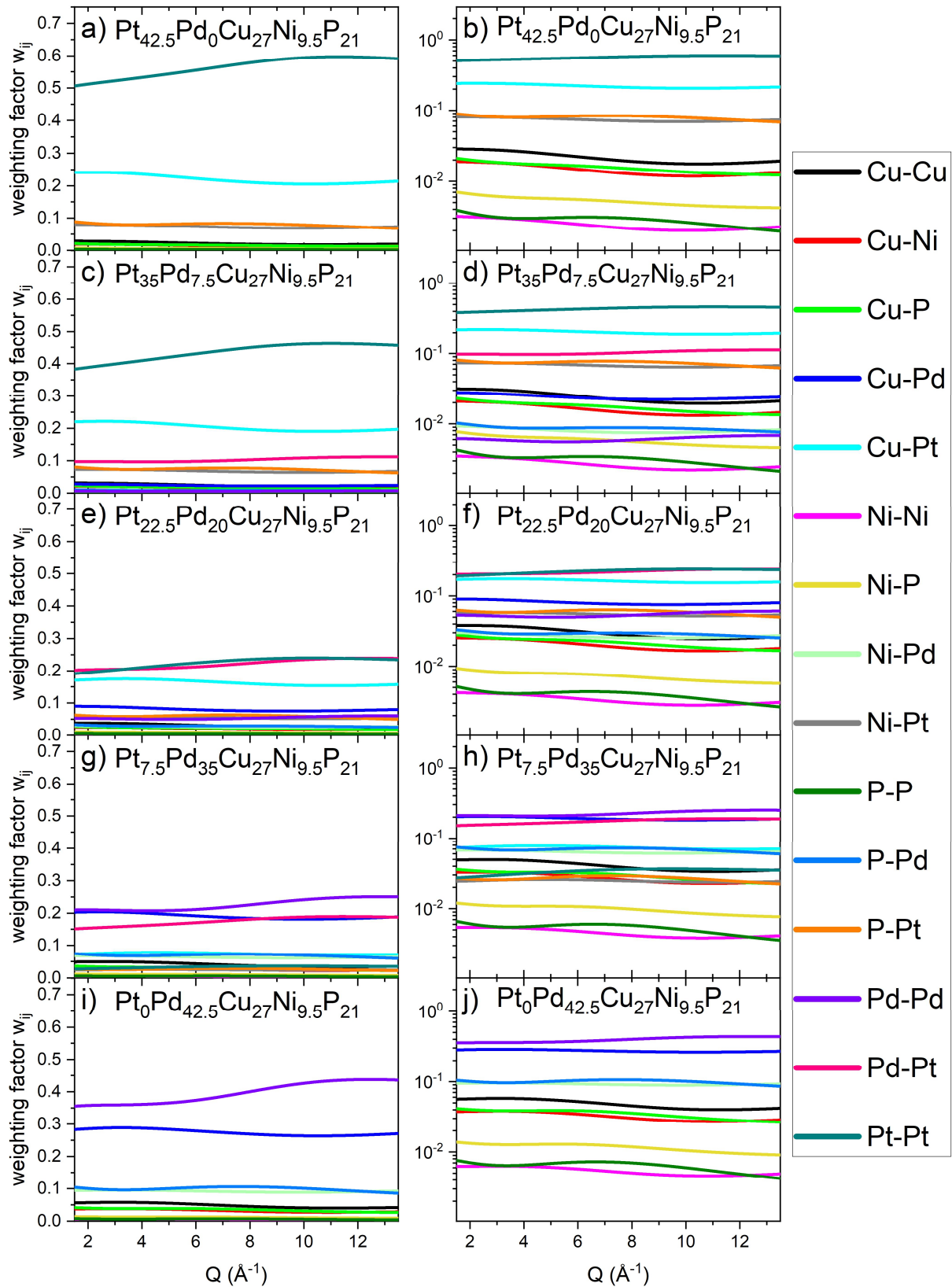
Figure 6-30: Change of the atomic weighting factors as a function of the wave-vector relating to the individual contribution of the atomic pairs to the overall scattering signal for a chosen number of different compositions of the $Pt_{42.5-x}Pd_xCu_{27}Ni_{9.5}P_{21}$ alloy series. The data was derived with eq. (3.28) and the atomic form factor was calculated based on the tables of Ref. [229].
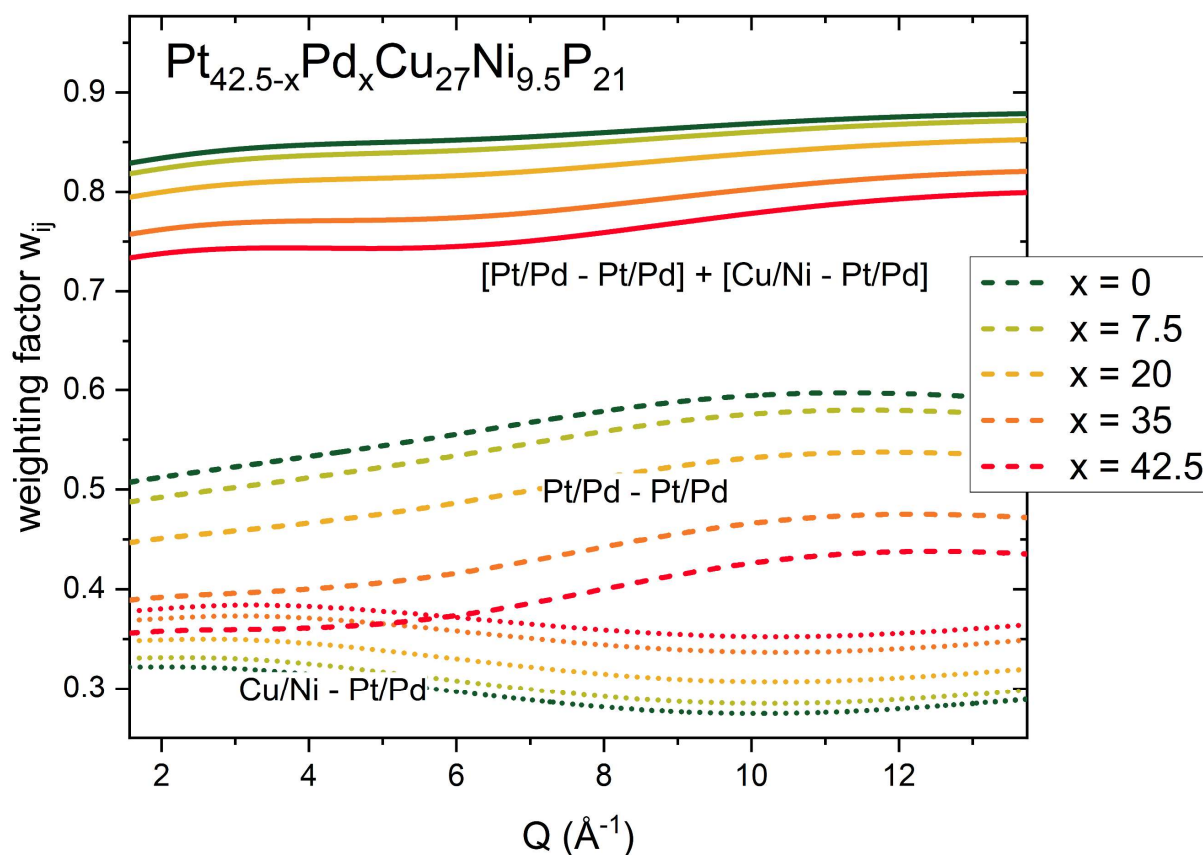
Figure 6-31: Change of the atomic weighting factors as a function of the wave-vector relating to the individual contribution of different groups of elements to the overall scattering signal for a chosen number of different compositions of the $Pt_{42.5-x}Pd_xCu_{27}Ni_{9.5}P_{21}$ alloy series. The main contributions are divided into two groups: First all noble metal – noble metal (Pt and Pd) correlations, depicted in a dashed line, which add up between 35% to above 50% contribution with rising Pt content. Secondly, the pair correlations of the noble metals with Cu and Ni each, which account also for roughly 30 % up to nearly 40% with rising Pd content. Additionally, the sum of both of these noble-metal related contributions is shown, adding up to the vast majority of the scattering signal with ~75 % to 85 % with rising Pt content.

To quantify the changes in scattering contribution to the overall signal, which basically condenses in a change of the observable atomic pair correlations, the changes of the weighting factors at a specific wave-vector Q with varying Pt/Pd content need to be reviewed. In Figure 6-32 a) the weighting factors at a $Q = 2.9$ Å^{-1}, which is in the direct vicinity of the FSDP, is used to quantify the changing contributions of the Pt/Pd-Pt/Pd, the Cu/Ni-Pt/Pd and their combined contribution. From this depiction the rising contribution of Cu/Ni and decreasing trend of the noble-metal – noble-metal contribution with increasing Pd content is well visible. To validate the changes, it is needed to examine the relative changes due to the different scattering contributions, to exclude that observed changes in the structural signal are based on this changed atomic contrast. In Figure 6-32b) the relative changes with respect to the initial

composition of $Pt_{42.5}Cu_{27}Ni_{9.5}P_{21}$ show a maximal change of around 30 % in the noble-metal contribution and a 20 % increase in the Cu/Ni – noble metal contribution, while the combined contributions remain almost constant with minor changes of around 10 %. This means that the interpretation of the direct scattering signal within the series of Pt/Pd has to be carried out with care and that these changes are far from neglectable. For example the changes in the connecting schemes with changing Pd content, shown in Publication III (e.g. Figure 7 of Ref. [230]), would need to be larger than the changes in the scattering contribution to be somehow reliable. In Figure 6-33 the relative changes in the reduced pair distribution function G(r) at the length-scale of 3-atom connections (compare section 2.5.2) with composition with respect to the initial composition of $Pt_{42.5}Cu_{27}Ni_{9.5}P_{21}$ are added from Ref. [230]. The relative changes observed are about two times larger than the changes of the scattering contribution. It supports the interpretability of the diffraction data, strongly suggesting that the observed changes are really related to changes in the atomic structure, instead of being simply an artifact due to the changes in contrast. However, it needs to be noted that the large changes of 30 % in the individual contrast is only a limiting factor when comparing the absolute signals of S(Q) or G(r). Anyhow, most quantities derived in this work are normalized values or normalized derivatives with respect to temperature. Also changes below the changes in the weighting factors can be taken into account, while still its specific atomic origin cannot be identified.

In summary, any structural information derived from the diffraction experiments mainly contains information on the behavior of the noble metal atoms with themselves and Cu/Ni. As a result, the current diffraction data merely allow inferences about the behavior of noble metal partials and to a combined degree on the Cu/Ni-noble metal interaction. Therefore, the small volume dilation of the Pd sub-system on the MRO length scale might lead to the apparent structurally strong behavior of the liquid. In that case the fragile behavior of the system could be determined by the interaction with or among the other atomic species involved that only give minor contributions to the diffraction signal. Especially the metal-P partials, which are almost not observable in the current measurements since they have the smallest contributions to the scattering signal, could be responsible for the fragile behavior of the system in thermodynamic and kinetic-dynamic regards.
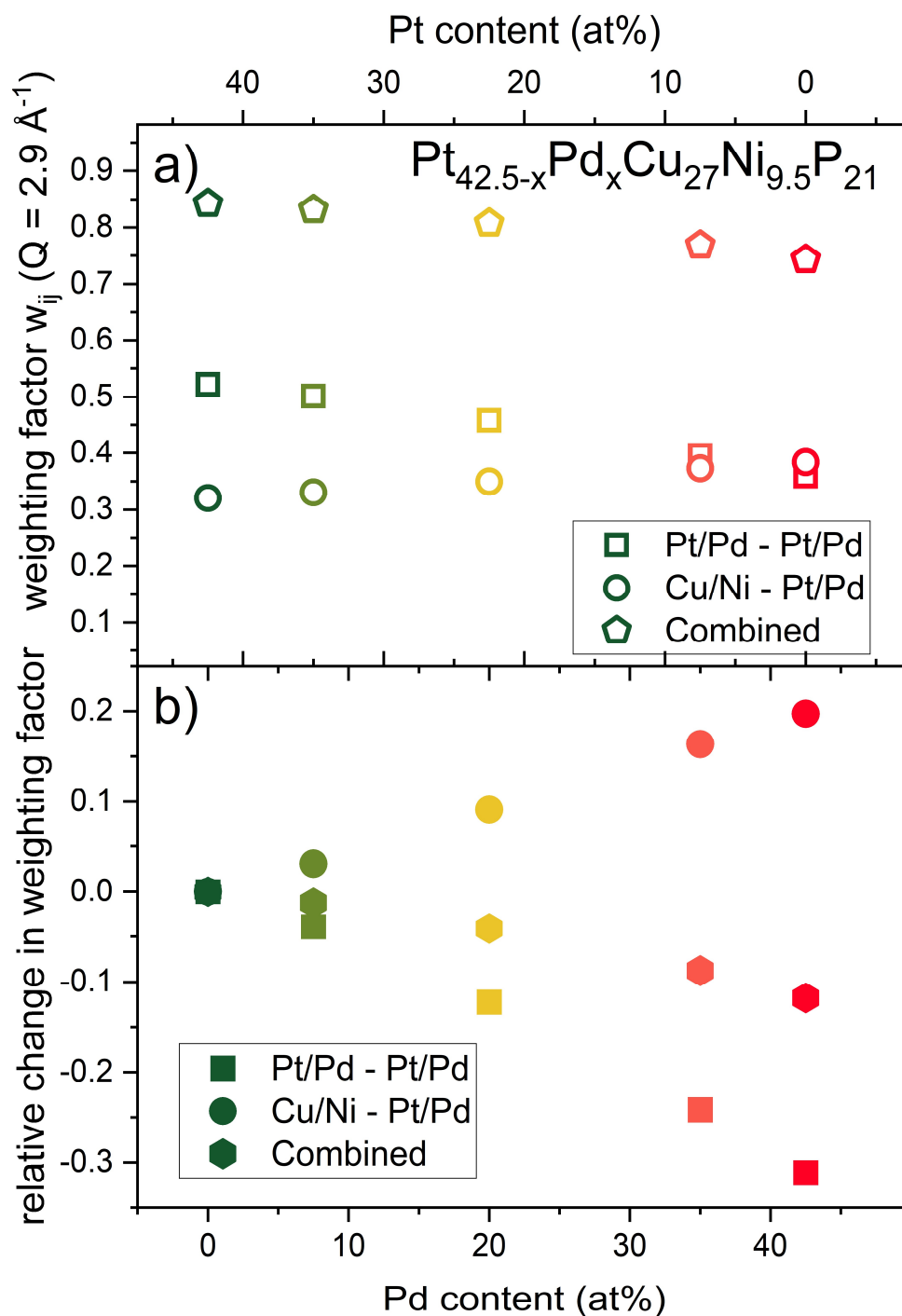
Figure 6-32: a) Weighting factor at a wave-vector of 2.9 Å⁻¹, located in the vicinity of the first sharp diffraction peak for the noble metal – noble metal contribution (squares) and the pair correlations of the noble metals with Cu and Ni each (triangles) and the combination of both (hexagons).

b) Relative change of the weighting factor with composition with respect to the initial composition of $Pt_{42.5}Cu_{27}Ni_{9.5}P_{21}$.
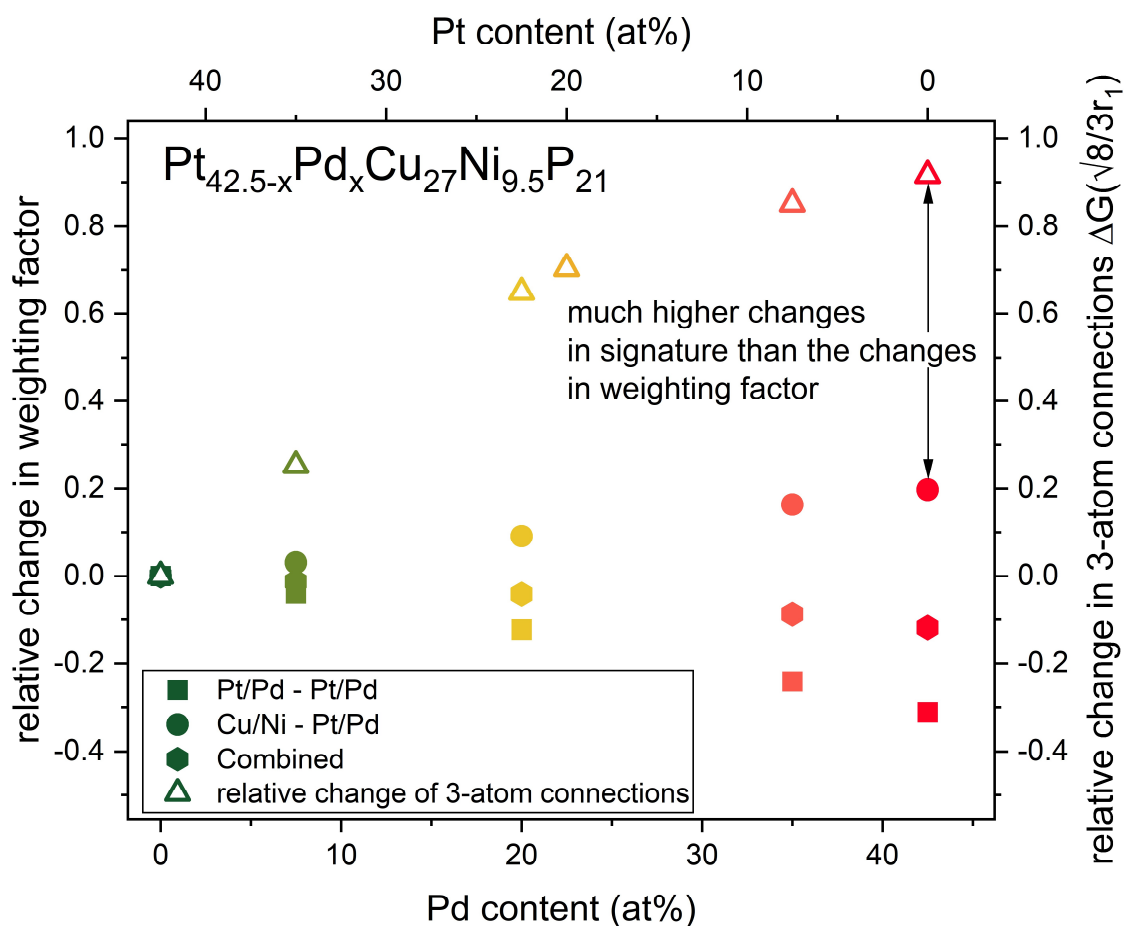
Figure 6-33: Relative change of the weighting factor (left axis) and relative change of the intensity of the reduced pair distribution function G(r) at the length-scale of 3-atom connections (compare section 2.5.2) with composition with respect to the initial composition of $Pt_{42.5}Cu_{27}Ni_{9.5}P_{21}$. The observed changes of the structural signature of 3-atom connections is larger than the changes in the atomic weighting factors, supporting the interpretation of the signal to be caused by actual compositionally induced structural changes. Data of the relative changes in G(r) is taken from Ref. [230]

6.3.4.2 Structural Changes in the Liquid during Cooling – a Perspective from Diffusion

At elevated temperatures a large slope is observed in the ε_{4-3} data of $Pd_{42.5}Cu_{27}Ni_{9.5}P_{21}$ followed by an abrupt flattening at around 690 K (1.2 T_g) into a slope that matches the slope observed during the heating experiments. The region at elevated temperatures yields a m_{str}^{V4-3} of 0.06, converting to a D^* of around 13, fitting the fragility expected for the Pd liquid. For $Pt_{7.5}Pd_{35}Cu_{27}Ni_{9.5}P_{21}$ and $Pt_{2.5}Pd_{40}Cu_{27}Ni_{9.5}P_{21}$ a similar behavior as for $Pd_{42.5}Cu_{27}Ni_{9.5}P_{21}$ is observed (compare Figure 6-27). Again, the high temperature data are fitting much better to the fragilities expected from thermodynamic and kinetic/dynamic data. In the m_{4-3}^{str} for the additional high temperature data is added to the overall fragility plot (Figure 6-28).

Hence, the empirical connection of volume dilation on the MRO length-scale and fragility seems to be restored at elevated temperatures, but at certain undercooling the volume dilation decreases towards an apparent stronger behavior mirroring the behavior observed in the heating experiments (Figure 6-27). With the argument that the information obtained from the X-ray scattering experiment is governed by the Pd-atoms, this change in the structural behavior should also be related to the behavior of the Pd atoms.

Interestingly, in the deeply undercooled liquid state of $Pd_{43}Cu_{27}Ni_{10}P_{20}$, which is compositionally very similar to the $Pd_{42.5}Cu_{27}Ni_{9.5}P_{21}$ alloy studied in this work, significant decoupling of the diffusion coefficient of Pd compared to other atomic species was reported in literature [56,231]. Thus, the question arises whether the small volume dilatation of the Pd-Pd correlations on the MRO length scale might be related to this highly decoupled, significantly smaller mobility of the Pd atoms. Possibly, the structural data could support the idea and be connected to the reported creation of a slow Pd subsystem after crossing a decoupling temperature (DCT), which the authors of Refs. [56,231] associate to the mode coupling temperature T_{MC} [56,231]. Furthermore, the rather high heterogeneity of the diffusion coefficients i.e. atomic motion supports well the observed heterogeneous dynamics in XPCS in the vicinity of the glass transition region.
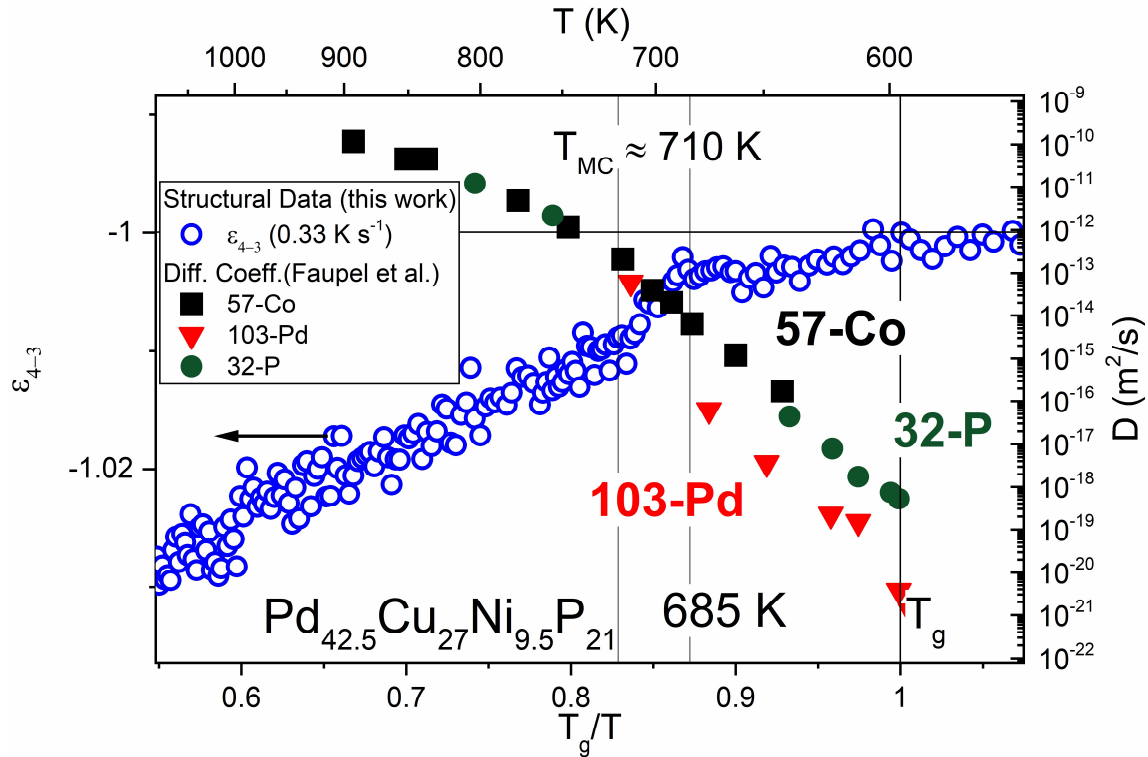
Figure 6-34: Volume dilation ε_{4-3} of $Pd_{42.5}Cu_{27}Ni_{9.5}P_{21}$ during cooling with 0.33 K s^{-1}, reflecting the change of the local volume V_{4-3} between r_3 and r_4 of the reduced pair distribution function G(r) (open blue circles, left axis) combined with diffusion data of different atomic species taken from Ref. [56]. Vertical lines are added to clarify different significant temperatures such as the mode-coupling temperature determined in Ref. [56], the bending point of the ε_{4-3} data at $T_{\varepsilon 4-3} = 685$ K and the glass transition temperature. A horizontal line referring to a volume dilation of zero is added to guide the eye.

In Figure 6-34 the structural data of ε_{4-3} of $Pd_{42.5}Cu_{27}Ni_{9.5}P_{21}$ during cooling from the liquid state (data from Figure 6-27c)) are compared to the mobility of the different atomic species in $Pd_{43}Cu_{27}Ni_{10}P_{20}$ from Ref. [56], namely the diffusion coefficients of Pd, P and Co, with the latter being representative for Ni. Interestingly, the flattening of ε_{4-3} occurs about 30 K below the determined DCT, where the Pd diffusion has already slowed down tremendously compared to the other atomic species (about three orders of magnitude slower than Co and P, compare Appendix Figure 8-10). Hence, the decoupled Pd-subsystem might rather appear 'solid-like' in relation to the other, much faster atomic species. Since Pd is also the species dominating the structural information, the decoupling might be significant enough to cause a collapse of the structural fragility model of Wei et al., ultimately making the m_{str}^{V43} metric incapable to describe the overall fragility of the system. The almost temperature invariant behavior of ε_{4-3} is typically observed for most systems below its thermal glass transition temperature because it is frozen into an iso-configurational state. When reviewing the decoupling by taking a look at the

change of the peak positions of G(r) on different length scales during cooling, it becomes obvious that the effect becomes weaker for smaller distances, turning out to be almost invisible at the average interatomic distance r_1 (see Appendix Figure 8-11) This apparent length-scale dependence could support the idea of decreasing mobility of the Pd that should most significantly influence rearrangements on increasing length scales. Ultimately, the three orders of magnitudes slower Pd subsystem, described by literature, that at the same time is the most significant part of the scattering signal, could fit the observation of almost stable evolution of structure on the medium-range order length-scale. This small dilation of the 3rd and 4th shell is then wrongly interpreted as a structurally strong behavior of the (whole) liquid, whereas it is merely the already more rigid sluggish behavior of only the Pd that can be observed with X-rays.

7. Summary and Outlook

In summary the different parts of the current work provide an overview on the thermodynamic, kinetic, dynamic, and mechanical properties and give new insights on their connection to structure for the exemplary model system of Pt/Pd-Cu-Ni-P liquids and glasses. Particular focus is laid upon the thermally induced changes of these properties as well as their responses upon variations of the chemical composition, namely the ratio of Pt to Pd, two presumably topologically equal species. All properties are characterized utilizing state-of-the-art methodology e.g. calorimetry, thermomechanical and micromechanical testing and synchrotron based diffraction and spectroscopy methods e.g. X-ray photon correlation spectroscopy.

Besides the assumed topological equality of Pt and Pd significant changes in almost every examined property can be observed. The main points can be summarized by the categories Thermodynamics, Kinetics and Dynamics, Structure and Mechanics in the following:

Thermodynamics

- The variation in GFA between the different alloys is dominated by the reduced driving force for crystallization, described in first approximation by the smaller enthalpy and entropy of fusion
- High Pd contents also lead to a smaller jump of the specific isobaric heat capacity during the glass transition, which is connected to the absolute change in configurational entropy during the undercooling of the liquid. However, it was shown, that a direct correlation with fragility can only be achieved, when the relative changes of entropy are used. This effect becomes eminent in this system due to the significant changes in the enthalpy of fusion (almost a change of 100%), often neglectable in other systems.
- Residual enthalpy in the glassy state, which is connected to the free volume, is drastically reduced upon the addition of Pd to the system. The potential low amount of free volume in the Pd-rich glasses, compared to the Pt-rich ones, partially explains their lower ductility.
- The systematic diffraction studies on the Pt/Pd-Cu-Ni-P suggested that the change of the FWHM of the FSDP is scaling to with the absolute entropic changes due to the structural rearrangements in the deeply supercooled liquid. This means that the width of the peak is changing stronger with temperature for systems that undergo more structural rearrangements/ordering during cooling.

Kinetics and Dynamics

- Investigations on the Kinetics of the glass transition and dynamics of the glass and liquid suggest a V-shaped compositional dependence of fragility, with the strongest liquids being in the intermediate compositions with equal Pt and Pd content, suggesting an additional interaction between both atomic species.

- Microscopic dynamics support the idea of similar dynamics in the solely Pt or Pd containing systems, while revealing significant differences in the change of their dynamic heterogeneities in the deeply undercooled liquid state in the vicinity of T_g.

  It was observed that the changes on the MRO length scale mimic the thermally induced changes of the relaxation spectrum in the vicinity of the glass transition, connecting structural observations with the dynamic behavior of the Pt-based and Pd-based liquids. While the Pd-liquid shows a constant degree of dynamic heterogeneity and small changes in the MRO length scale associated with structurally strong behavior, the Pt-liquid is constantly becoming more heterogeneous when approaching the glass transition, mimicking the changes observed on the MRO length scale, typically connected to structurally fragile behavior. Through this the importance of the actual shape of the relaxation spectrum, which is not included in the actual fragility concept, is highlighted and experimentally shown.

- The XPCS study also revealed that the dynamics of deeply supercooled liquids is showing a wave-vector dependence, so-called "De Gennes narrowing". For the Pt-based system this effect was demonstrated for the first time in deeply undercooled metallic liquids at wave-vectors smaller than the first sharp diffraction peak, relating to a length scale beyond the average interatomic distance.

Mechanics

- Mechanically the glasses with increased Pd content show higher hardness, but also a consequential higher tendency towards embrittlement, validated by micromechanical methods.

- Strain-Rate-Sensitivity of the alloy series is decreasing with higher Pd content, mirroring their smaller ability to multiple shear banding, which is crucial for macroscopically ductile deformation processes.

- The embrittlement tendency at higher Pd-contents was supported by micropillar compression tests.

- The embrittlement was traced back to the structural changes and a growing amount of more rigid, but brittle 3-atom connections in the Pd-rich glasses.

Structure

- X-ray diffraction experiments suggested significant structural differences between the Pt-rich and the Pd-rich liquids. Whereas the Pt-rich systems tend to show a significant MRO with trigonal prisms as the main structural unit, Pd-rich systems feature a larger number of icosahedra, leading to a pronounced icosahedral SRO. From geometrical considerations this leads to a higher number of 3-atom connections in Pd-rich systems, compared to a more diverse number of 1-, 2- and 4-atom connections in the Pt-rich systems.
- These 3-atom connecting schemes are, suggested by simulations, a structural signature of embrittlement. Through the experimentally observed mechanical behavior for the Pt/Pd-Cu-Ni-P system this hypothesis is strongly supported. The increased number of 3-atom connections on the Pd-rich side of the system was connected to increased brittleness. Additionally, aging leads to the growth of the structural signature of aforementioned 3-atom connections and is connected to embrittlement, further supporting the hypothesis.
- From the structural observations the so-called structural fragility was determined following the formalism of Wei et al. Consequently, the Pd-rich liquids are suggested to show structurally strong behavior, derived from their small changes on the MRO length scale. This effect is in line with the observations of the dynamic heterogeneities of the liquid in the vicinity of T_g. Extended studies to explain the misfit to the fragile behavior of the Pd-rich systems in dynamic and kinetic properties, did not find convincing evidence. However, a connection to the decoupling of the diffusion coefficients may be responsible for the break-down of the structural fragility model in this case. Here future works will help to shed further light on this open topic.

In total, the study has answered many questions and enlarged the understanding of highly undercooled melts and their resultant glasses combined with their properties. However, also many new questions arose, motivating new studies. Especially regarding the structure, additional simulations, as well as experimental validations utilizing even more elaborate scattering techniques will be needed. Without the knowledge of the partial structure factors and further sophisticated and systematic variations of the components, no complete picture of the

structure can be drawn. In particular this means additional studies with neutron diffraction and anomalous X-ray scattering will be needed to extend the amount of independent structural measurements, needed to gain insights into the partial structure factors. Especially the change of the Cu/Ni ratio might be helpful to further understand the structural features, as both elements are scattering similarly and can also be assumed topologically equal. Hence, any structural changes in the total structure factor can be related easier to actual structural changes, compared to the changing contrast through the Pt/Pd substitution, which was discussed in this work. However, one drawback here will be the limited glass forming ability, which was observed to deteriorate outside the approximate 3:1 ratio of Cu to Ni in the current alloys. Promising preliminary studies on this topic were already performed, paving the way for continued work on this topic. Further, in-situ X-ray investigations of the structure without the interference of crystallization will be helpful to finally solve the anomalous behavior on the MRO length scale of the Pd-rich systems. Here aerodynamic levitation experiments are already successfully scheduled at synchrotron facilities, that will allow a fast cooling to circumvent the heterogeneous crystallization events for all alloys studied in this work, connecting the high and low temperature structural data. Aerodynamic levitation technique is crucial, as the conventional method of electrostatic levitation is unfortunately not feasible for the P-containing alloys, as P tends to evaporate under the low ambient pressures needed for the electrostatic levitation.

Together with this outlook on the basic scientific impact that the current study on the used alloys can provide also their possible applications should be mentioned. Regarding the application of these unique alloys, outside of jewelry and decorative applications, their superior performance in catalytic reactions needs to be emphasized. In the framework of this thesis also this property was examined and showed promising results in combination with the unique thermoplastic formability, that can be utilized for nano-forming [25]. Hopefully, further studies on the catalytic properties of these amorphous Pt-Pd-alloys will be triggered by our works.

8. Appendix
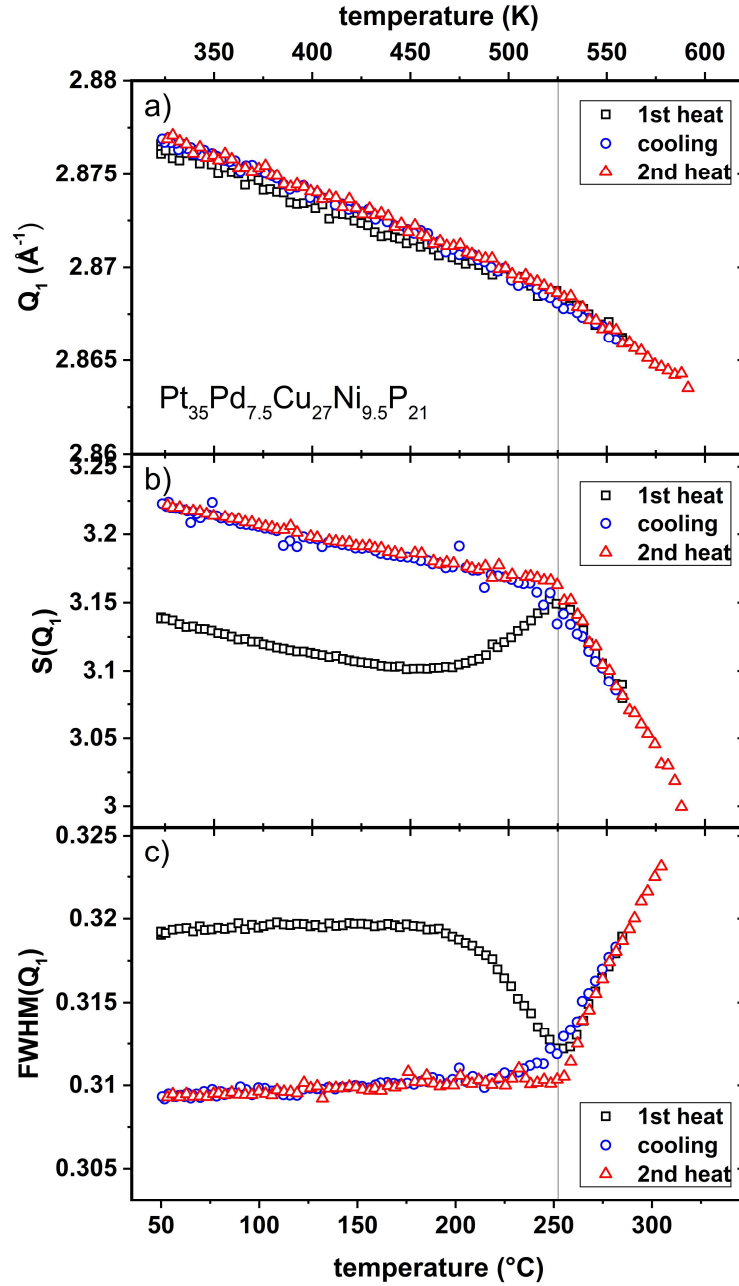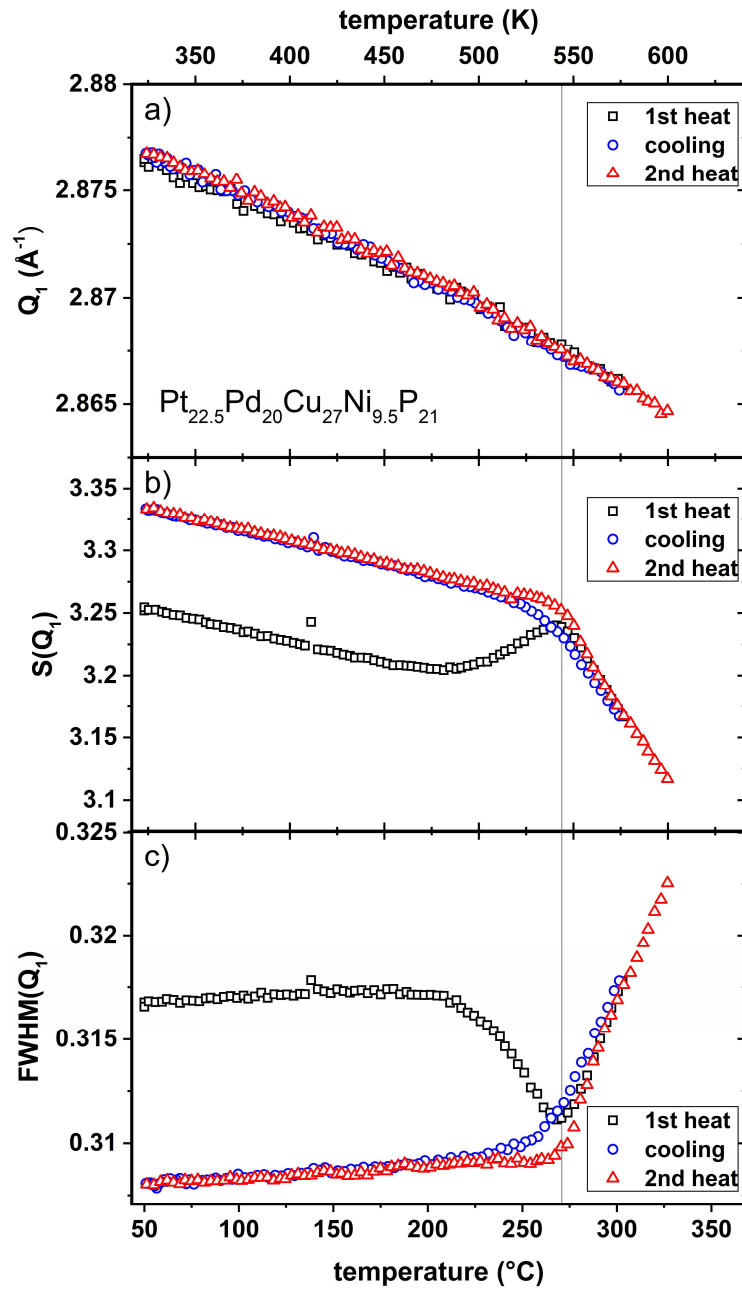
8.1 Additional Figures

Figure 8-1: Evolution of the first sharp diffraction peak during heating and cooling with 0.33 K s⁻¹ in an in-situ high energy synchrotron X-ray diffraction experiment of $Pt_{35}Pd_{7.5}Cu_{27}Ni_{9.5}P_{21}$. The shape of the peak is described using the different parameters of a) peak position Q_1, peak height $S(Q_1)$ and full-width at half maximum $FWHM(Q_1)$. An initial heating into the SCL to $T_{g,end}$ +15 K (black) is used to erase the thermal history of the casting (0.5 mm plate), followed by a controlled cooling to 50 °C and a consecutive 2nd heating, until the sample crystallized.
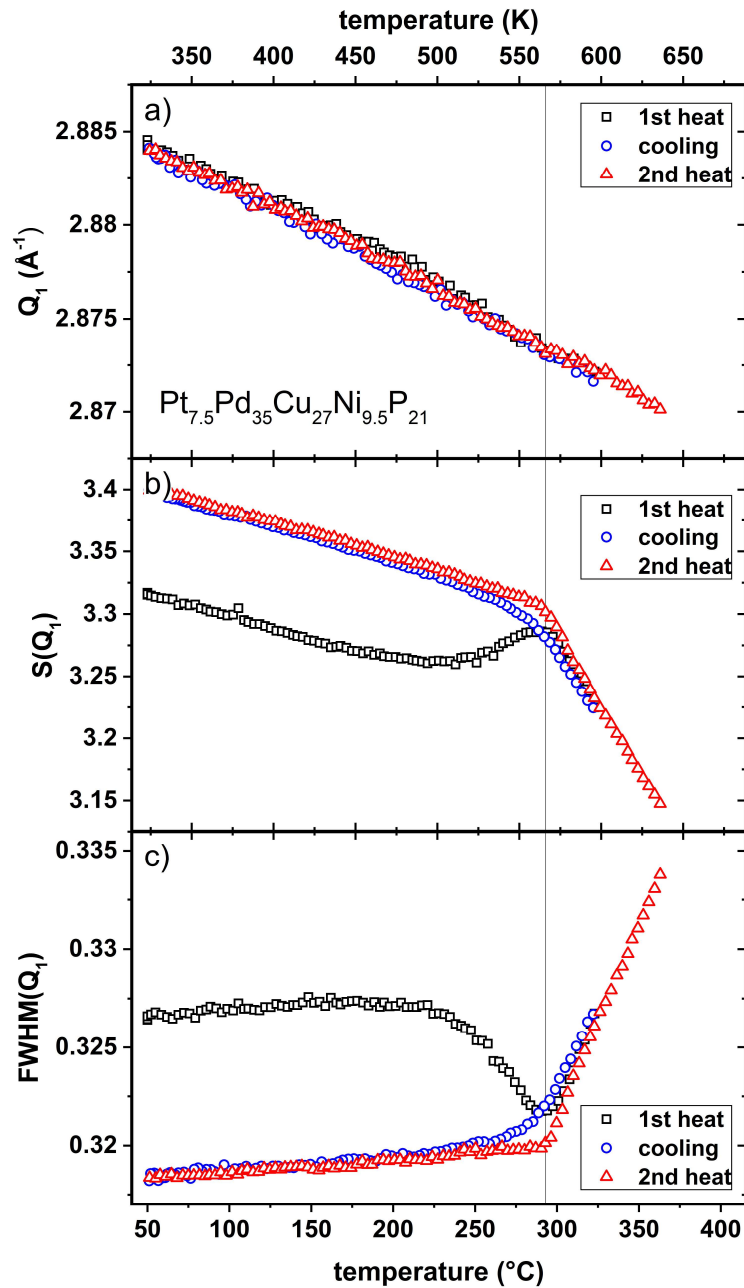
Figure 8-2: Evolution of the first sharp diffraction peak during heating and cooling with 0.33 K s^{-1} in an in-situ high energy synchrotron X-ray diffraction experiment of Pt$_{22.5}$Pd$_{20}$Cu$_{27}$Ni$_{9.5}$P$_{21}$. The shape of the peak is described using the different parameters of a) peak position Q$_1$, peak height S(Q$_1$) and full-width at half maximum FWHM(Q$_1$). An initial heating into the SCL to T$_{g,end}$ +15 K (black) is used to erase the thermal history of the casting (0.5 mm plate), followed by a controlled cooling to 50 °C and a consecutive 2nd heating, until the sample crystallized.
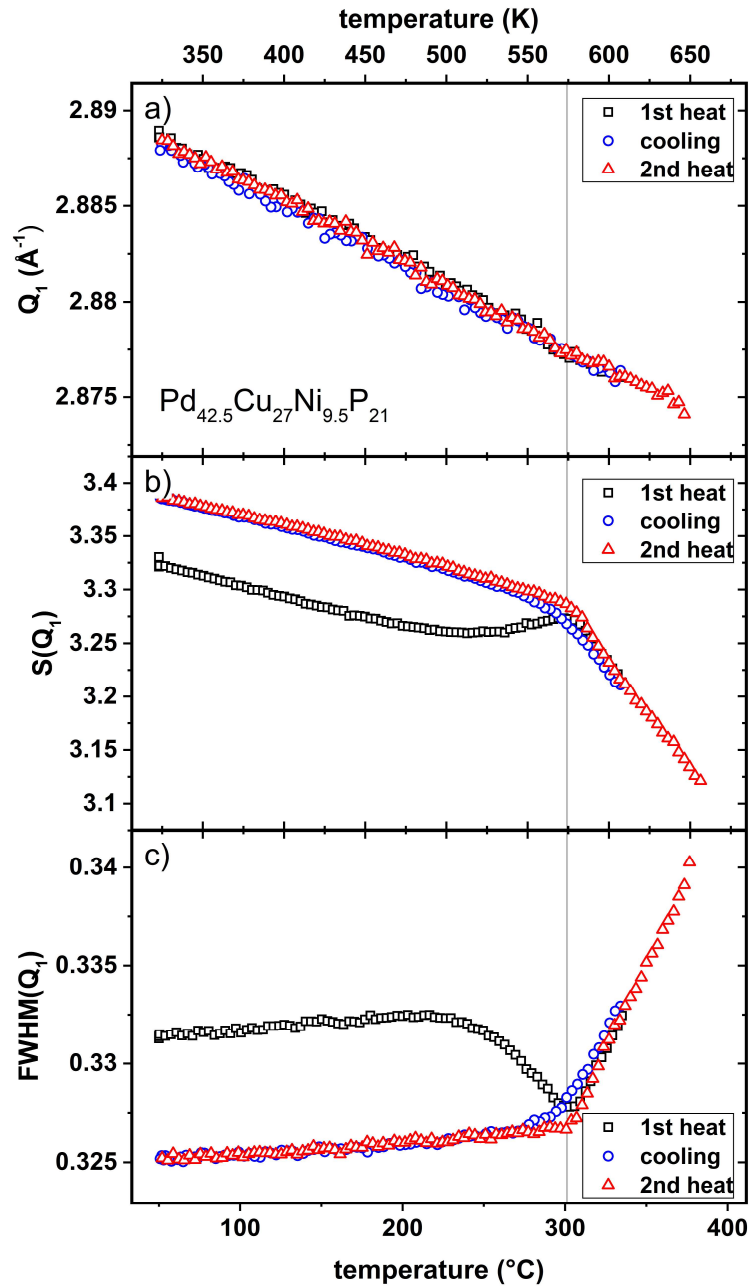
Figure 8-3: Evolution of the first sharp diffraction peak during heating and cooling with 0.33 K s^{-1} in an in-situ high energy synchrotron X-ray diffraction experiment of Pt$_{7.5}$Pd$_{35}$Cu$_{27}$Ni$_{9.5}$P$_{21}$. The shape of the peak is described using the different parameters of a) peak position Q$_1$, peak height S(Q$_1$) and full-width at half maximum FWHM(Q$_1$). An initial heating into the SCL to T$_{g,end}$ +15 K (black) is used to erase the thermal history of the casting (0.5 mm plate), followed by a controlled cooling to 50 °C and a consecutive 2nd heating, until the sample crystallized.

Figure 8-4: Evolution of the first sharp diffraction peak during heating and cooling with 0.33 K s^{-1} in an in-situ high energy synchrotron X-ray diffraction experiment of $Pd_{42.5}Cu_{27}Ni_{9.5}P_{21}$. The shape of the peak is described using the different parameters of a) peak position Q_1, peak height $S(Q_1)$ and full-width at half maximum $FWHM(Q_1)$. An initial heating into the SCL to $T_{g,end}$ +15 K (black) is used to erase the thermal history of the casting (0.5 mm plate), followed by a controlled cooling to 50 °C and a consecutive 2nd heating, until the sample crystallized.
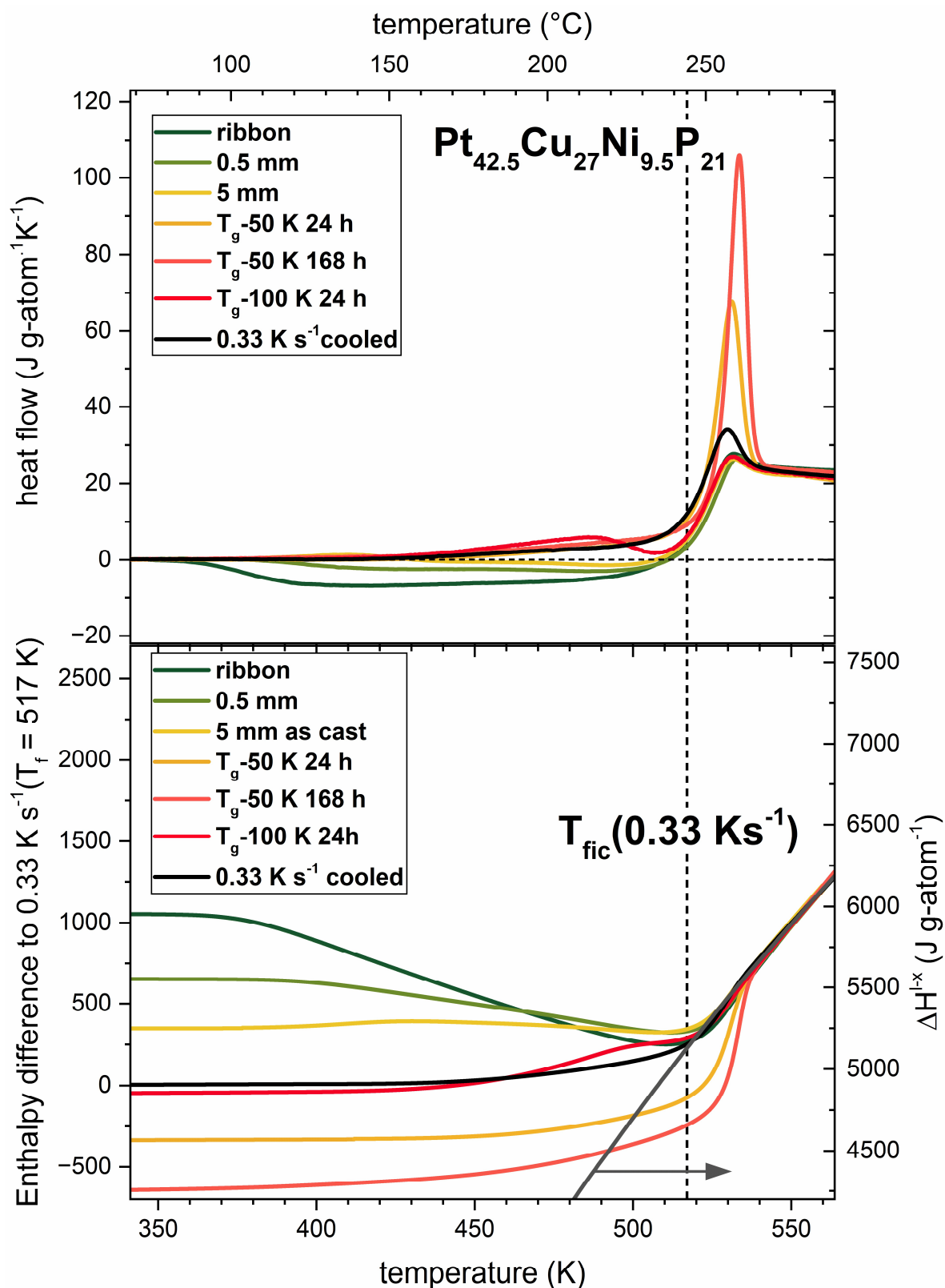
Figure 8-5: Heat flow and respective enthalpy difference obtained by differential scanning calorimetry (DSC) for $Pt_{42.5}Cu_{27}Niu_{9.5}P_{21}$ with different thermal histories, either by different cooling during casting, by different casting thicknesses or by isothermal annealing. The enthalpies are constructed by integration of the DSC traces with the state of a vitrification at 0.33 K^{-1} being the reference state.
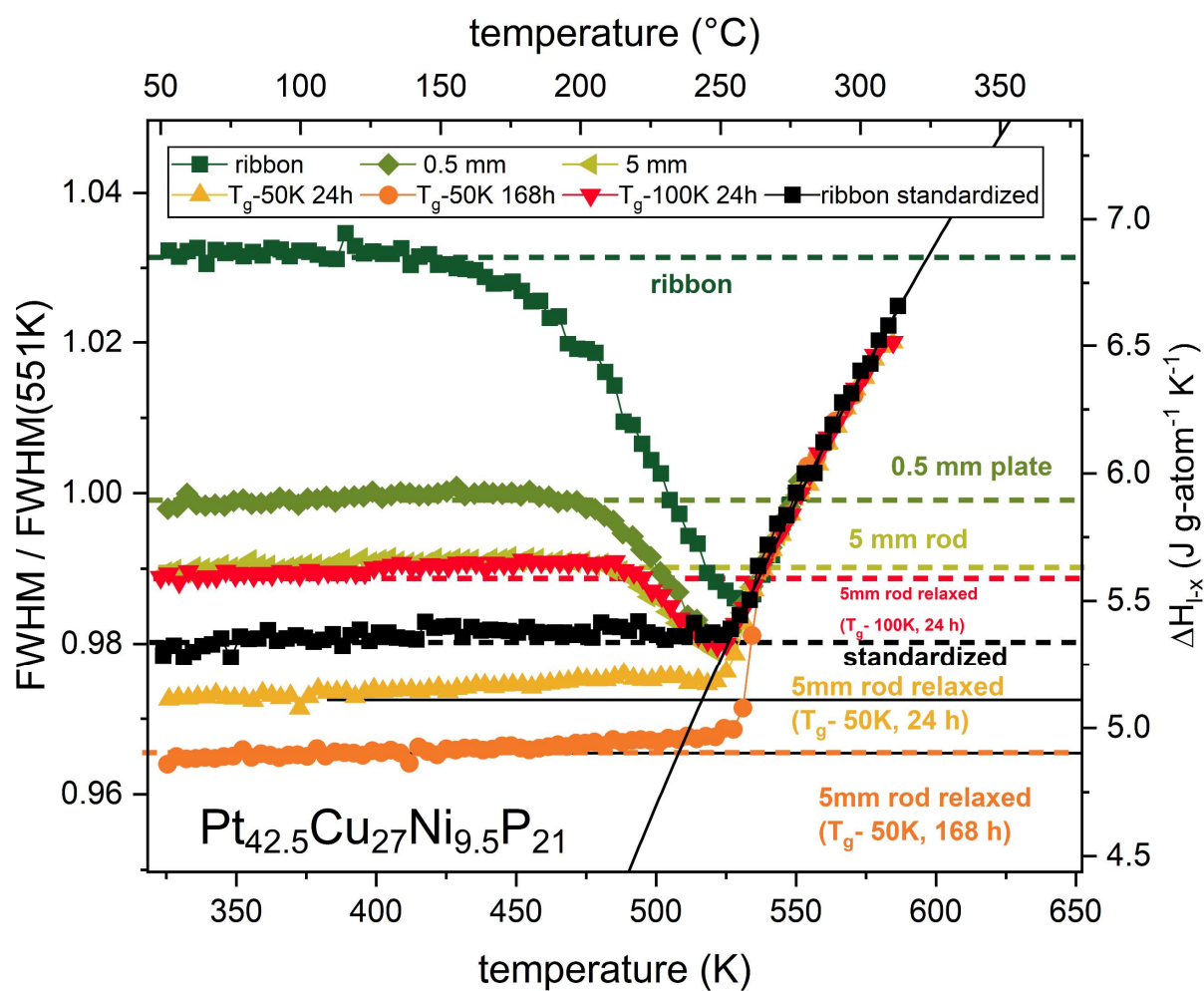
Figure 8-6: Evolution of the FWHM of the FSDP of for $Pt_{42.5}Cu_{27}Niu_{9.5}P_{21}$ with different thermal histories. The curves reproduce well the enthalpic states determined by DSC in Figure 8-5.
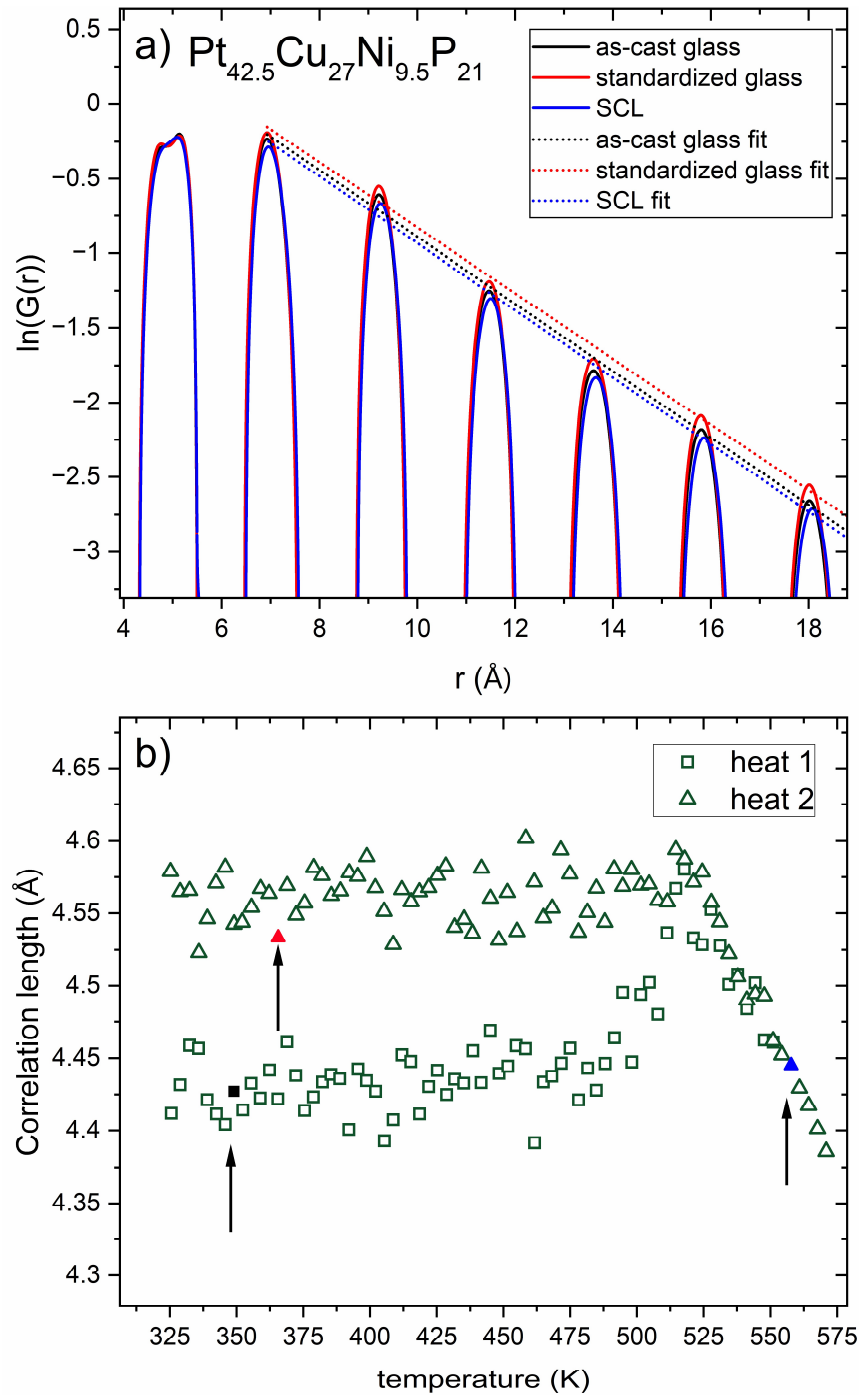
Figure 8-7: Fitting procedure of the Ornstein-Zernicke analysis and respective resulting correlation length for three different states. The fast cooled initial state of the as-cast glass shows a smaller correlation length compared to the relaxed one that has undergone structural ordering. An analogous behavior to the FWHM of the FSDP is observed.
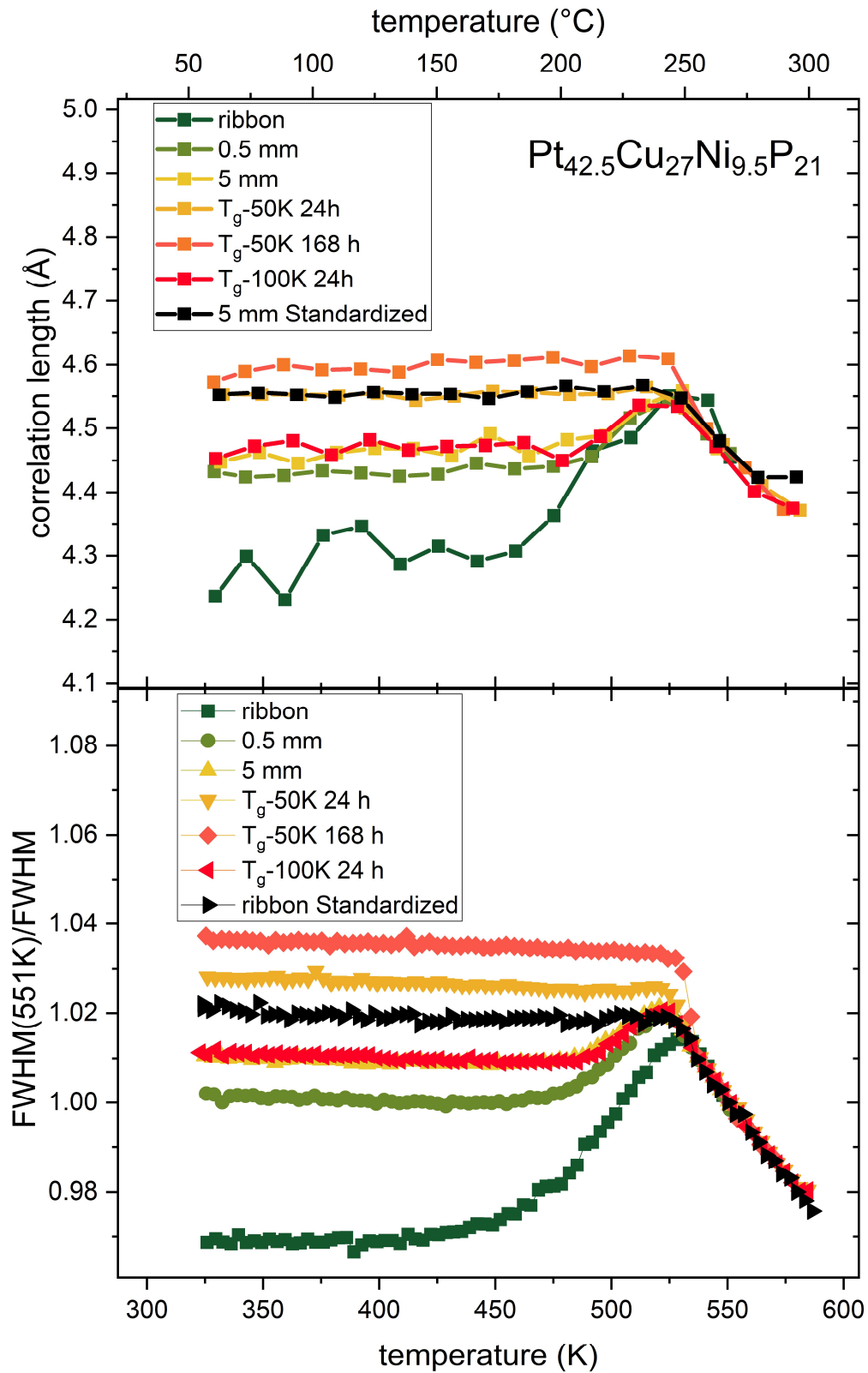
Figure 8-8: Evolution of the correlation length and the FWHM of the FSDP of for $Pt_{42.5}Cu_{27}Niu_{9.5}P_{21}$ with different thermal histories. For a better comparison of the amount of data the correlation length data has been binned by averaging 5 consecutive data points. Similar trends for both properties can be observed inversely resembling the enthalpic states of the different thermal histories.
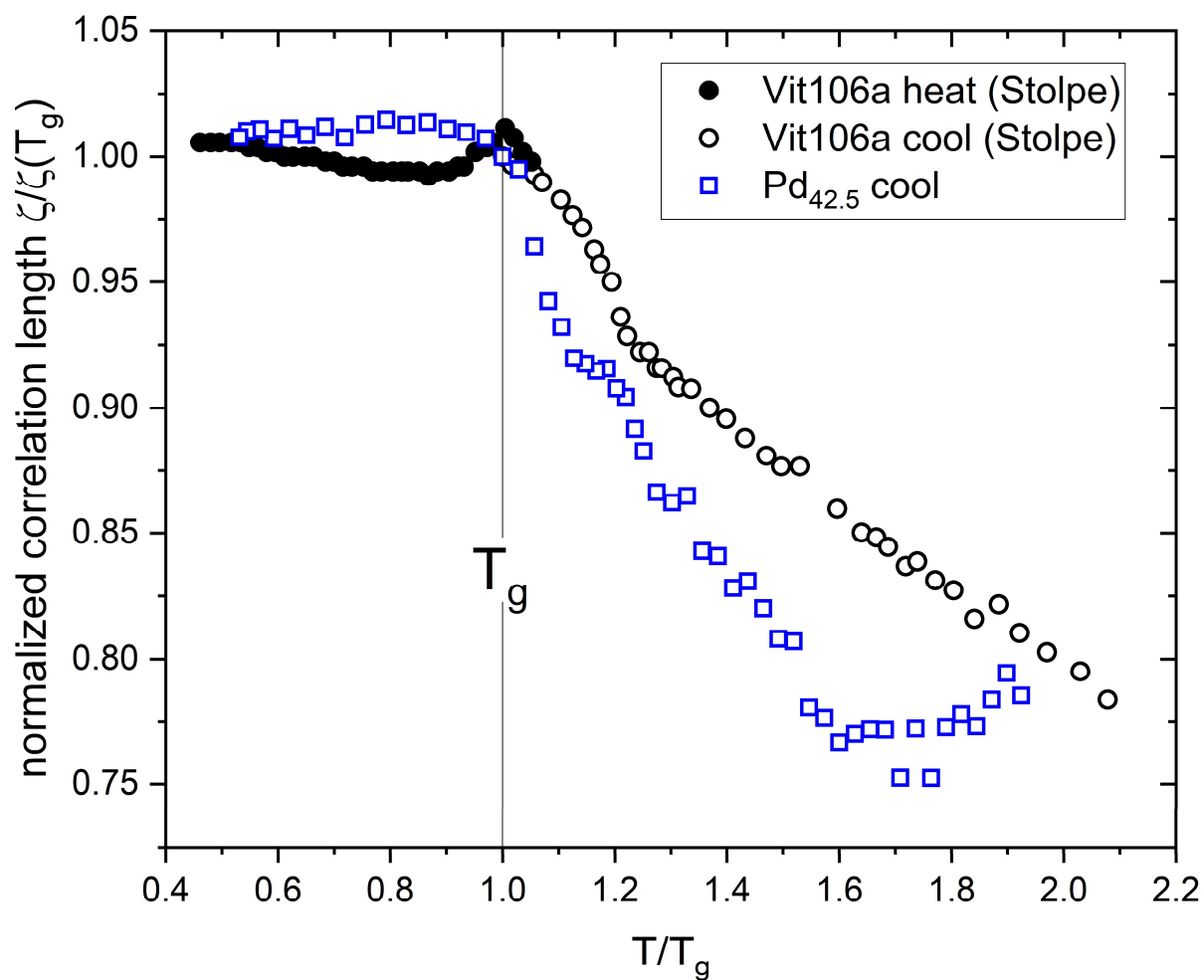
Figure 8-9: Normalized correlation length of two different glass forming systems, $Pd_{42.5}Cu_{27}Ni_{9.5}P_{21}$ (this work) and Vitreloy 106a (Vit 106a) reproduced from the work of Stolpe [78]
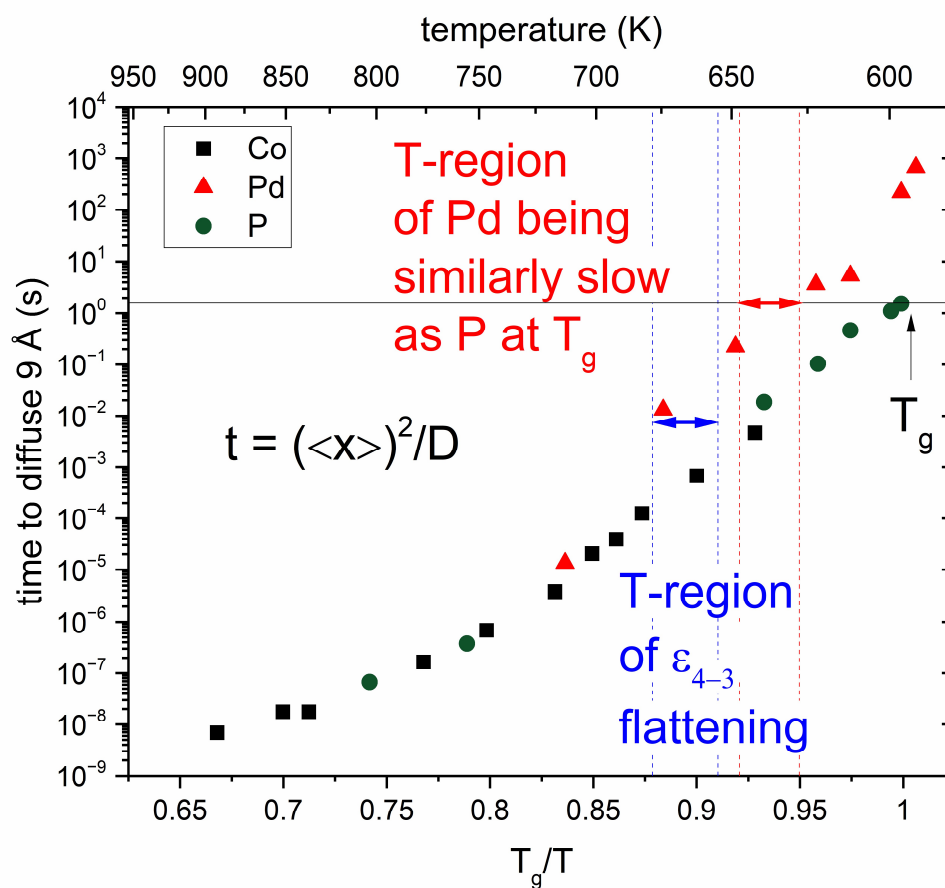
Figure 8-10: Time for the diffusion of an average distance of 9 Å (~4th peak of G(r)) for the different atomic species. Calculations are based on the atomic diffusion coefficients taken from Ref. [232] assuming stationary diffusion.
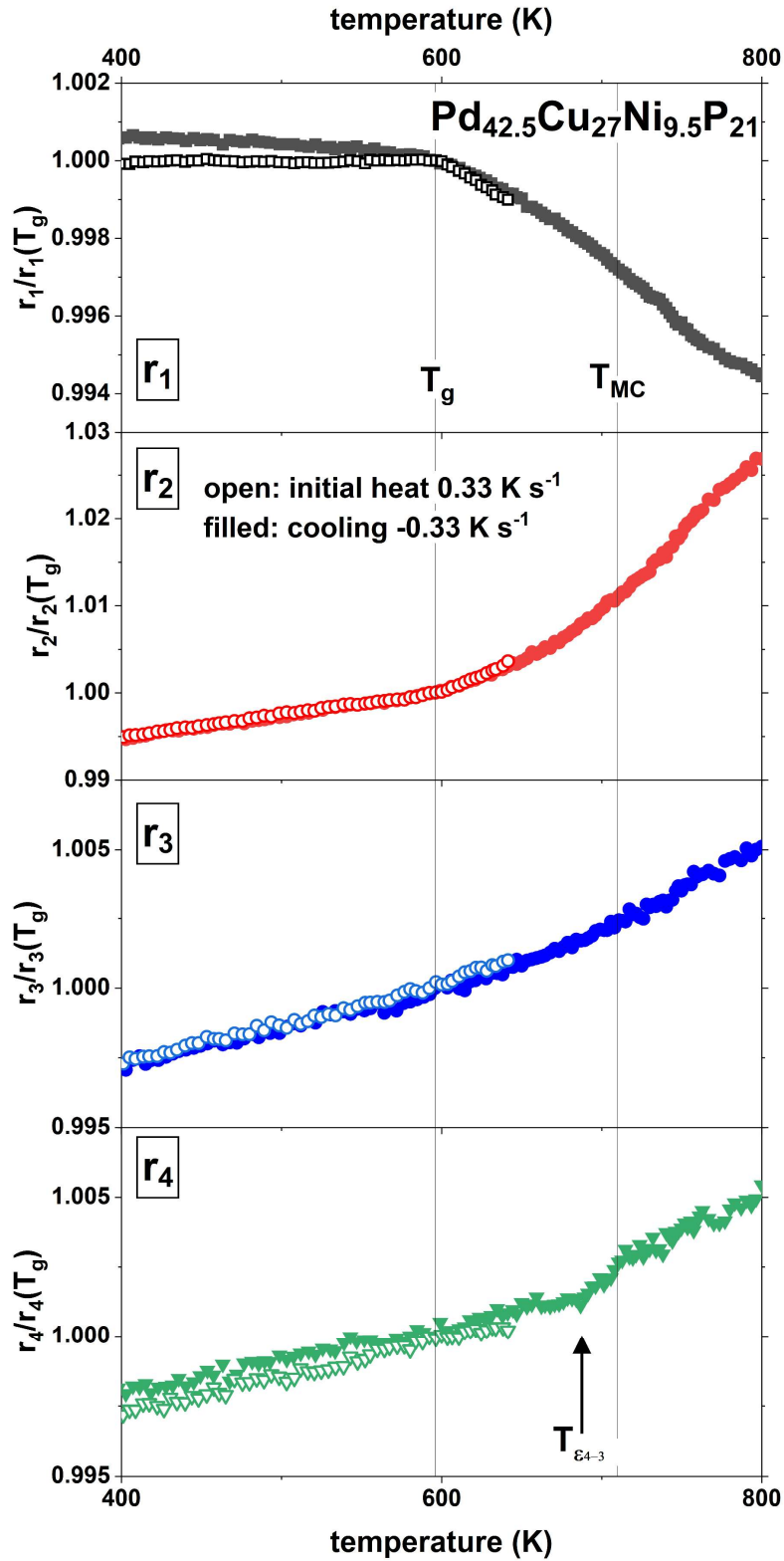
Figure 8-11: Evolution of the normalized peak position of the reduced pair distribution function as a function of temperature. The influence of the decoupled atomic mobility seems to increase with the length-scale of the respective shell, leading to the strongest influence at r_4 and an almost invisible influence on r_1.

8.2 Reprint permissions

8.2.1 Licences for used Figures

Table 8-1: Overview of the sources used in Figures of this work, with the respective Licence of reprint

Figure	Source	Licence
1-1	[4] Duwez et al.	5857490948155
2-12	[79]Ma et al.	5857510210424
2-13	[79] Ma et al.	5857510210424
2-14	[91] Miracle et al.	5857640404608
2-15	[88] Ding et al.	CC 4.0
2-19	[102] Ding et al.	RNP/24/AUG/082755
2-20	[102] Ding et al.	RNP/24/AUG/082755
2-23	[71] Schuh et al.	5857650628350
2-34	[71] Schuh et al.	5857650628350
2-26	[117] Kumar et al.	CC 3.0
2-27	[33] Kumar et al.	5857651063803
2-28	[88] Ding et al.	CC 4.0
3-9	[146] Frey et al.	1520163-1
3-13	[152] Gross et al.	CC 4.0
3-14	[154] Hechler et al.	CC 4.0

8.2.2 Permission for Publication I:

8.2.3 Permission for Publication II:

Licence to Publish - Open Access   SPRINGER NATURE

Licensee:	Springer Nature Limited	(the 'Licensee')
Journal Name:	Scientific Reports	(the 'Journal')
Manuscript Number:	94b7c366-7075-490b-8d83-d01093992ec0	
Proposed Title of Article:	Effect of composition and thermal history on deformation behavior and cluster connections in model bulk metallic glasses	(the 'Article')
Author(s) [Please list all named Authors]:	Nico Neuber, Maryam Sadeghilaridjani, Nandita Ghodki, Oliver Gross, Bastian Adam, Lucas Ruschel, Maximilian Frey, Saideep Muskeri, Malte Blankenburg, Isabella Gallino, Ralf Busch, Sundeep Mukherjee	(the 'Author')
Corresponding Author Name:	Nico Neuber	

Licence Applicable to the Article:

Creative Commons licence CC BY: This licence allows readers to copy, distribute and transmit the Article as long as it is attributed back to the author. Readers are permitted to alter, transform or build upon the Article, and to use the Article for commercial purposes. Please read the full licence for further details at -
http://creativecommons.org/licenses/by/4.0/

Subject to editorial acceptance of the Article, it will be published under the Creative Commons licence shown above.

1   Grant of Rights

   a)   For good and valuable consideration, the Author hereby grants to the Licensee the perpetual, non-exclusive, irrevocable, world-wide, assignable, sublicensable and unlimited right to: publish, reproduce, copy, distribute, communicate, display publicly, sell, rent and/ or otherwise make available the article identified above, including any supplementary information and graphic elements therein (e.g. illustrations, charts, moving images) (the "Article") in any language, in any versions or editions in any and all forms and/or media of expression (including without limitation in connection with any and all end-user devices), whether now known or developed in the future. Without limitation, the above grant includes: (i) the right to edit, alter, adapt, adjust and prepare derivative works; (ii) all advertising and marketing rights including without limitation in relation to social media; (iii) rights for any training, educational and/or instructional purposes; (iv) the right to add and/or remove links or combinations with other media/works; and (v) the right to create, use and/or license and/or sublicense content data or metadata of any kind in relation to the Article (including abstracts and summaries) without restriction. The above rights are granted in relation to the Article as a whole or any part and with or in relation to any other works.

   b)   Without limiting the rights granted above, Licensee is granted the rights to use the Article for the purposes of analysis, testing, and development of publishing- and research-related workflows, systems, products, projects, and services; to confidentially share the Article with select third parties to do the same; and to retain and store the Article and any associated correspondence/files/forms to maintain the historical record, and to facilitate research integrity investigations. The grant of rights set forth in this clause (b) is irrevocable.

   c)   The Licensee will have the right, but not the obligation, to exercise any or all of the rights granted herein. If the Licensee elects not to publish the Article for any reason, all publishing rights under this Agreement as set forth in clause 1.a) above will revert to the Author.

2   Copyright

Ownership of copyright in the Article will be vested in the name of the Author. When reproducing the Article or extracts from it, the Author will acknowledge and reference first publication in the Journal.

3   Use of Article Versions

   a)   For purposes of this Agreement: (i) references to the "Article" include all versions of the Article; (ii) "Submitted Manuscript" means the version of the Article as first submitted by the Author; (iii) "Accepted Manuscript" means the version of the Article accepted for publication, but prior to copy-editing and typesetting; and (iv) "Version of Record" means the version of the Article published by the Licensee, after copy-editing and typesetting. Rights to all versions of the Manuscript are granted on a non-exclusive basis.

b) The Author may make the Submitted Manuscript available at any time and under any terms (including, but not limited to, under a CC BY licence), at the Author's discretion. Once the Article has been published, the Author will include an acknowledgement and provide a link to the Version of Record on the publisher's website: "This preprint has not undergone peer review (when applicable) or any post-submission improvements or corrections. The Version of Record of this article is published in [insert journal title], and is available online at https://doi.org/[insert DOI]".

c) Immediately after acceptance the Author may deposit the Accepted Manuscript to any location, and under any terms (including, but not limited to, under a CC BY licence), provided it is not made publicly available until after publication. The Author will include an acknowledgement in the Accepted Manuscript, together with a link to the Version of Record on the publisher's website: "This version of the article has been accepted for publication, after peer review (when applicable) but is not the Version of Record and does not reflect post-acceptance improvements, or any corrections. The Version of Record is available online at: http://dx.doi.org/[insert DOI]".

4   Warranties & Representations

Author warrants and represents that:

a)

    i.   the Author is the sole copyright owner or has been authorised by any additional copyright owner(s) to grant the rights defined in clause 1,

    ii.   the Article does not infringe any intellectual property rights (including without limitation copyright, database rights or trade mark rights) or other third party rights and no licence from or payments to a third party are required to publish the Article,

    iii.   the Article has not been previously published or licensed, nor has the Author committed to licensing any version of the Article under a licence inconsistent with the terms of this Agreement,

    iv.   if the Article contains materials from other sources (e.g. illustrations, tables, text quotations), Author has obtained written permissions to the extent necessary from the copyright holder(s), to license to the Licensee the same rights as set out in clause 1 and has cited any such materials correctly;

b) all of the facts contained in the Article are according to the current body of research true and accurate;

c) nothing in the Article is obscene, defamatory, violates any right of privacy or publicity, infringes any other human, personal or other rights of any person or entity or is otherwise unlawful and that informed consent to publish has been obtained for any research participants;

d) nothing in the Article infringes any duty of confidentiality owed to any third party or violates any contract, express or implied, of the Author;

e) all institutional, governmental, and/or other approvals which may be required in connection with the research reflected in the Article have been obtained and continue in effect;

f) all statements and declarations made by the Author in connection with the Article are true and correct; and

g) the signatory who has signed this agreement has full right, power and authority to enter into this agreement on behalf of all of the Authors.

5   Cooperation

a) The Author will cooperate fully with the Licensee in relation to any legal action that might arise from the publication of the Article, and the Author will give the Licensee access at reasonable times to any relevant accounts, documents and records within the power or control of the Author. The Author agrees that any Licensee affiliate through which the Licensee exercises any rights or performs any obligations under this Agreement is intended to have the benefit of and will have the right to enforce the terms of this Agreement.

b) Author authorises the Licensee to take such steps as it considers necessary at its own expense in the Author's name(s) and on their behalf if the Licensee believes that a third party is infringing or is likely to infringe copyright in the Article including but not limited to initiating legal proceedings.

6   Author List

Changes of authorship, including, but not limited to, changes in the corresponding author or the sequence of authors, are not permitted after acceptance of a manuscript.

7   Post Publication Actions

The Author agrees that the Licensee may remove or retract the Article or publish a correction or other notice in relation to the Article if the Licensee determines that such actions are appropriate from an editorial, research integrity, or legal perspective.

8   Controlling Terms

The terms of this Agreement will supersede any other terms that the Author or any third party may assert apply to any version of the Article.

9   Governing Law

This Agreement will be governed by, and construed in accordance with, the laws of England and Wales. The courts of London, UK will have exclusive jurisdiction.

Signed for and on behalf of the Author(s)
Corresponding Author: Nico Neuber
Email: nico.neuber@uni-saarland.de
IP Address: 134.96.58.8

Time Stamp: 2022-09-27 05:38:23

8.2.4 Permission for Publication III:

CCC RightsLink

Disentangling structural and kinetic components of the α-relaxation in supercooled metallic liquids

SPRINGER NATURE

Author: Nico Neuber et al
Publication: Communications Physics
Publisher: Springer Nature
Date: Dec 6, 2022

Copyright © 2022, The Author(s)

Creative Commons

This is an open access article distributed under the terms of the Creative Commons CC BY license, which permits unrestricted use, distribution, and reproduction in any medium, provided the original work is properly cited.

You are not required to obtain permission to reuse this article.

To request permission for a type of use not listed, please contact Springer Nature

8.2.5 Permission for Publication IV:

8.2.5 Permission for Publication V:

American Physical Society
Reuse and Permissions License

18-Jul-2022

This license agreement between the American Physical Society ("APS") and Nico Neuber ("You") consists of your license details and the terms and conditions provided by the American Physical Society and SciPris.

Licensed Content Information

License Number:	**RNP/22/JUL/055843**
License date:	18-Jul-2022
DOI:	10.1103/PhysRevLett.125.055701
Title:	Wave-Vector Dependence of the Dynamics in Supercooled Metallic Liquids
Author:	B. Ruta et al.
Publication:	Physical Review Letters
Publisher:	American Physical Society
Cost:	USD $ 0.00

Request Details

Does your reuse require significant modifications: No

Specify intended distribution locations:	Germany
Reuse Category:	Reuse in a thesis/dissertation
Requestor Type:	Student
Items for Reuse:	Whole Article
Format for Reuse:	Print and Electronic
Total number of print copies:	Up to 1000

Information about New Publication:

University/Publisher:	Saarland University
Title of dissertation/thesis:	Intercorrelation of Thermodynamics, Kinetics, Structure and Mechanics in a model metallic glass forming system
Author(s):	Nico Neuber
Expected completion date:	Nov. 2022

License Requestor Information

Name:	Nico Neuber
Affiliation:	Individual
Email Id:	nico.neuber@uni-saarland.de
Country:	Germany

APS physics — American Physical Society Reuse and Permissions License
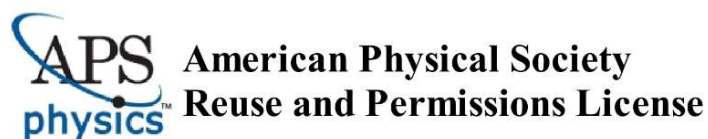
TERMS AND CONDITIONS

The American Physical Society (APS) is pleased to grant the Requestor of this license a non-exclusive, non-transferable permission, limited to Print and Electronic format, provided all criteria outlined below are followed.

1. You must also obtain permission from at least one of the lead authors for each separate work, if you haven't done so already. The author's name and affiliation can be found on the first page of the published Article.

2. For electronic format permissions, Requestor agrees to provide a hyperlink from the reprinted APS material using the source material's DOI on the web page where the work appears. The hyperlink should use the standard DOI resolution URL, http://dx.doi.org/{DOI}. The hyperlink may be embedded in the copyright credit line.

3. For print format permissions, Requestor agrees to print the required copyright credit line on the first page where the material appears: "Reprinted (abstract/excerpt/figure) with permission from [(FULL REFERENCE CITATION) as follows: Author's Names, APS Journal Title, Volume Number, Page Number and Year of Publication.] Copyright (YEAR) by the American Physical Society."

4. Permission granted in this license is for a one-time use and does not include permission for any future editions, updates, databases, formats or other matters. Permission must be sought for any additional use.

5. Use of the material does not and must not imply any endorsement by APS.

6. APS does not imply, purport or intend to grant permission to reuse materials to which it does not hold copyright. It is the requestor's sole responsibility to ensure the licensed material is original to APS and does not contain the copyright of another entity, and that the copyright notice of the figure, photograph, cover or table does not indicate it was reprinted by APS with permission from another source.

7. The permission granted herein is personal to the Requestor for the use specified and is not transferable or assignable without express written permission of APS. This license may not be amended except in writing by APS.

8. You may not alter, edit or modify the material in any manner.

9. You may translate the materials only when translation rights have been granted.

10. APS is not responsible for any errors or omissions due to translation.

11. You may not use the material for promotional, sales, advertising or marketing purposes.

12. The foregoing license shall not take effect unless and until APS or its agent, Aptara, receives payment in full in accordance with Aptara Billing and Payment Terms and Conditions, which are incorporated herein by reference.

13. Should the terms of this license be violated at any time, APS or Aptara may revoke the license with no refund to you and seek relief to the fullest extent of the laws of the USA. Official written notice will be made using the contact information provided with the permission request. Failure to receive such notice will not nullify revocation of the permission.

14. APS reserves all rights not specifically granted herein.

15. This document, including the Aptara Billing and Payment Terms and Conditions, shall be the entire agreement between the parties relating to the subject matter hereof.

9. References

[1]   M.F. Ashby, A.L. Greer, Metallic glasses as structural materials, Scr. Mater. 54 (2006) 321–326. https://doi.org/10.1016/j.scriptamat.2005.09.051.

[2]   M. Telford, The case for bulk metallic glass, Mater. Today. 7 (2004) 36–43. https://doi.org/10.1016/S1369-7021(04)00124-5.

[3]   J. Schroers, Bulk metallic glasses, Phys. Today. 66 (2013) 32–37. https://doi.org/10.1063/PT.3.1885.

[4]   W. Klement, R.H. Willens, P. Duwez, Non-crystalline structure in solidified Gold-Silicon alloys, Nature. 187 (1960) 869–870. https://doi.org/10.1038/187869b0.

[5]   D. Turnbull, Under What Conditions Can A Glass Be Formed?, Contemp. Phys. 10 (1969) 473–488. https://doi.org/10.1080/00107516908204405.

[6]   X.H. Lin, W.L. Johnson, Formation of Ti – Zr – Cu – Ni bulk metallic glasses Formation of Ti-Zr-Cu-Ni bulk metallic glasses, 6514 (2005). https://doi.org/10.1063/1.360537.

[7]   N. Nishiyama, K. Takenaka, H. Miura, N. Saidoh, Y. Zeng, A. Inoue, The world's biggest glassy alloy ever made, Intermetallics. 30 (2012) 19–24. https://doi.org/10.1016/j.intermet.2012.03.020.

[8]   A. Inoue, T. Zhang, T. Masumoto, Zr-Al-Ni Amorphous Alloys with High Glass Transition Temperature and Significant Supercooled Liquid Region, Mater. Trans. JIM. 31 (1990) 177–183. https://doi.org/10.2320/matertrans1989.31.177.

[9]   J. Heinrich, R. Busch, B. Nonnenmacher, Processing of a bulk metallic glass forming alloy based on industrial grade Zr, Intermetallics. 25 (2012) 1–4. https://doi.org/10.1016/j.intermet.2012.02.011.

[10]   A. Kuball, O. Gross, B. Bochtler, R. Busch, Sulfur-bearing metallic glasses: A new family of bulk glass-forming alloys, Scr. Mater. 146 (2018) 73–76. https://doi.org/10.1016/j.scriptamat.2017.11.011.

[11]   M. Frey, R. Busch, W. Possart, I. Gallino, On the thermodynamics, kinetics, and sub-T_g

relaxations of Mg-based bulk metallic glasses, Acta Mater. 155 (2018) 117–127. https://doi.org/10.1016/j.actamat.2018.05.063.

[12]   A. Inoue, A. Kato, T. Zhang, S.G. Kim, T. Masumoto, Mg-Cu-Y Amorphous-Alloys with High Mechanical Strengths Produced by a Metallic Mold Casting Method, Mater. Trans. Jim. 32 (1991) 609–616. https://doi.org/10.2320/matertrans1989.32.609.

[13]   B. Bochtler, O. Gross, I. Gallino, R. Busch, Thermo-physical characterization of the $Fe_{67}Mo_6Ni_{3.5}Cr_{3.5}P_{12}C_{5.5}B_{2.5}$ bulk metallic glass forming alloy, Acta Mater. 118 (2016) 129–139. https://doi.org/10.1016/j.actamat.2016.07.031.

[14]   C. Suryanarayana, A. Inoue, Iron-based bulk metallic glasses, Int. Mater. Rev. 58 (2013) 131–166. https://doi.org/10.1179/1743280412Y.0000000007.

[15]   A. Kuball, B. Bochtler, O. Gross, V. Pacheco, M. Stolpe, S. Hechler, R. Busch, On the bulk glass formation in the ternary Pd-Ni-S system, Acta Mater. 158 (2018) 13–22. https://doi.org/10.1016/j.actamat.2018.07.039.

[16]   X.M. Wang, I. Yoshii, A. Inoue, Y.-H.H. Kim, I.-B.B. Kim, Bulk amorphous Ni75-xNb5MxP20-yBy (M = Cr, Mo) alloys with large supercooling and high strength, Mater. Trans. Jim. 40 (1999) 1130–1136. https://doi.org/10.2320/matertrans1989.40.1130.

[17]   L.Y. Schmitt, N. Neuber, M. Eisenbart, L. Cifci, O. Gross, U.E. Klotz, R. Busch, Study on technical parameters and suitability of Pt-based metallic glasses for jewellery applications, Johnson Matthey Technol. Rev. 44 (2022) 1–33. https://doi.org/10.1595/205651323x16577027080875.

[18]   O. Gross, M. Eisenbart, L.-Y.Y.L.-Y. Schmitt, N. Neuber, L. Ciftci, U.E.U.E. Klotz, R. Busch, I. Gallino, Development of novel 18-karat, premium-white gold bulk metallic glasses with improved tarnishing resistance, Mater. Des. 140 (2018) 495–504. https://doi.org/10.1016/j.matdes.2017.12.007.

[19]   J. Schroers, W.L. Johnson, Highly processable bulk metallic glass-forming alloys in the Pt-Co-Ni-Cu-P system, Appl. Phys. Lett. 84 (2004) 3666–3668. https://doi.org/10.1063/1.1738945.

[20]   O.S. Houghton, A.L. Greer, A conflict of fineness and stability: Platinum- And

palladium-based bulk metallic glasses for jewellery: Part II processing, tarnish resistance and future developments, Johnson Matthey Technol. Rev. 65 (2021) 519–534. https://doi.org/10.1595/205651321X16248976623399.

[21]   N. Neuber, O. Gross, M. Frey, B. Bochtler, A. Kuball, S. Hechler, I. Gallino, R. Busch, On the thermodynamics and its connection to structure in the Pt-Pd-Cu-Ni-P bulk metallic glass forming system, Acta Mater. 220 (2021) 117300. https://doi.org/10.1016/j.actamat.2021.117300.

[22]   R.C. Sekol, G. Kumar, M. Carmo, F. Gittleson, N. Hardesty-Dyck, S. Mukherjee, J. Schroers, A.D. Taylor, Bulk metallic glass micro fuel cell, Small. 9 (2013) 2081–2085. https://doi.org/10.1002/smll.201201647.

[23]   Y. Yan, C. Wang, Z. Huang, J. Fu, Z. Lin, X. Zhang, J. Ma, J. Shen, Highly efficient and robust catalysts for the hydrogen evolution reaction by surface nano engineering of metallic glass, J. Mater. Chem. A. 9 (2021) 5415–5424. https://doi.org/10.1039/d0ta10235k.

[24]   Z. Jia, Y. Yang, Q. Wang, C. Kong, Y. Yao, Q. Wang, L. Sun, B. Shen, J.J. Kruzic, An Ultrafast and Stable High-Entropy Metallic Glass Electrode for Alkaline Hydrogen Evolution Reaction, ACS Mater. Lett. 4 (2022) 1389–1396. https://doi.org/10.1021/acsmaterialslett.2c00371.

[25]   C. Mahajan, V. Hasannaeimi, N. Neuber, X. Wang, R. Busch, I. Gallino, S. Mukherjee, Model Metallic Glasses for Superior Electrocatalytic Performance in a Hydrogen Oxidation Reaction, ACS Appl. Mater. Interfaces. 15 (2023) 6697–6707. https://doi.org/10.1021/acsami.2c18266.

[26]   H.F. Li, Y.F. Zheng, Recent advances in bulk metallic glasses for biomedical applications, Acta Biomater. 36 (2016) 1–20. https://doi.org/10.1016/j.actbio.2016.03.047.

[27]   J. Schroers, G. Kumar, T.M. Hodges, S. Chan, T.R. Kyriakides, Bulk metallic glasses for biomedical applications, Jom. 61 (2009) 21–29. https://doi.org/10.1007/s11837-009-0128-1.

[28]   A.M. Loye, H.-K. Kwon, D. Dellal, R. Ojeda, S. Lee, R. Davis, N. Nagle, P.G. Doukas,

J. Schroers, F.Y. Lee, T.R. Kyriakides, Biocompatibility of platinum-based bulk metallic glass in orthopedic applications, Biomed. Mater. 16 (2021) 45018. https://doi.org/10.1088/1748-605X/abf981.

[29] A. Inoue, Stabilization of metallic supercooled liquid and bulk amorphous alloys, Acta Mater. 48 (2000) 279–306. https://doi.org/10.1016/S1359-6454(99)00300-6.

[30] J.H. Na, M.D. Demetriou, M. Floyd, A. Hoff, G.R. Garrett, W.L. Johnson, Compositional landscape for glass formation in metal alloys, Proc. Natl. Acad. Sci. 111 (2014) 9031–9036. https://doi.org/10.1073/pnas.1407780111.

[31] K.J. Laws, D.B. Miracle, M. Ferry, A predictive structural model for bulk metallic glasses, Nat. Commun. 6 (2015) 1–10. https://doi.org/10.1038/ncomms9123.

[32] D.B. Miracle, A structural model for metallic glasses, Microsc. Microanal. 10 (2004) 786–787. https://doi.org/10.1038/nmat1219.

[33] G. Kumar, S. Prades-Rodel, A. Blatter, J. Schroers, Unusual brittle behavior of Pd-based bulk metallic glass, Scr. Mater. 65 (2011) 585–587. https://doi.org/10.1016/j.scriptamat.2011.06.029.

[34] N. Nishiyama, K. Takenaka, A. Inoue, Pd30 Pt17.5 Cu32.5 P20 alloy with low critical cooling rate of 0.067 K/s, Appl. Phys. Lett. 88 (2006) 30–33. https://doi.org/10.1063/1.2186512.

[35] K. Takenaka, T. Wada, N. Nishiyama, H. Kimura, A. Inoue, New Pd-based bulk glassy alloys with high glass-forming ability and large supercooled liquid region, Mater. Trans. 46 (2005) 1720–1724. https://doi.org/10.2320/matertrans.46.1720.

[36] O. Gross, B. Bochtler, M. Stolpe, S. Hechler, W. Hembree, R. Busch, I. Gallino, The kinetic fragility of Pt-P- and Ni-P-based bulk glass-forming liquids and its thermodynamic and structural signature, Acta Mater. 132 (2017) 118–127. https://doi.org/10.1016/j.actamat.2017.04.030.

[37] O. Gross, Precious metal based bulk glass-forming liquids: Development, thermodynamics, kinetics and structure, Diss. Saarl. Univ. (2018). https://doi.org/10.22028/D291-27993.

[38]   O. Kubaschewski, C.B. Alcock, P.J. Spencer, Materials thermochemistry, (1993) 363. https://doi.org/10.2170/physiolsci.RP009208.

[39]   Z. Evenson, On the thermodynamic and kinetic properties of bulk glass forming metallic systems, Univ. Des Saarlandes. (2012). https://doi.org/doi:10.22028/D291-22851.

[40]   D.A. Porter, K.E. Easterling, K.E. Easterling, Phase Transformations in Metals and Alloys (Revised Reprint), CRC press, 2009. https://doi.org/10.1201/9781439883570.

[41]   O. Gross, S.S. Riegler, M. Stolpe, B. Bochtler, A. Kuball, S. Hechler, R. Busch, I. Gallino, On the high glass-forming ability of Pt-Cu-Ni/Co-P-based liquids, Acta Mater. 141 (2017) 109–119. https://doi.org/10.1016/j.actamat.2017.09.013.

[42]   D.M. Herlach, Non-equilibrium solidification of undercooled metallic metls, Mater. Sci. Eng. R Reports. 12 (1994) 177–272. https://doi.org/10.1016/0927-796X(94)90011-6.

[43]   D.R. Uhlmann, Glass formation, J. Non. Cryst. Solids. 25 (1977) 42–85. https://doi.org/http:// dx.doi.org/10.1016/0022-3093(77)90090-4.

[44]   D.R. Uhlmann, A kinetic treatment of glass formation, J. Non. Cryst. Solids. 7 (1972) 337–348. https://doi.org/10.1016/0022-3093(72)90269-4.

[45]   K.F. Kelton, A.L. Greer, Nucleation in Condensed Matter, Elsevier, 2010. https://doi.org/10.1016/S1470-1804(09)01515-6.

[46]   W.L. Johnson, J.H. Na, M.D. Demetriou, Quantifying the origin of metallic glass formation, Nat. Commun. 7 (2016). https://doi.org/10.1038/ncomms10313.

[47]   N. Neuber, M. Frey, O. Gross, J. Baller, I. Gallino, R. Busch, Ultrafast scanning calorimetry of newly developed Au-Ga bulk metallic glasses, J. Phys. Condens. Matter. 32 (2020). https://doi.org/10.1088/1361-648X/ab8252.

[48]   R. Böhmer, C.A. Angell, Correlations of the nonexponentiality and state dependence of mechanical relaxations with bond connectivity in Ge-As-Se supercooled liquids, Phys. Rev. B. 45 (1992) 10091–10094. https://doi.org/10.1103/PhysRevB.45.10091.

[49]   R. Böhmer, K.L. Ngai, C.A. Angell, D.J. Plazek, R. Böhmer, K.L. Ngai, C.A. Angell, D.J. Plazek, R. Böhmer, K.L. Ngai, C.A. Angell, D.J. Plazek, Nonexponential

relaxations in strong and fragile glass formers, J. Chem. Phys. 99 (1993) 4201–4209. https://doi.org/10.1063/1.466117.

[50] N.A. Mauro, M. Blodgett, M.L. Johnson, A.J. Vogt, K.F. Kelton, A structural signature of liquid fragility, Nat. Commun. 5 (2014) 1–7. https://doi.org/10.1038/ncomms5616.

[51] C.A. Angell, Formation of glasses from liquids and biopolymers, Science (80-.). 267 (1995) 1924–1935. https://doi.org/10.1002/hlca.19690520729.

[52] C.A. Angell, Relaxation in liquids, polymers and plastic crystals - strong/fragile patterns and problems, J. Non. Cryst. Solids. 131–133 (1991) 13–31. https://doi.org/10.1016/0022-3093(91)90266-9.

[53] R. Busch, A. Masuhr, W.L. Johnson, Themodynamics and kinetics of Zr-Ti-Cu-Ni-Be bulk metallic glass forming liquids, Mater. Sci. Eng. A. 304–306 (2001) 97–102. https://doi.org/10.1016/S0921-5093(00)01458-1.

[54] S. V. Nemilov, Structural aspect of possible interrelation between fragility (length) of glass forming melts and Poisson's ratio of glasses, J. Non. Cryst. Solids. 353 (2007) 4613–4632. https://doi.org/10.1016/j.jnoncrysol.2007.08.045.

[55] D.N. Perera, Compilation of the fragility parameters for several glass-forming metallic alloys, J. Phys. Condens. Matter. 11 (1999) 3807–3812. https://doi.org/10.1088/0953-8984/11/19/303.

[56] A. Bartsch, K. Rätzke, A. Meyer, F. Faupel, Dynamic arrest in multicomponent glass-forming alloys, Phys. Rev. Lett. 104 (2010) 1–4. https://doi.org/10.1103/PhysRevLett.104.195901.

[57] S. Wei, Z. Evenson, M. Stolpe, P. Lucas, C. Austen Angell, Breakdown of the Stokes-Einstein relation above the melting temperature in a liquid phase-change material, Sci. Adv. 4 (2018). https://doi.org/10.1126/sciadv.aat8632.

[58] R. Busch, W. Liu, W.L. Johnson, Thermodynamics and kinetics of the Mg65Cu25Y10bulk metallic glass forming liquid, J. Appl. Phys. 83 (1998) 4134–4141. https://doi.org/10.1063/1.367167.

[59] G. Adam, J.H. Gibbs, On the temperature dependence of cooperative relaxation properties in glass-forming liquids, J. Chem. Phys. 43 (1965) 139–146. https://doi.org/10.1063/1.1696442.

[60] H.L. Smith, C.W. Li, A. Hoff, G.R. Garrett, D.S. Kim, F.C. Yang, M.S. Lucas, T. Swan-Wood, J.Y.Y. Lin, M.B. Stone, D.L. Abernathy, M.D. Demetriou, B. Fultz, Separating the configurational and vibrational entropy contributions in metallic glasses, Nat. Phys. 13 (2017) 900–905. https://doi.org/10.1038/nphys4142.

[61] M. Goldstein, Viscous liquids and the glass transition. V. Sources of the excess specific heat of the liquid, J. Chem. Phys. 64 (1976) 4767–4774. https://doi.org/10.1063/1.432063.

[62] L.M. Martinez, C.A. Angell, A thermodynamic connection to the fragility of glass-forming liquids, Nature. 410 (2001) 663–667. https://doi.org/10.1038/35070517.

[63] A. van den Beukel, J. Sietsma, The glass transition as a free volume related kinetic phenomenon, Acta Metall. Mater. 38 (1990) 383–389. https://doi.org/10.1016/0956-7151(90)90142-4.

[64] Z. Evenson, R. Busch, Equilibrium viscosity, enthalpy recovery and free volume relaxation in a Zr44Ti11Ni10Cu10Be25 bulk metallic glass, Acta Mater. 59 (2011) 4404–4415. https://doi.org/10.1016/j.actamat.2011.03.064.

[65] A. Slipenyuk, J. Eckert, Correlation between enthalpy change and free volume reduction during structural relaxation of Zr55Cu30Al10Ni 5 metallic glass, Scr. Mater. 50 (2004) 39–44. https://doi.org/10.1016/j.scriptamat.2003.09.038.

[66] O. Haruyama, Y. Nakayama, R. Wada, H. Tokunaga, J. Okada, T. Ishikawa, Y. Yokoyama, Volume and enthalpy relaxation in Zr55Cu30Ni5Al10 bulk metallic glass, Acta Mater. 58 (2010) 1829–1836. https://doi.org/10.1016/j.actamat.2009.11.025.

[67] M.E. Launey, J.J. Kruzic, C. Li, R. Busch, Quantification of free volume differences in a Zr 44Ti 11Ni 10Cu 10Be 25bulk amorphous alloy, Appl. Phys. Lett. 91 (2007) 8–11. https://doi.org/10.1063/1.2766659.

[68] D. Turnbull, M.H. Cohen, Free-volume model of the amorphous phase: Glass transition,

J. Chem. Phys. 34 (1961) 120–125. https://doi.org/10.1063/1.1731549.

[69]   G. Ruitenberg, P. De Hey, F. Sommer, J. Sietsma, Pressure dependence of the free volume in amorphous Pd40Ni40P20 and its implications for the diffusion process, Mater. Sci. Eng. A. 226–228 (1997) 397–400. https://doi.org/10.1016/s0921-5093(96)10651-1.

[70]   W.L. Johnson, J. Lu, M.D. Demetriou, Deformation and flow in bulk metallic glasses and deeply undercooled glass forming liquids - A self consistent dynamic free volume model, Intermetallics. 10 (2002) 1039–1046. https://doi.org/10.1016/S0966-9795(02)00160-7.

[71]   C.A. Schuh, T.C. Hufnagel, U. Ramamurty, Mechanical behavior of amorphous alloys, Acta Mater. 55 (2007) 4067–4109. https://doi.org/10.1016/j.actamat.2007.01.052.

[72]   G. Williams, D.C. Watts, Non-symmetrical dielectric relaxation behaviour arising from a simple empirical decay function, Trans. Faraday Soc. 66 (1970) 80. https://doi.org/10.1039/tf9706600080.

[73]   K. Trachenko, A. Zaccone, Slow stretched-exponential and fast compressed-exponential relaxation from local event dynamics, J. Phys. Condens. Matter. 33 (2021) 315101. https://doi.org/10.1088/1361-648X/ac04cd.

[74]   Z. Evenson, B. Ruta, S. Hechler, M. Stolpe, E. Pineda, I. Gallino, R. Busch, X-ray photon correlation spectroscopy reveals intermittent aging dynamics in a metallic glass, Phys. Rev. Lett. 115 (2015) 1–5. https://doi.org/10.1103/PhysRevLett.115.175701.

[75]   Y. Fan, T. Iwashita, T. Egami, How thermally activated deformation starts in metallic glass, Nat. Commun. 5 (2014) 1–7. https://doi.org/10.1038/ncomms6083.

[76]   D. Soriano, H. Zhou, S. Hilke, E. Pineda, B. Ruta, G. Wilde, Relaxation dynamics of Pd-Ni-P metallic glass: Decoupling of anelastic and viscous processes, J. Phys. Condens. Matter. 33 (2021). https://doi.org/10.1088/1361-648X/abef27.

[77]   V.M. Giordano, B. Ruta, Unveiling the structural arrangements responsible for the atomic dynamics in metallic glasses during physical aging, Nat. Commun. 7 (2016). https://doi.org/10.1038/ncomms10344.

[78] M. Stolpe, Synchrotron x-ray diffraction studies of bulk metallic glass forming liquids and glasses, Diss. Saarl. Univ. (2019). https://doi.org/10.22028/D291-32093.

[79] Y.Q. Cheng, E. Ma, Atomic-level structure and structure-property relationship in metallic glasses, Prog. Mater. Sci. 56 (2011) 379–473. https://doi.org/10.1016/j.pmatsci.2010.12.002.

[80] J.L. Finney, Bernal's road to random packing and the structure of liquids, Philos. Mag. 93 (2013) 3940–3969. https://doi.org/10.1080/14786435.2013.770179.

[81] J.D. Bernal, A geometrical approach to the structure Of liquids, Nature. 183 (1959) 141–147. https://doi.org/10.1038/183141a0.

[82] J.D. Bernal, Geometry of the Structure of Monatomic Liquids, Nature. 185 (1960) 68–70. https://doi.org/10.1038/185068a0.

[83] J.D. Bernal, The Bakerian Lecture, 1962 The structure of liquids, Proc. R. Soc. London. Ser. A. Math. Phys. Sci. 280 (1997) 299–322. https://doi.org/10.1098/rspa.1964.0147.

[84] P.H. Gaskell, A new structural model for transition metal–metalloid glasses, Nature. 276 (1978) 484–485. https://doi.org/10.1038/276484a0.

[85] P.H. Gaskell, A new structural model for amorphous transition metal silicides, borides, phosphides and carbides, J. Non. Cryst. Solids. 32 (1979) 207–224. https://doi.org/https://doi.org/10.1016/0022-3093(79)90073-5.

[86] D.B. Miracle, The efficient cluster packing model - An atomic structural model for metallic glasses, Acta Mater. 54 (2006) 4317–4336. https://doi.org/10.1016/j.actamat.2006.06.002.

[87] D.B. Miracle, A physical model for metallic glass structures: An introduction and update, JOM. 64 (2012) 846–855. https://doi.org/10.1007/s11837-012-0359-4.

[88] J. Ding, E. Ma, M. Asta, R.O. Ritchie, Second-nearest-neighbor correlations from connection of atomic packing motifs in metallic glasses and liquids, Sci. Rep. 5 (2015) 1–9. https://doi.org/10.1038/srep17429.

[89] S.P. Pan, J.Y. Qin, W.M. Wang, T.K. Gu, Origin of splitting of the second peak in the

pair-distribution function for metallic glasses, Phys. Rev. B - Condens. Matter Mater. Phys. 84 (2011) 092201. https://doi.org/10.1103/PhysRevB.84.092201.

[90]   C.H. Bennett, Serially deposited amorphous aggregates of hard spheres, J. Appl. Phys. 43 (1972) 2727–2734. https://doi.org/10.1063/1.1661585.

[91]   N. Neuber, Alloy Development and Thermophysical Characterization of Amorphous 18kt White Gold Bulk Metallic Glasses with Improved Tarnishing Resistance, Master-Thesis. (2017) 64.

[92]   A.R. Yavari, A. Le Moulec, A. Inoue, N. Nishiyama, N. Lupu, E. Matsubara, W.J. Botta, G. Vaughan, M. Di Michiel, Å. Kvick, Excess free volume in metallic glasses measured by X-ray diffraction, Acta Mater. 53 (2005) 1611–1619. https://doi.org/10.1016/j.actamat.2004.12.011.

[93]   C.W. Ryu, W. Dmowski, K.F. Kelton, G.W. Lee, E.S. Park, J.R. Morris, T. Egami, Curie-Weiss behavior of liquid structure and ideal glass state, Sci. Rep. 9 (2019) 18579. https://doi.org/10.1038/s41598-019-54758-y.

[94]   A.P. Sokolov, A. Kisliuk, M. Soltwisch, D. Quitmann, Medium-range order in glasses: Comparison of Raman and diffraction measurements, Phys. Rev. Lett. 69 (1992) 1540–1543. https://doi.org/10.1103/PhysRevLett.69.1540.

[95]   T. Egami, S.J.L. Billinge, Underneath the Bragg Peaks: structural analysis of complex materials, 2nd ed., 2003. https://doi.org/10.1016/B978-0-08-097133-9.00013-7.

[96]   S. Wei, M. Stolpe, O. Gross, Z. Evenson, I. Gallino, W. Hembree, J. Bednarcik, J.J. Kruzic, R. Busch, Linking structure to fragility in bulk metallic glass-forming liquids, Appl. Phys. Lett. 106 (2015) 10–15. https://doi.org/10.1063/1.4919590.

[97]   H.R. Jiang, J. Tseng, N. Neuber, J. Barrirero, B. Adam, M. Frey, A.C. Dippel, S. Banerjee, I. Gallino, A.H. Feng, G. Wang, F. Mücklich, R. Busch, J. Shen, On the devitrification of Cu–Zr–Al alloys: Solving the apparent contradiction between polymorphic liquid-liquid transition and phase separation, Acta Mater. 226 (2022) 117668. https://doi.org/10.1016/j.actamat.2022.117668.

[98]   B. Nowak, D. Holland-Moritz, F. Yang, T. Voigtmann, T. Kordel, T.C. Hansen, A.

Meyer, Partial structure factors reveal atomic dynamics in metallic alloy melts, Phys. Rev. Mater. 1 (2017) 3–7. https://doi.org/10.1103/PhysRevMaterials.1.025603.

[99] T. Nakamura, E. Matsubara, M. Sakurai, M. Kasai, A. Inoue, Y. Waseda, Structural study in amorphous Zr-noble metal (Pd, Pt and Au) alloys, J. Non. Cryst. Solids. 312–314 (2002) 517–521. https://doi.org/10.1016/S0022-3093(02)01738-6.

[100] S. Hosokawa, J.F. Bérar, N. Boudet, T. Ichitsubo, E. Matsubara, N. Nishiyama, Partial structure of Pd42:5Ni7:5Cu30P 20 bulk metallic glass, J. Phys. Conf. Ser. 144 (2009) 3–8. https://doi.org/10.1088/1742-6596/144/1/012055.

[101] S. Hosokawa, W.C. Pilgrim, J.F. Bérar, S. Kohara, Anomalous X-ray scattering studies on semiconducting and metallic glasses, Eur. Phys. J. Spec. Top. 208 (2012) 291–304. https://doi.org/10.1140/epjst/e2012-01625-0.

[102] J. Ding, Y.-Q.Q. Cheng, H. Sheng, E. Ma, Short-range structural signature of excess specific heat and fragility of metallic-glass-forming supercooled liquids, Phys. Rev. B. 85 (2012) 060201. https://doi.org/10.1103/PhysRevB.85.060201.

[103] L. Berthier, G. Biroli, J.P. Bouchaud, L. Cipelletti, W. van Saarloos, Dynamical Heterogeneities in Glasses, Colloids, and Granular Media, 2011. https://doi.org/10.1093/acprof:oso/9780199691470.001.0001.

[104] J. Wang, R. Li, N. Hua, T. Zhang, Co-based ternary bulk metallic glasses with ultrahigh strength and plasticity, J. Mater. Res. 26 (2011) 2072–2079. https://doi.org/10.1557/jmr.2011.187.

[105] J. Schroers, The superplastic forming of bulk metallic glasses, JOM J. Miner. Met. Mater. (2005) 35–39. https://doi.org/doi.org/10.1007/s11837-005-0093-2.

[106] A.S. Argon, Plastic deformation in metallic glasses, Acta Metall. 27 (1979) 47–58. https://doi.org/10.1016/0001-6160(79)90055-5.

[107] J. Bokeloh, S. V. Divinski, G. Reglitz, G. Wilde, Tracer measurements of atomic diffusion inside shear bands of a bulk metallic glass, Phys. Rev. Lett. 107 (2011) 1–5. https://doi.org/10.1103/PhysRevLett.107.235503.

[108] B. Yang, M.L. Morrison, P.K. Liaw, R.A. Buchanan, G. Wang, C.T. Liu, M. Denda,

Dynamic evolution of nanoscale shear bands in a bulk-metallic glass, Appl. Phys. Lett. 86 (2005) 1–3. https://doi.org/10.1063/1.1891302.

[109] J. Schroers, Wi.L. Johnson, Ductile bulk metallic glass, Phys. Rev. Lett. 93 (2004) 255506. https://doi.org/10.1103/PhysRevLett.93.255506.

[110] F. Spaepen, Metallic glasses: Must shear bands be hot?, Nat. Mater. 5 (2006) 7–8. https://doi.org/10.1038/nmat1552.

[111] F. Guo, H.-J. Wang, S.J. Poon, G.J. Shiflet, Ductile titanium-based glassy alloy ingots, Appl. Phys. Lett. 86 (2005) 091907. https://doi.org/10.1063/1.1872214.

[112] A.L. Greer, Y.Q. Cheng, E. Ma, Shear bands in metallic glasses, Mater. Sci. Eng. R Reports. 74 (2013) 71–132. https://doi.org/10.1016/j.mser.2013.04.001.

[113] D. Klaumünzer, A. Lazarev, R. Maaß, F.H. Dalla Torre, A. Vinogradov, J.F. Löffler, Probing shear-band initiation in metallic glasses, Phys. Rev. Lett. 107 (2011) 1–5. https://doi.org/10.1103/PhysRevLett.107.185502.

[114] D. Klaumünzer, R. Maaß, J.F. Löffler, Stick-slip dynamics and recent insights into shear banding in metallic glasses, J. Mater. Res. 26 (2011) 1453–1463. https://doi.org/10.1557/jmr.2011.178.

[115] Y.H. Liu, G. Wang, R.J. Wang, D.Q. Zhao, M.X. Pan, W.H. Wang, Super plastic bulk metallic glasses at room temperature, Science (80-.). 315 (2007) 1385–1388. https://doi.org/10.1126/science.1136726.

[116] L.F. Liu, L.H. Dai, Y.L. Bai, B.C. Wei, J. Eckert, Behavior of multiple shear bands in Zr-based bulk metallic glass, Mater. Chem. Phys. 93 (2005) 174–177. https://doi.org/10.1016/j.matchemphys.2005.03.011.

[117] G. Kumar, P. Neibecker, Y.H. Liu, J. Schroers, Critical fictive temperature for plasticity in metallic glasses, Nat. Commun. 4 (2013) 1536. https://doi.org/10.1038/ncomms2546.

[118] J.J. Lewandowski, W.H. Wang, A.L. Greer, Intrinsic plasticity or brittleness of metallic glasses, Philos. Mag. Lett. 85 (2005) 77–87. https://doi.org/10.1080/09500830500080474.

[119] W.L. Johnson, K. Samwer, A universal criterion for plastic yielding of metallic glasses with a (T/Tg)2/3 temperature dependence, Phys. Rev. Lett. 95 (2005) 2–5. https://doi.org/10.1103/PhysRevLett.95.195501.

[120] M.D. Demetriou, J.S. Harmon, M. Tao, G. Duan, K. Samwer, W.L. Johnson, Cooperative shear model for the rheology of glass-forming metallic liquids, Phys. Rev. Lett. 97 (2006) 41–44. https://doi.org/10.1103/PhysRevLett.97.065502.

[121] P.G. Debenedetti, F.H. Stillinger, Supercooled liquids and the glass transition, Nature. 410 (2001) 259–267. https://doi.org/10.1038/35065704.

[122] J. Jellinek, Energy Landscapes: With Applications to Clusters, Biomolecules and Glasses , Cambridge University Press, 2005. https://doi.org/10.1063/1.1996481.

[123] D. Pan, A. Inoue, T. Sakurai, M.W. Chen, Experimental characterization of shear transformation zones for plastic flow of bulk metallic glasses, Proc. Natl. Acad. Sci. U. S. A. 105 (2008) 14769–14772. https://doi.org/10.1073/pnas.0806051105.

[124] J. Shen, Y.J. Huang, J.F. Sun, Plasticity of a TiCu-based bulk metallic glass: Effect of cooling rate, J. Mater. Res. 22 (2007) 3067–3074. https://doi.org/10.1557/jmr.2007.0410.

[125] B. Ruta, E. Pineda, Z. Evenson, Relaxation processes and physical aging in metallic glasses, J. Phys. Condens. Matter. 29 (2017). https://doi.org/10.1088/1361-648X/aa9964.

[126] G. Kumar, D. Rector, R.D. Conner, J. Schroers, Embrittlement of Zr-based bulk metallic glasses, Acta Mater. 57 (2009) 3572–3583. https://doi.org/10.1016/j.actamat.2009.04.016.

[127] M.E. Launey, R. Busch, J.J. Kruzic, Effects of free volume changes and residual stresses on the fatigue and fracture behavior of a Zr-Ti-Ni-Cu-Be bulk metallic glass, Acta Mater. 56 (2008) 500–510. https://doi.org/10.1016/j.actamat.2007.10.007.

[128] M.E. Launey, R. Busch, J.J. Kruzic, Influence of structural relaxation on the fatigue behavior of a Zr 41.25Ti13.75Ni10Cu12.5Be 22.5 bulk amorphous alloy, Scr. Mater. 54 (2006) 483–487. https://doi.org/10.1016/j.scriptamat.2005.09.048.

[129] R. Raghavan, P. Murali, U. Ramamurty, On factors influencing the ductile-to-brittle transition in a bulk metallic glass, Acta Mater. 57 (2009) 3332–3340. https://doi.org/10.1016/j.actamat.2009.03.047.

[130] P. Murali, U. Ramamurty, Embrittlement of a bulk metallic glass due to sub-Tg annealing, Acta Mater. 53 (2005) 1467–1478. https://doi.org/10.1016/j.actamat.2004.11.040.

[131] M. Song, Y.Y. Sun, Y.H. He, S.F. Guo, Structure related hardness and elastic modulus of bulk metallic glass, J. Appl. Phys. 111 (2012). https://doi.org/10.1063/1.3692568.

[132] J. Tan, Y. Zhang, B.A. Sun, M. Stoica, C.J. Li, K.K. Song, U. Kühn, F.S. Pan, J. Eckert, Correlation between internal states and plasticity in bulk metallic glass, Appl. Phys. Lett. 98 (2011) 2009–2012. https://doi.org/10.1063/1.3580774.

[133] L.Y. Chen, A.D. Setyawan, H. Kato, A. Inoue, G.Q. Zhang, J. Saida, X.D. Wang, Q.P. Cao, J.Z. Jiang, Free-volume-induced enhancement of plasticity in a monolithic bulk metallic glass at room temperature, Scr. Mater. 59 (2008) 75–78. https://doi.org/10.1016/j.scriptamat.2008.02.025.

[134] M. Stolpe, J.J. Kruzic, R. Busch, Evolution of shear bands, free volume and hardness during cold rolling of a Zr-based bulk metallic glass, Acta Mater. 64 (2014) 231–240. https://doi.org/10.1016/j.actamat.2013.10.035.

[135] M.H. Lee, K.S. Lee, J. Das, J. Thomas, U. Kühn, J. Eckert, Improved plasticity of bulk metallic glasses upon cold rolling, Scr. Mater. 62 (2010) 678–681. https://doi.org/10.1016/j.scriptamat.2010.01.024.

[136] K.M. Flores, E. Sherer, A. Bharathula, H. Chen, Y.C. Jean, Sub-nanometer open volume regions in a bulk metallic glass investigated by positron annihilation, Acta Mater. 55 (2007) 3403–3411. https://doi.org/10.1016/j.actamat.2007.01.040.

[137] C.T. Moynihan, A.J. Easteal, M.A. DeBolt, J. Tucker, Dependence of the Fictive Temperature of Glass on Cooling Rate, J. Am. Ceram. Soc. 59 (1976) 12–16. https://doi.org/10.1111/j.1151-2916.1976.tb09376.x.

[138] E. Ma, Tuning order in disorder, Nat. Mater. 14 (2015) 547–552.

https://doi.org/10.1038/nmat4300.

[139] H.W. Sheng, W.K. Luo, F.M. Alamgir, J.M. Bai, E. Ma, Atomic packing and short-to-medium-range order in metallic glasses, Nature. 439 (2006) 419–425. https://doi.org/10.1038/nature04421.

[140] L. Sun, Q. Wu, Y. Xu, W. Wang, Study on solidification behaviour of Pd40Ni40P20 alloy by fluxing method, Phys. B Condens. Matter. 240 (1997) 205–210. https://doi.org/10.1016/s0921-4526(97)00425-0.

[141] R.W. Cahn, J.A. Jackson, Processing of metals and alloys, VCH Heinheim, 1991.

[142] C.A. Angell, Liquid fragility and the glass transition in water and aqueous solutions, Chem. Rev. 102 (2002) 2627–2650. https://doi.org/10.1021/cr000689q.

[143] M. Reading, D. Elliott, V.L. Hill, A new approach to the calorimetric investigation of physical and chemical transitions, J. Therm. Anal. 40 (1993) 949–955. https://doi.org/10.1007/BF02546854.

[144] P.S. Gill, S.R. Sauerbrunn, M. Reading, Modulated differential scanning calorimetry, J. Therm. Anal. 40 (1993) 931–939. https://doi.org/10.1007/BF02546852.

[145] Z. Jiang, C.T. Imrie, J.M. Hutchinson, An introduction to temperature modulated differential scanning calorimetry (TMDSC): A relatively non-mathematical approach, Thermochim. Acta. 387 (2002) 75–93. https://doi.org/10.1016/S0040-6031(01)00829-2.

[146] M. Frey, N. Neuber, O. Gross, B. Zimmer, W. Possart, R. Busch, Determining the fragility of bulk metallic glass forming liquids via modulated DSC, J. Phys. Condens. Matter. 32 (2020) 324004. https://doi.org/10.1088/1361-648X/ab8526.

[147] W.H. Bragg, The reflection of X-rays by crystals [3], Nature. 91 (1913) 477. https://doi.org/10.1038/091477b0.

[148] O. Gross, N. Neuber, A. Kuball, B. Bochtler, S. Hechler, M. Frey, R. Busch, Supplementary Information to Signatures of structural differences in Pt–P- and Pd–P-based bulk glass-forming liquids, Commun. Phys. 2 (2019). https://doi.org/https://doi.org/10.1038/s42005- 019-0180-2.

[149] Sample Environments P02 DESY, (n.d.). https://photon-science.desy.de/e58/e176720/e177229/e293004/e296665/index_eng.html?preview=preview (accessed March 11, 2023).

[150] X. Qiu, J.W. Thompson, S.J.L. Billinge, PDFgetX2: A GUI-driven program to obtain the pair distribution function from X-ray powder diffraction data, J. Appl. Crystallogr. 37 (2004) 678. https://doi.org/10.1107/S0021889804011744.

[151] S. Wei, M. Stolpe, O. Gross, W. Hembree, S. Hechler, J. Bednarcik, R. Busch, P. Lucas, Structural evolution on medium-range-order during the fragile-strong transition in Ge15Te85, Acta Mater. 129 (2017) 259–267. https://doi.org/10.1016/j.actamat.2017.02.055.

[152] O. Gross, N. Neuber, A. Kuball, B. Bochtler, S. Hechler, M. Frey, R. Busch, Signatures of structural differences in Pt–P- and Pd–P-based bulk glass-forming liquids, Commun. Phys. 2 (2019). https://doi.org/10.1038/s42005-019-0180-2.

[153] M. Sutton, S.G.J. Mochrie, T. Greytak, S.E. Nagler, L.E. Berman, G.A. Held, G.B. Stephenson, Observation of speckle by diffraction with coherent X-rays, Nature. 352 (1991) 608–610. https://doi.org/10.1038/352608a0.

[154] S. Hechler, On the thermophysical and structural properties of the Au49Cu26.9Si16.3Ag5.5Pd2.3 bulk metallic glass-forming alloy and their connection to the liquid-liquid transition in the deeply supercooled liquid, PHD Thesis. (2018). https://doi.org/doi:10.22028/D291-27565.

[155] P.G. De Gennes, Liquid dynamics and inelastic scattering of neutrons, Physica. 25 (1959) 825–839. https://doi.org/10.1016/0031-8914(59)90006-0.

[156] M. Fuchs, I. Hofacker, A. Latz, Primary relaxation in a hard-sphere system, Phys. Rev. A. 45 (1992) 898–912. https://doi.org/10.1103/PhysRevA.45.898.

[157] F. Sciortino, L. Fabbian, S.H. Chen, P. Tartaglia, Supercooled water and the kinetic glass transition. II. Collective dynamics, Phys. Rev. E - Stat. Physics, Plasmas, Fluids, Relat. Interdiscip. Top. 56 (1997) 5397–5404. https://doi.org/10.1103/PhysRevE.56.5397.

[158] F. Weysser, A.M. Puertas, M. Fuchs, T. Voigtmann, Structural relaxation of polydisperse

hard spheres: Comparison of the mode-coupling theory to a Langevin dynamics simulation, Phys. Rev. E - Stat. Nonlinear, Soft Matter Phys. 82 (2010) 1–21. https://doi.org/10.1103/PhysRevE.82.011504.

[159] J. Colmenero, A. Arbe, Recent progress on polymer dynamics by neutron scattering: From simple polymers to complex materials, J. Polym. Sci. Part B Polym. Phys. 51 (2013) 87–113. https://doi.org/10.1002/polb.23178.

[160] B. Ruta, G. Baldi, Y. Chushkin, B. Rufflé, L. Cristofolini, A. Fontana, M. Zanatta, F. Nazzani, Revealing the fast atomic motion of network glasses, Nat. Commun. 5 (2014). https://doi.org/10.1038/ncomms4939.

[161] V.N. Novikov, K.S. Schweizer, A.P. Sokolov, Coherent neutron scattering and collective dynamics on mesoscale, J. Chem. Phys. 138 (2013). https://doi.org/10.1063/1.4802771.

[162] A. Tölle, Neutron scattering studies of the model glass former ortho-terphenyl, Reports Prog. Phys. 64 (2001) 1473–1532. https://doi.org/10.1088/0034-4885/64/11/203.

[163] F. Yang, T. Kordel, D. Holland-Moritz, T. Unruh, A. Meyer, Structural relaxation as seen by quasielastic neutron scattering on viscous Zr-Ti-Cu-Ni-Be droplets, J. Phys. Condens. Matter. 23 (2011). https://doi.org/10.1088/0953-8984/23/25/254207.

[164] S.M. Bhattacharyya, B. Bagchi, P.G. Wolynes, Subquadratic wavenumber dependence of the structural relaxation of supercooled liquid in the crossover regime, J. Chem. Phys. 132 (2010). https://doi.org/10.1063/1.3330911.

[165] R. Bandyopadhyay, D. Liang, H. Yardimci, D.A. Sessoms, M.A. Borthwick, S.G.J. Mochrie, J.L. Harden, R.L. Leheny, Evolution of particle-scale dynamics in an aging clay suspension, Phys. Rev. Lett. 93 (2004) 2–5. https://doi.org/10.1103/PhysRevLett.93.228302.

[166] L. Cipelletti, L. Ramos, S. Manley, E. Pitard, D.A. Weitz, E.E. Pashkovski, M. Johansson, Universal non-diffusive slow dynamics in aging soft matter, Faraday Discuss. 123 (2003) 237–251. https://doi.org/10.1039/b204495a.

[167] P.H. Handle, L. Rovigatti, F. Sciortino, Q-Independent Slow Dynamics in Atomic and Molecular Systems, Phys. Rev. Lett. 122 (2019) 175501.

https://doi.org/10.1103/PhysRevLett.122.175501.

[168] G. Nava, M. Rossi, S. Biffi, F. Sciortino, T. Bellini, Fluctuating Elasticity Mode in Transient Molecular Networks, Phys. Rev. Lett. 119 (2017) 1–5. https://doi.org/10.1103/PhysRevLett.119.078002.

[169] E.D. Zanotto, a. R. Migliore, Viscous Flow of Glass-Forming Liquids: Experimental Techniques for the High Viscosity Range., in: J.M. Rincon, M. Romero (Eds.), Charact. Tech. Glas. Ceram., Springer Berlin Heidelberg, Berlin, Heidelberg, 1999: pp. 138–149. https://doi.org/10.1007/978-3-662-03871-0_7.

[170] F.T. Trouton, On the Coefficient of Viscous Traction and Its Relation to that of Viscosity, Proc. R. Soc. A Math. Phys. Eng. Sci. 77 (1906) 426–440. https://doi.org/10.1098/rspa.1906.0038.

[171] H.E. Hagy, Experimental Evaluation of Beam???Bending Method of Determining Glass Viscosities in the Range 108 to 1015 Poises, J. Am. Ceram. Soc. 46 (1963) 93–97. https://doi.org/10.1111/j.1151-2916.1963.tb11684.x.

[172] N. Neuber, O. Gross, M. Frey, B. Bochtler, A. Kuball, S. Hechler, F. Yang, E. Pineda, F. Westermeier, M. Sprung, F. Schäfer, I. Gallino, R. Busch, B. Ruta, Disentangling structural and kinetic components of the α-relaxation in supercooled metallic liquids, Commun. Phys. 5 (2022) 316. https://doi.org/10.1038/s42005-022-01099-4.

[173] C.A. Schuh, Nanoindentation studies of materials, Mater. Today. 9 (2006) 32–40. https://doi.org/10.1016/S1369-7021(06)71495-X.

[174] W.C. Oliver, G.M. Pharr, An improved technique for determining hardness and elastic modulus using load and displacement sensing indentation experiments, J. Mater. Res. 7 (1992) 1564–1583. https://doi.org/DOI: 10.1557/JMR.1992.1564.

[175] A.C. Lund, A.M. Hodge, C.A. Schuh, Incipient plasticity during nanoindentation at elevated temperatures, Appl. Phys. Lett. 85 (2004) 1362–1364. https://doi.org/10.1063/1.1784891.

[176] C.A. Schuh, T.G. Nieh, A nanoindentation study of serrated flow in bulk metallic glasses, Acta Mater. 51 (2003) 87–99. https://doi.org/10.1016/S1359-6454(02)00303-8.

[177] C.A. Schuh, A.S. Argon, T.G. Nieh, J. Wadsworth, The transition from localized to homogeneous plasticity during nanoindentation of an amorphous metal, Philos. Mag. 83 (2003) 2585–2597. https://doi.org/10.1080/1478643031000118012.

[178] N. Amini, F. Yang, E. Pineda, B. Ruta, M. Sprung, A. Meyer, Intrinsic relaxation in a supercooled ZrTiNiCuBe glass forming liquid, Phys. Rev. Mater. 5 (2021) 1–8. https://doi.org/10.1103/physrevmaterials.5.055601.

[179] T. Scopigno, G. Ruocco, F. Sette, G. Monaco, Is the Fragility of a Liquid Embedded in the Properties of Its Glass?, Science (80-.). 302 (2003) 849–852. https://doi.org/10.1126/science.1089446.

[180] V.N. Novikov, A.P. Sokolov, Poisson's ratio and the fragility of glass-forming liquids, Nature. 431 (2004) 961–963. https://doi.org/10.1038/nature02947.

[181] A. Bhattacharyya, G. Singh, K. Eswar Prasad, R. Narasimhan, U. Ramamurty, On the strain rate sensitivity of plastic flow in metallic glasses, Mater. Sci. Eng. A. 625 (2015) 245–251. https://doi.org/10.1016/j.msea.2014.12.004.

[182] S.T. Liu, Z. Wang, H.L. Peng, H.B. Yu, W.H. Wang, The activation energy and volume of flow units of metallic glasses, Scr. Mater. 67 (2012) 9–12. https://doi.org/10.1016/j.scriptamat.2012.03.009.

[183] S.Y. Kim, H.S. Oh, E.S. Park, A hidden variable in shear transformation zone volume versus Poisson's ratio relation in metallic glasses, APL Mater. 5 (2017). https://doi.org/10.1063/1.4999653.

[184] J.C. Ye, J. Lu, Y. Yang, P.K. Liaw, Study of the intrinsic ductile to brittle transition mechanism of metallic glasses, Acta Mater. 57 (2009) 6037–6046. https://doi.org/10.1016/j.actamat.2009.08.029.

[185] R.T. Qu, Z.Q. Liu, R.F. Wang, Z.F. Zhang, Yield strength and yield strain of metallic glasses and their correlations with glass transition temperature, J. Alloys Compd. 637 (2015) 44–54. https://doi.org/10.1016/j.jallcom.2015.03.005.

[186] J. Orava, A.L. Greer, B. Gholipour, D.W. Hewak, C.E. Smith, Characterization of supercooled liquid Ge2Sb2Te 5 and its crystallization by ultrafast-heating calorimetry,

Nat. Mater. 11 (2012) 279–283. https://doi.org/10.1038/nmat3275.

[187] R. Busch, E. Bakke, W.L. Johnson, Viscosity of the supercooled liquid and relaxation at the glass transition of the Zr46.75Ti8.25Cu7.5Ni10Be27.5bulk metallic glass forming alloy, Acta Mater. 46 (1998) 4725–4732. https://doi.org/10.1016/S1359-6454(98)00122-0.

[188] J.E.K. Schawe, Vitrification in a wide cooling rate range: The relations between cooling rate, relaxation time, transition width, and fragility, J. Chem. Phys. 141 (2014). https://doi.org/10.1063/1.4900961.

[189] I.G. X. Monnier, D. Cangialosi, B. Ruta, R. Busch, Vitrification kinetics versus atomic mobility in a metallic glass forming liquid, Sci. Adv. (2020). https://doi.org/DOI: 10.1126/sciadv.aay1454.

[190] J.W.P. Schmelzer, Kinetic criteria of glass formation and the pressure dependence of the glass transition temperature, J. Chem. Phys. 136 (2012) 1–11. https://doi.org/10.1063/1.3685510.

[191] Z. Evenson, I. Gallino, R. Busch, The effect of cooling rates on the apparent fragility of Zr-based bulk metallic glasses, J. Appl. Phys. 107 (2010) 1–7. https://doi.org/10.1063/1.3452381.

[192] R. Böhmer, K.L. Ngai, C.A. Angell, D.J. Plazek, R. Böhmer, K.L. Ngai, C.A. Angell, D.J. Plazek, Nonexponential relaxations in strong and fragile glass formers, J. Chem. Phys. 99 (1993) 4201–4209. https://doi.org/10.1063/1.466117.

[193] X. Monnier, D. Cangialosi, B. Ruta, R. Busch, I. Gallino, Vitrification decoupling from α-relaxation in a metallic glass, Sci. Adv. 6 (2020). https://doi.org/10.1126/sciadv.aay1454.

[194] J. Jiang, Z. Lu, J. Shen, T. Wada, H. Kato, M. Chen, Decoupling between calorimetric and dynamical glass transitions in high-entropy metallic glasses, Nat. Commun. 12 (2021) 1–10. https://doi.org/10.1038/s41467-021-24093-w.

[195] W.H. Wang, Dynamic relaxations and relaxation-property relationships in metallic glasses, Prog. Mater. Sci. 106 (2019) 100561.

https://doi.org/https://doi.org/10.1016/j.pmatsci.2019.03.006.

[196] D. Ma, A.D. Stoica, X.L. Wang, Power-law scaling and fractal nature of medium-range order in metallic glasses, Nat. Mater. 8 (2009) 30–34. https://doi.org/10.1038/nmat2340.

[197] I. Gallino, On the fragility of bulk metallic glass forming liquids, Entropy. 19 (2017). https://doi.org/10.3390/e19090483.

[198] I. Gallino, J. Schroers, R. Busch, Kinetic and thermodynamic studies of the fragility of bulk metallic glass forming liquids, J. Appl. Phys. 108 (2010) 063501. https://doi.org/10.1063/1.3480805.

[199] G.J. Fan, J.F. Löffler, R.K. Wunderlich, H.J. Fecht, Thermodynamics, enthalpy relaxation and fragility of the bulk metallic glass-forming liquid Pd43Ni10Cu27P20, Acta Mater. 52 (2004) 667–674. https://doi.org/10.1016/j.actamat.2003.10.003.

[200] G.J. Fan, H.J. Fecht, E.J. Lavernia, Viscous flow of the Pd43Ni10Cu27P 20 bulk metallic glass-forming liquid, Appl. Phys. Lett. 84 (2004) 487–489. https://doi.org/10.1063/1.1644052.

[201] G. Wilde, I.R. Lu, R. Willnecker, Fragility, thermodynamic properties, and thermal stability of Pd-rich glass forming liquids, Mater. Sci. Eng. A. 375–377 (2004) 417–421. https://doi.org/10.1016/j.msea.2003.10.218.

[202] T.E. Faber, R.S. Allgaier, Introduction to the Theory of Liquid Metals , Cambridge University Press, 1973. https://doi.org/10.1063/1.3128232.

[203] F. Spaepen, A survey of energies in materials science, Philos. Mag. 85 (2005) 2979–2987. https://doi.org/10.1080/14786430500155080.

[204] O. Gross, N. Neuber, A. Kuball, B. Bochtler, S. Hechler, M. Frey, R. Busch, Peer Review File to Signatures of structural differences in Pt–P- and Pd–P-based bulk glass-forming liquids, Commun. Phys. 2 (2019) 83. https://doi.org/10.1038/s42005-019-0180-2.

[205] L.M. Wang, C.A. Angell, R. Richert, Fragility and thermodynamics in nonpolymeric glass-forming liquids, J. Chem. Phys. 125 (2006). https://doi.org/10.1063/1.2244551.

[206] J.D. Stevenson, P.G. Wolynes, Thermodynamic - Kinetic correlations in supercooled

liquids: A critical survey of experimental data and predictions of the random first-order transition theory of glasses, J. Phys. Chem. B. 109 (2005) 15093–15097. https://doi.org/10.1021/jp052279h.

[207] I.R. Lu, G. Wilde, G.P. Görler, R. Willnecker, Thermodynamic properties of Pd-based glass-forming alloys, J. Non. Cryst. Solids. 250-252 (I (1999) 577–581. https://doi.org/10.1016/S0022-3093(99)00135-0.

[208] C.W. Ryu, T. Egami, Origin of liquid fragility, Phys. Rev. E. 102 (2020) 1–8. https://doi.org/10.1103/PhysRevE.102.042615.

[209] D.L. Sidebottom, B. V. Rodenburg, J.R. Changstrom, Connecting structure and dynamics in glass forming materials by photon correlation spectroscopy, Phys. Rev. B - Condens. Matter Mater. Phys. 75 (2007) 1–4. https://doi.org/10.1103/PhysRevB.75.132201.

[210] Q.K. Jiang, C.L. Qin, K. Amiya, S. Nagata, A. Inoue, R.T. Zheng, G.A. Cheng, X.P. Nie, J.Z. Jiang, Enhancement of corrosion resistance in bulk metallic glass by ion implantation, Intermetallics. 16 (2008) 225–229. https://doi.org/10.1016/j.intermet.2007.09.009.

[211] Y.Q. Cheng, H.W. Sheng, E. Ma, Relationship between structure, dynamics, and mechanical properties in metallic glass-forming alloys, Phys. Rev. B - Condens. Matter Mater. Phys. 78 (2008) 1–7. https://doi.org/10.1103/PhysRevB.78.014207.

[212] G.S. Cargill III, Solid state physics, Acad. Press. Ed. by H. Ehrenreich, F. Seitz D. Turnbull. 30 (1975) 227.

[213] J. Wilden, F. Yang, D. Holland-Moritz, S. Szabó, W. Lohstroh, B. Bochtler, R. Busch, A. Meyer, Impact of Sulfur on the melt dynamics of glass forming Ti75Ni25-xSx, Appl. Phys. Lett. 117 (2020) 3–8. https://doi.org/10.1063/5.0012409.

[214] J. Kruzic, S. Naleway, Z. Evenson, S. Wei, O. Gross, I. Gallino, R. Busch, Beta Relaxation and Low Temperature Aging of a Gold Based Bulk Metallic Glass, TMS 2015 144th Annu. Meet. Exhib. (2015). http://bib-pubdb1.desy.de/record/209322.

[215] M. Gao, J.H. Perepezko, Separating β relaxation from α relaxation in fragile metallic

glasses based on ultrafast flash differential scanning calorimetry, Phys. Rev. Mater. 4 (2020) 25602. https://doi.org/10.1103/PhysRevMaterials.4.025602.

[216] J. Qiao, R. Casalini, J.M. Pelletier, H. Kato, Characteristics of the structural and johari-goldstein relaxations in pd-based metallic glass-forming liquids, J. Phys. Chem. B. 118 (2014) 3720–3730. https://doi.org/10.1021/jp4121782.

[217] H.B. Yu, K. Samwer, Y. Wu, W.H. Wang, Correlation between β relaxation and self-diffusion of the smallest constituting atoms in metallic glasses, Phys. Rev. Lett. 109 (2012) 1–5. https://doi.org/10.1103/PhysRevLett.109.095508.

[218] J. Bednarcik, S. Michalik, M. Sikorski, C. Curfs, X.D. Wang, J.Z. Jiang, H. Franz, Thermal expansion of a La-based bulk metallic glass: Insight from insitu high-energy x-ray diffraction, J. Phys. Condens. Matter. 23 (2011). https://doi.org/10.1088/0953-8984/23/25/254204.

[219] Z. Evenson, S.E. Aleway, S. Wei, O. Gross, J.J. Kruzic, I. Gallino, W. Possart, M. Stommel, R. Busch, β relaxation and low-temperature aging in a Au-based bulk metallic glass: From elastic properties to atomic-scale structure, Phys. Rev. B - Condens. Matter Mater. Phys. 89 (2014) 1–14. https://doi.org/10.1103/PhysRevB.89.174204.

[220] Y. Su, X. Wang, Q. Cao, D. Zhang, J.Z. Jiang, Different Thermal Responses of Local Structures in Pd43Cu27Ni10P20Alloy from Glass to Liquid, J. Phys. Chem. C. 124 (2020) 19817–19828. https://doi.org/10.1021/acs.jpcc.0c05171.

[221] S. Wei, Anomalous liquids on a new landscape: From water to phase-change materials, J. Non-Crystalline Solids X. 14 (2022) 100094. https://doi.org/10.1016/j.nocx.2022.100094.

[222] I. Gallino, P. Wadhwa, R. Busch, The effect of shear on the liquid-liquid transition and crystallization of the undercooled Zr41.2Ti13.8Cu12.5Ni10.0Be22.5(Vit1) bulk metallic glass forming alloy, J. Phys. Condens. Matter. 33 (2021). https://doi.org/10.1088/1361-648X/ac2272.

[223] J. Shen, Y.H. Sun, J. Orava, H.Y. Bai, W.H. Wang, Liquid-to-liquid transition around the glass-transition temperature in a glass-forming metallic liquid, Acta Mater. 225 (2022) 117588. https://doi.org/10.1016/j.actamat.2021.117588.

[224] M. Stolpe, I. Jonas, S. Wei, Z. Evenson, W. Hembree, F. Yang, A. Meyer, R. Busch, Structural changes during a liquid-liquid transition in the deeply undercooled Z r58.5 C u15.6 N i12.8 A l10.3 N b2.8 bulk metallic glass forming melt, Phys. Rev. B. 93 (2016) 1–7. https://doi.org/10.1103/PhysRevB.93.014201.

[225] Y.F. Lo, X.C. Wang, Z.D. Wu, W.Z. Zhou, H.W. Kui, Direct imaging of a first-order liquid-liquid phase transition in undercooled molten Pd[sbnd]Ni[sbnd]P alloys and its thermodynamic implications, J. Non. Cryst. Solids. 472 (2017) 75–85. https://doi.org/10.1016/j.jnoncrysol.2017.07.020.

[226] J. Pries, H. Weber, J. Benke-Jacob, I. Kaban, S. Wei, M. Wuttig, P. Lucas, Fragile-to-Strong Transition in Phase-Change Material Ge3Sb6Te5, Adv. Funct. Mater. 2202714 (2022). https://doi.org/10.1002/adfm.202202714.

[227] S. Wei, F. Yang, J. Bednarcik, I. Kaban, O. Shuleshova, A. Meyer, R. Busch, Liquid-liquid transition in a strong bulk metallic glass-forming liquid, Nat. Commun. 4 (2013). https://doi.org/10.1038/ncomms3083.

[228] S. Mukherjee, Z. Zhou, J. Schroers, W.L. Johnson, W.K. Rhim, Overheating threshold and its effect on time-temperature-transformation diagrams of zirconium based bulk metallic glasses, Appl. Phys. Lett. 84 (2004) 5010–5012. https://doi.org/10.1063/1.1763219.

[229] P.J. Brown, A.G. Fox, E.N. Maslen, M.A. O'Keefe, B.T.M. Willis, Intensity of diffracted intensities, Int. Tables Crystallogr. C (2006) 554–595. https://doi.org/10.1107/97809553602060000600.

[230] N. Neuber, M. Sadeghilaridjani, N. Ghodki, O. Gross, B. Adam, L. Ruschel, M. Frey, S. Muskeri, M. Blankenburg, I. Gallino, R. Busch, S. Mukherjee, Effect of composition and thermal history on deformation behavior and cluster connections in model bulk metallic glasses, Sci. Rep. 12 (2022) 17133. https://doi.org/10.1038/s41598-022-20938-6.

[231] V. Zöllmer, K. Rätzke, F. Faupel, A. Meyer, Diffusion in a Metallic Melt at the Critical Temperature of Mode Coupling Theory, Phys. Rev. Lett. 90 (2003) 4. https://doi.org/10.1103/PhysRevLett.90.195502.

[232] A. Bartsch, V. Zöllmer, K. Rätzke, A. Meyer, F. Faupel, Diffusion and viscous flow in

bulk glass forming alloys, J. Alloys Compd. 509 (2011) S2–S7. https://doi.org/10.1016/j.jallcom.2010.11.123.